UNIVERSITÀ DEGLI STUDI DI TRIESTE

Università Ca'Foscari Venezia

UNIVERSITÀ DEGLI STUDI DI TRIESTE
UNIVERSITÀ CA' FOSCARI VENEZIA

XXXVIII CICLO DEL DOTTORATO DI RICERCA IN

CHIMICA

Finanziato dall'Unione europea – NextGenerationEU e Bracco Imaging S.p.A.

Towards new metal-based radiopharmaceuticals for imaging and therapy

Settore scientifico-disciplinare: Chimica generale ed inorganica (CHIM/03)

DOTTORANDA
Ileana Merdžo

COORDINATORE
Prof. Enzo Alessio

SUPERVISORE
Prof. Enzo Alessio

CO-SUPERVISORI
Dr. Zsolt Baranyai

Dr. Federica Battistin

ANNO ACCADEMICO 2024/2025

Finanziato dall'Unione europea NextGenerationEU
Ministero dell'Università e della Ricerca
Italiadomani
UNIVERSITÀ DEGLI STUDI DI TRIESTE

Table of Contents

Abstract

This thesis is structured into four chapters, each addressing key challenges in the design, characterization, and application of metal chelators in nuclear medicine and radiopharmacy, with particular emphasis on thermodynamic stability, kinetic inertness, and structural dynamics. The research described in Chapters 1 and 2 was done at Bracco Imaging SpA (Basovizza, Trieste); the research concerning the topic treated in Chapter 3 was done during a 3-month stage at Seoul National University Hospital (College of Medicine), Seoul (South Korea), whereas that described in Chapter 4 was started during a 3-month stage at the University of Western Brittany in Brest (France), and continued at the University of Trieste.

Chapter 1 examines a new AAZTA-derived hexadentate spirobicyclic chelating agent, TRASUTA, designed to evaluate whether this type of conformational constraint enhanced the stability of metal−ligand complexes with biologically and diagnostically relevant metal ions such as Ga^{3+}, Cu^{2+}, Zn^{2+} and Ca^{2+}. Contrary to expectations, the studied TRASUTA complexes exhibited reduced thermodynamic stability and kinetic inertness compared to those formed with more flexible analogues, including AAZTA. In fact, detailed multinuclear variable-temperature NMR studies showed that, despite its spirobicyclic framework, TRASUTA complexes exhibited pronounced conformational dynamics. The observed isomerization processes are entropy-controlled and are likely to proceed through transient heptacoordinate intermediates involving coordination of a water molecule. These findings suggest that the presence of spirobicyclic structures alone does not necessarily result in enhanced physico-chemical properties of the complex, and highlight the need to balance rigidity and flexibility in ligand design. The work was published in *Inorganic Chemistry* (*Inorg. Chem.* **2024**, 63, 27, 12525 – 12537).

Chapter 2 presents a comprehensive equilibrium, kinetic, and structural study of Pb(II) complexes with chelators of clinical interest, including DOTA, DOTAM, DOTP, DTPA, and EDTA. Using potentiometric, spectroscopic, electrophoretic, and crystallographic techniques, substantial differences in metal-binding strength, selectivity, and kinetic behavior were elucidated. DOTA emerged as the most selective ligand for Pb^{2+} under physiological conditions, while the DOTP complex displayed markedly reduced kinetic inertness due to proton-assisted dissociation pathways. Structural studies revealed similar coordination geometries among all DOTA-type complexes, *i.e.* twisted square antiprismatic (TSAP), but emphasized the role of ligand rigidity, hydration, and conformational motions in governing kinetic stability. Collectively, these results identify $[Pb(DOTA)]^{2-}$ as the most promising candidate for the development of $^{212}Pb/^{212}Bi$-based radiopharmaceuticals for Targeted Alpha Therapy (TAT). A manuscript concerning this work is under preparation.

Chapter 3 shifts focus to diagnostic imaging and describes the development of a modular albumin-based platform labelled with radiometals for positron emission tomography (PET). By exploiting the abundance of lysine residues on albumin, the protein was functionalized via click-chemistry with the linker dibenzocyclooctyne-*N*-hydroxysuccinimide (DBCO), the chelator NOTA, and the prostate cancer-targeting peptide glutamate-ureido-lysine (GUL). The

degree of functionalization (DOF) of albumin, *i.e.* the number of moieties of DBCO, NOTA and GUL, was shown to be a fundamental parameter controlling pharmacokinetics and biodistribution. Dynamic Light Scattering (DLS) studies of the albumin platforms showed that the native size of the protein is preserved, while radiolabeling with the metal ions $^{68}Ga^{3+}$ and $^{64}Cu^{2+}$ was found to be highly efficient (≥ 98%). Moreover, preliminary *in vivo* PET studies in mice demonstrated that a lower DOF of GUL favored rapid renal clearance, whereas a higher one led to increased hepatic accumulation. These results highlight the versatility of albumin as a carrier for radiometal-based PET probes and emphasize the importance of fine-tuning probe loading for optimal imaging results.

Lastly, Chapter 4 investigates the synthesis and characterization of two new decadentate *macropa*-derived macrocyclic chelators − *bpycropa* and *phencropa* − incorporating rigid aromatic bipyridine and phenanthroline moieties, respectively. They were developed with the aim of enhancing the stability of complexes with metal ions for targeted alpha therapy (TAT). The complexes of *bpycropa* and *phencropa* with Ba^{2+}, Pb^{2+}, La^{3+}, and Bi^{3+} − used as non-radioactive analogues of clinically relevant radiometals ($^{223}Ra^{2+}$, $^{212}Pb^{2+}$, $^{225}Ac^{3+}$, $^{212}Bi^{3+}$) − were studied by NMR spectroscopy, mass spectrometry, potentiometry, and X-ray diffraction. All complexes displayed an asymmetric coordination geometry, different from that of the *macropa* analogues. The *phencropa* complexes generally afforded higher thermodynamic stability and kinetic inertness compared to *bpycropa*. Nonetheless, kinetic transchelations with EDTA studies revealed that inertness remains insufficient for long-lived α-emitting radiopharmaceutical applications, highlighting the need for further ligand structural optimization.

Overall, this work provides key insights into how ligand structure, rigidity, and conformational dynamics influence metal complex stability and reactivity, which can contribute to establishing guidelines for the rational design of novel chelators and carrier systems, for both diagnostic and therapeutic nuclear medicine.

Riassunto

Questo lavoro di tesi è strutturato in quattro capitoli, ciascuno dei quali affronta aspetti fondamentali nella progettazione, caratterizzazione e applicazione di chelanti per ioni metallici in medicina nucleare e radiofarmacia, con particolare attenzione alla stabilità termodinamica, all'inerzia cinetica e alle proprietà strutturali. I lavori presentati nei Capitoli 1 e 2 sono stati svolti presso Bracco Imaging SpA (Basovizza, Trieste). Il Capitolo 3 trae origine da uno stage di tre mesi svolto presso il Seoul National University Hospital (College of Medicine), a Seoul (Corea del Sud). Infine, il lavoro descritto nel Capitolo 4 è stato avviato durante uno stage di tre mesi presso l'Università della Bretagna Occidentale di Brest (Francia) e successivamente proseguito presso l'Università di Trieste.

Il primo capitolo esamina un nuovo derivato del legante AAZTA, un chelante esadentato spirobiciclico denominato TRASUTA, progettato per valutare se tale rigidità conformazionale sia in grado di aumentare la stabilità di complessi con ioni metallici di rilevanza biologica e diagnostica, tra i quali Ga^{3+}, Cu^{2+}, Zn^{2+} e Ca^{2+}. Contrariamente alle aspettative, i complessi studiati di TRASUTA dimostrano una stabilità termodinamica e un'inerzia cinetica inferiore rispetto a quelli formati con analoghi aventi maggiore flessibilità, compreso l'AAZTA. Infatti, studi approfonditi di NMR multinucleare a temperatura variabile evidenziano che, nonostante la struttura spirobiciclica, i complessi di TRASUTA presentano una marcata dinamicità conformazionale. I processi di isomerizzazione osservati sono entropicamente dipendenti e avvengono attraverso intermedi eptacoordinati che coinvolgono la coordinazione di una molecola d'acqua. Complessivamente, questi risultati suggeriscono che la presenza di strutture spirobicicliche non si traduce necessariamente in un miglioramento delle proprietà chimico-fisiche del complesso, evidenziando l'importanza di bilanciare rigidità e flessibilità nella progettazione dei leganti. Questo lavoro è stato pubblicato nella rivista *Inorganic Chemistry* (*Inorg. Chem.* **2024**, 63, 27, 12525 – 12537).

Il secondo capitolo presenta uno studio approfondito dei complessi di Pb(II) con chelanti di rilevanza clinica, tra cui DOTA, DOTAM, DOTP, DTPA ed EDTA. Combinando tecniche potenziometriche, spettroscopiche, elettroforetiche e cristallografiche, sono state evidenziate differenze significative nella forza di legame metallo-chelante, nella selettività e nel comportamento cinetico. Tra i leganti studiati, si individua il DOTA come il legante più selettivo per il Pb^{2+} in condizioni fisiologiche, mentre i complessi di DOTP sono caratterizzati da una scarsa inerzia cinetica dovuta a meccanismi di dissociazione acido-catalizzati. Gli studi strutturali rivelano geometrie di coordinazione simili tra i complessi esaminati, ovvero di tipo antiprismatico quadrato distorto, tuttavia mettono in evidenza il ruolo della rigidità del legante, dell'idratazione e dei moti conformazionali nella determinazione della stabilità cinetica. Complessivamente, $[Pb(DOTA)]^{2-}$ emerge come il candidato più promettente per lo sviluppo di radiofarmaci basati sul sistema $^{212}Pb/^{212}Bi$, volti alla terapia alfa mirata.

Il terzo capitolo è dedicato all'imaging diagnostico, descrivendo lo sviluppo di una piattaforma modulare basata sull'albumina marcata con radiometalli per tomografia a emissione di positroni (PET). Sfruttando l'abbondanza intrinseca di residui di lisina, l'albumina viene funzionalizzata mediante reazioni di *click-chemistry* con il linker dibenzocicloottino-*N*-

idrossisuccinimide (DBCO), il chelante macrociclico NOTA, e il peptide *targeting* glutammato-ureido-lisina (GUL), selettivo per il cancro alla prostata. Il grado di funzionalizzazione dell'albumina, ovvero il numero delle unità presenti di DBCO, NOTA e GUL, si è dimostrato fondamentale per il controllo della farmacocinetica e biodistribuzione. Gli studi di *Dynamic Light Scattering* (DLS) evidenziano che le dimensioni native dell'albumina vengono preservate, mentre la radiomarcatura con gli ioni metallici $^{68}Ga^{3+}$ e $^{64}Cu^{2+}$ risulta altamente efficiente (≥ 98%). Inoltre studi preliminari *in vivo* hanno evidenziato che gradi di funzionalizzazione bassi di GUL favoriscono un'escrezione renale più rapida, mentre quelli più elevati aumentano l'accumulo epatico. Questi risultati suggeriscono la versatilità dell'albumina come vettore per sonde PET basate su radiometalli, nonché l'importanza di modulare il carico di sonda per ottimizzare le prestazioni e la qualità di imaging.

Infine, il quarto capitolo riguarda la sintesi e caratterizzazione di due nuovi chelanti macrociclici decadentati derivanti dal *macropa* − *bpycropa* e *phencropa* − i quali presentano rispettivamente unità rigide aromatiche di bipiridina e fenantrolina per potenzialmente aumentare la stabilità dei complessi rispetto al *macropa*. I loro complessi con gli ioni metallici Ba^{2+}, Pb^{2+}, La^{3+} e Bi^{3+} − selezionati come analoghi non radioattivi (*cold*) di radiometalli di interesse clinico ($^{223}Ra^{2+}$, $^{212}Pb^{2+}$, $^{225}Ac^{3+}$, $^{212}Bi^{3+}$) − sono stati studiati mediante tecniche di spettroscopia NMR, spettrometria di massa, potenziometria e diffrazione a raggi X. Per tutti i complessi si è riscontrata una geometria di coordinazione asimmetrica, di cui quelli con il *phencropa* presentano generalmente una maggiore stabilità termodinamica e inerzia cinetica rispetto al *bpycropa*. Tuttavia, studi cinetici di transchelazione con EDTA evidenziano che l'inerzia rimane insufficiente per applicazioni con radiofarmaci α-emettitori aventi tempi di emivita lunghi, indicando la necessità di ulteriori ottimizzazioni strutturali dei leganti.

In sintesi, questo lavoro di tesi offre una visione approfondita di come la struttura, la rigidità e i moti conformazionali dei leganti influenzino la stabilità e la reattività dei complessi metallici, fornendo basi importanti per la progettazione di nuovi chelanti e sistemi vettoriali per applicazioni diagnostiche e terapeutiche in medicina nucleare.

List of abbreviations

18-crown-6: 1,4,7,10,13,16-hexaoxacyclooctadecane

AAZTA: 6-amino-6-methylperhydro-1,4-diazepine-*N*, *N*',*N*'',*N*'''-tetraacetic acid

acac: Acetylacetonate

CHX-A″-DTPA: 2-[[(1*R*)-2-[bis(carboxymethyl)amino]cyclohexyl]-[(2*S*)-2-[bis(carboxymethyl)amino]-3-(4-isothiocyanatophenyl)propyl]amino]acetic acid

CN: Coordination number

CT: Computed Tomography

CyAAZTA: 1,4-bis(carboxymethyl)-6-[bis(carboxymethyl)amino]-6-methylperhydro-1,4-diazepine

CZE: Capillary Zone Electrophoresis

DATA^{m}: 6-methyl-6-amino-1,4-diazepane-1,4-diacetic acid

DBCO-NHS: Dibenzocyclooctyne-*N*-hydroxysuccinimide

DLS: Dynamic Light Scattering

DO2AtBu: 2-(7-(2-amino-2-oxoethyl)-4,10-bis(2-tert-butoxy-2-oxoethyl)-1,4,7,10-tetraazacyclododecan-1-yl)ethanoic acid

DOF: Degree of Functionalization

DOTA: 1,4,7,10-Tetraazacyclododecane-1,4,7,10-tetraacetic acid

DOTAM: 1,4,7,10-tetrazacyclododecan-1,4,7,10-tetraacetamide

DOTP: 1,4,7,10-Tetraazacyclododecane-1,4,7,10-tetra(methylene phosphonic acid)

DTPA: Dietilene-triamine-*N,N,N',N''N''*-pentaacetic acid

DUPA: (2S,2′S)-2,2′-(carbonyldiimino)dipentanedioic acid

EDTA: 2,2′,2″,2‴-(1,2-ethanediyldinitrilo)tetraacetic acid)

EGTA: 3,12-Bis(carboxymethyl)-6,9-dioxa-3,12-diazatetradecane-1,14-dioic acid

FDG: Fluorodeoxyglucose

GUL: Glutamate-Ureido-Lysine

HER2: Human Epidermal Growth Factor Receptor 2

HSA: Human Serum Albumin

IgG: Immunoglobulin G

Kryptofix: 4,7,13,16,21,24-hexaoxa-1,10-diazabicyclo[8.8.8]hexacosane

mAb: Monoclonal antibody

macropa: 6-[[16-[(6-carboxypyridin-2-yl)methyl]-1,4,10,13-tetraoxa-7,16-diazacyclooctadec-7-yl]methyl]pyridine-2-carboxylic acid

MALDI-TOF: Matrix-Assisted Laser Desorption Ionization Time of Flight

MC1R: Melanocortin Receptor 1

mCRPC: Metastatic Castration-Resistant Prostate Cancer

MRI: Magnetic Resonance Imaging

NET: Neuroendocrine Tumors

NMR: Nuclear Magnetic Resonance

NOTA: 2,2′,2″-(1,4,7-triazacyclononane-1,4,7-triyl)triacetic acid

PBS: Phosphate-Buffered Saline

PEG: Polyethylene glycol

PET: Positron Emission Tomography

PIDAZTA: 4-amino-4-methylperhydro-pyrido[1,2-*a*][1,4]diazepin-N,N′,N′-triacetic acid

PSC: Pb-Specific-Chelator

PSMA: Prostate-Specific Membrane Antigen

radio-iTLC-SG: radio-instant thin layer chromatography on silica gel

RDx: Radiodiagnostics

RIT: Radioimmunotherapy

RTx: Radiotherapeutics

SAP: Square antiprism

SP: Substance P

SPAAC: Strain-Promoted Alkyne-Azide Cycloaddition

SPARC: Secreted Protein Acidic and Rich in Cysteine

SPECT: Single-Photon Emission Computed Tomography

SSTR2: Somatostatin Receptor Subtype 2

TAT: Targeted Alpha Therapy

TRASUTA: 1,7,10-triazaspiro[4.6]-undecane-1,7,10-triacetic acid

TSAP: Twisted square antiprism

UV-Vis: Ultraviolet-Visible

Introduction

This short introductive Chapter is meant to give a succint, and by all means not comprehensive, overview of radiopharmaceuticals, in terms of techniques and radionuclides. A more detailed introduction to specific aspects of the topics dealt within this thesis is to be found at the beginning of each of the following Chapters.

Radiopharmaceuticals, types of ionizing radiations and clinical applications

Radiopharmaceuticals play a crucial role in nuclear medicine, enabling the diagnosis, staging, monitoring, and treatment of numerous diseases, including cancer and lesions of different types and origins.[1] They can be broadly classified according to their application, namely as diagnostic (γ or β^+ emitters) or therapeutic (β^- or α emitters) agents. For both categories, the radionuclides employed – besides having the appropriate emission(s) – must exhibit properties compatible with the preparation and administration of the radiolabelled compounds, i.e. a suitable decay half-time ($t_{1/2}$), as well as (for the diagnostic agents) with the detection of the emitted signal once inside the organism.[2]

In addition, cost and accessibility of radionuclide production must be considered. Among all the different methods of production, generator systems are usually preferred, in which a long-lived parent isotope is retained on a sorbent column while its daughter radionuclide is periodically eluted or "milked" (*vide infra*).[3] Moreover, radionuclides are commonly categorized as either *non-metal-based* (*e.g.* ^{18}F, ^{11}C) or *metal-based* (*e.g.* ^{68}Ga, ^{99m}Tc).[4][5] This work will primarily focus on the latter category.

Approaches in radioimaging: SPECT and PET

Single-photon emission computed tomography (SPECT) relies on radiotracers that emit single gamma photons as they decay within the body. As the detector, a gamma camera, rotates around the patient, it records these emissions from multiple viewpoints, enabling the reconstruction of a three-dimensional map of tracer distribution. SPECT scans are widely used in cardiac and bone imaging and rely on the emission of gamma photons from metastable nuclides. Among these, ^{99m}Tc ($t_{1/2}$ = 6 h) is the most extensively used diagnostic radiotracer. A well-known agent is technetium-sestamibi (commercially *Cardiolite*), particularly applied in cardiac, bone, and kidney imaging (Figure 1). ^{99m}Tc is conveniently obtained from a ^{99}Mo/^{99m}Tc generator, where it is eluted as $[^{99m}TcO_4]^-$, pertechnetate, from an alumina column loaded with molibdate, $[^{99}MoO_4]^{2-}$, using a saline solution. However, the generator typically requires replacement after about a week due to declining elution efficiency and the occurrence of a process known as the ^{99}Mo breakthrough, *i.e.* contamination of the ^{99m}Tc eluate with the parent radionuclide.[6][7]

Other metal-based SPECT agents gaining attention include ^{111}In-oxine for white blood cell imaging and ^{67}Ga-citrate for lymphoma imaging.[8][9] Recent studies also explore heavy isotopes such as ^{203}Pb because of its potential theranostic pairing with the therapeutic β^- emitter

^{212}Pb[10] – which decays to the α emitter ^{212}Bi – discussed separately in a later chapter. On the other hand, non-metallic SPECT tracers remain fundamental as well. Namely, iodine-131, obtained as a by-product of ^{99}Mo decay, and iodine-123 are well-established agents for imaging thyroid disorders.[11][12]

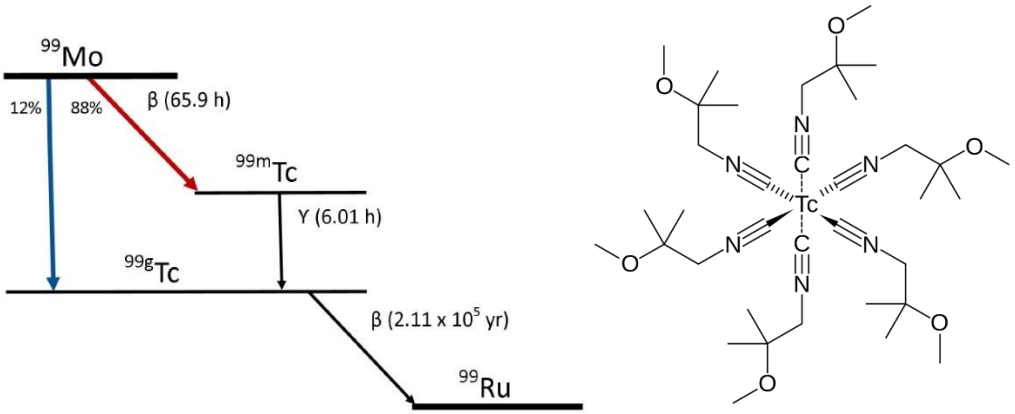

Figure 1. Decay scheme of the ^{99}Mo/^{99m}Tc (a) and the cardiac imaging SPECT agent ^{99m}Tc-sestamibi, commercially known as *Cardiolite* (b).

Another fundamental imaging technique is given by *Positron Emission Tomography* (PET). PET imaging is based on radiotracers that emit positrons, which travel only a short distance before encountering electrons in the surrounding tissue. Ideally, the emitted positron has a relatively low energy, as this minimizes its travel distance and improves the spatial resolution of the reconstructed image. When a positron and an electron collide, they undergo an annihilation process, producing two 511 keV photons emitted in nearly opposite directions. A ring of detectors simultaneously records these coincident photon pairs, allowing the system to determine their point of origin with high spatial accuracy.

In nuclear medicine there are generally two main strategies to introduce radiotracers in the organism, namely the *non-targeted* and *targeted* approach. In the first one, imaging relies on molecules that are intrinsically taken up by specific cell types exhibiting characteristic biological behaviours. For example, cancer cells typically exhibit accelerated and energy-demanding metabolism compared to healthy tissue. This principle is harnessed particularly for PET imaging employing fluorine-18, a positron emitter ($t_{1/2}$ = 110 min, 97%), typically produced in a cyclotron via proton irradiation of a ^{18}O-enriched water target. In fact, one of the most commonly used tracers for PET is [^{18}F]Fluorodeoxyglucose (FDG), a glucose analogue that follows endogenous metabolic pathways but remains trapped in tumor cells following phosphorylation, enabling sensitive metabolic imaging.[13][14]

The targeted approach, on the other hand, is employed when metal nuclides are the radiotracers of choice.[15] These radionuclides must be strongly chelated by appropriate ligands and exhibit a half-life suitable for biodistribution, accumulation in the target tissue, and decay.[16] Ligands employed in nuclear medicine fall into two major categories, linear (*e.g.* EDTA, DTPA) and

macrocyclic (*e.g.* DOTA, NOTA). The latter is generally preferred because of their high stability and inertness, and several of these will be discussed in detail in the following chapters. Selectivity is achieved through a *targeting vector*, typically a peptide or antibody, conjugated to the radiometal complex.[17] These type of vectors bind preferentially to specific receptors or antigens overexpressed in tumors (Figure 2).

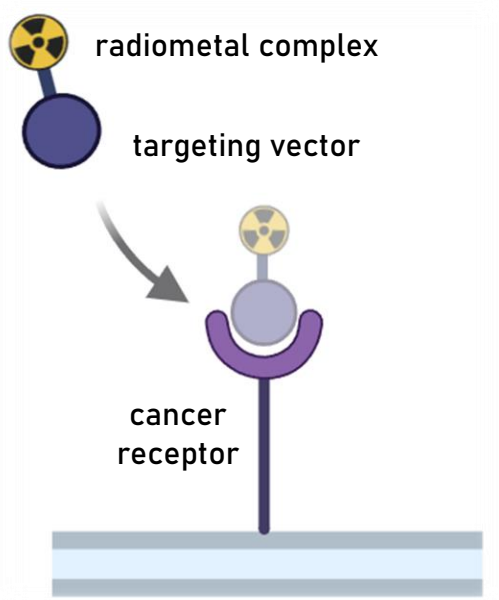

Figure 2. Schematic representation of a targeting vector that selectively localizes the radionuclide onto the target.

The use of metal ions allows straightforward one-step complexations with the chelator, which are not possible in the case of fluorine-based organic reactions, due to the intrinsically different chemistry. Among metal ions, ^{68}Ga ($t_{1/2}$ = 68 min) and ^{64}Cu ($t_{1/2}$ = 12.7 h) are increasingly prominent positron emitters for PET.[18] For example, ^{68}Ga-labelled PSMA-targeted ligands show high sensitivity in prostate cancer imaging. Furthermore, a range of ^{68}Ga-DOTA complexes (^{68}Ga-DOTATOC, ^{68}Ga-DOTATATE, ^{68}Ga-DOTANOC)[19] coupled to the cyclic peptide analogue of somatostatin, octreotide, are widely used for imaging different somatostatin receptor subtypes overexpressed in neuroendocrine tumors (Figure 3a).

Other biological targets include integrins − transmembrane proteins involved in adhesion, motility and cell-extracellular matrix interactions. Specifically, peptides displaying the RGD motif (arginine–glycine–aspartic acid) are able to selectively bind integrins. Correspondingly, radiolabelled integrin-targeting agents, such as fibroblast activation protein inhibitors (*e.g.* ^{68}Ga-FAPI-RGD) are currently in clinical trials.[20] A practical advantage of ^{68}Ga is its availability from the ^{68}Ge/^{68}Ga generator (Figure 3b), considered cost-effective for routine production. However, some major drawbacks of this system include high eluate volume, low radionuclide concentration, short physical half-life, short physical half-life and high energy of

the β^+ particle resulting in lower resolution of PET images.[21] For this reason, radionuclides with longer half-lives, such as ^{64}Cu ($t_{1/2}$ = 12.7 h), help mitigate these limitations.

^{64}Cu is produced via proton irradiation of ^{64}Ni and has been applied in the form of bis(thiosemicarbazone) complexes (Figure 4) for imaging hypoxia, blood flow, and copper transport.[22] However, its use is hindered by the high cost and limited availability of enriched ^{64}Ni (natural abundance of 0.926%). An alternative production route is provided by neutron irradiation of ^{64}Zn, although it yields lower quantities and co-produces ^{67}Cu.[23]

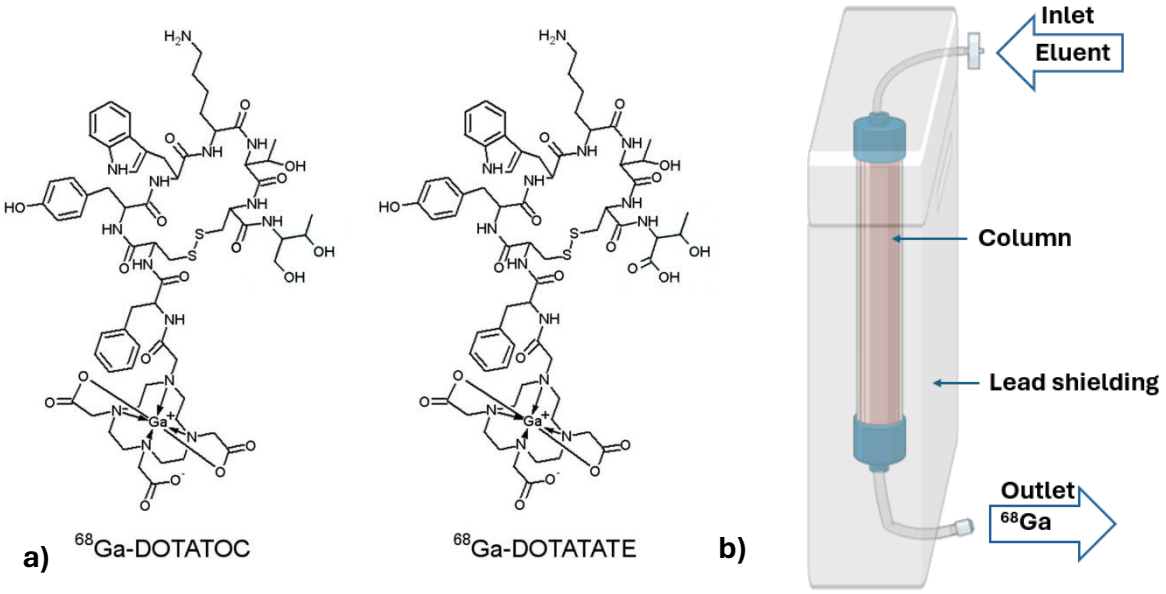

Figure 3. (a) ^{68}Ga-based radiopharmaceuticals bearing DOTATOC and DOTATATE targeting vectors for neuroendocrine tumors PET imaging, (b) simplified illustration of a ^{68}Ge/^{68}Ga generator for $^{68}Ga^{3+}$ production.

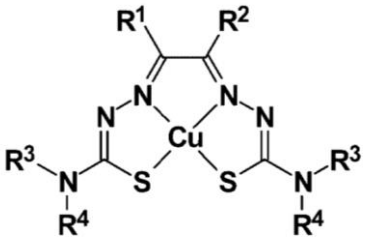

Figure 4. Example of a copper-64 agent ([^{64}Cu]Cu-bis(thiosemicarbazone)) for hypoxia PET imaging.

Another advantage of longer-lived radionuclides is given by a more effective clearance of non-specific background activity, improving tumor-to-organ contrast. Furthermore, the lower positron energy of ^{64}Cu (0.65 MeV) compared to ^{68}Ga (1.90 MeV) results in higher spatial

resolution. Moreover, for significantly slower biodistribution processes, such as those in which the radiotracer is conjugated to an antibody, the long half-life of zirconium-89 ($t_{1/2}$ = 3.3 days) offers a favourable match.[24]

Approaches in radiotherapeutics: alpha and beta therapy

Therapeutic radiopharmaceuticals rely on the emission of ionizing radiation, principally α- and β^- particles. *Targeted Alpha Therapy* (TAT) is a rapidly evolving field based on radionuclides capable of delivering high energy over short distances. In fact, in the domain of radiotherapy, an important parameter is given by the linear energy transfer (LET), which quantifies the amount of energy a charged particle deposits per unit distance as it passes through tissues, typically expressed in keV/µm. In the case of alpha particles, their pathlength is only about 40 – 90 µm, but exhibit a high LET of approximately 100 keV/µm, thus enabling highly localized and potent biological damage via double strand break of DNA. On the other hand β^- particles, due to their much smaller mass, have a lower average LET of 0.2 keV/µm, but travel a longer distance in tissues (≈ 10 mm), compared to alpha particles.[25]

In summary, an optimal alpha emitter must accumulate efficiently in cancer cells, possess a high LET, and a suitable half-life. Examples include radionuclides such as ^{233}U, ^{223}Ra, ^{225}Ac, ^{232}Th, and ^{212}Bi. Clinically, $^{223}RaCl_2$ (commercially *Xofigo*) is currently the only approved alpha-emitter, and it is used for treating bone metastases due to the chemical similarity between Ra(II) and Ca(II) ions.[26] Another radionuclide of critical importance is ^{225}Ac and several actinium-based compounds are currently in clinical trials.[27] However, the increasing demand and limited availability poses a substantial challenge since the amount of available ^{233}U/^{229}Th is sufficient to generate ^{225}Ac in MBq/mCi quantities, which cover less than a thousand of TAT per year.[28]

By contrast, β^- particles exhibit a less-confined, more penetrating behaviour which is suitable for larger tumors that are not located in sites compromising vital functions (the larger range of these particles implies that, even when the emitting nuclide is localized in tumor tissue, they can reach and damage nearby healthy tissue). The mechanism of β^- particles is more indirect compared to alpha particles, since the former are smaller in size and charge and able to generate reactive oxygen species (ROS).[29] In fact, β^- particles can only cause single strand break of DNA which is easier to repair, resulting in lower therapy efficiency. Due to the lower radiation energy of beta particles, dosage and regulatory aspects are less restrictive compared to the high-energy, more damaging alpha emitters. Some radionuclides of interest for β^- therapy such as ^{90}Y and ^{177}Lu are already used in clinics in targeted compounds as [^{90}Y]Y-Ibritumomab-Tiuxetan (*Zevalin*) and [^{177}Lu]Lu-DOTATATE (*Lutathera*) for the treatment of non-Hodgkin's lymphoma and neuroendocrine tumors, respectively.[30][31]

Growing attention is also directed towards terbium, since it provides a wide and versatile variety of radioisotopes with theranostic properties for all modalities: ^{152}Tb and ^{155}Tb for PET/SPECT imaging, and ^{149}Tb and ^{161}Tb for α- and β^--therapy. From the standpoint of

production and availability in larger scales, ^{161}Tb and ^{155}Tb are the most promising, thus potentiating their translation to hospitals.[32][33]

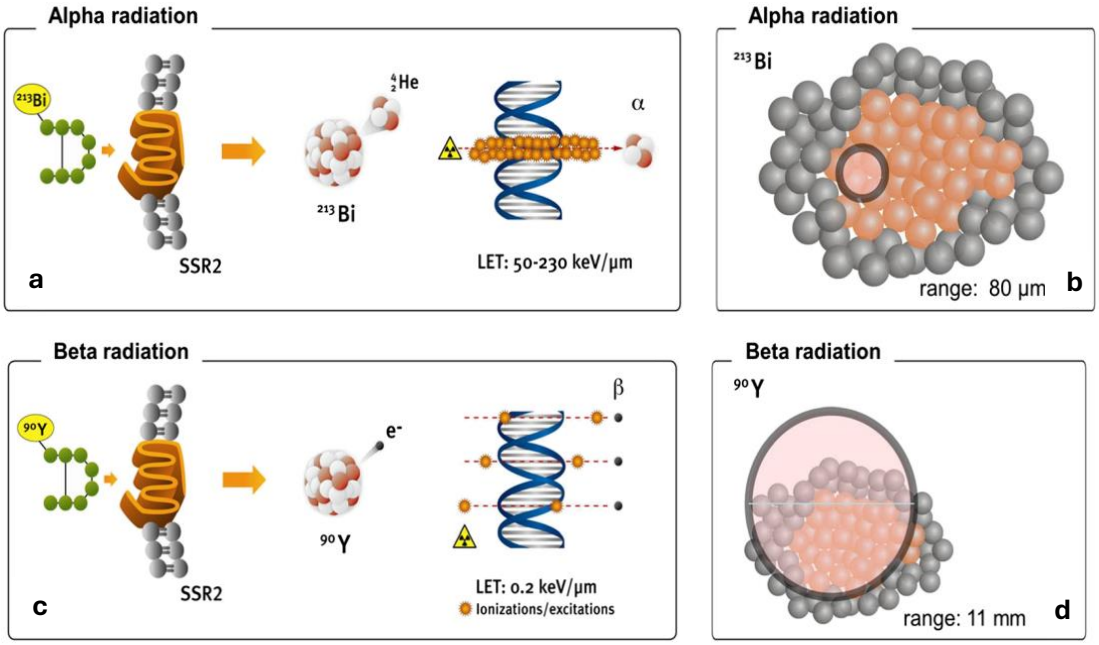

Figure 5. Differences between alpha (top) and beta (bottom) particles useful for radiotherapy. The boxes on the right define the range of action of the particles.

Bioconjugation strategies of targeting vector to metal complexes

To conjugate a targeting vector to a bifunctional chelator containing the radiometal, generally a linker is required as a connecting bridge between the two moieties. Therefore, a critical aspect to consider for the efficacy of a radiopharmaceutical resides not only in the selection of the optimal radionuclide and chelating agent, but also on the chemical strategy used to conjugate the targeting vector to the metal complex.[34] Despite the variable nature of the targeting vector, *i.e.* whether it is a small molecule, peptide or antibody, the established linkage must preserve both the biological activity of the targeting moiety and the chemical stability of the metal-chelate complex. This applies to all targeted radiopharmaceuticals due to the need for *in vivo* stability during decay, including in locally acidic environments in the organism (*e.g.* within lysosomes), and in the presence of possible enzymatic degradation.[35]

There are several strategies used for conjugation such as formation of thioureidic bonds, achieved by reacting isothiocyanate group, typically found on the chelator, with *N*-terminal amino groups of the targeting vector (Scheme 1a). Formation of amides is also commonly adopted, specifically via coupling reactions between carboxylic acids and amines in the presence of condensing crosslinkers (EDC, DCC *etc.*, Scheme 1b), or by using molecules bearing reactive ester groups which usually incorporate *N*-hydroxysuccinimide (NHS, Scheme 1c). Other approaches harness click-chemistry reactions such as azide-alkyne cycloadditions in the presence of copper(I) as catalyst (Scheme 1d), or copper-free if the reacting alkyne is strained (*e.g.* cyclooctyne, Scheme 1e), resulting in a stable 1,2,3-triazole linkage. Since the

majority of targeting vectors are composed of aminoacidic residues, most of these methodologies involve the amino group of lysine residues, however nucleophilic −OH in tyrosines and −SH groups of cysteine residues can also be exploited. In fact, a common reaction is the thiol-maleimide coupling that leads to a thioether bond, known for its stability under physiological and acidic conditions (Scheme 1f).

Regardless of the adopted strategy, these types of functionalizations must provide several advantages such as high reactivity, adequate solubility, minimal structural changes to the targeting vector and stability in different conditions (physiological, acidic, oxidative...).

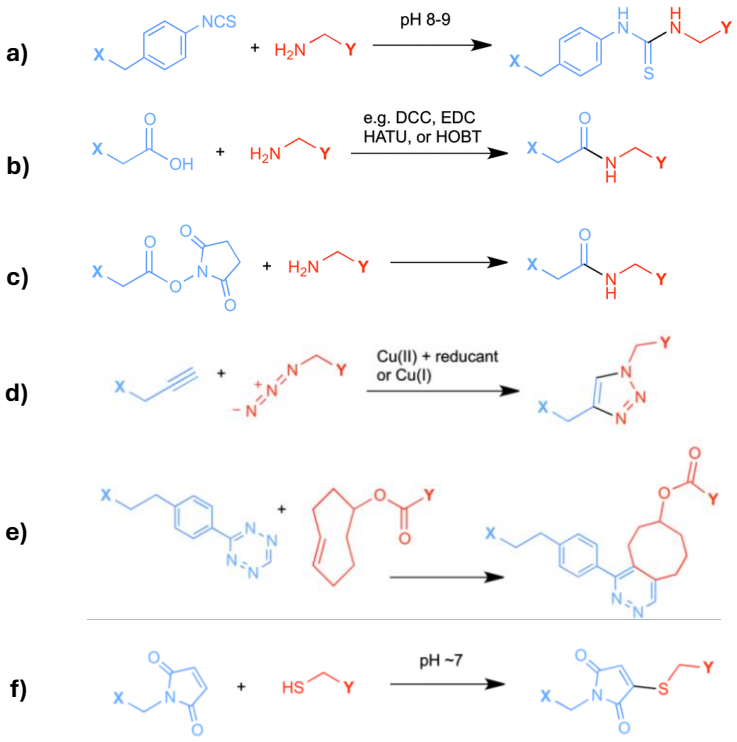

Scheme 1. Different approaches in bioconjugation of targeting vectors to a linker.

Another factor to consider, especially when working with highly selective macromolecules such as antibodies, is steric hindrance, since an increase in the bulkyness and/or number of linked radioactive moieties (linker + bifunctional chelate + metal ion) can modify the pharmacokinetics and binding affinity of the targeting moiety.[36] Thus, albeit the insertion of spacers (*e.g.* PEGylation) is fundamental to improve stability and reduce immunogenicity, if applied excessively the steric effects can decrease the affinity between the antibody and the antigen site. As a general principle, it is acceptable to bind a maximum of two PEG moieties per macromolecule.[37] Moreover, in the antibody-based frameworks, conjugation is mostly performed site-selectively to prevent heterogeneous products that affect biodistribution.[38] Some of the site-selective conjugation strategies implicate enzyme-mediated coupling,

engineered cysteines, glyco-conjugation, all of which improve reproducibility and pharmacokinetic predictability (Figure 6).[39]

On the other hand, the targeting vector + linker moiety should not affect negatively the binding properties on the bifunctional chelate towards the metal ion (*i.e.* it should not trigger the release of the metal ion).

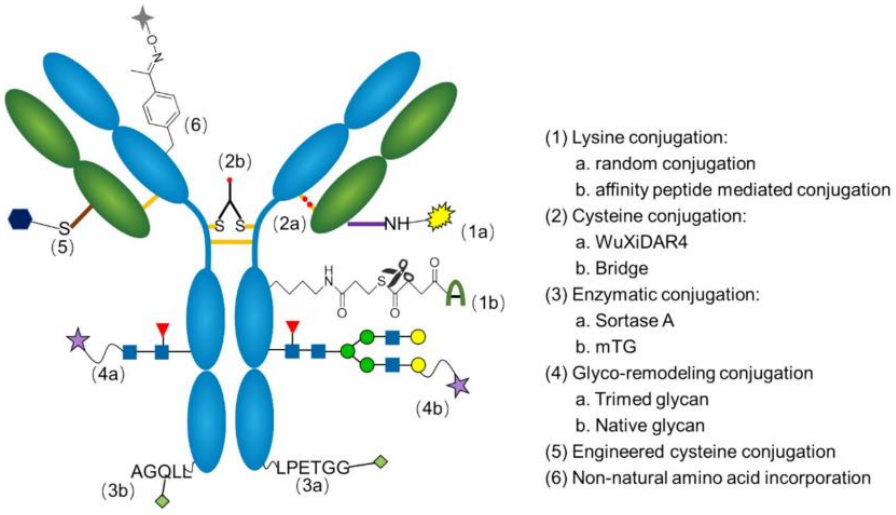

Figure 6. Representation of site-specific conjugation techniques, highlighting key reaction mechanisms and conjugation sites.[39]

References

(1) Dhoundiyal, S.; Srivastava, S.; Singh, S. K.; Singh, G.; Ashique, S; Pal, R.; Mishra, N.; Taghizadeh-Hesary, F. Radiopharmaceuticals: Navigating the Frontier of Precision Medicine and Therapeutic Innovation. *Eur. J. Med. Res.* **2024**, *29*(1).

(2) Lindsley, C. W.; Müller, C. E.; Bongarzone, S. Diagnostic and Therapeutic Radiopharmaceuticals: A "Hot" Topic. *J. Med. Chem.* **2023**, *66*(24), 16457−16463.

(3) Lebowitz, E.; Richards, P. Radionuclide Generator Systems. *Semin. Nucl. Med.* **1974**, *4*(3), 257−268.

(4) MacPherson, D. S.; Fung, K.; Cook, B. E.; Francesconi, L. C.; Zeglis, B. M. A Brief Overview of Metal Complexes as Nuclear Imaging Agents. *Dalton Trans.* **2019**, *48*(39), 14547–14565.

(5) Sun, A.; Liu, X.; Tang, G. Carbon-11 and Fluorine-18 Labeled Amino Acid Tracers for Positron Emission Tomography Imaging of Tumors. *Front. Chem.* **2018**, *5*.

(6) National Research Council (US) Committee. *Medical Isotope Production Without Highly Enriched Uranium, 2, Molybdenum-99/Technetium-99m: Production and Use.*; Washington (DC): National Academies Press (US), **2009**.

(7) Ramadhanti, N. Z.; Febriana, S. Verification on Molybdenum-99 (^{99}Mo) Breakthrough from Non-Fission ^{99}Mo/^{99m}Tc Generator to Produce Technetium-99m (^{99m}Tc) Medical Radionuclide. *J. Phys. Conf. Ser.* **2024**, *2866*, 012056.

(8) Becker, W.; Fischbach, W.; Jenett, M.; Reiners, C.; Börner, W. ^{111}In-Oxine-Labelled White Blood Cells in the Diagnosis and Follow-up of Crohn's Disease. *Klin. Wochenschr.* **1986**, *64(3)*, 141–148.

(9) Seabold, J. E.; Votaw, M. L.; Keyes, J. W.; Foley, J.; Balachandran, W. D.; Gill, S. P. Gallium Citrate Ga-67 Scanning: Clinical Usefulness in Lymphoma Patients. *Arch. Intern. Med.* **1976**, *136(12)*, 1370–1374.

(10) McNeil, B. L.; Mastroianni, S. A.; McNeil, S. W.; Zeisler, S.; Kumlin, J.; Borjian, S.; McDonagh, A. W.; Cross, M.; Schaffer, P.; Ramogida, C. F. Optimized Production, Purification, and Radiolabeling of the ^{203}Pb/^{212}Pb Theranostic Pair for Nuclear Medicine. *Sci. Rep.* **2023**, *13(1)*, 10623.

(11) Bitgen, N.; Bayram, F.; Hamurcu, Z.; Baskol, G.; Ozturk, F.; Abdulrezzak, U.; Donmez-Altuntas, H. The Effects of Iodine-131 Treatment on Chromosomal and Oxidative DNA Damage in Papillary Thyroid Carcinoma. Mutation Research. *Genet. Toxicol. Environ. Mutagen.* **2024**, *898* (503797).

(12) Bourguignon, M. H.; Pauwels, E. K.; Loc'h, C.; Mazière, B. Iodine-123 Labelled Radiopharmaceuticals and Single-Photon Emission Tomography: A Natural Liaison. *Eur. J. Nucl. Med. Mol. Imaging* **1997**, *24(3)*, 331–344.

(13) Ozaki, K.; Harada, K.; Terayama, N.; Kosaka, N.; Kimura, H.; Gabata, T. FDG-PET/CT Imaging Findings of Hepatic Tumors and Tumor-like Lesions Based on Molecular Background. *Jpn. J. Radiol.* **2020**, *38(8)*, 687–718.

(14) Almuhaideb, A.; Papathanasiou, N.; Bomanji, J. ^{18}F-FDG PET/CT Imaging in Oncology. *Ann. Saudi Med.* **2011**, *31(1)*, 3–13.

(15) Oyen, W. J. G.; Bodei, L.; Giammarile, F.; Maecke, H. R.; Tennvall, J.; Luster, M.; Brans, B. Targeted Therapy in Nuclear Medicine—Current Status and Future Prospects. *Ann. Oncol.* **2007**, *18(11)*, 1782–1792.

(16) Sneddon, D.; Cornelissen, B. Emerging Chelators for Nuclear Imaging. *Curr. Opin. Chem. Biol.* **2021**, *63*, 152–162.

(17) Chaturvedi, S.; Mishra, A. K. Vectors for the Delivery of Radiopharmaceuticals in Cancer Therapeutics. *Ther. Deliv.* **2014**, *5(8)*, 893−912.

(18) Fonseca, A. I.; Sereno, J.; Almeida, S.; Ferreira, H.; Hrynchak, I.; Falcão, A.; Alves, F.; Gomes, C.; Abrunhosa, A. J. Unveiling the Potential of Copper-64 vs. Gallium-68 for SSTR PET Imaging. *Eur. J. Nucl. Med. Mol. Imaging* **2025**, *52(7)*, 2671–2684.

(19) Filippi, L.; Pizzichini, P.; Bagni, O.; Scopinaro, F. Somatostatin Receptor Analogs (^{68}Ga-DOTATOC, ^{68}Ga-DOTANOC, ^{68}Ga-DOTATATE). In *Radiopharmaceuticals*; Springer, Cham.: Calabria; pp 105–119.

(20) Javid, H.; Oryani, M. A.; Rezagholinejad, N.; Esparham, A.; Tajaldini, M.; Karimi-Shahri, M. RGD Peptide in Cancer Targeting: Benefits, Challenges, Solutions, and Possible Integrin-RGD Interactions. *Cancer Med.* **2024**, *13(2)*, e6800.

(21) Velikyan, I. 68Ga-Based Radiopharmaceuticals: Production and Application Relationship. *Molecules* **2015**, *20(7)*, 12913−12943.

(22) Paterson, B. M.; Donnelly, P. S. Copper Complexes of Bis(Thiosemicarbazones): From Chemotherapeutics to Diagnostic and Therapeutic Radiopharmaceuticals. *Chem. Soc. Rev.* **2011**, *40(5)*, 3005.

(23) Jauregui-Osoro, M.; De Robertis, S.; Halsted, P.; Gould, S. M.; Yu, Z.; Paul, R. L.; Marsden, P. K.; Gee, A. D.; Fenwick, A.; Blower, P. J. Production of Copper-64 Using a Hospital Cyclotron: Targetry, Purification and Quality Analysis. *Nucl. Med. Commun.* **2021**, *42(9)*, 1024−1038.

(24) Badier, L., Quelven, I. Zirconium-89 and Copper-64 for ImmunoPET: From Antibody Bioconjugation and Radiolabeling to Molecular Imaging. *Pharmaceutics* **2024**, *16*(7), 882.

(25) Marcu, L.; Bezak, E.; Allen, B. J. Global Comparison of Targeted Alpha vs Targeted Beta Therapy for Cancer: *In Vitro*, *In Vivo* and Clinical Trials. *Crit. Rev. Oncol. Hematol.* **2018**, *123*, 7–20.

(26) Liepe, K.; Shinto, A. From Palliative Therapy to Prolongation of Survival: $^{223}RaCl_2$ in the Treatment of Bone Metastases. *Ther. Adv. Med. Oncol.* **2016**, *8(4)*, 294–304.

(27) Bidkar, A. P.; Zerefa, L.; Yadav, S.; VanBrocklin, H. F.; Flavell, R. R. Actinium-225 Targeted Alpha Particle Therapy for Prostate Cancer. *Theranostics* **2024**, *14(7)*, 2969–2992.

(28) Miederer, M.; Benešová-Schäfer, M.; Mamat, C.; Kästner, D.; Pretze, M.; Michler, E.; Brogsitter, C.; Jörg Kotzerke; Kopka, K.; Scheinberg, D. A.; McDevitt, M. R. Alpha-Emitting Radionuclides: Current Status and Future Perspectives. *Pharmaceuticals* **2024**, *17*(1), 76.

(29) Mu, W.; Liu, L.-Z. Reactive Oxygen Species Signaling in Cancer Development. *Reactive Oxygen Species* **2017**, *4(10),* 251–265.

(30) Krasner, C.; Joyce, R. M. ZevalinTM: 90Yttrium-Labeled Anti-CD20 (Ibritumomab Tiuxetan), A New Treatment for Non-Hodgkin's Lymphoma. *Curr. Pharm. Biotechnol.* **2001**, *2(4)*, 341–349.

(31) Hromadik, L. K.; Sturges, L. Caring for Patients Receiving ^{177}Lu-DOTATATE, Lutathera®: A Treatment of Hope for Patients with Gastroenteropancreatic Neuroendocrine Tumors. *J. Radiol. Nurs.* **2019**, *38(1)*, 28–32.

(32) Koniar, H.; McNeil, S.; Wharton, L.; Ingham, A.; Van de Voorde, M.; Ooms, M.; Sekar, S.; Rodríguez-Rodríguez, C.; Kunz, P.; Radchenko, V.; Rahmim, A.; Uribe, C.; Yang, H.; Schaffer, P. Quantitative SPECT Imaging of 155Tb and 161Tb for Preclinical Theranostic Radiopharmaceutical Development. *EJNMMI physics* **2024**, 11(1), 77.

(33) Van Laere, C.; Koole, M.; Deroose, C. M.; Van Baete, K.; Cocolios, T. E.; Duchemin, C.; Ooms, M.; Cleeren, F. Terbium Radionuclides for Theranostic Applications in Nuclear Medicine: From Atom to Bedside. *Theranostics* **2024**, *14(4)*, 1720−1743.

(34) Samieipour, F.; Dianat-Moghadam, H.; Khanahmad, H. Recent Developments in Bioconjugation: From Strategies to Design and Clinical Applications. *Biomed. Pharmacother.* **2025**, *192*, 118593.

(35) Bisht, T.; Adhikari, A.; Patil, S.; Dhoundiyal, S. Bioconjugation Techniques for Enhancing Stability and Targeting Efficiency of Protein and Peptide Therapeutics. *Curr. Protein Pept. Sci.* **2024**, *25(3)*, 226−243.

(36) Su, D.; Zhang, D. Linker Design Impacts Antibody-Drug Conjugate Pharmacokinetics and Efficacy via Modulating the Stability and Payload Release Efficiency. *Front. Pharmacol.* **2021**, *12*.

(37) Kanellopoulos, P.; Lymperis, E.; Kaloudi, A.; de Jong, M.; Krenning, E. P.; Nock, B. A.; Maina, T. [99mTc]Tc-DB1 Mimics with Different-Length PEG Spacers: Preclinical Comparison in GRPR-Positive Models. *Molecules* **2020**, *25(15)*, 3418.

(38) Agarwal, P.; Bertozzi, C. R. Site-Specific Antibody–Drug Conjugates: The Nexus of Bioorthogonal Chemistry, Protein Engineering, and Drug Development. *Bioconjugate Chem.* **2015**, *26(2)*, 176−192.

(39) Fan, Q.; Chen, H.; Wei, G.; Wei, D.; Wang, Z.; Zhang, L.; Wang, J.; Zhu, M. A Review of Conjugation Technologies for Antibody Drug Conjugates. *Antib. Ther.* **2025**, *8(2)*, 157−170.

Chapter 1

TRASUTA: The effect of the structural rigidity of a mesocyclic AAZTA-like chelating agent on the thermodynamic, kinetic, and structural properties of some divalent metal and Ga^{3+} complexes

The work reported in this Chapter was performed at the Bracco Imaging laboratories of Basovizza (TS) under the supervision of Dr. Zsolt Baranyai with the assistance of Dr.ssa Mariangela Boccalon and Dr.ssa Nicol Guidolin.

Introduction

The ability of chelating agents to form complexes with metal ions is widely employed in domestic, agricultural, industrial, and medical applications and witnessed by an impressive annual consumption in the range of hundreds of thousands tons.[1] Medical applications of chelating agents include diagnostics for MRI,[2] PET, and SPECT,[3][4][5] targeted radiotherapy,[6] and chelation therapy,[7] in which the rapid and selective formation of particularly stable metal complexes is mandatory. High thermodynamic and kinetic stability is usually associated with macrocyclic chelating agents, with the coordinating functional groups preorganized in or onto a large *n*-membered ring ($n \geq 9$).[8] The structural rigidity imposed by some macrocyclic structures takes its toll in the formation kinetics of the metal complex, requiring long times and/or forcing conditions to reach completion, hardly compatible with the often short-lived metal isotopes used in nuclear medicine and with sensitive biomolecules and in vivo conditions.[9] Rapid formation of metal complexes is achieved with acyclic and small (3–6 membered) cyclic chelators, but the thermodynamic and kinetic inertness of these chelates is usually lower, leading to a potential and unwanted loss of the metal ions.

A good compromise between fast complexation kinetics and thermodynamic stability has been achieved with AAZTA, a heptadentate mesocyclic polyaminocarboxylic chelating agent, as well as with its hexadentate derivative $DATA^{m}$[10] (Figure 1). AAZTA[11] can be easily obtained from inexpensive starting materials, and its complexes with several divalent and trivalent metal ions show good thermodynamic stability associated with fast formation kinetics.[12-15] Owing to these valuable features, several AAZTA-like bifunctional chelating agents[16][17] were synthesized, conjugated to diagnostic-relevant biomolecules, and labeled with metal ions to give a vast array of diagnostic imaging probes.[18-25]

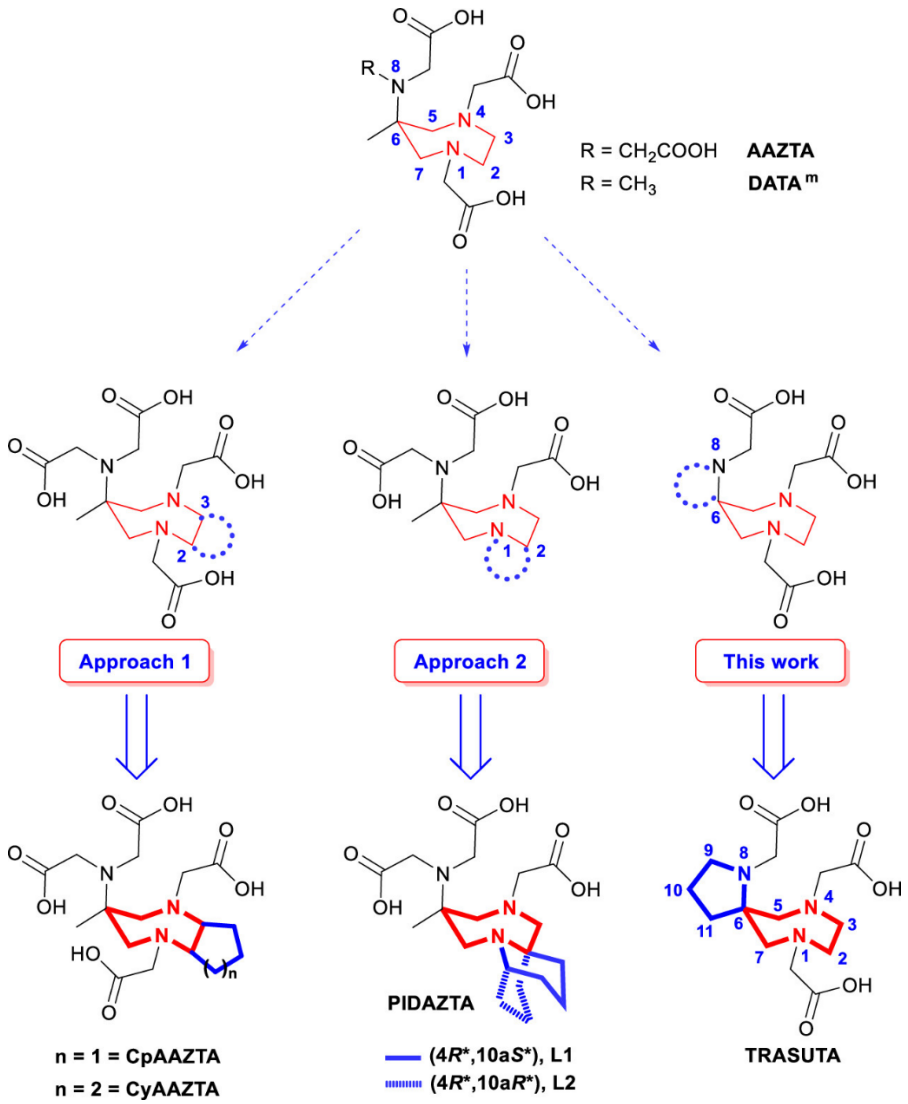

Figure 1. AAZTA and its bicyclic derivatives.

Among them, $^{68}Ga^{3+}$ complexes recently gained a widespread interest as PET contrast agents, culminated in the approval for clinical use by FDA and EMA of ^{68}Ga-edotreotide ([^{68}Ga]-Ga-DOTATOC) to detect somatostatin receptor-positive neuroendocrine tumors.[26]

The slow complexation kinetics associated with DOTA-like macrocyclic chelators led to investigating the possibility of employing AAZTA-based ligands as the chelating moiety in $^{68}Ga^{3+}$-based PET imaging probes due to their prompt formation of the stable chelate. Recent reports demonstrated the superior efficiency in detecting liver and bone metastases of the AAZTA -related [^{68}Ga]Ga-DATA^{5m}-LM4 over the macrocyclic [^{68}Ga]Ga-DOTANOC[27] and the potential of [^{68}Ga]Ga-DATA^{5m}.SA.FAPi for the visualization of cancer-associated fibroblasts of different tumors and metastases thereof.[28]

Prompted by these results, several AAZTA derivatives have been studied in order to improve their coordination properties or (bio)conjugation to molecular targeting vectors.[29] Rigidification of a flexible ligand is commonly undertaken for increasing the stability of its

metal complexes. Reducing the conformational freedom of the metal complex generally makes metal release more difficult. Only two different successful approaches to make AAZTA-type ligands more rigid have been reported to date, both involving the formation of bicyclic derivatives.[30-33]

A first approach (#1, Figure 1) is based on the fusion of the C2/C3 positions of the diazepane ring with a five- or six-membered ring, providing "CpAAZTA"[30] and "CyAAZTA",[32][33] respectively. A second approach (#2, Figure 1) leads to the "PIDAZTA" stereoisomers (L1 and L2), bearing a six-membered ring fused on N-1 and C-2 of the diazepane ring.[31]

This article focuses on the design and synthesis of a new rigidified spirobicyclic hexadentate AAZTA derivative ("TRASUTA" = H_3L, 1,7,10-**tri**a**z**a**s**piro[4.6]-**u**ndecane-1,7,10-triacetic acid), with a five-membered ring locking C-6 and N-8 (Figure 1).

Herein, we report also a comprehensive investigation of the coordination behavior of TRASUTA toward an array of selected divalent metal ions spanning a range of sizes and hard–soft features (Ca^{2+}, Mn^{2+}, Zn^{2+}, Cu^{2+}, Pb^{2+}, and Cd^{2+}) and the PET-relevant Ga^{3+} ion, aimed at obtaining useful correlations between the structural features of related meso(bi)cyclic ligands and the thermodynamic and kinetic inertness of the corresponding chelates, to be subsequently translated in the design of improved chelating agents.

Results and Discussion

Synthesis

TRASUTA was synthesized by Prof. Giovanni B. Giovenzana (Dipartimento di Scienze del Farmaco, Università Degli Studi Del Piemonte Orientale). The synthesis of TRASUTA is breafly reported in Scheme 1 and detailed in the Supporting Information.

Acid-base properties of TRASUTA

The protonation constants of the TRASUTA ligand (H_3L), defined by *Eq. 1*, were determined by pH potentiometry and ^1H NMR spectroscopy. The $\log K_i^H$ values of TRASUTA obtained in 0.15 M NaCl or in 0.15 M $NaNO_3$ solutions are listed in Table 1 (standard deviation is shown in parentheses). The $\log K_i^H$ values determined by ^1H NMR are in good agreement with the values determined by pH-potentiometry.

$$K_i^H = \frac{[H_iL]}{[H_{i-1}][H^+]} \quad (i = 1, 2\ldots5) \qquad \textit{Eq. 1}$$

Table 1. Protonation constants of TRASUTA, PIDAZTA (L1, L2), DATA^m, CyAAZTA, and AAZTA (25 °C).

	TRASUTA			L1[31]	L2[31]	DATA^m[38]	CyAAZTA[33]	AAZTA[13]	
I	0.15 M NaCl		0.15 M $NaNO_3$	0.15 M NaCl			0.1 M KCl	0.15 M NaCl	0.1 M KCl
logK_1^H	9.76 (2)	10.30 (3)*	10.06 (2)	11.37	11.67	11.51	10.48	10.06	11.23
logK_2^H	6.15 (2)	6.14 (1)*	6.15 (2)	5.88	5.22	5.15	6.43	6.50	6.53
logK_3^H	4.14 (2)	3.90 (8)*	3.99 (3)	3.56	3.67	3.49	4.23	3.77	3.81
logK_4^H	2.53 (3)	2.50 (9)*	2.08 (4)	2.69	3.02	1.30	2.76	2.33	2.26
logK_5^H					1.28		1.68	1.51	1.61
ΣlogK_ix^H	22.57	22.79*	22.27	23.50	24.85	21.45	25.58	24.16	25.44

*Obtained by ^{1}H NMR studies (0.15 M NaCl, 25 °C).

The comparison of the logK_i^H values of TRASUTA with those of the hexadentate AAZTA derivatives PIDAZTA (L1 and L2) and DATA^m (Table 1) reveals that the main differences are observed for logK_1^H and logK_2^H, ascribed to the protonation of the exo- and one of the endocyclic N-atoms, respectively. The first protonation constant is lower, whereas the second one is slightly higher than the related logK_i^H values of the hexadentate PIDAZTA (L1, L2) and DATA^m. The data in Table 1 also show that the first protonation constant of AAZTA obtained in NaCl solution is lower than that obtained in KCl solution due to the higher stability of the complex with Na^+ compared to K^+.[15][38] The lower affinity of DATA^m and PIDAZTA (L1, L2) toward Na^+, indicated by their higher logK_1^H values compared to AAZTA, is attributed to the lower denticity.[38] The lower logK_1^H of TRASUTA compared to those of the hexadentate analogues L1, L2, and DATA^m indicates a higher Na^+ affinity of the TRASUTA ligand, similar to those of the heptadentate ligands CyAAZTA and AAZTA. Consistent with this hypothesis, the logK_2^H value of TRASUTA is similar to those of CyAAZTA and AAZTA and higher than those of hexadentate DATA^m and PIDAZTA (L1 and L2). The further protonation constants of TRASUTA, taking place on the carboxylic groups, are similar to those of the corresponding logK_i^H values of DATA^m, PIDAZTA (L1, L2), CyAAZTA, and AAZTA. Finally, the ΣlogK_i^H values (Table 1), show that the total basicity of TRASUTA is lower than those of PIDAZTA (L1, L2), CyAAZTA, and AAZTA and higher than that of DATA^m. It is worth noting that the logK_i^H values of TRASUTA measured in 0.15 M NaCl and $NaNO_3$ are practically identical, indicating that chloride and nitrate anions do not affect the protonation behavior of TRASUTA. It is commonly accepted that less basic donor groups bind more weakly to metal ions. On this base, TRASUTA is expected to overcome DATA^m (both ligands having three N- and three carboxylate O-donor atoms) in terms of the stability constants of the corresponding metal complexes. However, the size match between the metal ion and the coordination cage, rigidified by the spiro-fusion, must be taken into account.

Complexation properties of TRASUTA

The stability and protonation constants of M^{n+}—TRASUTA (H_3L) complexes (Ca^{2+}, Mn^{2+}, Zn^{2+}, Pb^{2+}, Cu^{2+}, Cd^{2+}, and Ga^{3+}) are defined by *Eq. 2* and 3.

$$K_{\mathrm{ML}} = \frac{[\mathrm{ML}]}{[\mathrm{M}][\mathrm{L}]} \qquad \textit{Eq. 2}$$

$$K_{\mathrm{MH_iL}} = \frac{[\mathrm{MH_iL})]}{[\mathrm{MH_{i-1}L})][\mathrm{H^+}]} \qquad i = 1, 2 \qquad \textit{Eq. 3}$$

The equilibrium constants, displayed in Table 2, were obtained for TRASUTA (H_3L)−M^{n+} complexes by pH-potentiometric and/or UV–vis spectrophotometric measurements (1:1 metal/ligand concentration ratio). The model including the formation at equilibrium of the species ML, MHL, and MH_2L led to the best fitting. The titrimetric data of H_3L obtained with equimolar concentrations of Zn^{2+} and Cu^{2+} at pH > 7 show the presence of an extra base-consuming step, rationalized with the coordination of OH^- (*Eq. 4*).

$$K_{\mathrm{M(L)OH}} = \frac{[\mathrm{ML}]}{[\mathrm{M(L)OH}][\mathrm{H^+}]} \qquad \textit{Eq. 4}$$

Table 2. Stability and protonation constants of the divalent metal ion complexes with TRASUTA, PIDAZTA (L1, L2), $DATA^m$, CyAAZTA, and AAZTA ligands (25 °C).

	TRASUTA	**L1**[31]	**L2**[31]	**$DATA^m$**[38]	**CyAAZTA**[32][33]	**AAZTA**[15][38]
I		**0.15 M NaCl**			**0.1 M KCl**	**0.15 M NaCl/0.1 M KCl or KNO_3**
CaL	**6.67 (6)**	**7.41**	**8.89**	**8.70**	**12.38**	**11.75/12.76**
CaHL	7.42 (6)	6.92	5.62	5.49	4.00	3.41/3.34
MnL	**8.55 (4)**	**11.32**	**12.40**	**11.43**		**14.19/15.44**
MnHL	5.97 (5)	4.02	3.75	3.36		2.61/2.83
ZnL	**12.82 (5)**	**15.11**	**16.13**	**16.54**	**17.09**	**16.02/18.01**
ZnHL	3.76 (3)	3.25	3.66	1.76	4.17	3.95/3.87
ZnH_2L	3.50 (4)	1.97	2.22		2.83	2.53/2.36
$ZnLH_{-1}$	7.87 (3)	11.18	10.54	11.94	9.43	11.36/11.25
CdL*	**11.48 (3)**					**17.94**[31]
CdHL*	4.22 (3)					3.25[31]

	TRASUTA	L1[31]	L2[31]	DATA^m[38]	CyAAZTA[32][33]	AAZTA[15][38]
I	**0.15 M NaCl**				**0.1 M KCl**	**0.15 M NaCl/0.1 M KCl or KNO_3**
CdH_2L*						2.05[31]
PbL*	**13.41 (2)**					**19.84**[31]
PbHL*	3.71 (4)					3.22[31]
PbH_2L*						2.50[31]
CuL**	**16.22 (2)**	**18.17**	**19.14**	**18.36**	**20.11**	**20.60/22.27**
CuHL	3.97 (1)	2.99	3.78	3.56	4.24	3.86/3.93
CuH_2L	2.44 (2)	1.51	2.07	1.52	3.08	2.43/2.68
$CuLH_{-1}$	9.35 (6)	11.51	10.30	10.88	9.62	10.62/10.79

*25 °C, 0.15 M $NaNO_3$, **By spectrophotometry ($I = [Na^+] + [H^+] = 0.15$ in the samples where $[H^+] \leq 0.15$ M).

The stability and protonation constants of $[Cu(TRASUTA)]^-$ were determined by spectrophotometry. The equilibrium reaction (*Eq. 5*) was studied in the $[H^+]$ range of 0.01–1.0 M (the ionic strength was constant $I = [Na^+] + [H^+] = 0.15$ in the samples where $[H^+] \leq 0.15$ M), where the presence of Cu^{2+}, [CuHL], $[CuH_2L]^+$, and H_xL species was assumed ($x = 4$ and 5; $y = 2$ and 3, *Eq. 5*). Some characteristic absorption spectra are shown in Figure S23.

$$Cu^{2+} + H_xL \rightleftharpoons [Cu(H_{x-y}L)] + yH^+ \qquad \textit{Eq. 5}$$

In the absorption spectra of the Cu^{2+}–TRASUTA system, a decrease in the proton concentration results in the increase of the absorbance values, attributable to the progressive formation of the $[Cu(H_2L)]^+$ and [Cu(HL)] species in the $[H^+] = 0.01 – 1.0$ M range.

In the pH range of 1.7 – 12.0, where $[CuL]^-$, [Cu(HL)], $[Cu(H_2L)]^+$, and $[Cu(L)OH]^{2-}$ species are present, the protonation constants of $[Cu(TRASUTA)]^-$ were determined by pH-potentiometric titrations.

The stability constants of Ca^{2+}, Mn^{2+}, Zn^{2+}, Cd^{2+}, Pb^{2+}, and Cu^{2+} complexes formed with TRASUTA are lower by 2–5 log*K* units than those of the corresponding PIDAZTA, DATA^m, CyAAZTA, and AAZTA complexes (Table 2). A comparison of the $\log K_{ML}$ values of metal complexes formed with the TRASUTA and DATA^m indicates that the stability constants of the DATA^m complexes (Table 2) are generally higher by 2–4 log*K* units than those of the corresponding complexes of TRASUTA. This finding indicates that the potential ligand rigidification induced by incorporation of the pyrrolidine group in the exocyclic pendant arm does not improve the thermodynamic properties of the TRASUTA complexes with respect to the corresponding DATA^m complexes.

The complexes formed with TRASUTA, as for other AAZTA derivatives, can undergo protonation at low pH; pH potentiometry was used to determine the corresponding protonation constants, listed in Table 2. For $[ZnL]^-$ and $[CuL]^-$ complexes, two protonation constants were determined in the pH range of 2.0 – 5.0, presumably associated with the protonation of two weakly coordinated carboxylate groups. For the $[CaL]^-$, $[MnL]^-$, $[PbL]^-$, and $[CdL]^-$ complexes, a single protonation step was found that, according to the higher $\log K_{MHL}$ values, might take place on one of the carboxylate donor atoms.

Equilibrium properties of the Ga^{3+}–TRASUTA system

The stability constants of aminopolycarboxylate or aminopolyphosphonate Ga^{3+} complexes have been commonly measured by pH potentiometry following the competition/decomplexation reactions with OH^- at pH > 6.[13][39–41] To determine the stability and protonation constants of the Ga^{3+}–TRASUTA system, the titration was made at a 1:1 metal:ligand concentration ratio.

The complexation of Ga^{3+} with TRASUTA and the competition between TRASUTA and OH^- for Ga^{3+} are fast enough to follow the processes by direct pH-potentiometric titration. The optimal fitting of data was achieved with a model including the species [GaL], $[Ga(HL)]^+$, and $[Ga(H_2L)]^{2+}$ at equilibrium. The data also indicate the occurrence of an extra base-consuming process at pH > 4.0, rationalized by assuming the coordination of a hydroxide ion – and the concomitant release of a carboxylate group – with the formation of the $[Ga(L)OH]^-$ species according to *Eq. 3* and *Eq. 6*.

$$\mathbf{Ga^{3+} + L^{3-} + OH^- \rightleftharpoons [Ga(L)OH]^-}$$

$$\beta_{Ga(L)OH} = \frac{[Ga(L)OH]}{[Ga^{3+}][L^{3-}][OH^-]} \qquad \textit{Eq. 6}$$

For equilibrium constant calculation, the hydrolysis constants of free Ga^{3+} ions have also been considered ($\log K_{[Ga(OH)]2+} = -2.41$, $\log K_{[Ga(OH)2]+} = -5.92$, $\log K_{[Ga(OH)3]} = -10.63$, and $\log K_{[Ga(OH)4]-} = -16.87$).[42–44] The stability and protonation constants of the [Ga(TRASUTA)] complex are reported in Table 3, along with the corresponding values for [Ga(L1/L2)], $[Ga(DATA^m)]$, $[Ga(CyAAZTA)]^-$, and $[Ga(AAZTA)]^-$. The species distribution diagram for the Ga^{3+}–TRASUTA system, calculated on the base of the equilibrium data, is reported in Figure 2.

Table 3. Stability and protonation constants of Ga^{3+} complexes formed with TRASUTA PIDAZTA (L1, L2), $DATA^m$, CyAAZTA, and AAZTA (25 °C).

	I	GaL	Ga(HL)	$Ga(H_2L)$	Ga(L)OH	$log\beta_{Ga(L)OH}$
[Ga(TRASUTA)]	0.15 M $NaNO_3$	17.2 (1)*	3.53 (2)	2.38 (3)	5.41(2) / 5.28 (3)*	**12.2 (1)***
[Ga(L1)][31]	**0.15 M NaCl**	**18.77**	2.41		4.04	**14.74**
[Ga(L2)][31]		**21.70**	2.51		3.75	**17.94**
[Ga(DATA^m)][38]		**21.54**	2.42		6.25	**15.29**
[Ga(CyAAZTA)][33]	**0.1 M KCl**	**21.39**	4.09	2.32	7.31	**14.08**
[Ga(AAZTA)][13]	**0.15 M NaCl**	**21.15**	3.14	1.14	4.60	**16.57**

*Obtained by ^{71}Ga NMR spectroscopy at 25 °C in 0.15 M $NaNO_3$ solution.

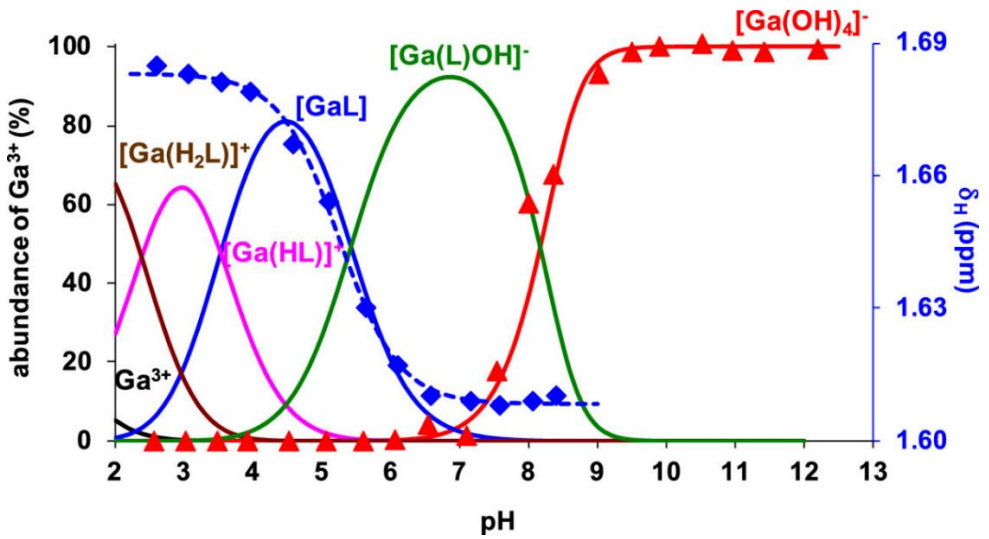

Figure 2. Species distribution in the Ga^{3+}–TRASUTA system. The chemical shift of the overlapping resonances of hydrogen atoms in [Ga(TRASUTA)] (blue ◆, see Scheme 2) and the amount of $[Ga(OH)_4]^-$ (red ▲) were obtained by ^1H and ^{71}Ga NMR spectroscopy ($[Ga^{3+}]$ = [TRASUTA] = 2.0 mM, 9.4 T, 0.15 M NaCl, 298 K).

The stability constant of the [Ga(TRASUTA)] complex ($\log K_{GaL}$ = 17.2, 0.15 M $NaNO_3$, 25 °C) is about 1.5–4.5 log*K* lower than those of [Ga(L1/L2)], [Ga($DATA^m$)], [Ga(CyAAZTA)]$^-$, and [Ga(AAZTA)]$^-$, suggesting that the incorporation of the pyrrolidine group in the exocyclic side chain leads to a slightly less optimal coordination of the Ga^{3+} ion. The cumulative stability constant of the [Ga(TRASUTA)OH]$^-$ species dominating at pH > 4.0 ($\log\beta_{Ga(L)H-1}$ = 12.2, 0.15 M $NaNO_3$, 25 °C) is the lowest among the Ga^{3+} complexes of AAZTA-like chelating agents. The equilibrium data suggest that the presence of the pyrrolidine group may distort the coordination cage of the AAZTA skeleton, hindering the easy achievement of optimal conformations for the coordination of the amine-N and carboxylate-O donor atoms to Ga^{3+}.

The Ga^{3+}–TRASUTA system was also investigated by ^{1}H and ^{71}Ga NMR in the pH range of 2.0–11.0 (Figures 2, S24 and S25). The integral values of the ^{71}Ga-NMR signal of $[Ga(OH)_4]^-$ (δ_{Ga} = 223 ppm, $\nu_{1/2}$ = 100 Hz, Figure S25) were used to calculate the amount of $[Ga(OH)_4]^-$ formed at pH > 7.0 in the decomplexation of [GaL]. The percentages of $[Ga(OH)_4]^-$ species determined by ^{71}Ga NMR spectroscopy and the distribution of the $[Ga(L)OH]^-$ species obtained by ^{1}H NMR spectroscopy (Figure 2) are in good agreement with the values calculated with the equilibrium data obtained from the pH potentiometric studies.

The species distribution diagrams and the ^{1}H and ^{71}Ga NMR spectra (Figures 2, S24 and S25) reveal that the complexation of Ga^{3+} with TRASUTA is complete at pH ≥ 2.0 and the species [Ga(TRASUTA)] dominates in the pH range of 4–5. However, the ^{71}Ga NMR signal in [Ga(TRASUTA)] is broad (Figure S25) and basically undetectable, which can be explained by the fact that ^{71}Ga is quadrupolar, so the line width is strongly dependent on the symmetry of the Ga^{3+} complex, and the Ga^{3+} ion in [Ga(TRASUTA)] is in a less-symmetric coordination environment. The ^{1}H NMR spectra of the Ga^{3+}-TRASUTA system are complex with several overlapping multiplets (Figure S24). The deprotonation of the residual $[Ga(HTRASUTA)]^+$ and the formation of $[Ga(TRASUTA)OH]^-$ at 5 < pH < 7.5 result in a modest upfield shift of all ^{1}H NMR signals. Based on the upfield shift of the ^{1}H NMR signals, it might be assumed that the deprotonation of $[Ga(HTRASUTA)]^+$ might occur at one weakly and/or noncoordinated carboxylate group of TRASUTA. On the other hand, the formation of $[Ga(TRASUTA)OH]^-$ presumably takes place by the replacement of a coordinated COO^- group with hydroxide ions in the coordination sphere. Similar phenomena have been observed in the Ga^{3+}–$DATA^m$ and Ga^{3+}–AAZTA systems.[13][38] At pH > 7.5, competition between TRASUTA and OH^- for Ga^{3+} is confirmed by the formation of $[Ga(OH)_4]^-$ (Figure S25) and free TRASUTA (Figure S24). The slight upfield shift of ^{1}H NMR resonances of free TRASUTA compared to the spectrum in D_2O (Figure S14) is explained by the deprotonation of the HL^{2-} species leading to the fully deprotonated L^{3-} species at pH > 8.2 (Figure S24).

Transmetallation kinetics of the $[Ga(TRASUTA)OH]^-$ complex with Cu^{2+}

The kinetic inertness of metal chelates for *in vivo* applications as radiopharmaceuticals must be assessed to ensure the delivery of the radioisotope as an intact complex to the target tissue. Although Ga^{3+} chelates are usually associated with relatively high thermodynamic stability and kinetic inertness, body fluids contain an excess of competing endogenous species either in the form of powerful ligands (e.g., transferrin) or of metal ions (e.g., Zn^{2+} and Cu^{2+}), potentially leading to the transchelation or transmetalation of the administered Ga^{3+} chelates.[13][15][31][33][38]

The dissociation yield of a Ga^{3+} chelate is a function of the stability constants of the different complexes formed with competing endogenous species. According to the equilibrium data (Table 2), the endogenous metal ions (mainly Cu^{2+} and Zn^{2+}) and transferrin (Tf) may take a part in the exchange reactions of $[Ga(TRASUTA)OH]^-$ which starts to be predominant at pH ≥ 5.5 (Figure 2), with the release of Ga^{3+} and the formation of Ga(Tf) and Ga_2(Tf) complexes ($\log K_{GaTf}$ = 18.88 and $\log K_{Ga2(Tf)}$ = 17.65).[45] The kinetic properties of Ga^{3+} chelates are usually determined under strongly acidic and basic conditions ($[H^+]$ > 1.0 M and $[OH^-]$ > 0.1

M, respectively).[46–48] To approach physiological conditions, the kinetic stability of $[Ga(TRASUTA)OH]^-$ was determined by spectrophotometry, following the exchange reactions of the Ga^{3+} complex with Cu^{2+} in the presence of excess Cu^{2+} and of citrate (Cit) to prevent hydrolysis of free Ga^{3+} and Cu^{2+} ions in the pH range of 6.0–8.0 (Figure S26). The k_d pseudo-first-order rate constants of the transmetalation reaction of $[Ga(TRASUTA)OH]^-$ (Figure S27) indicate that the rate of the exchange reaction is directly proportional to the concentration of OH^-, but it does not depend on $[Cu^{2+}]$ and [Cit] (the increase of $[Cu^{2+}]$ in the presence of constant $[Cit]_{tot}$ results in the formation of more $[Cu(Cit)H_{-1}]^{2-}$ species and the decrease of $[Cit]_{free}$ in the pH range of 6.0–8.0). By taking into account the kinetic data, we can assume that the reactions of $[Ga(TRASUTA)OH]^-$ occur through two parallel dissociation pathways, the spontaneous (k_0) and the OH^- ion-assisted (k_{OH}) dissociation (Scheme 1), followed by a fast reaction between free TRASUTA and the Cu^{2+} ions. The rate and protonation constants of the transmetalation reaction of $[Ga(TRASUTA)OH]^-$ with Cu^{2+} are reported in Table 4 along with those of $[Ga(PIDAZTA)OH]^-$, $[Ga(DATA^m)OH]^-$, $[Ga(CyAAZTA)OH]^{2-}$, and $[Ga(AAZTA)OH]^{2-}$. Experimental details, definitions, and equations used for the evaluation of the kinetic data are summarized in the Supporting Information.

$$Ga^{3+} + TRASUTA \xleftarrow{k_0} [Ga(TRASUTA)OH]^- \xrightarrow[OH^-]{k_{OH}} Ga^{3+} + TRASUTA$$

Scheme 1. Dissociation mechanism of $[Ga(TRASUTA)OH]^-$

Table 4. Rate (k_i), equilibrium constants (K_i), and half-life values ($t_{1/2} = \ln 2/k_d$) for the dissociation of the Ga^{3+} complexes with mesocyclic chelating agents (298 K) in the presence of Cu^{2+}

	TRASUTA	PIDAZTA (4aR*,10aS*)[31] (L1)	PIDAZTA (4aR*,10aR*)[31] (L2)	$DATA^m$[38]	CyAAZTA[33]	AAZTA[13]
I	0.15 M NaCl				0.1 M KCl	
$k_0/(s^{-1})$	$(2.3 \pm 0.1) \times 10^{-4}$	1.4×10^{-4}	4.3×10^{-7}	8.0×10^{-6}	1.7×10^{-5}	3.0×10^{-6}
$k_{OH}\,(M^{-1}\,s^{-1})$	2100 ± 100		0.6	31	68	10
$K_{Ga(L)OH}\,(M^{-1})$	2.4×10^5	1.1×10^4	5.6×10^3	1.8×10^6	2.0×10^7	5.2×10^4
$k_d\,(s^{-1})$ (pH = 7.4)	1.1×10^{-3}	7×10^{-4}	6.5×10^{-7}	1.7×10^{-5}	2.3×10^{-5}	9.2×10^{-6}
$t_{1/2}$ (h) (pH = 7.4)	**0.18**	**0.27**	**295**	**11.2**	**8.5**	**21**

The kinetic data in Table 4 show that the k_0 rate constant of the spontaneous dissociation of $[Ga(TRASUTA)OH]^-$ is about 2, 540, 29, 14, and 77 times higher than those of the $[Ga(L1))OH]^-$, $[Ga(L2)OH]^-$, $[Ga(DATA^m)OH]^-$, $[Ga(CyAAZTA)OH]^{2-}$, and $[Ga(AAZTA)OH]^{2-}$ complexes, respectively. The spontaneous demetalation of the $[Ga(L)OH]^-$ species may take place by the rearrangement of the coordinated donor atoms, triggering the fission of metal ion-donor atom bonds and the concomitant release of the Ga^{3+} ion.

The exchange reaction of $[Ga(TRASUTA)OH]^-$ with Cu^{2+}, that occurs through the OH^--assisted dissociation (k_{OH}) path, has a rate constant (k_{OH}) that is about 3500, 68, 31, and 210 times higher than the corresponding k_{OH} of $[Ga(L2)OH]^-$, $[Ga(DATA^m)OH]^-$, $[Ga(CyAAZTA)OH]^{2-}$, and $[Ga(AAZTA)OH]^{2-}$, respectively. The OH^--assisted dissociation of $[Ga(L)OH]^-$ species presumably takes place through the replacement of another coordinated COO^- donor group by a hydroxide ion, generating the labile $[Ga(L)(OH)_2]^{2-}$ intermediate, the latter rapidly releasing the Ga^{3+} ion, thus explaining the significantly larger rate constant of the OH^--assisted dissociation pathway. By considering the above-mentioned equilibrium and rate constants, the rate and the half-life ($t_{1/2} = \ln 2/k_d$) of the dissociation reactions of $[Ga(TRASUTA)OH]^-$ were calculated close to physiological conditions (pH = 7.4, 25 °C) and compared with the corresponding values of Ga^{3+} complexes formed with L1, L2, $DATA^m$, CyAAZTA, and AAZTA (Table 4). The calculated dissociation half-life of $[Ga(TRASUTA)OH]^-$ at pH = 7.4 is about 1.5, 1640, 62, 47, and 117 times shorter than those of $[Ga(L1)OH]^-$, $[Ga(L2)OH]^-$, $[Ga(DATA^m)OH]^-$, $[Ga(CyAAZTA)OH]^{2-}$, and $[Ga(AAZTA)OH]^{2-}$, respectively, due to the faster spontaneous and OH^--assisted Ga^{3+}-release pathways. The lower $t_{1/2}$ value of $[Ga(TRASUTA)OH]^-$ highlights that the fusion of the pyrrolidine ring with the exocyclic pendant moiety of the AAZTA ligand results in a $[Ga(L)OH]^-$ species with significantly lower inertness under physiological conditions.

Transchelation kinetics of the $[Ga(TRASUTA)OH]^-$ complex with human serum transferrin

Transferrins are well-known Fe^{3+}-transporting proteins. On the base of their biological function, three types of transferrin are identified: serum transferrin (sTf), lactoferrin (LTf), and ovotransferrin (OTf). [49] Transferrins are ~80 kDa single-chain bilobal glycoproteins with one Fe^{3+}-binding site in each lobe. Both sTf and LTf interact strongly with Ga^{3+} ions ($\log K_{GaTf} = 18.88$ and $\log K_{Ga2Tf} = 17.65$) due to the similar coordination behavior of Ga^{3+} and Fe^{3+} ions.[45] Since sTf is generally only partially saturated with Fe^{3+}, it retains a relatively high capacity to bind other metal ions, like Ga^{3+}. The saturation of human sTf with Fe^{3+} was determined by titrating a solution of sTf (8.4×10^{-5} M) with $Ga(NO_3)_3$ ($0 - 3 \times 10^{-4}$ M). The exchange reaction between Ga^{3+} and the coordinated Fe^{3+} ions of sTf is neglected due to the large difference between the stability constants of the corresponding complexes.[45][49] All titrations were made in the presence of $NaHCO_3$ (25 mM) at pH = 7.4 and 298 K. The absorption spectra of the Ga^{3+}–sTf system are shown in Figure S28, and the plot of absorbance as a function of $[Ga^{3+}]/[sTf]$ are shown in Figures S28 and S29. The increase in absorbance at 246 nm as a function of $[Ga^{3+}]/[sTf]$ (Figure S29) reflects the binding of Ga^{3+} at the iron-

binding sites of sTf. The saturation curves reach a plateau at about $[Ga^{3+}]/[sTf] \approx 1.5$. The intersection of absorbance values vs. $[Ga^{3+}]/[sTf]$ in Figure S29 ($[Ga^{3+}]/[sTf] = 1.53$) reveals that the saturation of human sTf with Fe^{3+} is 23.5%, close to the physiological saturation of sTf (ca. 30%).[45]

To investigate the extent and the rate of the competition reactions between TRASUTA and transferrin, the ligand-exchange reaction between the $[Ga(TRASUTA)OH]^-$ complex and sTr was followed by spectrophotometry at the absorption band of the Ga^{3+}–sTf complex in the 240–250 nm range (*Eq. 7* and Figure 3).

$$[Ga(TRASUTA)OH]^- + sTf \rightleftharpoons Ga(sTf) + TRASUTA \qquad Eq.\ 7$$

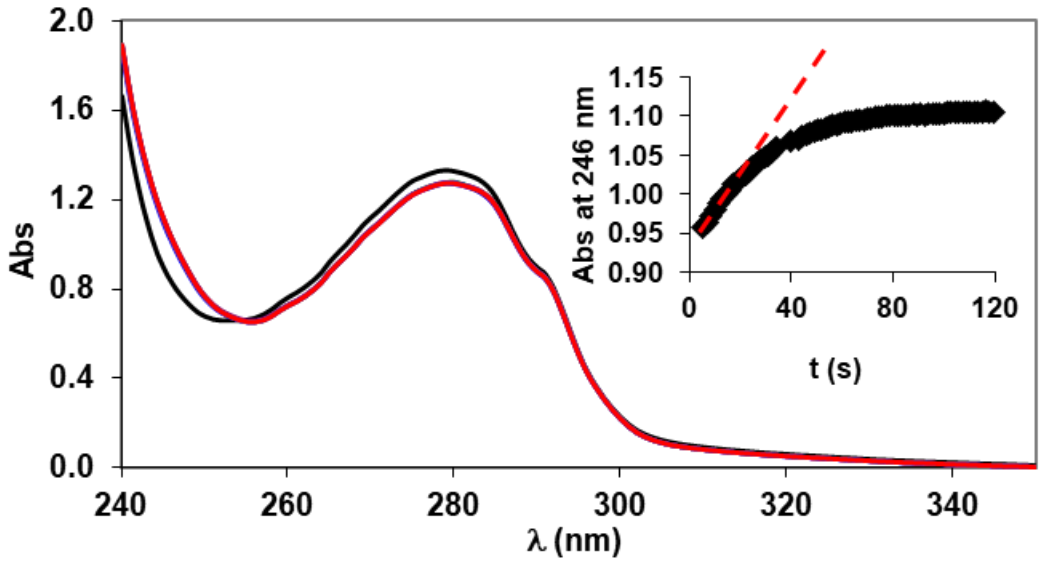

Figure 3. Absorption spectra of the $[Ga(TRASUTA)OH]^-$ − sTf system. $[Ga(TRASUTA)OH]^- = 1.0 \times 10^{-4}$ M, $[sTf] = 2.0 \times 10^{-5}$ M, pH = 7.5, 25.0 mM $NaHCO_3$, 0.15 M NaCl, 298 K, $l = 0.875$ cm.

The rates of the ligand-exchange reaction were studied in the presence of a high excess of $[Ga(TRASUTA)OH]^-$ ($[Ga(TRASUTA)OH]^- = 0.1$ mM, $[sTf] = 20$ μM, pH = 7.5, 25.0 mM $NaHCO_3$, 0.15 M NaCl, 298 K). The rate of the transchelation reactions between $[Ga(AAZTA)OH]^{2-}$, $[Ga(DATA^m)OH]^-$, $[Ga(L1)OH]^-$, and $[Ga(L2)OH]^-$ chelates and human sTf were investigated in the presence of various concentration of Ga^{3+} complexes and human sTf.[13][31][38] In these experiments, Ga^{3+} complex was applied in a large excess with respect to [sTf] to ensure pseudo-first order conditions. These kinetic experiments reveal that the rate of the reactions was independent of [sTf] and increases with the concentration of the Ga^{3+} complex, which can be explained by a rate-determining dissociation of the Ga^{3+} complex, followed by a rapid reaction between the Ga^{3+} and human sTf. Based on analogy, it is assumed that the rate of the transmetalation between $[Ga(TRASUTA)OH]^-$ and human sTf is independent of the [sTf] and increases with the concentration of the Ga^{3+} complex. The ligand-exchange reaction in such a condition can be considered as a pseudo-first-order process and, consequently, the reaction rate is expressed with *Eq. S3*. Keeping in mind the molar absorptivity

of Ga(sTf) (ε_{246} = 14758 cm^{-1} M^{-1}), the rate constants (k_d) were calculated from the slope of the kinetic curve ($\Delta Abs/\Delta t$, inset of Figure 3) with *Eq. 8*. The slope of the kinetic curve has been considered to be up to 40% conversion in order to be sure of the Ga(sTf) complex formation. The rate constant (k_d) obtained at 20 μM human sTf concentration was 2.0×10^{-3} s^{-1}.

$$k_{\mathrm{d}} = \frac{\Delta \mathrm{Abs}}{\mathrm{dt}} \times \frac{1}{\varepsilon_{\mathrm{Ga(sTf)}}} \times \frac{1}{[\mathrm{GaL}]_{\mathrm{t}}} \qquad \textit{Eq. 8}$$

In our experimental conditions, the rate of the formation of the Ga(sTf) adduct by the reaction of the free Ga^{3+} ion and sTf is about 2-3 times faster than that of the transchelation reaction between $[Ga(TRASUTA)OH]^-$ and sTf. The rate-determining step of the transchelation between $[Ga(TRASUTA)OH]^-$ and sTf is the dissociation of the $[Ga(TRASUTA)OH]^-$ complex. The k_d rate constants characterizing the ligand-exchange reaction of $[Ga(TRASUTA)OH]^-$ with sTf ($k_d = 2.0 \times 10^{-3}$ s^{-1}) and the metal-exchange reaction between $[Ga(TRASUTA)OH]^-$ and Cu^{2+} in the presence of citrate ($k_d = 1.1 \times 10^{-3}$ s^{-1}) at pH = 7.4 and 25 °C in 0.1 M NaCl are practically equal. On the base of these results, human sTf has no effect on the rate of dissociation, the latter taking place through the spontaneous and hydroxide-assisted dissociations of $[Ga(TRASUTA)OH]^-$, followed by a fast reaction between the released Ga^{3+} ions and human sTf.

Solution structure of the $[Zn(TRASUTA)]^-$, [Ga(TRASUTA)], $[Ga(TRASUTA)OH]^-$, and $[Pb(TRASUTA)]^-$ complexes

To acquire a deeper insight into the structural properties of $[M(TRASUTA)]^{0,1-}$ complexes, the solution structures of $[Zn(TRASUTA)]^-$, [Ga(TRASUTA)], $[Ga(TRASUTA)OH]^-$, and $[Pb(TRASUTA)]^-$ were investigated by multinuclear NMR spectroscopy. 1D/2D NMR spectra of Zn^{2+}, Ga^{3+}, and Pb^{2+} complexes with TRASUTA obtained at 298–353 K, are shown in Figures 4 and 5, as well as in Figures S30 – S48. The structure and the possible isomerization of $[M(TRASUTA)]^{0,1-}$ with the assignment of selected ^1H and ^{13}C NMR signals are shown in Scheme 2.

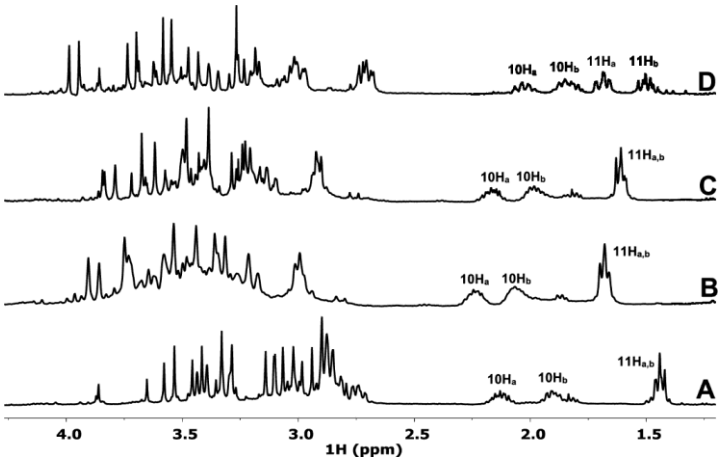

Figure 4. ^1H NMR spectra of $[Zn(TRASUTA)]^-$ (A), $[Ga(TRASUTA)]^-$ (B), $[Ga(TRASUTA)OH]^-$ (C), and $[Pb(TRASUTA)]^-$ (D) ([ML] = 20 mM, pD = 6.46 (ZnL), 4.9 (GaL), and 7.44 (GaLOH) and pH = 7.05, 9.4 T, 298 K, D_2O).

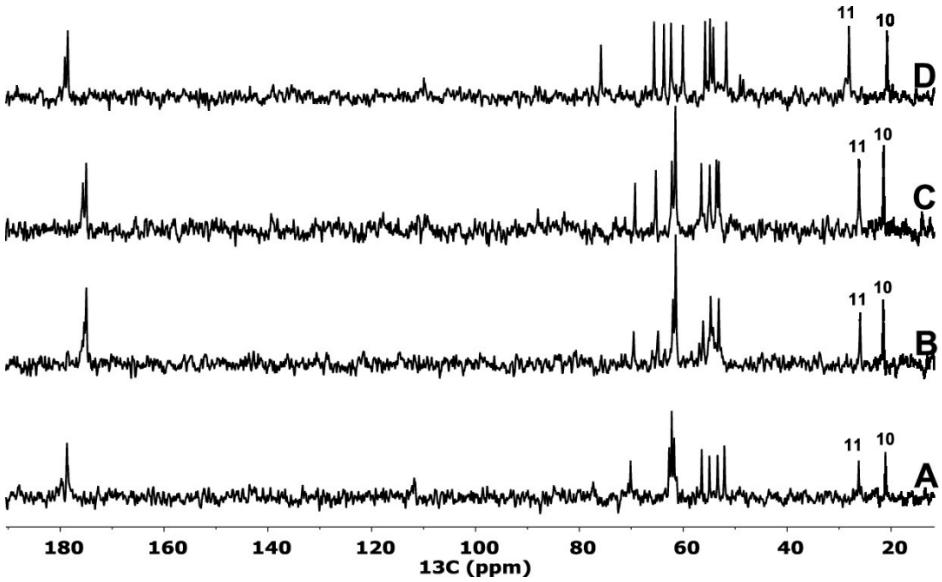

Figure 5. ^{13}C NMR spectra of $[Zn(TRASUTA)]^-$ (**A**), $[Ga(TRASUTA)]^-$ (**B**), $[Ga(TRASUTA)OH]^-$ (**C**), and $[Pb(TRASUTA)]^-$ (**D**) ([ML] = 20 mM, pD = 6.46 (ZnL), 4.9 (GaL), and 7.44 [Ga(L)OH] and pH = 7.05 (PbL), 9.4 T, 298 K, D_2O).

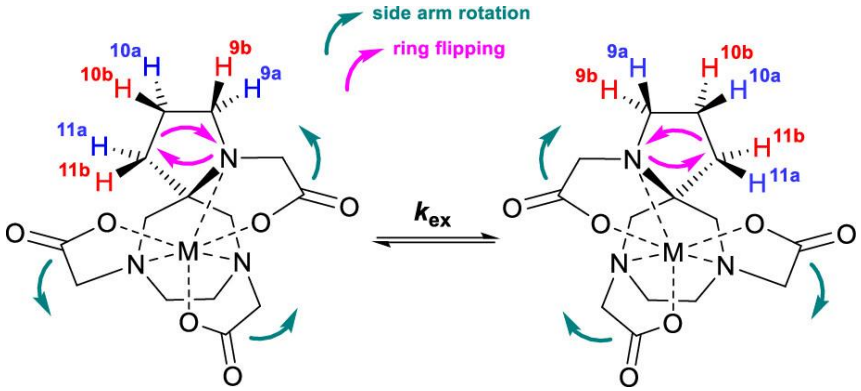

Scheme 2. Structural interconversion process in $[M(TRASUTA)]^{0,1-}$ complexes (M^{n+} = Zn^{2+}, Ga^{3+}, and Pb^{2+}; charges omitted for clarity)

Multinuclear NMR studies of $[Zn(TRASUTA)]^-$, $[Ga(TRASUTA)]^-$, $[Ga(TRASUTA)OH]^-$, and $[Pb(TRASUTA)]^-$ indicate that these complexes have C_1 symmetry in solution. It could be assumed that the structures of $[Zn(TRASUTA)]^-$ and $[Ga(TRASUTA)]^-$ are quite similar to that reported for $[Ga(DATA^m)]$ in the solid state,[38][50] in which the Ga^{3+} ion is coordinated in a distorted octahedral geometry by the N_3O_3 donor set of the chelating agent. The exocyclic N atom, one endocyclic N atom, the exocyclic COO^-, and one of the ring-COO^- atoms bind the Ga^{3+} ion in the equatorial positions. The remaining endocyclic N atom and ring-COO^- occupy the axial positions of the Ga^{3+} ion.[50] Single crystals of $[Ga(DATA^m)]$ contain enantiomeric Ga^{3+} complexes with opposite conformations of the ring and helicities of the acetate pendant arms. Based on the torsion angle values, the conformation of the seven-membered ring is close to that of the twisted-chair found in the single crystal of the free AAZTA ligand.[51] In all the

isomers of [Ga(DATA^m)], two acetate pendant arms have the same helicities, whereas the third acetate arm has the opposite orientation. The ^{1}H NMR spectrum of the [Ga(DATA^m)] complex shows two singlets for the methyl groups (on C6 and N_{exo}), whereas the remaining protons are all diastereotopic, with 5 AB-doublets for C5, C7, and for the side arms methylene protons and an AA'BB' multiplet for the C2–C3 annular ethylene moiety (Figure 1).[50] The ^{1}H NMR studies of the [Ga(DATA^m)]─[Ga(DATA^m)OH]$^-$ systems also reveal that the formation of [Ga(DATA^m)OH]$^-$ in the pH range of 4.0–8.0 results in the upfield shifts of the N_{exo}-CH_3 and C–CH_3 singlets, reasonably attributed to the hydroxide ion replacing one ring-COO^- group in the coordination sphere of the metal ion. In addition, the ^{1}H NMR signals of the [Ga(DATA^m)OH]$^-$ species are broader than those of [Ga(DATA^m)] presumably due to the significantly higher flexibility of the five-coordinated ligand in [Ga(DATA^m)OH]$^-$. The exchange between [Ga(DATA^m)] and [Ga(DATA^m)OH]$^-$ complexes is slow on the NMR time scale at 273 K (the singlets of N_{exo}–CH_3 and C–CH_3 protons of the two species collapse at $T \geq$ 298 K).[38]

The ^{1}H and ^{13}C NMR spectra of the [M(TRASUTA)]$^{0,1-}$ complexes (M^{n+} = Zn^{2+}, Ga^{3+}, and Pb^{2+}) obtained at 298 K (Figure 4, 5, S30, S31, S35, S36, S40, S41, S45 and S46) contain one set of signals, consistent with the presence of a single species in solution. The ^{1}H resonances of the 10 methylene protons in [M(TRASUTA)]$^{0,1-}$ are sharp up to 313 K, with only a modest upfield shift. The ^{1}H and ^{13}C NMR signals of the [Pb(TRASUTA)]$^-$ complex remain practically unchanged up to 343 K (Figures S45 and S46). This can be explained by a strong interaction between the N donor atoms of TRASUTA and soft Pb^{2+}, resulting in the hindrance of the intramolecular rearrangement (Scheme 2). Since the ^{13}C NMR spectra of the [M(TRASUTA)]$^-$ complexes remain unchanged up to 353 K (Figures S31, S36, S41 and S46), it can be assumed that the dissociation of the Zn^{2+}, Ga^{3+}, and Pb^{2+} complexes does not take place with the release of the free TRASUTA ligand. In the VT ^{1}H NMR spectra of [Zn(TRASUTA)]$^-$, [Ga(TRASUTA)]$^-$, and [Ga(TRASUTA)OH]$^-$, the ^{1}H resonances gradually broaden upon increasing the temperature, especially those of the ^{1}H NMR signals of the $10H_{a,b}$ and $11H_{a,b}$ protons of the pyrrolidine group, possibly due to exchange between respective mutual positions in each pair of diastereotopic protons, via a process involving the acetate arm rotation and the ring flipping with inversion of the amino N donor atom (either stepwise or concerted, Scheme 2). Since the ^{1}H and ^{13}C NMR spectra of [Zn(TRASUTA)]$^-$, [Ga(TRASUTA)]$^-$, and [Ga(TRASUTA)OH]$^-$ contain only one set of signals, it can be assumed that the motion of the carboxymethyl pendant arms and the flipping of the N donor atom result in the interconversion between the two enantiomers of each complex. The motion of the carboxymethyl pendant arms and the flipping of the N donor atom might occur simultaneously or in subsequent steps. Similar phenomena have been observed by NMR for the axial─equatorial exchange of the acetate arms in [Zn(EDTA)]$^{2-}$, [Pb(EDTA)]$^{2-}$, [Al(EDTA)]$^-$, [Ga(EDTA)]$^-$, and [In(EDTA)]$^-$ complexes.[52–54] The ^{1}H NMR signals of the $11H_{a,b}$ protons of [Zn(TRASUTA)]$^-$, [Ga(TRASUTA)], and [Ga(TRASUTA)OH]$^-$ were chosen for line-shape analysis, simulating the ^{1}H NMR spectra in the temperature range of 298–353 K (Figures S34, S39 and S44). The NMR spectral parameters for the resonances of $10H_{a,b}$ and $11H_{a,b}$ protons in [Zn(TRASUTA)]$^-$, [Ga(TRASUTA)], [Ga(TRASUTA)OH]$^-$, and [Pb(TRASUTA)]$^-$ complexes are summarized in Table S1. The activation parameters (Table 5)

for the interconversion process in $[Zn(TRASUTA)]^-$, [Ga(TRASUTA)], and $[Ga(TRASUTA)OH]^-$ have been estimated with the Eyring equation by using the k_{ex} rate constant obtained by the line-shape analysis (Figure S49).

Table 5. Rate constants and activation parameters for the interconversion process in the $[Zn(TRASUTA)]^-$, [Ga(TRASUTA)], and $[Ga(TRASUTA)OH]^-$ complexes

	$[Zn(TRASUTA)]^-$	**[Ga(TRASUTA)]**	**$[Ga(TRASUTA)OH]^-$**
$\Delta H^{\ddagger}$/kJ·mol^{-1}	13.6 ± 0.6	14.2 ± 0.9	19 ± 1
$\Delta S^{\ddagger}$/J·mol^{-1}·K^{-1}	–179 ± 2	–176 ± 5	–164 ± 7
$\Delta G^{\ddagger}_{298}$/kJ·mol^{-1}	**66.9**	**66.6**	**68.2**
k_{ex}^{298}/s^{-1}	**11.4**	**12.9**	**6.7**

The activation enthalpy ($\Delta H^{\ddagger}$) and entropy ($\Delta S^{\ddagger}$) values characterizing the interconversion process in $[Zn(TRASUTA)]^-$ and [Ga(TRASUTA)] are very similar and smaller than those of $[Ga(TRASUTA)OH]^-$. These data indicate that the motion of the carboxymethyl pendant arms and the flipping of the N donor atom in the pyrrolidine ring are slower in $[Ga(TRASUTA)OH]^-$ than in $[Zn(TRASUTA)]^-$ and [Ga(TRASUTA)]. Based on this experimental finding, the formation of $[Ga(TRASUTA)OH]^-$ with the substitution of the ring acetate group of [Ga(TRASUTA)] by OH^- resulted in a more favorable accommodation of Ga^{3+} in the coordination environment of TRASUTA. Surprisingly, the activation enthalpy values of the interconversion process are relatively low for all the investigated species. However, the negative and rather large activation entropy values, which can be explained by the formation of a temporarily ordered transition state, indicate that the interconversion process is mainly entropy-controlled.

According to the result of the detailed NMR studies and theoretical calculations, the exchange between axial and equatorial carboxymethyl arms in $[Zn(EDTA)]^{2-}$, $[Pb(EDTA)]^{2-}$, $[Al(EDTA)]^-$, $[Ga(EDTA)]^-$, and $[In(EDTA)]^-$ chelates may take place by two distinct routes: (i) *direct exchange*, which might take place through the complete dissociation of the whole iminodiacetate moiety, followed by the N atom inversion[52][53] and (ii) *indirect rearrangement*, involving several reversible elementary steps and the formation of heptacoordinated intermediates.[54] DFT calculations revealed that in the $[Al(EDTA)]^-$ complex, the complete displacement of the carboxymethyl groups out from the first coordination sphere of the Al^{3+} ion is characterized by very high activation free energy ($\Delta G^{\ddagger}_{298}$ = 125 kJ·mol^{-1}).[54] Conversely, the formation of the heptacoordinated $[Al(EDTA)(H_2O)]^-$ species requires significantly lower activation energy (the binding energy of H_2O in $[Al(EDTA)(H_2O)]^-$ is about 32 kJ·mol^{-1}), and the presence of H_2O in the inner-sphere of Al^{3+} results in the weakening of the Al–O^- and Al–N bonds, which may facilitate the decoordination of the acetate arm and the inversion of the N donor atom.[54] This theory is confirmed by the X-ray structure of $[Zn(CDTA)]^{2-}$ in $[\{Zn(H_2O)_5\}\{Zn(CDTA\}]\cdot H_2O$ and $[Zn(CDTA)(H_2O)]^{2-}$ in

[{Zn(H_2O)$_4$}{Zn(CDTA)(H_2O)}]·4H_2O. In [Zn(CDTA)]$^{2-}$, the Zn^{2+} ion is hexacoordinated with two N and two carboxylate O donor atoms in the equatorial positions, and by two other carboxylate O donor atoms in axial positions which complete the coordination sphere in a distorted octahedral geometry. In [Zn(CDTA)(H_2O)]$^{2-}$, the Zn^{2+} ion is pseudoheptacoordinated in a monocapped trigonal prism geometry. Importantly, the seventh donor atom is a water oxygen and an in-plane carboxylate oxygen donor atom has a distance of 3.135 Å from the Zn^{2+} ion.[55][56]

Based on analogy, it can be assumed that the interconversion process in the [Zn(TRASUTA)]$^-$, [Ga(TRASUTA)], and [Ga(TRASUTA)OH]$^-$ complexes might similarly occur by the formation of the heptacoordinated [M(L)H_2O]$^{0,1-}$ species that might also provide a rational explanation for the large negative value of the activation entropy. In the heptacoordinated [M(L)H_2O]$^{0,1-}$ species, the displacement of the acetate group and the inversion of the N donor atom are likely followed by the substitution of the inner-sphere H_2O with the O^- donor atom of the acetate group.

Conclusions

This chapter reports the thermodynamic properties of the corresponding Ca^{2+}, Mn^{2+}, Zn^{2+}, Cu^{2+}, Pb^{2+}, Cd^{2+}, and Ga^{3+} complexes with a new hexadentate spirobicyclic chelating agent (H_3TRASUTA). For the Ga^{3+} complex, in-depth kinetic investigations were also performed. Finally, the structural features and dynamic behavior of the Zn^{2+}, Pb^{2+}, and Ga^{2+} complexes with TRASUTA were assessed.

TRASUTA is devised to study the effect of the conformational constraint imposed by the spirobicyclic structure on the stability of the corresponding metal chelates. Quite surprisingly, the presence of the spiro-fused bicyclic system does not increase the stability and the inertness of the metal complexes. The thermodynamic stability of selected metal complexes of TRASUTA is slightly lower than the corresponding chelates with the structurally related flexible ligand DATA^m. Moreover, the kinetic inertness of Ga^{3+}–TRASUTA is about 10 times lower than that of Ga^{3+}–DATA^m due to the lability of the [Ga(L)OH]$^-$ species dominating under physiological conditions.

The structural features and the dynamic behavior of the [Zn(TRASUTA)]$^-$, [Pb(TRASUTA)]$^-$, [Ga(TRASUTA)], and [Ga(TRASUTA)OH]$^-$ complexes were determined by multinuclear variable-temperature NMR studies. The dynamics of the Zn^{2+}– and Ga^{3+}–TRASUTA complexes in solution are dominated by a coordination isomerization involving the side arms and the concomitant inversion of the exocyclic nitrogen atom. In [Zn(TRASUTA)]$^-$, [Ga(TRASUTA)], and [Ga(TRASUTA)OH]$^-$, the isomerization processes is entropy controlled, and on the basis of the highly negative entropy values, it is assumed to take place by the formation of heptacoordinated [M(L)H_2O]$^{0,1-}$ intermediates.

The bicyclic system of TRASUTA retains significant dynamics, despite the conformational constraint imposed by the spiro-fusion, resulting in a lower inertness of the corresponding metal complexes. The flexibility of the spiro-fused system must be considered in the design of

mesocyclic chelating agents, in order to obtain metal chelates with improved thermodynamic and kinetic properties.

Experimental Section

Materials

All chemicals employed were of analytical grade. The concentrations of the $CaCl_2$, $MnCl_2$, $Pb(NO_3)_2$, $CdCl_2$, $ZnCl_2$, and $CuCl_2$ stock solutions were determined by complexometric titration against standard Na_2H_2EDTA solutions and xylenol orange ($ZnCl_2$, $Pb(NO_3)_2$, $CdCl_2$), murexide ($CuCl_2$), eriochrome black t ($MnCl_2$), and Patton& Reeder ($CaCl_2$) as indicators. The solution of gallium nitrate was prepared by dissolving Ga_2O_3 (99.9%, Fluka) in 6 M nitric acid, followed by evaporation; the residue was then redissolved in a 0.1 M HNO_3 solution. The final concentration of Ga^{3+} was assessed by adding a known excess of standardized Na_2H_2EDTA and back-titration with a standardized $ZnCl_2$ solution. The acid excess of the $Ga(NO_3)_3$ solution was measured by pH potentiometric titration in the presence of excess Na_2H_2EDTA. TRASUTA ligand was synthesized by Prof. Giovanni B. Giovenzana (Dipartimento di Scienze del Farmaco, Università Degli Studi Del Piemonte Orientale) and it was used without further purification. The concentration and protonation constants of H_3TRASUTA were calculated from the pH-potentiometric titration data obtained with standardized 0.2 M NaOH in the presence and absence of a large (40-fold) excess of $CaCl_2$. No uncommon hazards were noted.

pH-potentiometry

The stability and protonation constants of the complexes were evaluated from the data obtained by pH-potentiometric titrations of the systems with a 1:1 metal-to-ligand concentration ratio (the concentration of the ligand was generally 0.002 M). A *Metrohm 888 Titrando* automatic titration workstation with a *Metrohm-6.0234.110* combined electrode were used for the pH measurements and titrations. pH potentiometric titrations were performed at a constant ionic strength (0.15 M NaCl) in 6 mL samples at 298 K under magnetic stirring and a N_2 atmosphere. The titrations were carried out in the pH range of 1.7–12.0. For the calibration of the pH meter, KH-phthalate (pH = 4.005) and borax (pH = 9.177) buffers were used. The method reported by Irving et al. was employed[34] for the calculation of $[H^+]$ from the measured pH values. A 0.01 M HCl solution was titrated with the standardized NaOH solution at 298 K in the presence of 0.15 M NaCl ionic strength. Differences (A) of the measured (pH_{read}) and calculated ($-\log[H^+]$) pH values were used to evaluate the equilibrium H^+ concentration from the pH values obtained in the titration experiments (A = 0.015). A waiting time of 60 s between two pH measurements was applied. In the equilibrium calculations, the stoichiometric water ionic product (pK_w) was also used for the calculation of $[OH^-]$ values under basic conditions. The V_{NaOH}─pH_{read} data pairs of the HCl-NaOH titration in the pH range 10.5–12.0 were used for the calculation of the pK_w value (pK_w = 13.80).

Spectrophotometry

The stability constants of $[Cu(TRASUTA)]^-$ were calculated by using the spectrophotometric data of the Cu^{2+}─TRASUTA systems at the absorption band of Cu^{2+} complexes (λ = 400–800 nm) in the $[H^+]$ range of 0.01–1.0 M. In these experiments, the concentrations of Cu^{2+} and H_3TRASUTA were identical ($[Cu^{2+}]$ = [L] = 0.0016 M). The adjustment of the H^+ concentration in the samples was performed by the addition of calculated amounts of 3 M HCl. In samples with $[H^+] \leq 0.15$ M, the ionic strength was also maintained constant (I = 0.15 M) by the addition of calculated amounts of NaCl ($I = [Na^+] + [H^+] = 0.15$ M). The samples were stored at 298 K for 1 week. The absorbance of the samples was measured at 615, 635, 655, 675, 695, 715, 735, 755, and 775 nm. The stability and protonation constants of $[Cu(TRASUTA)]^-$ were calculated by using the molar absorptivities of $CuCl_2$, $[Cu(TRASUTA)]^-$, [Cu(HTRASUTA)], and $[Cu(H_2TRASUTA)]^+$, which were determined by recording the Vis spectra of 1.0×10^{-3}, 1.5×10^{-3}, 2.0×10^{-3}, and 2.5×10^{-3} M solutions of $CuCl_2$ and $[Cu(TRASUTA)]^-$ in the pH range of 1.7–7.5. The pH was adjusted by the addition of concentrated NaOH or HCl solutions. The spectrophotometric measurements were carried out with a *PerkinElmer Lambda 365* UV–vis spectrophotometer with 1.0 cm cells at 298 K. The PSEQUAD program was used to calculate the protonation and stability constants.[35]

NMR experiments

^{1}H, ^{13}C, and ^{71}Ga NMR spectra were acquired with a *Bruker Avance III* (9.4 T) spectrometer, equipped with *Bruker Variable Temperature Unit* (BVT), *Bruker Cooling Unit*, and a BB inverse *z* gradient probe (5 mm). The protonation processes of TRASUTA have been investigated by ^{1}H NMR spectroscopy on solutions containing 2.0 mM ligand and 0.15 M NaCl in H_2O (a capillary with D_2O was used for locking). The complexation and protonation processes in the Ga^{3+}─TRASUTA system were followed by ^{1}H and ^{71}Ga NMR spectroscopy at 298 K on solutions containing 2.0 mM aqueous [Ga(TRASUTA)] and 0.15 M NaCl (a capillary with D_2O was used for locking). The pH was adjusted by addition of concentrated NaOH and HCl solutions. The amount of $[Ga(OH)_4]^-$ formed by the decomplexation of [Ga(TRASUTA)] was evaluated by means of the integrals of the ^{71}Ga NMR signal of $[Ga(OH)_4]^-$. The molar integral value of the $[Ga(OH)_4]^-$ complex in the ^{71}Ga NMR spectrum was calculated using 0.001, 0.0015, 0.002, and 0.0025 M solutions of $[Ga(OH)_4]^-$ (pH = 12.5, 0.1 M NaCl, 25 °C). Calculations were carried out using the computer program *Micromath Scientist, version 2.0* (Salt Lake City, UT, USA).

VT ^{1}H and ^{13}C NMR spectra of $[Zn(TRASUTA)]^-$, [Ga(TRASUTA)], $[Ga(TRASUTA)OH]^-$, and $[Pb(TRASUTA)]^-$ were measured on 20 mM samples prepared at pD = 6.46, 4.90, and 7.44 and pH = 7.05 in D_2O and H_2O, respectively. The ^{1}H – ^{1}H (COSY) and ^{1}H – ^{13}C (HSQC) correlation spectra were collected by standard Bruker pulse programs. Band-shape analyses were performed with the DNMR program of the Bruker Topspin software package. Chemical shift, spin–spin coupling constants, intensity, and LB values under chemical-exchange free condition were fixed as input parameters during the fitting procedure. The similarity of the

measured and calculated ^{1}H NMR spectra obtained at different temperature was always greater than 92%.

Transmetallation reactions

The rates and kinetics of the exchange reactions between [Ga(TRASUTA)OH]$^{-}$ and Cu^{2+} in the presence of citrate (Cit^{3-}) were investigated by spectrophotometry on the absorption band of the resulting [Cu(TRASUTA)]$^{-}$ complex (λ = 277 nm). The experiments were carried out with a *PerkinElmer Lambda 365 UV–vis* spectrophotometer in 1.0 cm cells. The concentrations of the [Ga(TRASUTA)OH]$^{-}$ complex and Cu^{2+} were 0.1, and 0.3, and 0.5 mM in order to ensure pseudo-first-order conditions. [Ga(TRASUTA)OH]$^{-}$ was prepared just before the experiments by adjusting the pH of the [Ga(TRASUTA)] solution to the required value with concentrated NaOH and HCl solutions. The transmetalation reactions were studied in the presence of large excess of citrate ($[Cit]_t$ = 1.0 mM) to prevent the hydrolysis of Ga^{3+} and Cu^{2+} ions. The exchange rates were determined in the pH range of 6.0–8.0. Constant pH values were maintained by HEPES buffers (0.01 M). Pseudo-first-order rate constants (k_d) were calculated by fitting the absorbance data to *Eq. 9*.

$$A_t = (A_0 - A_e)e^{-k_d t} + A_e \qquad \textit{Eq. 9}$$

where A_t, A_0, and A_p are the absorbance values at time t, at the start of the reaction and at equilibrium, respectively. Calculations of the kinetic parameters were made by the fitting of the absorbance–time and relaxation rate–time data pairs to *Eq. 9* with the *Micromath Scientist* computer program (version 2.0, Salt Lake City, UT, USA).

Transchelation Reactions

The ligand-exchange reaction of [Ga(TRASUTA)OH]$^{-}$ with human serum transferrin (*Sigma*, partially Fe^{3+} saturated) has been followed by spectrophotometry, monitoring the formation of a Ga-transferrin complex at 246 nm and pH = 7.4 with a *PerkinElmer Lambda 365 UV–vis* spectrophotometer. The concentration of the human serum transferrin solution was determined by measuring the absorbance at 280 nm with the use of the molar absorptivity published in the literature (ε_{280} = 91200 cm^{-1} M^{-1}).[36] The temperature was maintained at 298 K, and 0.15 M NaCl ionic strength and 0.025 M $NaHCO_3$ of the samples were kept constant. The Fe^{3+} saturation of the human serum transferrin was determined by spectrophotometric titration of the transferrin solution with $Ga(NO_3)_3$ monitored in the wavelength range of 240–250 nm ([sTf] = 8.4 × 10^{-5} M, [Ga^{3+}] = 0–3 × 10^{-4} M, 0.025 M $NaHCO_3$, and 0.15 M NaCl, pH = 7.4, 25 °C, l = 1 mm).

References

(1) Hart, J. R. Ethylenediaminetetraacetic Acid and Related Chelating Agents. *Ullmann's Encyclopedia of Industrial Chemistry*; Wiley-VCH, 2011.

(2) Wahsner, J.; Gale, E. M.; Rodríguez-Rodríguez, A.; Caravan, P. Chemistry of MRI Contrast Agents: Current Challenges and New Frontiers. *Chem. Rev.* **2019**, *119* (2), 957–1057.

(3) Wadas, T. J.; Wong, E. H.; Weisman, G. R.; Anderson, C. J. Coordinating Radiometals of Copper, Gallium, Indium, Yttrium, and Zirconium for PET and SPECT Imaging of Disease. *Chem. Rev.* **2010**, *110* (5), 2858–2902.

(4) Kostelnik, T. I.; Orvig, C. Radioactive Main Group and Rare Earth Metals for Imaging and Therapy. *Chem. Rev.* **2019**, *119* (2), 902–956.

(5) Boros, E.; Packard, A. B. Radioactive Transition Metals for Imaging and Therapy. *Chem. Rev.* **2019**, *119* (2), 870–901.

(6) Grieve, M. L.; Paterson, B. M. The Evolving Coordination Chemistry of Radiometals for Targeted Alpha Therapy. *Aust. J. Chem.* **2021**, *75* (2), 65–88.

(7) Crisponi, G.; Nurchi, V. M. Chapter 2─Chelating Agents as Therapeutic Compounds─Basic Principles. *Chelation Therapy in the Treatment of Metal Intoxication*; Aaseth, J., Crisponi, G., Andersen, O., Eds.; Academic Press: Boston, 2016; pp 35–61.

(8) Delgado, R.; Félix, V.; Lima, L. M. P.; Price, D. W. Metal Complexes of Cyclen and Cyclam Derivatives Useful for Medical Applications: A Discussion Based on Thermodynamic Stability Constants and Structural Data. *Dalton Trans.* **2007**, *26*, 2734–2745.

(9) Jackson, J. A.; Hungnes, I. N.; Ma, M. T.; Rivas, C. Bioconjugates of Chelators with Peptides and Proteins in Nuclear Medicine: Historical Importance, Current Innovations, and Future Challenges. *Bioconjugate Chem.* **2020**, *31* (3), 483–491.

(10) Waldron, B. P.; Parker, D.; Burchardt, C.; Yufit, D. S.; Zimny, M.; Roesch, F. Structure and Stability of Hexadentate Complexes of Ligands Based on AAZTA for Efficient PET Labelling with Gallium-68. *Chem. Commun.* **2013**, *49* (6), 579–581.

(11) Aime, S.; Calabi, L.; Cavallotti, C.; Gianolio, E.; Giovenzana, G. B.; Losi, P.; Maiocchi, A.; Palmisano, G.; Sisti, M. [Gd-AAZTA]-: A New Structural Entry for an Improved Generation of MRI Contrast Agents. *Inorg. Chem.* **2004**, *43* (24), 7588–7590.

(12) Nagy, G.; Szikra, D.; Trencsényi, G.; Fekete, A.; Garai, I.; Giani, A. M.; Negri, R.; Masciocchi, N.; Maiocchi, A.; Uggeri, F.; Tóth, I.; Aime, S.; Giovenzana, G. B.; Baranyai, Z. AAZTA: An Ideal Chelating Agent for the Development of ^{44}Sc PET Imaging Agents. *Angew. Chem. Int. Ed. Engl.* **2017**, *56* (8), 2118–2122.

(13) Baranyai, Z.; Uggeri, F.; Maiocchi, A.; Giovenzana, G. B.; Cavallotti, C.; Takács, A.; Tóth, I.; Bányai, I.; Bényei, A.; Brucher, E.; Aime, S. Equilibrium, Kinetic and Structural

Studies of AAZTA Complexes with Ga^{3+}, In^{3+} and Cu^{2+}. *European Journal of Inorganic Chemistry* **2013**, *2013*(1), 147–162.

(14) Kálmán, F. K.; Tircsó, G. Kinetic Inertness of the Mn^{2+} Complexes Formed with AAZTA and Some Open-Chain EDTA Derivatives. *Inorg. Chem.* **2012**, *51* (19), 10065–10067.

(15) Baranyai, Z.; Uggeri, F.; Giovenzana, G. B.; Bényei, A.; Brücher, E.; Aime, S. Equilibrium and Kinetic Properties of the Lanthanoids(III) and Various Divalent Metal Complexes of the Heptadentate Ligand AAZTA. *Chem. Eur. J.* **2009**, *15* (7), 1696–1705.

(16) Giovenzana, G. B.; Lattuada, L.; Negri, R. Recent Advances in Bifunctional Paramagnetic Chelates for MRI. *Isr. J. Chem.* **2017**, *57* (9), 825–832.

(17) Lattuada, L.; Barge, A.; Cravotto, G.; Giovenzana, G. B.; Tei, L. The Synthesis and Application of Polyamino Polycarboxylic Bifunctional Chelating Agents. *Chem. Soc. Rev.* **2011**, *40* (5), 3019–3049.

(18) Ghiani, S.; Hawala, I.; Szikra, D.; Trencsényi, G.; Baranyai, Z.; Nagy, G.; Vágner, A.; Stefania, R.; Pandey, S.; Maiocchi, A. Synthesis, Radiolabeling, and Pre-Clinical Evaluation of [^{44}Sc]Sc-AAZTA Conjugate PSMA Inhibitor, a New Tracer for High-Efficiency Imaging of Prostate Cancer. *Eur. J. Nucl. Med. Mol. Imaging* **2021**, *48* (8), 2351–2362.

(19) Greifenstein, L.; Grus, T.; Nagel, J.; Sinnes, J. P.; Rösch, F. Synthesis and Labeling of a Squaric Acid Containing PSMA-Inhibitor Coupled to AAZTA5 for Versatile Labeling with ^{44}Sc, ^{64}Cu, ^{68}Ga and ^{177}Lu. *Appl. Radiat. Isot.* **2020**, *156*, 108867.

(20) Orteca, G.; Sinnes, J.-P.; Rubagotti, S.; Iori, M.; Capponi, P. C.; Piel, M.; Rösch, F.; Ferrari, E.; Asti, M. Gallium-68 and Scandium-44 Labelled Radiotracers Based on Curcumin Structure Linked to Bifunctional Chelators: Synthesis and Characterization of Potential PET Radiotracers. *J. Inorg. Biochem.* **2020**, *204*, 110954.

(21) Sinnes, J.-P.; Nagel, J.; Rösch, F. AAZTA5/AAZTA5-TOC: Synthesis and Radiochemical Evaluation with 68Ga, 44Sc and 177Lu. *EJNMMI radiopharm. chem.* **2019**, *4* (1), 18.

(22) Pfister, J.; Summer, D.; Rangger, C.; Petrik, M.; von Guggenberg, E.; Minazzi, P.; Giovenzana, G. B.; Aloj, L.; Decristoforo, C. Influence of a Novel, Versatile Bifunctional Chelator on Theranostic Properties of a Minigastrin Analogue. *EJNMMI Res.* **2015**, *5* (1), 74.

(23) Manzoni, L.; Belvisi, L.; Arosio, D.; Bartolomeo, M. P.; Bianchi, A.; Brioschi, C.; Buonsanti, F.; Cabella, C.; Casagrande, C.; Civera, M.; De Matteo, M.; Fugazza, L.; Lattuada, L.; Maisano, F.; Miragoli, L.; Neira, C.; Pilkington-Miksa, M.; Scolastico, C. Synthesis of Gd and ^{68}Ga Complexes in Conjugation with a Conformationally Optimized RGD Sequence as Potential MRI and PET Tumor-Imaging Probes. *Chem. Med. Chem.* **2012**, *7* (6), 1084–1093.

(24) Gianolio, E.; Cabella, C.; Colombo Serra, S.; Valbusa, G.; Arena, F.; Maiocchi, A.; Miragoli, L.; Tedoldi, F.; Uggeri, F.; Visigalli, M.; Bardini, P.; Aime, S. B25716/1: A Novel Albumin-Binding Gd-AAZTA MRI Contrast Agent with Improved Properties in Tumor Imaging. *J. Biol. Inorg. Chem.* **2014**, *19* (4–5), 715–726.

(25) Liu, X.; Chen, L.; Li, Y.; He, C.; Zhang, X.; Zhou, H.; Bao, G.; Zhu, X.; Xiang, G.; Ma, X. Synthesis of Novel DOTA-/AAZTA-Based Bifunctional Chelators: Solution Thermodynamics, Peptidomimetic Conjugation, and Radiopharmaceutical Evaluation. *Biomed. Pharmacother.* **2023**, *165*, 115114.

(26) Hennrich, U.; Benešová, M. [^{68}Ga]Ga-DOTA-TOC: The First FDA-Approved ^{68}Ga-Radiopharmaceutical for PET Imaging. *Pharmaceuticals* **2020**, *13* (3), 38.

(27) Viswanathan, R.; Ballal, S.; Yadav, M. P.; Roesch, F.; Sheokand, P.; Satapathy, S.; Tripathi, M.; Agarwal, S.; Moon, E. S.; Bal, C. Head-to-Head Comparison of SSTR Antagonist [^{68}Ga]Ga-DATA^{5m}-LM4 with SSTR Agonist [^{68}Ga]Ga-DOTANOC PET/CT in Patients with Well Differentiated Gastroenteropancreatic Neuroendocrine Tumors: A Prospective Imaging Study. *Pharmaceuticals* **2024**, *17* (3), 275.

(28) Greifenstein, L.; Kramer, C. S.; Moon, E. S.; Rösch, F.; Klega, A.; Landvogt, C.; Müller, C.; Baum, R. P. From Automated Synthesis to *In Vivo* Application in Multiple Types of Cancer − Clinical Results with [^{68}Ga]Ga-DATA5m.SA.FAPi. *Pharmaceuticals* **2022**, *15* (8), 1000.

(29) Travagin, F.; Lattuada, L.; Giovenzana, G. B. AAZTA: The Rise of Mesocyclic Chelating Agents for Metal Coordination in Medicine. *Coord. Chem. Rev.* **2021**, *438*, 213908–213931.

(30) Martinelli, J.; Martorana, E.; Tei, L. Synthesis of a Rigidified Bicyclic AAZTA-like Ligand and Relaxometric Characterization of Its GdIII Complex. *Tetrahedron Lett.* **2020**, *61* (48), 152573.

(31) Farkas, E.; Vágner, A.; Negri, R.; Lattuada, L.; Tóth, I.; Colombo, V.; Esteban-Gómez, D.; Platas-Iglesias, C.; Notni, J.; Baranyai, Z.; Giovenzana, G. B. PIDAZTA: Structurally Constrained Chelators for the Efficient Formation of Stable Gallium-68 Complexes at Physiological pH. *Chem. Eur. J.* **2019**, *25* (45), 10698–10709.

(32) Vágner, A.; Gianolio, E.; Aime, S.; Maiocchi, A.; Tóth, I.; Baranyai, Z.; Tei, L. High Kinetic Inertness of a Bis-Hydrated Gd-Complex with a Constrained AAZTA-like Ligand. *Chem. Commun.* **2016**, *52* (75), 11235–11238.

(33) Vágner, A.; D'Alessandria, C.; Gambino, G.; Schwaiger, M.; Aime, S.; Maiocchi, A.; Tóth, I.; Baranyai, Z.; Tei, L. A Rigidified AAZTA-like Ligand as Efficient Chelator for ^{68}Ga Radiopharmaceuticals. *ChemistrySelect* **2016**, *1* (2), 163–171.

(34) Irving, H. M.; Miles, M. G.; Pettit, L. D. A Study of Some Problems in Determining the Stoicheiometric Proton Dissociation Constants of Complexes by Potentiometric Titrations Using a Glass Electrode. *Anal. Chim. Acta* **1967**, *38*, 475–488.

(35) Zekany, L.; Nagypal, I. PSEQUAD. *Computational Methods for the Determination of Formation Constants*; Leggett, D. J., Ed.; Modern Inorganic Chemistry; Springer US: Boston, MA, **1985**; pp 291–353.

(36) Oe, H.; Takahashi, N.; Doi, E.; Hirose, M. Effects of Anion Binding on the Conformations of the Two Domains of Ovotransferrin. *J. Biochem.* **1989**, *106* (5), 858–863.

(37) Noble, A.; Anderson, J. C. Nitro-Mannich Reaction. *Chem. Rev.* **2013**, *113* (5), 2887–2939.

(38) Farkas, E.; Nagel, J.; Waldron, B. P.; Parker, D.; Tóth, I.; Brücher, E.; Rösch, F.; Baranyai, Z. Equilibrium, Kinetic and Structural Properties of Gallium(III) and Some Divalent Metal Complexes Formed with the New $DATA^{m}$ and $DATA^{5m}$ Ligands. *Chem. Eur. J.* **2017**, *23* (43), 10358–10371.

(39) Motekaitis, R. J.; Martell, A. E. Gallium Complexes of Multidentate Ligands in Aqueous Solution. *Inorg. Chem.* **1980**, *19* (6), 1646–1651.

(40) Delgado, R.; Sun, Y.; Motekaitis, R. J.; Martell, A. E. Stabilities of Divalent and Trivalent Metal Ion Complexes of Macrocyclic Triazatriacetic Acids. *Inorg. Chem.* **1993**, *32* (15), 3320–3326.

(41) Geraldes, C. F. G. C.; Delgado, R.; Urbano, A. M.; Costa, J.; Jasanada, F.; Nepveu, F. Complexes of Ga^{3+} and In^{3+} with the N,N″-Bis(Butylamide) Derivative of Diethylenetriaminepentaacetic Acid: Stability Constants and Nuclear Magnetic Resonance Studies in Aqueous Solution. *J. Chem. Soc., Dalton Trans.* **1995**, (3), 327–335.

(42) Baes, C. F.; Mesmer, R. E. *The Hydrolysis of Cations*; Wiley: New York, **1976**.

(43) Akitt, J. W.; Kettle, D. ^{71}Ga Nuclear Magnetic Resonance Investigation of Aqueous Gallium(III) and Its Hydrolysis. *Magn. Reson. Chem.* **1989**, *27* (4), 377–379.

(44) Tóth, I.; Zékány, L.; Brücher, E. Equilibrium Study of the Systems of Aluminium(III), Gallium(III) and Indium(III) with Mercaptoacetate, 3-Mercaptopropionate and 2-Mercaptobenzoate. *Polyhedron* **1984**, *3* (7), 871–877.

(45) Harris, W. R.; Pecoraro, V. L. Thermodynamic Binding Constants for Gallium Transferrin. *Biochemistry* **1983**, *22* (2), 292–299.

(46) Kubíček, V.; Havlíčková, J.; Kotek, J.; Tircsó, G.; Hermann, P.; Tóth, É.; Lukeš, I. Gallium(III) Complexes of DOTA and DOTA-Monoamide: Kinetic and Thermodynamic Studies. *Inorg. Chem.* **2010**, *49* (23), 10960–10969.

(47) Šimeček, J.; Schulz, M.; Notni, J.; Plutnar, J.; Kubíček, V.; Havlíčková, J.; Hermann, P. Complexation of Metal Ions with TRAP (1,4,7-Triazacyclononane Phosphinic Acid) Ligands and 1,4,7-Triazacyclononane-1,4,7-Triacetic Acid: Phosphinate-Containing Ligands as Unique Chelators for Trivalent Gallium. *Inorg. Chem.* **2012**, *51* (1), 577–590.

(48) Broan, C. J.; Cox, J. P. L.; Craig, A. S.; Kataky, R.; Parker, D.; Harrison, A.; Randall, A. M.; Ferguson, G. Structure and Solution Stability of Indium and Gallium Complexes of 1,4,7-Triazacyclononanetriacetate and of Yttrium Complexes of 1,4,7,10-Tetraazacyclododecanetetraacetate and Related Ligands: Kinetically Stable Complexes for Use in Imaging and Radioimmunotherapy. X-Ray Molecular Structure of the Indium and Gallium Complexes of 1,4,7-Triazacyclononane-1,4,7-Triacetic Acid. *J. Chem. Soc., Perkin Trans. 2* **1991**, *2* (1), 87–99.

(49) Li, Y.; Liu, B.; Ge, Z.; Yang, B. Spectroscopic Analysis of the Interaction between Gallium(III) and Apoovotransferrin. *J. Photochem. Photobiol.,* **2008**, *91* (2–3), 137–142.

(50) Parker, D.; Waldron, B. P.; Yufit, D. S. Crystallographic and Solution NMR Structural Analyses of Four Hexacoordinated Gallium(Iii) Complexes Based on Ligands Derived from 6-Amino-Perhydro-1,4-Diazepine. *Dalton Trans.* **2013**, *42* (22), 8001–8008.

(51) Aime, S.; Bombieri, G.; Cavallotti, C.; Giovenzana, G. B.; Imperio, D.; Marchini, N. An unusual gadolinium ten-coordinated dimeric complex in the series of MRI contrast agents: Na[Gd(H2O)AAZTA]·3H2O. *Inorg. Chim. Acta* **2008**, *361* (5), 1534–1541.

(52) Day, R. J.; Reilley, C. N. Nuclear Magnetic Resonance Studies of Metal Aminopolycarboxylate Complexes. Lability of Individual Metal Ligand Bonds in (Ethylenedinitrilo)-Tetraacetate Complexes. *Anal. Chem.* **1964**, *36* (6), 1073–1076.

(53) Day, R. J.; Reilley, C. N. Nuclear Magnetic Resonance Studies of Metal Aminopolycarboxylate Complexes. Structural Effects on the Labilities of Individual Metal-Ligand Bonds. *Anal. Chem.* **1965**, *37* (11), 1326–1333.

(54) Jószai, R.; Purgel, M.; Pápai, I.; Wakita, H.; Tóth, I. Multinuclear NMR and DFT Studies of the Structure and Fluxionality for MIII-Ethylenediamine-Tetraacetate Complexes (M(EDTA)-, M = Al, Ga and In) in Solution. *J. Mol. Liq.* **2007**, *131–132*, 72–80.

(55) Polynova, T. N.; Filippova, T. V.; Porai-Koshits, M. A.; Belskii, V. K.; Sobolev, A. N.; Myachina, L. I. *Koord. Khim.* **1988**, *14*, 405.

(56) Fuertes, A.; Miravitlles, C.; Escriva, E.; Coronado, E.; Beltran, D.; Padel, L. J. Bimetallic compounds of trans-cyclohexane-1,2-diamine-NNN′N′-tetra-acetate (cdta). Part 3. Structural and magnetic characterization of the dinuclear $[M(OH_2)_5]$ $[M'(cdta)]\cdot H_2O$ (M,M′= Ni,Ni; Mn,Ni; Mn,Cu; Co,Ni; or Co,Cu) and the tetranuclear $[M(OH_2)_4]$ $[M'(cdta)(OH_2)]\cdot 4H_2O$ (M,M′= Zn,Zn; Zn–Co; Co,Co; or Mn,Co) complexes. *J. Chem. Soc., Dalton Trans.* **1989**, 863.

Supplementary information

I. Synthesis of TRASUTA

I.1 Materials and methods

Solvents and starting materials were purchased from Merck or TCI and used without further purification. All aqueous solutions were prepared from ultrapure laboratory grade water (18 MΩ· cm) obtained from Millipore/MilliQ purification system. ^{1}H and ^{13}C NMR spectra were recorded at 300 and 75 MHz, respectively on a Jeol Eclipse ECP300 spectrometer. Chemical shifts are reported in ppm with the protic impurities of the deuterated solvent as the internal reference. Mass spectra were obtained with a Thermo Finnigan LCQ-Deca XP-

PLUS ion trap spectrometer equipped with an electrospray source. High resolution mass spectra were registered on a ThermoScientific Q-Exactive Plus spectrometer. TLC were performed with silica gel (MN Kieselgel 60F254) and visualized by UV or sprayed with Dragendorff reagent or alkaline $KMnO_4$. Column chromatography was carried out on Macherey-Nagel Silica gel 60 (0.063–0.200 mm).

I.2 Synthetic procedures

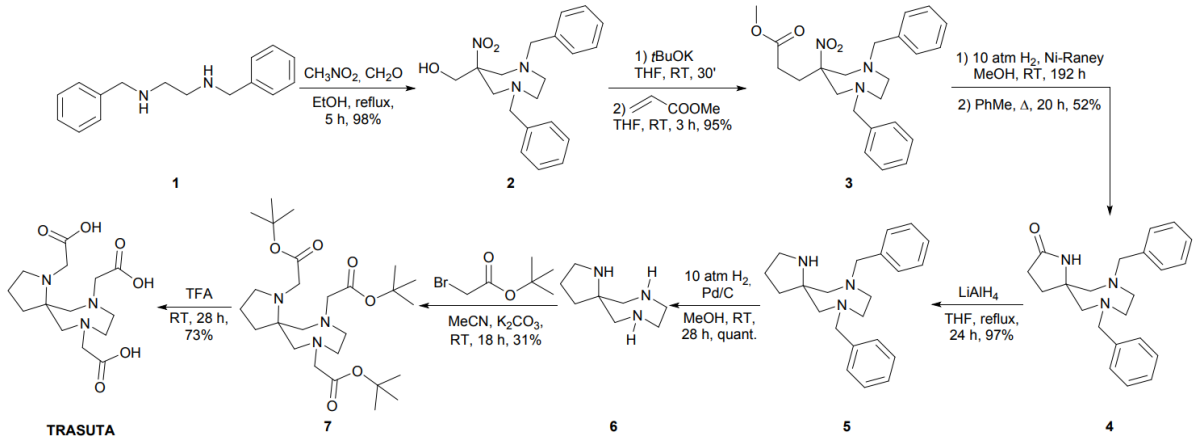

Figure S1. Synthesis of TRASUTA.

1,4-Dibenzyl-6-nitro-1,4-diazepan-6-yl)methanol (2): *N*,*N*'-dibenzylethylendiamine (**1**) (freshly obtained by extraction with DCM of a NaOH aqueous solution of *N*,*N*'-dibenzylethylendiamine diacetate, 29.6 g, 82.0 mmol) and nitromethane (4.4 mL, 82.0 mmol) were dissolved in ethanol (100 mL). Formaldehyde solution (37 wt. % in water, 26.6 g, 354 mmol) was added in small portions under stirring, and the suspension was heated to reflux for 5 h. The reaction mixture was evaporated *in vacuo*, and the crude product was dissolved in basified water ($NaHCO_3$) and extracted three times with ethyl acetate. The organic phase was then dried over Na_2CO_3 and Na_2SO_4, filtered and evaporated. The waxy residue was purified on silica gel chromatography column (DCM) to give compound **2** as a brown oil (28.6 g, 98 %).

^{1}H NMR (300 MHz, $CDCl_3$, 298 K) δ 7.39 – 7.30 (m, 10H), 3.77 – 3.63 (m, 6H), 3.54 (d, J = 14.4 Hz, 2H), 3.06 (d, J = 14.3 Hz, 2H), 2.73 – 2.58 (m, 4H), 2.33 (br s, 1H) ppm.

^{13}C NMR (75 MHz, $CDCl_3$, 298 K) δ 138.8 (C), 129.0 (CH), 128.4 (CH), 127.4 (CH), 94.7 (C), 65.7 (CH_2), 63.7 (CH_2), 59.0 (CH_2), 58.6 (CH_2) ppm.

MS (ESI^+): *m*/z = 356.20 (100%, $[M+H]^+$). Calc. for $C_{20}H_{25}N_3O_3$: 355.19.

Methyl 3-(1,4-dibenzyl-6-nitro-1,4-diazepan-6-yl)propanoate (3): Compound **2** (20 g, 56,3 mmol) was dissolved in anhydrous THF (148 mL), potassium *tert*-butoxide (9.47 g, 84.4 mmol) was added and the suspension was stirred at RT for 30 min. Methyl acrylate (10 mL, 113 mmol) was then added, and the mixture was stirred at room temperature for 3 hours. After that 1 mL of methanol and an aqueous solution saturated with $NaHCO_3$ were added to the reaction. The organic layer was separated, and the aqueous phase was extracted 2 times with ethyl acetate. The organic phase was dried over Na_2SO_4 and Na_2CO_3 and evaporated to dryness. The product was purified by column chromatography (Pet/EtOAc 9:1) to give compound **3** as a yellow oil (22.0 g, 95 %).

^{1}H NMR (300 MHz, $CDCl_3$, 298 K) δ 7.30 – 7.23 (m, 10H), 3.75 – 3.48 (m, 9H), 2.94 (d, J = 14.2 Hz, 2H), 2.68 – 2.54 (m, 4H), 1.97 – 1.91 (m, 2H), 1.76 – 1.70 (m, 2H) ppm.

^{13}C NMR (75 MHz, $CDCl_3$, 298 K) δ 138.6 (C), 128.6 (CH), 127.9 (CH), 126.8 (CH), 93.3 (C), 63.3 (CH_2), 60.9 (CH_2), 58.1 (CH_2), 51.0 (CH_3), 30.8 (CH_2), 27.1 (CH_2) ppm.

MS (ESI^+): *m*/z = 412.52 (100%, $[M+H]^+$). Calc. for $C_{23}H_{29}N_3O_4$: 411.22.

7,10-Dibenzyl-1,7,10-triazaspiro[4.6]undecan-2-one (4) Procedure 4A.: A 50 % Raney-Nickel slurry (26 g) was washed with methanol and centrifuged 3 times to completely remove water. This Raney-Nickel slurry in methanol was added to a solution of compound **3** (13.0 g, 31.6 mmol) and methanol (120 mL total). The mixture was stirred at RT under hydrogen atmosphere (10 bar) for 192 h then filtered through Celite and dried under vacuum. The residue was taken up in toluene, refluxed for 20 h and then evaporated to dryness. The product was purified by crystallization from ethyl acetate, vacuum filtration and washing with Et_2O to give compound **4** as white needles (5.76 g, 52 %).

Procedure 4B.: A mixture of compound **3** (1.00 g, 2.43 mmol), iron powder (0.679 g, 12.2 mmol) and acetic acid (5 mL) was refluxed for 20 h. Then the mixture was quenched in water, basified with $NaHCO_3$ and treated with 5 g of EDTA disodium. The resulting suspension was filtered and extracted three times with ethyl acetate. The organic phase was dried (Na_2SO_4, Na_2CO_3) and the solvent was removed under vacuum. The product is purified by crystallization from ethyl acetate, vacuum filtration and washing with Et_2O to give **4** as white needles (0.419 g, 49 %).

Procedure 4C.: A mixture of compound **3** (11.7 g, 28.5 mmol), zinc powder (9.31 g, 142 mmol) and acetic acid (70 mL) was refluxed for 20 h. Then the mixture was quenched in water, basified with $NaHCO_3$ and treated with 14 g of EDTA disodium. The resulting suspension was filtered and extracted three times with ethyl acetate. The organic phase was dried (Na_2SO_4, Na_2CO_3) and the solvent was removed under vacuum. The product was purified by crystallization from ethyl acetate, vacuum filtration and washing with Et_2O to give **4** as white needles (1.53 g, 15 %).

^{1}H NMR (300 MHz, $CDCl_3$, 298 K) δ 7.32 – 7.26 (m, 10H), 3.71 – 3.45 (m, 4H), 2.84 – 2.57 (m, 6H), 2.21 (s, 1H), 2.04 (t, J = 7.9 Hz, 2H), 1.57 (t, J = 7.8 Hz, 2H) ppm.

^{13}C NMR (75 MHz, $CDCl_3$, 298 K) δ 176.5 (C), 129.0 (C), 128.5 (CH), 127.4 (CH), 65.3 (CH_2), 64.0 (CH_2), 62.3 (C), 58.5 (CH_2), 29.9 (CH_2), 29.2 (CH_2) ppm.

MS (ESI^+): *m*/z = 350.37 (100%, $[M+H]^+$). Calc. for $C_{22}H_{27}N_3O$: 349.22.

HRMS (ESI^+): *m*/z = 350.22240 (100%, $[M+H]^+$). Calc. for $C_{22}H_{27}N_3O$: 349.21541.

7,10-Dibenzyl-1,7,10-triazaspiro[4.6]undecane (5): Compound **4** (4.10 g, 11.7 mmol) was dissolved in dry THF (20 mL) and $LiAlH_4$ (1.34 g, 35.2 mmol) was added portionwise under nitrogen atmosphere. The reaction was stirred and refluxed under a nitrogen atmosphere for 24 h. The mixture was quenched with NaOH 50% aqueous solution and then with water and the organic phase was separated. The aqueous layer was extracted three times with DCM, the organic phases were collected and dried under vacuum. The product was purified by column chromatography (EtOAc/MeOH 95:5 – 8:2) to yield compound **5** as a yellow oil (3.80 g, 97 %).

^{1}H NMR (300 MHz, $CDCl_3$, 298 K) δ 1H NMR (300 MHz, $CDCl_3$, 298K) δ 7.33 – 7.19 (m, 10H), 6.19 (s, 1H), 3.64 (d, J = 13.1 Hz, 2H), 3.58 (d, J = 13.1 Hz, 2H), 2.81 – 2.50 (m, 8H), 1.95 – 1.91 (m, 4H), 1.51 – 1.47 (m, 2H) ppm.

^{13}C NMR (75 MHz, $CDCl_3$, 298 K) δ 139.9 (C), 129.2 (CH), 128.3 (CH), 127.1 (CH), 65.0 (CH_2), 64.8 (C), 63.7 (CH_2), 57.6 (CH_2), 44.5 (CH_2), 35.4 (CH_2), 24.0 (CH_2) ppm.

MS (ESI^+): m/z = 336.26 (100%, $[M+H]^+$). Calc. for $C_{22}H_{29}N_3$: 335.24.

HRMS (ESI^+): m/z = 336.24296 (100%, $[M+H]^+$). Calc. for $C_{22}H_{29}N_3$: 335.23615.

1,7,10-Triazaspiro[4.6]undecane (6): Compound **5** (3.60 g, 10,7 mmol) was dissolved in methanol, Pd/C (5 %, 3.60 g) was added, and the mixture was stirred under hydrogen atmosphere (10 atm) at room temperature for 28 h. The reaction mixture was than filtered through Celite and evaporated to give compound **6** as a brown oil (1.67 g, quant.).

^{1}H NMR (300 MHz, D_2O, 298 K) δ 3.56 (t, J = 7.0 Hz, 2H), 3.47 – 3.34 (m, 6H), 2.32 – 2.11 (m, 6H) ppm.

^{13}C NMR (75 MHz, D_2O, 298 K) δ 58.2 (C), 54.7 (CH_2), 48.7 (CH_2), 45.5 (CH_2), 33.9 (CH_2), 23.2 (CH_2).

MS (ESI^+): m/z = 156.15 (100%, $[M+H]^+$). Calc. for $C_8H_{17}N_3$: 155.14.

HRMS (ESI^+): m/z = 156.14949 (100%, $[M+H]^+$). Calc. for $C_8H_{17}N_3$: 155.14225.

Tri-tert-Butyl 2,2',2''-(1,7,10-triazaspiro[4.6]undecane-1,7,10-triyl)triacetate (7), Procedure 7A.: Compound **6** (0.542 g, 3.49 mmol) was dissolved in acetonitrile (10 mL) and potassium carbonate (1.93 g, 14.0 mmol) was added. *tert*- Butyl bromoacetate (1.7 mL, 11.5 mmol) was added dropwise over 1 h at 0°C and then the reaction was stirred at room temperature for 18 h. The mixture was filtered, evaporated and purified by column chromatography (Pet/EtOAc 9:1 – 85:15) to give compound **7** as a yellow oil (0.531 g, 31 %).

Procedure 7B.: Compound **6** (0.513 g, 3.30 mmol) was dissolved in *N*,*N*-dimethylacetamide (2 mL) and potassium carbonate (2.74 g, 0.0198 mmol) was added. The *tert*-butyl bromoacetate (2.9 mL, 0.0198 mmol) was added dropwise over 1 h at 0°C and then the reaction was stirred at room temperature for 18 h. Then water was added to the mixture which was extracted three times with ether, dried (Na_2SO_4, Na_2CO_3), evaporated under vacuum and purified by column chromatography (Pet/EtOAc 9:1 – 85:15) to give compound **7** as a yellow oil (0.477 g, 29 %).

Procedure 7C.: Compound **6** (0.500 g, 3.22 mmol) was dissolved in acetonitrile (10 mL) and potassium carbonate (1.93 g, 14.0 mmol) and sodium sulfate (1.83 g, 13.0 mmol) were added. *tert*-Butyl bromoacetate (1.7 mL, 11.5 mmol) was added dropwise over 3 h at 0 °C and then the reaction was stirred at room temperature for 18 h. The mixture was filtered, evaporated and purified by column chromatography (Pet/EtOAc 9:1 – 85:15) to give compound **7** as a yellow oil (0.485 g, 30 %).

^{1}H NMR (300 MHz, $CDCl_3$, 298 K) δ 3.37 (s, 2H), 3.04 (br s, 4H), 2.69 – 2.44 (m, 10H), 1.49 (br s, 2H), 1.35 – 1.24 (m, 29H) ppm.

^{13}C NMR (75 MHz, $CDCl_3$, 298 K) δ 171.5 (C), 170.3 (C), 80.4 (C), 79.8 (C), 65.3 (C), 63.4 (CH_2), 61.9 (CH_2), 58.8 (CH_2), 51.9 (CH_2), 51.0 (CH_2), 35.9 (CH_2), 27.9 (CH_3), 27.8 (CH_3), 21.7 (CH_2) ppm.

MS (ESI$^+$): *m*/z = 498.35 (100%, $[M+H]^+$). Calc. for $C_{26}H_{47}N_3O_6$: 497.35.

HRMS (ESI$^+$): *m*/z = 498.35368 (100%, $[M+H]^+$). Calc. for $C_{26}H_{47}N_3O_6$: 497.34649.

1,7,10-Triazaspiro[4.6]undecane-1,7,10-triacetic acid (TRASUTA): Compound **7** (0.262 g, 0.526 mmol) was dissolved in trifluoroacetic acid (2 mL) and left at room temperature for 28 h. The mixture was dried under vacuum and the residue was dissolved in methanol, precipitated with ether, centrifugated and the supernatant was poured away. This procedure was repeated three times. The product was purified by chromatography on XAD (eluent: H_2O) to give compound TRASUTA as an off-white solid (0.126 g, 73 %).

^{1}H NMR (300 MHz, D_2O, 298 K) δ 4.32 (s, 2H), 3.94 (br s, 4H), 3.83 – 3.64 (m, 6H), 3.53 – 3.36 (m, 6H), 2.24 (s, 2H) ppm.

^{13}C NMR (75 MHz, D_2O, 298 K) δ 172.7 (C), 170.7 (C), 74.7 (C), 59.1 (CH_2), 59.0 (CH_2), 58.6 (CH_2), 54.3 (CH_2), 54.1 (CH_2), 33.9 (CH_2), 21.2 (CH_2) ppm.

MS (ESI^+): *m*/z = 330.17 (100%, $[M+H]^+$). Calc. for $C_{14}H_{23}N_3O_6$: 329.16.

HRMS (ESI^+): *m*/z = 330.16595 (100%, $[M+H]^+$). Calc. for $C_{14}H_{23}N_3O_6$: 329.15869.

I. NMR spectra

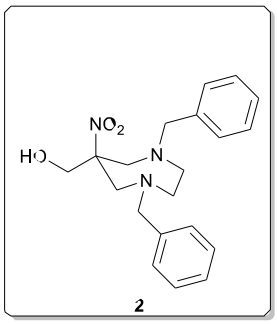

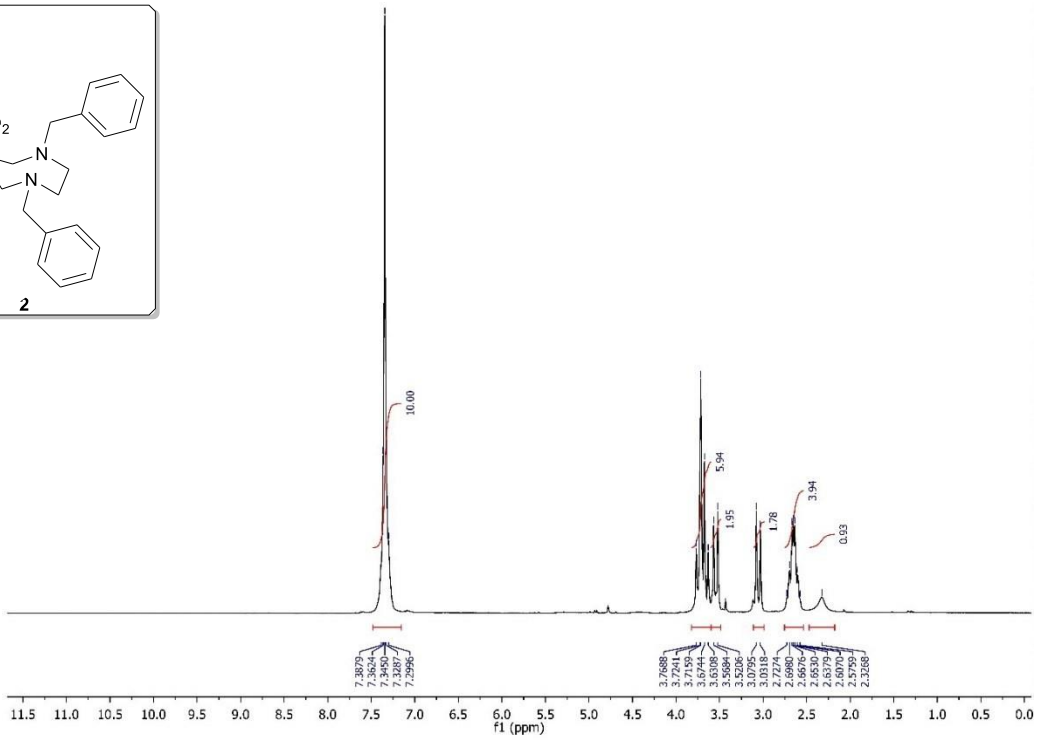

Figure S2. ^{1}H NMR spectrum of compound **2** (7 T, $CDCl_3$, 298 K)

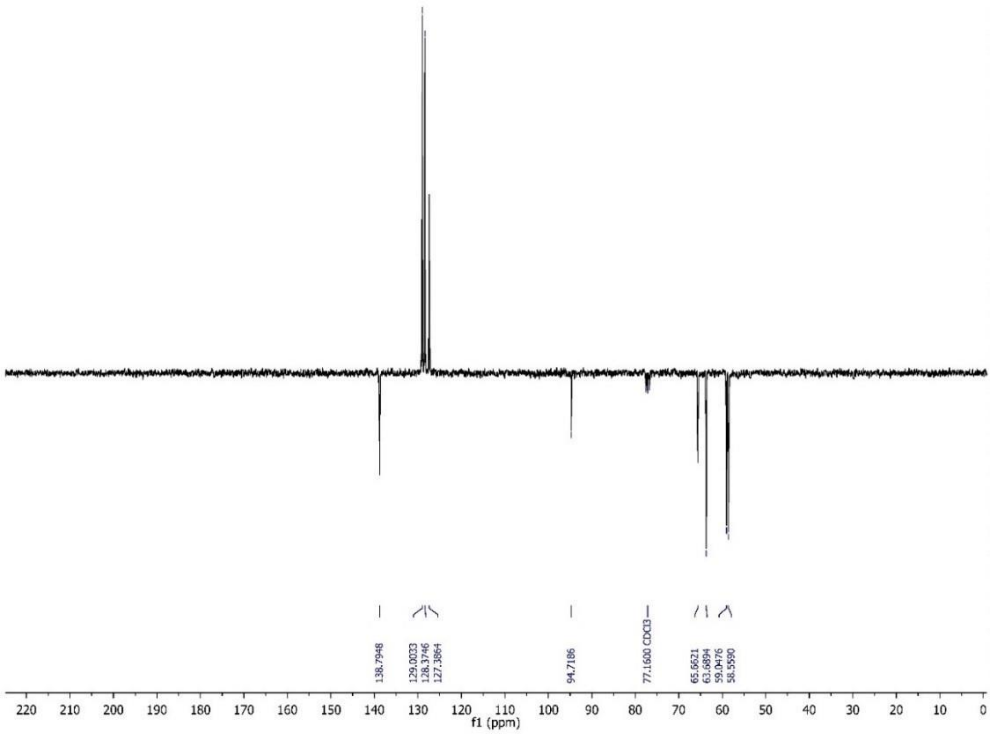

Figure S3. ^{13}C APT NMR spectrum of compound **2** (7 T, $CDCl_3$, 298 K)

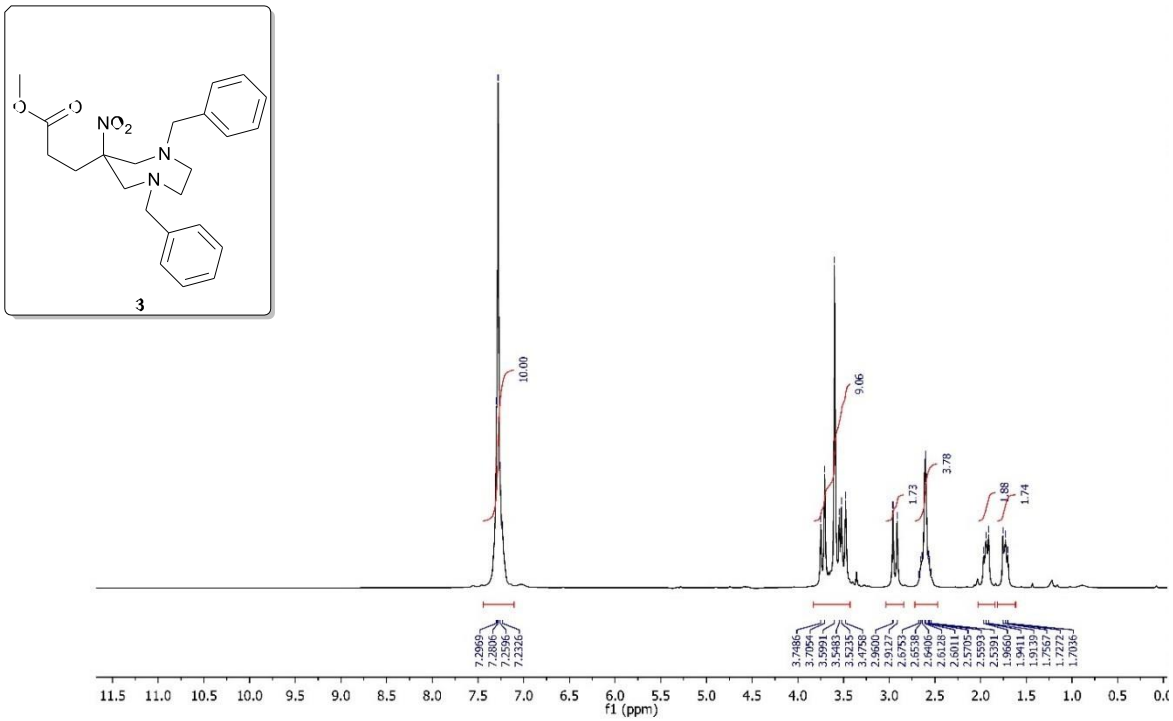

Figure S4. ^{1}H NMR spectrum of compound **3** (7 T, $CDCl_3$, 298 K).

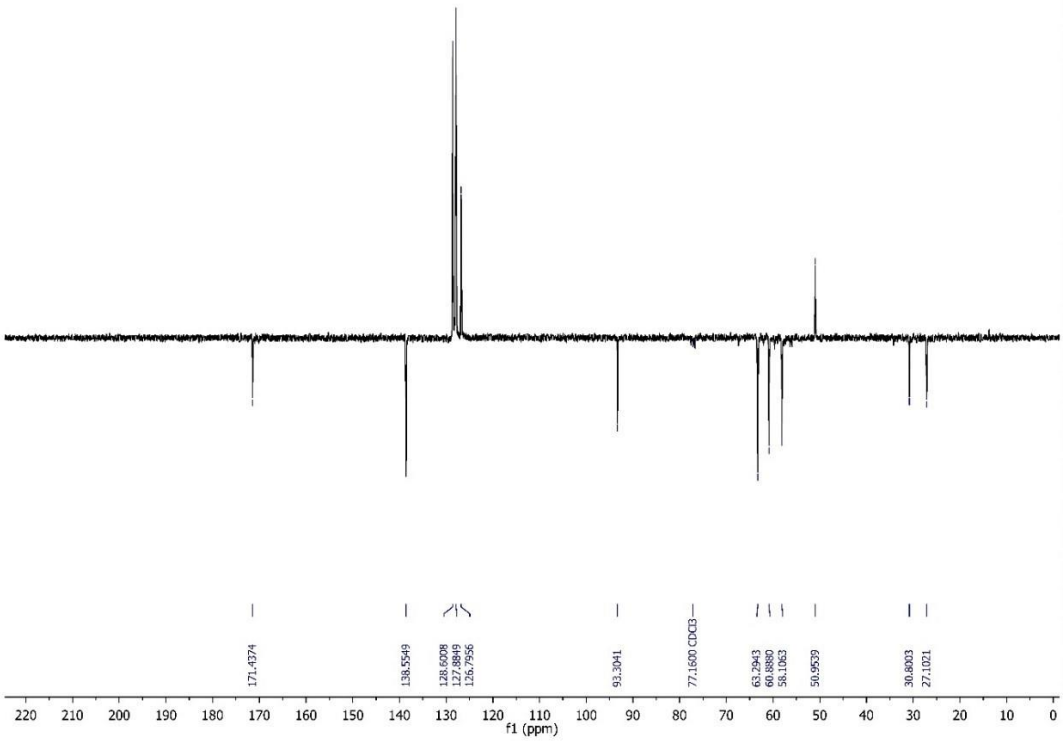

Figure S5. ^{13}C APT NMR spectrum of compound **3** (7 T, $CDCl_3$, 298 K).

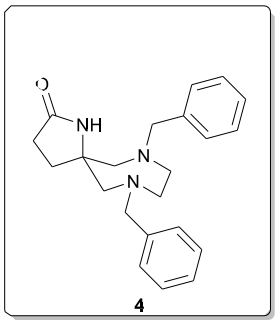

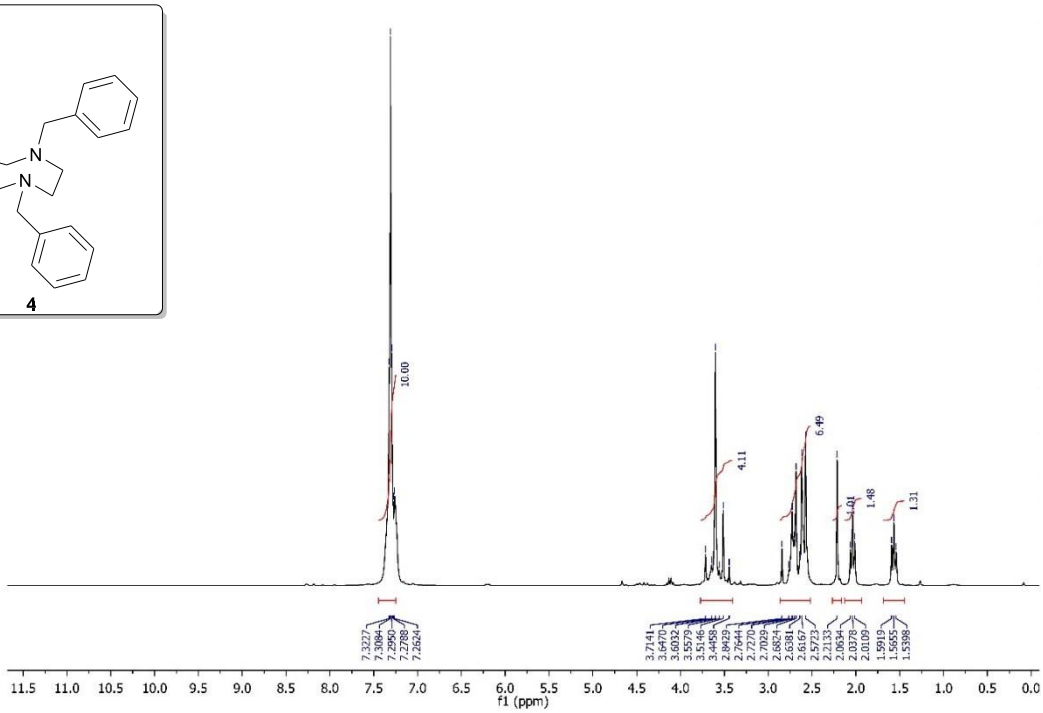

Figure S6. ^{1}H NMR spectrum of compound **4** (7 T, $CDCl_3$, 298 K).

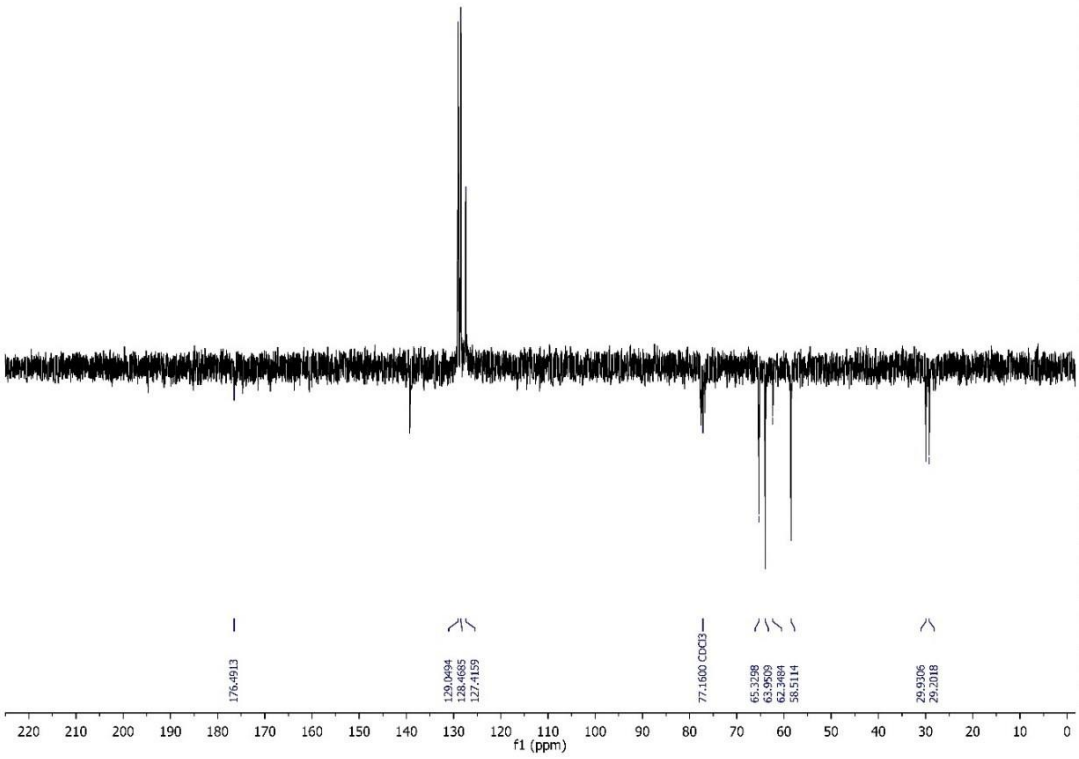

Figure S7. ^{13}C APT NMR spectrum of compound **4** (7 T, $CDCl_3$, 298 K).

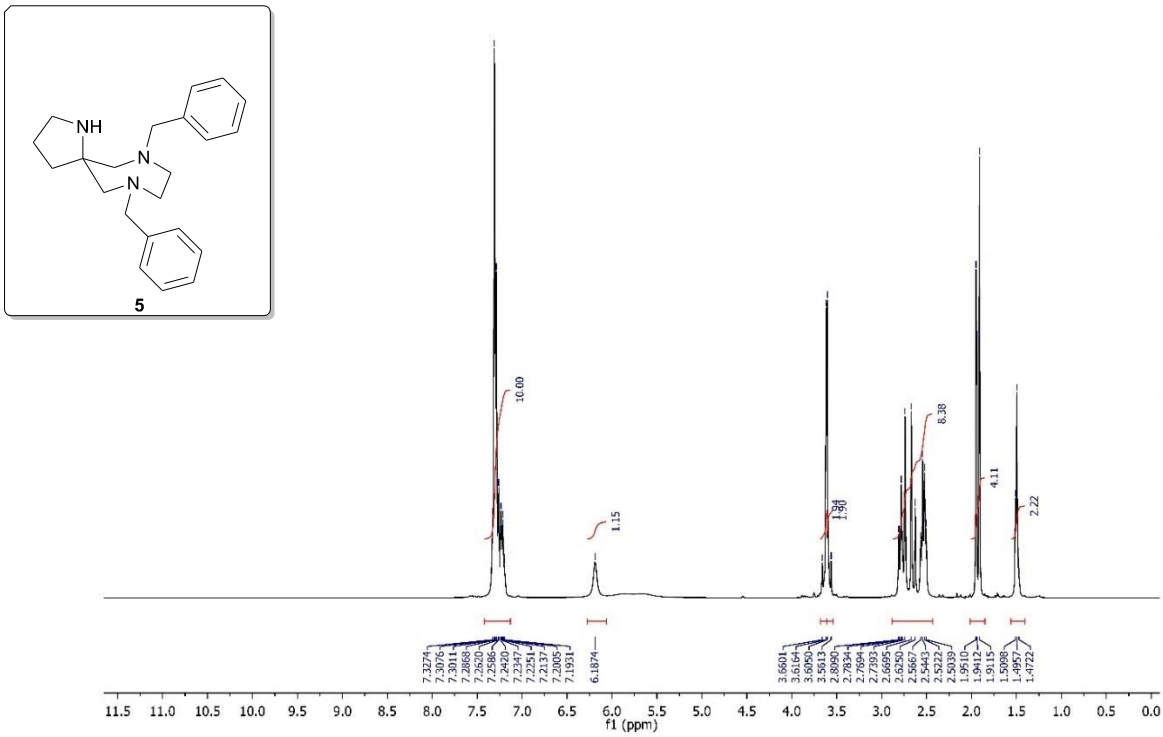

Figure S8. ^{1}H NMR spectrum of compound **5** (7 T, $CDCl_3$, 298 K).

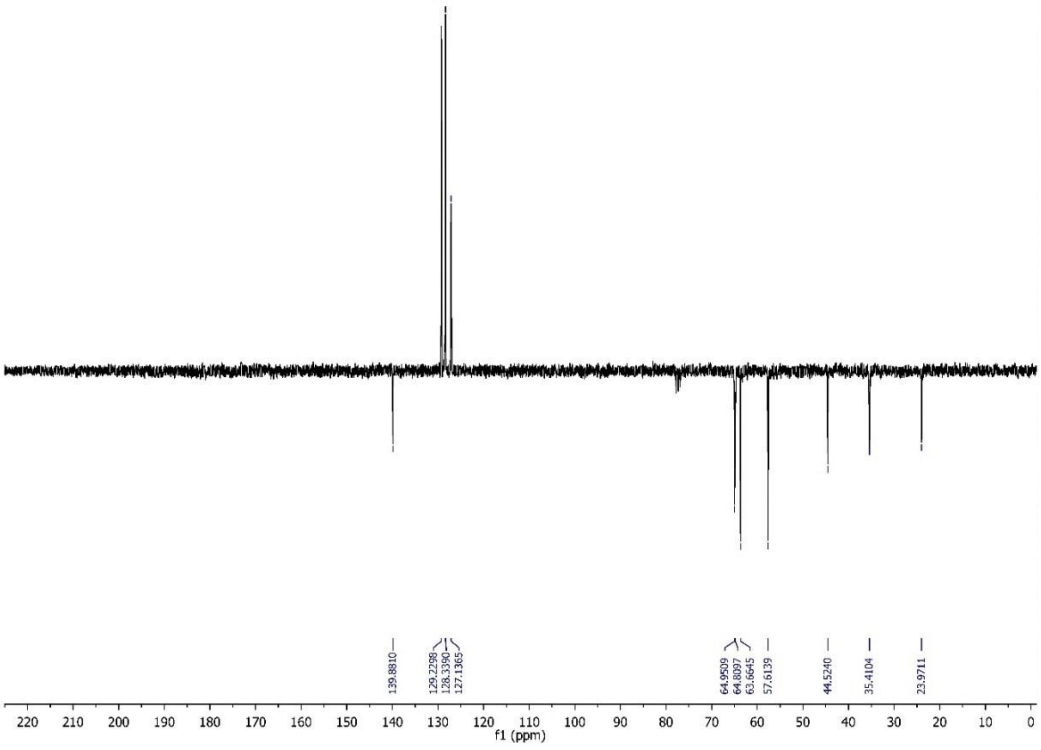

Figure S9. ^{13}C APT NMR spectrum of compound 5 (7 T, $CDCl_3$, 298 K).

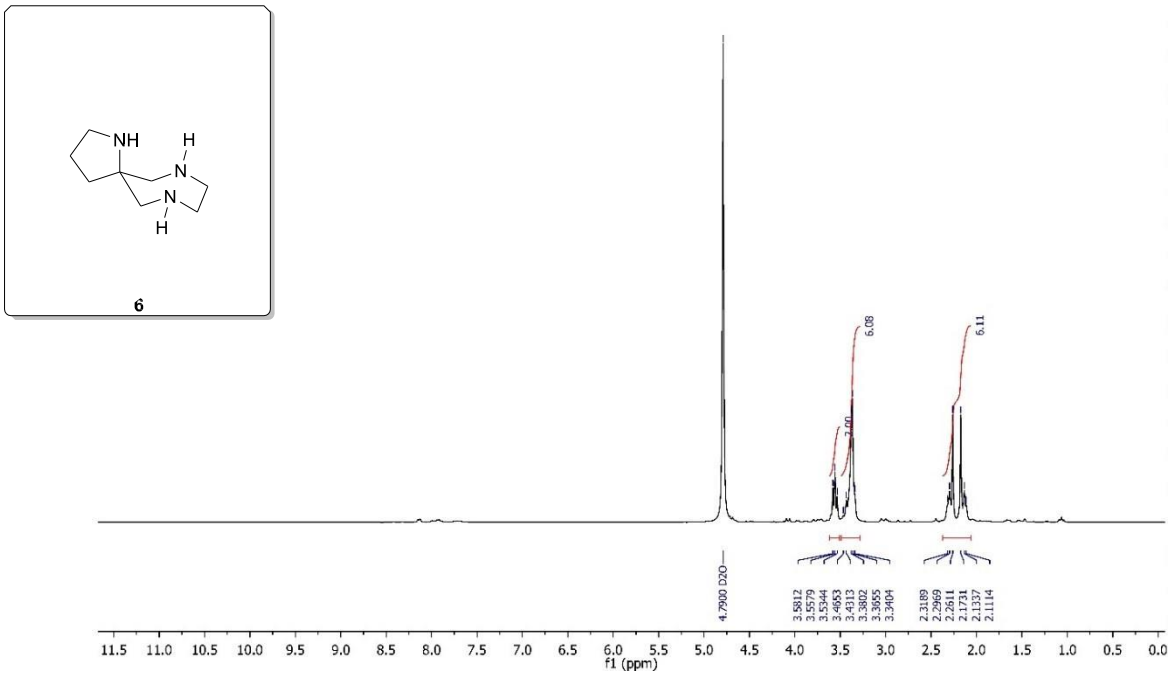

Figure S10. ^{1}H NMR spectrum of compound **6** (7 T, D_2O, 298 K).

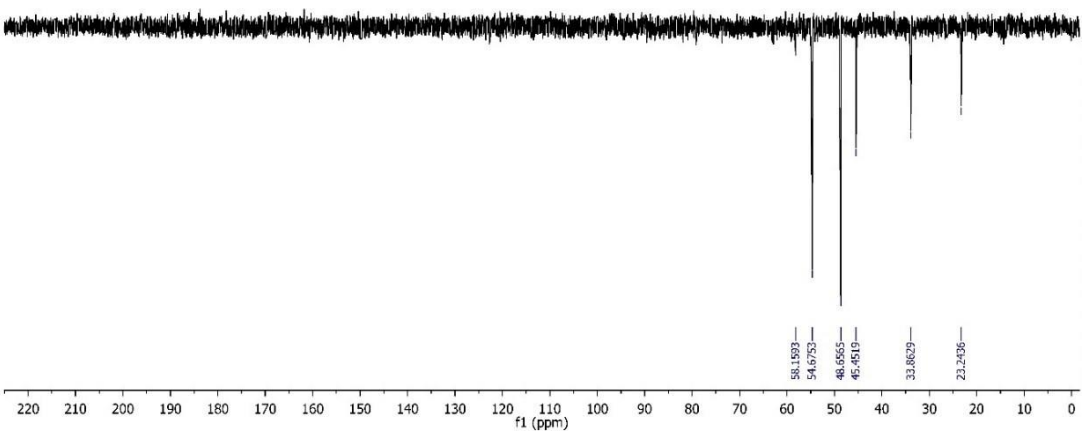

Figure S11. ^{13}C APT NMR spectrum of compound **6** (7 T, D_2O, 298 K).

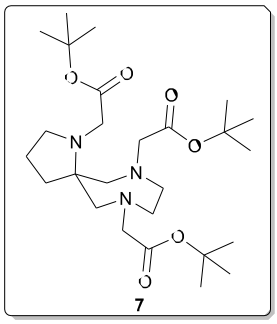

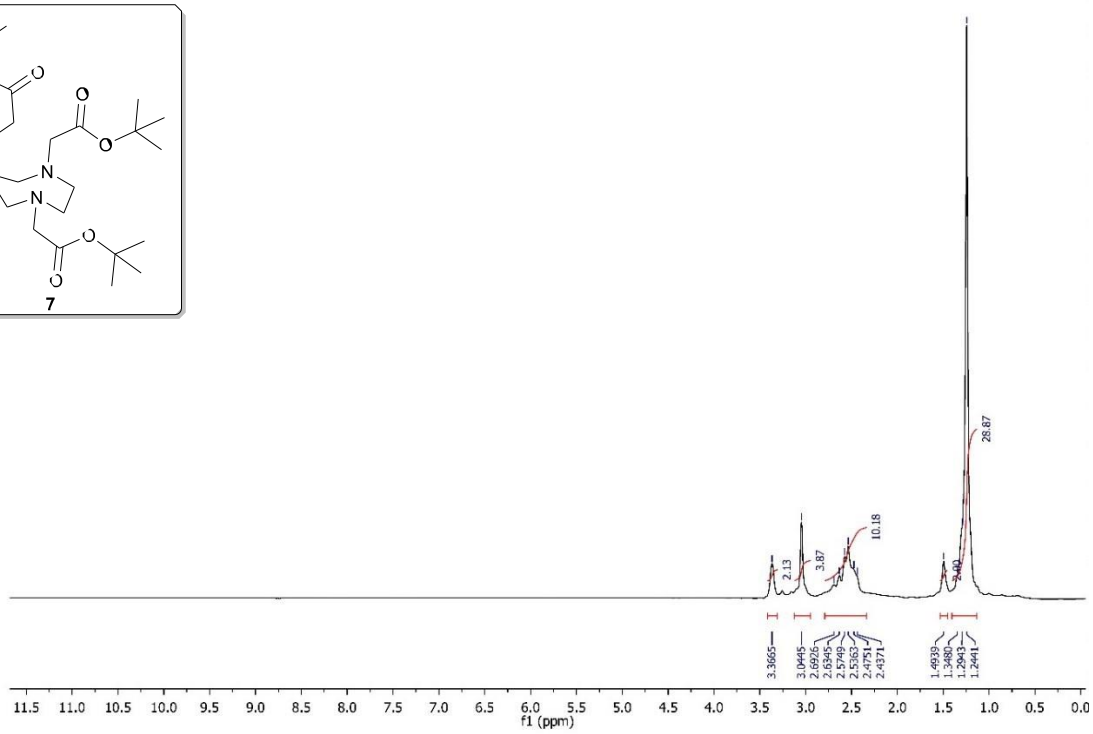

Figure S12. ^{1}H NMR spectrum of compound **7** (7 T, D_2O, 298 K).

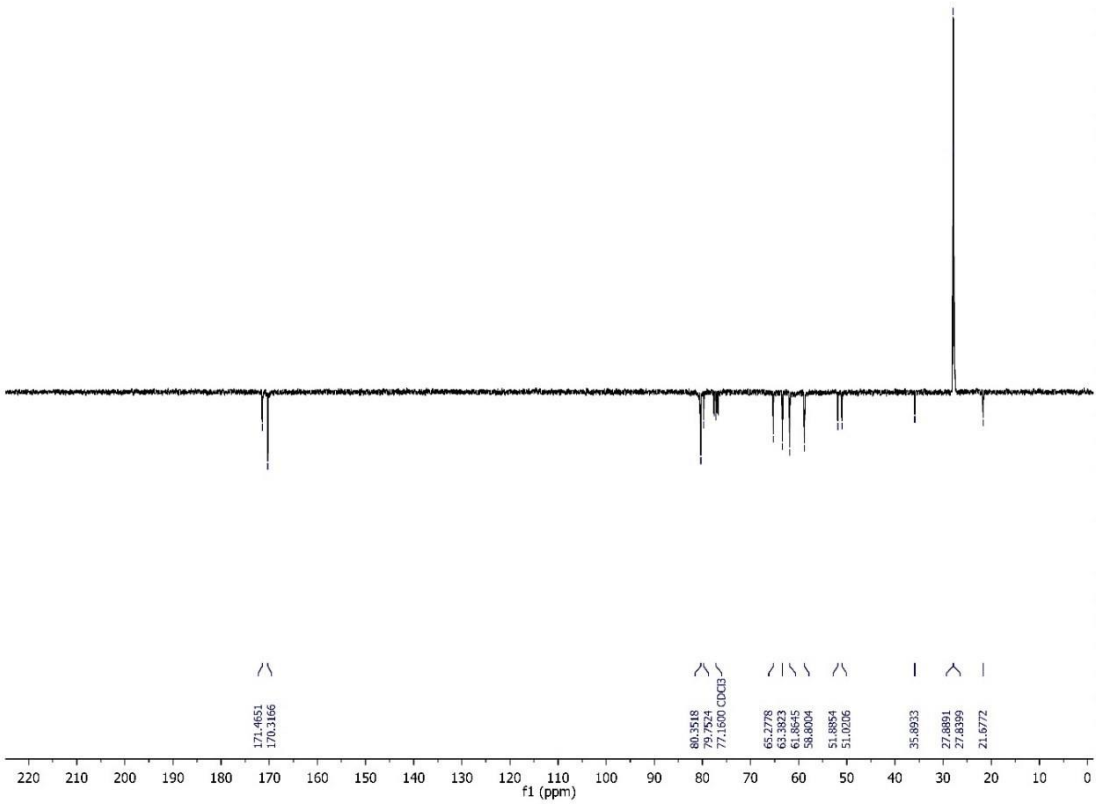

Figure S13. ^{13}C APT NMR spectrum of compound **7** (7 T, D_2O, 298 K).

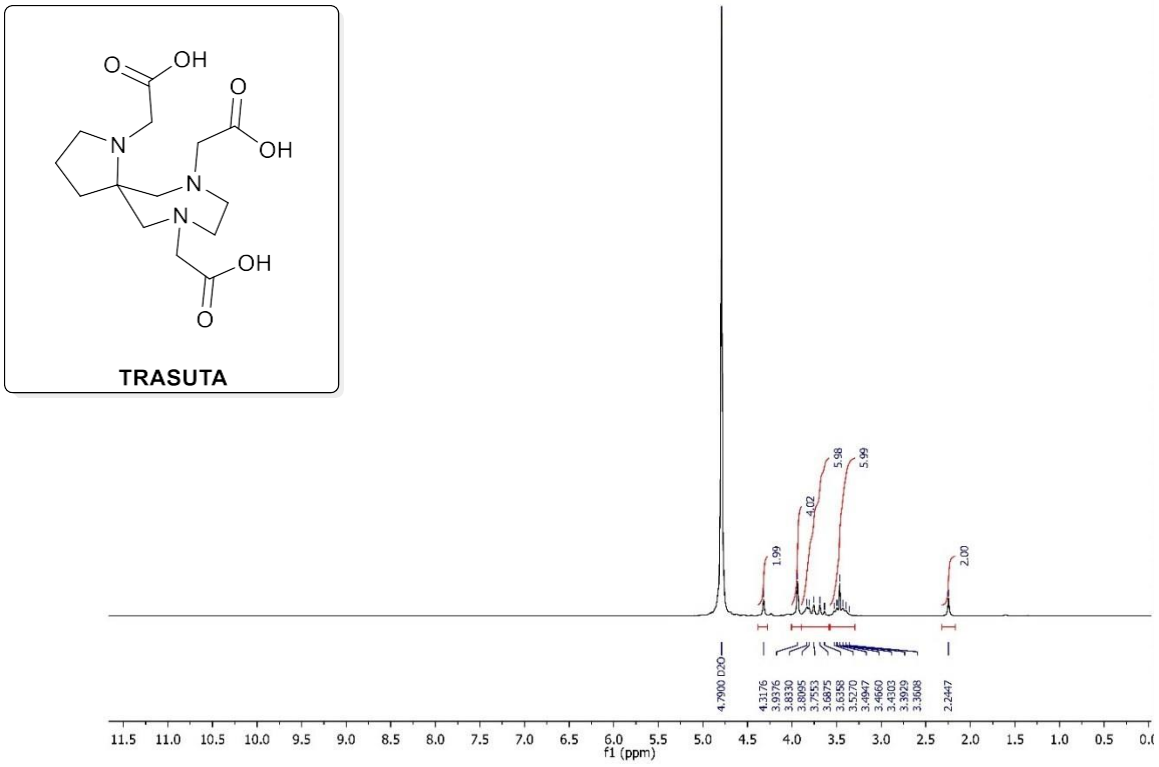

Figure S14. 1H NMR spectrum of TRASUTA (7 T, D_2O, 298 K).

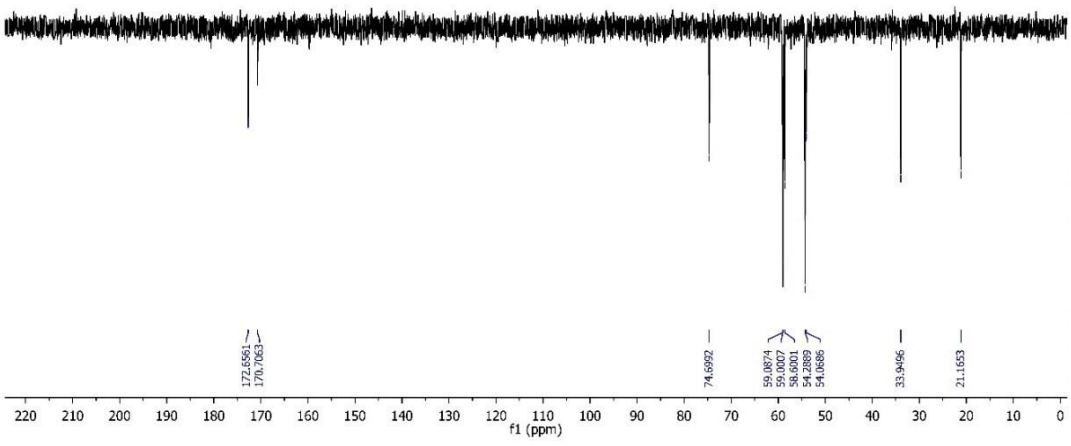

Figure S15. ^{13}C APT NMR spectrum of TRASUTA (7 T, D_2O, 298 K).

II. High resolution mass spectra

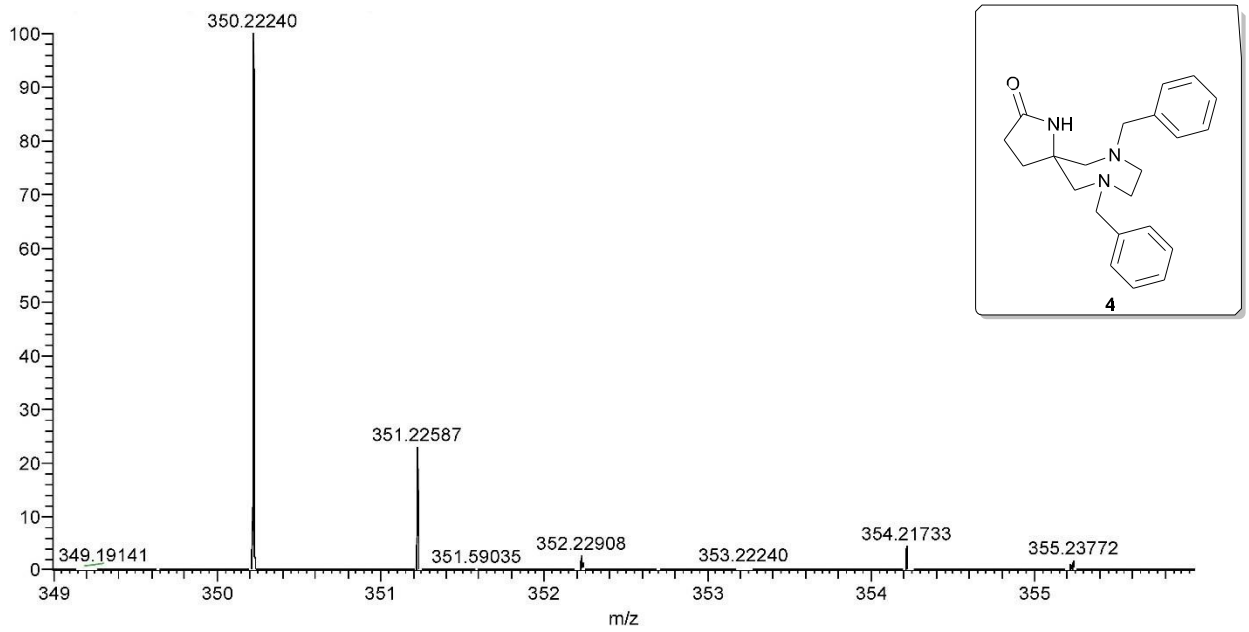

Figure S16. High resolution mass spectrum of compound **4**.

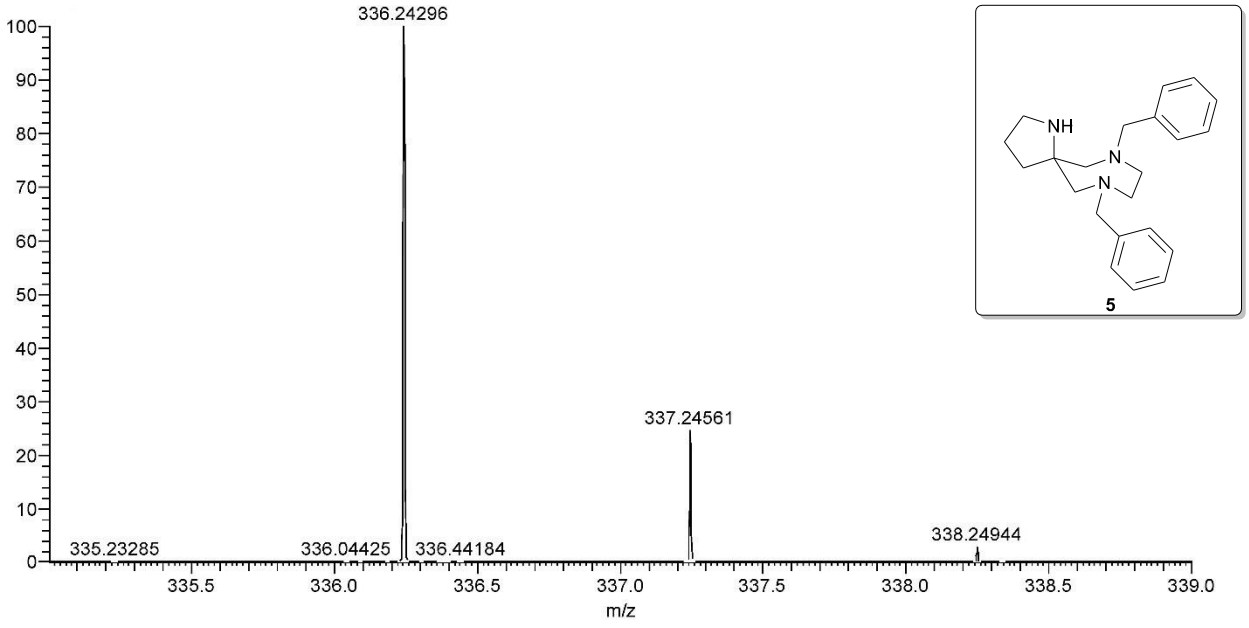

Figure S17. High resolution mass spectrum of compound **5**.

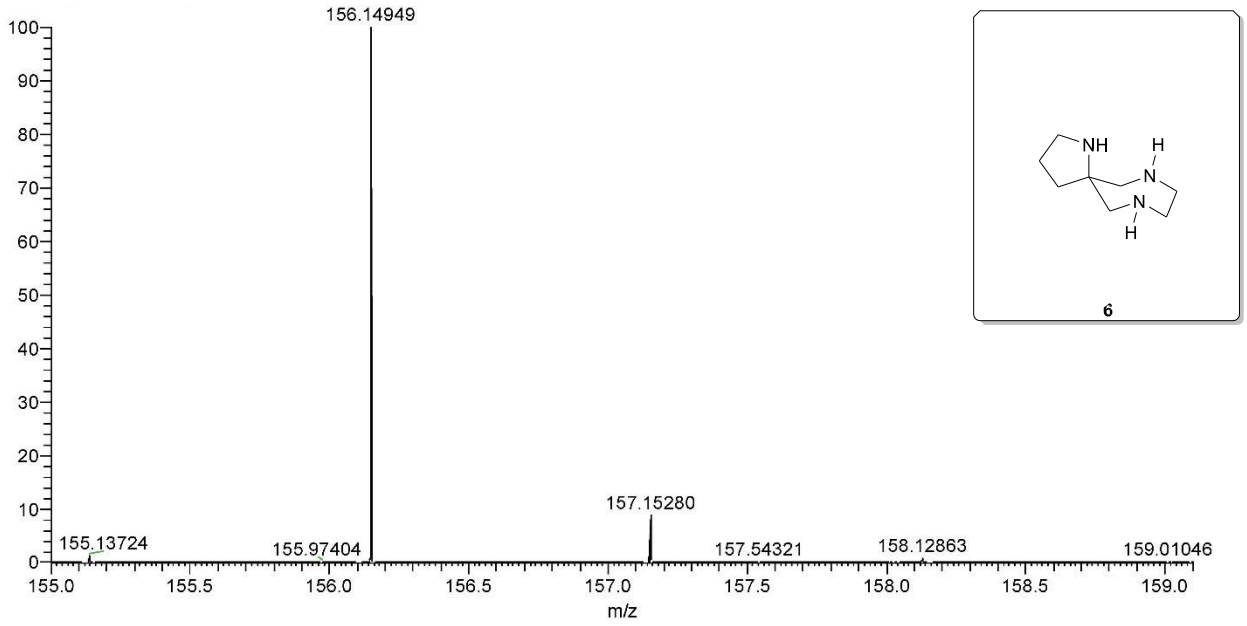

Figure S18. High resolution mass spectrum of compound **6**.

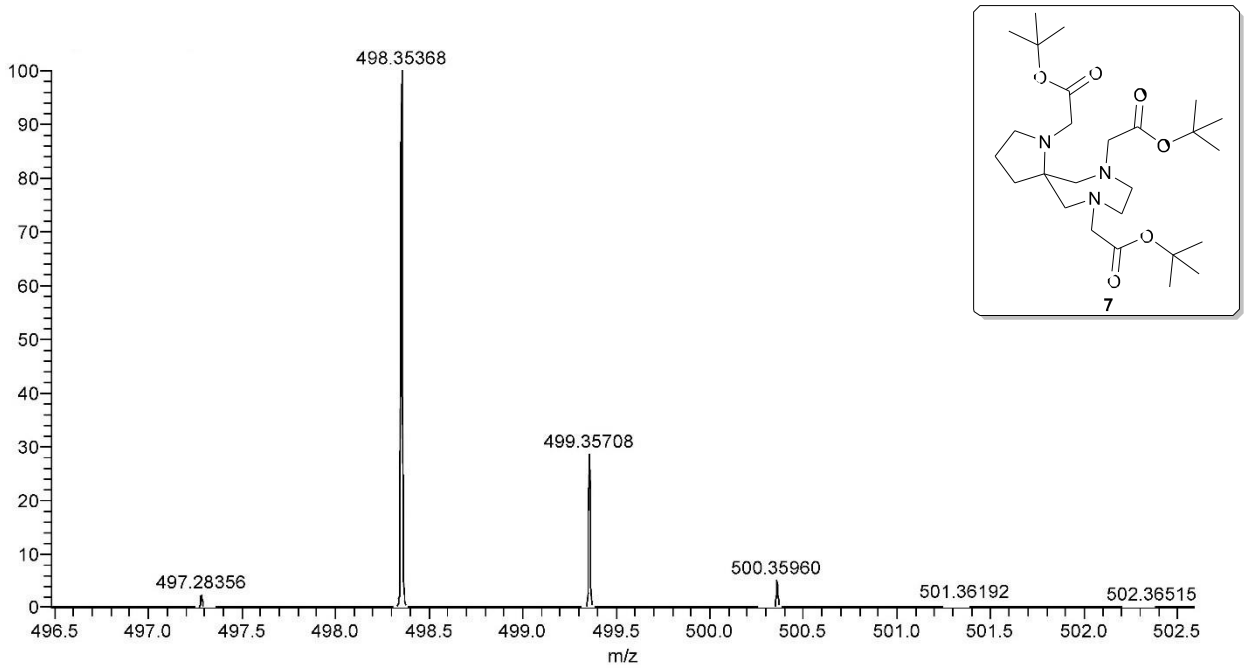

Figure S19. High resolution mass spectrum of compound **7**.

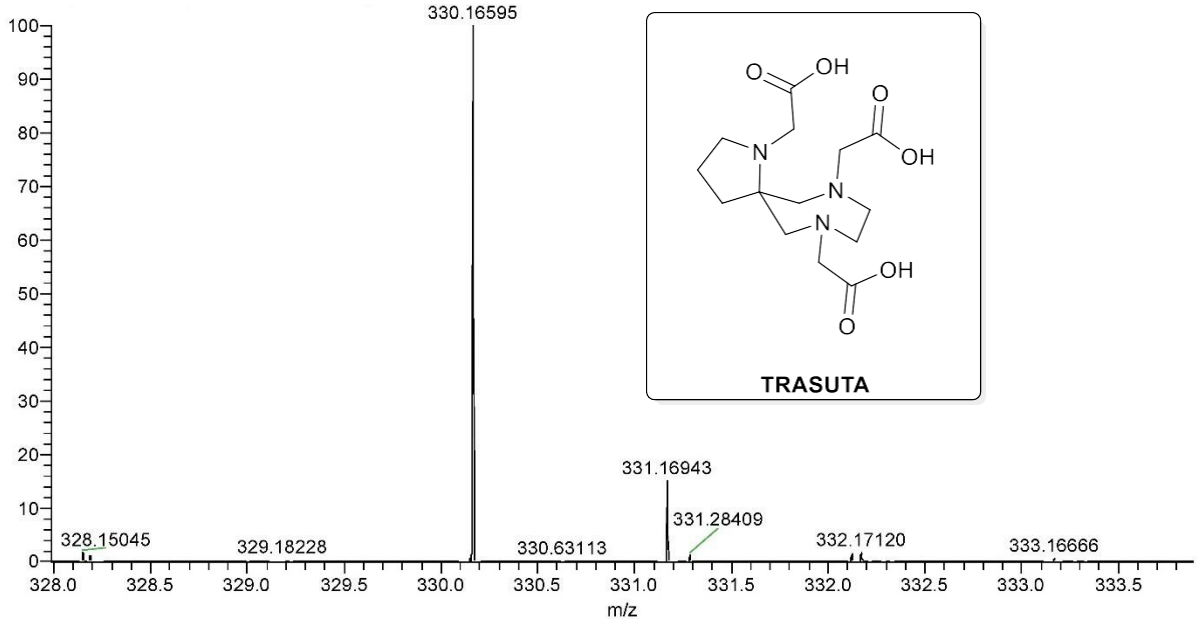

Figure S20. High resolution mass spectrum of TRASUTA.

III. Equilibrium properties of TRASUTA and $M^{2+/3+}$ - TRASUTA systems

III.1 ^{1}H NMR titration of TRASUTA ligand

The protonation constants were also determined with the use of the pH-dependent ^{1}H NMR chemical shifts of the non-labile protons in the TRASUTA ligand (Figure S21).

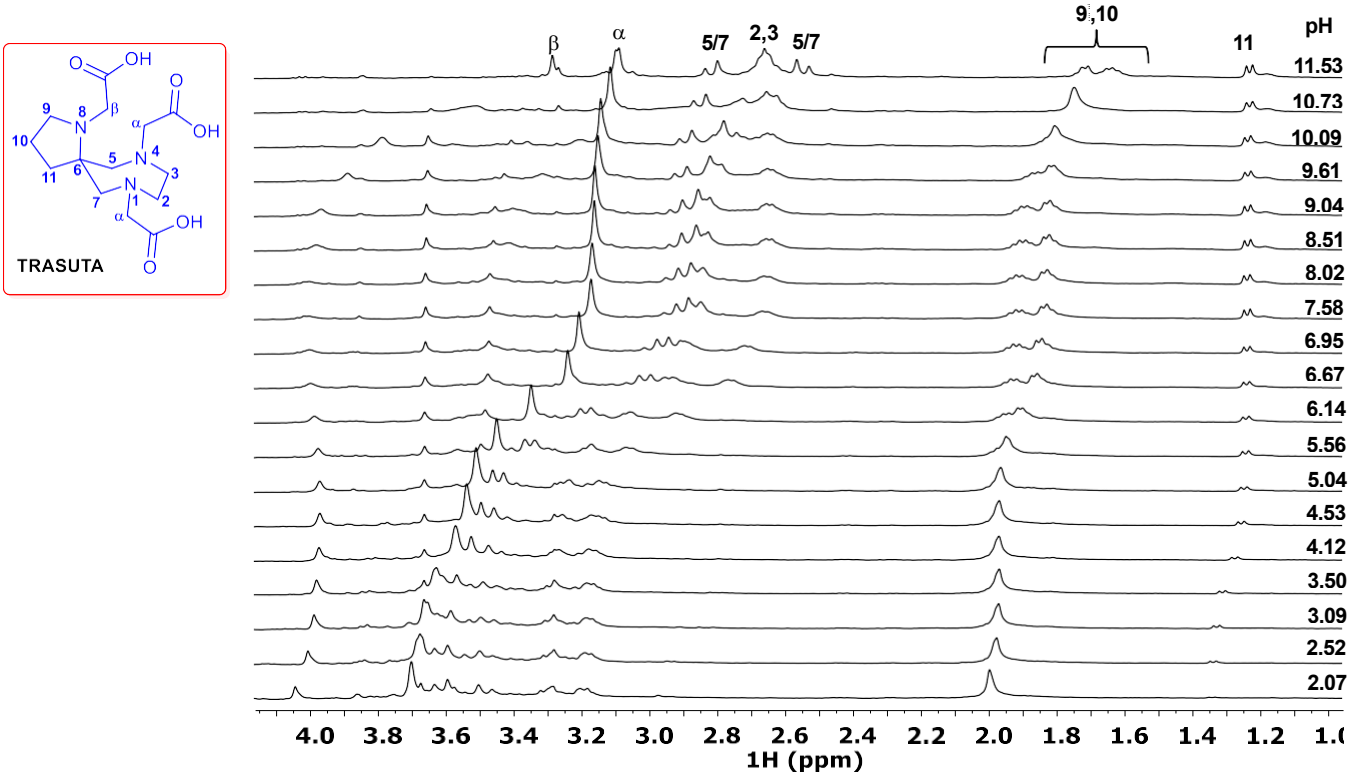

Figure S21. ^{1}H NMR spectra of TRASUTA as a function of pH ([TRASUTA]=0.002 M, 9.4 T, H_2O, 0.15 M NaCl, 298 K).

The ^{1}H NMR titration profile (Figure S22) displays sharp changes as a function of pH, which are related to the protonation-deprotonation of the ligand. Since the protonation-deprotonation processes are generally fast on the NMR time scale, the chemical shifts of the ^{1}H NMR signals represent the weighted average of the chemical shifts of the ligand in different protonation states (Eq. S1).[3]

$$\delta_H = \sum x_i \delta_H^{HiL} \qquad (S1)$$

where, δ_H is the observed chemical shift of a given signal, x_i and δ^{HiL}_{H} are the molar fraction and the chemical shift of the involved species, respectively. The observed chemical shifts were fitted with Eq. S1. (the molar fractions x_i of the different protonated species were expressed with the use of the protonation constants K_i^H). The fits of the experimental data points are shown in Figure S22, and the corresponding $\log K_i^H$ values are listed in Table 1.

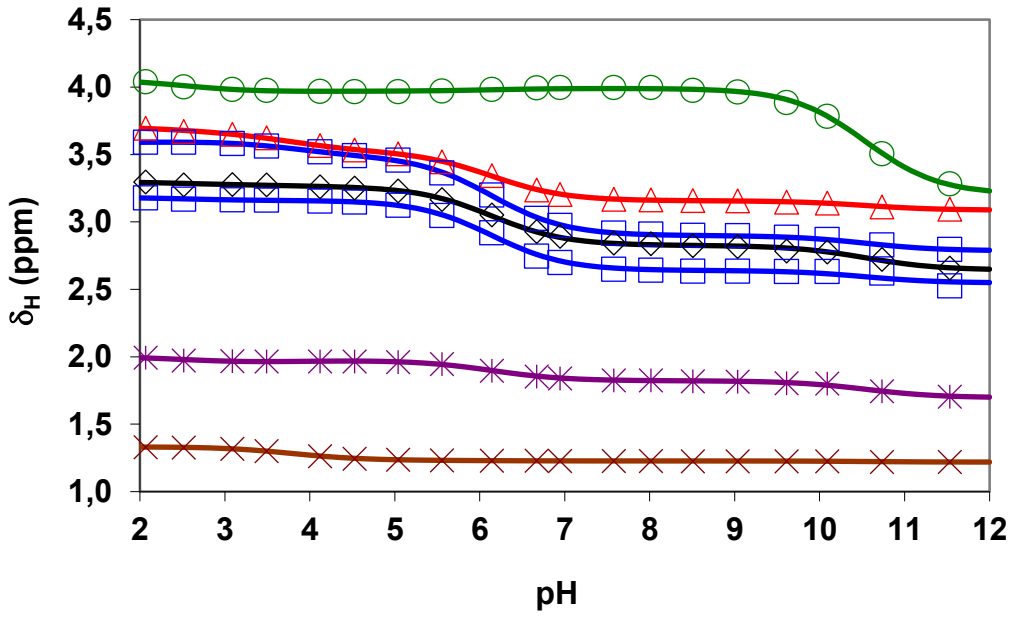

Figure S22. The chemical shifts of the CH_2 protons of TRASUTA *vs* pH (H-2,3 (◇), H-5,7 (□), H-α (△), H-β (◯), H-9, H-10, H-11 (✳)(×), 0.15 M NaCl, 298 K). The open symbols and the curves represent the experimental and the calculated chemical shift values, respectively.

The ^{1}H NMR spectra of TRASUTA are quite complex especially at pH>10 (Figure S21). Based on the integral values and the multiplicities of the ^{1}H NMR signals the resonances were assigned to the hydrogen atoms of TRASUTA in Figure S21. The methylene protons of the 7-membered ring and of the two acetate groups located on the same ring give rise to a broad multiplet (H-α), two AB doublets (H-5,7) and another broad multiplet (H-2,3). The signals of the pyrrolidine methylene protons (H-9, H-10, H-11) and the central acetate (H-β) are broad multiplets and a singlet, respectively. In basic conditions, the Na^+ complex is presumably present as it was found for AAZTA ligand.[4,5] At pH<10 the methylene proton of the acetate pendant arm (H-β) give a very broad multiplet, which may arise from the involvement of the carboxylate groups in strong

intramolecular H-bonds in the monoprotonated ligand. Interestingly, the ^{1}H NMR signal of the methylene proton of the ring-acetate groups (H-β) in the entire pH range is a singlet which indicates the weak H-bonding interaction of the ring-carboxylate group with the protonated N donor atoms (Figure S21).

At pH ≥ 11.5 a significant downfield shift of the H-β, H-9, H-10, H-11 methylene proton resonances of TRASUTA^{3-} occurs, indicating that the first protonation takes place at the N atoms of the pyrrolidine group (N-8). In the pH range 5 – 8, the signals of the 7-membered ring and of the lateral acetate methylene protons are mainly affected by the second protonation process, which thus probably occurs at N-1/N-4. The downfield shift of resonances of protons belonging to the 7-membered ring and to the lateral acetate methylene protons in the pH range 2 – 4.5 confirms that the logK_3^H and logK_4^H are related to the protonation of the carboxylate groups of the lateral arms and to the last non-protonated ring N atom (N-4/N-1).

III.2 Equilibrium studies of $M^{2+/3+}$ – TRASUTA systems

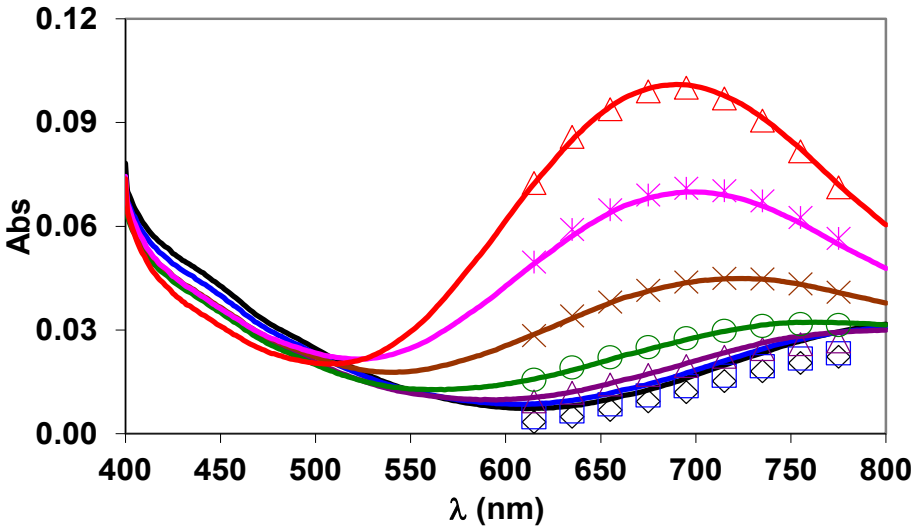

Figure S23. Absorption spectra of Cu^{2+}- TRASUTA system as a function of $[H^+]$. The curves and the open symbols represent the experimental and the calculated absorbance values, respectively. $[H^+]$= 0.60 (◇), 0.30 (□), 0.15 (△), 0.10 (○), 0.06 (×), 0.03 (✳) and 0.01 M (△); $[Cu^{2+}]$=[TRASUTA]=0.0016 M, $[H^+]\leq 0.15$ M → [HCl]+[NaCl]=0,15 M, 25°C, l=1 cm

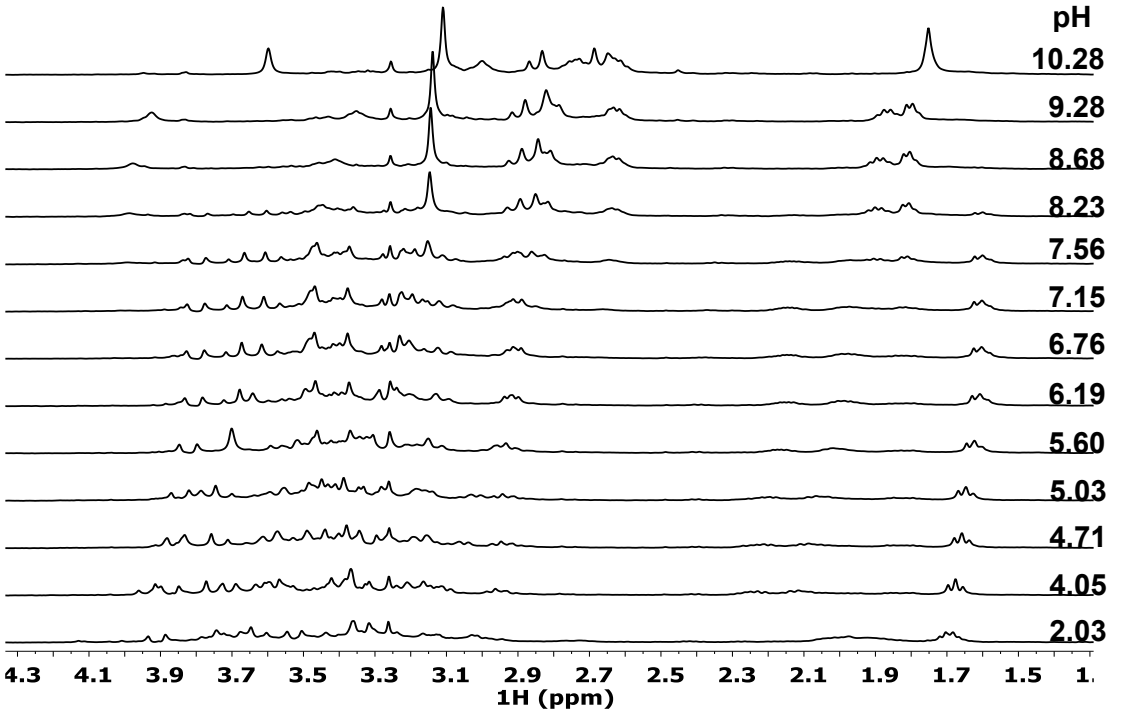

Figure S24. ^{1}H NMR spectra of the Ga^{3+} - TRASUTA system in the pH range 2.0 – 11.0 ([Ga^{3+}]=[TRASUTA]=2.0 mM, 9.4 T, H_2O, 0.15 M NaCl, 25°C)

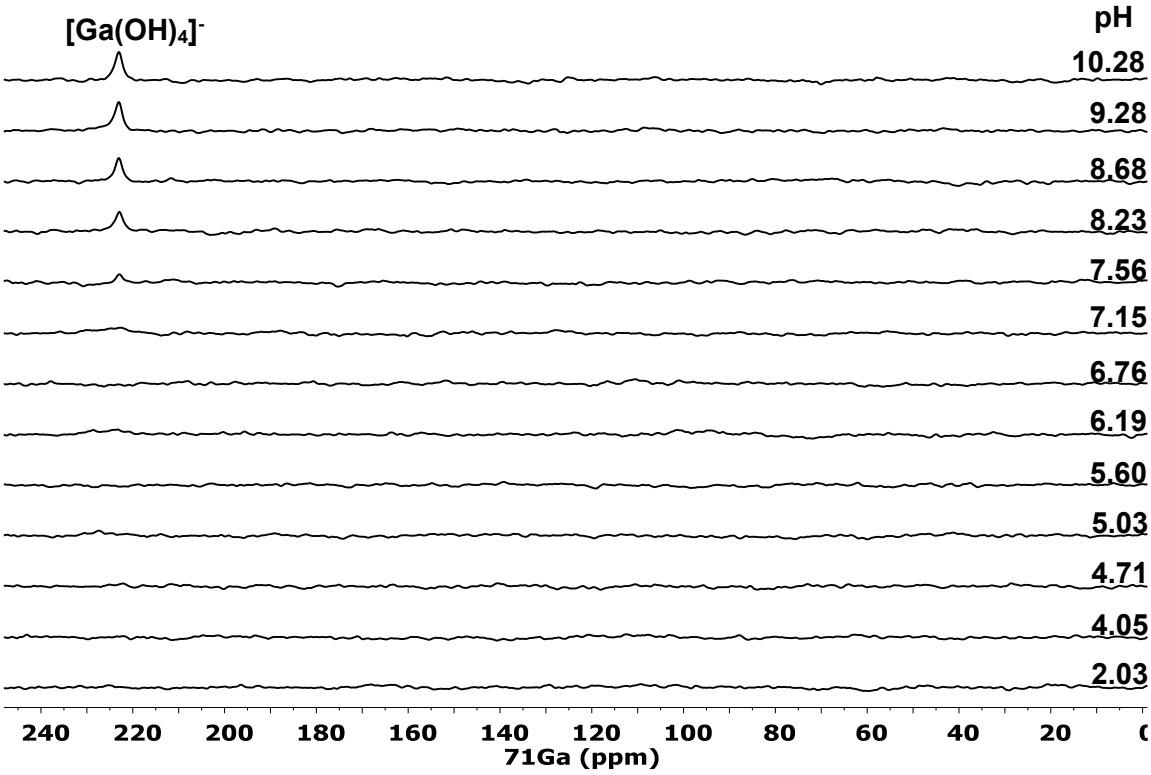

Figure S25. ^{71}Ga NMR spectra of the Ga^{3+} - TRASUTA system in the pH range 2.0 – 12.3 ([Ga^{3+}]=[TRASUTA]=2.0 mM, 9.4 T, H_2O, 0.15 M NaCl, 25°C)

IV. Transmetallation of the $[Ga(TRASUTA)OH]^-$ with Cu^{2+} in the presence of citrate

The transmetallation reactions between $[Ga(TRASUTA)OH]^-$ and Cu^{2+} ions (Eq. S2), TRASUTA = H_3L) have been studied in the pH ranges 6.0 – 8.0. Excess citrate (Cit^{3-}) was used to prevent the hydrolysis of the exchanging Cu^{2+} – and the releasing Ga^{3+} ions. Under such conditions Cu^{2+} was predominantly present as $[Cu(Cit)H_{-1}]^{2-}$, while the released Ga^{3+}-ion forms $[Ga(Cit)H_{-1}]^{2-}$ and $[Ga(Cit)_2]^{4-}$ complexes.[5–8] The absorption spectra of the $[Ga(TRASUTA)OH]^-$ – Cu^{2+}-citrate reacting systems as a function of time are shown in Figure S26.

$$[Ga(L)OH]^- + Cu^{2+} \rightleftharpoons [CuL]^- + Ga^{3+} \qquad (S2)$$

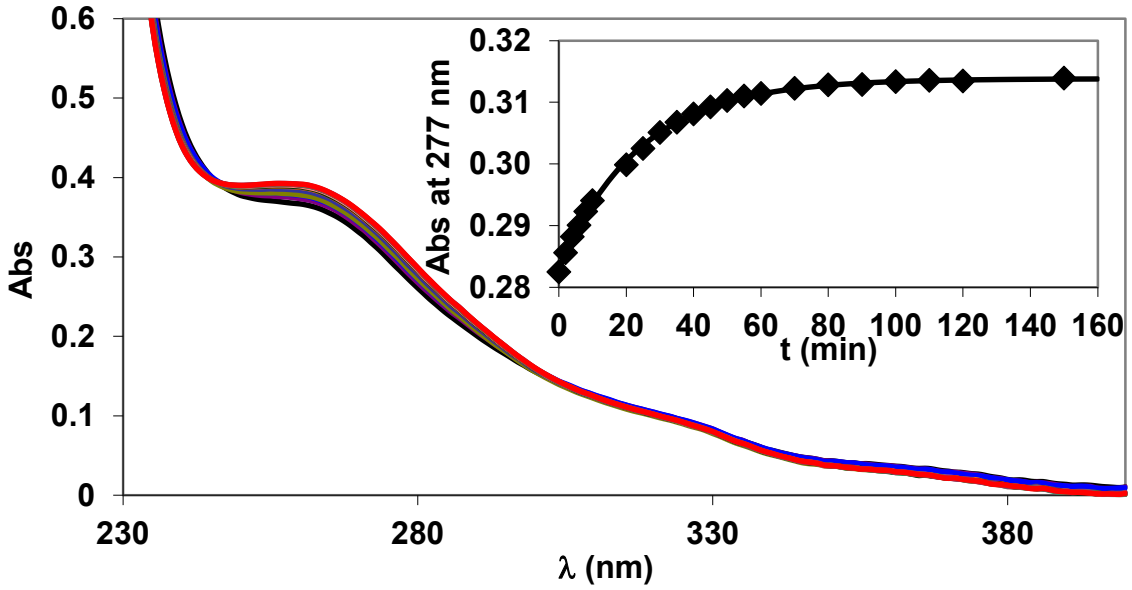

Figure S26. Absorption spectra and absorbance values of the $[Ga(TRASUTA)OH]^-$ - Cu^{2+} reacting system (insertion) at 277 nm in the presence of citrate excess ($[GaL]_{tot}$=0.1 mM, $[Cu^{2+}]_{tot}$=0.1 mM, $[Cit]_{tot}$=1.0 mM, 0.15 M NaCl, 25°C)

Rates of the transmetallation reaction have been studied in the presence of Cu^{2+}-citrate excess, so it can be treated as a pseudo-first order kinetic process and the rates of reaction can be expressed by Eq. S3:

$$-\frac{d[GaL]_t}{dt} = k_d[Ga(L)OH_t \qquad (S3)$$

where k_d is a pseudo-first-order rate constant and $[Ga(L)OH]_t$ is the total concentration of Ga^{3+} complex, respectively. The pseudo-first-order rate constants characterizing the transmetallation reactions of $[Ga(TRASUTA)OH]^-$ with Cu^{2+} at different pH-values in the presence of citrate are shown in Figure S27.

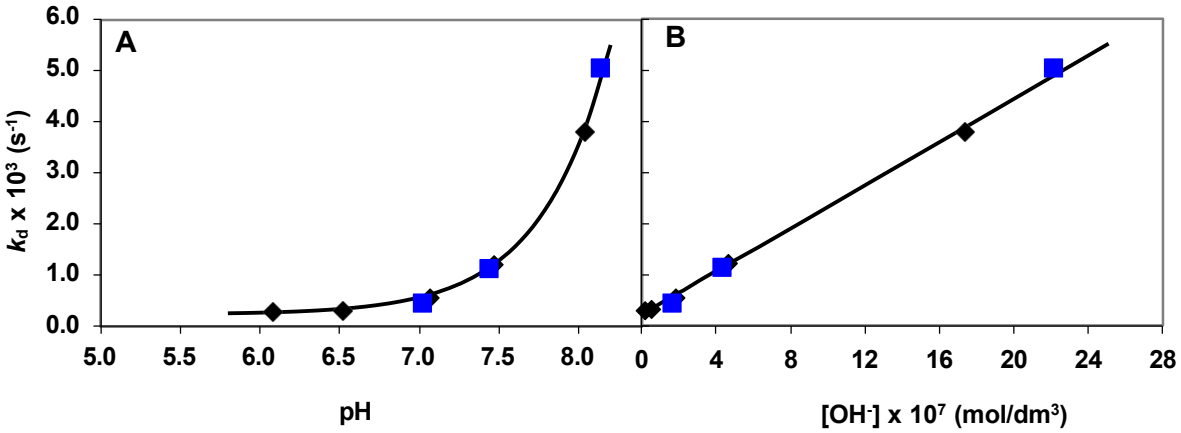

Figure S27. Pseudo-first-order (k_d) rate constants characterizing the transmetallation reaction of the Ga(TRASUTA)] - Cu^{2+} reacting system as a function of pH (**A**) and $[OH^-]$ (**B**) in the presence of citrate ($[GaL]_{tot}$=0.1 mM, $[Cu^{2+}]_{tot}$=0.3 (■) and 0.5 mM (◆), $[Cit]_{tot}$=1.0 mM, 0.15 M NaCl, 25°C).

The k_d values are independent on the concentration of Cu^{2+} and $[Cu(Cit)H_{-1}]^{2-}$. Since the $[Cu(Cit)H_{-1}]^{2-}$ dominates in the pH range 6.0 – 8.0, the increase of the $[Cu^{2+}]$ in the presence of constant $[Cit]_{tot}$ results in the decrease of the $[Cit]_{free}$. Because of the k_d values are independent on the $[Cu^{2+}]$ in the presence of constant $[Cit]_{tot}$, it can be assumed that the rate of the exchange reaction is also independent of the citrate concentration. By considering these evidences, it is reasonable to assume that the rate controlling step of the transmetallation reactions is the dissociation of the $[Ga(TRASUTA)OH]^-$ followed by the fast reaction between the free TRASUTA and Cu^{2+} ion. By taking into account the species distribution of the Ga^{3+}-TRASUTA system, the $[Ga(L)OH]^-$ species predominate in the pH range 6.0 – 8.0. The k_d values of

[Ga(TRASUTA)OH]$^{-}$ – Cu^{2+}-citrate reacting systems are shown in Figure S27 increase with the [OH^{-}]. The dependence of the k_d values on pH can be interpreted in terms of the spontaneous (k_0, Eq. S4), and OH^{-} (k_{OH}, Eq. S5) assisted dissociation of the [Ga(TRASUTA)OH] $^{-}$ complex.

$$[Ga(L)OH]^{-} \xrightarrow{k_0} Ga^{3+} + H_xL \qquad (S4)$$

$$[Ga(L)OH]^{-} + OH^{-} \xrightarrow{k_{OH}} Ga^{3+} + H_xL \qquad (S5)$$

In the ternary [Ga(L)OH]$^{-}$ species, TRASUTA coordinates by 5 donor atoms (three N and two O donor atoms) whereas the remaining coordination sites of the Ga^{3+} ion is occupied by on OH^{-} ions. The formation of mono-hydroxo [Ga(L)OH] ternary species with L1, L2, DATA^{m}, CyAAZTA and AAZTA have been also confirmed by pH-potentiometry, ^{1}H and ^{71}Ga-NMR spectroscopy.[4,5,9–11] By taking into account all possible pathways and Eq. S3, the dissociation rate of [Ga(TRASUTA)OH]$^{-}$ can be expressed by Eq. S6 and the k_d pseudo-first-order rate constant can be expressed by Eq. S7.

$$-\frac{\mathrm{d[GaL]_t}}{\mathrm{dt}} = k_{\mathrm{d}}[\mathrm{Ga(L)OH}]_{\mathrm{t}} = k_0[\mathrm{Ga(L)OH}] + k_{\mathrm{OH}}[\mathrm{Ga(L)OH}] \qquad (S6)$$

$$k_{\mathrm{d}} = k_0 + k_{\mathrm{OH}}[\mathrm{OH^-}] \qquad (S7)$$

where k_0, and k_{OH} are the rate constants characterizing the spontaneous and OH^{-}-assisted dissociation of [Ga(TRASUTA)OH]$^{-}$. The rate constants characterize the transmetallation reaction of [Ga(TRASUTA)OH]$^{-}$ with Cu^{2+} in the presence of citrate have been calculated by fitting the k_d values presented in Figure S27 to the Eq. S7.

V. Saturation of serum transferrin with Ga^{3+}

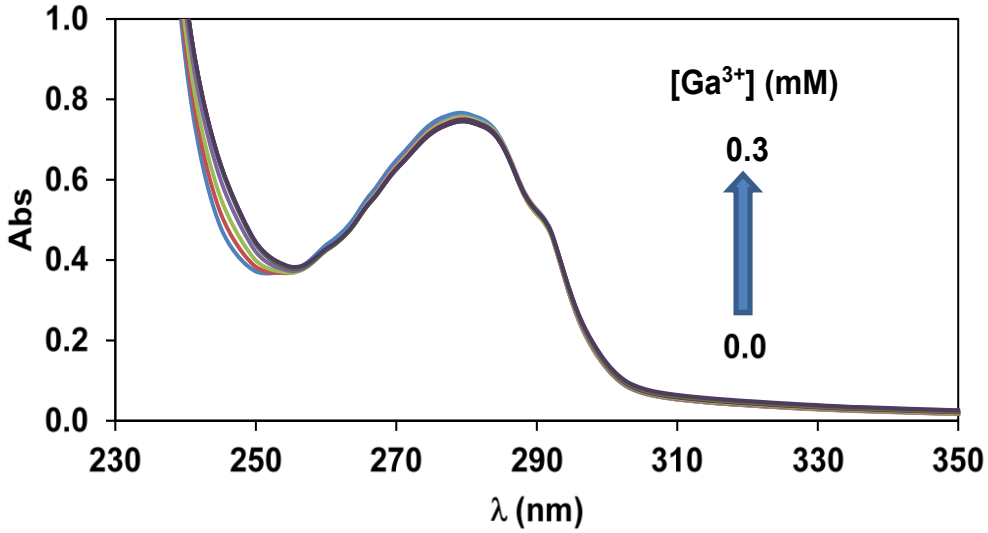

Figure S28. Absorption spectra human serum transferrin (sTf) - Ga^{3+} system ([sTf]=8.4×10^{-5} M, $[Ga^{3+}]_{tot}$=0 – 0.3 mM, 0.025 M $NaHCO_3$, 0.15 M NaCl, 25°C, l=1.0 mm).

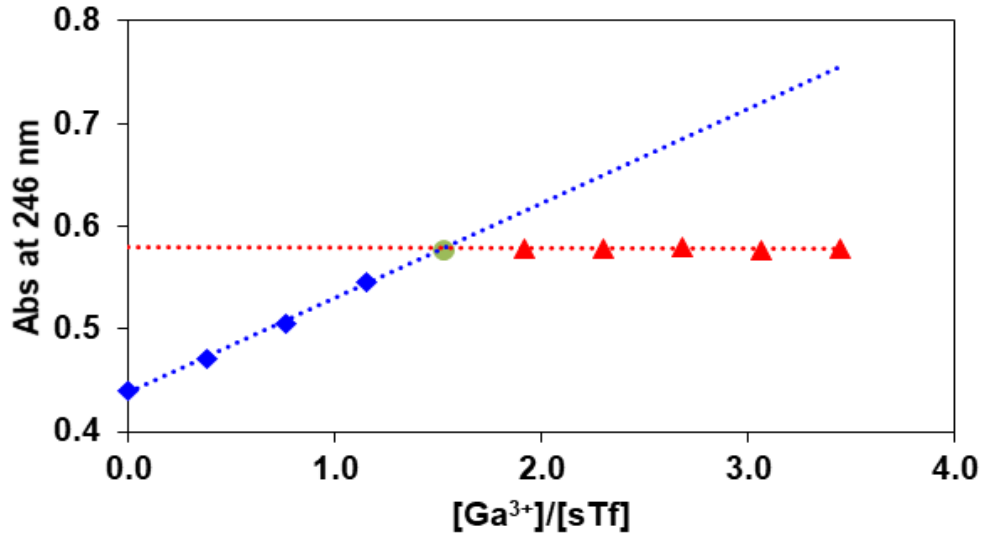

Figure S29. Absorbance values of the human serum transferrin (sTf) - Ga^{3+} system as a function of $[Ga^{3+}]/[sTf]$ at 246 nm ([sTf]=8.4×10^{-5} M, $[Ga^{3+}]_{tot}$=0 – 0.3 mM, 0.025 M $NaHCO_3$, 0.15 M NaCl, 25°C, l=1.0 mm).

VI. VT- ^{1}H and ^{13}C NMR studies of Ga(III), Zn(II) and Pb(II) complexes with TRASUTA

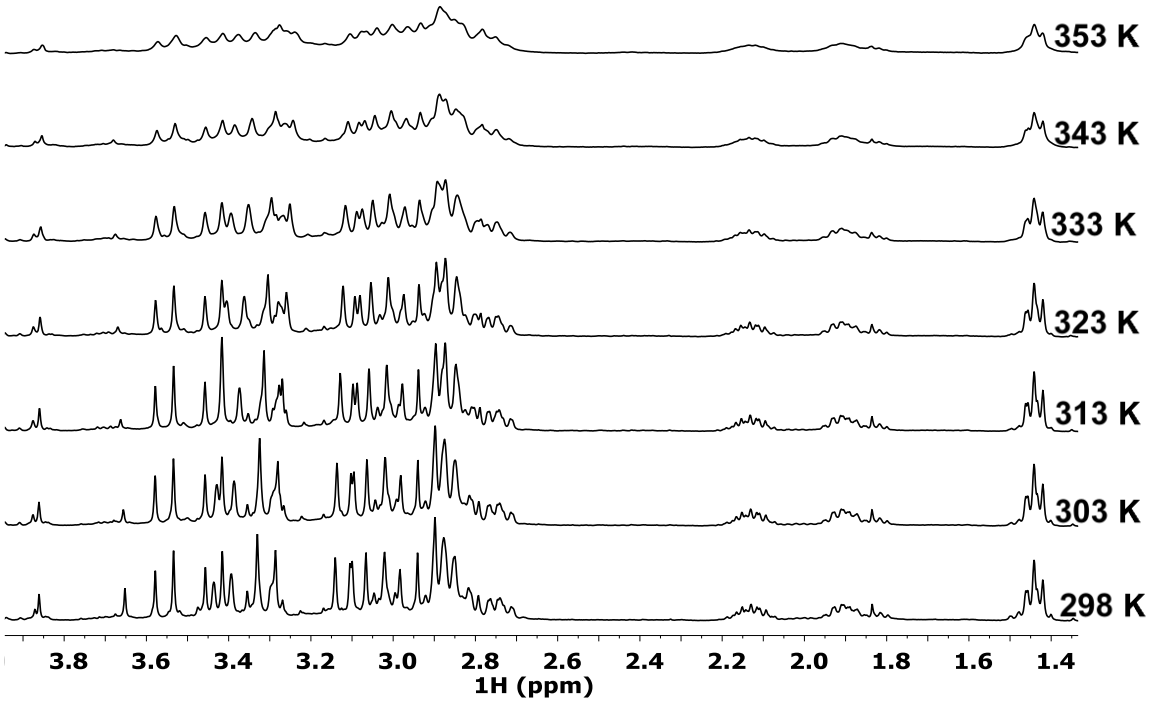

Figure S30. VT-^{1}H NMR spectra of $[Zn(TRASUTA)]^{-}$ ([ZnL]=20 mM, pD=6.46, 9.4 T, D_2O).

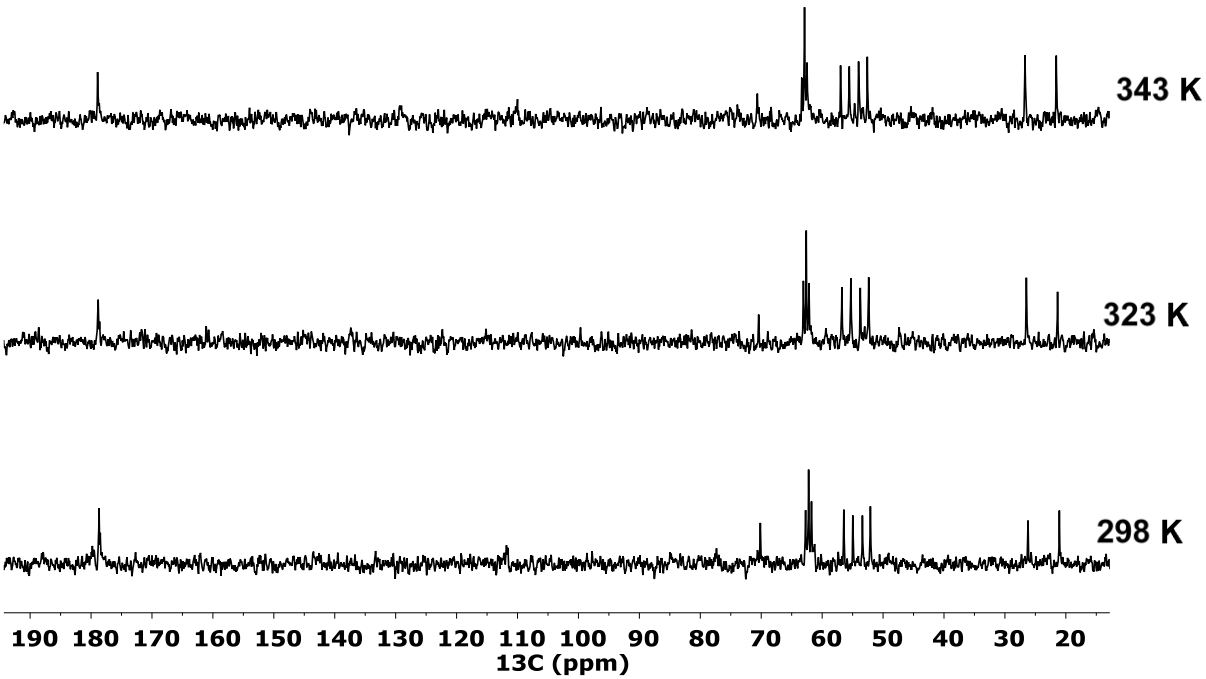

Figure S31. VT-^{13}C NMR spectra of $[Zn(TRASUTA)]^{-}$ ([ZnL]=20 mM, pD=6.46, 9.4 T, D_2O).

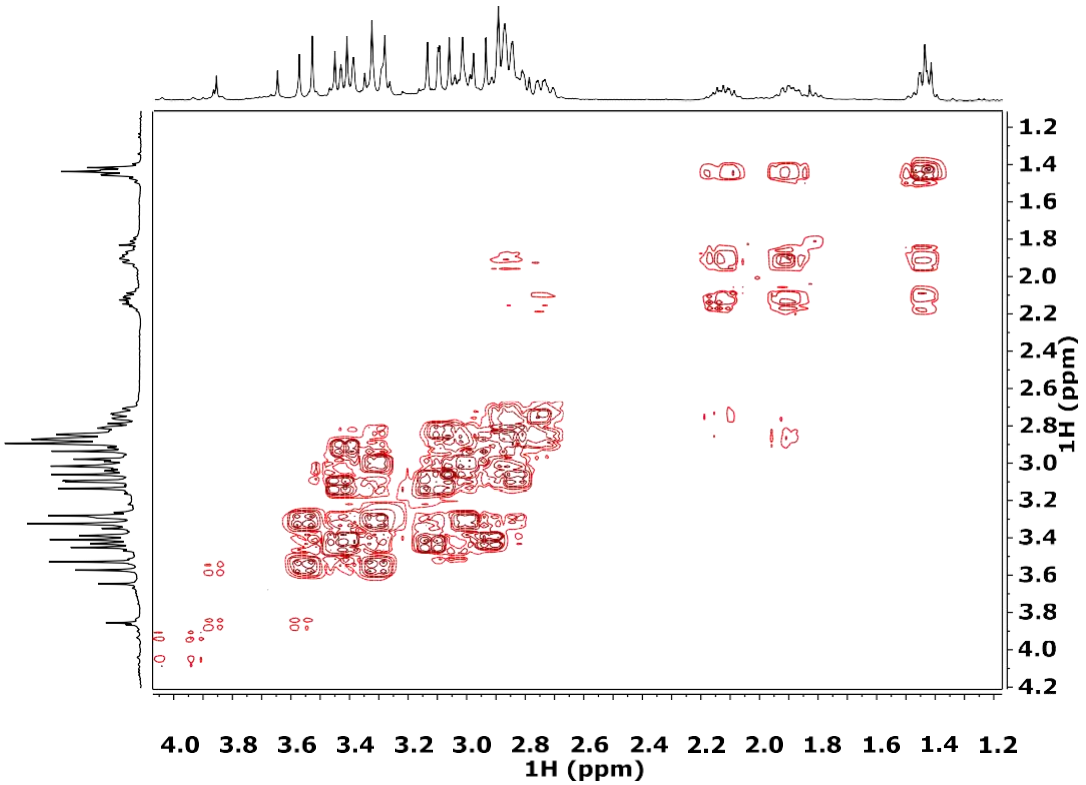

Figure S32. $^{1}H - {}^{1}H$ COSY spectra of $[Zn(TRASUTA)]^{-}$ ([ZnL]=20 mM, pD=6.46, 298K, 9.4 T, D_2O).

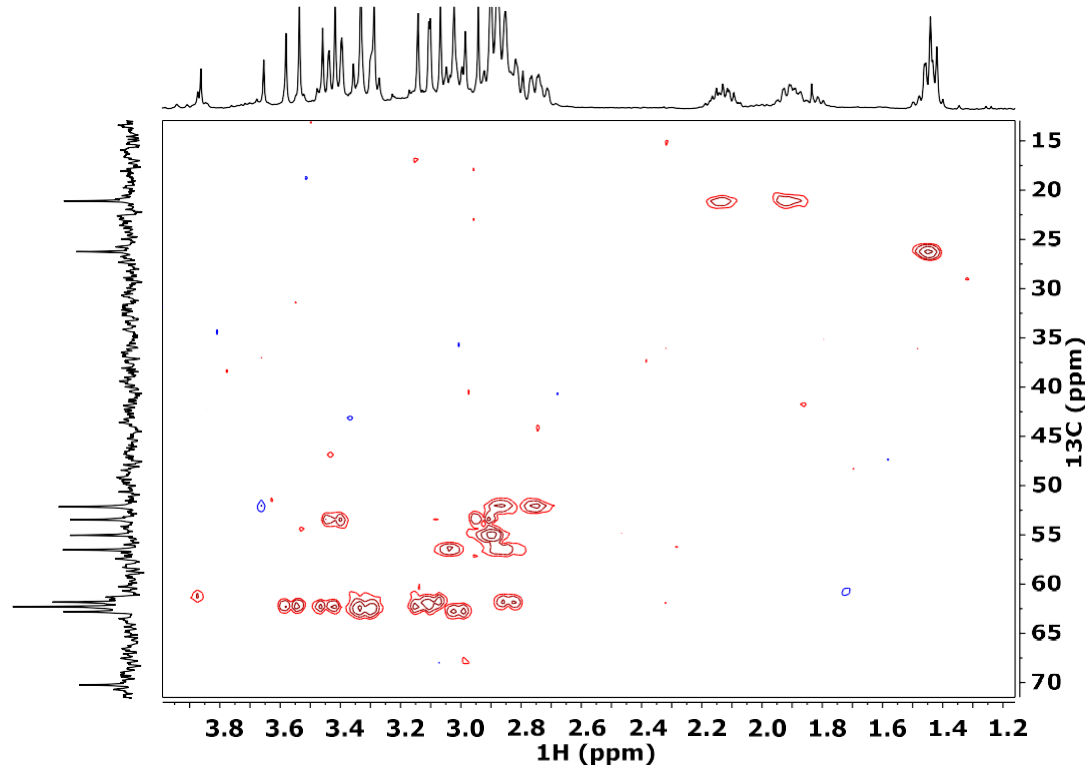

Figure S33. $^{1}H - {}^{13}C$ HSQC spectra of $[Zn(TRASUTA)]^{-}$ ([ZnL]=20 mM, pD=6.46, 298K, 9.4 T, D_2O).

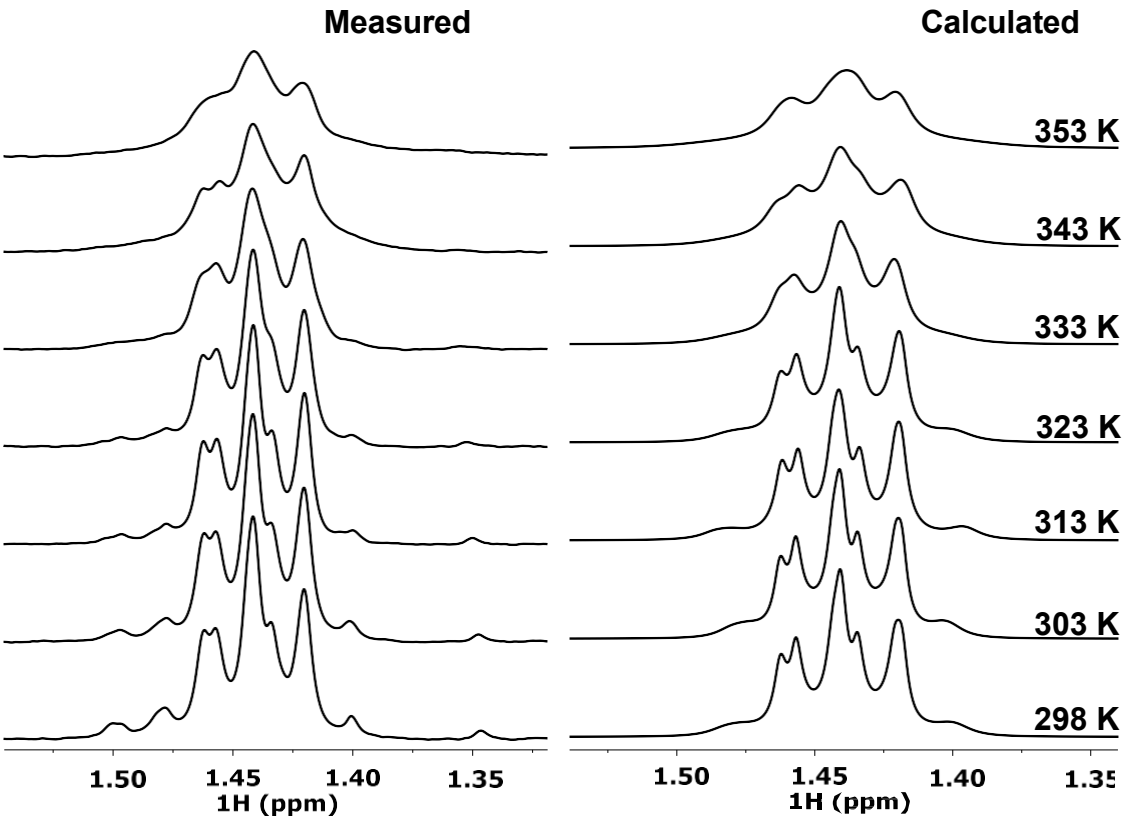

Figure S34. Measured and calculated VT-^{1}H NMR spectra of $[Zn(TRASUTA)]^{-}$ ([ZnL]=20 mM, pD=6.46, 9.4 T, D_2O).

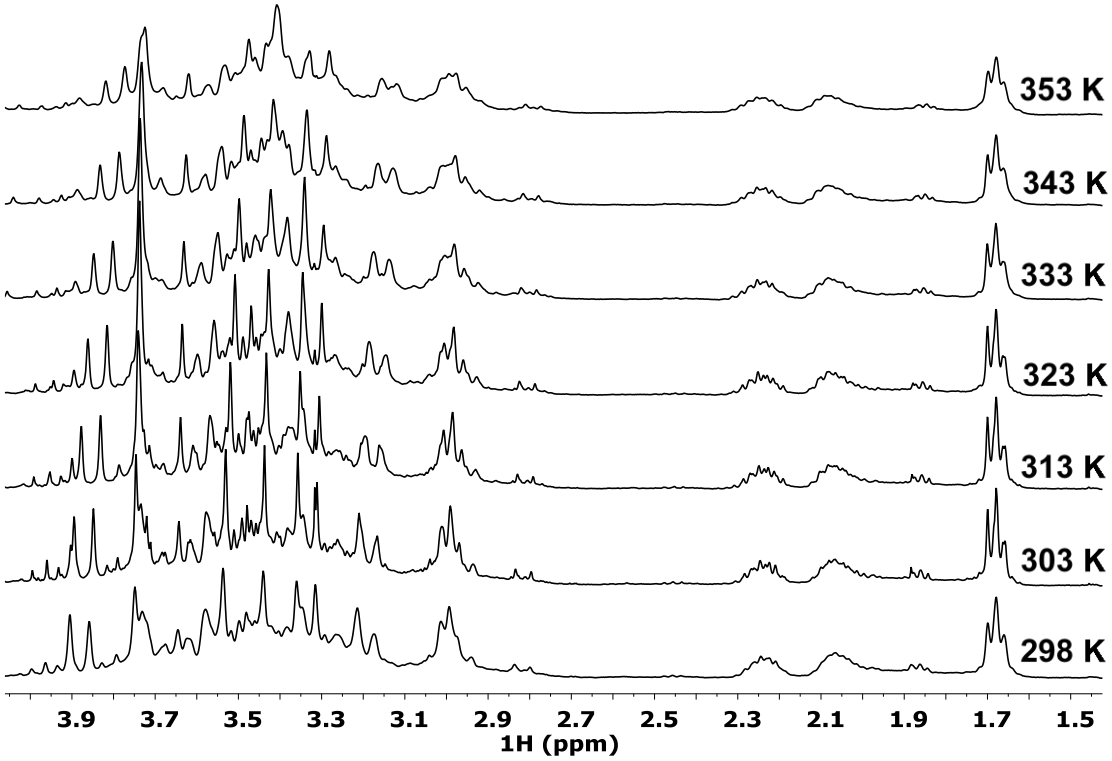

Figure S35. VT-^{1}H NMR spectra of [Ga(TRASUTA)] ([GaL]=20 mM, pD=4.90, 9.4 T, D_2O).

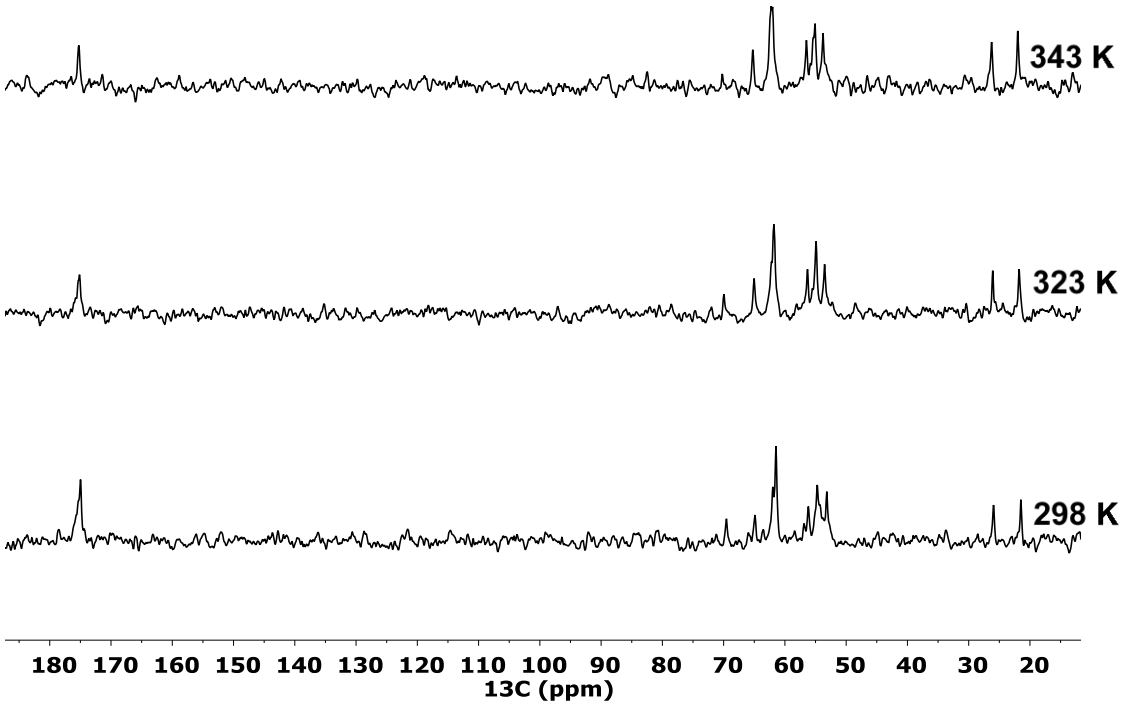

Figure S36. VT-^{13}C NMR spectra of [Ga(TRASUTA)] ([GaL]=20 mM, pD=4.90, 9.4 T, D_2O)

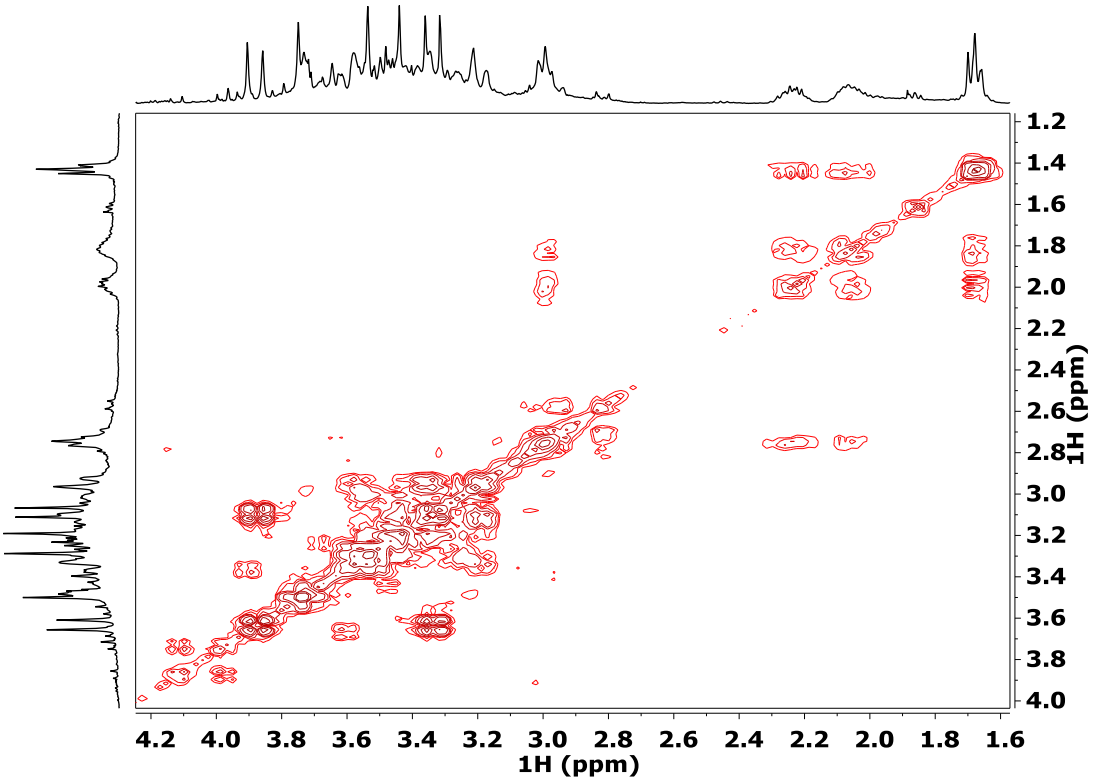

Figure S37. $^{1}H - {}^{1}H$ COSY spectra of [Ga(TRASUTA)] ([GaL]=20 mM, pD=4.90, 298K, 9.4 T, D_2O)

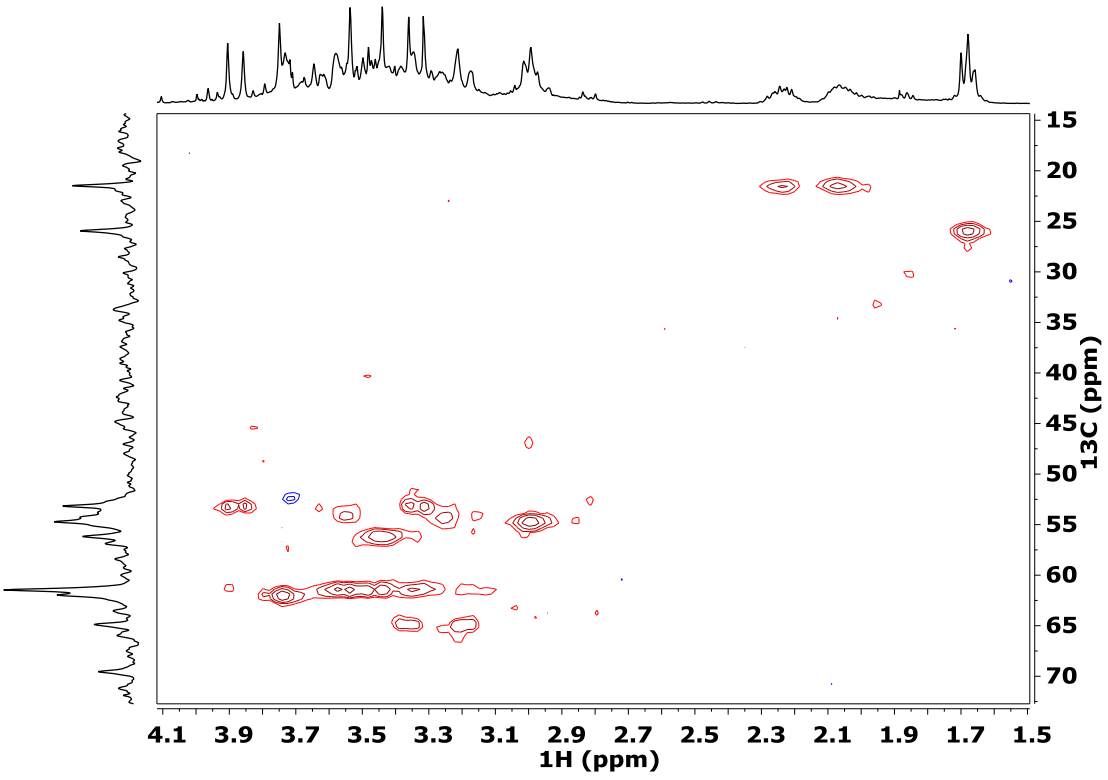

Figure S38. $^{1}H - {}^{13}C$ HSQC spectra of [Ga(TRASUTA)] ([GaL]=20 mM, pD=4.90, 298K, 9.4T, D_2O).

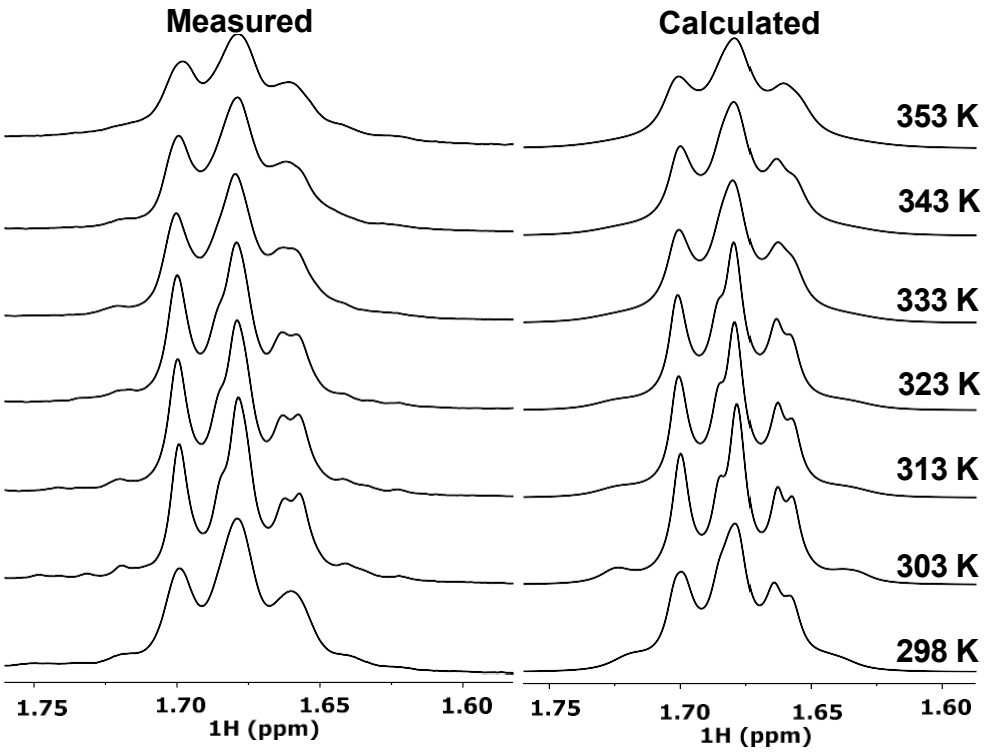

Figure S39. Measured and calculated VT-^{1}H NMR spectra of [Ga(TRASUTA)] ([GaL]=20 mM, pD=4.90, 9.4 T, D_2O).

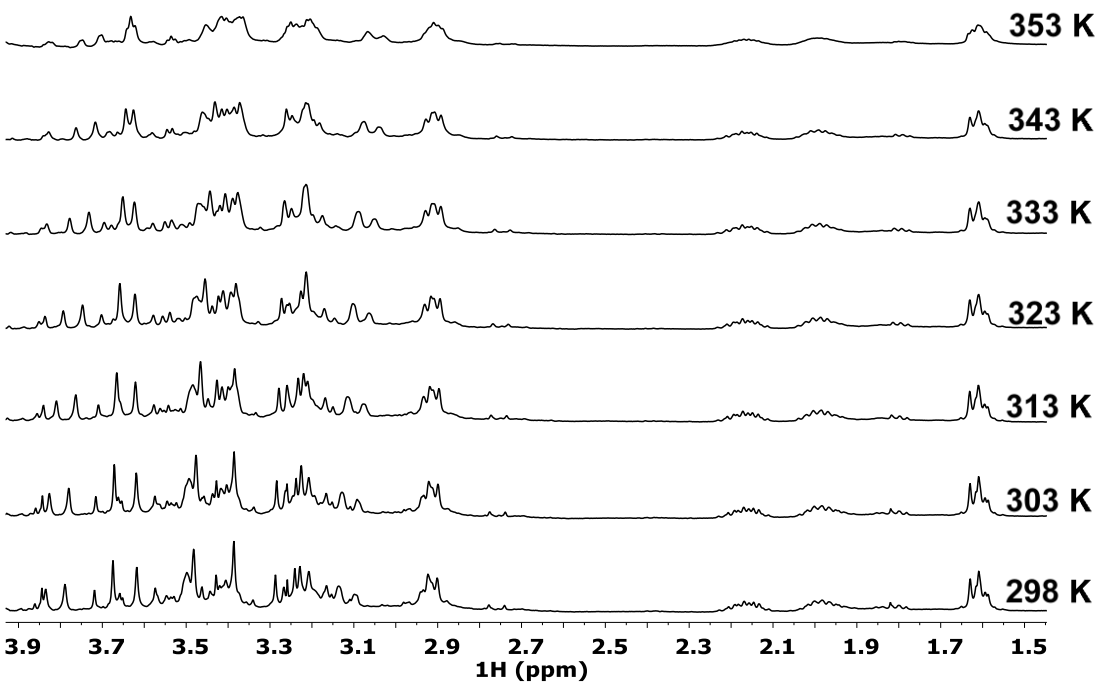

Figure S40. VT-^{1}H NMR spectra of [Ga(TRASUTA)OH]$^{-}$
([GaL]=20 mM, pD=7.44, 9.4 T, D_2O)

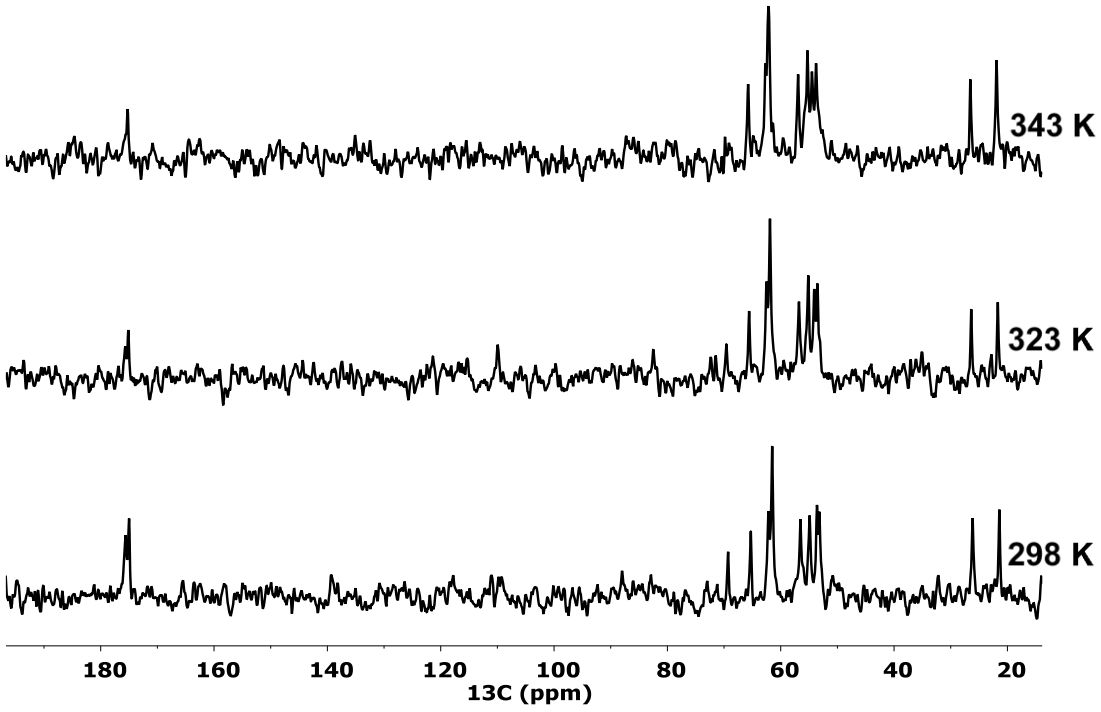

Figure S41. VT-^{13}C NMR spectra of [Ga(TRASUTA)OH]$^{-}$
([GaL]=20 mM, pD=7.44, 9.4 T, D_2O).

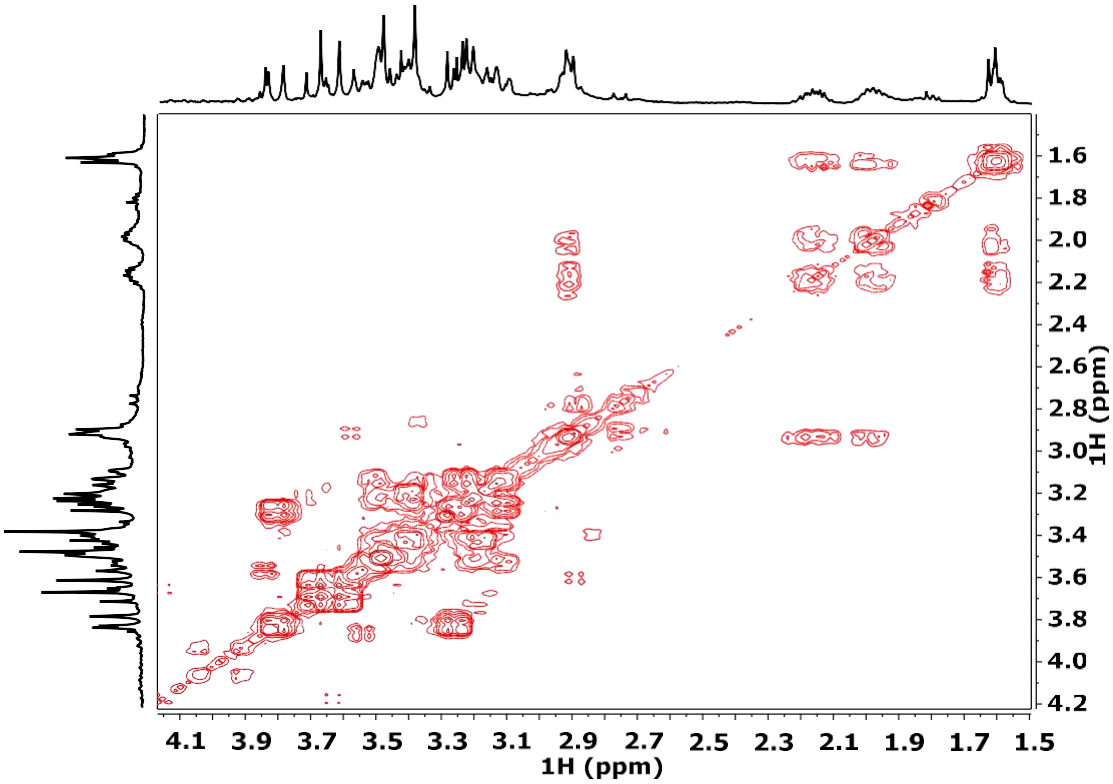

Figure S42. $^{1}H - {}^{1}H$ COSY spectra of [Ga(TRASUTA)OH]$^{-}$ ([GaL]=20 mM, pD=7.44, 298K, D_2O

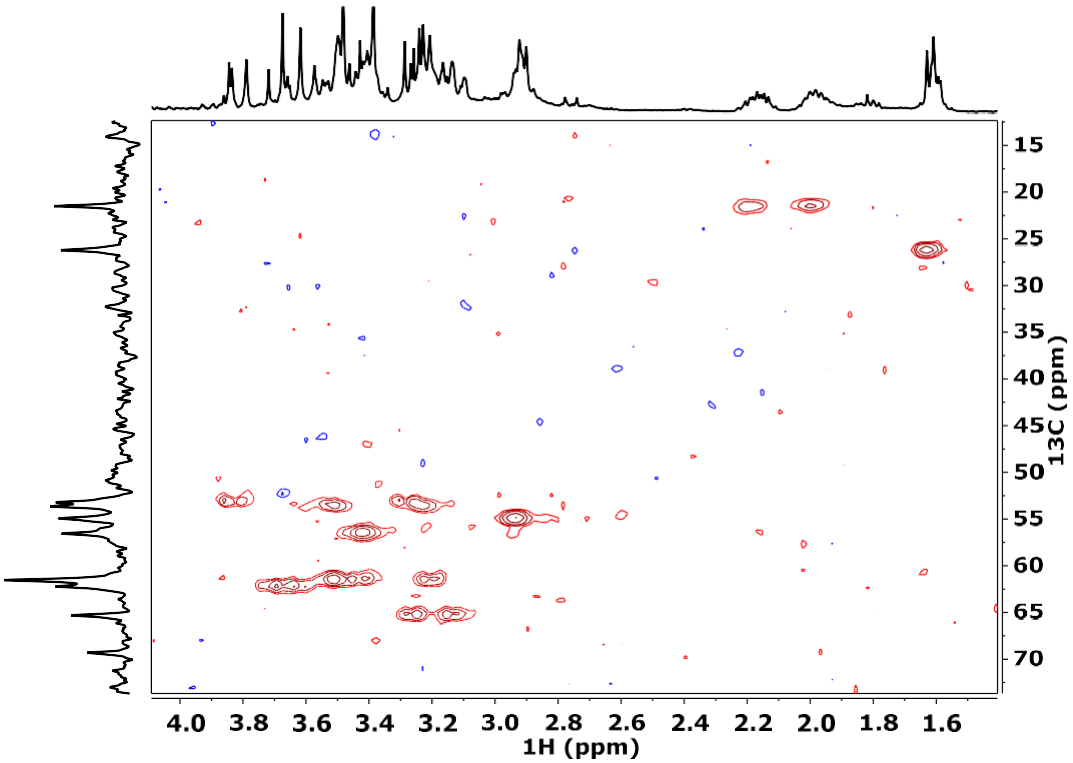

Figure S43. $^{1}H - {}^{13}C$ HSQC spectra of [Ga(TRASUTA)OH]$^{-}$ ([GaL]=20 mM, pD=7.44, 298K, 9.4 T, D_2O).

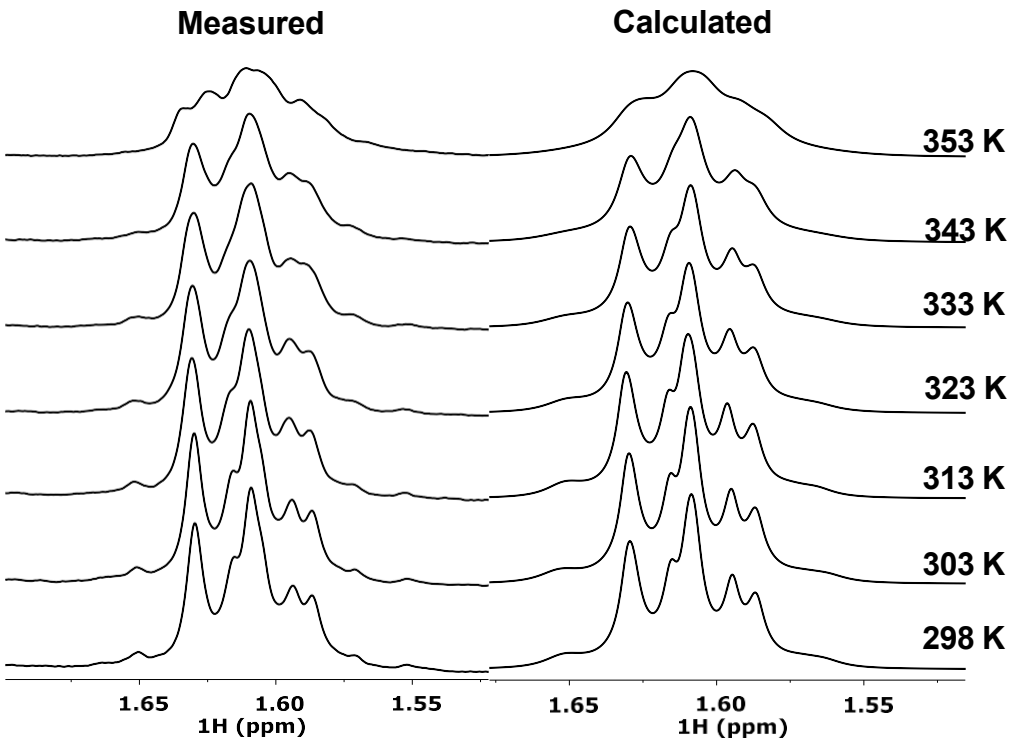

Figure S44. Measured and calculated VT-^{1}H NMR spectra of [Ga(TRASUTA)OH]$^{-}$ ([GaL]=20 mM, pD=7.44, 9.4 T, D_2O)

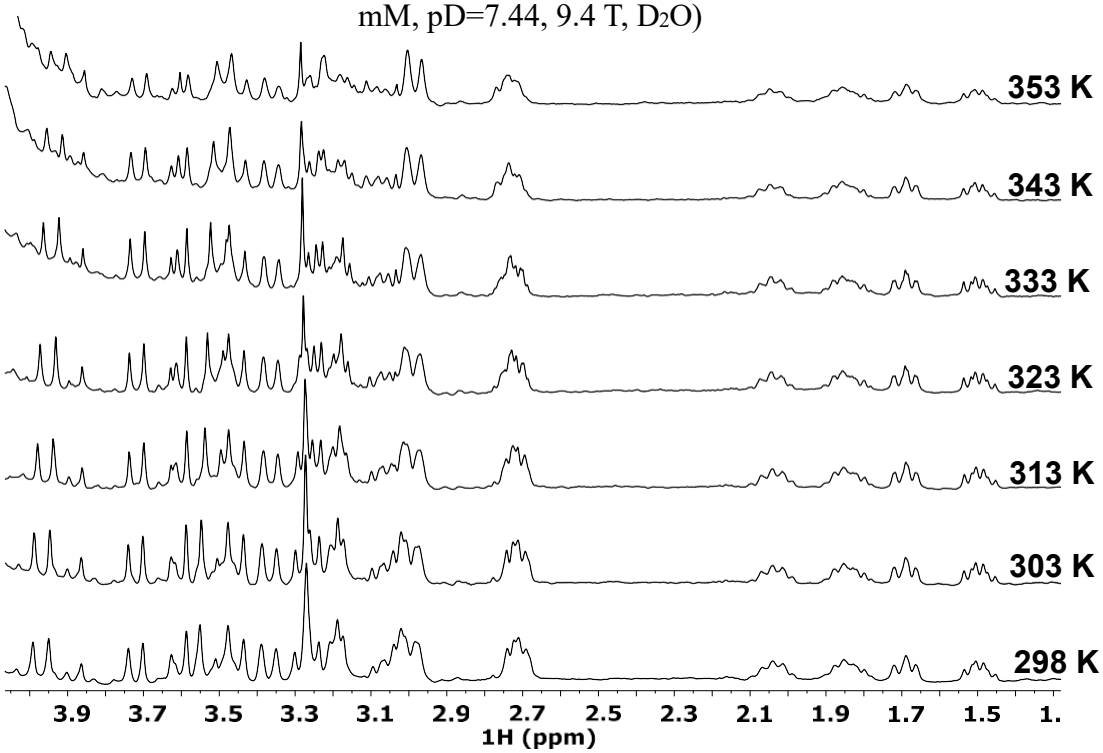

Figure S45. VT-^{1}H NMR spectra of [Pb(TRASUTA)]$^{-}$ ([PbL]=20 mM, pH=7.05, 9.4 T, H_2O)

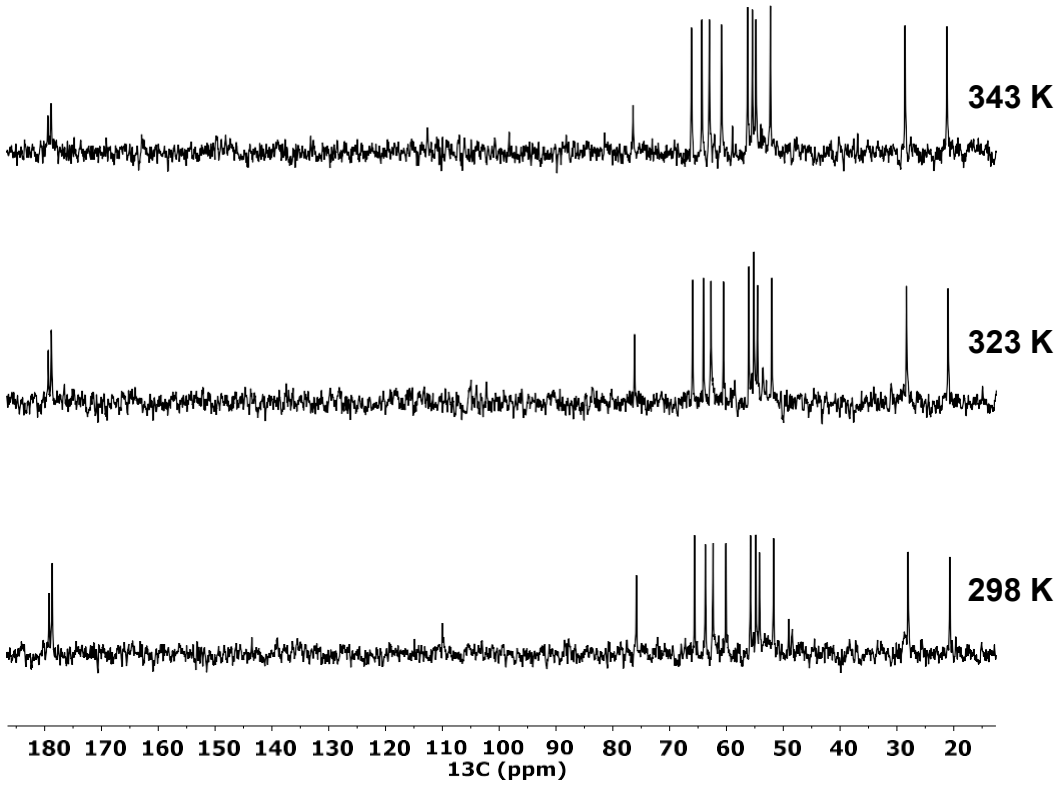

Figure S46. VT $-^{13}$C NMR spectra of $[Pb(TRASUTA)]^-$ ([PbL]=20 mM, pH=7.05, 9.4 T, H_2O)

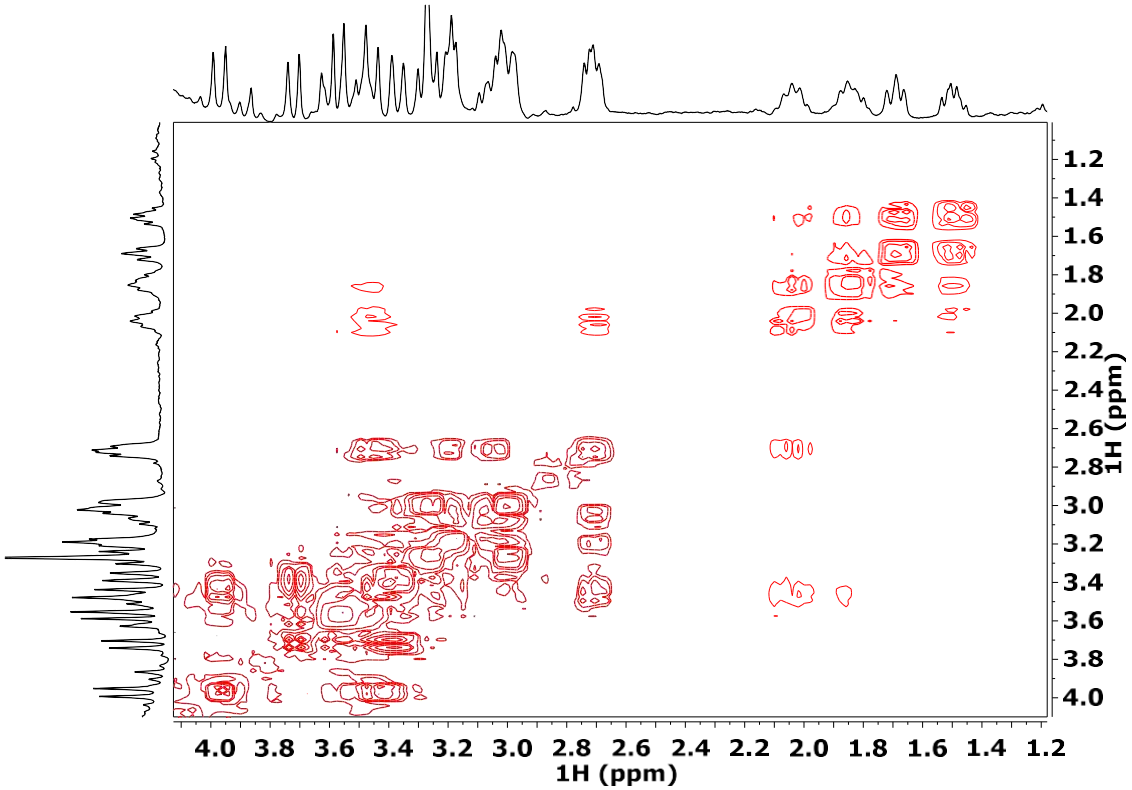

Figure S47. ^{1}H – ^{1}H COSY spectra of $[Pb(TRASUTA)]^-$ ([PbL]=20 mM, pH=7.05, 298K, 9.4 T, H_2O).

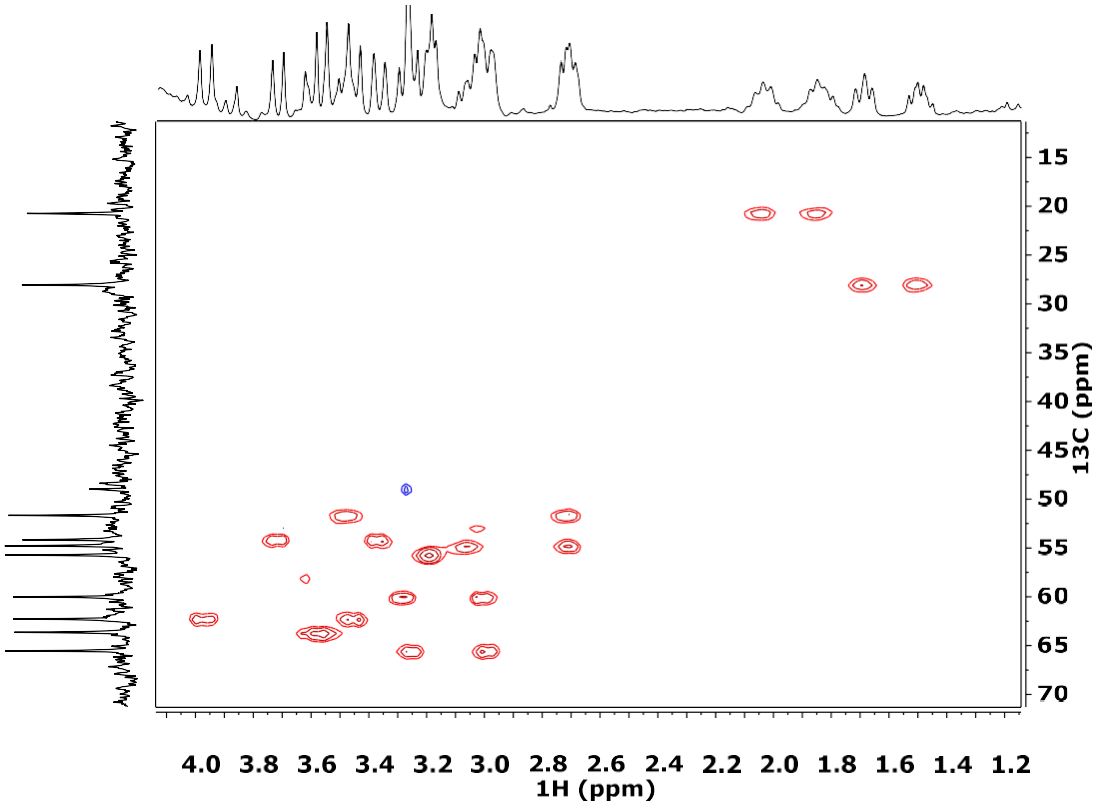

Figure S48. $^{1}H - {}^{1}H$ HSQC spectra of $[Pb(TRASUTA)]^{-}$ ([PbL]=20 mM, pH=7.05, 298K, 9.4 T, H_2O).

Table S1. NMR spectral parameters for $[Zn(TRASUTA)]^{-}$, [Ga(TRASUTA)], $[Ga(TRASUTA)OH]^{-}$ and $[Pb(TRASUTA)]^{-}$ complexes.

	[Zn(TRASUTA)]$^{-}$		**[Ga(TRASUTA)]**		**[Ga(TRASUTA)OH]$^{-}$**		**[Pb(TRASUTA)]$^{-}$**	
1H / ppm	1.42	1.45	1.66	1.70	1.59	1.63	1.50	1.69
2H / ppm	1.89	2.13	2.07	2.24	1.98	2.17	1.83	2.02
$^{1}J_{1H1H}$ / Hz	8.3		10.2		9.4		13.2	
$^{3}J_{1H2H}$ / Hz	8.9	9.0	8.8	8.8	8.2	8.4	9.8	7.7
$^{3}J_{1H2H}$ / Hz	2.4	0.9	2.6	0.5	3.5	0.5	3.5	2.7

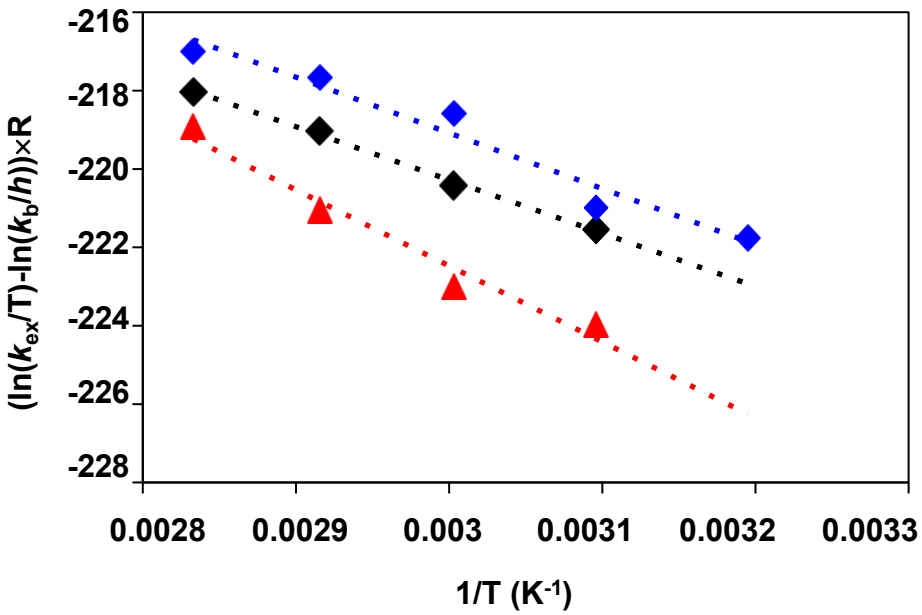

Figure S49. *Eyring* plot for determining the activation parameters of the isomerization in the pyrrolidine group of **[Zn(TRASUTA)]**$^{-}$, **[Ga(TRASUTA)]** and **[Ga(TRASUTA)OH]**$^{-}$ complexes.

References

(1) Irving, H. M.; Miles, M. G.; Pettit, L. D. A Study of Some Problems in Determining the Stoicheiometric Proton Dissociation Constants of Complexes by Potentiometric Titrations Using a Glass Electrode. *Anal. Chim. Acta*, **1967**, *38*, 475–488.

(2) Zekany, L.; Nagypal, I. in Computational Methods for the Determination of Formation Constants, ed. D. J. Leggett, Springer US, Boston, MA, **1985**, pp. 291–353.

(3) Submeier J. L.; Reilley, C. N. Nuclear Magnetic Resonance Studies of Protonation of Polyamine and Aminocarboxylate Compounds in Aqueous Solution. *Anal. Chem.*, **1964**, 36, 1698–1706.

(4) Farkas, E.; Nagel, J.; Waldron, B. P.; D. Parker, D.; Tóth, I.; Brücher, E.; Rösch F.; Baranyai, Z. Equilibrium, Kinetic and Structural Properties of Gallium(III) and Some Divalent Metal Complexes Formed with the New $DATA^{m}$ and $DATA^{5m}$ Ligands. *Chem. Eur. J.*, **2017**, *23*, 10358–10371.

(5) Baranyai, Z.; Uggeri, F.; Maiocchi, A.; Giovenzana, G. B.; Cavallotti, C.; Takács, A.; Tóth, I.; Bányai, I.; Bényei, A.; Brucher E.; Aime, S. Equilibrium, Kinetic and Structural Studies of AAZTA Complexes with Ga^{3+} , In^{3+} and Cu^{2+}. *Eur. J. Inorg. Chem.* **2013**, 147–162.Z.

(6) Baranyai, Z.; Brucher E.; Uggeri, F.; Maiocchi, A.; Tóth, I.; Andrási, M.; Gáspár, A.; Zékány L.; Aime, S. The role of equilibrium and kinetic properties in the dissociation of Gd[DTPA-bis(methylamide)] (Omniscan) at near to physiological conditions**.** *Chem. Eur. J.*, **2015**, *21*, 4789–4799.

(7) A. E. Martell and R. M. Smith, Critical stability constants, Plenum Press: New York, **1974**, vol. 1−6.

(8) Farkas, E.; Vágner, A.; Negri, R.; Lattuada, L.; Tóth, I.; Colombo, V.; D. Esteban-Gómez, D.; Platas-Iglesias, C.; Notni, J.; Baranyai, Z.; Giovenzana, G. B. PIDAZTA: Structurally Constrained Chelators for the Efficient Formation of Stable Gallium-68 Complexes at Physiological pH. *Chem. Eur. J.*, **2019**, *25*, 10698– 10709.

(9) Vágner, A.; D'Alessandria, C.; Gambino, G.; Schwaiger, M.; Aime, S.; Maiocchi, A.; Tóth, I.; Baranyai, Z.; Tei, L. A rigidified AAZTA-like ligand as efficient chelator for ^{68}Ga radiopharmaceuticals. *ChemistrySelect*, **2016**, *1*, 163–171.

(10) Baranyai, Z.; Uggeri, F.; Giovenzana, G. B.; Bényei, A.; Brücher E.; Aime, S. Equilibrium and kinetic properties of the lanthanoids(III) and various divalent metal complexes of the heptadentate ligand AAZTA. *Chem. Eur. J.*, **2009**, *15*, 1696–1705.

Chapter 2

Pb(II) and Bi(III)-complexes with azamacrocyclic and open-chain ligands for *in vivo* applications of the $^{212}Pb/^{212}Bi$ isotope pair in targeted alpha therapy (TAT)

The work reported in this Chapter was performed at the Bracco Imaging laboratories of Basovizza (TS) under the supervision of Dr. Zsolt Baranyai with the assistance of Dr. Mariangela Boccalon and Dr. Nicol Guidolin.

Introduction

Physicochemical and radiochemical properties of $^{203/212}Pb$ and $^{212/213}Bi$

Radionuclides of lead (Pb^{2+}) and bismuth (Bi^{3+}) ions have emerged in the last years as key elements in the development of radiopharmaceuticals due to their favorable decay characteristics and their potential application in medical diagnosis and therapy. In particular, some of their isotopes – ^{203}Pb, ^{212}Pb, ^{212}Bi, and ^{213}Bi – represent viable probes of radiodiagnostics (RDx) and radiotherapeutics (RTx) that show promise in the growing demand for personalized medicine in oncology.[1] In the following chapter we will consider both their physico-chemical properties, radiochemical and clinical aspects of their applications.

Lead: chemistry and production of radioisotopes ^{212}Pb and ^{203}Pb

In standard conditions and aqueous solutions, the lead cation is primarily found in the 2+ oxidation state. Due to its relatively low affinity to OH^- ion, hydrolysis of Pb^{2+} ion is usually negligible under acidic conditions (Figure 1). However, it was observed that Pb^{2+} can form mono- (e.g. $[Pb(OH)]^+$, $[Pb(OH)_2]$, and $[Pb(OH)_3]^-$) and poly-nuclear hydroxides (*e.g.* $[Pb_2(OH)]^{3+}$, $[Pb_3(OH)_4]^{2+}$, $[Pb_4(OH)_4]^{4+}$, $[Pb_6(OH)_8]^{4+}$) with various solubility at pH > 6 even in dilute aqueous solutions.

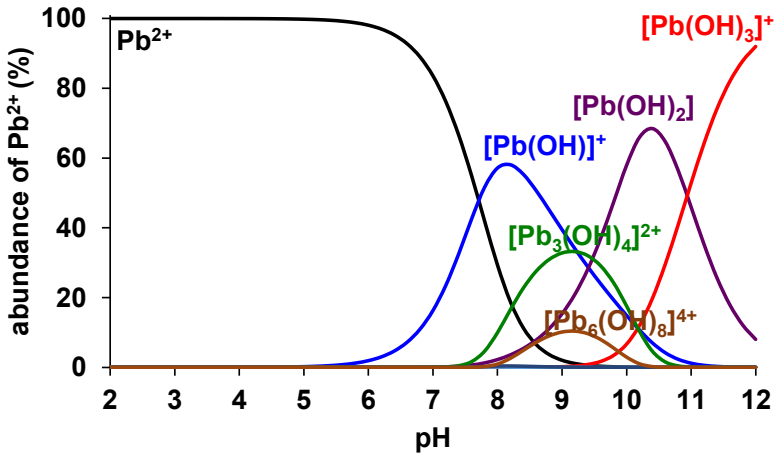

Figure 1. Species distribution of Pb^{2+} ion ($[Pb^{2+}] = 1.0 \times 10^{-4}$ M). Equilibrium constants characterizing the hydrolysis of the Pb^{2+} ion.[2]

The large ionic radius of Pb^{2+} ion shows modest variations depending on the coordination number. For instance, the effective ionic radius of Pb^{2+} is 1.19 and 1.29 Å in hexa- and octa-coordinate complexes, respectively.[3] A peculiarity of Pb^{2+} is the presence of the lone pair $6s^2$ in its electron shell, which is characterized by the so-called "inert pair effect" seen commonly in heavier elements due to relativistic effects. This phenomenon typically translates in an increased stability for the lower 2+ compared to the 4+ oxidation state. Moreover, it may have a stereochemical effect and influence its coordination geometry, causing it to be more asymmetric. In fact, the stereochemical activity of the lone pair can be present to different extents and has been debated for a long time. It was found that high coordination numbers (> 8) typically present a scarce stereochemical influence of such electron pair and these systems are defined as holodirected, exhibiting a spherical symmetry (Figure 2). Conversely, complexes with low coordination numbers (< 6) possess a well-defined stereochemically-active lone pair and these systems are defined as hemidirected, in which the uneven electron density translates into an overall asymmetry with a visual gap in its coordination sphere (Figure 2). Thus, it is characteristic of hemidirected complexes to present distorted geometries (twisted square pyramidal, seesaw, capped octahedral with lone pair gap).[4][5] This phenomenon is typically observed for complexes with smaller open-chain ligands such as EDTA and acac, in which a notable space in the first coordination sphere is present (Figure 3). With multidentate ligands such as 18-crown-6 and EGTA (Figure 3) Pb–L bond distances are longer and differ less between each other. Additionally, the donor atoms are far from each other, thus cannot occupy preferentially one side of Pb^{2+}. In this sort of complexes, the lone pair of Pb^{2+} is stereochemically inactive because of the homogeneous distribution of electron density around the cation with respect to the distant location of donor atoms.[6] It is worth noting that each complex should be treated case-by-case, since the lone pair activity depends on several factors, such as the hard/soft nature and the electrostatic interactions between the donor atoms of the ligand.

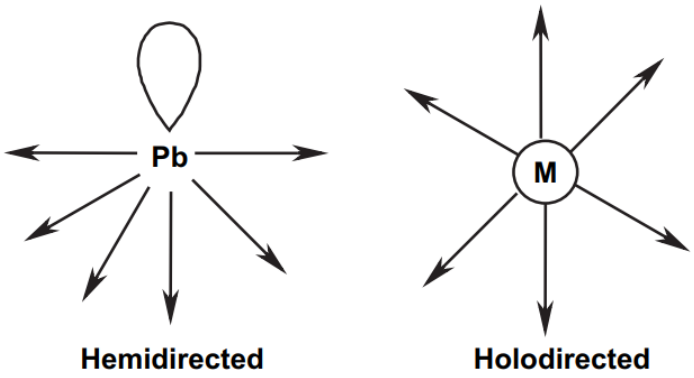

Figure 2. Hemidirected and holodirected coordination spheres.

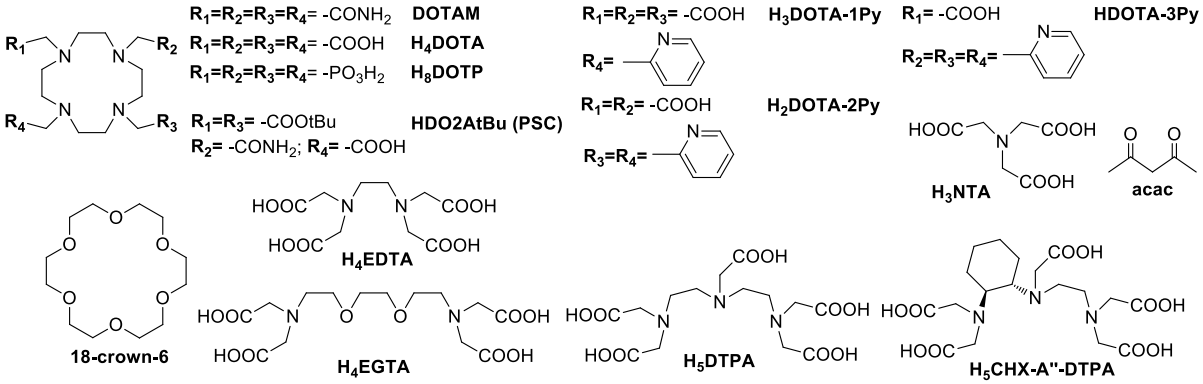

Figure 3. Structure of ligands mentioned in this chapter (DOTAM: 1,4,7,10-tetrazacyclododecan-1,4,7,10-tetraacetamide, H_4DOTA: 1,4,7,10-tetrazacyclododecan-1,4,7,10 tetraacetic acid, H_8DOTP: 1,4,7,10-tetraazacyclododecane-1,4,7,10-tetramethylenephosphonic acid, HDO2AtBu: 2-(7-(2-amino-2-oxoethyl)-4,10-bis(2-tert-butoxy-2-oxoethyl)-1,4,7,10-tetraazacyclododecan-1-yl)ethanoic acid, H_4EDTA: 2,2′,2″,2‴-(1,2-ethanediyldinitrilo)tetraacetic acid).

Despite being a pure β^--emitter ($t_{1/2}$ = 10.6 h), ^{212}Pb is investigated for targeted alpha therapy (TAT) since it acts as an *in vivo* generator of the alpha emitters ^{212}Bi ($t_{1/2}$ = 60.6 min, $E_{\alpha,avg}$ = 6.2 MeV, 36%) and ^{212}Po ($t_{1/2}$ = 0.3 µs, $E_{\alpha\ avg}$ = 8.9 MeV) (Scheme 1). Due to its relatively long half-life, ^{212}Pb allows an extended radiopharmaceutical preparation and efficient shipping across longer distances compared to its alpha-emitting daughter nuclides. Moreover, the half-life of ^{212}Pb is compatible with the pharmacokinetics of slowly targeting large vectors (*e.g.,* affibodies, engineered proteins that mimic the selective binding of antibodies), providing an opportunity for the development of efficient ^{212}Pb-based RTx using highly selective peptides. The ^{212}Pb isotope is typically obtained as $^{212}Pb^{2+}$ ion from ^{228}Th ($t_{1/2}$ = 1.9 y) or ^{224}Ra ($t_{1/2}$ = 3.64 d) generators. The cross section of ^{228}Th/^{212}Pb generator is shown in Figure 4. The resin traps the parent nuclide (^{228}Th or ^{224}Ra) and the ^{220}Rn formed in the decay is moved to the other chamber by using air steam (Figure 4). As the decay chain progresses from ^{220}Rn, ^{212}Pb deposits on the chamber walls and can be collected by washing it with aqueous solutions

of strong acids (HCl or HNO_3) or complexing agents, with yields of 70 – 90%. In such way, ^{212}Pb production is considerably facilitated and safer, as it does not require chromatographic purification or extensive handling of the parent nuclide, maintaining the system functional over a long period.

Another important radioisotope of lead in clinical application is ^{203}Pb. In fact, ^{203}Pb can be employed as a diagnostic pair of ^{212}Pb due to its decay via electron capture, emitting a 279 keV photon suitable for SPECT imaging. However, the cyclotron production of ^{203}Pb via proton bombardment of thallium targets poses significant challenges due to the high toxicity of the thallium and small cross section of ^{203}Tl.[7]

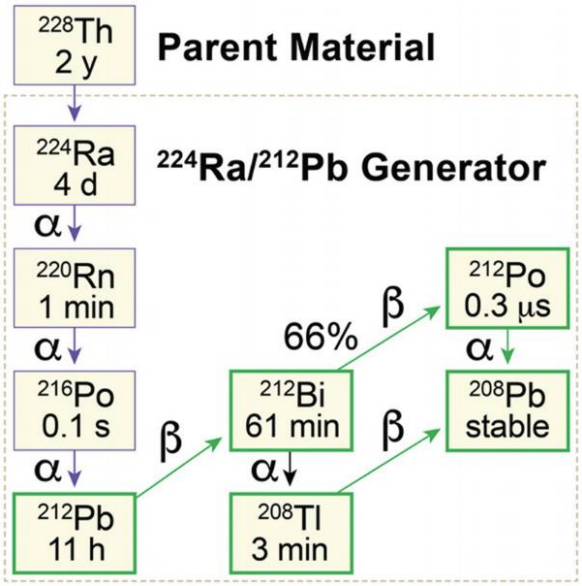

Scheme 1. Decay chain of ^{228}Th leading to therapeutic pair $^{212}Pb/^{212}Bi$.

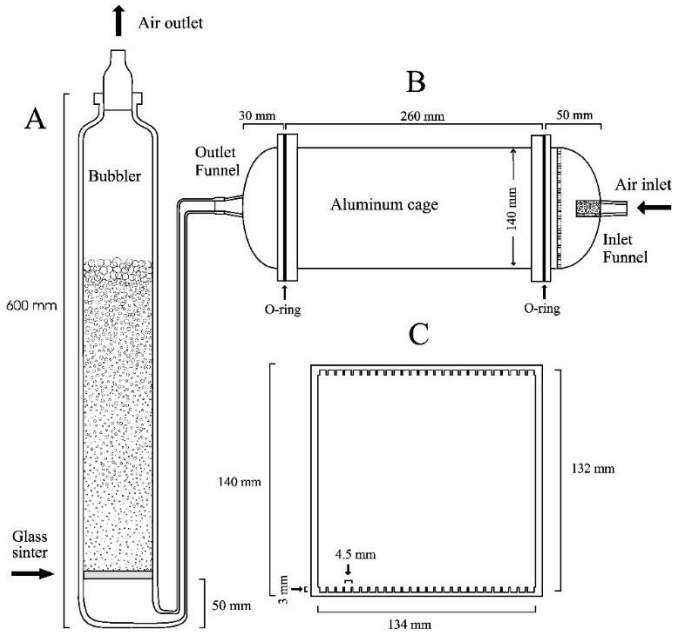

Figure 4. Example of ^{212}Pb generator consisting of two major compartments, the ^{228}Th and ^{220}Rn chambers. [^{228}Th] is introduced on a barium stearate support inside a cage (**B, C**) where dry air flows continuously, carrying ^{220}Rn into the collection chamber (**A**) filled with an organic solvent at low temperature (< –71°C). This enables the extraction and solidification of the radon gas. The decay product of interest ^{212}Pb is entrapped in the collection chamber and can be recovered with a HNO_3 solution.[8]

Bismuth: chemistry and production of radioisotopes ^{212}Bi and ^{213}Bi

Bismuth has two alpha-emitting nuclides of potential therapeutic use, ^{212}Bi ($t_{1/2}$ = 60.6 min, $E_{\alpha,avg}$ = 6.2 MeV, 36%) and ^{213}Bi ($t_{1/2}$ = 45.6 min, $E_{\alpha,avg}$ = 8.5 MeV, 97.2%). The decay chains leading to the formation of ^{212}Bi and ^{213}Bi isotopes are shown in Scheme 2. ^{212}Bi is produced via the decay of natural ^{232}Th, appearing as the direct daughter of ^{212}Pb (Scheme 2b), whereas ^{213}Bi is obtained from the decay of ^{229}Th, the longest-lived daughter of ^{225}Ac (Scheme 2a). Bismuth in aqueous solution is prevalently found as a trivalent ion, with the $6s^2$ valence electrons acting as a stereochemically inert lone pair in most of the coordination complexes. It was found that even in very acidic solution (1 M $HClO_4$), the Bi^{3+} ion is hydrolysed via the formation of mono- and polynuclear hydroxo species (Figure 6). Only few inorganic salts are known with bismuth in +5 oxidation state (e.g. BiF_5 and $NaBiO_3$ which are strong oxidizing agents).

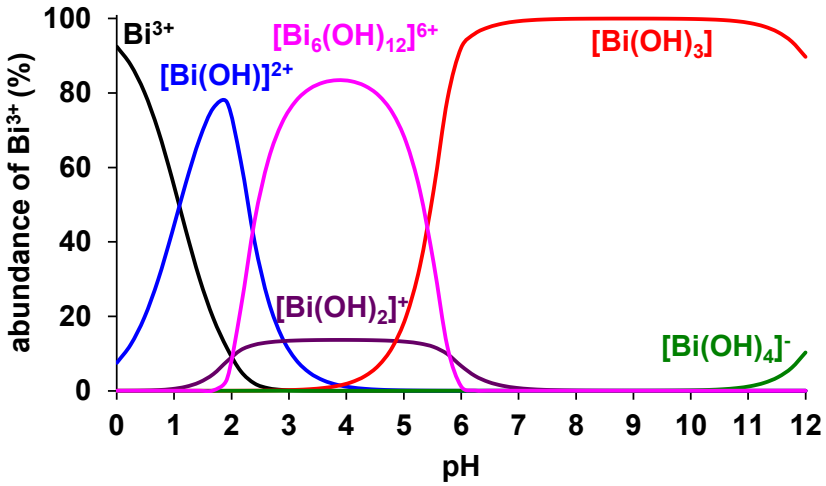

Figure 6. Species distribution of Bi^{3+} ion ($[Bi^{2+}] = 1.0\times10^{-4}$ M). Equilibrium constants characterizing the hydrolysis of Bi^{2+} ion.[2]

The coordination behaviour of the Bi^{3+} ion was studied thoroughly and, similarly to Pb^{2+}, it exhibits a variety of coordination numbers and irregular coordination geometries with oxygen and nitrogen donor atoms, as well as sulphur-containing groups, given its borderline/soft nature. Bi^{3+} complexes with varying coordination numbers (3 – 10) have been examined, with the typical ionic radius for CN = 8 reported as 1.17 Å.

Although ^{212}Bi can be generated *in vivo* via a $^{212}Pb/^{212}Bi$ generator (Scheme 2b), certain applications, such as targeting colon carcinoma and myeloma tumors, require ^{212}Bi that is free of its parent isotope.[9,10] State-of-the-art $^{212}Pb/^{212}Bi$ generators include newly developed column materials which incorporate specialized resins and sorbents capable of efficiently retaining the parent radionuclide, while ensuring a straightforward elution of the daughter isotope. Developments in elution methodologies, such as optimized eluent compositions and flow rates, have been critical in increasing $^{212}Bi^{3+}$ yield while minimizing $^{212}Pb^{2+}$ residual impurities. By varying the acid content in the mobile phase, the selective elution of $^{212}Bi^{3+}$ is achievable. Namely, it is favoured by relatively diluted HCl solutions (~ 0.4 M), while more concentrated acid solutions (up to 2 M) are required for the elution of $^{212}Pb^{2+}$.[11] The clinical significance of $^{212}Pb/^{212}Bi$ generators can be extended across a wide spectrum of cancer types including, but not limited to, prostate, ovarian, and pancreatic cancers. Hence their respective radiolabelled compounds offer a promising therapeutic modality, particularly for metastasis and radioresistant tumors (*vide infra*).

The ^{213}Bi isotope is also clinically accessible, namely through automated $^{225}Ac/^{213}Bi$ isotope generators. These systems rely on cation exchange chromatography to retain ^{225}Ac on the resin and elute $^{213}Bi^{3+}$ using a 1:1 ratio mixture of HCl and NaI. Owing to the long half-life of ^{225}Ac ($t_{1/2}$ = 10 days), this generator can be shipped and stored for up to two weeks, enabling in-house production of ^{213}Bi. Regardless of the source, radionuclides of bismuth are continuing to emerge as promising tools against cancer, possibly heralding a new era of precision medicine and personalized therapeutics.

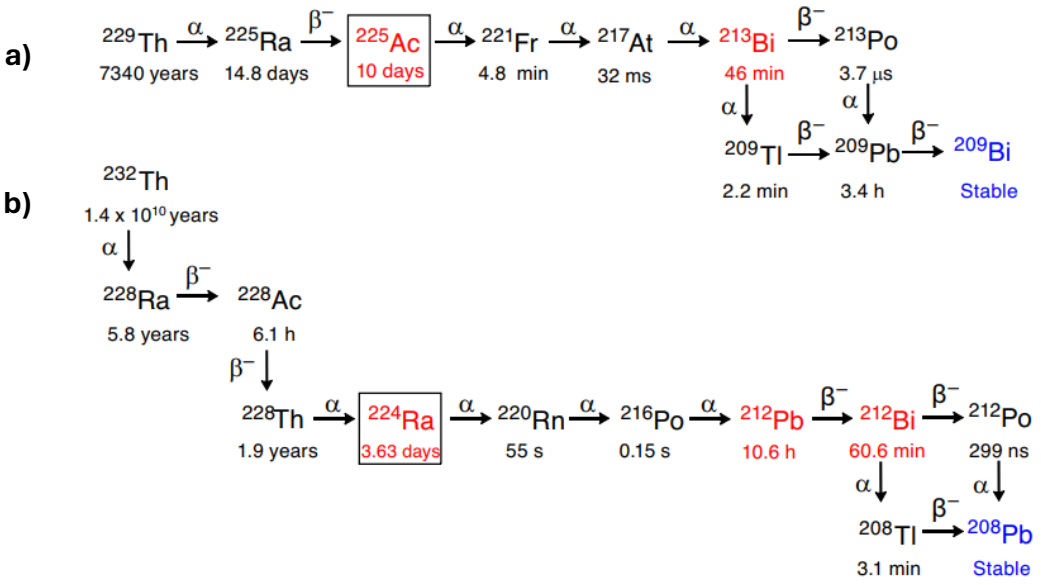

Scheme 2.[12] Decay chains for the production of: a) ^{213}Bi and b) ^{212}Pb/^{212}Bi therapeutic radionuclides.

$^{212}Pb^{2+}/^{212}Bi^{3+}$ radiopharmaceuticals for prostate, neuroendocrine and melanoma tumor therapies

In the last decade, TAT showed great promise for a variety of cancers, especially those exhibiting targetable moieties on their surfaces. In fact, the $^{212}Pb^{2+}$ ion does not exhibit an inherent preference to accumulate in tumors as it localizes primarily in the bones, while its ^{212}Bi daughter ion is retained by the kidneys, spleen and liver.[13] Thus, a strategy to induce tumor localisation must be employed. The target should ideally be expressed by metastasised cells in addition to the primary tumor and be located extracellularly for being accessible to the circulating radiopharmaceutical.

The targetable tumors include prostate cancer, which is one of the most common type of malignancies affecting male patients worldwide. The prostate-specific membrane antigen (PSMA) is a transmembrane protein overexpressed in > 90% of prostate cancers, hence is used as a target in radiotherapy. In particular, the Glu-Urea-Lys motif allows the selective binding to PSMA and is used in most small-molecule PSMA inhibitors.[14] In addition to PSMA, alternative prostate cancer cell surface receptors were recently identified, such as the CD46 antigen. Furthermore, it was also found overexpressed in primary tumor tissue of not only prostatic cancer, but also of neuroendocrine and adenocarcinoma while being expressed at low levels in healthy tissues.[15]

Neuroendocrine tumors (NET) are a heterogeneous group of tumors originating from neuroendocrine cells. They can occur in various parts of the body, although most commonly in the gastrointestinal tract and lungs. For NET the somatostatin receptor subtype 2 (SSTR2),

highly overexpressed by these malignancies, is the standard target. The current standard of care for SSRT2-positive neuroendocrine tumors includes the β^- emitter [^{177}Lu]Lu-DOTATATE, which contains the SSRT2 targeting peptide octreotide. However, on-going clinical trials are also exploring $^{212}Pb^{2+}$ complexes with DOTA-PEGylated peptides such as ^{212}Pb-PSC-PEG$_2$-TOC (Figure 7b) and [^{212}Pb]Pb-VMT-α-NET, which is currently in phase I/IIa to assess safety and optimal dosing.[16]

[^{212}Pb]Pb^{2+} complexes are being studied for the treatment of metastatic melanoma by targeting the MC1R receptor, which is overexpressed on the cell membrane of these tumor cells. Radiopharmaceuticals such as [^{212}Pb]Pb-VMT01, comprised of a slightly more lipophilic DOTA-PEGylated peptide, are an emerging class of targeted alpha-particle tumor drugs that could improve the delivery and efficacy of radiation doses (Figure 7c).

A favourable scenario would be the internalization of the targeting vector upon receptor binding, resulting in intracellular confinement and retention of ^{212}Pb at the tumor site. Internalization typically occurs with antibodies, therefore one of the alternative promising strategies that has been developed is radioimmunotherapy (RIT). By labelling a monoclonal antibody (mAb) with ^{212}Pb, which serves as an *in vivo* generator of ^{212}Bi, it is possible to improve the radiotherapeutic efficacy of ^{212}Bi, since its decay occurs mainly in the tumor, and not during the labelling process. Another major advantage of using ^{212}Pb as the "payload" that targets the tumor instead of ^{212}Bi is that the former delivers a more than 10 times larger amount of energy per administered unit compared to ^{212}Bi alone or the α-emitter ^{213}Bi.[17] A widely studied antibody for radiopharmaceutical applications of ^{212}Pb is trastuzumab, an immunoglobulin G (IgG) mAb which is internalised upon binding to the human epidermal growth factor receptor 2 (HER2), a membrane receptor present on a variety of solid tumors. Another commonly employed antibody is rituximab, which consists in a mAb conjugate targeting a transmembrane protein expressed by B-cells known as CD20, which greatly extended the survival times in early- and late-stage lymphoma models compared to the untreated and aspecific controls.[18]

Historically, ^{213}Bi was the first α emitter to be studied in humans, after complexation with the bifunctional chelating agent SCN-CHX-A''-DTPA (Figure 3) conjugated with lintuzumab (HuM195), a humanized anti-CD33 antibody targeting myeloid leukemia cells.[19] Although no complete remission was observed, 14 of 18 patients (78%) showed a significant reduction in marrow blasts. A follow-up study demonstrated that sequential administration of the chemotherapeutic agent cytarabine prior to ^{213}Bi-lintuzumab treatment induced complete remission in some patients. These results were attributed to the reduction of tumor volume induced by cytarabine, improving the impact of radiations of ^{213}Bi-lintuzumab.[20] Thereafter, ^{213}Bi-radioimmunoconjugates were also investigated for treatment of malignant melanoma or of bladder cancer.[21,22]

Macrocyclic ligands (*e.g.* DOTA and DOTP, Figure 3) bind Bi(III) with an exceptionally high stability, thus most of the investigated Bi(III)-based radiopharmaceuticals were developed starting from the "gold standard" DOTA.[23] ^{213}Bi(III)- and ^{225}Ac(III)-complexes of DOTA-peptides conjugates are currently in clinical trials as TAT-agents for the treatment of NETs.[23,24] It has been demonstrated that [^{213}Bi(DOTA-TATE)] can serve as a radiotracer for SPECT imaging, expanding the application of ^{213}Bi(III) complexes from therapy to diagnosis, and

theranostics.[25] Furthermore, [^{213}Bi(DOTATOC)] was also successful in the treatment of tumors that are not responsive to β^--therapy.[26]

Nevertheless, the formation of $[Bi(DOTA)]^-$ is quite slow and requires high temperatures for long reaction times and high concentration of ligand (30 – 60 min at 95 °C, pH 4 – 9, [DOTA] = 10 μM),[23] whereas the formation of $[Bi(DOTP)]^{5-}$ is significantly faster.[27] However, $[^{212/213}Bi(DOTP)]^{5-}$ exhibits high bone uptake and rapid renal clearance, which can limit its utility for targeted treatment of neuroendocrine tumors and prostate cancer.[28] On the other hand, the short half-life of ^{213}Bi reduces the risk of systemic organ toxicity, but poses challenges for tracer development.

Several phase I studies were reported with ^{213}Bi-DOTA-Substance P for treatment of glioblastoma, where Substance P (SP) is an undecapeptide composed of the amino acid chain sequence Arg-Pro-Lys-Pro-Gln-Gln-Phe-Phe-Gly-Leu-Met, with an amidated C-terminus.[29] Despite positive results on reducing tumor volume and improving survival, the comparison with the analog ^{225}Ac-SP showed advantages for the latter when dealing with large tumors, mainly due to its longer half-life.[29] For the evaluation of ^{213}Bi in peptide receptor targeted therapy, ^{213}Bi(DOTA-TOC) was studied in patients that had developed resistance to ^{177}Lu(DOTA-TATE) therapy and resulted in a considerable number of long-lasting antitumor responses, including one complete remission. [29,30] Analogously, ^{213}Bi(PSMA-617) was tested in a patient with mCRPC (metastatic castration-resistant prostate cancer) that was progressive under conventional therapy. After eleven months, ^{68}Ga(PSMA) PET/CT showed an outstanding molecular imaging response.[31] The relative merits of ^{213}Bi-PSMA-617 or ^{225}Ac-PSMA-617 are still under debate.[32]

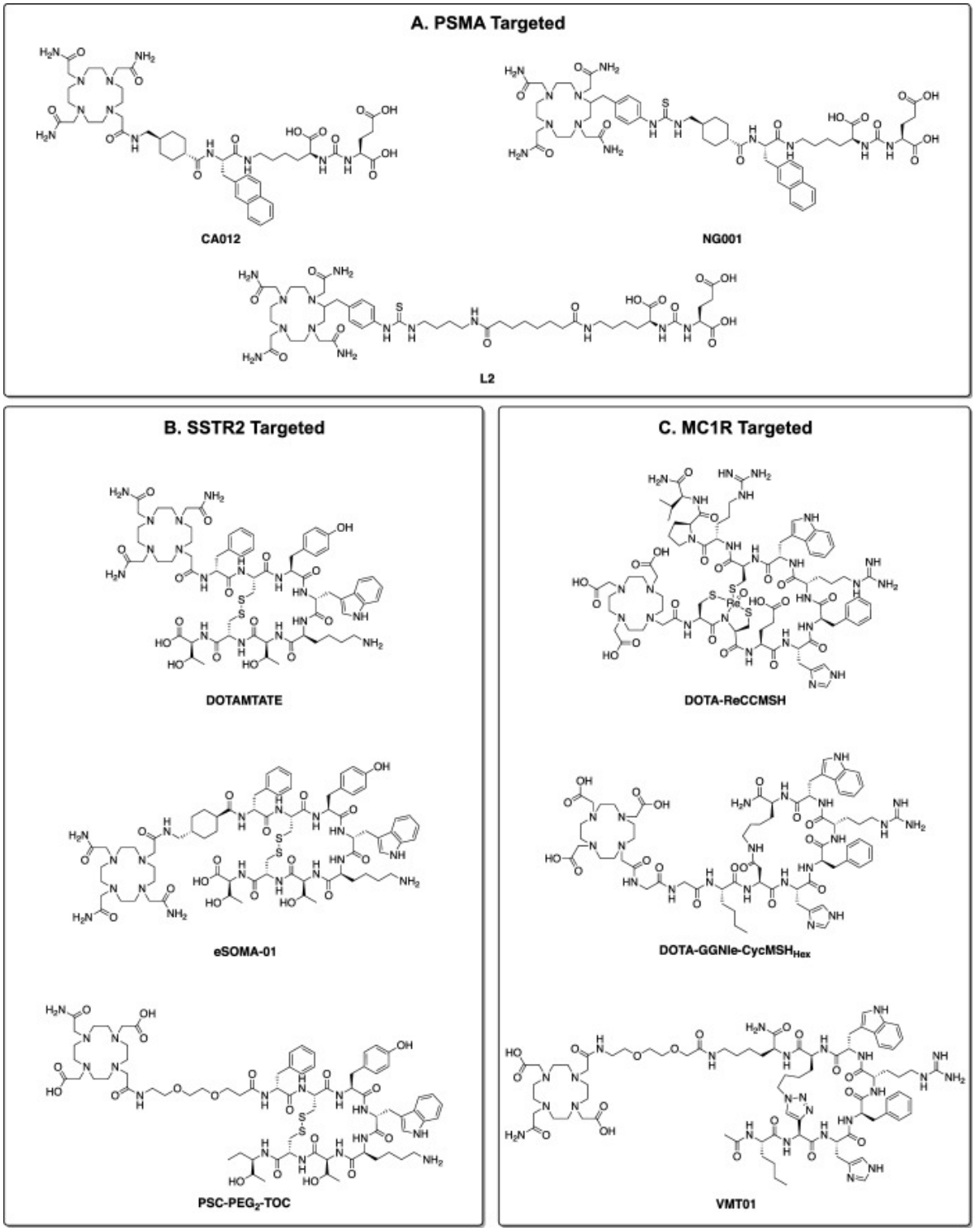

Figure 7. Clinically investigated small $^{212}Pb^{2+}$ complexes with peptide targeting vectors for: **A** prostate specific membrane antigen (PSMA); **B** somatostatin receptor subtype 2 (SSTR2); **C** melanocortin receptor 1 (MC1R).

Conformational dynamics of DOTA-derived complexes with heavy metals

Due to the widespread interest for DOTA and its derivatives for magnetic resonance imaging (MRI) and radiopharmaceutical applications, a vast amount of research was conducted to study their in-solution properties, specifically their conformational changes.[33][34][35] As mentioned above, the backbone of DOTA-like macrocycles consists in the 12-membered tetraazamacrocycle (cyclen), in which the four nitrogen atoms are linked through flexible ethylene (−CH_2−CH_2−) bridges and functionalized with acetate, acetamide and phosphonate pendant arms, in DOTA, DOTAM and DOTP, respectively (Figure 3). This type of backbone provides potentially an eight donor atom set (four nitrogens and four oxygens), enabling the ligand to bind metal ions with large ionic radii and high coordination numbers, such as Pb(II) and Bi(III).

The $DOTA^{4-}$ anion typically binds to large metal ions with all four ring nitrogen atoms and four carboxylate oxygens. The nitrogen atoms as well as the oxygen atoms form N4 and O4 roughly planar squares. Detailed multi nuclear NMR studies in solution and X-ray diffraction investigations in the solid phase reveal that the $[Ln(DOTA)]^-$ complexes (Ln stands for a generic lanthanide 3+ cation) can exist in two different coordination geometries. A larger torsion angle (39°) between the two square planes is associated with the square antiprismatic geometry (SAP), whereas a smaller torsion angle (25°) is related to the twisted square antiprism (TSAP)[36] (Figure 8). Depending on the size of the metal ion, the O4 plane can be capped by a coordinated water molecule.

Upon metal ion coordination, the ethylene groups of the cyclen ring form four flexible five-membered chelates with clockwise (δδδδ) or anticlockwise (λλλλ) helical conformation. Based on the two arrangements of the ethylene bridges the carbon atoms can lay alternatively above or below the 4N plane with the axial and equatorial positions of the –CH_2–CH_2– protons in the cyclen ring.

The four pendant acetate arms have two orientations that lead to two enantiomers of the complex, Λ (clockwise) or Δ (counter clockwise). By considering the helicities of the ethylene groups (δδδδ, λλλλ) and the pendant arms (Δ, Λ), four isomers (*i.e.* two enantiomeric pairs) can be present in solution: Δ(λλλλ)/Λ(δδδδ) (SAP) and Δ(δδδδ)/Λ(λλλλ) (TSAP) (Figure 8). Simultaneous rotation of the arms and inversion of ethylene rings result in the interconversion between the enantiomers. The X-ray structures of $Na[Bi(DOTA)]\cdot H_2O$ and $Na[Bi(H_4DOTP)]\cdot 4H_2O$ show that in the solid state all four ethylene rings typically have the same helical conformation, either all δδδδ or all λλλλ with Δ or Λ orientation of the pendant arms. The two enantiomers of TSAP (Λ(λλλλ) and Δ(δδδδ)) were characterized, with a 30° and 25.4° torsion angle between the N4 and O4 planes for $[Bi(DOTA)]^-$ and $[Bi(H_4DOTP)]^-$, respectively.[27,37]

Based on the single crystal X-ray structures, similar considerations can be made for $Na_3[Pb(DOTA)](NO_3)\cdot 2H_2O$ and $[Pb(DOTAM)](NO_3)_2\cdot 3.5H_2O$.[34,38] In both $[Pb(DOTA)]^{2-}$ and $[Pb(DOTAM)]^{2+}$ complexes, the Pb^{2+} ion is coordinated by four nitrogen and four oxygen atoms in TSAP geometry (Λ(λλλλ) and Δ(δδδδ)). The torsion angle between the N4 and O4 planes is 25.9° in $[Pb(DOTA)]^-$ and 26.1° in $[Pb(DOTAM)]^{2+}$.

As it is shown by the single crystal structures, the rotation of the arms and the inversion of ethylene rings are critical for achieving optimal coordination geometry, particularly for heavy metal ions such as Pb(II) and Bi(III), where steric and electronic characteristics induced by the metal can potentially favor specific combinations of ring and arm conformations.[39] In summary, the concerted processes of ring inversion and arm rotation, which define the overall structure of Pb(II)- and Bi(III)-DOTA complexes, affect both their thermodynamic behavior and the kinetics of complex formation and dissociation.

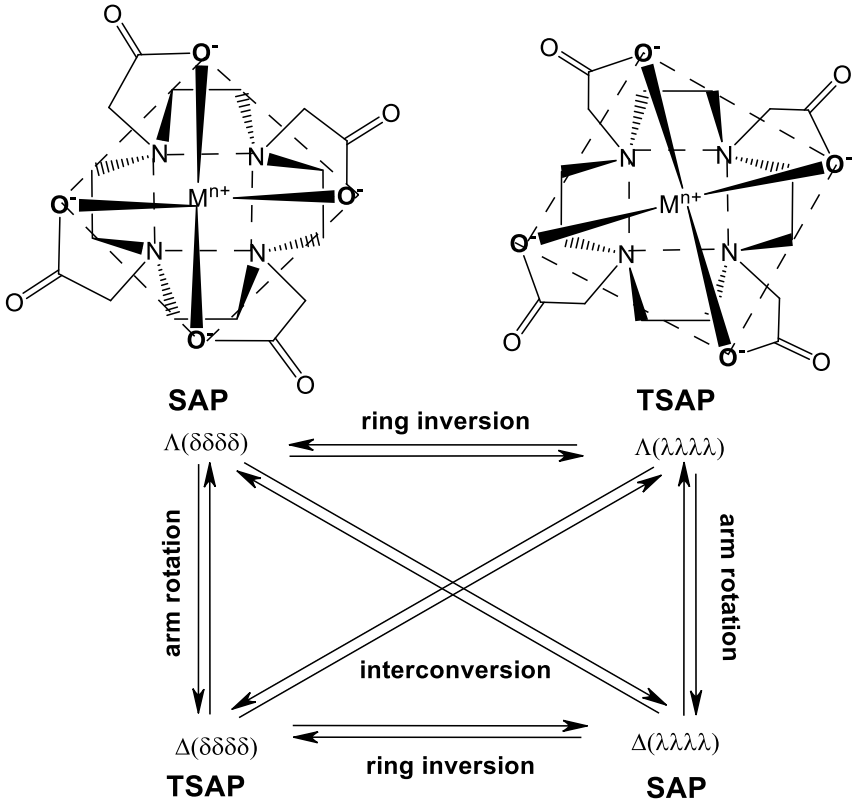

Figure 8. Conformation isomers of $[M(DOTA)]^{n-4}$ complexes (M^{n+}= Ln^{3+}, Bi^{3+} and Pb^{2+})

Investigated chelators for Pb^{2+}/Bi^{3+} radiotherapy

As both ^{212}Bi and ^{213}Bi alpha-emitting isotopes are available through commercial benchtop generators and therefore are of great interest, the objective of this study was to investigate chelators that might be suitable for both the long-lived mother nuclide ^{212}Pb and the short-lived daughters $^{212/213}$Bi.

Previous works have investigated a series of chelating agents such as DO2AtBu monoamide-monoacid, later named as Pb-specific-chelator (PSC). PSC is a DOTA-derivative bearing only one of the four original carboxylate groups, the others being transformed to one acetamide and two tert-butyl ester groups (Figure 3). It was hypothesized that this mixed donor set of ligands would reduce the net charge of the Pb(II) complex, while also maintaining a fair affinity for Bi^{3+} ion. Indeed, PSC afforded a > 96% radiolabeling efficiency of ^{212}Bi at 80 °C within 15 min.[40] Other studies investigated cyclen-based chelators DOTA-1Py, DOTA-2Py and DOTA-3Py, which have one, two and three pyridine pendant arms, respectively (Figure 3). Among

them, DOTA-3Py exhibited the highest radiolabeling yield with $^{203}Pb/^{212}Pb$.[41] In contrast, because DOTA-type chelators require relatively harsh radiolabelling conditions (high temperature, long reaction times), open-chain chelators such as DTPA and its analogues have also been studied. DTPA is a first generation radiometal chelator and has the advantage of undergoing quick radiolabelling at room temperature. Nonetheless, because of its low-to-moderate *in-vivo* stability it was soon replaced by other derivatives such as CHX-A″-DTPA (Figure 3), a ligand with a cyclohexyl ring in the backbone that confers rigidity and imposes a degree of pre-organization on the metal ion binding site.[42]

To establish a reference set of useful chelators for Pb^{2+}/Bi^{3+} systems, in this work we revised thoroughly the most widely used amino-polycarboxylate, -polyphosphonate and -polyamide ligands, starting from the cyclen-based macrocycles DOTA, DOTAM and DOTP (Figure 3), and evaluated their coordination ability towards Pb^{2+} and Bi^{3+} ions in terms of stability, inertness, and selectivity. Furthermore, with multinuclear NMR spectroscopy we characterized the solution structures of the respective Pb(II) complexes, as well as the dynamic properties that cause the interconversion between enantiomers. For comparison, also the open-chain ligands DTPA and EDTA (Figure 3) were investigated.

Results and discussion

Complexation properties of macrocyclic and open-chain polyamino-polycarboxylate ligands

To assess the complexation behavior of the polyamino-polycarboxylate, -polyphosphonate, and -polyamide macrocyclic ligands (DOTA, DOTP, and DOTAM) as well as the open-chain ligands (DTPA and EDTA, Figure 3) toward the selected metal ions, their protonation constants were first determined. The protonation constants defined by *Eq. 1* were calculated from pH-potentiometric titration data obtained at 25 °C in 0.15 M $NaClO_4$ solution and are listed in Table 1, along with literature values for comparison (standard deviations, 3σ, are given in parentheses).

$$K_i^H = \frac{[H_iL]}{[H_{i-1}L][H^+]} \quad (i = 1, 2\ldots7) \qquad \textit{Eq. 1}$$

In such manner, it was possible to gain insight into the acid-base properties of these ligands, that usually reflect the coordinative ability of the set of donor atoms towards metal ions. Firstly, it is important to make a distinction between the protonation constants relative to the different types of donor atoms: sp^3 nitrogens and carboxylate/phosphonate oxygen atoms. We observed that the first two protonation constants of DOTA ($\log K_1^H$ and $\log K_2^H$) fall in the pH range 9.1 – 9.5 and are relative to the sp^3 nitrogen atoms, the most basic in the set. Two consecutive protonation events occur on two opposite ring-*N* atoms.[43] For DOTAM lower values were observed, around 5.9 – 7.7, depending on the ionic strength. The lower basicity of the ring N atoms of DOTAM is consistent with the presence of the neutral, less basic and highly electron withdrawing amide substituents (compared to carboxylates in DOTA) on the pendant arms. Conversely, the first two protonation constants of DOTP are exceptionally high ($\log K_1^H = 13.60$

and $\log K_2^H$ = 12.21, respectively) due to the phosphonate groups which contribute to a larger negative total charge, hence increasing the basicity of the ring N donor atoms. It should be noted that in this case, due to intrinsic instrumental limitations that prevent the determination of constants at pH > 12, it is not possible to determine the $\log K_1^H$ and $\log K_2^H$ with conventional pH-potentiometry. Therefore, the protonation constants of DOTP were determined using complementary techniques, including ^{1}H and ^{31}P NMR spectroscopy experiments, where the sample pH was adjusted by adding a precisely calculated amount of concentrated NaOH.

The subsequent $\log K_i^H$ values fall in the mostly acidic pH range (1.1 – 9.1) and correspond to the protonation processes of the carboxylate or phosphonate oxygen atoms, starting from those bound to the non-protonated ring nitrogen atoms, in order to minimize the electrostatic repulsions.[44] Further protonation constants cannot be calculated for DOTAM due to the lack of the protonable donor atoms in the pendant arms.

The first and second protonations of DTPA occur at the central and terminal nitrogen atoms of the ligand backbone, whereas the first proton is transferred to the remaining unprotonated terminal N atom due to electrostatic repulsion between protonated donor atoms. The third protonation occurs partially on the central nitrogen and carboxylate oxygen donor atoms, while subsequent protonations take place on the carboxylate oxygen atoms of the terminal amino groups. In contrast, for EDTA, the first two protonations occur on the nitrogen atoms of the ligand backbone, and the remaining three occur on the oxygen donor atoms of the carboxylate pendant arms.[45,46]

Considering the overall basicity expressed as the sum of the protonation constants $\Sigma\log K_i^H$, it can be observed that macrocycles (except for DOTAM) exhibit higher total basicity compared to the open-chain ligands EDTA and DTPA (Table 1).

Table 1. Protonation constants of polyamino-polycarboxylate ligands (25°C). Values in blue are experimental data obtained in this work, the remaining values are taken from literature.

	DOTAM		DOTA		DOTP	DTPA		EDTA
I	**0.15 M $NaClO_4$**	**0.1 M $NaNO_3$**[25]	**0.15 M $NaClO_4$**[27]	**0.15 M NaCl**[47]	**0.15 M $NaClO_4$**[27]	**0.15 M $NaClO_4$**	**0.15 M NaCl**[47]	**0.15 M $NaClO_4$**
$\log K_1^H$	7.29(1)	7.70(1)	9.12(1)	9.14(1)	13.60(1)	9.72(1)	9.93(1)	9.24(1)
$\log K_2^H$	5.99(1)	6.21(1)	9.50(1)	9.21(1)	12.21(4)	8.26(1)	8.37(1)	6.04(1)
$\log K_3^H$	–	–	4.51(1)	4.48(1)	8.62(2)	4.19(1)	4.18(1)	2.68(1)
$\log K_4^H$	–	–	4.05(1)	4.03(1)	7.53(2)	2.71(1)	2.71(1)	2.10(1)
$\log K_5^H$	–	–	2.05(1)	1.99(1)	5.82(3)	2.14(1)	2.00(1)	1.01(1)
$\log K_6^H$	–	–	1.14(2)	–	5.11(3)	0.90(1)	–	–
$\log K_7^H$	–	–	–	–	1.64(3)	–	–	–
$\Sigma\log K_i^H$	13.28	13.91	30.37	28.85	54.53	27.92	27.19	21.07

Protonation constants in Table 1 reveal that there is no significant difference between the logK_i^H values obtained in 0.15 M NaCl, 0.15 M $NaClO_4$, or 0.15 M $NaNO_3$, suggesting a negligible effect of the anions. However, according to the literature, the cation plays a more substantial role. In fact, it is known that the Na^+ cation – due to its higher charge density – forms stable complexes with these ligands compared to K^+. As a result of the competition between protons and such cations, protonation constants measured in a Na^+-containing medium are typically lower compared to those obtained in a K^+-containing medium.[48] This is exemplified by the protonation constants of DOTA in 0.1 M KCl and 0.15 M NaCl solutions, which are reported in Table 2. We also observe that in NaCl the second protonation constant is slightly larger than the first one, log K_2^H > log K_1^H. This can be explained by the initial formation of a Na^+-complex in which the proton competes with the cation for the ligand, thus the first protonation constant appears lower than expected (log$K_{Na(DOTA)}$= 4.03 – 4.38).[49,50] The first protonation event displaces the Na^+ cation, hence further protonation occurs on the $HDOTA^{3-}$ ligand. This effect is less relevant for the weaker binding K^+ cation.

Table 2. Protonation constants of the DOTA ligand obtained in different ionic media (25°C).

	DOTA	
I	**0.15 M NaCl**[47]	**0.1 M KCl**[51]
logK_1^H	9.14(1)	11.14(1)
logK_2^H	9.21(1)	9.69(2)
logK_3^H	4.48(1)	4.85(2)
logK_4^H	4.03(1)	3.95(1)
logK_5^H	1.99(1)	–
logK_6^H	–	–
logK_7^H	–	–

While the protonation constants of each individual ligand may afford an estimation of its general coordinative behaviour, the stability constants with each metal ion of interest must be determined experimentally for having a comprehensive picture. In this work we focused on Pb(II) and Bi(III).

The stability and protonation constants of the complexes formed by Pb(II) with the above mentioned polyamino-polycarboxylate, -polyphosphonate and -polyamide ligands were determined by pH-potentiometry, UV-Vis spectrophotometry and Capillary Zone Electrophoresis (CZE) (Table 3). In the case of the last two techniques, the ligand-ligand competition reactions for the Pb^{2+} ions have been monitored in acidic (pH = 1 – 3) or basic conditions (pH > 8). Stability (logK_{ML}), protonation (log$K_{M(HiL)}$) and conditional (logK^c_{ML}) constants of the metal complexes are defined by the equations *Eq. 2 – 4*, respectively. To

compare the metal ion binding ability of different ligands, the $\log K^{c}_{ML}$ conditional stability constant of the given metal-complex is calculated by considering all possible side reactions of components in the complexing equilibria. In biological systems, the free ligand L can be protonated and form complexes with endogenous metal ions (Ca^{2+}, Zn^{2+} and Cu^{2+}), while the M^{n+} metal ion can interact with endogenous ligands (citrate, phosphate, carbonate, etc.). Moreover, the metal complex can undergo protonation at the more labile sites, such as carboxylate or phosphonate groups, which may lead to partial de-coordination from the metal center; in other words, protonated complexes are generally characterized by lower stabilities. For the calculation of the conditional stability constant (K^{c}_{ML}), the portion of the protonated ligand, the protonated metal-complex, and the hydrolysed metal ion have been considered by the alpha coefficients for the ligand (α_L), the metal-complex (α_{ML}) and the metal ion (α_M), respectively.

$$K_{ML} = \frac{[ML]}{[M^{n+}][L]} \qquad \textit{Eq. 2}$$

$$K_{M(H_iL)} = \frac{[M(H_iL)]}{[M(H_{i-1}L)][H^+]} \qquad \textit{Eq. 3}$$

$$K^{c}_{ML} = \frac{[ML]_t}{[M]_t[L]_t} = \frac{[ML]}{[M][L]}\frac{\alpha_{ML}}{\alpha_M\alpha_L} = K_{ML}\frac{\alpha_{ML}}{\alpha_M\alpha_L} \qquad \textit{Eq. 4}$$

where $[M]_t = [M] + [M(OH)] + [M(OH)_2] + \ldots$, $[L]_t = [L] + [HL] + [H_2L] + \ldots + [H_nL]$, $[ML]_t = [ML] + [MHL] + [MH_2L] + \ldots$, $\alpha_M = 1 + K_{MOH}/[H^+] + K_{MOH}K_{M(OH)2}/[H^+]^2 + \ldots$, $\alpha_L = 1+K_1[H^+] + K_1K_2[H^+]^2 + \ldots + K_1K_2\ldots K_n[H^+]^n +$, $\alpha_{ML} = 1+K_{MHL}[H^+] + K_{MHL}K_{MH2L}[H^+]^2 + \ldots$

By taking into account the protonation constants of the ligand (K_i^H, Table 1), the stability and protonation constants of the complexes (Table 3) and the hydrolysis constant of the M^{n+} metal ion,[2] the conditional stability constant (K^{c}_{ML}) of a given metal complex can be calculated for a specific condition. It must be noted that the conditional stability constants are generally lower than their corresponding stoichiometric stability constants (*Eq. 2*), which describe the simple M + L = ML equilibrium.

Although the $[^{212}Pb][Pb(DOTAM)]^{2+}$ complex and its derivatives have already been used in clinical trials, its stability constant had not been determined yet due to its high inertness (slow dissociation) and complete formation (~100%) in acid conditions (pH < 2).[34] A limiting value for the stability constant of $[Pb(DOTAM)]^{2+}$, determined by Hancock *et al*., was found to be significantly higher than that of the closest analogue $[Hg(DOTAM)]^{2+}$ complex ($\log K_{Pb(DOTAM)} > 19$, $\log K_{Hg(DOTAM)} = 15.53$, 25°C, 0.1 M $NaNO_3$).[52] Since the formation of the $[Pb(DOTAM)]^{2+}$ occurs in very acidic conditions (pH < 2), the stability constant cannot be determined precisely by pH-potentiometry. Therefore, the competition reaction between EDTA and DOTAM for Pb^{2+} has been followed by CZE, due to its high sensitivity. Specifically, the competition between $[Pb(EDTA)]^{2-}$ and DOTAM ligand was monitored via the formation of $[Pb(DOTAM)]^{2+}$ (*Eq. 5*). For these experiments, 8 samples were prepared with 0.2 mM $[Pb(EDTA)]^{2-}$, 0.8 mM EDTA and 0 – 2.0 mM DOTAM at pH = 8.5 and 25°C in 0.15 M $NaClO_4$ solution (monoprotonated HEDTA ligand is predominant at pH = 8.5). The samples

were kept for about 2 months at 25°C to reach the equilibrium (the time needed to attain the equilibrium was determined by CZE). The electropherograms and the species distribution of the $[Pb(EDTA)]^{2-}$ – DOTAM reacting system in the presence of 4-fold HEDTA excess obtained at pH = 8.5 are shown in Figure 9. The first electropherogram shows the predominant species $[Pb(EDTA)]^{2-}$ at 15.9 min, in addition to a broad signal in the range 12 – 13.7 min relative to the free EDTA excess. In the subsequent electropherograms – in which the concentration of free DOTAM (peak at 3.0 minutes) is progressively increased – the peak of $[Pb(DOTAM)]^{2+}$, with a migration time of 2.5 minutes, progressively increases due to the competition reaction between $[Pb(EDTA)]^{2-}$ and DOTAM, and the formation of the $[Pb(DOTAM)]^{2+}$ complex (*Eq. 5*).

$$[Pb(EDTA)]^{2-} + H_xDOTAM \leftrightharpoons [Pb(DOTAM)]^{2+} + H_yEDTA \qquad x = 0, 1; y = 1, 2 \qquad Eq.5$$

$$K_{PbX} = \frac{[Pb(DOTAM)][EDTA]_{free}}{[Pb(EDTA)][DOTAM]_{free}} \qquad Eq.\ 5a$$

$$K_{PbX} = \frac{K_{Pb(DOTAM)}\alpha_{EDTA}}{K_{Pb(EDTA)}\alpha_{DOTAM}} \qquad Eq.\ 5b$$

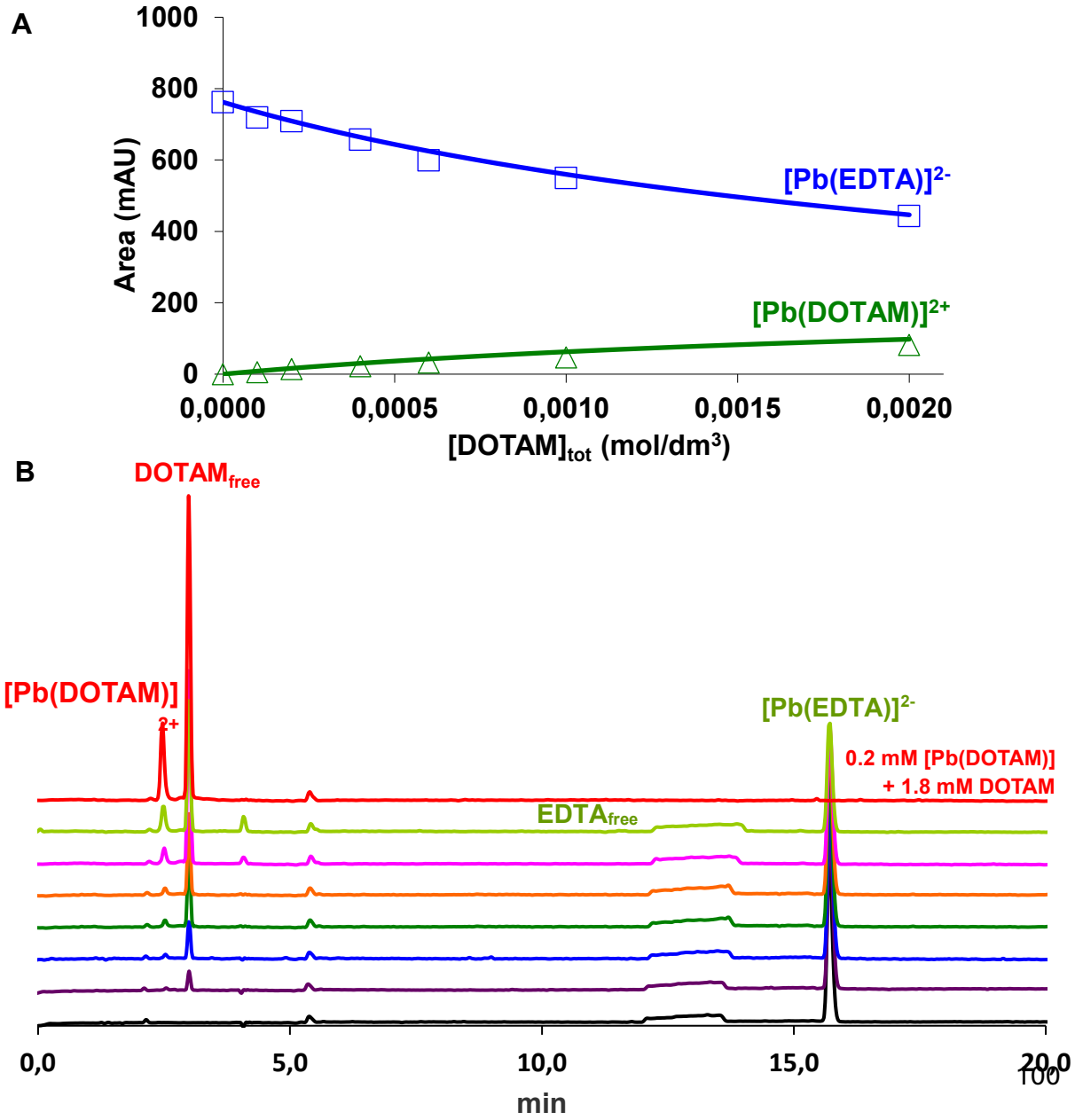

Figure 9. Species distribution (**A**) of the $[Pb(EDTA)]^{2-}$ – DOTAM reacting system and CZE electropherograms (**B**). In **A** the solid lines and the open symbols represent the calculated and the experimental area values, respectively. ($[Pb^{2+}]$ = 0.2 mM, [EDTA] = 1.0 mM, [DOTAM] = **0**, **0.1**, **0.2**, **0.4**, **0.6**, **0.8**, **1.0** and **2.0** mM; pH = 8.5, 0.15 M $NaClO_4$, 25°C. (CZE condition: 100 mM sodium-tetraborate, 50 mbar, 10 s, 30 kV, pH = 9.2, 25°C).

By taking into account the total concentration of EDTA and DOTAM ligands ($[EDTA]_t$ = $[HEDTA] + [H_2EDTA] + [Pb(EDTA)]^{2-}$; $[DOTAM]_t$ = $[DOTAM] + [HDOTAM]^{+} + [Pb(DOTAM)]^{2+}$), the molar integral values of $[Pb(EDTA)]^{2-}$ and $[Pb(DOTAM)]^{2+}$ determined in separate experiments ($[Pb(EDTA)]^{2-}$= 3.81×10^6 mAu/M and $[Pb(DOTAM)]^{2+}$ = 1.18×10^6 mAu/M at λ = 200 nm), the value of K_{PbX} was calculated with *Eq. 5a* (K_{PbX} = 0.36(1)). Considering the stability constant of $[Pb(EDTA)]^{2+}$ complex obtained via pH-potentiometric studies ($\log K_{Pb(EDTA)}$ = 16.55(1) at 25°C in 0.15 M $NaClO_4$ (Table 3)), the α_{EDTA} = 4.61 and α_{DOTAM} = 1.04 at pH = 8.5, the stability constant of $[Pb(DOTAM)]^{2+}$ was calculated with *Eq. 5b* ($\log K_{Pb(DOTAM)}$ = 15.51(2) at 25°C in 0.15 M $NaClO_4$).

$$Pb^{2+} + H_zDTPA \leftrightharpoons [Pb(H_pDTPA)]^{p-3} + z\text{-}pH^{+} \qquad z = 2,3,4,5,6;\ p = 0,1,2,3 \qquad Eq.6$$

Among the Pb(II) complexes proposed for TAT applications $[^{212}Pb][Pb(DTPA)]^{3-}$ is characterized by the fastest formation rate.[12] The thermodynamic properties of the $[Pb(DTPA)]^{3-}$ complex have been investigated in several studies.[54,55] In order to compare the thermodynamic properties of the most common $[^{212}Pb]$Pb(II) complexes in TAT, the stability and protonation constants of $[Pb(DTPA)]^{3-}$ has been determined at 25°C in 0.15M $NaClO_4$ solution. The stability constants of $[Pb(DTPA)]^{3-}$ was determined with pH-potentiometry and spectrophotometry by recording the absorption spectra of the Pb^{2+} – H_zDTPA system (z = 2,3,4,5 and 6) in the pH range 1.5 – 7.0 (Figure 10). The spectrophotometric data reveal a progressive increase of absorbance values at pH < 2 in the region 230 – 260 nm due to the formation of the $[Pb(H_3DTPA)]$ species. In the pH range 2.5 – 7.0 the absorption maximum of the Pb^{2+} – H_zDTPA system is shifted from 247 nm to 253 nm by the stepwise deprotonation $[Pb(H_3DTPA)]$ via the formation of $[Pb(H_2DTPA)]$, [Pb(HDTPA)] and [Pb(DTPA)] species (charges omitted). By considering the protonation constants of the $[Pb(DTPA)]^{3-}$ obtained by pH-potentiometry and the absorbance values of the Pb^{2+} – H_zDTPA system in the pH range 1.5 – 7.0, the stability constant $[Pb(DTPA)]^{3-}$ complex was calculated with the PSEQUAD program ($\log K_{Pb(DTPA)}$ = 18.41(2) at 25°C in 0.15 M $NaClO_4$). Moreover, by considering the protonation constant of the DTPA ligand (Table 1), stability and protonation constant of the $[Pb(DTPA)]^{3-}$ complex (Table 3), the species distribution of the Pb^{2+} – H_zDTPA system have been calculated and presented in Figure 10.

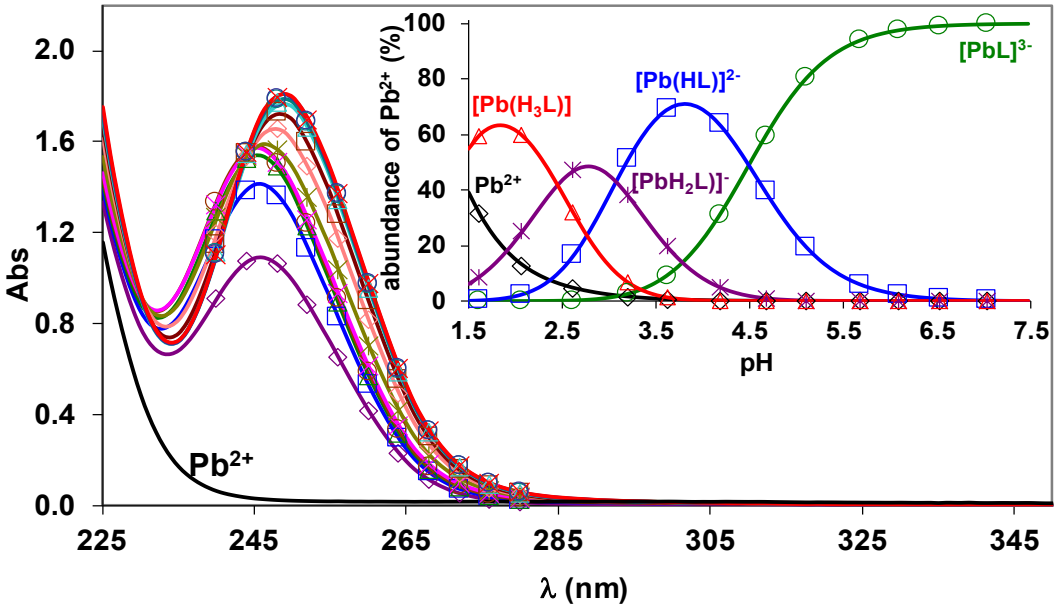

Figure 10. Absorption spectra and species distribution for the Pb^{2+} – DTPA (L in the insert) system. The solid lines and the open symbols represent the experimental and the calculated abundance of the Pb^{2+}, $[Pb(H_3DTPA)]$, $[Pb(H_2DTPA)]$, $[Pb(HDTPA)]$ and $[Pb(DTPA)]$ species (charges omitted), respectively. ($[Pb^{2+}]$ = [DTPA] = 0.2 mM, pH = **1.57**, **2.03**, **2.58**, **3.16**, **3.58**, **4.14**, **4.64**, **5.07**, **5.64**, **6.06**, **6.49** and **7.02**, l = 1.0 cm, 0.15 M $NaClO_4$, 25°C).

In the late 1990s there were few studies that revisited the thermodynamic properties of the $[Pb(DOTA)]^{2-}$ complex due to the wide application of the DOTA ligand in the chelation of $^{203/212}Pb^{2+}$ radioisotopes.[56,57] In the studies of Tosato *et al.*, the stability and protonation constants of the $[Pb(DOTA)]^{2-}$ complex were calculated from UV-Vis spectrophotometric data of the Pb^{2+} – DOTA systems acquired in 0.1 M NaCl solution. The stability constant of the $[Pb(DOTA)]^{2-}$ complex in this work was found to be $\log K_{Pb(DOTA)} = 25.3$ which is about 3 $\log K$ units higher than the $\log K_{Pb(DOTA)}$ value previously obtained by Chaves *et al.* ($\log K_{Pb(DOTA)} = 22.69$, 25°C, 0.1 M Me_4NNO_3).[50] It should be noted that the formation of the $PbCl_x$ species[58] has not been considered in the calculation of the equilibrium constants characterizing the species formed in the Pb^{2+} – DOTA system. Moreover, the protonation constant of the DOTA ligand obtained in 0.1 M KCl and 0.1 M Me_4NCl solutions were used by Tosato *et al.* and Pippin *et al.*, respectively, for the calculations of the stability constant of the $[Pb(DOTA)]^{2-}$ complex, whereas the investigations were performed in 0.1 M NaCl and 0.1 M $NaClO_4$ solutions, respectively.[56,57] Because of the large difference in the published $\log K_{Pb(DOTA)}$ values, the stability and protonation constants of the $[Pb(DOTA)]^{2-}$ complex have been re-determined in this work with pH-potentiometry and UV-spectrophotometry by following the competition reaction between the DOTA and DTPA ligands for the Pb^{2+} ion at 25°C in 0.15 M $NaClO_4$ solution (*Eq. 6*, x = 2 and 3, y = 2 and 3, z = 5, q = 6). The UV-spectrophotometric monitoring is possible due to the different absorption maxima (6p ← 6s transitions of Pb(II)) of $[Pb(H_yDTPA)]$ (λ_{max} = 246 nm) and $[Pb(H_xDOTA)]$ (λ_{max} = 260 nm) (Figure 11).[39][59] For

these experiments, 8 samples were prepared with 1.0 mM $[Pb(H_xDOTA)]^{2-}$ and 0 – 10.0 mM H_zDTPA at pH = 1.7 and 25°C in 0.15 M $NaClO_4$ solution. The samples were kept for about 1 month at 25°C in order to reach the equilibrium (the time needed to attain the equilibrium was determined by UV spectrophotometry). At pH = 1.70 DTPA can successfully compete with DOTA for Pb^{2+}, via the dissociation of $[Pb(H_xDOTA)]$ and the formation of $[Pb(H_3DTPA)]$ and $[Pb(H_2DTPA)]^{2-}$ species. By considering the protonation constants of the DTPA and DOTA ligands (Table 1), the stability and protonation constants of $[Pb(DTPA)]^{3-}$ (Table 3), the protonation constants of $[Pb(DOTA)]^{2-}$ obtained by pH-potentiometry (Table 3), and the molar absorptivity values of the [PbL], [Pb(HL)], $[Pb(H_2L)]$ and $[Pb(H_3L)]$ species determined through the spectrophotometric titrations of the $[Pb(DTPA)]^{3-}$ and $[Pb(DOTA)]^{2-}$ complexes in the pH range 2.0 – 7.0, the stability constant of the $[Pb(DOTA)]^{2-}$ complex was calculated with the PSEQUAD program from the UV spectrophotometric data (Figure 11) obtained at pH = 1.7 from the $[Pb(H_xDOTA)]^{2-}$ – H_zDTPA system ($\log K_{Pb(DOTA)}$ = 22.32 (2) at 25°C in 0.15 M $NaClO_4$). The species distribution of the $[Pb(H_xDOTA)]^{2-}$ – H_zDTPA system at pH = 1.7 is also shown in Figure 11. According to the species distribution for the $[Pb(H_xDOTA)]^{2-}$ – H_zDTPA system, DTPA can successfully compete with DOTA for the Pb^{2+} ion at pH = 1.7 even in equimolar system. The effective transchelation of $[Pb(H_xDOTA)]$ by the H_zDTPA ligand can be explained by the lower conditional stability of the $[Pb(H_2DOTA)]$ and $[Pb(H_3DOTA)]^{+}$ complexes compared to those of the $[Pb(H_2DTPA)]^{-}$ and $[Pb(H_3DTPA)]$ species.

$$[Pb(H_xDOTA)]^{x-2} + H_zDTPA \leftrightharpoons [Pb(H_yDTPA)] + H_qDOTA \qquad Eq.6$$

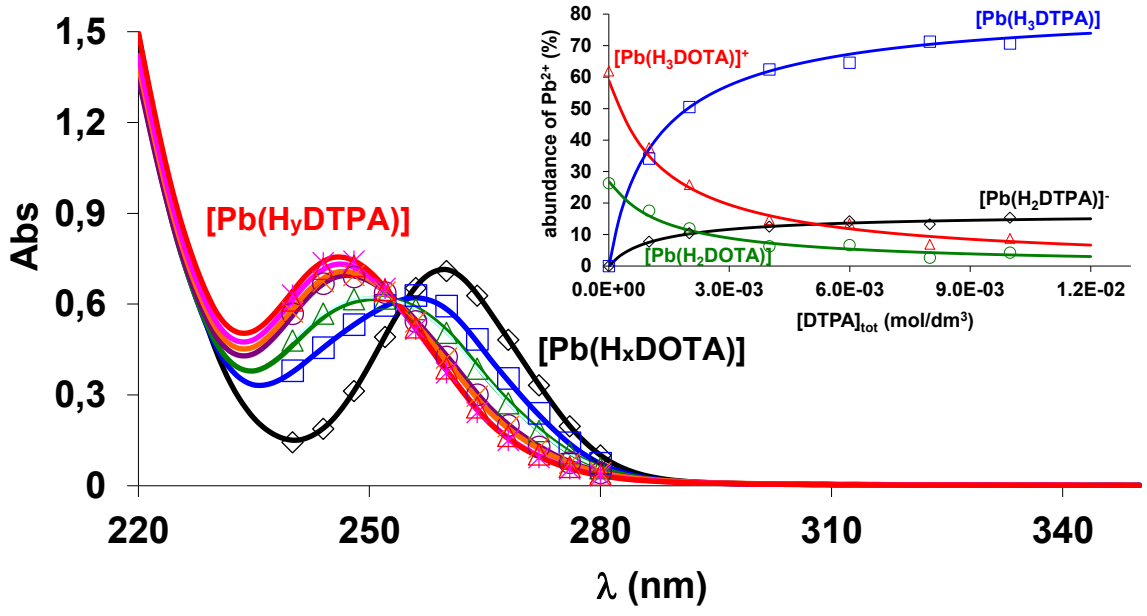

Figure 11. Absorption spectra and species distribution for the [Pb(DOTA)] – DTPA system (x = 2 and 3, y = 2 and 3). The solid lines and the filled symbols represent the experimental and the calculated absorbance values, respectively. ([Pb(DOTA)] = 1.0 mM, $[DTPA]_{tot}$ = **0**, **1**, **2**, **4**, **6**, **8** and **10** mM, pH = 1.70, l = 0.1 cm, 0.15 M $NaClO_4$, 25°C).

It was shown that the [^{212}Pb][Pb(DOTP)] complex can be applied for the TAT of metastases to the skeleton from prostate, breast, and lung cancers.[28] However, the equilibrium and the dissociation kinetic properties of $[Pb(DOTP)]^{6-}$ have not been investigated so far.

The stability and protonation constants of $[Pb(DOTP)]^{6-}$ were thus determined in this work through pH potentiometry and UV-spectrophotometry (Figure 12) by following the competition reaction between the DOTP and EDTA ligands for the Pb^{2+} ion at pH = 9.44 and 25°C in 0.15 M $NaClO_4$ solution (*Eq. 7*, x = 0 and 1, y = 0 and 1, z = 2 and 3) due to their distinctive absorption bands at 240 nm for $[Pb(EDTA)]^{2-}$ and 275 nm for $[Pb(H_xDOTP)]^{x-6}$.[60] For these experiments, 9 samples were prepared with 1.0 mM $[Pb(DOTP)]^{6-}$ and 0 – 2.0 mM H_yEDTA at pH = 9.44 and 25°C in 0.15 M $NaClO_4$ solution. The samples were kept for about 1 months at 25°C in order to reach the equilibrium (the time needed to attain the equilibrium was determined by UV spectrophotometry). The species distribution of the $[Pb(H_xDOTP)]^{x-6}$ – H_xEDTA system at pH = 9.44 is also shown in Figure 12. According to the species distribution of the $[Pb(H_xDOTP)]^{x-6}$ – H_xEDTA system, the relative abundances of the $[Pb(H_xDOTP)]^{x-6}$ and $[Pb(EDTA)]^{2-}$ complexes are about 50 and 43%, respectively, which confirms the comparable conditional stability of the $[Pb(H_xDOTP)]^{x-6}$ and $[Pb(EDTA)]^{2-}$ complexes at pH = 9.44.

$$[Pb(H_xDOTP)]^{6-} + H_yEDTA \leftrightharpoons [Pb(EDTA)]^{2-} + H_zDOTP \qquad Eq.7$$

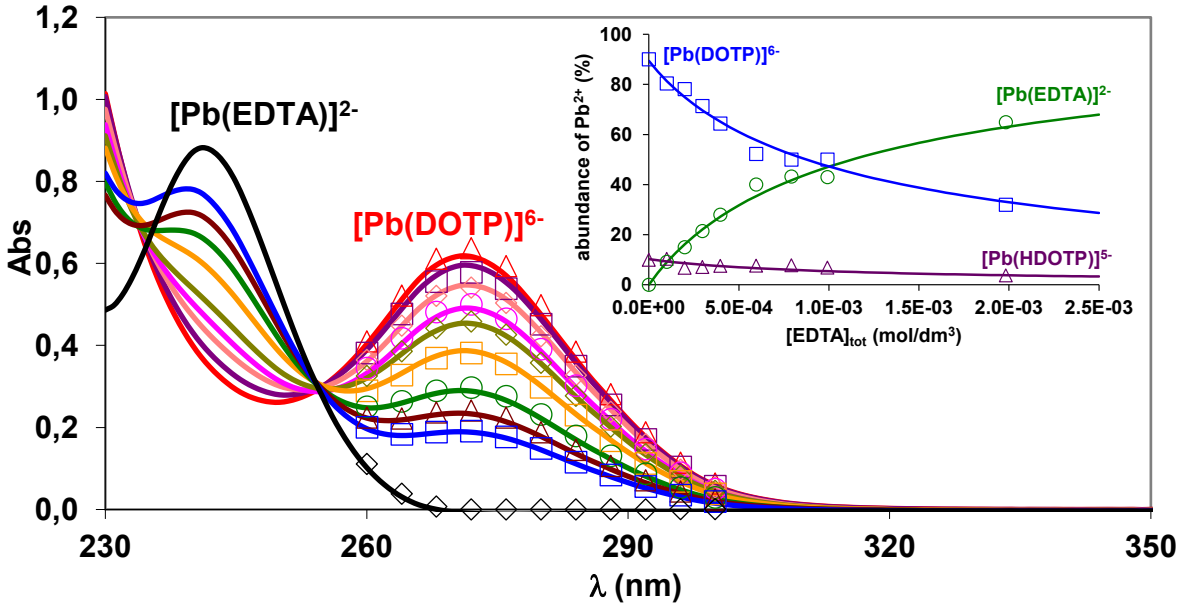

Figure 12. Absorption spectra and species distribution for the $[Pb(H_xDOTP)]$ – H_yEDTA system (x = 0 and 1, y = 0 and 1). The solid lines and the open symbols represent the experimental and the calculated absorbance values, respectively. ($[Pb(DOTP)]$ = 1.0 mM, $[EDTA]_{tot}$ = **0.0**, **0.1**, 0.2, **0.3**, **0.4**, **0.6**, **0.8**, **1.0** and **2.0** mM, $[Pb(EDTA)]$ = 1.0 mM, pH = 9.44, l = 0.1 cm, 0.15 M $NaClO_4$, 25°C).

The stability, protonation and conditional stability constants (K^{c}_{ML} at pH = 7.4) of the Pb(II), Bi(III), Cu(II) and Zn(II) complexes with DOTAM, DOTA, DOTP, DTPA and EDTA ligands are listed and compared with data taken from the literature in Table 3 (standard deviations - 3σ - are shown in parenthesis).

Table 3. Stability, protonation and conditional stability (K^{c}_{ML} at pH = 7.4) constants for the Pb(II), Bi(III), Cu(II) and Zn(II) complexes with DOTAM, DOTA, DOTP, DTPA and EDTA ligands (25 °C). Values in blue are experimental data obtained during this work, the remaining values are taken from literature.

	DOTAM	**DOTA**	**DOTP**	**DTPA**	**EDTA**
I	**0.15 M $NaClO_4$**				
logK_{PbL}	**15.51(2)** **>19**[52]	**22.32(2)** **25.3**(1) [56]	**23.40(3)** –	**18.41(2)** **19.1**[54]	**16.55(1)** **16.50(5)**[61]
log$K_{Pb(HL)}$	–	3.64(2) 3.98(6)[56]	8.50(4) –	4.49(1) –	2.72(2) 3.28(2)[61]
log$K_{Pb(H2L)}$	–	2.52(2) 2.72(6)[56]	7.58(4) –	3.08(1) –	1.57(2)[61]
log$K_{Pb(H3L)}$	–	2.10(2) 1.1(2)[56]	6.45(4) –	2.45(1) –	–
log$K_{Pb(H4L)}$	–	–	5.51(5)	–	–
logK^{c}_{PbL}	**15.20**	**18.50**	**12.33**	**15.18**	**14.69**
logK_{BiL}	–	**30.86**(7)[27]	**38.67**(2)[27]	**29.29**(3)[62]	**26.7**[63]
log$K_{Bi(HL)}$	–	1.38(4)[27]	7.04(3)[27]	2.55[27]	1.7[63]
log$K_{Bi(H2L)}$	–	–	5.86(3)[27]	–	–
log$K_{Bi(H3L)}$	–	–	4.81(4)[27]	–	–
log$K_{Bi(H4L)}$	–	–	4.27(2)[27]	–	–
logK^{c}_{BiL}	–	**27.0**[27]	**26.1**[27]	**26.0**[27]	**24.8**
logK_{CuL}	**16.3(1)**[52]	**22.00**(1)[47]	**25.4**[64]	**23.40**(6)[47]	**19.02**[65]
log$K_{Cu(HL)}$	–	4.10(1)[47]	7.41[64]	4.63(1)[47]	3.15[65]
log$K_{Cu(H2L)}$	–	3.4(1)[47]	6.42[64]	2.67(1)[47]	2.04[65]
logK^{c}_{CuL}	**16.04**	**18.15**	**13.15**	**20.30**	**17.12**
logK_{ZnL}	**10.47**(3)[52]	**17.35**[65]	**24.8**[64]	**17.58**(2)[47]	**15.92**[65]
log$K_{Zn(HL)}$	–	4.16[65]	7.68[64]	5.37(1)[47]	3.23[65]
log$K_{Zn(H2L)}$	–	3.40[65]	6.92[64]	2.38(2)[47]	–
logK^{c}_{ZnL}	**10.21**	**13.53**	**11.77**	**14.35**	**14.02**
logK_{CaL}	**7.54**(1)[52]	**13.84**[52]	**11.12**[66]	**10.63**[67]	**9.53**[65]
log$K_{Ca(HL)}$	–	3.90[52]	8.70[66]	6.02[67]	2.92[65]
log$K_{Ca(H2L)}$	–	–	8.52[66]	4.51[67]	–
log$K_{Ca(H3L)}$	–	–	6.86[66]	3.39[67]	–
logK^{c}_{CaL}	**7.28**	**10.02**	**1.05**	**7.39**	**7.63**

Stability constants of the Pb(II) complexes in Table 3 reveal that the $[Pb(DOTAM)]^{2+}$ complex has a very low stability ($\log K_{Pb(DOTAM)}$ = 15.51, 0.15 M $NaClO_4$, 25°C), which is similar to that of the closest analogue $[Hg(DOTAM)]^{2+}$ ($\log K_{Hg(DOTAM)}$ = 15.53, 25°C, 0.1 M $NaNO_3$) and significantly lower than the $\log K_{Pb(DOTAM)} > 19$ value estimated by Hancock *et al*.[52] Based on this evidence, the stability constant of $[Pb(DOTAM)]^{2+}$ is clearly overestimated in the literature ($\log K_{Pb(DOTAM)} > 19$).[34,52] The comparison of the $\log K_{PbL}$ values indicates that the stability constant of the $[Pb(DOTP)]^{6-}$ species is the highest among the Pb(II) complexes formed with the macrocyclic DOTAM, DOTA and DOTP ligands. However, the conditional stability constants K^{c}_{PbL} calculated at physiological pH = 7.4 indicate that DOTA forms the most stable Pb(II) complex due to the presence of several protonated species of $[Pb(DOTP)]^{6-}$ near physiological condition. A similar trend was found in the literature for the stability and conditional stability constants of the corresponding Bi(III) complexes with DOTA and DOTP ligands.[12][27] The stability constants of the $[Pb(DTPA)]^{3-}$ species is 1.86 log*K* unit higher than that of the corresponding $[Pb(EDTA)]^{2-}$ complex. By considering the significantly higher total basicity of the DTPA ligand ($\Sigma \log K_i^H$ = 27.92) compared to EDTA ($\Sigma \log K_i^H$ = 21.07, Table 1), the presence of three nitrogen and five carboxylate oxygen donor atoms does not improve substantially the stability of the $[Pb(DTPA)]^{3-}$ complex compared to $[Pb(EDTA)]^{2-}$.

As for the endogenous Cu^{2+} and Zn^{2+} metal ions, the conditional stability constants in Table 3 show that the affinity for DOTA ($\log K^{c}_{CuL}$ = 18.15, $\log K^{c}_{ZnL}$ = 13.53) is lower than that for DTPA ($\log K^{c}_{CuL}$ = 20.30, $\log K^{c}_{ZnL}$ = 14.35), suggesting the importance of an optimal size match between the ionic radii and the ligand-binding cavities, as well as between the coordination preferences of the ion and the type and number of donor atoms. Moreover, this behaviour is also in agreement with the Irving-Williams series, *i.e.* in each case the stability constant is higher for the Cu(II) complex compared to the Zn(II) complex ($\log K_{CuL} > \log K_{ZnL}$).

The extremely low concentration of the radiopharmaceuticals and the high excess of possible endogenous competition partners (Ca^{2+}, Zn^{2+}, Cu^{2+}, cysteine, cystine and other proteins with -SH groups) might determine the thermodynamic force for the *in vivo* dissociation of the Pb(II) complexes. Moreover, the presence of the large HCO_3^- excess in body fluids ($[HCO_3^-]_{tot}$ = 25 mM)[68] might result in the precipitation of the free Pb^{2+} ion due to the relatively low solubility of $PbCO_3$ ($\log K_{sol}$ = –12.51).[69] To estimate the metal ion binding properties of the polyamino-polycarboxylate and -polyphosphonate ligands in physiological conditions, Cacheris *et al*. introduced the selectivity constant (K_{sel}).[70] This is a conditional stability constant that takes into account the possible side reactions of the ligand with H^+, Zn^{2+}, Cu^{2+} and Ca^{2+} ions in physiological conditions:

$$K_{sel}^{PbL} = \frac{K_{PbL}^{c}}{\alpha_L^H + \alpha_L^{Ca} + \alpha_L^{Zn} + \alpha_L^{Cu}} \qquad Eq.8$$

where $\alpha_L{}^H = 1 + K_1[H^+] + K_1K_2[H^+]^2 + \ldots + K_1K_2\ldots K_n[H^+]^n$, $\alpha_L{}^{Ca} = 1 + K_{CaL}[Ca^{2+}] + K_{CaL}K_{CaHL}[Ca^{2+}][H^+] + \ldots + K_{CaL}K_{CaHL}\ldots K_{CaHnL}[Ca^{2+}][H^+]^n$, $\alpha_L{}^{Zn} = 1 + K_{ZnL}[Zn^{2+}] + K_{ZnL}K_{ZnHL}[Zn^{2+}][H^+] + K_{ZnL}K_{ZnHL}\ldots K_{ZnHnL}[Zn^{2+}][H^+]^n$ and $\alpha_L{}^{Cu} = 1 + K_{CuL}[Cu^{2+}] + K_{CuL}K_{CuHL}[Cu^{2+}][H^+] + K_{CuL}K_{CuHL}\ldots K_{CuHnL}[Cu^{2+}][H^+]^n$. By taking into account the concentration of the Ca^{2+}, Zn^{2+} and Cu^{2+} ions in the body fluids ($[Ca^{2+}] = 1.5\times10^{-3}$ M, $[Zn^{2+}] = 1.6\times10^{-5}$ M and $[Cu^{2+}] = 1.0 \times 10^{-6}$ M),[68] the stability and protonation constants of the

Ca(II), Zn(II) and Cu(II) complexes formed with DOTAM, DOTA, DOTP, DTPA and EDTA ligands (Tables 1 and 3), the K_{sel} values of DOTAM, DOTA, DOTP, DTPA and EDTA for Pb^{2+} over Ca^{2+}, Zn^{2+} and Cu^{2+} ion were calculated and compared in Table 4.

Table 4. Conditional stability constants ($\log K^{ML}_{cond}$) of the Ca^{2+}, Zn^{2+} and Cu^{2+}, and Pb^{2+} complexes of the DOTAM, DOTA, DOTP, DTPA and EDTA ligands, and the selectivity constants ($\log K^{PbL}_{sel}$) of the DOTAM, DOTA, DOTP, DTPA and EDTA ligands for Pb^{2+} over Ca^{2+}, Zn^{2+} and Cu^{2+} ions at pH = 7.4 and 25°C.

	DOTAM	DOTA	DOTP	DTPA	EDTA
$\log K^{CaL}_{cond}$	7.28	10.02	1.05	7.39	7.63
$\log K^{ZnL}_{cond}$	10.21	13.53	11.77	14.35	14.02
$\log K^{CuL}_{cond}$	16.04	18.15	13.15	20.30	17.12
$\log K^{PbL}_{cond}$	**15.20**	**18.50**	**12.33**	**15.18**	**14.69**
$\log K^{PbL}_{sel}$	**5.21**	**6.35**	**1.72**	**0.21**	**3.52**

Comparison of the $\log K^{PbL}_{sel}$ values show that the DOTA ligand has the highest selectivity for Pb^{2+} over Ca^{2+}, Zn^{2+} and Cu^{2+} ions due to the high conditional stability of the [Pb(DOTA)] complex. The selectivity of DOTAM for Pb^{2+} ion in body fluids is somewhat lower than that of DOTA due to the lower conditional stability of the $[Pb(DOTAM)]^{2+}$ complex. Surprisingly, the selectivity of the DOTP and DTPA ligands for Pb^{2+} ion is very low in physiological media due to the low conditional stability of the $[Pb(DOTP)]^{6-}$ and $[Pb(DTPA)]^{3-}$complexes and the relatively high $\log K^{CuL}_{cond}$ value of $[Cu(DOTP)]^{6-}$ and $[Cu(DTPA)]^{3-}$. Even the EDTA ligand shows higher selectivity for Pb^{2+} over Ca^{2+}, Zn^{2+} and Cu^{2+} ions. On the other hand, the calculation of the $\log K^{PbL}_{sel}$ values reveals that the Cu^{2+} ion might be the most important competitor for the Pb(II) complexes in biological systems.

Kinetic inertness of [Pb(DOTP)], [Pb(DOTA)], and [Pb(DOTAM)] complexes

While thermodynamic stability describes the intrinsic propensity for metal complex formation, kinetic inertness, especially within the physiologically relevant pH range, is an equally critical parameter, as it largely determines suitability for therapeutic and diagnostic applications. The kinetic inertness of $[Pb(DOTA)]^{2-}$ was investigated by following the dissociation reactions in 0.02 – 0.3 M $HClO_4$ solutions. However, the dissociation of the $[Pb(DOTAM)]^{2+}$ complex could not be detected even in 0.5 M HCl solution.[34] Because the dissociation of $[Pb(DOTP)]^{6-}$ was too fast to be monitored by conventional methods under strongly acidic conditions, the kinetic inertness of the $[Pb(DOTP)]^{6-}$ complex was evaluated by tracking its transmetallation reactions with Cu^{2+} (*Eq. 9*, x = 4 and 5; y = 4 and 5) via spectrophotometry, specifically by monitoring the absorption band of the resulting $[Cu(H_yDOTP)]^{6-}$ complex (λ = 330 nm) in the pH range 2.5 – 4.5. The absorption spectra of the $[Pb(H_xDOTP)]^{x-6}$ – Cu^{2+} reacting system at pH = 4.0 are shown in Figure 13.

$$[Pb(H_xDOTP)]^{x-6} + Cu^{2+} \leftrightharpoons [Cu(H_yDOTP)]^{y-6} + Pb^{2+} \qquad Eq.\ 9$$

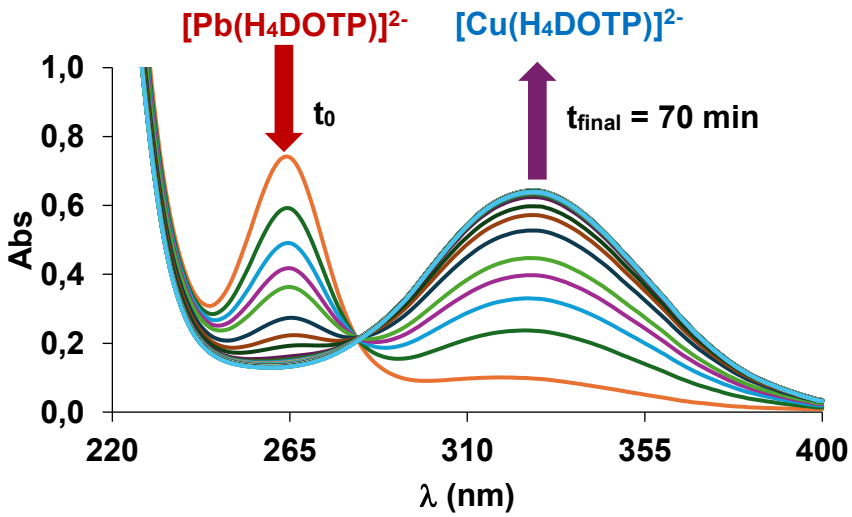

Figure 13. Absorption spectra of the $[Pb(H_xDOTP)]^{x-6}$ – Cu^{2+} reacting system at pH = 4.0 ($[Pb(DOTP)] = 1.0\times10^{-4}$ M, $[Cu(ClO_4)_2] = 1.0\times10^{-3}$ M, [*N*-methyl-piperaizne] = 0.01 M, pH = 4.0, 25°C, 0.15 M $NaClO_4$).

The transmetallation reactions of $[Pb(H_xDOTP)]^{x-6}$ were monitored in the presence of a large excess of the exchanging Cu^{2+} ion ($[Pb(DOTP)] = 1.0 \times 10^{-4}$ M, $[Cu(ClO_4)_2] = 1.0 \times 10^{-3}$ – 4.0×10^{-3} M, 25°C, 0.15 M $NaClO_4$). In these conditions, the transmetallation can be treated as a pseudo-first-order process, and the reaction rate can be expressed with *Eq. 10*, where k_d is a pseudo-first-order rate constant and $[PbL]_{tot}$ is the total concentration of the $[Pb(H_xDOTP)]^{x-6}$ complex.

$$-\frac{d[PbL]_{tot}}{dt} = k_d[PbL]_{tot} \qquad \textit{Eq. 10}$$

The rate of transmetallation has been studied at different concentrations of the exchanging Cu^{2+} ion in the pH range 2.3 – 4.5. The obtained rate constants k_d are presented in Figure 14 as a function of $[H^+]$.

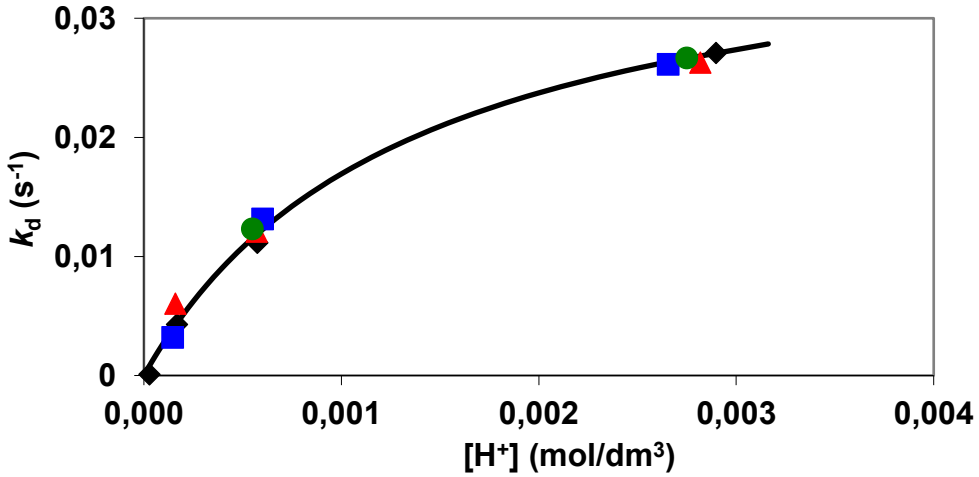

Figure 14. Pseudo-first order (k_d) rate constants characterizing the transmetallation reaction of the $[Pb(H_xDOTP)]^{x-6}$ with Cu^{2+} as a function of $[H^+]$. ($[Pb(DOTP)] = 1.0\times10^{-4}$ M, $[Cu(ClO_4)_2] = 1.0\times10^{-3}$ M (◆), 2.0×10^{-3} M (■), 3.0×10^{-3} M (▲) and 4.0×10^{-3} M (●), 0.15 M $NaClO_4$, 25°C)

As shown in Figure 14, the k_d values are independent of the Cu^{2+} concentration and increase as the pH decreases. Since the k_d values are independent from $[Cu^{2+}]$, it can be assumed that the transmetallation reaction takes place by the rate determining dissociation of $[Pb(H_xDOTP)]^{x-6}$, followed by a fast reaction between the free DOTP ligand and the exchanging Cu^{2+}. The k_d values as a function of $[H^+]$ show a saturation profile (Figure 14), which can be explained by the equilibrium formation of a reaction intermediate. Based on the speciation of the Pb^{2+} – DOTP system (Table 3), the $[Pb(H_5DOTP)]^-$ complex forms at pH < 4. The fifth protonation of $[Pb(DOTP)]^{6-}$ is likely to occur on the coordinated phosphonate oxygen donor atom, resulting in the formation of the labile $[Pb(H_5DOTP)]^-$ intermediate. The dependence of k_d on $[H^+]$ can be interpreted by the spontaneous dissociation of the $[Pb(H_4DOTP)]^{2-}$ (k_0, *Eq. 11*), the equilibrium formation ($K_{Pb(H5L)}$, *Eq. 12*) and dissociation ($k_{Pb(H5L)}$, *Eq. 13*) of the $[Pb(H_5DOTP)]^-$ complex.

$$[Pb(H_4DOTP)]^{2-} \xrightarrow{k_0} Pb^{2+} + H_6DOTP^{2-} \qquad \textit{Eq. 11}$$

$$[Pb(H_4DOTP)]^{2-} + H^+ \overset{K^H_{Pb(H5L)}}{\rightleftharpoons} [Pb(H_5DOTP)]^- \qquad \textit{Eq. 12}$$

$$K^{\mathrm{H}}_{\mathrm{Pb(H_5L)}} = \frac{[\mathrm{Pb(H_5L)}]}{[\mathrm{Pb(H_4L)}][\mathrm{H^+}]}$$

$$[\mathrm{Pb(H_5DOTP)}]^{2-} \xrightarrow{k_{\mathrm{Pb(H5L)}}} \mathrm{Pb^{2+}} + \mathrm{H_6DOTP^{2-}} \qquad \textit{Eq. 13}$$

By considering all the possible pathways, the rate of the transmetallation of $[\mathrm{Pb(H_xDOTP)}]^{x-6}$ can be expressed by *Eq. 14*:

$$-\frac{[\mathrm{PbL}]_{\mathrm{tot}}}{\mathrm{dt}} = k_0[\mathrm{Pb(H_4L)}] + k_{\mathrm{Pb(H5L)}}[\mathrm{Pb(H_5L)}] \qquad \textit{Eq. 14}$$

Considering the total concentration of the $[\mathrm{Pb(H_xDOTP)}]^{x-6}$ complex ($[\mathrm{PbL}]_{\mathrm{tot}} = [\mathrm{Pb(H_4L)}] + [\mathrm{Pb(H_5L)}]$, the equation defining the formation of $[\mathrm{Pb(H_5DOTP)}]^-$ (*Eq. 12* and *Eq. 10*), the pseudo-first-order rate constant can be expressed as follows:

$$k_{\mathrm{d}} = \frac{k_0 + k_1[\mathrm{H^+}]}{1 + K^{\mathrm{H}}_{\mathrm{Pb(H5L)}}[\mathrm{H^+}]} \qquad \textit{Eq. 15}$$

The rate constants, k_0 and $k_1 = k_{Pb(H5L)} \times K^{\mathrm{H}}_{\mathrm{Pb(H5L)}}$ are characteristic for the reactions which occur by the spontaneous and proton-assisted dissociation of the $[\mathrm{Pb(H_4DOTP)}]^{2-}$ species, respectively. The rate and equilibrium constants characterizing the dissociation of $[\mathrm{Pb(H_4DOTP)}]^{2-}$ have been calculated by fitting the k_{d} values presented in Figure 14 to the *Eq. 15* and the values obtained are compared with the corresponding values for $[\mathrm{Pb(DOTA)}]^{2-}$, $[\mathrm{Bi(DOTA)}]^-$ and $[\mathrm{Bi(DOTP)}]^{5-}$ in Table 5.

Table 5. The rate (k_{i}) and equilibrium constants (K_{i}) and dissociation half-life values ($t_{1/2} = \ln 2/k_{\mathrm{d}}$) at pH = 7.4 characterizing the dissociation of the [Pb(DOTP)] and [Pb(DOTA)] complexes (25 ºC, 0.15 M $NaClO_4$)

	$[\mathrm{Pb(H_4DOTP)}]^{2-}$	**$[\mathrm{Pb(HDOTA)}]^-$** [71]	**$[\mathrm{Bi(H_4DOTP)}]^-$** [27]	**$[\mathrm{Bi(DOTA)}]^-$**
k_0 (s^{-1})	–	–	–	2.4×10^{-8}
k_1 ($M^{-1}s^{-1}$)	30 ± 2	3.4×10^{-3}	4.0×10^{-6}	5.8×10^{-5}
$K^{\mathrm{H}}_{\mathrm{i}}$ (M^{-1})	740 ± 120	5.05 ($[\mathrm{Pb(H_2L)}]$)	–	337
k_{d} (s^{-1}) at pH=3.0	0.017	3.4×10^{-6}	4.0×10^{-9}	6.2×10^{-8}
$t_{1/2}$ (h) at pH=3.0	0.012	57	4.8×10^{4}	3.1×10^{3}

The k_0 values obtained are very low and exhibit large relative uncertainties, indicating that spontaneous dissociation of $[\mathrm{Pb(H_4DOTP)}]^{2-}$ is of limited relevance under our experimental conditions (pH = 2.5 – 4.5 and 25°C). The rate constants k_1, characterizing the proton-assisted dissociation of the $[\mathrm{Pb(H_4DOTP)}]^{2-}$ complex is 8800 times higher than that of the $[\mathrm{Pb(HDOTA)}]^-$ complex. On the basis of the solid state structure of the $[\mathrm{Pb(DOTA)}]^{2-}$ complex,

the Pb^{2+} ion is coordinated by four nitrogen and four oxygen atoms in a twisted square antiprism geometry.[38] Protonation to form the $[Pb(HDOTA)]^{-}$ complex most likely occurs at a carboxylate group upon transient formation of a free COOH group. However, the resulting protonated complex is not reactive, as protonation/deprotonation of the carboxylate group is rapid and the COO^{-} group can readily rebind. Dissociation is more likely when proton transfer occurs to a nitrogen atom of the macrocycle, forming a relatively labile protonated intermediate in which the H^{+} effectively displaces the Pb^{2+} ion from the coordination cage. It can be assumed that the proton assisted dissociation of $[Pb(H_4DOTP)]^{2-}$ occurs in a similar manner. In the $[Pb(H_4DOTP)]^{2-}$ complex, the Pb^{2+} ion is coordinated by four nitrogen and four less basic oxygen atoms of the phosphonate pendant arms, whereas the four basic oxygen donor atoms of the phosphonate groups are protonated. In the $[Pb(H_5DOTP)]^{-}$ intermediate, the fifth proton is attached presumably to a weakly coordinated phosphonate oxygen atom. Since the Pb(II) ion is coordinated by the less basic phosphonate oxygen atoms, proton transfer to a macrocyclic nitrogen atom is more likely, which may lead to the faster proton-assisted dissociation of the $[Pb(H_5DOTP)]^{-}$ intermediate. It should be noted that the protonation constant of the $[Pb(H_4DOTP)]^{2-}$ complex was also determined by pH-potentiometric titration ($\log K_{Pb(H5L)}$ = 2.89(7) at 25°C in 0.15 M $NaClO_4$). The protonation constant of $[Pb(H_4DOTP)]^{2-}$ calculated from the kinetic data using *Eq. 15* ($\log K_{Pb(H5L)}$ = 2.87(6) at 25°C in 0.15 M $NaClO_4$) is in very good agreement with the value obtained by the pH-potentiometric method.

Comparison of the corresponding rate constants and half-life values for the Pb(II) and Bi(III) complexes formed with DOTA and DOTP (Table 5) reveals that the Bi(III) complexes exhibit greater resistance to acid-catalyzed dissociation, attributable to the higher affinity of Bi(III) for the more basic macrocyclic nitrogen donor atoms. Surprisingly, the H^{+}-assisted dissociation of the $[Bi(H_4DOTP)]^{-}$ is significantly slower than that of $[Bi(DOTA)]^{-}$.[27] Because Bi(III) is coordinated by the more basic macrocyclic nitrogen donor atoms of the DOTP ligand, proton transfer from the weakly basic phosphonate oxygen donor atoms to the ring nitrogen atoms is less favored than in $[Bi(DOTA)]^{-}$, where Bi(III) is coordinated by the less basic ring nitrogen atoms (Table 1).

Structural features of the $[Pb(DOTA)]^{2-}$, $[Pb(DOTAM)]^{2+}$, $[Pb(DOTP)]^{6-}$, $Pb(H_4DOTP)]^{2-}$ and $[Bi(DOTAM)]^{3+}$ complexes

In order to investigate the structural properties of Pb(II) and Bi(III)-complexes with DOTA-derivatives, multinuclear NMR spectroscopy studies have been performed with both 1D (^{1}H, ^{13}C) and 2D (COSY, HSQC, HMBC) NMR techniques. In addition, variable temperature (VT) ^{1}H and ^{13}C NMR spectra of the Pb(II) and Bi(III)-complexes were also acquired for gaining insight into their dynamic features, *i.e.* the two concerted processes, macrocyclic ring flipping and pendant arm rotation that interconvert the enantiomers (Figures 8 and 15). In fact, VT ^{13}C NMR experiments in the range 273 – 343 K allowed us to determine the respective exchange rate constants k_{ex}, associated to the interconversion of the enantiomers formed by the $[Pb(DOTA)]^{2-}$, $[Pb(DOTAM)]^{2+}$, $[Pb(H_4DOTP)]^{2-}$ and $[Pb(DOTP)]^{6-}$ complexes. Moreover, $[Bi(DOTAM)]^{3+}$ was also synthesized and its structural properties were compared to those of the previously characterized $[Bi(DOTP)]^{5-}$ and $[Bi(DOTA)]^{-}$ complexes.[27][72]

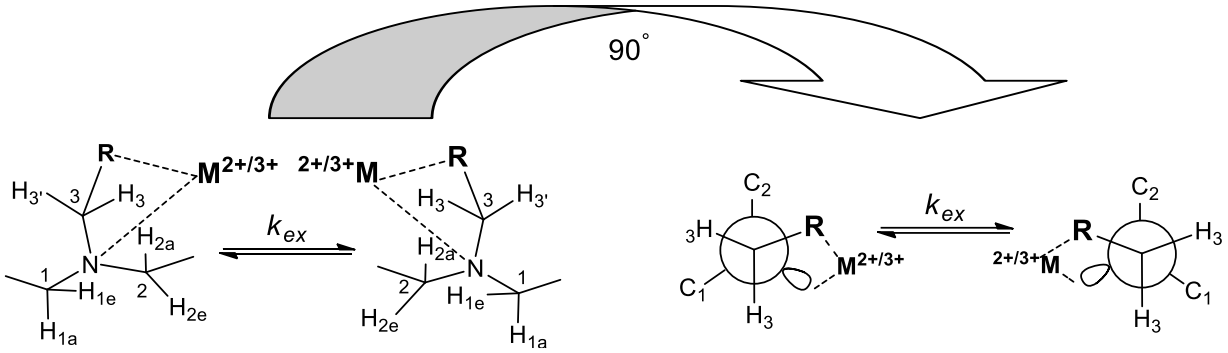

Figure 15. Illustration of the interconversion with explicit proton labelling for the Pb(II) and Bi(III)-complexes of DOTA, DOTAM and DOTP ligands (**R**:–COO^-, –$CONH_2$ and –PO_3^{2-}).

We began by characterizing the $[Pb(DOTA)]^-$ complex by ^1H NMR spectroscopy in D_2O (Figure 16), where – consistent with literature data – the number of signals suggested a C_4 symmetry for the complex, *i.e.* the two carbon atoms adjacent to each N atom of the macrocyclic ring are inequivalent, being one above and the other below the average 4N square plane. According to the single crystal X-ray structure of $Na_3[Pb(DOTA)](NO_3)\cdot 2H_2O$,[38] the Pb(II) ion in $[Pb(DOTA)]^{2-}$ is coordinated by four nitrogen and four oxygen atoms in twisted square antiprism geometry (TSAP: Λ(λλλλ) and Δ(δδδδ)). The ^1H and ^{13}C NMR spectra of $[Pb(DOTA)]^{2-}$ contain a single set of signals, indicating the presence of a single isomer in solution, which might be very similar to that of the crystalline form.

The ^1H NMR spectrum exhibits a pattern of doublets and (pseudo) triplets in the range 2.30 – 3.45 ppm, relative to the axial and equatorial protons of the macrocyclic ring; in addition, the diastereotopic protons of the pendant arm resonate as two doublets at higher ppm values. In fact, the H_3 and $H_{3'}$ protons are deshielded by the carboxylate group and strongly coupled to each other ($^2J_{HH}$ = 16.4 Hz), representing an AB system. Assignment of the resonances of the macrocyclic ring protons was done through proton-decoupled ^{13}C NMR studies and literature data (Figure 17). Based on previous studies,[73][37][74] the three methylene carbon resonances were assigned in the following order from higher to lower frequency: C_3 (55.76 ppm) C_1 (52.74 ppm), and C_2 (49.38 ppm); the resonance of the carboxylate carbon falls at 177.90 ppm. This attribution is in agreement with C_3 being adjacent to the electron withdrawing $-COO^-$ group, followed by C_1 and C_2 of the macrocyclic ring. Furthermore, the ^1H – ^{13}C HSQC spectrum enabled us to determine the connectivity between the carbon atoms with their respective protons (Figure 18). Each carbon presents two signals corresponding to the diastereotopic protons for C_3, and the respective axial-equatorial proton pairs on C_2 and C_1. The distinction between the axial and equatorial protons was made based on their multiplicity and scalar coupling patterns. Specifically, axial protons present two observable ^3J couplings relative to the axial-axial ($^3J_{ax\text{-}ax}$ = 11 – 16 Hz) and axial-equatorial ($^3J_{eq\text{-}ax}$ = 3 – 7 Hz) interactions, while the equatorial protons typically exhibit only the axial-equatorial coupling since the J value relative to equatorial-equatorial protons is very small ($^3J_{eq\text{-}eq}$ = 2 – 5 Hz). This causes the signals of axial protons to resonate as triplets, and equatorial protons as a pseudo triplet (or doublet of

doublets). The described coupling pattern was also confirmed by the $^{1}H - {}^{1}H$ COSY spectrum (Figure 19).

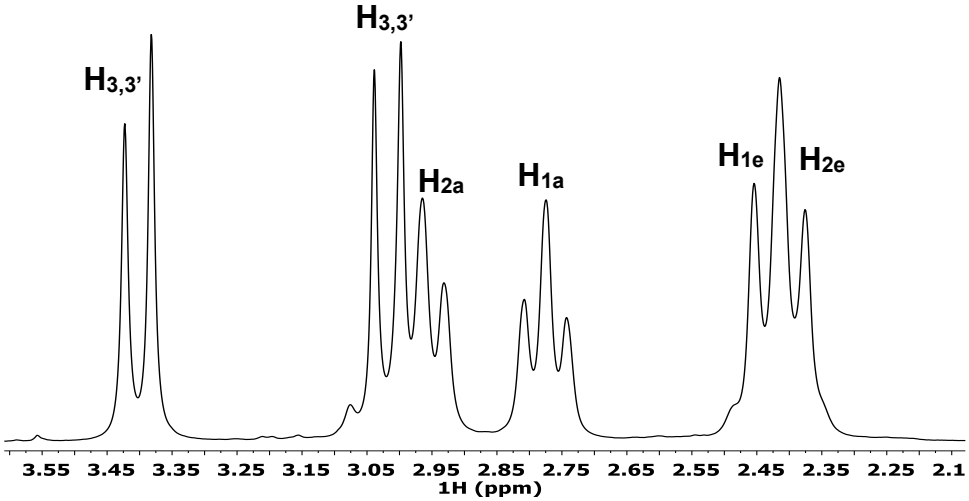

Figure 16. ^{1}H NMR spectrum of $[Pb(DOTA)]^{2-}$ at pD = 7.5 and 273 K ($[Pb(DOTA)]^{2-}$ = 0.02 M, D_2O).

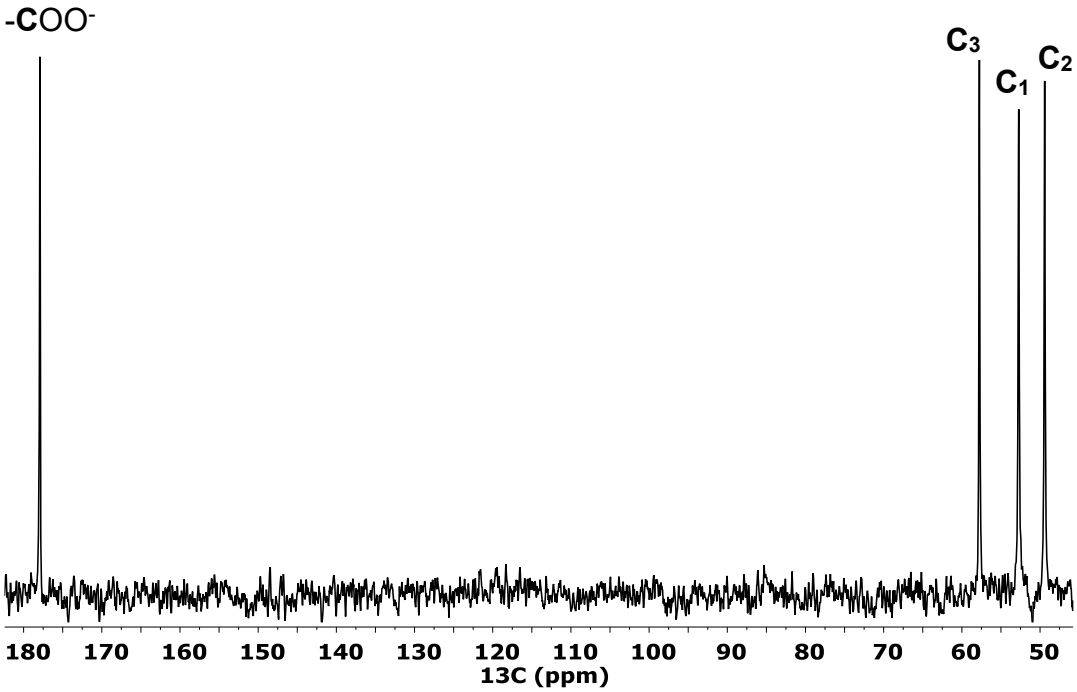

Figure 17. $^{13}C\{^{1}H\}$ NMR spectrum of $[Pb(DOTA)]^{2-}$ at pD = 7.5 and 273 K ($[Pb(DOTA)]^{2-}$ = 0.02 M, D_2O).

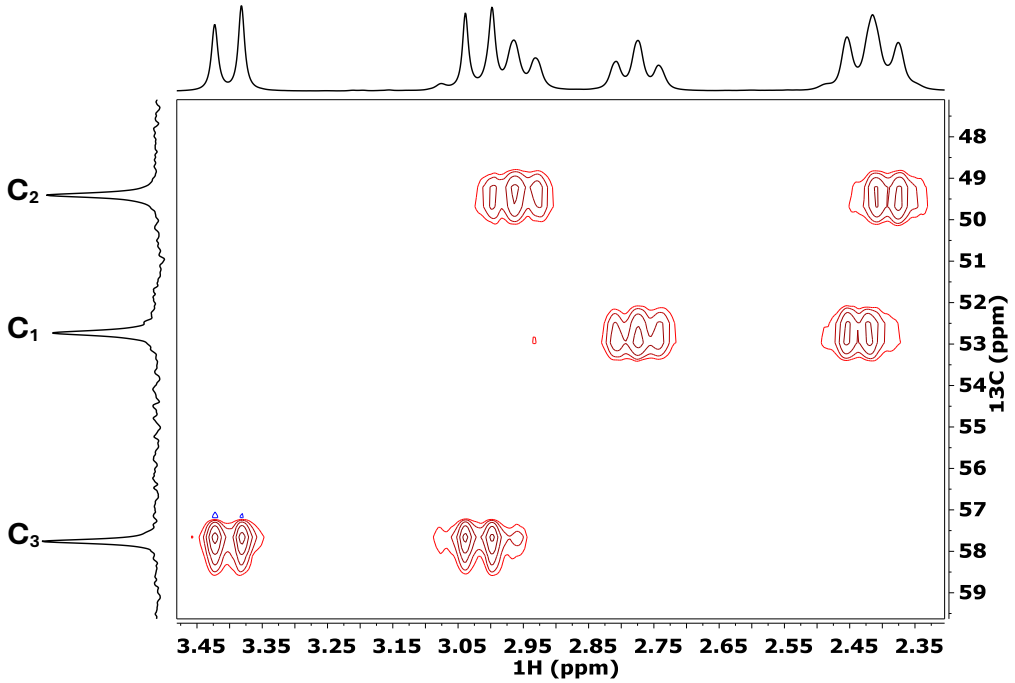

Figure 18. $^{1}H - {}^{13}C$ HSQC spectrum of $[Pb(DOTA)]^{2-}$ at pD = 7.5 and 273 K ($[Pb(DOTA)]^{2-}$ = 0.02 M, D_2O).

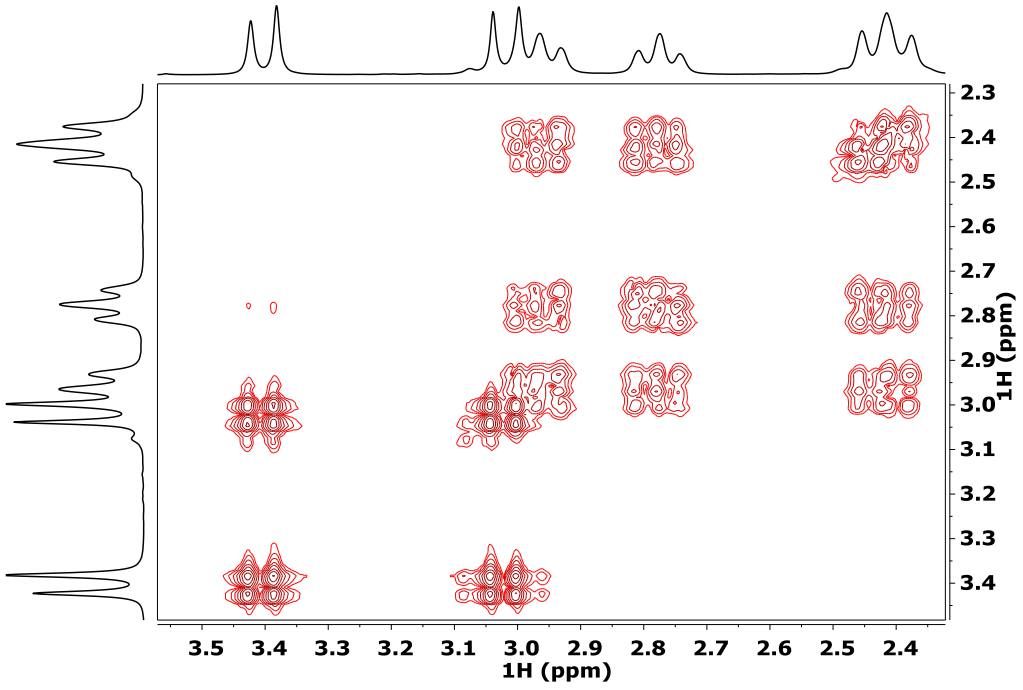

Figure 19. $^{1}H - {}^{1}H$ COSY spectrum of $[Pb(DOTA)]^{2-}$ at pD = 7.5 and 273 K ($[Pb(DOTA)]^{2-}$ = 0.02 M, D_2O).

VT ^{1}H and ^{13}C NMR spectra of $[Pb(DOTA)]^{2-}$ have been recorded in the temperature range 273 – 343 K (Figures 20 and 21). At 273 K (0 °C), the ^{1}H NMR spectrum contains relatively sharp ^{1}H signals with a well-defined multiplicity. As temperature increased, the signals exhibited a progressive broadening leading to coalescence at 333 K (60 °C). Remarkably, the coalescence of the resonances of the ring protons, due to the ring flipping motion *i.e.* $\delta \leftrightharpoons \lambda$ ring inversion, occurs at the same temperature of that of the two protons on the pendant arms H_3 and $H_{3'}$, due to the pendant arm rotation *i.e.* $\Delta \leftrightharpoons \Lambda$, indicating that the two motions, leading to the interconversion of the TSAP enantiomers ($\Lambda(\lambda\lambda\lambda\lambda) \leftrightharpoons \Delta(\delta\delta\delta\delta)$), are not independent, even though they might occur simultaneously or subsequently. The same phenomenon was observed in the VT ^{13}C NMR spectra of $[Pb(DOTA)]^{2-}$ (Figure 21).

The ^{13}C NMR signals of the C_1 and C_2 carbons were suitable to carry out line-shape analysis by simulating the ^{13}C NMR spectra of $[Pb(DOTA)]^{2-}$ obtained in the temperature range 273 – 343 K (Figure 21). By simulating each spectrum at a given temperature, it was possible to determine the corresponding k_{ex} rate constant characterizing the $\Lambda(\lambda\lambda\lambda\lambda) \leftrightharpoons \Delta(\delta\delta\delta\delta)$ interconversion of the TSAP enantiomers. These experiments reveal that the fluxionality of the $[Pb(DOTA)]^{2-}$ complex increases with temperature, pointing to a faster interconversion between its enantiomers, hence the broadening of the signals that ultimately lead to coalescence of the resonances of C_1 and C_2 at higher temperatures (T = 333 K).

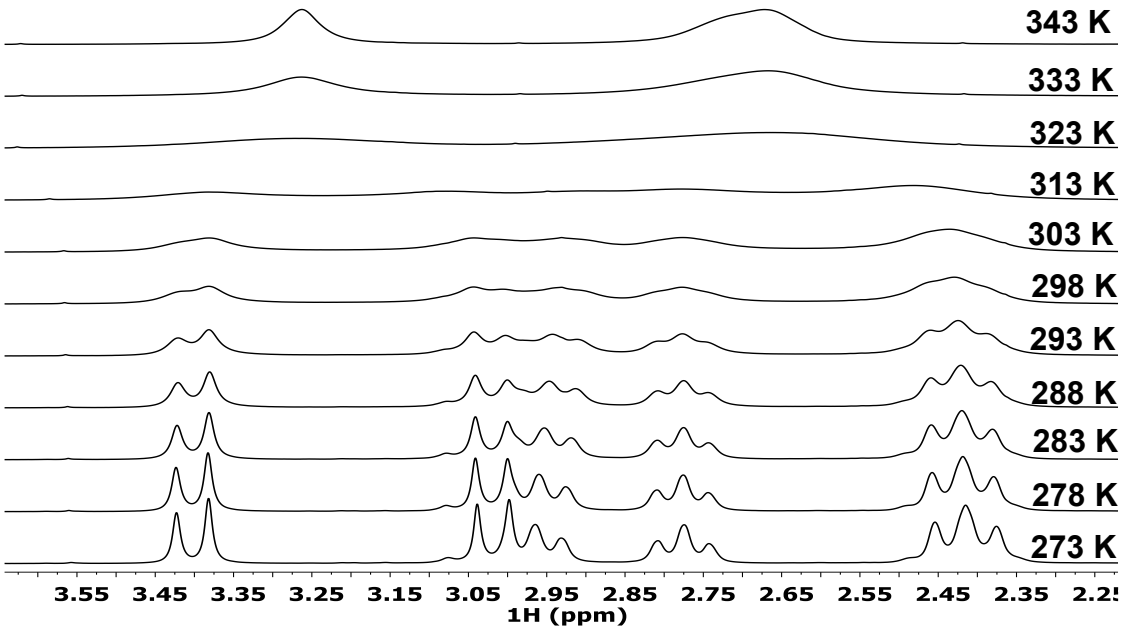

Figure 20. VT ^{1}H NMR spectra of $[Pb(DOTA)]^{2-}$ at pD = 7.5 in the temperature range 273–343 K ($[Pb(DOTA)]^{2-}$ = 0.02 M, D_2O).

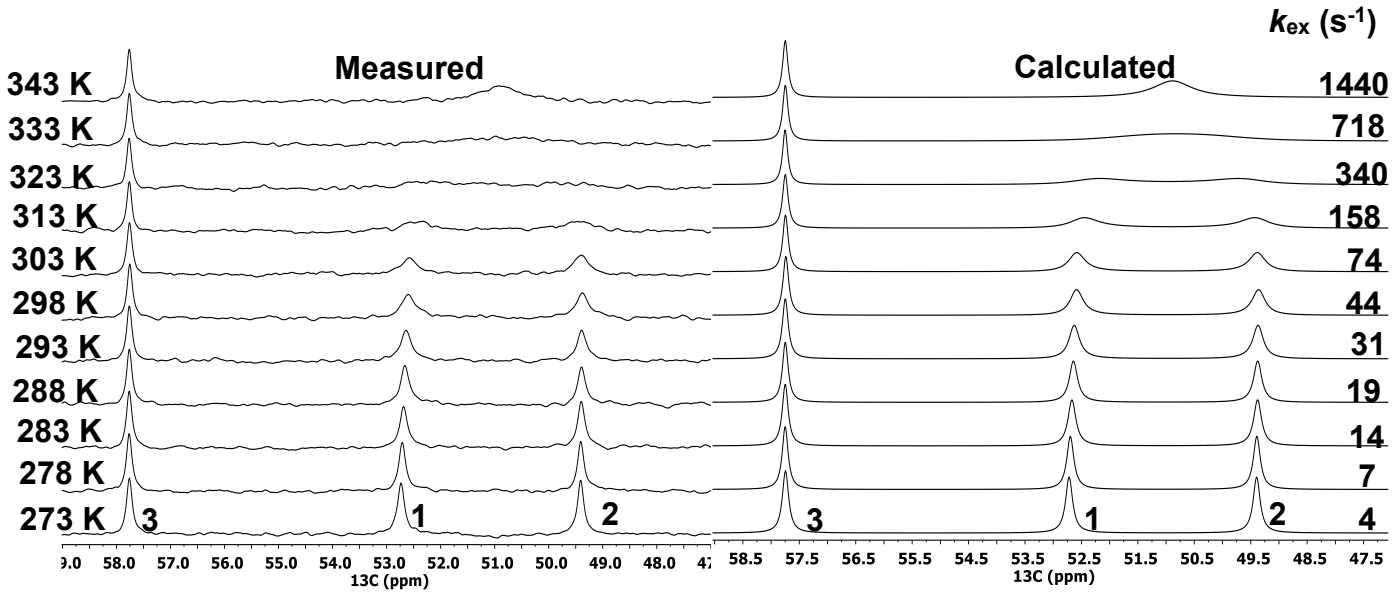

Figure 21. Measured (left) and calculated (right) VT $^{13}C\{^{1}H\}$ NMR spectra of $[Pb(DOTA)]^{2-}$ at pD = 7.5 in the temperature range 273–343 K, ($[Pb(DOTA)]^{2-}$ = 0.02 M, D_2O).

The dynamic properties of $[Pb(DOTAM)]^{2+}$ have been previously investigated in $[D_7]$DMF solution.[34,75] In order to compare the solution structure of $[Pb(DOTAM)]^{2+}$ with that of $[Pb(DOTA)]^{2-}$ in the same conditions, we performed a detailed NMR characterization of $[Pb(DOTAM)]^{2+}$ in D_2O. The single crystal X-ray diffraction study of $[Pb(DOTAM)](NO_3)_2 \cdot 3.5H_2O$[34] revealed that the $[Pb(DOTAM)]^{2+}$ complex is also characterized by the twisted square antiprism structure (TSAP: Λ(λλλλ) and Δ(δδδδ)). As for the DOTA complex, the ^{1}H and ^{13}C NMR spectra of $[Pb(DOTAM)]^{2+}$ show a single set of signals confirming the presence of a single isomer (presumably TSAP enantiomers with Λ(λλλλ) and Δ(δδδδ) configurations) in solution (Figures 22, 23 and S1). In fact, the ^{1}H NMR spectrum of $[Pb(DOTAM)]^{2+}$ (Figure 22) is very similar to that of $[Pb(DOTA)]^{2-}$. In this case the ^{1}H NMR signals appeared slightly less sharp, the doublets relative to the H_3 and $H_{3'}$ protons (AB system) did not overlap with other resonances, whereas those of the equatorial protons on C_1 and C_2 still largely overlap with each other, as seen for $[Pb(DOTA)]^{2-}$. In the ^{13}C NMR spectrum the signal of the $-CONH_2$ group falls at 174.97 ppm (Figure S1). Assignments of the ^{1}H and ^{13}C NMR signals of $[Pb(DOTAM)]^{2+}$ were performed by recording $^{1}H - {}^{1}H$ COSY and $^{1}H - {}^{13}C$ HSQC spectra (Figures S2 and S3). Additionally, the VT ^{1}H and ^{13}C NMR experiments carried out in the temperature range 273 – 323 K revealed similar broadening of the ^{1}H and ^{13}C signals (Figures S4 and 23), that achieved coalescence at lower temperatures compared to $[Pb(DOTA)]^{2-}$ (T = 313 *vs* 333 K). The k_{ex} rate constants for the interconversion of the TSAP enantiomers (Λ(λλλλ) ⇋ Δ(δδδδ)) formed by $[Pb(DOTAM)]^{2+}$ were determined with line-shape analysis by simulating the ^{13}C NMR spectra obtained in the temperature range 273 – 323 K (Figure S23).

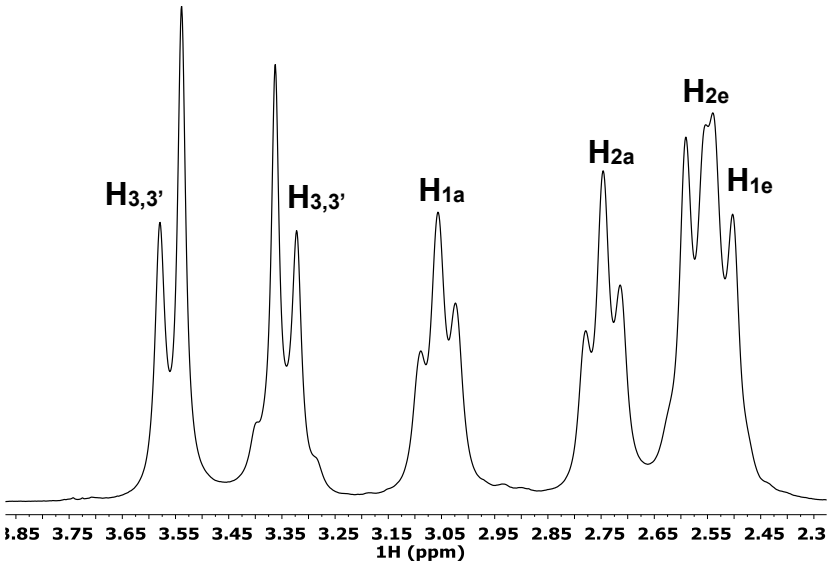

Figure 22. ^{1}H NMR spectrum of $[Pb(DOTAM)]^{2+}$ at pD = 7.6 and 273 K ($[Pb(DOTAM)]^{2+}$ = 0.02 M, D_2O).

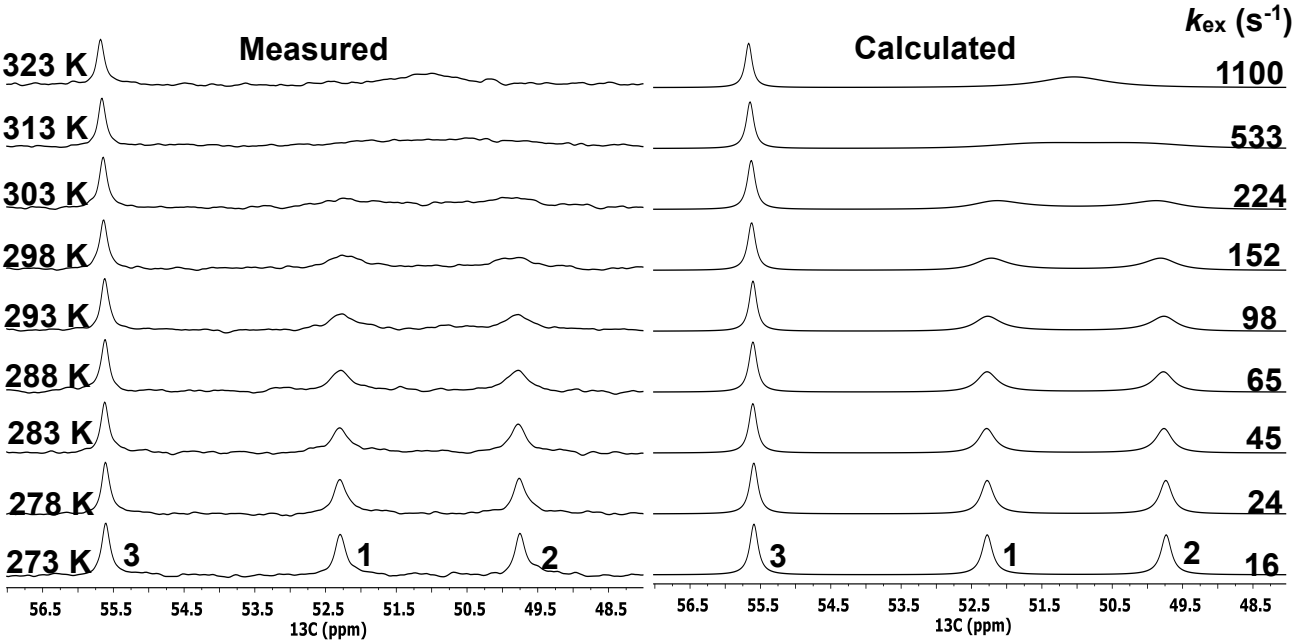

Figure 23. Measured (left) and calculated (right) VT $^{13}C\{^{1}H\}$ NMR spectra of $[Pb(DOTAM)]^{2+}$ at pD = 7.6 in the temperature range 273 – 323 K, ($[Pb(DOTAM)]^{2+}$ = 0.02 M, D_2O).

Since the solution structure and dynamic processes of $[Bi(DOTAM)]^{3+}$ complex have not been investigated before, the multinuclear 1D and 2D NMR studies of $[Bi(DOTAM)]^{3+}$ were performed in a similar manner as for $[Pb(DOTAM)]^{2+}$. By analogy, it can be assumed that the structure of the $[Bi(DOTAM)]^{3+}$ and $[Bi(DOTA)]^{-}$ complexes are very similar and that both adopt a TSAP geometry in solution.[37] The ^{1}H NMR spectrum of $[Bi(DOTAM)]^{3+}$ was recorded in H_2O with a D_2O capillary in the sample for the locking. This allowed us to determine the resonances of the $–NH_2$ protons of the amide function that resonate as two singlets at 7.88 and 8.58 ppm (Figure 24). This assignment was also confirmed by the $^{1}H – ^{13}C$ HMBC spectrum (Figure 25), where correlation cross peaks between the singlets of the two amidic protons and that of the carbonyl carbon of the amide group are present, as well as with the signal of the adjacent methylene carbon C_3 in the pendant arm. The assignments of the ^{1}H and ^{13}C NMR signals were completed by the acquisition of the $^{1}H – ^{1}H$ COSY, $^{1}H – ^{1}H$ NOESY and $^{1}H – ^{13}C$ HSQC spectra of the $[Bi(DOTAM)]^{3+}$ complex (Figures S6 – S8). In the ^{1}H NMR spectrum of $[Bi(DOTAM)]^{3+}$ the resonances of the protons on the pendant arms and macrocyclic ring are well separated, as in the spectrum of $[Pb(DOTAM)]^{2+}$, at lower frequencies compared to the amide singlets (range 3 – 4.4 ppm). However, in this case the equatorial protons resonate at higher frequencies compared to the axial ones, whereas the opposite was observed for $[Pb(DOTAM)]^{2+}$.

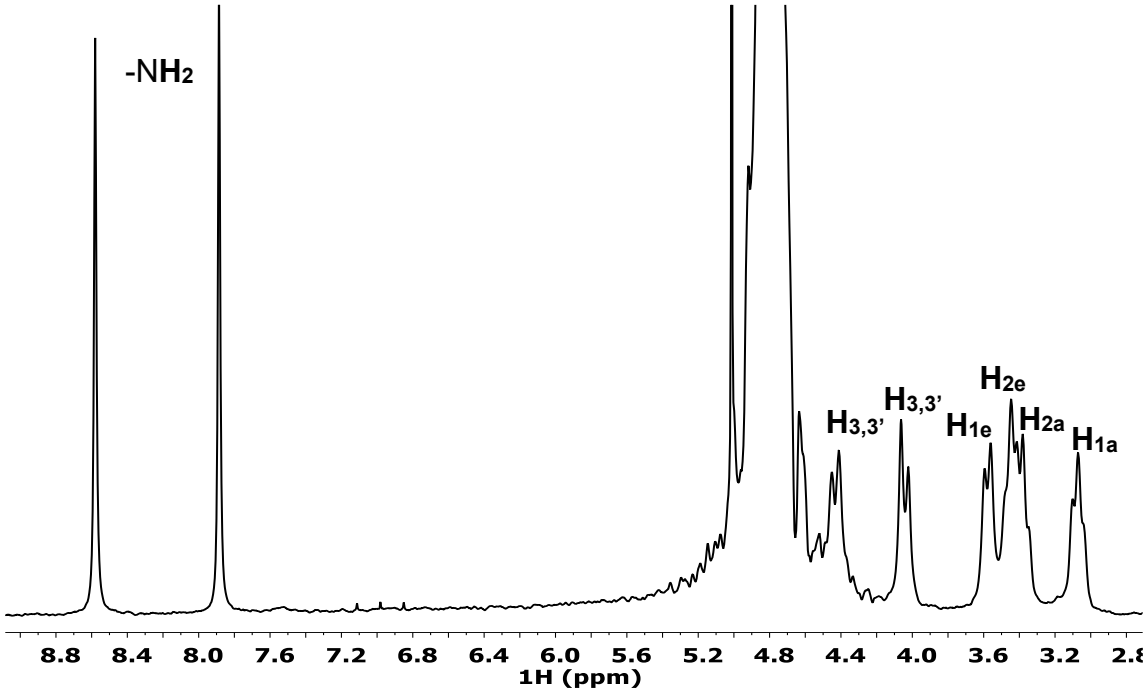

Figure 24. ^{1}H NMR spectrum of $[Bi(DOTAM)]^{3+}$ at pH = 4.5 and 273 K ($[Bi(DOTAM)]^{3+}$ = 0.04 M, H_2O).

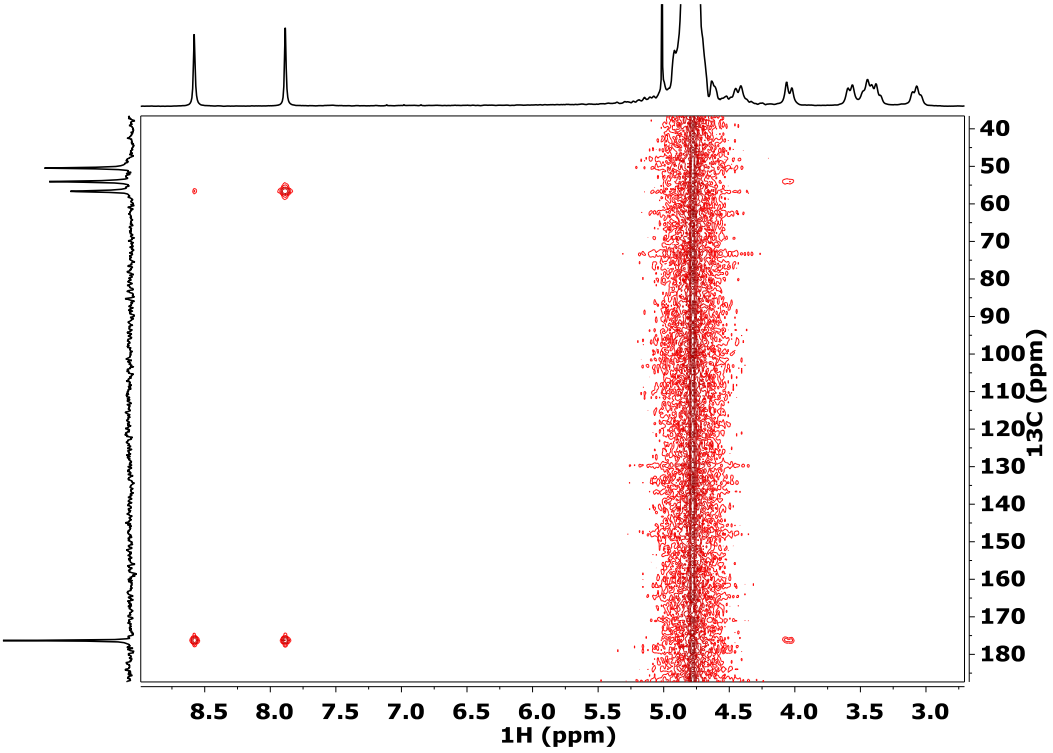

Figure 25. ^{1}H – ^{13}C HMBC spectrum of $[Bi(DOTAM)]^{3+}$ at pH = 4.5 and 273 K ($[Bi(DOTAM)]^{3+}$ = 0.04 M, H_2O).

Variable temperature ^{1}H NMR spectra of $[Bi(DOTAM)]^{3+}$ also showed an increased broadening of the resonances of the methylene protons proportional to the temperature in the range 273 – 328 K. Conversely, the signals of the amide protons were not significantly affected by the temperature (Figure 26). Likewise, VT ^{13}C NMR spectra of $[Bi(DOTAM)]^{3+}$ (Figures S5 and 27) were suitable to carry out line-shape analysis for calculating the k_{ex} rate constants characterizing the interconversion of the TSAP enantiomers ($\Lambda(\lambda\lambda\lambda\lambda) \leftrightharpoons \Delta(\delta\delta\delta\delta)$).

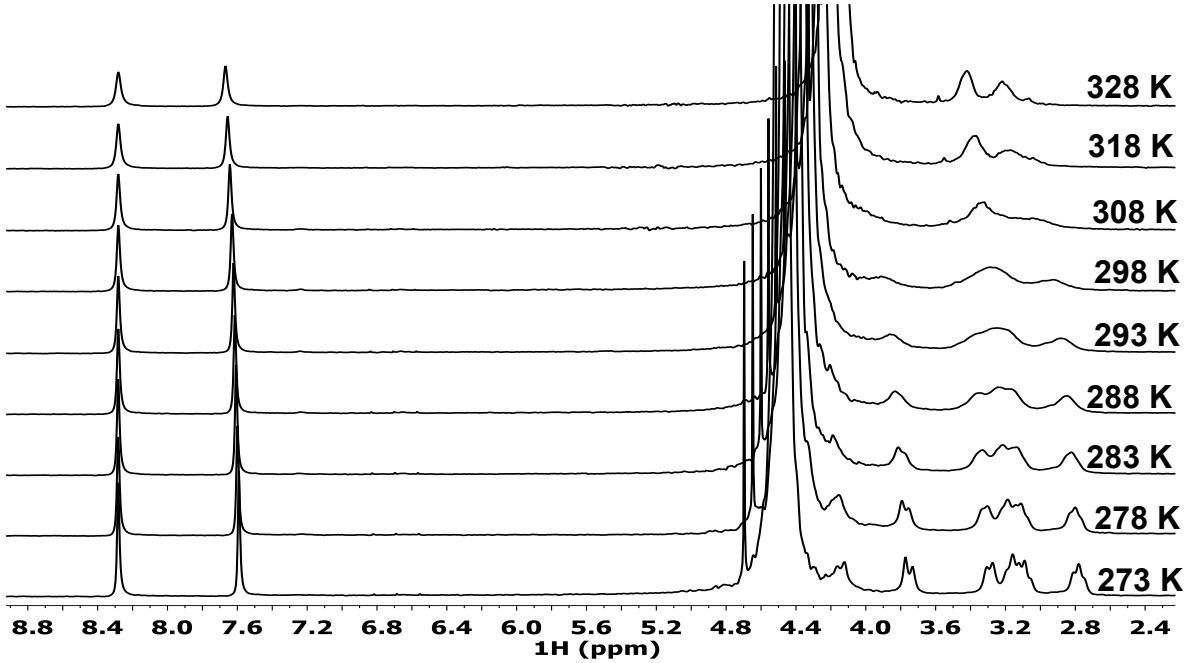

Figure 26. VT ^{1}H NMR spectra of $[Bi(DOTAM)]^{3+}$ at pH = 4.5 in the temperature range 273 –328 K ($[Bi(DOTAM)]^{3+}$ = 0.04 M, H_2O).

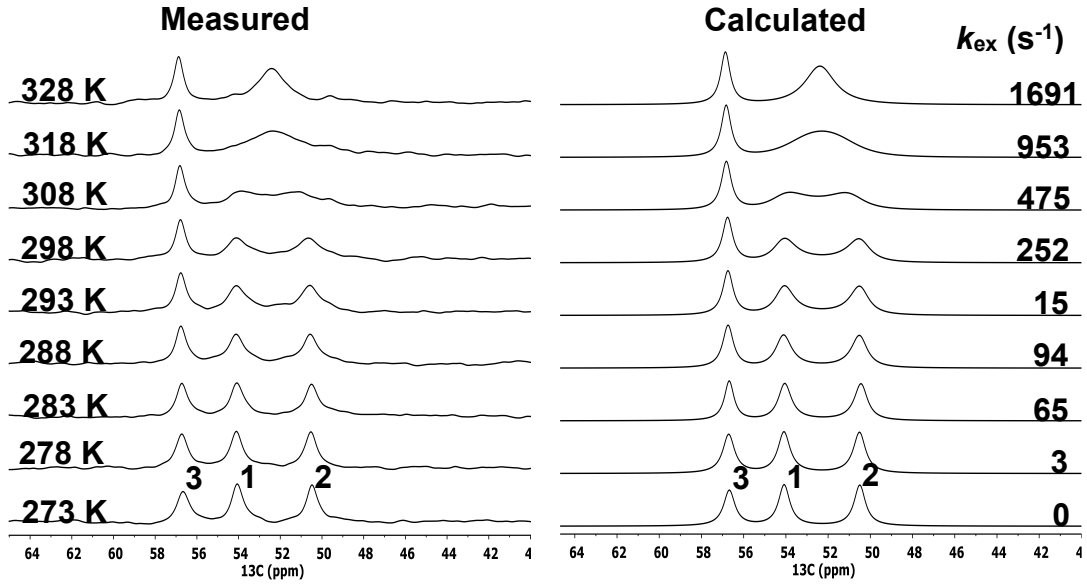

Figure 27. Measured (left) and calculated (right) VT $^{13}C\{^{1}H\}$ NMR spectra of $[Bi(DOTAM)]^{3+}$ at pH = 4.5 in the temperature range 273 – 328 K ($[Bi(DOTAM)]^{3+}$ = 0.04 M, H_2O).

Finally, the Pb(II) complex with DOTP was studied by multinuclear NMR spectroscopy at two different pD values (pD = 4.6 and 10.95) in order to investigate the influence of the protonation state on the structural and dynamic processes of the $[Pb(H_4DOTP)]^{2-}$ and $[Pb(DOTP)]^{6-}$ species in solution. According to the X-ray diffraction studies, $[Pb(H_4DOTP)]^{2-}$ is characterized by TSAP structure (*vide infra* "*X-ray diffraction studies of [Pb(H4DOTP)]2– and comparison with*

solid-state data of the selected complexes"). The ^{1}H and ^{13}C NMR spectra of $[Pb(H_4DOTP)]^{2-}$ show a single set of signals, confirming the presence of a single isomer in solution (Figures 28 and 29). The phosphonate methylene protons resonate as two broad multiplets at slightly lower frequencies (2.58 and 2.97 ppm) compared to the previous Pb(II) complexes, one of which is partially overlapping with the multiplet of axial proton H_{1a} at 3.03 ppm (Figure 28). The methylene protons of the macrocycle exhibit the usual four proton signals (two triplets and two doublets) as seen previously for the other Pb(II) complexes.

The ^{13}C NMR spectrum of $[Pb(H_4DOTP)]^{2-}$ exhibits four signals (Figure 29), one of which clearly indicating an overlap, confirmed also by the ^{1}H – ^{13}C HSQC and ^{1}H – ^{1}H COSY spectra (Figures 30 and S9). The increased number of ^{13}C resonances can be explained by the ^{13}C – ^{31}P coupling. The doublet with the larger coupling constant ($^{1}J_{3CP}$ = 142.9 Hz) can be ascribed to the methylene phosphonate carbon C_3, while the other doublet is relative to the macrocyclic carbon C_1 ($^{3}J_{C1P}$ = 17.4 Hz). The resonance of the C_2 carbon falls under that of C_3 at 52.7 ppm, and is characterized by a very small coupling constant with ^{31}P ($^{3}J_{C2P}$ < 2 Hz). By considering these coupling constants of the C_1 and C_2 carbons with the ^{31}P nucleus, the dihedral angles ϕ for the C_1–N–C_3–P and C_2–N–C_3–P bonds were calculated with the Karplus equation:[76]

$$^{3}J_{CP} = 17.3\cos^{2}\phi - 4.7\cos\phi - 0.9 \qquad \textit{Eq. 16}$$

The dihedral angles were found to be ϕ = 55.5° and 154.3° for C_2–N–C_3–P and C_1–N–C_3–P bonds, respectively.

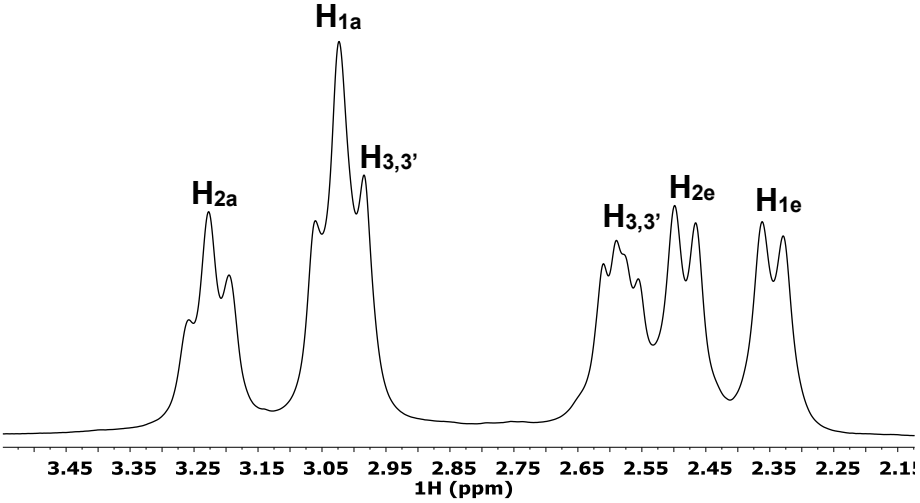

Figure 28. ^{1}H NMR spectrum of $[Pb(H_4DOTP)]^{2-}$ at pD = 4.6 and 268 K ($[Pb(H_4DOTP)]^{2-}$ = 0.02 M, D_2O).

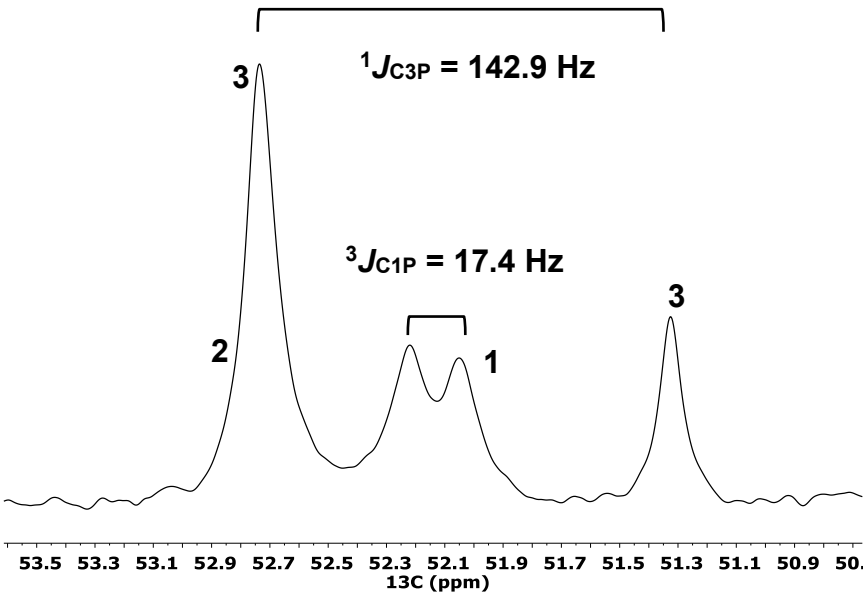

Figure 29. $^{13}C\{^1H\}$ NMR spectrum of $[Pb(H_4DOTP)]^{2-}$ at pD = 4.6 and 268 K ($[Pb(H_4DOTP)]^{2-}$ = 0.02 M, D_2O).

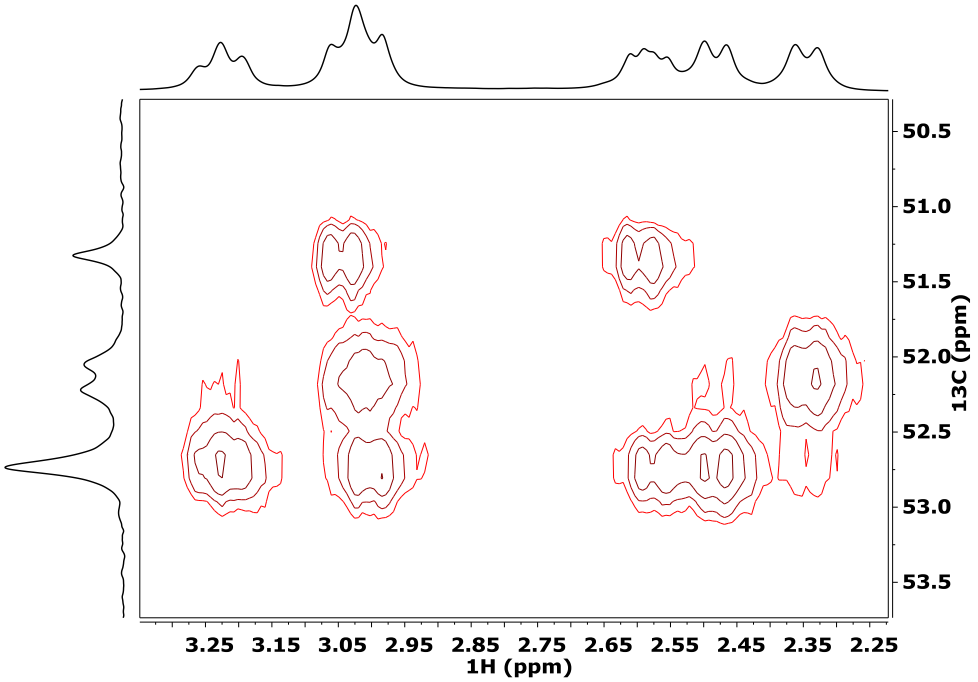

Figure 30. ^1H – ^{13}C HSQC spectrum of $[Pb(H_4DOTP)]^{2-}$ at pD = 4.6 and 268 K ($[Pb(H_4DOTP)]^{2-}$ = 0.02 M, D_2O).

Line-shape analysis was also performed in the temperature range 268 – 333 K by simulating the ^{13}C NMR spectra of $[Pb(H_4DOTP)]^{2-}$ (Figure 31) to calculate the k_{ex} rate constants characterizing the interconversion of the TSAP enantiomers ($\Lambda(\lambda\lambda\lambda\lambda) \leftrightharpoons \Delta(\delta\delta\delta\delta)$).

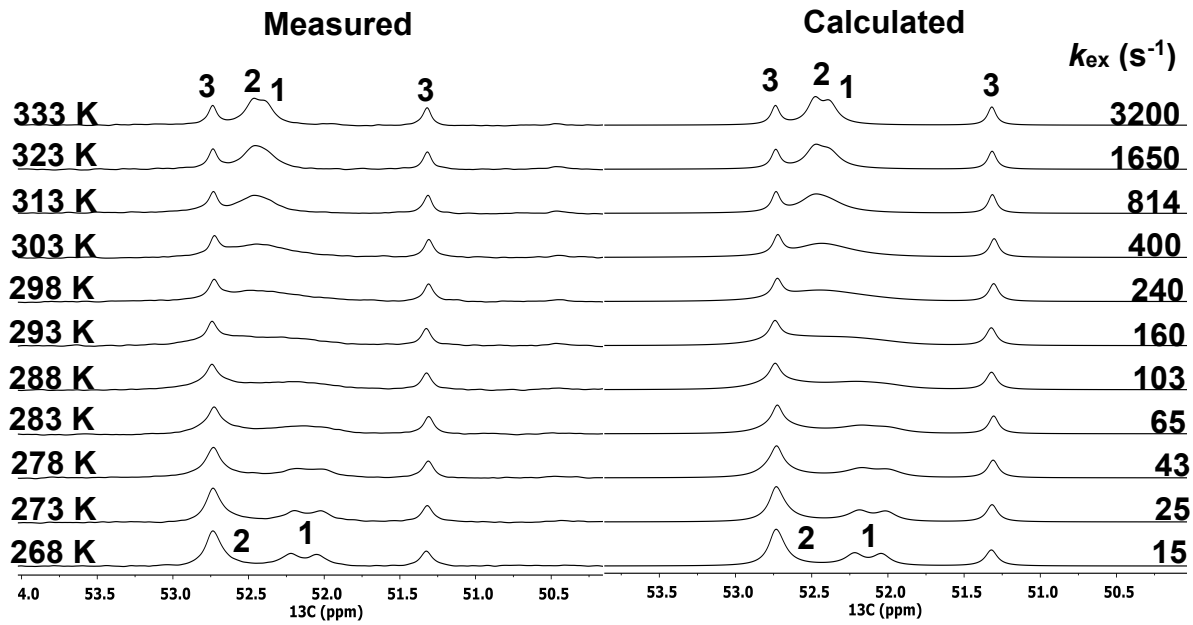

Figure 31. Measured (left) and calculated (right) VT $^{13}C\{^{1}H\}$ NMR spectra of $[Pb(H_4DOTP)]^{2-}$ at pD = 4.6 in the temperature range 268 – 333 K, ($[Pb(H_4DOTP)]^{2-}$ = 0.02 M, D_2O).

Compared to the protonated form $[Pb(H_4DOTP)]^{2-}$, the ^{1}H NMR signals of $[Pb(DOTP)]^{6-}$ were much broader and overlapped, suggesting the occurrence of an even faster fluctional motion (Figure 32). A similar phenomenon was observed in the ^{13}C NMR spectrum as the signals of C_1 and C_2 are each overlapped with those of carbon C_3, which is coupled to ^{31}P with a large coupling constant ($^{1}J_{C3P}$ = 134.5 Hz, Figure 33). Assignments of the ^{1}H and ^{13}C NMR signals were performed by recording the ^{1}H – ^{1}H COSY and ^{1}H – ^{13}C HSQC spectra of the complex (Figures S10 and S11). Considering the $^{1}J_{C3P}$ value, the dihedral angles ϕ of the C_2–N–C_3–P and C_1–N–C_3–P bonds calculated with *Eq. 15* (ϕ = 55.5° and 152.9°, respectively) were found to be almost identical to those of the tetraprotonated $[Pb(H_4DOTP)]^{2-}$ complex.

Finally, the line-shape analysis was also carried out in the temperature range 273 – 333 K by simulating the ^{13}C NMR spectra of $[Pb(DOTP)]^{2-}$ (Figure 34) to calculate the k_{ex} rate constants for the interconversion of the TSAP enantiomers (Λ(λλλλ) ⇋ Δ(δδδδ)).

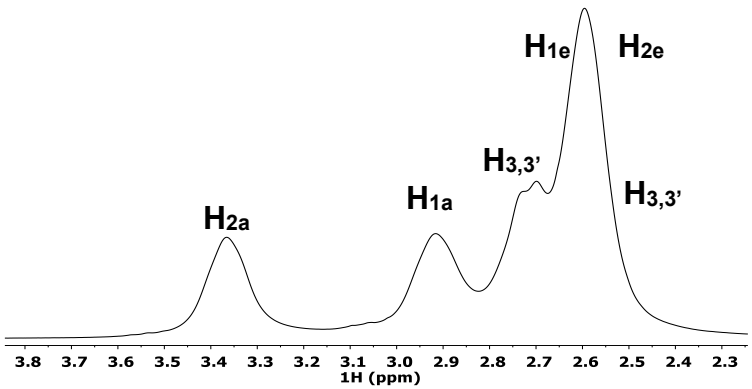

Figure 32. ^{1}H NMR spectrum of $[Pb(DOTP)]^{6-}$ at pD = 10.95 and 273 K ($[Pb(DOTP)]^{6-}$ = 0.1 M, D_2O).

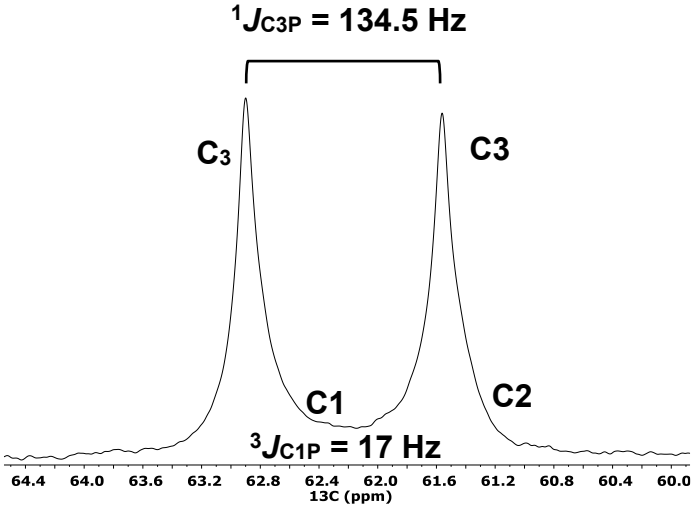

Figure 33. $^{13}C\{^1H\}$ NMR spectrum of $[Pb(DOTP)]^{6-}$ at pD = 10.95 and 273 K ($[Pb(DOTP)]^{6-}$ = 0.1 M, D_2O).

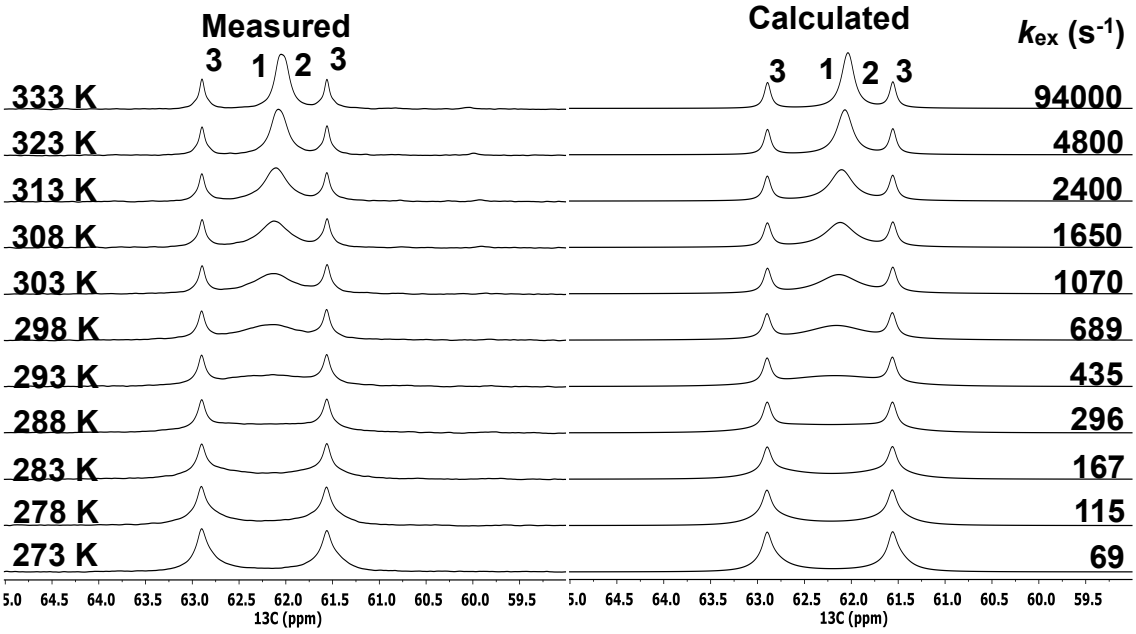

Figure 34. Measured (left) and calculated (right) VT $^{13}C\{^1H\}$ NMR spectra of $[Pb(DOTP)]^{6-}$ at pD = 10.95 in the temperature range 273 – 333 K ($[Pb(DOTP)]^{6-}$ = 0.1 M, D_2O).

Eyring plot for the determination of the activation parameters

The activation parameters ($\Delta H^{\neq}$: activation enthalpy , $\Delta S^{\neq}$: activation entropy, $\Delta G^{\neq}_{298}$: Gibbs free energy and k_{ex}^{298}: exchange rate) of the interconversion process of the TSAP enantiomers ($\Lambda(\lambda\lambda\lambda\lambda) \leftrightharpoons \Delta(\delta\delta\delta\delta)$) for the $[Pb(DOTA)]^{2-}$, $[Pb(DOTAM)]^{2+}$, $[Pb(H_4DOTP)]^{2-}$ and $[Bi(DOTAM)]^{2+}$ complexes were estimated with the Eyring equation (*Eq. 16*), by using the k_{ex} rate constant obtained via line-shape analysis in the temperature range 273 – 333 K (Figure 35, Table 6).

$$\ln\frac{k}{T} = \frac{-\Delta H^{\neq}}{R}\cdot\frac{1}{T} + \ln\frac{k_B}{h} + \frac{\Delta S^{\neq}}{R} \qquad \textit{Eq. 16}$$

It was observed that the interconversion of the enantiomers for the Pb(II) complexes is characterized by very similar activation enthalpy values ($\Delta H^{\neq} \approx 60$ kJ mol^{-1}), but very different entropy, Gibbs free energy and exchange rate values. The main difference was observed between $[Pb(DOTA)]^{2-}$ and $[Pb(DOTP)]^{6-}$ with activation entropy values $\Delta S^{\neq} = -9$ J mol^{-1} K^{-1} and $\Delta S^{\neq} = 10.9$ J mol^{-1} K^{-1}, respectively. Surprisingly the interconversion of the enantiomers formed by the protonated $[Pb(H_4DOTP)]^{2-}$ and the fully deprotonated $[Pb(DOTP)]^{6-}$ complexes were also characterized by very different activation entropy values ($[Pb(H_4DOTP)]^{2-}$: $\Delta S^{\neq} = -0.1$ J mol^{-1} K^{-1}; $[Pb(DOTP)]^{6-}$: $\Delta S^{\neq} = 10.9$ J mol^{-1} K^{-1}, Table 6). The activation entropy is likely related to the different hydration features of the pendant arms (carboxylate *vs* phosphonate) in the ground and the transition states. Based on the similar $\Delta H^{\neq}$ and the different $\Delta S^{\neq}$ values, it can be assumed that the interconversion of the enantiomers formed by the Pb(II) complexes with DOTA-derivatives is an entropy-controlled process which is mainly influenced by their different hydration in the ground and transition states. In fact, the activation entropy of the $[Pb(DOTAM)]^{2+}$ and $[Pb(H_4DOTP)]^{2-}$ was roughly zero, which can be explained by the similarly ordered system in the ground and transition states due to the presence of the less basic amide and protonated phosphonate groups. Additionally, the reduced net charge of the Pb(II) complexes induce a milder reorganization of the solvent shell during the interconversion processes. On the other hand, the interconversion of $[Pb(DOTA)]^{2-}$ is characterized by a negative activation entropy value, which can be linked to a highly organized hydration sphere of the carboxylate groups in the transition state. This hypothesis is further supported by the positive activation entropy for the interconversion of the enantiomers of $[Pb(DOTP)]^{6-}$, which is likely to have a more reorganized solvent shell in the ground state than in the transition state.

Among the Pb(II) complexes, $[Pb(DOTP)]^{6-}$ had the highest interconversion rate ($k_{ex}^{298} = 689$ s^{-1}), followed by its protonated form $[Pb(H_4DOTP)]^{2-}$ ($k_{ex}^{298} = 240$ s^{-1}), $[Pb(DOTAM)]^{2+}$ ($k_{ex}^{298} = 152$ s^{-1}) and lastly $[Pb(DOTA)]^{2-}$ ($k_{ex}^{298} = 44$ s^{-1}). In contrast, the interconversion of the enantiomers of $[Bi(DOTP)]^{5-}$ were characterized by the slowest exchange rate ($k_{ex}^{298} = 8$ s^{-1}), followed by $[Bi(DOTA)]^{-}$ ($k_{ex}^{298} = 65$ s^{-1}) and $[Bi(DOTAM)]^{3+}$ ($k_{ex}^{298} = 252$ s^{-1}). According to the proposed mechanism for the dissociation reaction of Pb(II) and Bi(III) complexes, the release of the metal ions requires the transfer of a proton from the pendant arm to the macrocyclic nitrogen atom, resulting in a relatively labile protonated intermediate in which the

H^+ effectively displaces the Pb^{2+} ion from the coordination cage. Comparison of the enantiomerization rates (Table 6) with the dissociation rates (Table 5) shows that the flexibility of the Pb(II) and Bi(III) complexes correlates with their kinetic lability. In general, more flexible systems are more prone to metal ion release than rigid ones, as faster intramolecular rearrangements increase the likelihood of dissociation.

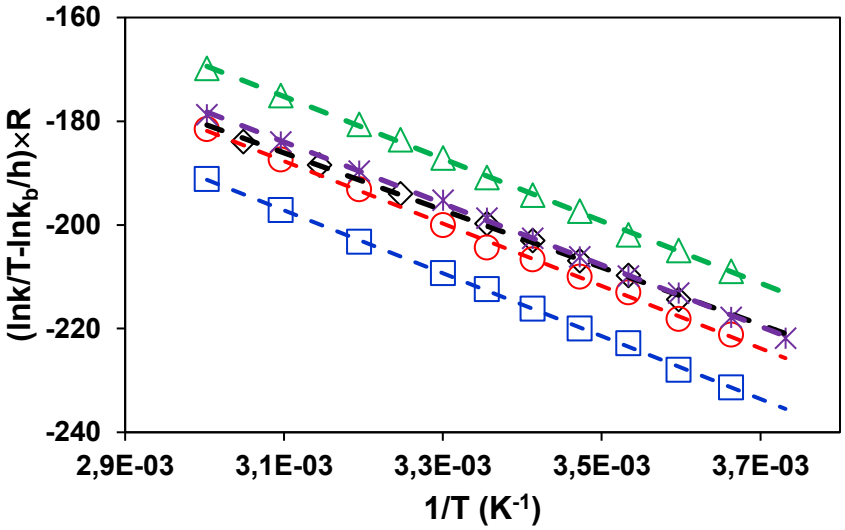

Figure 35. Eyring plots that afforded the activation parameters for the dynamic equilibrium Δ(δδδδ) ⇌ Λ(λλλλ) for **[Pb(DOTAM)]$^{2+}$**, **[Pb(DOTA)]$^{2-}$**, **[Pb(DOTP)]$^{6-}$**, **[Pb(H$_4$DOTP)]$^{2-}$** and **[Bi(DOTAM)]$^{3+}$**.

Table 6. Rate constants and activation parameters for the dynamic equilibrium Δ(δδδδ) ⇌ Λ(λλλλ) of the Pb(II) and Bi(III) complexes formed with DOTAM, DOTA and DOTP ligands.

	[Pb(DOTAM)]$^{2+}$	**[Pb(DOTA)]$^{2-}$**	**[Pb(H$_4$DOTP)]$^{2-}$**	**[Pb(DOTP)]$^{6-}$**
$\Delta H^{\ddagger}$/ kJ·mol^{-1}	60.2 ± 0.9 58 ± 0.7[34]	60.9 ± 0.5	59.4 ± 0.5	60.0 ± 0.5
$\Delta S^{\ddagger}$/J·mol^{-1} K^{-1}	**–1.1 ± 0.2** –13 ± 0.2[34]	**–9.0 ± 0.5**	**–0.1 ± 0.5**	**10.9 ± 0.9**
$\Delta G^{\ddagger}_{298}$/kJ·mol^{-1}	60.5 62[34]	63.6	59.4	56.8
k_{ex}^{298}/s^{-1}	152 79[34]	44	240	689
	[Bi(DOTAM)]$^{3+}$	**[Bi(DOTA)]$^{-}$**[37]	**[Bi(DOTP)]$^{5-}$**[27]	
$\Delta H^{\ddagger}$/ kJ·mol^{-1}	56 ± 1	40	64 ± 1	
$\Delta S^{\ddagger}$/J·mol^{-1} K^{-1}	–11 ± 2	–76	–14 ± 2	

$\Delta G^{\ddagger}_{298}$/kJ·mol^{-1}	59	63	68
k_{ex}^{298}/s^{-1}	252	65	8

X-ray diffraction studies of $[Pb(H_4DOTP)]^{2-}$ and comparison with solid-state data of selected complexes

To confirm the structural properties of the Pb(II) complex with the DOTP ligand, the crystal structure of $[Pb(H_4DOTP)]^{2-}$ complex was determined by X–ray diffraction studies. In particular, single crystals of formula $\{2(C(NH_2)_3)[Pb(H_4DOTP)]\}\cdot 7H_2O$ suitable for X-ray diffraction studies, were grown by the slow diffusion of an EtOH and Et_2O mixture into an aqueous solution of $[Pb(H_4DOTP)]^{2-}$ prepared by mixing equimolar amounts of $PbCO_3$ and of the H_8DOTP ligand. To obtain the tetraprotonated $[Pb(H_4DOTP)]^{2-}$ complex, the pH of the aqueous solution was adjusted to 4.2 with guanidine-carbonate. A simplified structure of the $[Pb(H_4DOTP)]^{2-}$ complex anion is shown in Figure 36. Other details regarding the structure of the complex are reported in the Supporting Information.

In the $[Pb(H_4DOTP)]^{2-}$ anionic complex the Pb(II) ion is hepta-coordinated, with four sp^3 nitrogen atoms and three oxygen atoms of the phosphonate groups (one fully deprotonated and two monoprotonated), whereas the fully protonated phosphonate group is not bound to Pb^{2+} as it is indicated by the long distance between the metal center and the O atoms of this group (Pb – O4: 3.324 Å; Pb – O5: 3.819 Å). The Pb(II) ion is sandwiched between the plane formed by the four N atoms of the macrocycle at a distance of 0.941 Å, and a trigonal plane defined by the three coordinated phosphonate O atoms at a distance of 1.326 Å. The torsion angle between these two planes is 25.4°. The coordination polyhedron around the Pb(II) ion in $[Pb(H_4DOTP)]^{2-}$ can be described as a twisted square antiprism (TSAP). The bond distances between the Pb(II) ion and the coordinated donor atoms (Pb–N: 2.69 – 2.86 Å; Pb–O: 2.67 – 2.92 Å, see Table 7) point to a slightly distorted coordination sphere, possibly due to the uncoordinated phosphonate arm.

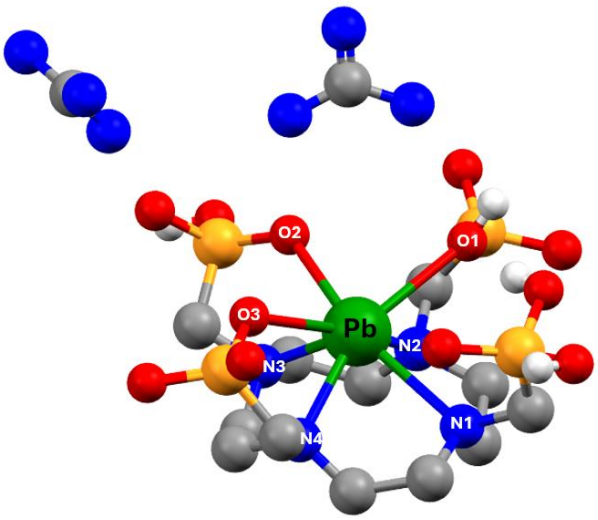

Figure 36: X-ray molecular structure of $\{2(C(NH_2)_3)[Pb(H_4DOTP)]\}\cdot 7H_2O$. The water molecules are omitted for simplicity.

The Pb(II) ion in $[Pb(DOTA)]^-$ and $[Pb(DOTAM)]^{2+}$ is octa-coordinated with a twisted square antiprism geometry.[34,38] The coordination sphere is formed by the four nitrogen atoms of the macrocycle (average Pb−N bond distance: 2.617 – 2.687 Å, and by the four oxygen atoms of the carboxylate (DOTA) or amide (DOTAM) groups located on the pendant arms (average Pb−O distance: 2.687 − 2.717 Å).[38] In the $[Pb(DOTA)]^-$ and $[Pb(DOTAM)]^{2+}$ complexes the donor atoms of the ligands encapsulate the central Pb(II) ion, which is placed between the four roughly coplanar nitrogen atoms of the ring (N1, N2, N3 and N4) and the four roughly coplanar oxygen atoms of the pendant arms (O1, O2, O3 and O4). Compared to $[Pb(H_4DOTP)]^{2-}$, both complexes exhibit on average shorter, hence stronger bonds, between Pb(II) and the donor atoms. In fact, the average Pb–N and Pb–O bond distances in $[Pb(H_4DOTP)]^{2-}$fall in the range of 2.69 – 2.86 Å and 2.67 – 2.92 Å, respectively.

Based on the X-ray diffraction studies, the structural features in solid state of $[Bi(DOTA)]^-$ and $[Bi(DOTP)]^{5-}$ (Figure 38)[12] are very similar to those of the $[Pb(DOTA)]^-$, $[Pb(H_4DOTP)]^{2-}$ and $[Pb(DOTAM)]^{2+}$complexes. In $[Bi(DOTA)]^-$ and $[Bi(DOTP)]^{5-}$, the Bi(III) ion is octa-coordinated, with four macrocyclic nitrogen and four carboxylate or phosphonate oxygen donor atoms.[37,77] In both $[Bi(DOTA)]^-$ and $[Bi(DOTP)]^{5-}$, the coordination geometry of Bi(III) ion can also be described as a twisted square antiprism (TSAP).

Table 7: Comparison of the Pb−X (X = N, O) bond lengths in $[Pb(H_4DOTP)]^{2-}$, $[Pb(DOTA)]^{2-}$ and $[Pb(DOTAM)]^{2+}$.

Bond distance (Å)	$[Pb(H_4DOTP)]^{2-}$	$[Pb(DOTA)]^{2-}$[38]	$[Pb(DOTAM)]^{2+}$[34]
Pb−N1	2.689(10)	2.676(9)	2.630(9)
Pb−N2	2.744(9)	2.687(9)	2.617(8)
Pb−N3	2.859(9)	2.638(9)	2.625(9)
Pb−N4	2.727(10)	2.660(9)	2.628(8)
Pb−O1	2.671(7)	2.796(8)	2.819(5)
Pb−O2	2.924(7)	2.827(9)	2.657(6)
Pb−O3	2.890(7)	2.586(8)	2.785(6)
Pb−O4	–	2.609(8)	2.756(6)

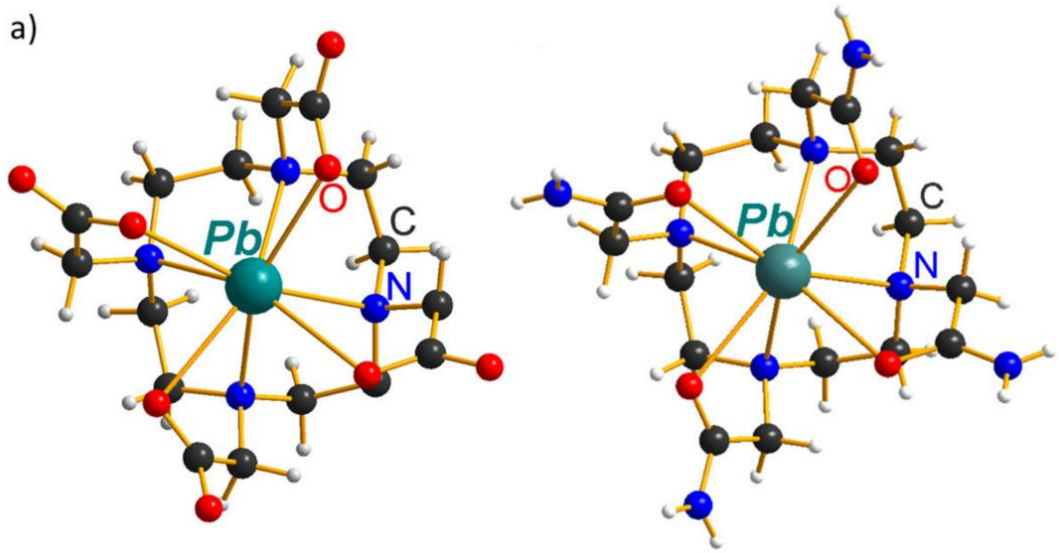

Figure 37: X-ray crystal structures of the (a) $[Pb(DOTA)]^{2-}$ complex anion and (b) $[Pb(DOTAM)]^{2+}$ complex cation.[6]

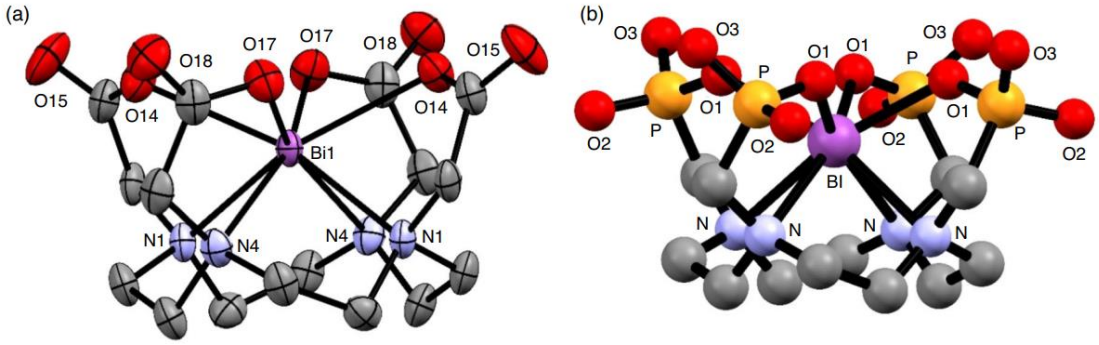

Figure 38: X-ray crystal structures of the $[Bi(DOTA)]^{-}$ and $[Bi(DOTP)]^{5-}$ complex anions.[12]

The solid-state X-ray structures of the complexes of Zn^{2+} and Cu^{2+} with DOTA and DOTAM are also described in the literature and, due to their biological relevance, are discussed here for comparative purposes. Consistent with the smaller ionic radius and lower coordination number of Zn^{2+} and Cu^{2+}, it was found that not all the donor atoms of DOTA and its derivatives participate in the formation of the complexes (Figure 39 and Figure 40). In fact, in both $[Cu(H_2DOTA)]$ and $[Zn(H_2DOTA)]$ the metal ions are hexacoordinated, with the coordination sphere defined by the four nitrogen atoms of the cyclen ring and two opposite carboxylate arms, while the two other protonated carboxyl groups are not interacting with the metal center. Moreover, for the Cu^{2+} complex two Cu–N bonds are elongated (≈ 2.32 Å) compared to the other two (≈ 2.04 Å) indicating a distorted octahedral geometry, which can be attributed to the Jahn-Teller effect, typical of d^9 ions.

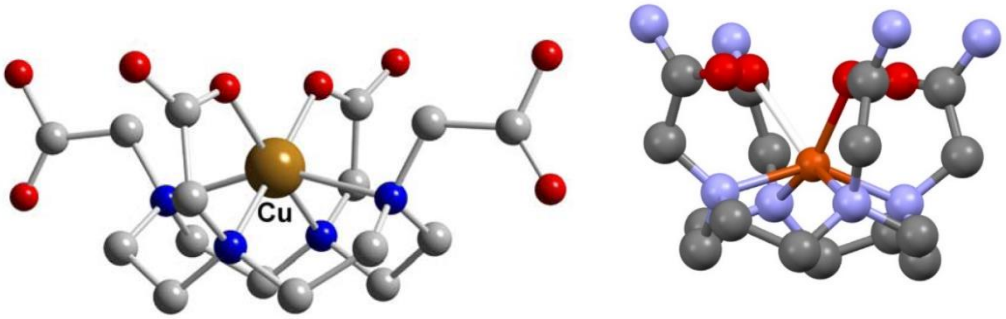

Figure 39: X-ray crystal structures of [Cu(H_2DOTA)] and [Cu(DOTAM)] (protons omitted).[78,79]

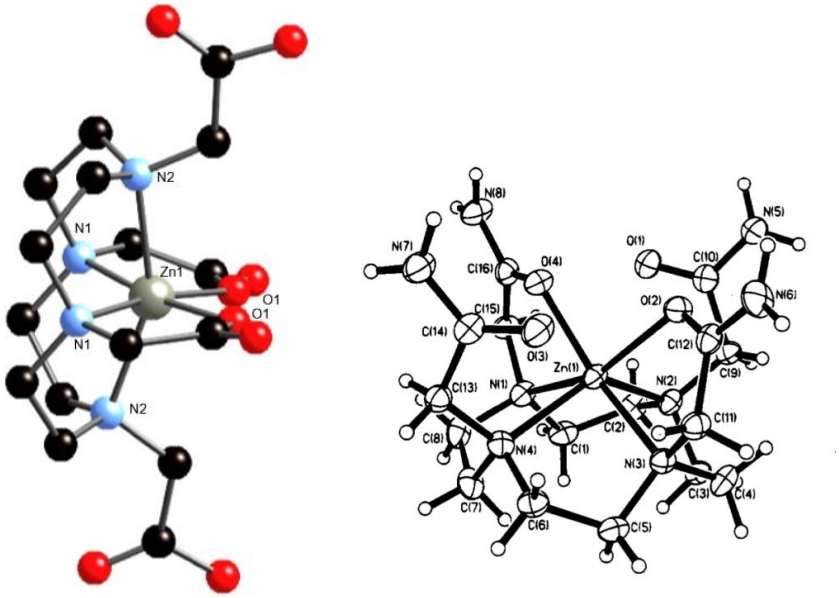

Figure 40: X-ray crystal structure of [Zn(H_2DOTA)]and [Zn(DOTAM)].[80][81]

Conclusions

In this work the equilibrium properties of the Pb(II) complexes with DOTA, DOTAM, DOTP, DTPA and EDTA ligands and the kinetic inertness of $[Pb(DOTP)]^{6-}$ have been investigated by pH-potentiometry, UV-Vis spectrophotometry and Capillary Zone Electrophoresis methods. The structural properties of $[Pb(DOTA)]^{2-}$, $[Pb(DOTAM)]^{2+}$, $[Pb(DOTP)]^{6-}$, $[Pb(H_4DOTP)]^{2-}$ and $[Bi(DOTAM)]^{2+}$ complexes have been studied by multinuclear NMR spectroscopy in solution, and – in the case of $[Pb(H_4DOTP)]^{2-}$ – by single crystal X-ray diffraction studies in the solid state.

The stability constant of the $[Pb(DOTAM)]^{2+}$ complex was found to be $\log K_{Pb(DOTAM)}$ = 15.51 (25°C, 0.15 M $NaClO_4$), which is significantly lower than that estimated by Hancock *et al.* ($\log K_{Pb(DOTAM)} > 19$, 25°C, 0.1 M $NaNO_3$)[52] and similar to that of the closest analogue $[Hg(DOTAM)]^{2+}$ complex ($\log K_{Hg(DOTAM)}$ = 15.53, 25°C, 0.1 M $NaNO_3$).[75]

The selectivity constant (K_{sel}) values reveal that the DOTA ligand has the highest selectivity for Pb^{2+} ion, over the most important biological metal ions (Ca^{2+}, Zn^{2+}, Cu^{2+}) among DOTAM, DOTP, DTPA and EDTA ligands near physiological conditions (pH = 7.4, 25°C, 0.15 M $NaClO_4$). Surprisingly, the selectivity of DTPA for Pb^{2+} ion is very poor.

The transmetallation reactions of $[Pb(DOTP)]^{6-}$ with Cu^{2+} takes place by the rate determining spontaneous and acid-catalysed dissociation of the $[Pb(H_4DOTP)]^{2-}$ complex followed by the rapid reaction between the free DOTP ligand and the incoming Cu^{2+} ion. The acid catalysed dissociation of $[Pb(DOTP)]^{6-}$ is about 9000 times faster than that of $[Pb(DOTA)]^{2-}$, possibly due to the more probable H^+ transfer from the protonated phosphonate pendant arm to the macrocyclic nitrogen atom in the $[Pb(H_5DOTP)]^-$ intermediate.

In addition, the large difference between the kinetic inertness of the $[Pb(DOTP)]^{6-}$ and $[Pb(DOTA)]^{2-}$ complexes might be caused by the different rigidity of the Pb(II) complexes. Detailed NMR studies revealed that the interconversion processes between the enantiomers of the Pb(II) complex are characterized by nearly identical activation enthalpy values ($\Delta H^{\neq}$) and different activation entropy ($\Delta S^{\neq}$), Gibbs free energy ($\Delta G^{\neq}_{298}$) and exchange rate values (k_{ex}^{298}). The exchange between the enantiomers formed by the Pb(II) complexes are entropy-controlled processes, which can be explained by their different hydration spheres in the ground and transition states.

X-ray diffraction studies of the single crystals of $\{2(C(NH_2)_3)[Pb(H_4DOTP)]\}\cdot 7H_2O$ revealed that the Pb(II) ion is hepta-coordinated, with four sp^3 nitrogen atoms and three oxygen atoms of the phosphonate functionalities (one fully deprotonated and two monoprotonated), whereas the fully protonated phosphonate group is not bound to the Pb^{2+} ion. The Pb(II) ion is sandwiched between the plane formed by the four N atoms of the cyclen macrocycle and the trigonal plane defined by the three coordinated phosphonate O atoms. The coordination polyhedron around Pb(II) ion in $[Pb(H_4DOTP)]^{2-}$ can be described as a twisted square antiprism (TSAP), as it was found for the $[Pb(DOTA)]^{2-}$ and $[Pb(DOTAM)]^{2+}$ complexes.

Based on the detailed equilibrium, kinetic and structural studies of the Pb(II) complexes with DOTA, DOTAM, DOTP, DTPA and EDTA ligands, $[Pb(DOTA)]^{2-}$ exhibits optimal features for the development of $^{212}Pb/^{212}Bi$ based radiopharmaceuticals in TAT applications.

Experimental Section

Materials

The chemicals used for the experiments were of the highest analytical grade. The concentrations of the $Pb(ClO_4)_2$, $Bi(NO_3)_3$ and $Cu(ClO_4)_2$ stock solutions were determined by complexometric titration with standardized 0.2 M Na_2H_2EDTA solutions and xylenol orange indicator in the case of $Pb(ClO_4)_2$ and $Bi(NO_3)_3$, whereas for $Cu(ClO_4)_2$ murexide was used as indicator. The solution of bismuth nitrate was prepared by dissolving Bi_2O_3 in 65% nitric acid, followed by evaporation; the residue was then re-dissolved in a 0.1 M HNO_3 solution. The lead perchlorate solution was prepared by dissolving $PbCO_3$ in a 0.1 M $HClO_4$ solution. The acid excess of the $Bi(NO_3)_3$ and $Pb(ClO_4)_2$ solutions was determined by pH potentiometric titration in the presence of Na_2H_2EDTA excess. The concentration and protonation constants of the DOTAM, DOTA, DOTP, DTPA and EDTA ligands provided by Bracco Imaging S.p.A were calculated from the pH-potentiometric titration data obtained with standardized 0.2 M NaOH in the presence and absence of a large excess of $CaCl_2$, to detect the acid content of the stock solution.

Caution! Dry powder perchlorate samples are prone to explosion and should be handled with special care, especially in larger quantities.

Potentiometric titrations

All the equilibrium measurements were made at constant ionic strength maintained by 0.15 M $NaClO_4$ at 25°C. The protonation constant of DOTAM, DOTA, DOTP, DTPA and EDTA ligands, the stability and protonation constants of Pb(II) formed with EDTA ligand were determined by pH-potentiometric titration. The metal-to-ligand concentration ratios were 1:1 (the concentration of the ligand was generally 0.002 M). The protonation constants of the Pb(II) complexes with DOTA, DOTP and DTPA were determined using pH-potentiometry by titrating the pre-prepared complexes from pH = 1.7 to pH = 12.0 with 0.2 M NaOH. In calculating the equilibrium constants of the metal complexes, the best fitting of the NaOH - pH data pairs, were obtained by assuming the formation of ML, MHL, MH_2L, MH_3L, MH_4L and MH_5L complexes in the pH range 1.7 − 12.0.

pH-potentiometric titrations were performed using a *Metrohm 888 Titrando* automatic titration workstation equipped with a *Metrohm 6.0234.110* combined glass electrode. Measurements were carried out at 298 K in 6 mL samples under a nitrogen atmosphere with continuous magnetic stirring, maintaining a constant ionic strength of 0.15 M $NaClO_4$. The investigated pH range was 1.7 – 12.0.

The pH meter was calibrated with standard KH-phthalate (pH = 4.005) and borax (pH = 9.177) buffer solutions. The calculation of proton concentrations ($[H^+]$) from the measured pH values followed the method of Irving *et al*.[82] For this purpose, a 0.01 M $HClO_4$ solution was titrated with a standardized NaOH solution at 298 K in the presence of 0.15 M $NaClO_4$. The differences

(A) between the measured pH (pH_{read}) and calculated $-\log[H^+]$ values were used to correct the experimental pH readings obtained in the titrations (A=-0.02). A waiting time of 60 s between consecutive measurements was applied to ensure equilibrium.

In the equilibrium calculations, the stoichiometric ionic product of water (pK_w) was also taken into account for the determination of $[OH^-]$ under basic conditions. The $V_{NaOH} - pH_{read}$ data obtained in the 10.5 – 12.0 pH range from the $HClO_4$–NaOH titration were used for the calculation of the pK_w value (pK_w = 13.65). The protonation and stability constants were calculated using the PSEQUAD program.[83]

UV-Vis spectrophotometry measurements

The stability and protonation constants of the Pb(II)-complex with DTPA ligands were determined by spectrophotometry studying the formation of the PbL, Pb(HL), $Pb(H_2L)$ and $Pb(H_3L)$ species on the absorption band of Pb(II)-complex (λ=210-400 nm) in the pH range 1.7 – 7.0. The concentrations of $Pb(ClO_4)_2$ and DTPA ligand were 0.0002 M. The pH of the samples was adjusted with the addition of concentrate $HClO_4$ and NaOH solutions. Constant ionic strength was maintained by 0.15 M $NaClO_4$. The absorbance values of the samples were determined at 11 wavelengths (240, 244, 248, 252, 256, 260, 264, 268, 272, 276 and 280 nm). For the calculations of the stability and protonation constants of the $[Pb(DTPA)]^{3-}$, the molar absorptivities of Pb^{2+} and PbL, Pb(HL), $Pb(H_2L)$ and $Pb(H_3L)$ species were determined by recording the spectra of 1.0×10^{-4}, 1.5×10^{-4}, 2.0×10^{-4} and 2.5×10^{-4} M $Pb(ClO_4)_2$ and $[Pb(DTPA)]^{3-}$ solutions in the pH range of 2.0 – 7.5. The pH was adjusted by stepwise addition of concentrated NaOH or $HClO_4$ solutions. In the equilibrium calculations, the protonation constants of $[Pb(DTPA)]^{3-}$ obtained by pH-potentiometric studies at 298 K in 0.15 M $NaClO_4$ solution were considered. The spectrophotometric measurements were made with a *PerkinElmer Lambda 365* UV-Vis spectrophotometer at 25 °C, using 1.0 cm cells.

The stability constant of $[Pb(DOTA)]^{2-}$ complexes was determined with spectrophotometry by following the competition reactions between DOTA and DTPA ligands for Pb^{2+} ion at pH=1.70 on the absorption band of the Pb(II) complexes (λ = 210 − 400 nm). For these experiments, seven samples were prepared, containing [DOTA] = 1.0×10^{-3} M, [DTPA] = 0.0 – 10.0×10^{-3} M, $[Pb^{2+}] = 1.0\times10^{-3}$ M at pH = 1.7 and 25°C in 0.15 M $NaClO_4$. The samples were kept at 25 °C for about 1 month in order of the equilibrium to be attained (the time needed to reach the equilibria were determined by spectrophotometry). The absorbance values of the samples were determined at 10 wavelengths (235, 240, 245, 250, 255, 260, 265, 270, 275 and 280 nm). For the calculations of the stability constants of the $[Pb(DOTA)]^{2-}$, the molar absorptivities of PbL, Pb(HL), $Pb(H_2L)$ and $Pb(H_3L)$ species were determined by recording the spectra of 1.0×10^{-3}, 1.5×10^{-3}, 2.0×10^{-3} and 2.5×10^{-3} M $[Pb(DOTA)]^{2-}$ solutions in the pH range of 2.0 – 7.5. The pH was adjusted by stepwise addition of concentrated NaOH or $HClO_4$ solutions. In the equilibrium calculations, the protonation constants of $[Pb(DTPA)]^{3-}$ and $[Pb(DOTA)]^{2-}$ complexes obtained by pH-potentiometric studies at 298 K in 0.15 M $NaClO_4$ solution were considered. The spectrophotometric measurements were made with a *PerkinElmer Lambda 365* UV-Vis spectrophotometer at 25 °C, using 0.1 cm cells.

The stability constant of $[Pb(DOTP)]^{6-}$ complexes was determined with spectrophotometry by following the competition reactions between DOTP and EDTA ligands for Pb^{2+} ion at pH = 1.70 in the wavelength range 210 – 400 nm. For these experiments, nine samples were prepared, containing [DOTP] = 1.0×10^{-3} M, [EDTA] = 0.0 – 2.0×10^{-3} M, $[Pb^{2+}] = 1.0\times10^{-3}$ M at pH = 9.44 and 25°C in 0.15 M $NaClO_4$. The samples were kept at 25 °C for about 1 month in order of the equilibrium to be attained (the time needed to reach the equilibria were determined by spectrophotometry). The absorbance values of the samples were determined at 11 wavelengths (260, 264, 268, 272, 276, 280, 284, 288, 292, 296 and 300 nm) on the absorption band of $[Pb(DOTP)]^{6-}$. For the calculations of the stability constants of the $[Pb(DOTP)]^{6-}$, the molar absorptivities of PbL, Pb(HL), $Pb(H_2L)$ and $Pb(H_3L)$, $Pb(H_4L)$ species were determined by recording the spectra of 1.0×10^{-3}, 1.5×10^{-3}, 2.0×10^{-3} and 2.5×10^{-3} M $[Pb(DOTP)]^{6-}$ and $[Pb(EDTA)]^{2-}$ solutions in the pH range of 2.0 – 11.5. The pH was adjusted by stepwise addition of concentrated NaOH or $HClO_4$ solutions. In the equilibrium calculations, the protonation constants of $[Pb(DOTP)]^{6-}$, stability and protonation constants of $[Pb(EDTA)]^{2-}$ complexes obtained by pH-potentiometric studies at 298 K in 0.15 M $NaClO_4$ solution were considered. The spectrophotometric measurements were made with a *PerkinElmer Lambda 365* UV-Vis spectrophotometer at 25 °C, using 0.1 cm cells. The protonation and stability constants were calculated using the PSEQUAD program.[83]

Transmetallation reactions

The kinetic inertness of the Pb(II) complex with DOTP was characterized by the rates of the exchange reactions taking place between the $[Pb(H_4DOTP)]^{2-}$ and Cu^{2+}. The exchange reactions with Cu^{2+} were studied by spectrophotometry, following the formation of the Cu(II) complex at 330 nm with *PerkinElmer Lambda 365* UV-Vis spectrophotometer. The concentration of the $[Pb(H_4DOTP)]^{2-}$ complex was 1×10^{-4} M, while the concentration of the Cu^{2+} was 10 to 40 times higher, in order to guarantee pseudo-first-order conditions. The temperature was maintained at 25°C and the ionic strength of the solutions was kept constant, 0.15 M for $NaClO_4$. The exchange rates were studied in the pH range about 2.5 – 4.5. For keeping the pH values constant, monochloroacetic acid (pH range 2.5 – 3.1), 1,4-dimethylpiperazine (pH range 3.1 – 4.1) and *N*-methylpiperazine (pH range 4.1 – 4.5) buffers (0.01 M) were used. The pseudo-first-order rate constants (k_d) were calculated by fitting the absorbance–time data pairs to *Eq. 17.*

$$\mathbf{A_t = (A_0 - A_p)e^{-k_d t} + A_p} \qquad \textit{Eq. 17}$$

where A_t, A_0 and A_p are the absorbance values at time *t*, the start of the reaction and at equilibrium, respectively. Calculations were performed with the *Micromath Scientist* computer program (version 2.0, Salt Lake City, UT, USA).

Capillary Zone Electrophoresis (CZE)

The stability constant of $[Pb(DOTAM)]^{2+}$ was determined by Capillary Zone Electrophoresis (CZE) studying the competition reaction of DOTAM and EDTA ligands for Pb^{2+} at pH=8.5 and 25°C in 0.15 M $NaClO_4$ solution. For capillary electrophoresis *Hewlett-Packard HP^{3D}* capillary electrophoresis system were used. Separations were performed using bare fused-silica capillaries of 64 cm x 50 mm i.d. (*Agilent*). Before the first use of the capillary it was washed with 1.0 M NaOH (15 min), with 0.1 M NaOH (30 min) and with the buffer electrolyte (30 min). Prior to CE analysis all buffers were filtered through a 0.45 mm syringe filter and stored in refrigerator at +4ºC. In the CZE the sample solutions were introduced at the anodic end of the capillary in normal mode (50 mbar, 10 s). The effective length of the capillary was 56 cm. The capillary was preconditioned with the buffer electrolyte (100 mM sodium tetraborate, pH=9.2) for 3 minutes. The separation was performed at 25°C with the application of 30 kV voltage. After analysis, the postconditioning (0.1 M NaOH (3 min) and buffer (3 min)) was applied to remove all possibly adsorbed materials from the capillary. In all measurements, 5 mM DMSO as internal standard was applied to correct the migration time of components on the electropherogram. The detection was carried out by on-column DAD measurement at 200 nm. The electropherograms were recorded and processed by *ChemStation* computer program of B.04.02 version (*Agilent*).

For CZE studies, the 0.2 mM $[Pb(EDTA)]^{2-}$ complex in the presence of 0.8 mM EDTA excess was prepared, while the concentration of DOTAM was varied between 0.0 and 2.0 mM (9×2 mL samples). The pH was adjusted to pH=8.5 by stepwise addition of concentrated NaOH or $HClO_4$. Constant ionic strength was maintained by 0.15 M $NaClO_4$. The samples were kept at 25°C for two months in order to attain the equilibrium (the time needed to reach the equilibria was determined by capillary electrophoresis). For the equilibrium calculations, the molar integral values of the $[Pb(EDTA)]^{2-}$ and $[Pb(DOTAM)]^{2+}$ were used. The molar integral values of the $[Pb(EDTA)]^{2-}$ and $[Pb(DOTAM)]^{2+}$ were determined by recording the electropherograms of 1, 2 and 3 mM $[Pb(EDTA)]^{2-}$ and $[Pb(DOTAM)]^{2+}$ solutions at pH=7.4 and 25°C in the presence of 0.15 M $NaClO_4$ ionic strength. The molar integral value of $[Pb(DOTAM)]^{2+}$ and $[Pb(EDTA)]^{2-}$ was found to be $(1.18\pm0.02)\times10^6$ and $(3.81\pm0.04)\times10^6$ $mAu^{-1}M^{-1}$, respectively. The individual linear regression equations (response-concentration) for $[Pb(EDTA)]^{2-}$ and $[Pb(DOTAM)]^{2+}$ were determined according to three concentrations. The peak integrals were found to be linear (R^2>0.998) in a concentration range 1.0 – 3.0 mM.

NMR studies

Multinuclear NMR studies were performed with a *Bruker Avance III* spectrometer (9.4 T) equipped with a *Bruker Variable Temperature Unit* (BVT), Bruker Cooling Unit, and a 5 mm broadband direct (BBO) probe with *z*-gradient. For the NMR experiments 0.02 M solution of $[Pb(DOTA)]^{2-}$ and $[Pb(DOTAM)]^{2+}$ complexes were prepared at pD=7.5 in D_2O. 1D and 2D NMR spectra of 0.02 M $[Pb(H_4DOTP)]^{2-}$ and $[Pb(DOTP)]^{6-}$ solutions were acquired at pD = 4.6 and 10.95, respectively. For the NMR studies of $[Bi(DOTAM)]^{3+}$, equimolar $Bi(NO_3)_3$ and DOTAM ligand were mixed at pH=3.5 in a diluted aqueous solution ([BiL] ≈ 0.1 mM) in order

to avoid the formation of the $[Bi_6(OH)_{12}]^{6+}$. After the completion of the complex formation, the pH of the solution was set to pH= 4.5 with the diluted NaOH solution. The water excess $[Bi(DOTAM)]^{3+}$ solution was removed by rotary vacuum evaporator. 1D and 2D NMR spectra of 0.04 M $[Bi(DOTAM)]^{2+}$ solution were measured in H_2O (using a D_2O-filled capillary for field locking).

Two-dimensional ^1H–^1H COSY, ^1H–^1H NOESY, ^1H–^{13}C HSQC and ^1H–^{13}C HMBC correlation spectra were collected by using standard Bruker pulse sequences. Line-shape analyses were performed with the DNMR module of the Bruker TopSpin software package. Chemical shifts, spin–spin coupling constants, signal intensities, and Lorentzian broadening (LB) parameters obtained under exchange-free conditions were fixed as input parameters during spectral fitting. The similarity between the experimental and calculated ^{13}C NMR spectra obtained at different temperatures consistently exceeded 95%.

X-ray diffraction studies of $[Pb(H_4DOTP)]^{2-}$[82–86]

Single crystals of formula $\{2(C(NH_2)_3)[Pb(H_4DOTP)]\}\cdot 7H_2O$ suitable for X-ray diffraction studies, were grown by the slow diffusion of ethanol and diethyl ether mixture to aqueous solution of $[Pb(H_4DOTP)]^{2-}$ prepared by mixing equimolar $PbCO_3$ and H_8DOTP ligand. In order to obtain the tetraprotonated $[Pb(H_4DOTP)]^{2-}$ complex, the pH of aqueous solution was adjusted to 4.2 with guanidine-carbonate. The mixture was heated to remove dissolved CO_2 and subsequently filtered through a 0.20 μm nylon syringe filter. The filtrate was concentrated to dryness using a rotary evaporator, and the residue was redissolved in 700 μL of deionized water. Solution was transferred into an NMR tube and carefully layered with ethanol and diethyl ether. The sample for crystallization was then stored at 4°C in a refrigerator.

The samples were given either as crystalline material or powder. If it was necessary after crystallization a crystal well-looking in polarized light, was fixed on a Hampton Research loop using high viscosity oil (Figure S12). Data were collected at 150 K or room temperature using a Bruker-D8 Venture diffractometer equipped with INCOATEC IμS 3.0 dual (Cu and Mo) sealed tube microsources and Photon 200 Charge-integrating Pixel Array detector. Several datasets were collected and the most reliable is used in this report for each compound. Data collection and integration was performed using the APEX4 software.[84] Data reduction and multi-scan absorption correction was applied[85] and numerical absorption correction did not improve the refinement. The structures could be solved using direct methods and refined on F^2 using SHELXL program[84] incorporated into the APEX4 suite. The statistics of the reflections as well as systematic absences indicated and supported the suggested space group. Finally, the PLUTON crystallographic software did not report any missed symmetry elements. Refinement was performed anisotropicaly for all non-hydrogen atoms. Hydrogens were placed into geometric positions except O-H or N-H protons which usually could be found at the electron density map, but the respective O-H or N-H distances were usually constrained. Tables were extracted from the edited CIF file using publCIF.[87] The PLATON program[88] was used for crystallographic calculations. The structures were not checked against crystallographic database (Cambridge Structural Database) or any other public checking service. However,

structural data are reasonable according to printed compilation[87] of bond distance data and stand-alone checking features of the PLATON[88] crystallographic software. The structure of $[Pb(H_4DOTP)]^{2-}$ with selected bond lengths are shown in Figures S13 and S14. Details of the structure determination are summarized in Table S1. Fractional atomic coordinates and isotropic or equivalent isotropic displacement parameters, atomic displacement parameters, selected bond distances and angles and hydrogen-bond geometry in $\{2(C(NH_2)_3)[Pb(H_4DOTP)]\}\cdot 7H_2O$ single crystal are compiled in Tables S2 – S5.

References

(1) Eychenne, R.; Chérel, M.; Haddad, F.; Guérard. F; Gestin, J. F. Overview of the Most Promising Radionuclides for Targeted Alpha Therapy: The "Hopeful Eight". *Pharmaceutics.* **2021**, *13(6):906.*

(2) Baes, C. F.; Mesmer, R. E. *The Hydrolysis of Cations*; Wiley: New York, **1976**.

(3) Persson, I., K. Lyczko, D. Lundberg, L. Eriksson, and A. Płaczek. Coordination Chemistry Study of Hydrated and Solvated Lead(II) Ions in Solution and Solid State. *Inorg. Chem.* **2011**, *50(3):*1058−1072.

(4) Shimoni-Livny, L.; Glusker, J. P.; Bock, C. W. Lone Pair Functionality in Divalent Lead Compounds. *Inorg. Chem.* **1998**, *37(8)*, 1853−1867.

(5) Catalano, J.; Murphy, A.; Yao, Y.; Yap, G. P.; Zumbulyadis, N.; Centeno, S. A.; Dybowski, C. Coordination Geometry of Lead Carboxylates - Spectroscopic and Crystallographic Evidence. **2015**, *44(5)*, 2340-2347.

(6) Kokov, K. V.; Egorova, B. V.; German, M. N.; Klabukov, I. D.; Krasheninnikov, M. E.; Larkin-Kondrov, A. A.; Makoveeva, K. A.; Ovchinnikov, M. V.; Sidorova, M. V.; Chuvilin, D. Y. ^{212}Pb: Production Approaches and Targeted Therapy Applications. *Pharmaceutics* **2022**, *14(1):189.*

(7) McNeil, B. L.; Mastroianni, S. A.; McNeil, S. W.; Zeisler, S.; Kumlin, J.; Sogol Borjian; McDonagh, A. W.; Cross, M.; Schaffer, P.; Ramogida, C. F. Optimized Production, Purification, and Radiolabeling of the ^{203}Pb/^{212}Pb Theranostic Pair for Nuclear Medicine. *Sci. Rep.* **2023**, *13 (1).*

(8) Hassfjell, S. P.; Hoff, P. A Generator for Production of ^{212}Pb and ^{212}Bi. *Appl. Radiat. Isot.* **1994**, *45* (10), 1021–1025.

(9) Simonson, R. B.; Ultee, M. E.; Hauler, J. A.; Alvarez, V. L. Radioimmunotherapy of Peritoneal Human Colon Cancer Xenografts with Site-Specifically Modified ^{212}Bi-Labeled Antibody. *Cancer Res.* **1990**, *50* (3 Suppl), 985s–988s.

(10) Hartmann, F.; Horak, E. M.; Garmestani, K.; Wu, C.; Brechbiel, M. W.; Kozak, R. W.; Tso, J.; Kosteiny, S. A.; Gansow, O. A.; Nelson, D. L. Radioimmunotherapy of Nude Mice Bearing a Human Interleukin 2 Receptor Alpha-Expressing Lymphoma Utilizing the Alpha-Emitting Radionuclide-Conjugated Monoclonal Antibody ^{212}Bi-Anti-Tac. *Cancer Res.* **1994**, *54* (16), 4362–4370.

(11) Despotopulos, J. D.; Kmak, K. N.; Moody, K. J.; Shaughnessy, D. A. Development of a ^{212}Pb and ^{212}Bi Generator for Homolog Studies of Flerovium and Moscovium. **2018**, *317(1),* 473-477.

(12) Grieve, M. L.; Paterson, B. M.. The Evolving Coordination Chemistry of Radiometals for Targeted Alpha Therapy. *Aust. J. Chem.* **2021**, *75(2)*, 65−88.

(13) Schwartz, J.; Jaggi, J. S.; O'Donoghue, J. A.; Ruan, S.; McDevitt, M.; Larson, S. M.; Scheinberg, D. A.; Humm, J. L. Renal Uptake of Bismuth-213 and Its Contribution to Kidney Radiation Dose Following Administration of Actinium-225-Labeled Antibody. *Phys. Med. Biol.* **2011**, *56(3)*, 721−733.

(14) Corpetti, M.; Müller, C.; Beltran, H.; de Bono, J.; Theurillat, J. P. Prostate-Specific Membrane Antigen–Targeted Therapies for Prostate Cancer: Towards Improving Therapeutic Outcomes. *Eur. Urol.* **2023**, *85(3)*, 193−204.

(15) Li, J.; Huang, T.; Hua, J.; Wang, Q.; Su, Y.; Chen, P.; Bidlingmaier, S.; Li, A.; Xie, Z.; Bidkar, A. P.; Shen, S.; Shi, W.; Seo, Y.; Flavell, R. R.; Gioeli, D.; Dreicer, R.; Li, H.; Liu, B.; He, J. CD46 Targeted ^{212}Pb Alpha Particle Radioimmunotherapy for Prostate Cancer Treatment. *J. Exp. Clin. Cancer Res.* **2023**, *42 (1).*

(16) NCT05636618. ClinicalTrials.Gov [Online]; National Library of Medicine (US): Bethesda, MD, **2023**. https://Clinicaltrials.Gov/Study/NCT05636618.

(17) Yong, K.; Brechbiel, M. W. Towards Translation of ^{212}Pb as a Clinical Therapeutic; Getting the Lead In! *Dalton Trans.* **2011**, *40(23)*, 6068−6076.

(18) Durand-Panteix, S.; Monteil, J.; Sage, M.; Garot, A.; Clavel, M.; Saidi, A.; Torgue, J.; Cogne, M.; Quelven, I. Preclinical Study of ^{212}Pb Alpha-Radioimmunotherapy Targeting CD20 in Non-Hodgkin Lymphoma. *Br. J. Cancer.* **2021**, *125(12),* 1657−1665.

(19) Jurcic, J. G.; Larson, S. M.; Sgouros, G.; McDevitt, M. R.; Finn, R. D.; Divgi, C. R.; Ballangrud, A. M.; Hamacher, K. A.; Ma, D.; Humm, J. L.; Brechbiel, M. W.; Molinet, R.; Scheinberg, D. A. Targeted Alpha Particle Immunotherapy for Myeloid Leukemia. *Blood* **2002**, *100* (4), 1233–1239.

(20) Rosenblat, T. L.; McDevitt, M. R.; Mulford, D. A.; Pandit-Taskar, N.; Divgi, C. R.; Panageas, K. S.; Heaney, M. L.; Chanel, S.; Morgenstern, A.; Sgouros, G.; Larson, S. M.; Scheinberg, D. A.; Jurcic, J. G. Sequential Cytarabine and α-Particle Immunotherapy with Bismuth-213–Lintuzumab (HuM195) for Acute Myeloid Leukemia. *Clin. Cancer Res.* **2010**, *16* (21), 5303–5311.

(21) Allen, B. J.; Singla, A. A.; Rizvi, S. M. A.; Graham, P.; Bruchertseifer, F.; Apostolidis, C.; Morgenstern, A. Analysis of Patient Survival in a Phase I Trial of Systemic Targeted α-Therapy for Metastatic Melanoma. *Immunotherapy* **2011**, *3* (9), 1041–1050.

(22) Autenrieth, M. E.; Seidl, C.; Bruchertseifer, F.; Horn, T.; Kurtz, F.; Feuerecker, B.; D'Alessandria, C.; Pfob, C.; Nekolla, S.; Apostolidis, C.; Mirzadeh, S.; Gschwend, J. E.; Schwaiger, M.; Scheidhauer, K.; Morgenstern, A. Treatment of Carcinoma in Situ of the Urinary Bladder with an Alpha-Emitter Immunoconjugate Targeting the Epidermal Growth Factor Receptor: A Pilot Study. *Eur. J. Nucl. Med. Mol. Imaging* **2018**, *45* (8), 1364–1371.

(23) Ahenkorah, S.; Cassells, I.; Deroose, C. M.; Cardinaels, T.; Burgoyne, A. R.; Bormans, G.; Ooms, M.; Cleeren, F. Bismuth-213 for Targeted Radionuclide Therapy: From Atom to Bedside. *Pharmaceutics* **2021**, *13* (5), 599.

(24) Kellerbauer, A.; Bruchertseifer, F.; Malmbeck, R.; Morgenstern, A. Targeted α Therapy with ^{213}Bi and ^{225}Ac. *J. Phys. Conf. Ser.* **2020**, *1643* (1), 012205.

(25) De Swart, J.; Chan, H. S.; Goorden, M. C.; Morgenstern, A.; Bruchertseifer, F.; Beekman, F. J.; De Jong, M.; Konijnenberg, M. W. Utilizing High-Energy γ-Photons for High-Resolution ^{213}Bi SPECT in Mice. *J. Nucl. Med.* **2016**, *57* (3), 486–492.

(26) Kratochwil, C.; Giesel, F. L.; Bruchertseifer, F.; Mier, W.; Apostolidis, C.; Boll, R.; Murphy, K.; Haberkorn, U.; Morgenstern, A. ^{213}Bi-DOTATOC Receptor-Targeted Alpha-Radionuclide Therapy Induces Remission in Neuroendocrine Tumours Refractory to Beta Radiation: A First-in-Human Experience. *Eur. J. Nucl. Med. Mol. Imaging* **2014**, *41* (11), 2106–2119.

(27) Horváth, D.; Travagin, F.; Guidolin, N.; Buonsanti, F.; Tircsó, G.; Tóth, I.; Bruchertseifer, F.; Morgenstern, A.; Notni, J.; Giovenzana, G. B.; Baranyai, Z. Towards ^{213}Bi Alpha-Therapeutics and Beyond: Unravelling the Foundations of Efficient Bi(III) Complexation by DOTP. *Inorg. Chem.* **2021**, *8(16)*, 3893−3904.

(28) Hassfjell, S. P.; Bruland, Ø. S.; Hoff, P. 212Bi-DOTMP: An Alpha Particle Emitting Bone-Seeking Agent for Targeted Radiotherapy. *Nucl. Med. Biol.* **1997**, *24* (3), 231–237.

(29) Królicki, L.; Kunikowska, J.; Bruchertseifer, F.; Koziara, H.; Królicki, B.; Jakuciński, M.; Pawlak, D.; Rola, R.; Morgenstern, A.; Rosiak, E.; Merlo, A. ^{225}Ac- and ^{213}Bi-Substance P Analogues for Glioma Therapy. *Semin. Nucl. Med.* **2020**, *50* (2), 141–151.

(30) Kratochwil, C.; Giesel, F. L.; Bruchertseifer, F.; Mier, W.; Apostolidis, C.; Boll, R.; Murphy, K.; Haberkorn, U.; Morgenstern, A. ^{213}Bi-DOTATOC Receptor-Targeted Alpha-Radionuclide Therapy Induces Remission in Neuroendocrine Tumours Refractory to Beta Radiation: A First-in-Human Experience. *Eur. J. Nucl. Med. Mol. Imaging* **2014**, *41* (11), 2106–2119.

(31) Sathekge, M.; Knoesen, O.; Meckel, M.; Modiselle, M.; Vorster, M.; Marx, S. ^{213}Bi-PSMA-617 Targeted Alpha-Radionuclide Therapy in Metastatic Castration-Resistant Prostate Cancer. *Eur. J. Nucl. Med. Mol. Imaging* **2017**, *44* (6), 1099–1100.

(32) Kratochwil, C.; Haberkorn, U.; Giesel, F. L. ^{225}Ac-PSMA-617 for Therapy of Prostate Cancer. *Semin. Nucl. Med.* **2020**, *50* (2), 133–140.

(33) Aime, S.; Botta, M.; Fasano, M.; Marques, M.; Carlos; Pubanz, D.; Merbach, A. E. Conformational and Coordination Equilibria on DOTA Complexes of Lanthanide Metal Ions in Aqueous Solution Studied by ^{1}H NMR Spectroscopy. *Inorg. Chem.* **1997**, *36 (10)*, 2059-2068.

(34) Cuenot, F.; Meyer, M.; Espinosa, E.; Bucaille, A.; Burgat, R.; Guilard, R.; Marichal-Westrich, C. New Insights into the Complexation of Lead(II) by 1,4,7,10-Tetrakis(Carbamoylmethyl)-1,4,7,10-Tetraazacyclododecane (DOTAM): Structural, Thermodynamic, and Kinetic Studies. *Eur. J. Inorg. Chem.* **2007**, *2008(2)*.

(35) Blahut, J.; Hermann, P.; Tošner, Z.; Platas-Iglesias, C. A Combined NMR and DFT Study of Conformational Dynamics in Lanthanide Complexes of Macrocyclic DOTA-like Ligands. *Phys. Chem. Chem. Phys.* **2017**, *19(39)*, 26662−26671.

(36) Benetollo, F.; Bombieri, G.; Calabi, L.; Aime, S.; Botta, M. Structural Variations across the Lanthanide Series of Macrocyclic DOTA Complexes: Insights into the Design of Contrast Agents for Magnetic Resonance Imaging. *Inorg. Chem.* **2003**, *42* (1), 148–157.

(37) Csajbók, É.; Baranyai, Z.; Bányai, I.; Brucher, E.; Király, R.; Muller-Fahrnow, A.; Platzek, J.; Raduchel, B.; Schäfer, M. Equilibrium, ^{1}H and ^{13}C NMR Spectroscopy, and X-Ray Diffraction Studies on the Complexes Bi(DOTA)- and Bi(DO3A-Bu). *Inorg. Chem.* **2003**, *42 (7)*, 2342−2349.

(38) Nugent, J. W.; Lee, H.-S.; Reibenspies, J. H.; Hancock, R. D. Spectroscopic, Structural, and Thermodynamic Aspects of the Stereochemically Active Lone Pair on Lead(II): Structure of the Lead(II) Dota Complex. *Polyhedron* **2015**, *91*, 120−127.

(39)Gourlaouen, C.; Piquemal, J.-P. On the Quantum Chemical Nature of Lead(II) "Lone Pair." *Molecules* **2021**, *27(1)*, 27.

(40) Li, M.; Baumhover, N. J.; Liu, D.; Preclinical Evaluation of a Lead Specific Chelator (PSC) Conjugated to Radiopeptides for ^{203}Pb and ^{212}Pb-Based Theranostics. *Pharmaceutics* **2023**, *15(2)*, 414.

(41) McNeil, B. L.; Robertson, A. K. H.; Fu, W.; Yang, H.; Hoehr, C.; Ramogida, C. F.; Schaffer, P. Production, Purification, and Radiolabeling of the $^{203}Pb/^{212}Pb$ Theranostic Pair. *EJNMMI Radiopharmacy and Chemistry* **2021**, *6(1).*

(42) Camera, L., Kinuya, S., Garmestani, K., Wu, C., Brechbiel, M. W., Pai, L. H., McMurry, T. J., Gansow, O. A., Pastan, I., & Paik, C. H. Evaluation of the Serum Stability and *in Vivo* Biodistribution of CHX-DTPA and Other Ligands for Yttrium Labeling of Monoclonal Antibodies. *J. Nucl. Med.* **1994**, *35(5)*, 882−889.

(43) C. F. G. C. Geraldes; Sherry, A. D.; Cacheris, W. P. Synthesis, Protonation Sequence, and NMR Studies of Polyazamacrocyclic Methylenephosphonates. *Inorg. Chem.* **1989**, *28 (17)*, 3336−3341.

(44) Wurzer, A.; Adrienn Vágner; Horvath, D. G.; Flóra Fellegi; Wester, H.; Kálmán, F. K.; Johannes Notni. Synthesis of Symmetrical Tetrameric Conjugates of the Radiolanthanide Chelator DOTPI for Application in Endoradiotherapy by Means of Click Chemistry. *Front. Chem.* **2018**, *6*.

(45) Geraldes, C. F. G. C.; Urbano, A. M.; Alpoim, M. C.; Sherry, A. D.; Kuan, K.-T.; Rajagopalan, R.; Maton, F.; Muller, R. N. Preparation, Physico-Chemical Characterization, and Relaxometry Studies of Various Gadolinium(III)-DTPA-Bis(Amide) Derivatives as Potential Magnetic Resonance Contrast Agents. *Magn. Reson. Imaging* **1995**, *13* (3), 401–420.

(46) Imura, H.; Choppin, G. R.; Cacheris, W. P.; De Learie, L. A.; Dunn, T. J.; White, D. H. Thermodynamics and NMR Studies of DTPA-Bis(Methoxyethylamide) and Its Derivatives. Protonation and Complexation with Ln(III). *Inorg. Chim. Acta* **1997**, *258* (2), 227–236.

(47) Pálinkás Z.; Baranyai, Z.; Ernő Brücher; Béla Rózsa. Kinetics of the Exchange Reactions between $Gd(DTPA)^{2-}$, $Gd(BOPTA)^{2-}$, and Gd(DTPA-BMA) Complexes, Used as MRI Contrast Agents, and the Triethylenetetraamine-Hexaacetate Ligand. *Inorg. Chem.* **2011**, *50(8)*, 3471–3478.

(48) Baranyai, Z.; Gyula Tircsó; Rösch, F. The Use of the Macrocyclic Chelator DOTA in Radiochemical Separations. *Eur. J. Inorg. Chem. 2020(1)*, 36−56.

(49) Bianchi, A.; Calabi, L.; Giorgi, C.; Losi, P.; Mariani, P.; Paoli, P.; Rossi, P.; Valtancoli, B.; Virtuani, M. Thermodynamic and Structural Properties of Gd3+ Complexes with Functionalized Macrocyclic Ligands Based upon 1,4,7,10-Tetraazacyclododecane. *J. Chem. Soc. Dalton Trans.* **2000**, No. 5, 697–705.

(50) Delgado, R.; Da Silva, J. J. R. F. Metal Complexes of Cyclic Tetra-Azatetra-Acetic Acids. *Talanta* **1982**, *29* (10), 815–822.

(51) Clarke, E. T.; Martell, A. E. Stabilities of Trivalent Metal Ion Complexes of the Tetraacetate Derivatives of 12-, 13- and 14-Membered Tetraazamacrocycles. *Inorg. Chim. Acta* **1991**, *190(1)*, 37−46.

(52) Maumela H.; Hancock, R. D.; Carlton, L.; Reibenspies, J. H.; Wainwright, K. P. The Amide Oxygen as a Donor Group. Metal Ion Complexing Properties of Tetra-N-Acetamide Substituted Cyclen: A Crystallographic, NMR, Molecular Mechanics, and Thermodynamic Study. *J. Am. Chem. Soc.* **1995**, *117(25)*, 6698−6707.

(53) Grieve, M. L.; Davey, R. W. J. P.; Bernhardt, P. V.; Forsyth, C. M.; Paterson, B. M. Rapid and stable complexation of the α-generators bismuth-212 and lead-212 with a tetraazamacrocyclic chelator bearing thiosemicarbazone pendant arms. *Inorg. Chem. Front.* **2024***, 11(21),* 7307−7323.

(54) Letkeman, P.; Westmore, J. B. Metal–Amino Polycarboxylic Acid Complexes. IV. A Polarographic Study of Lead (II) Complexes with Diethylenetriaminepentaacetic Acid in Aqueous Solution. *Can. J. Chem.* **1972**, *50(23)*, 3821−3831.

(55) Brechbiel, M. W.; Gansow, O. A.; Pippin, C. G.; Rogers, R. D.; Planalp, R. P. Preparation of the Novel Chelating Agent *N* -(2-Aminoethyl)- *Trans*-1,2-Diaminocyclohexane-*N,N',N''*-Pentaacetic Acid (H_5 CyDTPA), a Preorganized Analogue of Diethylenetriaminepentaacetic Acid (H_5 DTPA), and the Structures of Bi^{III} $(CyDTPA)^{2-}$ and Bi^{III} (H_2 DTPA) Complexes. *Inorg. Chem.* **1996**, *35* (21), 6343–6348.

(56) Tosato, M.; Lazzari, L.; Marco, V. D. Revisiting Lead(II)-1,4,7,10-Tetraazacyclododecane-1,4,7,10-Tetraacetic Acid Coordination Chemistry in Aqueous Solutions: Evidence of an Underestimated Thermodynamic Stability. *ACS Omega* **2022**, *7(18)*, 15596−15602.

(57) Pippin, C. G.; McMurry, T. J.; Brechbiel, M. W.; McDonald, M.; Lambrecht, R.; Milenic, D.; Roselli, M.; Colcher, D.; Gansow, O. A. Lead(II) Complexes of 1,4,7,10-Tetraazacyclododecane-N,N′,N″,N‴-Tetraacetate: Solution Chemistry and Application to Tumor Localization with ^{203}Pb Labeled Monoclonal Antibodies. *Inorganica Chim. Acta* **1995**, *239* (1–2), 43–51.

(58) Hefter, G. T. Stability Constants for the Lead(II)-Halide Systems. *Polyhedron* **1990**, *9* (19), 2429–2432.

(59) Tosato, M.; Randhawa, P.; Lazzari, L.; McNeil, B. L.; Tiezza, M. D.; Zanoni, G.; Fabrizio Mancin; Orian, L.; Ramogida, C. F.; Marco, V. D. Tuning the Softness of the Pendant Arms and the Polyazamacrocyclic Backbone to Chelate the $^{203}Pb/^{212}Pb$ Theranostic Pair. *Inorg. Chem.* **2024**, *63(4)*, 1745−1758.

(60) Yoshida, S.; Yoshida, K.; Hamada, Y.; Tsuruoka, T.; Usui, K. Development of Detection System for Lead Ions in Mixture Solutions Using UV-Vis Measurements with Peptide Immobilized Microbeads. *Sci. Rep.* **2025**, *15(1)*.

(61) Oyama, N.; Horie, M.; Matsuda, H.; Ohtaki, H. Potentiomeric and Polarographic Studies on Complex Formation of Cadmium(II) Ion with Ethylenediaminemonoacetic Acid. *Bull. Chem. Soc. Jpn.* **1977**, *50* (8), 1945–1949.

(62) Stavila, V.; Davidovich, R. L.; Gulea, A.; Whitmire, K. H. Bismuth(III) Complexes with Aminopolycarboxylate and Polyaminopolycarboxylate Ligands: Chemistry and Structure. *Coord. Chem. Rev.* **2006**, *250 (21-22)*, 2782−2810.

(63) Kleja, D. B.; Gustafsson, J. P.; Kessler, V.; Persson, I. Bismuth(III) Forms Exceptionally Strong Complexes with Natural Organic Matter. *Environ. Sci. Technol.* **2022**, *56 (5)*, 3076−3084.

(64) Delgado, R.; Costa, J.; Guerra, K. P.; Lima, L. M. P. Lanthanide Complexes of Macrocyclic Derivatives Useful for Medical Applications. *Pure Appl. Chem.* **2005**, *77(3)*, 569−579.

(65) Baranyai Z.. *Nonpublished Results (0.15 M NaCl, 25°C)*.

(66) Delgado, R.; Siegfried, L. C.; Kaden, T. A. Metal Complexes with Macrocyclic Ligands. Part XXXI. Protonation Studies and Complexation Properties of Tetraazamacrocyclic Methylenephosphonates with Earth-alkali Ions. *Helv. Chim. Acta* **1990**, *73* (1), 140–148.

(67) Baranyai, Z.; Brücher, E.; Uggeri, F.; Maiocchi, A.; Tóth, I.; Andrási, M.; Gáspár, A.; Zékány, L.; Aime, S. The Role of Equilibrium and Kinetic Properties in the Dissociation of Gd[DTPA-bis(Methylamide)] (Omniscan) at near to Physiological Conditions. *Chem. – Eur. J.* **2015**, *21* (12), 4789–4799.

(68) May, P. M.; Linder, P. W.; Williams, D. R. Computer Simulation of Metal-Ion Equilibria in Biofluids: Models for the Low-Molecular-Weight Complex Distribution of Calcium(II), Magnesium(II), Manganese(II), Iron(III), Copper(II), Zinc(II), and Lead(II) Ions in Human Blood Plasma. *J. Chem. Soc. Dalton Trans.* **1977**, No. 6, 588.

(69) Powell, K. J.; Brown, P. L.; Byrne, R. H.; Gajda, T.; Hefter, G.; Leuz, A.-K.; Sjöberg, S.; Wanner, H. Chemical Speciation of Environmentally Significant Metals with Inorganic Ligands. Part 3: The $Pb^{2+} + OH^-$, Cl^-, CO_3^{2-}, SO_4^{2-}, and PO_4^{3-} Systems (IUPAC Technical Report). *Pure Appl. Chem.* **2009**, *81* (12), 2425–2476.

(70) Cacheris, W. P.; Quay, S. C.; Rocklage, S. M. The Relationship between Thermodynamics and the Toxicity of Gadolinium Complexes. *Magn. Reson. Imaging* **1990**, *8* (4), 467–481.

(71) Mirzadeh, S.; Kumar, K.; Gansow, O. A. The Chemical Fate of ^{212}Bi-DOTA Formed by β^- Decay of ^{212}Pb(DOTA)$^{2-}$. *Radiochim. Acta* **1993**, *60* (1), 1–10.

(72) Desreux, J. F. Nuclear Magnetic Resonance Spectroscopy of Lanthanide Complexes with a Tetraacetic Tetraaza Macrocycle. Unusual Conformation Properties. *Inorg. Chem.* **1980**, *19(5)*, 1319–1324.

(73) Obuch, J.; Císařová, I.; Brus, J.; Hermann, P. DOTA Complexes with Divalent Zinc, Cadmium and Mercury: X-Ray and Solid-State NMR Studies and Solution Isomerism. *Dalton Trans.* **2025**.

(74) Aime, S.; Botta, M.; Ermondi, G. NMR Study of Solution Structures and Dynamics of Lanthanide(III) Complexes of DOTA. *Inorg. Chem. 31(21)*, 4291-4299.

(75) Hancock, R. D.; Reibenspies, J. H.; Maumela, H. Structural Effects of the Lone Pair on Lead(II), and Parallels with the Coordination Geometry of Mercury(II). Does the Lone Pair on Lead(II) Form H-Bonds? Structures of the Lead(II) and Mercury(II) Complexes of the Pendant-Donor Macrocycle DOTAM (1,4,7,10-Tetrakis(Carbamoylmethyl)-1,4,7,10-Tetraazacyclododecane). *Inorg. Chem.* **2004**, *43* (9), 2981–2987.

(76) Contreras, R. H.; R. Suardíaz; C. Pérez; R. Crespo-Otero; J. San Fabián; de, G. Karplus Equation for 3JHH Spin−Spin Couplings with Unusual ^{3}J(180°) < ^{3}J(0°) Relationship. *J. Chem. Theory Comput.* **2008**, *4(9)*, 14941500.

(77) Hassfjell, S.; Kongshaug, K. O.; Rømming, C. Synthesis, Crystal Structure and Chemical Stability of Bismuth(III) Complexed with 1,4,7,10-Tetraazacyclododecane-1,4,7,10-Tetramethylene Phosphonic Acid (H_8DOTMP). *Dalton Trans.* **2003**, No. 7, 1433–1437.

(78) Smith S. V. Molecular Imaging with Copper-64. *J. Inorg. Biochem.* **2008**, *98*, 1874–1901.

(79) Desreux, J. F.; Merciny, E.; Loncin, M. F. Copper(II) Complexes of Cyclen Derivatives: Structure and Reactivity. *Inorg. Chem.* **1981**, *20*, 987–991.

(80) Viola-Villegas, N.; Doyle, R. P. The Coordination Chemistry of 1,4,7,10-Tetraazacyclododecane-N,N′,N″,N‴-Tetraacetic Acid (H_4DOTA): Structural Overview and Analyses on Structure–Stability Relationships. *Coord. Chem. Rev.* **2009**, *253(13-14)*, 1906–1925.

(81) Nagata, M. K. C. T.; Brauchle, P. S.; Wang, S.; Briggs, S. K.; Hong, Y. S.; Laorenza, D. W.; Lee, A. G.; Westmoreland, T. D. Correlation of Solid State and Solution Coordination Numbers with Infrared Spectroscopy in Five-, Six-, and Eight-Coordinate Transition Metal Complexes of DOTAM. *Polyhedron* **2016**, *114*, 299–305. (81)

(82) Irving, H. M.; Miles, M. G.; Pettit, L. D. A Study of Some Problems in Determining the Stoicheiometric Proton Dissociation Constants of Complexes by Potentiometric Titrations Using a Glass Electrode. *Analytica Chimica Acta* **1967**, *38*, 475−488.

(83) Zekany, L.; Nagypal, I. PSEQUAD. Computational Methods for the Determination of Formation Constants. *Modern Inorganic Chemistry*; Springer US: Boston, MA, **1985**; pp. 291−353.

(84) *APEX4 V2017.3-0, Bruker AXS.*

(85) *SAINT V8.38A, Bruker AXS Inc., 2017. SADABS2016/2 - Bruker AXS Area Detector Scaling and Absorption Correction*.

(86) *SHELXT 2014/5 (Sheldrick, 2014); Program(s) Used to Refine Structure: SHELXL2016/6 (Sheldrick, 2016).*

(87) Allen, F. H.; Watson, D. G.; Brammer, L.; Orpen, A. G.; Taylor, R. Typical Interatomic Distances: Organic Compounds. In *International Tables for Crystallography*; Prince, E., Ed.; Fuess, H., Hahn, Th., Wondratschek, H., Müller, U., Shmueli, U., Prince, E., Authier, A., Kopský, V., Litvin, D. B., Rossmann, M. G., Arnold, E., Hall, S., McMahon, B., Series Eds.; International Tables for Crystallography; International Union of Crystallography: Chester, England, **2006**; Vol. C, pp 790–811.

(88) Spek, A. L. *PLATON* SQUEEZE: A Tool for the Calculation of the Disordered Solvent Contribution to the Calculated Structure Factors. *Acta Crystallogr. Sect. C Struct. Chem.* **2015**, *71* (1), 9–18.

Supporting Information

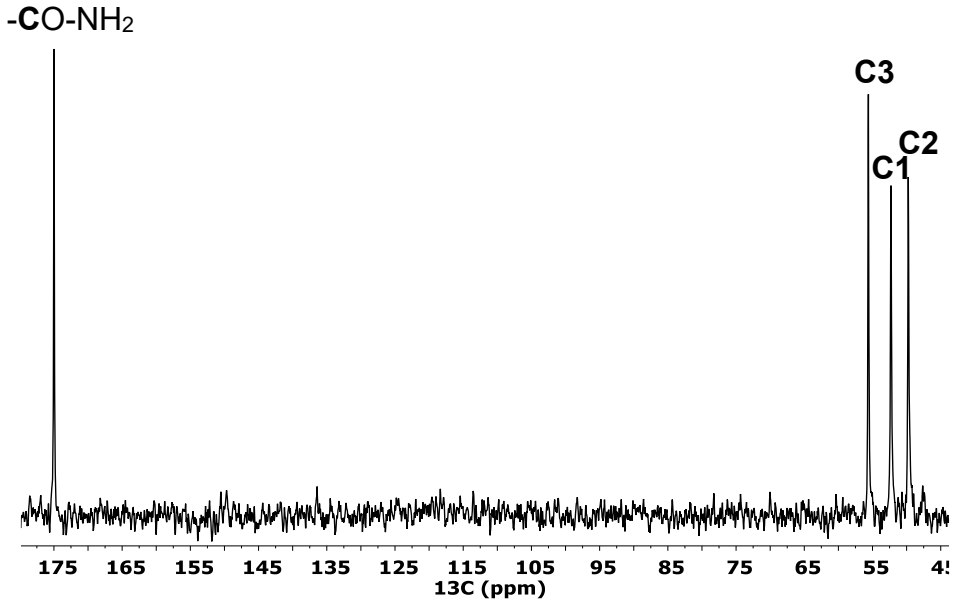

Figure S1. ^{13}C NMR spectrum of $[Pb(DOTAM)]^{2+}$ at pD = 7.6 and 273 K ([PbL] = 0.02 M, D_2O)

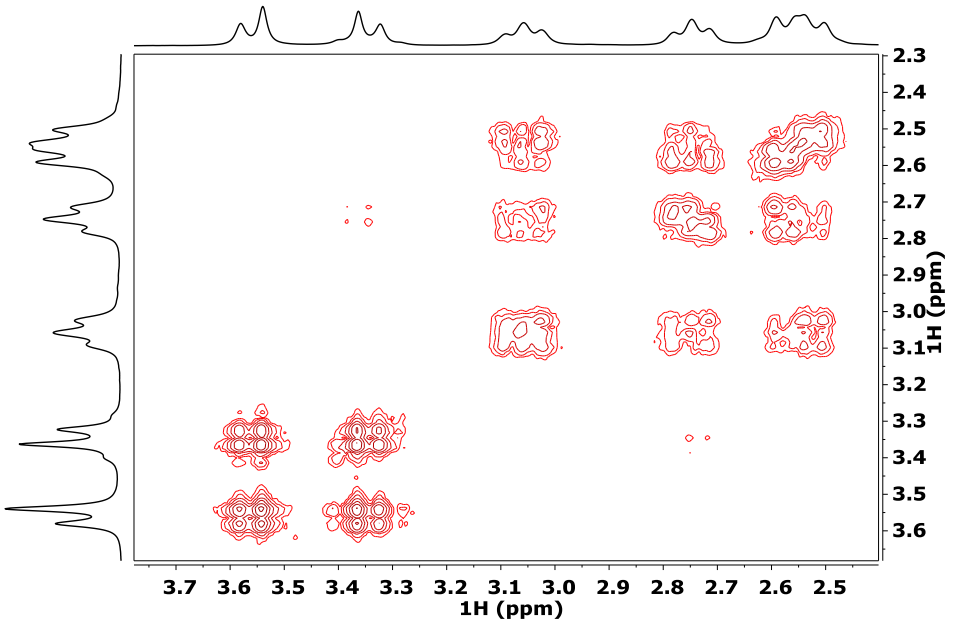

Figure S2. $^{1}H - {}^{1}H$ COSY spectrum of $[Pb(DOTAM)]^{2+}$ at pD = 7.6 and 273 K ([PbL] = 0.02 M, D_2O)

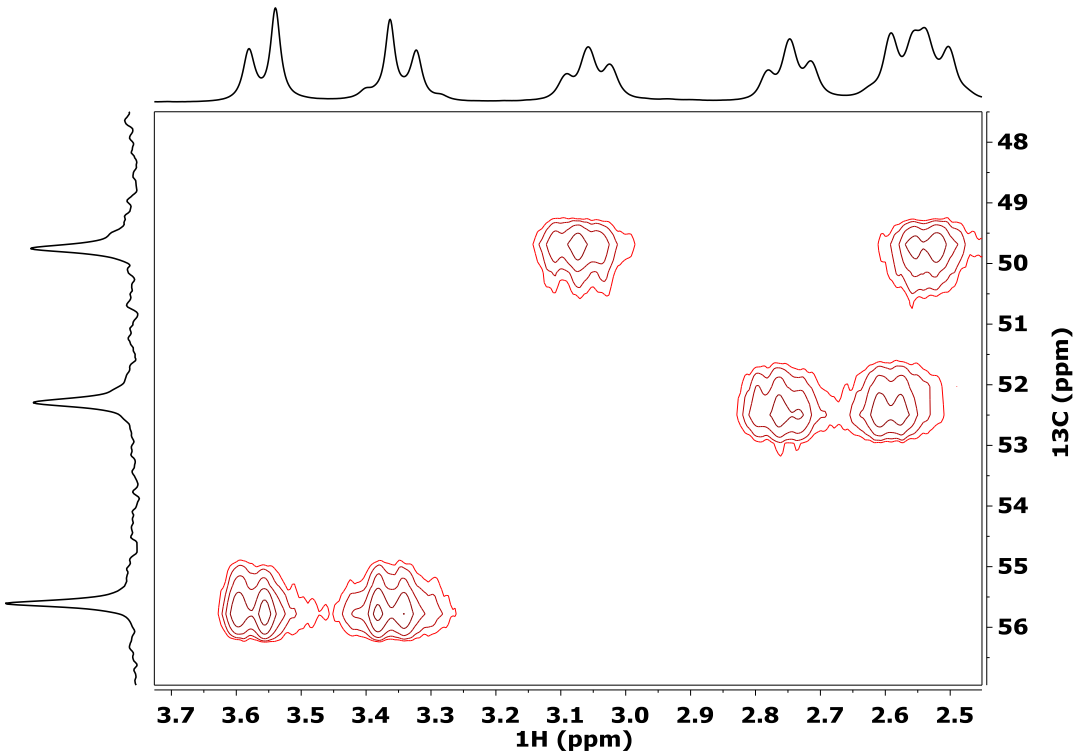

Figure S3. $^{1}H - {}^{13}C$ HSQC spectrum of $[Pb(DOTAM)]^{2+}$ at pD = 7.6 and 273 K ([PbL] = 0.02 M, D_2O)

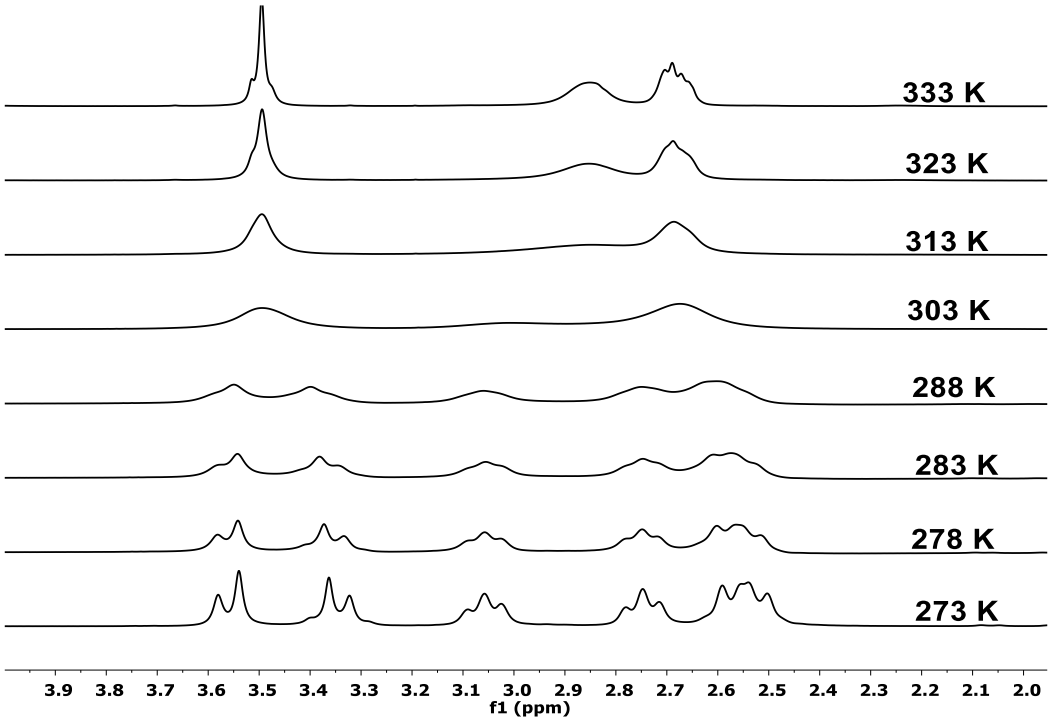

Figure S4. VT – ^{1}H NMR spectra of $[Pb(DOTAM)]^{2+}$ at pD = 7.2 in the temperature range 273 – 333 K ([PbL] = 0.02 M, D_2O)

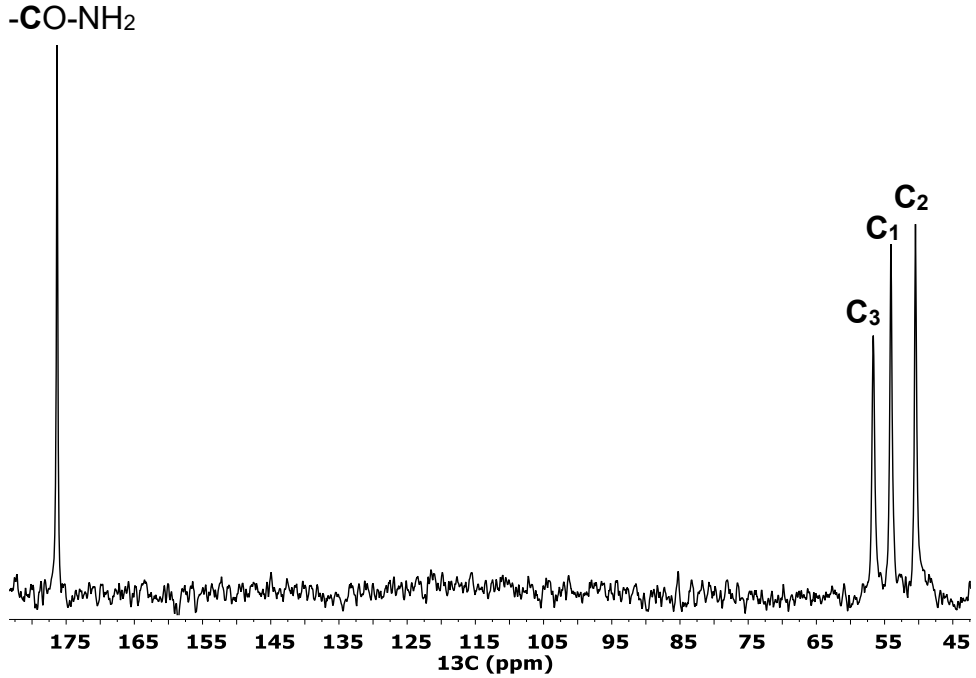

Figure S5. ^{13}C NMR spectra of $[Bi(DOTAM)]^{3+}$ at pH = 4.5 and 273 K ([BiL] = 0.04 M, H_2O)

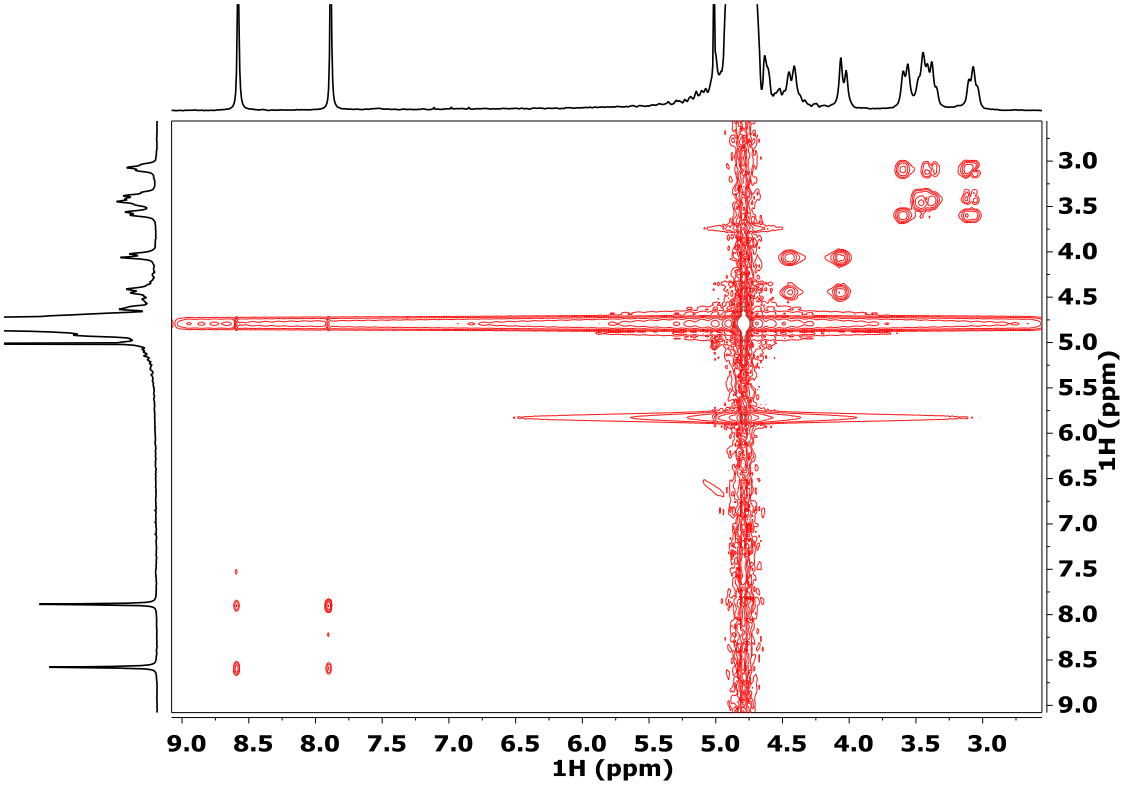

Figure S6. $^{1}H - {}^{1}H$ COSY spectrum of $[Bi(DOTAM)]^{3+}$ at pH = 4.5 and 273 K ([BiL] = 0.04 M, H_2O)

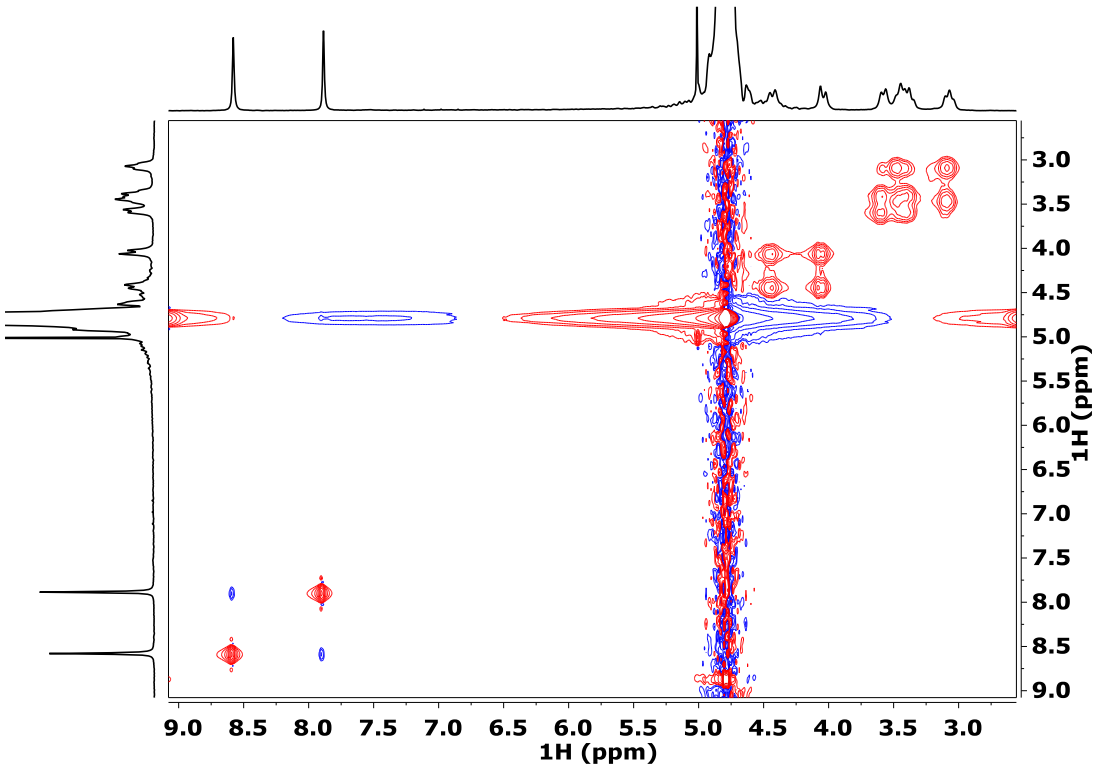

Figure S7. $^{1}H - {}^{1}H$ NOESY spectrum of $[Bi(DOTAM)]^{3+}$ at pH = 4.5 and 273K ([BiL] = 0.04 M, mixing time = 50 ms, H_2O).

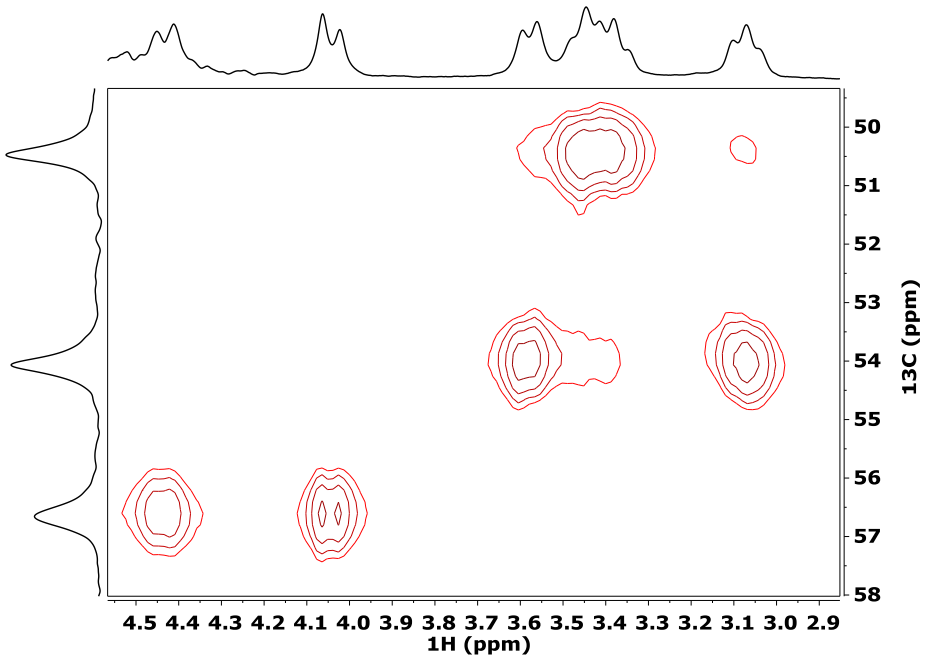

Figure S8. ^{1}H – ^{13}C HSQC spectra of $[Bi(DOTAM)]^{3+}$ at pH = 4.5 and 273 K ([BiL] = 0.04 M, H_2O)

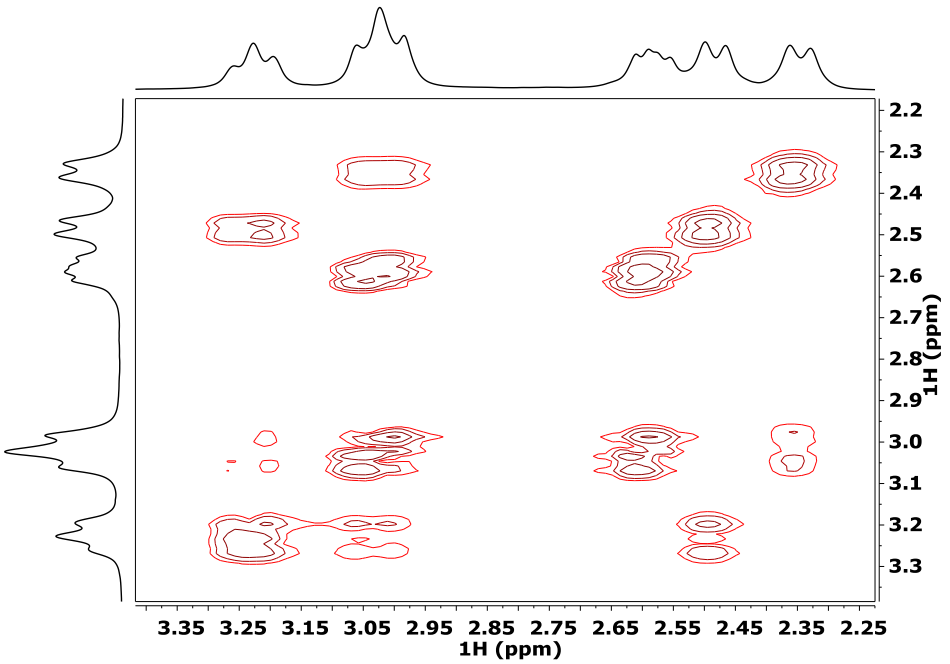

Figure S9. ^{1}H – ^{1}H COSY spectra of $[Pb(H_4DOTP)]^{2-}$ at pD = 4.6 and 268 K ([PbL] = 0.02 M, D_2O)

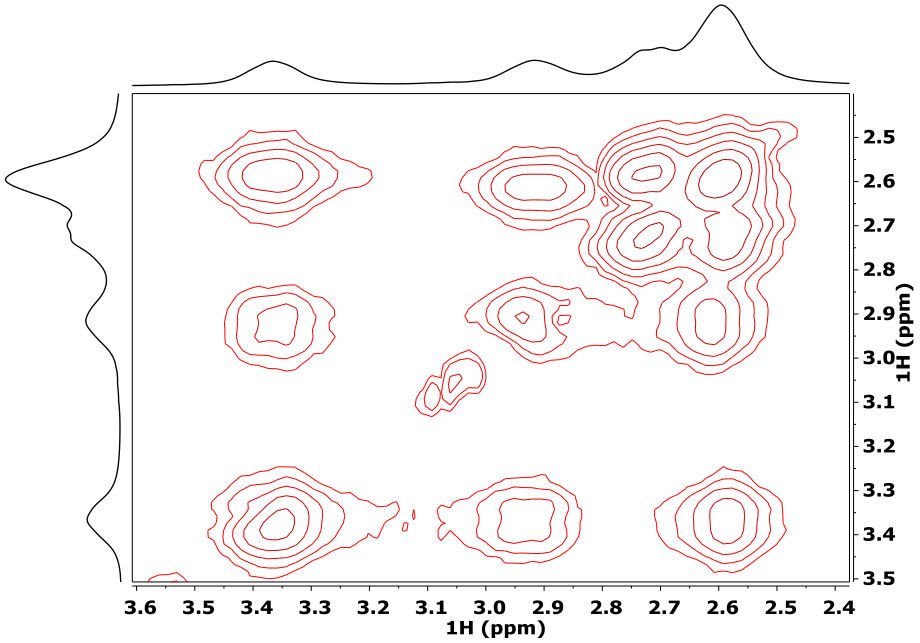

Figure S10. $^{1}H - {}^{1}H$ COSY spectra of $[Pb(DOTP)]^{6-}$ at pD = 10.95 and 273 K ([PbL] = 0.1 M, D_2O)

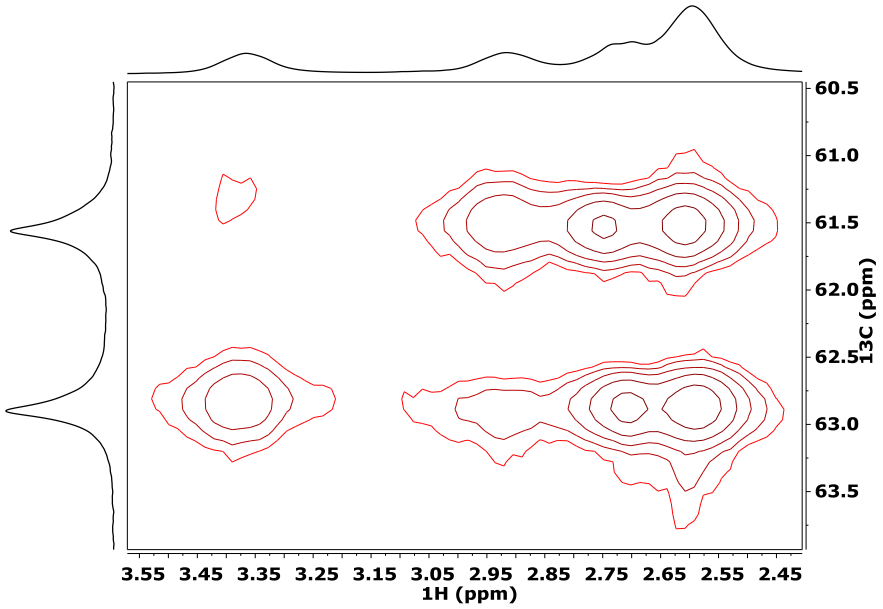

Figure S11. $^{1}H - {}^{13}C$ HSQC spectra of $[Pb(DOTP)]^{6-}$ at pD = 10.95 and 273 K ([PbL] = 0.1 M, D_2O)

XRD studies of $[Pb(H_4DOTP)]^{2-}$

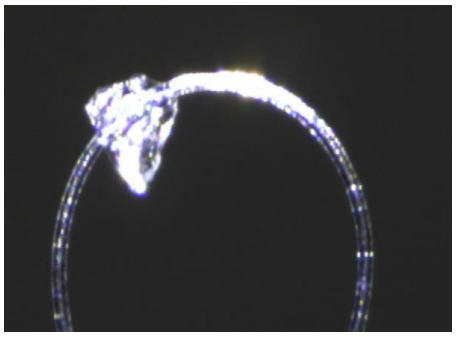

Figure S12. Crystals of $\{2(C(NH_2)_3)[Pb(H_4DOTP)]\}\cdot 7H_2O$ on Hampton Research loop mounted on a goniometer head.

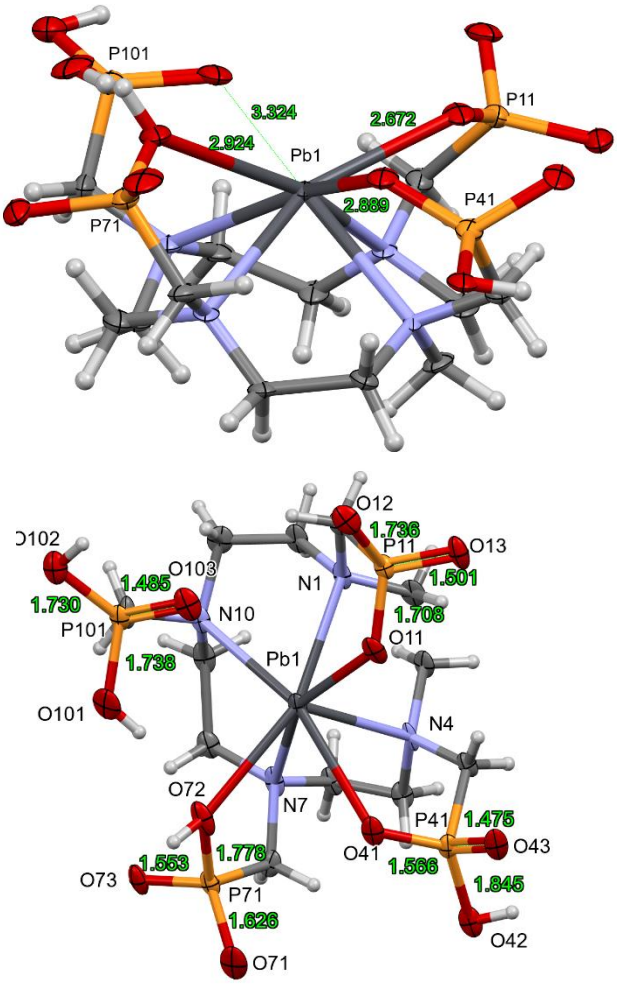

Figure S13. ORTEP view $[Pb(H_4DOTP)]^{2-}$ at 50 % probability level with partial numbering scheme from two directions and P…O as well as Pb…O distances. Solvent water molecules and guadinium counter cations are omitted for clarity.

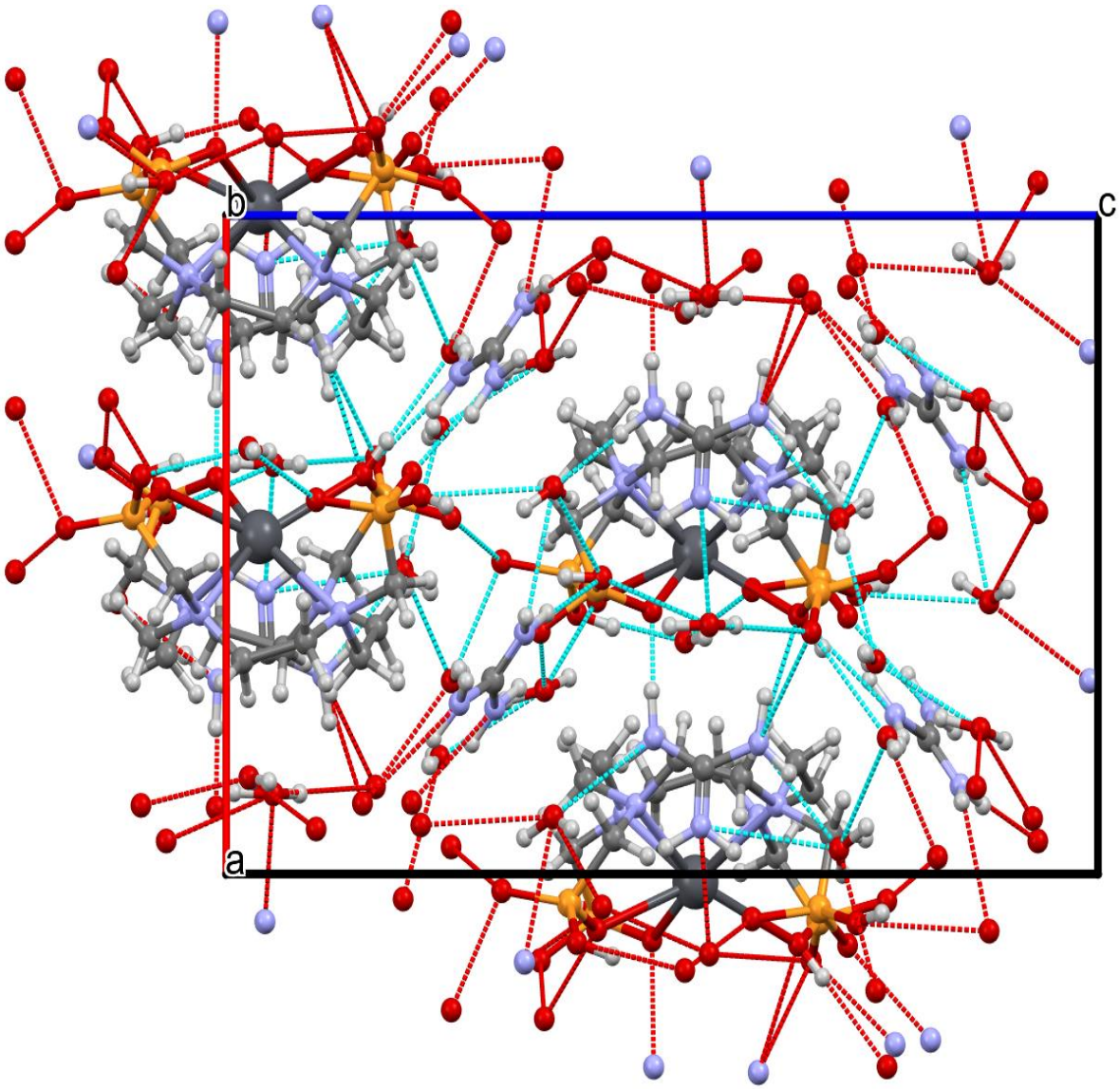

Figure S14. Packing diagram of $[Pb(H_4DOTP)]^{2-}$ showing hydrogen bond networks and the layered structure.

Table S1. Experimental data of X-ray structure determination of $\{2(C(NH_2)_3)[Pb(H_4DOTP)]\}\cdot 7H_2O$

Chemical formula	$C_{12}H_{24}N_4O_{12}P_4Pb\cdot 2(CH_6N_3)\cdot 7(H_2O)$
M_r	997.74
Crystal system, space group	Orthorhombic, *Pna*2$_1$
Temperature (K)	150
a, *b*, *c* (Å)	12.0854 (8), 15.0444 (16), 19.1100 (13)
V (Å^3)	3474.5 (5)
Z	4
Radiation type	Mo *K*α
μ (mm^{-1})	5.13
Crystal size (mm)	0.25 × 0.19 × 0.08
Data collection	
Diffractometer	Bruker D8 VENTURE
Absorption correction	Multi-scan Krause, L., Herbst-Irmer, R., Sheldrick, G. M., Stalke, D. (2015). "Comparison of silver and molybdenum microfocus X-ray sources for single-crystal structure determination" J. Appl. Cryst. 48, 3-10. doi:10.1107/S1600576714022985
T_{min}, T_{max}	0.35, 0.67
No. of measured, independent and observed [$I > 2\sigma(I)$] reflections	55349, 7097, 6184
R_{int}	0.108
$(\sin\theta/\lambda)_{max}$ (Å^{-1})	0.767
Refinement	
$R[F^2 > 2\sigma(F^2)]$, $wR(F^2)$, S	0.036, 0.086, 1.01
No. of reflections	7097
No. of parameters	488
No. of restraints	29
H-atom treatment	H atoms treated by a mixture of independent and constrained refinement
$\Delta\rangle_{max}$, $\Delta\rangle_{min}$ (e Å^{-3})	1.43, -1.08
Absolute structure	Flack x determined using 2618 quotients [(I+)-(I-)]/[(I+)+(I-)] (Parsons, Flack and Wagner, Acta Cryst. B69 (2013) 249-

	259).
Absolute structure parameter	0.064 (5)

Table S2. Fractional atomic coordinates and isotropic or equivalent isotropic displacement parameters (Å^2) for [Pb(H$_4$DOTP)]$^{2-}$

	x	*y*	*z*	U_{iso}*/U_{eq}
C2	0.3578 (7)	0.6559 (8)	0.4123 (6)	0.026 (3)
H2A	0.414286	0.657923	0.374835	0.031000*
H2B	0.288798	0.680564	0.392331	0.031000*
C3	0.3330 (7)	0.5439 (8)	0.4310 (5)	0.022 (3)
H3A	0.272293	0.544904	0.465785	0.027000*
H3B	0.300054	0.519871	0.387571	0.027000*
C5	0.3722 (7)	0.3751 (8)	0.4925 (5)	0.020 (2)
H5A	0.308706	0.347755	0.467895	0.024000*
H5B	0.435041	0.332829	0.492577	0.024000*
C6	0.3413 (7)	0.4022 (8)	0.5660 (5)	0.020 (3)
H6A	0.273427	0.438720	0.562167	0.024000*
H6B	0.319988	0.347113	0.590964	0.024000*
C8	0.3733 (7)	0.5040 (8)	0.6723 (5)	0.022 (3)
H8A	0.434149	0.506909	0.706925	0.026000*
H8B	0.310945	0.472293	0.694789	0.026000*
C9	0.3301 (7)	0.6133 (9)	0.6543 (6)	0.025 (3)
H9A	0.272240	0.606436	0.618083	0.030000*
H9B	0.290637	0.632135	0.697241	0.030000*
C10	0.4453 (7)	0.8173 (8)	0.4443 (5)	0.020 (2)
H10A	0.389414	0.852356	0.418339	0.024000*
H10B	0.474031	0.852786	0.483973	0.024000*
C11	0.3538 (7)	0.7879 (8)	0.5913 (6)	0.024 (3)
H11A	0.288742	0.814251	0.614957	0.029000*
H11B	0.413839	0.832625	0.589443	0.029000*
C12	0.3241 (7)	0.7557 (9)	0.5186 (5)	0.025 (3)
H12A	0.265348	0.710601	0.525307	0.030000*
H12B	0.288429	0.806788	0.495057	0.030000*
C40	0.4642 (7)	0.4396 (8)	0.3958 (5)	0.019 (2)
H40A	0.496742	0.489393	0.368907	0.023000*
H40B	0.411900	0.407328	0.365072	0.023000*
C70	0.4720 (6)	0.3558 (8)	0.6314 (5)	0.020 (2)
H70A	0.420449	0.316633	0.657277	0.024000*

H70B	0.499236	0.323930	0.589437	0.024000*
C90	0.7069 (7)	0.1142 (8)	0.3058 (5)	0.022 (3)
C91	0.8391 (6)	0.4192 (7)	0.5475 (8)	0.025 (3)
C100	0.4396 (7)	0.7458 (9)	0.6942 (5)	0.024 (3)
H10C	0.446107	0.704056	0.734017	0.029000*
H10D	0.386520	0.792913	0.707611	0.029000*
H42	0.544 (10)	0.247 (2)	0.3869 (17)	0.036000*
H72	0.665 (6)	0.495 (4)	0.682 (5)	0.036000*
H101	0.609 (11)	0.640 (5)	0.691 (6)	0.036000*
H102	0.585 (12)	0.918 (3)	0.686 (2)	0.036000*
H1WA	1.122 (11)	0.335 (7)	0.5092 (16)	0.036000*
H1WB	1.123 (11)	0.299 (5)	0.583 (4)	0.036000*
H2WA	0.849 (10)	0.643 (3)	0.236 (7)	0.036000*
H2WB	0.845 (10)	0.541 (3)	0.231 (7)	0.036000*
H3WA	0.686 (10)	0.853 (3)	0.274 (6)	0.036000*
H3WB	0.686 (10)	0.751 (3)	0.270 (6)	0.036000*
H4WA	0.752 (10)	0.575 (7)	0.324 (3)	0.036000*
H4WB	0.694 (10)	0.609 (5)	0.389 (5)	0.036000*
H5WA	0.967 (11)	0.392 (6)	0.736 (5)	0.036000*
H5WB	0.995 (9)	0.483 (4)	0.708 (6)	0.036000*
H6WA	0.934 (10)	0.332 (4)	0.386 (6)	0.036000*
H6WB	0.940 (10)	0.414 (6)	0.340 (5)	0.036000*
H7WA	0.642 (9)	0.997 (2)	0.535 (6)	0.036000*
H7WB	0.642 (11)	0.897 (4)	0.552 (5)	0.036000*
N1	0.3959 (6)	0.7200 (7)	0.4702 (4)	0.019 (2)
N4	0.4080 (6)	0.4726 (8)	0.4558 (4)	0.018 (2)
N7	0.4130 (7)	0.4481 (8)	0.6101 (5)	0.021 (3)
N10	0.3951 (6)	0.6965 (7)	0.6316 (5)	0.020 (2)
N91	0.7475 (6)	0.2112 (7)	0.3080 (5)	0.030 (2)
H91A	0.715350	0.249742	0.336080	0.036000*
H91B	0.802949	0.228083	0.281291	0.036000*
N92	0.6345 (7)	0.0965 (7)	0.3419 (5)	0.022 (2)
H92A	0.609077	0.041740	0.343108	0.027000*
H92B	0.604256	0.137756	0.368380	0.027000*
N93	0.7410 (6)	0.0320 (7)	0.2675 (4)	0.026 (2)
H93A	0.706059	–0.018378	0.275055	0.032000*
H93B	0.796030	0.034076	0.237387	0.032000*
N94	0.7932 (9)	0.4218 (9)	0.4904 (6)	0.044 (4)
H94A	0.832829	0.420900	0.451753	0.053000*
H94B	0.720560	0.424637	0.487973	0.053000*

N95	0.9278 (5)	0.4159 (6)	0.5444 (8)	0.036 (2)
H95A	0.960753	0.415252	0.503396	0.044000*
H95B	0.967429	0.413807	0.583035	0.044000*
N96	0.8012 (9)	0.4210 (10)	0.6105 (6)	0.060 (5)
H96A	0.847081	0.419454	0.646207	0.072000*
H96B	0.729355	0.423710	0.617792	0.072000*
O1W	1.1215 (6)	0.3438 (6)	0.5540 (4)	0.036 (2)
O2W	0.8219 (7)	0.5916 (8)	0.2454 (6)	0.050 (3)
O3W	0.7071 (8)	0.8026 (8)	0.2578 (8)	0.069 (3)
O4W	0.7201 (5)	0.5644 (6)	0.3648 (5)	0.034 (2)
O5W	0.9620 (7)	0.4315 (8)	0.7028 (5)	0.040 (2)
O6W	0.9129 (6)	0.3841 (8)	0.3749 (5)	0.043 (3)
O7W	0.6468 (5)	0.9420 (5)	0.5259 (4)	0.0250 (19)
O11	0.5841 (4)	0.6813 (5)	0.4252 (4)	0.0232 (17)
O12	0.6045 (5)	0.8867 (5)	0.4028 (4)	0.0259 (19)
O13	0.5257 (5)	0.7742 (6)	0.3160 (4)	0.0279 (19)
O41	0.6001 (5)	0.4275 (6)	0.4884 (4)	0.0243 (18)
O42	0.5500 (5)	0.2480 (6)	0.4312 (4)	0.0251 (18)
O43	0.6315 (5)	0.3865 (5)	0.3603 (4)	0.0277 (19)
O71	0.6324 (5)	0.2903 (6)	0.6712 (4)	0.034 (2)
O72	0.6071 (5)	0.4971 (6)	0.6563 (4)	0.0288 (19)
O73	0.5410 (5)	0.3991 (5)	0.7579 (4)	0.0258 (19)
O101	0.6083 (5)	0.6901 (6)	0.7132 (4)	0.033 (2)
O102	0.5744 (6)	0.8873 (6)	0.7240 (4)	0.0286 (19)
O103	0.5682 (5)	0.7945 (6)	0.6032 (4)	0.0283 (19)
P11	0.5444 (2)	0.7824 (3)	0.39336 (16)	0.0174 (8)
P41	0.5657 (2)	0.3697 (2)	0.42391 (15)	0.0190 (7)
P71	0.5715 (2)	0.3862 (2)	0.67959 (15)	0.0190 (7)
P101	0.5532 (2)	0.7882 (3)	0.68018 (16)	0.0204 (8)
Pb1	0.51219 (2)	0.59453 (2)	0.53830 (4)	0.01552 (13)

Table S3. Atomic displacement parameters (Å^2) for $[Pb(H_4DOTP)]^{2-}$

	U^{11}	U^{22}	U^{33}	U^{12}	U^{13}	U^{23}
C2	0.005 (3)	0.049 (9)	0.023 (6)	0.010 (5)	–0.002 (3)	–0.003 (6)
C3	0.006 (3)	0.041 (9)	0.020 (5)	0.004 (4)	–0.006 (3)	–0.007 (6)
C5	0.008 (4)	0.036 (8)	0.017 (5)	–0.002 (4)	0.003 (3)	0.000 (5)
C6	0.006 (3)	0.036 (8)	0.018 (5)	–0.005 (4)	–0.002 (3)	0.001 (5)
C8	0.010 (4)	0.036 (8)	0.019 (5)	–0.001 (4)	0.002 (3)	0.000 (5)
C9	0.007 (4)	0.048 (9)	0.021 (6)	–0.003 (5)	0.001 (3)	–0.005 (6)

C10	0.010 (3)	0.032 (7)	0.016 (5)	0.003 (4)	0.001 (3)	–0.002 (5)
C11	0.006 (3)	0.037 (8)	0.029 (6)	0.000 (4)	0.002 (3)	–0.006 (6)
C12	0.007 (3)	0.048 (8)	0.020 (6)	0.005 (4)	–0.001 (3)	–0.003 (5)
C40	0.010 (3)	0.032 (7)	0.015 (5)	0.000 (4)	0.000 (3)	0.003 (5)
C70	0.008 (3)	0.030 (7)	0.023 (5)	–0.003 (4)	–0.001 (3)	–0.009 (5)
C90	0.009 (4)	0.043 (8)	0.014 (5)	0.003 (4)	0.000 (3)	0.008 (5)
C91	0.010 (3)	0.036 (6)	0.030 (8)	0.000 (3)	–0.001 (5)	–0.002 (7)
C100	0.015 (4)	0.045 (8)	0.011 (5)	–0.005 (4)	0.001 (3)	–0.007 (5)
N1	0.003 (3)	0.042 (7)	0.013 (4)	0.001 (4)	–0.001 (3)	–0.003 (4)
N4	0.003 (3)	0.044 (7)	0.007 (4)	0.001 (4)	0.000 (3)	0.000 (4)
N7	0.003 (3)	0.047 (7)	0.014 (5)	0.002 (4)	0.000 (3)	–0.003 (5)
N10	0.006 (3)	0.038 (7)	0.016 (5)	–0.001 (4)	–0.002 (3)	–0.003 (5)
N91	0.007 (3)	0.054 (7)	0.029 (5)	0.000 (4)	0.006 (3)	0.000 (5)
N92	0.009 (3)	0.032 (7)	0.026 (5)	0.001 (4)	0.004 (3)	0.003 (4)
N93	0.011 (3)	0.045 (7)	0.022 (5)	–0.005 (4)	0.007 (3)	–0.005 (5)
N94	0.013 (4)	0.094 (11)	0.025 (6)	0.010 (5)	–0.006 (4)	–0.010 (6)
N95	0.005 (2)	0.069 (7)	0.036 (5)	0.001 (3)	0.001 (5)	–0.005 (7)
N96	0.009 (4)	0.137 (14)	0.034 (7)	–0.013 (6)	0.014 (4)	–0.006 (7)
O1W	0.020 (3)	0.063 (6)	0.026 (5)	–0.008 (3)	–0.009 (3)	0.005 (4)
O2W	0.009 (4)	0.090 (9)	0.052 (6)	–0.007 (4)	0.012 (4)	0.000 (6)
O3W	0.038 (5)	0.061 (8)	0.108 (10)	0.002 (6)	0.028 (6)	–0.007 (8)
O4W	0.010 (3)	0.049 (6)	0.041 (5)	0.000 (3)	0.007 (3)	–0.001 (4)
O5W	0.023 (4)	0.063 (7)	0.032 (5)	–0.013 (4)	–0.014 (3)	0.005 (5)
O6W	0.015 (3)	0.079 (8)	0.034 (5)	0.018 (4)	0.006 (3)	0.009 (5)
O7W	0.004 (2)	0.043 (5)	0.028 (5)	0.000 (3)	0.003 (2)	–0.002 (4)
O11	0.005 (2)	0.044 (5)	0.021 (4)	0.003 (3)	–0.002 (2)	0.005 (4)
O12	0.008 (3)	0.040 (5)	0.030 (4)	–0.005 (3)	0.000 (3)	0.006 (4)
O13	0.011 (3)	0.055 (6)	0.017 (4)	–0.002 (3)	–0.002 (2)	0.000 (4)
O41	0.006 (2)	0.046 (5)	0.021 (4)	0.001 (3)	–0.001 (2)	–0.004 (4)
O42	0.006 (2)	0.049 (6)	0.020 (4)	–0.002 (3)	0.001 (2)	–0.001 (4)
O43	0.006 (2)	0.056 (6)	0.021 (4)	0.007 (3)	0.003 (2)	–0.006 (4)
O71	0.007 (3)	0.062 (6)	0.033 (4)	0.005 (3)	–0.005 (3)	–0.008 (4)
O72	0.010 (3)	0.057 (6)	0.020 (4)	–0.007 (3)	–0.004 (2)	0.005 (4)
O73	0.013 (3)	0.049 (6)	0.016 (4)	0.002 (3)	–0.004 (2)	0.001 (4)
O101	0.011 (3)	0.050 (6)	0.038 (5)	0.000 (3)	–0.013 (3)	–0.003 (4)
O102	0.015 (3)	0.046 (6)	0.025 (4)	–0.007 (3)	0.000 (3)	–0.004 (4)
O103	0.008 (3)	0.051 (6)	0.026 (4)	–0.006 (3)	0.001 (2)	0.004 (4)
P11	0.0112 (12)	0.026 (2)	0.0152 (14)	–0.0033 (13)	0.0008 (10)	0.0010 (14)
P41	0.0095 (9)	0.031 (2)	0.0161 (14)	0.0021 (11)	0.0006 (10)	–0.0042 (14)
P71	0.0095 (9)	0.032 (2)	0.0154 (14)	–0.0014 (11)	–0.0021 (10)	0.0009 (14)

P101	0.0091 (11)	0.034 (2)	0.0179 (15)	0.0017 (13)	–0.0016 (11)	–0.0034 (15)
Pb1	0.00684 (11)	0.0262 (2)	0.01350 (16)	–0.00023 (11)	–0.0004 (2)	–0.0006 (3)

Table S4. Geometric parameters (Å, º) for $[Pb(H_4DOTP)]^{2-}$

C2—N1	1.536 (14)	C91—N95	1.074 (10)
C2—C3	1.748 (15)	C91—N94	1.225 (17)
C3—N4	1.482 (13)	C91—N96	1.289 (17)
C5—C6	1.510 (14)	C100—N10	1.507 (13)
C5—N4	1.682 (16)	C100—P101	1.537 (10)
C6—N7	1.391 (13)	N1—Pb1	2.689 (10)
C8—N7	1.534 (13)	N4—Pb1	2.727 (10)
C8—C9	1.759 (17)	N10—Pb1	2.744 (9)
C9—N10	1.540 (15)	O11—P11	1.708 (8)
C10—P11	1.629 (10)	O11—Pb1	2.671 (7)
C10—N1	1.658 (15)	O12—P11	1.738 (9)
C11—C12	1.513 (14)	O13—P11	1.501 (8)
C11—N10	1.653 (15)	O41—P41	1.564 (8)
C12—N1	1.378 (12)	O42—P41	1.846 (9)
C40—N4	1.422 (13)	O43—P41	1.475 (7)
C40—P41	1.703 (10)	O71—P71	1.627 (9)
C70—P71	1.582 (9)	O72—P71	1.779 (9)
C70—N7	1.613 (16)	O73—P71	1.554 (8)
C90—N92	1.145 (12)	O101—P101	1.738 (9)
C90—N93	1.495 (15)	O102—P101	1.729 (9)
C90—N91	1.541 (16)	O103—P101	1.486 (8)
N1—C2—C3	120.6 (8)	C9—N10—C11	130.8 (7)
N4—C3—C2	131.2 (7)	C100—N10—Pb1	127.4 (5)
C6—C5—N4	102.5 (9)	C9—N10—Pb1	89.6 (6)
N7—C6—C5	122.9 (8)	C11—N10—Pb1	108.6 (5)
N7—C8—C9	117.0 (8)	P11—O11—Pb1	129.2 (3)
N10—C9—C8	131.6 (7)	O13—P11—C10	120.3 (5)
P11—C10—N1	99.1 (7)	O13—P11—O11	108.6 (5)
C12—C11—N10	103.4 (9)	C10—P11—O11	106.3 (5)
N1—C12—C11	126.3 (8)	O13—P11—O12	103.8 (5)
N4—C40—P41	107.8 (7)	C10—P11—O12	87.4 (5)
P71—C70—N7	103.5 (7)	O11—P11—O12	130.5 (4)

N92—C90—N93	108.3 (11)	O43—P41—O41	114.3 (4)
N92—C90—N91	116.5 (11)	O43—P41—C40	91.3 (5)
N93—C90—N91	135.2 (8)	O41—P41—C40	95.5 (5)
N95—C91—N94	113.9 (16)	O43—P41—O42	106.7 (4)
N95—C91—N96	113.9 (16)	O41—P41—O42	121.3 (4)
N94—C91—N96	132.1 (9)	C40—P41—O42	124.2 (4)
N10—C100—P101	112.6 (7)	O73—P71—C70	114.7 (5)
C12—N1—C2	122.6 (7)	O73—P71—O71	108.2 (4)
C12—N1—C10	94.8 (9)	C70—P71—O71	91.7 (5)
C2—N1—C10	116.6 (8)	O73—P71—O72	100.4 (4)
C12—N1—Pb1	106.1 (7)	C70—P71—O72	108.0 (5)
C2—N1—Pb1	93.7 (6)	O71—P71—O72	134.2 (4)
C10—N1—Pb1	125.2 (5)	O103—P101—C100	107.9 (5)
C40—N4—C3	106.6 (8)	O103—P101—O102	114.0 (5)
C40—N4—C5	98.9 (9)	C100—P101—O102	114.0 (5)
C3—N4—C5	127.4 (7)	O103—P101—O101	111.5 (5)
C40—N4—Pb1	118.7 (6)	C100—P101—O101	85.8 (6)
C3—N4—Pb1	88.8 (6)	O102—P101—O101	120.0 (4)
C5—N4—Pb1	117.7 (5)	O11—Pb1—N1	55.6 (2)
C6—N7—C8	123.1 (8)	O11—Pb1—N4	90.6 (2)
C6—N7—C70	90.1 (9)	N1—Pb1—N4	87.2 (3)
C8—N7—C70	114.5 (8)	O11—Pb1—N10	114.8 (3)
C100—N10—C9	110.9 (8)	N1—Pb1—N10	69.7 (3)
C100—N10—C11	93.9 (8)	N4—Pb1—N10	120.9 (2)

Table S5. Hydrogen-bond geometry (Å, º) for $[Pb(H_4DOTP)]^{2-}$

D—H···*A*	*D*—H	H···*A*	*D*···*A*	*D*—H···*A*
C2—H2*A*···O13	0.99	2.48	3.267 (13)	136
C2—H2*A*···O73^{i}	0.99	2.45	3.300 (13)	143
C2—H2*B*···O12^{ii}	0.99	2.45	3.133 (11)	125
C3—H3*A*···O7*W*^{ii}	0.99	1.91	2.897 (11)	173
C3—H3*B*···N93^{iii}	0.99	2.53	3.509 (13)	171
C5—H5*B*···O42	0.99	2.22	3.106 (13)	148
C6—H6*A*···O7*W*^{ii}	0.99	2.46	3.408 (13)	160
C8—H8*A*···O72	0.99	2.31	2.843 (11)	113
C8—H8*A*···O73	0.99	2.29	3.045 (13)	132
C8—H8*B*···O2*W*^{iv}	0.99	2.11	3.096 (14)	178
C9—H9*A*···O7*W*^{ii}	0.99	2.44	3.410 (13)	168

C10—H10*A*···O4*W*^{ii}	0.99	2.61	3.589 (12)	171
C10—H10*B*···O7*W*	0.99	2.61	3.446 (12)	143
C11—H11*B*···O103	0.99	1.97	2.603 (10)	120
C100—H10*D*···N91^{iv}	0.99	2.51	3.205 (13)	127
O72—H72···N93^{v}	0.86 (3)	2.06 (5)	2.857 (10)	153 (10)
O101—H101···O72	0.86 (3)	2.25 (4)	3.101 (12)	168 (13)
O1*W*—H1*WA*···O42^{vi}	0.87 (3)	2.13 (8)	2.858 (11)	141 (11)
O1*W*—H1*WB*···O71^{vi}	0.87 (3)	2.17 (3)	3.018 (12)	167 (9)
O2*W*—H2*WA*···O71^{vii}	0.86 (3)	2.55 (6)	3.354 (15)	157 (13)
O2*W*—H2*WB*···O102^{viii}	0.85 (3)	2.51 (5)	3.345 (14)	164 (12)
O3*W*—H3*WA*···O5*W*^{vii}	0.86 (3)	2.55 (12)	3.007 (16)	115 (11)
O4*W*—H4*WA*···O2*W*	0.88 (3)	1.75 (3)	2.625 (13)	176 (12)
O4*W*—H4*WB*···O11	0.87 (3)	1.85 (6)	2.668 (11)	155 (13)
O5*W*—H5*WA*···O3*W*^{ix}	0.87 (3)	2.53 (11)	3.007 (16)	115 (10)
O5*W*—H5*WA*···O13^{ix}	0.87 (3)	2.35 (3)	3.210 (14)	174 (11)
O5*W*—H5*WB*···O102^{x}	0.88 (3)	2.19 (3)	3.072 (14)	178 (12)
O6*W*—H6*WA*···O42^{vi}	0.86 (3)	2.03 (8)	2.802 (12)	149 (12)
O6*W*—H6*WB*···O102^{viii}	0.87 (3)	2.26 (11)	2.889 (12)	129 (12)
O7*W*—H7*WA*···O1*W*^{ii}	0.85 (3)	2.43 (3)	3.282 (12)	176 (11)
O7*W*—H7*WB*···O103	0.84 (3)	2.03 (6)	2.830 (11)	157 (12)
N91—H91*A*···O43	0.88	2.34	3.149 (12)	153
N91—H91*B*···O101^{viii}	0.88	1.78	2.534 (10)	142
N92—H92*A*···O12^{xi}	0.88	2.60	3.384 (13)	149
N92—H92*B*···O6*W*^{iii}	0.88	2.34	2.767 (11)	110
N92—	0.88	2.15	3.025 (13)	173

H92*B*···O42				
N93—H93*A*···O5*W*^{viii}	0.88	2.57	3.136 (13)	123
N93—H93*B*···O72^{viii}	0.88	2.02	2.857 (10)	158
N94—H94*A*···O6*W*	0.88	1.84	2.698 (14)	163
N94—H94*B*···O41	0.88	1.46	2.336 (12)	177
N95—H95*A*···O6*W*	0.88	2.57	3.280 (17)	139
N95—H95*B*···O5*W*	0.88	2.30	3.063 (18)	144
N96—H96*A*···O5*W*	0.88	1.77	2.629 (14)	165
N96—H96*B*···O71	0.88	2.54	3.061 (15)	119
N96—H96*B*···O72	0.88	1.99	2.753 (14)	145

Symmetry codes: (i) –*x*+1, –*y*+1, *z*–1/2; (ii) *x*–1/2, –*y*+3/2, *z*; (iii) *x*–1/2, –*y*+1/2, *z*; (iv) –*x*+1, –*y*+1, *z*+1/2; (v) –*x*+3/2, *y*+1/2, *z*+1/2; (vi) *x*+1/2, –*y*+1/2, *z*; (vii) –*x*+3/2, *y*+1/2, *z*–1/2; (viii) –*x*+3/2, *y*–1/2, *z*–1/2; (ix) –*x*+3/2, *y*–1/2, *z*+1/2; (x) *x*+1/2, –*y*+3/2, *z*; (xi) *x*, *y*–1, *z*.

Chapter 3

Click-chemistry assisted labelling of albumin with positron-emitting metal ions for PET imaging of prostate cancer

The research described in this Chapter was performed during a period of 3 months (at least 6 months abroad are required for PNRR scholarships) in the group of professor Yun-Sang Lee at Seoul National University Hospital (College of Medicine), Seoul, South Korea. The study highlights some key aspects of albumin-based delivery systems of diagnostic PET radionuclides for detection of prostate cancer.

Introduction

Functionalization of Human Serum Albumin (HSA) and applications in medicine

Human Serum Albumin (HSA), whose biosynthesis occurs exclusively in the hepatocytes, is the most abundant protein in human blood plasma, constituting approximately 60% of the total plasma protein content (35 – 50 g per liter of serum). It is a 66.5 kDa globular heart-shaped protein (Figure 1) composed of three homologous domains (I, II, and III), each of which consists of two subdomains (A and B). It plays a key role in maintaining osmotic pressure and acting as carrier of various molecules and ions throughout the body. As a consequence of its highly diverse structure characterized by a multitude of binding sites, it enables the transport of a large variety of endogenous and exogenous compounds, such as hormones, vitamins, fatty acids, and drugs.[1] There are two main drug binding sites, called Sudlow site I and Sudlow site II. One of them is located in subdomain IIA, which is known for selectively recognizing warfarin, an anticoagulant drug, while the other is located in subdomain IIIA and shows affinity towards benzodiazepines.

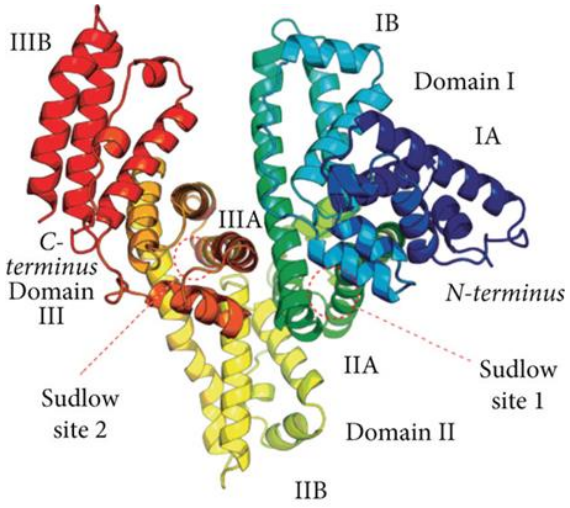

Figure 1. Structure of Human Serum Albumin (HSA).

HSA possesses a high thermal stability, as it maintains its native state for 10 hours at 60 °C, and its biological function is preserved over a broad pH range (4 − 9) as well.[1][2] In terms of receptor affinity, native albumin recognizes selectively glycoprotein receptors such as Gp60 (or albondin), Gp30, Gp18, and Cubilin, as well as SPARC (Secreted Protein, Acidic and Rich in Cysteine), also known as the osteonectin receptor. Specifically, SPARC receptors are overexpressed in several types of tumours (breast, liver and brain cancer), while Gp60 receptor mediates albumin cell transport in blood and lymphatic vessels, hence can be used as a tool to deliver antitumor drugs.[3] Furthermore, due to its versatile structure rich in different functional groups that can be chemically modified, selectivity towards other types of receptors can be also achieved. In fact, the interest for albumin has seen a continuous increase due to the presence of lysine-, cysteine- and tyrosine-rich domains which allows its functionalization for a wide range of applications. The reactivity of the nucleophilic groups on the side chains of these residues, namely amino, thiol and hydroxyl groups, respectively, can be exploited to bind several fragments of interest.

This array of properties makes albumin suitable, in particular, for drug formulations. In fact, the most outstanding clinical application of albumin is in the form of Abraxane, a drug composed of a chemotherapeutic agent for lung, breast and pancreatic cancer (Paclitaxel), bound to HSA.[4] Abraxane was officially approved by the FDA in 2005, however applications of HSA extend also to the radiopharmaceutical field, which dates back to 1965 when ^{131}I-labeled human serum albumin (RISA) for blood pool imaging was commercialized by Abbott Laboratories.[4] Nowadays, the role of albumin has expanded to a variety of drug delivery strategies, from binding small molecules and antibodies, to more advanced biomolecular techniques (*e.g.* genetic fusion). One of the most appealing attributes is the reversible binding of drugs in such manner that the formed adduct behaves as a drug reservoir, which can enhance its biodistribution and bioavailability.[5]

Conjugation of molecular drugs to macromolecules is a commonly adopted strategy, useful for improving their circulation time and biodistribution, especially for those with poor solubility and pharmacokinetics.

In the present work, the role of HSA for radiopharmaceutical applications was studied, acting as a carrier of both a radioprobe (a β^+ emitter) and a targeting peptide, with the purpose of using it for *in-vivo* PET imaging of prostate cancer.

Prostate cancer, accounting for 29% of all cancer incidence in men, is among the most recurrent cancers, along with lung, breast and colorectal malignancies.[6] When it comes to selectivity for this type of tumour, one of the most common approaches in clinical settings is to target the overexpressed Prostate-Specific Membrane Antigen (PSMA) with molecules (vectors) exhibiting high selectivity towards PSMA. Radiopharmaceutical agents for prostate cancer – such as PSMA-11 – are typically made of a targeting peptide with high affinity for PSMA, a linker and a (bifunctional) chelating agent which forms a stable complex with a radionuclide endowed with therapeutic and/or diagnostic properties (*e.g.* ^{68}Ga-PSMA-11 for PET imaging, Figure 2). In the case of PSMA-11 the targeting vector is the GUL peptide (Glutamate-Ureido-Lysine, Figure 2). As mentioned, the targeting peptide is connected to the radiometal complex through a linker, whose nature (e.g. length, flexibility, functionalities...) often helps to improve

the peptide's *in-vivo* stability and the solubility of the whole construct as well. In fact, some peptides may have a poor solubility and/or undergo rapid enzymatic degradation due to the *in-vivo* abundance of proteases. For the purpose of reducing enzymatic degradation certain types of modifications might be needed, *e.g.* insertion of analogous modified aminoacids or use of prosthetic groups.

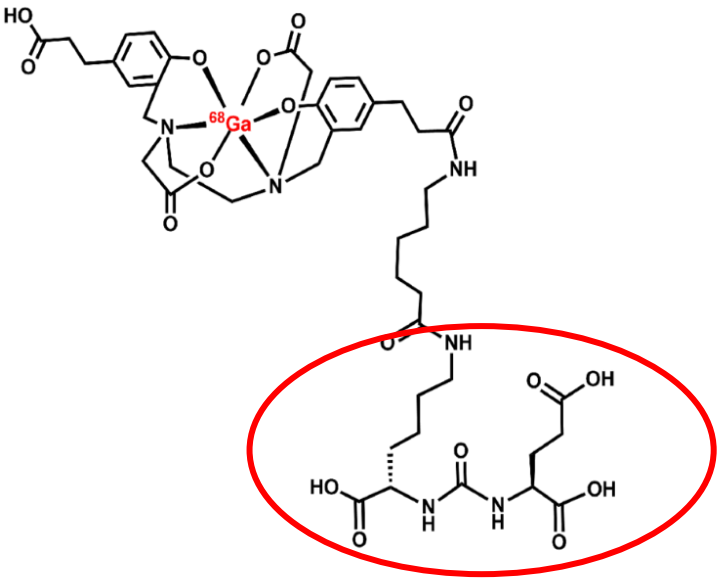

Figure 2. Structure of ^{68}Ga-PSMA-11, the first FDA-approved PET imaging agent for prostate cancer. The targeting peptide vector (GUL) is evidenced in the red frame.

Positron-emitting radionuclides for imaging and chelating agents

Positron emission tomography is a rapidly growing nuclear medicine technique, especially advantageous for the imaging of metabolic processes and blood flow, that relies on the emission of β^+ particles (positrons) from radioactive nuclides. The positron-based imaging confers increased sensitivity compared to other imaging techniques (*e.g.* SPECT) due to its mechanism that consists in the annihilation between a β^+ particle and an electron, which in turn produces two gamma rays (γ) at 180° (Figure 3). This phenomenon, as well as the absence of collimators in front of the detectors which can cause scattering and/or absorption of the particles, increases the signal-to-noise ratio.

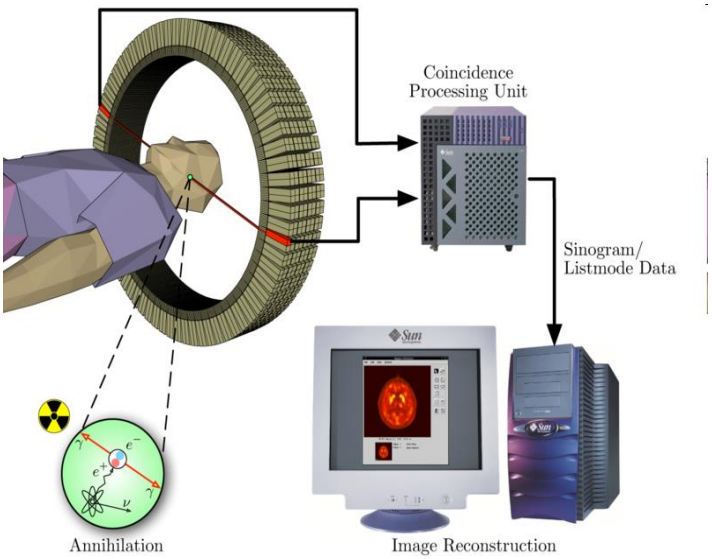

Figure 3. Simplified graphical representation of PET scans acquisition.

The most widely used positron-emitter radionuclide for clinical applications is fluorine-18, mainly in the form of ^{18}F-FDG (Fluorodeoxyglucose), an example of bio-isosteric substitution. In fact, ^{18}F-FDG undergoes the same metabolism as native glucose until the point of phosphorylation, but after this step fluorinated glucose cannot continue the usual reaction cascades of its native counterpart, hence it accumulates in tissues that exhibit increased metabolic activity, which is typically the case for most cancers. However, fluorine-18 has its setbacks, such as time-consuming purification steps compared to its relative short half-life ($t_{1/2}$ = 110 min), which could ultimately result in a less efficient imaging. Consequently, in recent years alternative options have emerged, and several positron emitting metal ions (*i.e.* ^{64}Cu, ^{68}Ga, ^{89}Zr) were found to be particularly promising. Metal ions generally engage in rapid complexation reactions with appropriate chelators that require little to no purification steps, unlike their non-metal counterpart ^{18}F.[7] A fundamental requisite a chelator must possess for bio-medical purposes is the ability to form a stable and inert metal complex. Finding a suitable chelating agent depends on the intrinsic characteristics of the metal ion such as ionic radius, charge, coordination number, overall hardness/softness etc. Furthermore, chelators can be divided into acyclic/linear, mesocyclic and macrocyclic agents, and each of them presents complementary properties. For example, acyclic ligands (*e.g.* EDTA, Figure 4a) undergo fast complexation reactions but their complexes are typically less thermodynamically stable than those of macrocycles (*e.g.* DOTA, Figure 4c), albeit the latter exhibits slower formation kinetics. An in-between situation is found with mesocyclic ligands (e.g. AAZTA, Figure 4b), which are typically 7 – 11 membered rings that exhibit intermediate properties between linear and macrocyclic chelators.[8]

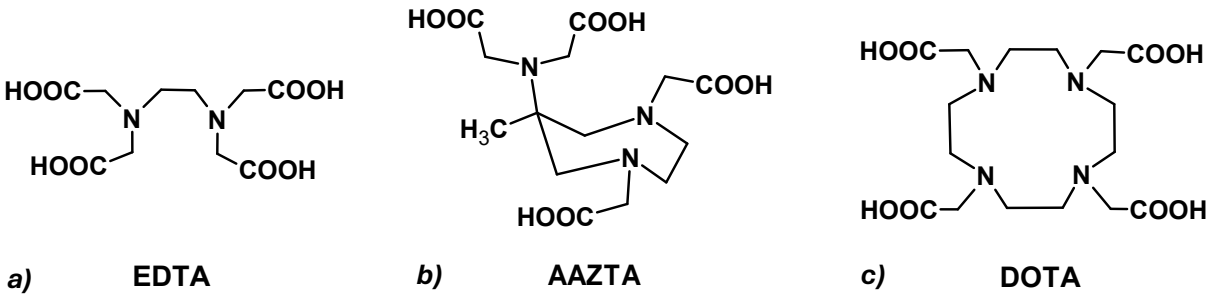

Figure 4. Examples of different chelators for metal ions *a)* acyclic/linear – EDTA, *b)* mesocyclic – AAZTA, *c)* macrocyclic – DOTA.

The general approach

In our approach HSA is progressively functionalized (Figure 5a): in the first step, a number of DBCO-NHS linkers (DBCO-NHS = dibenzocyclooctyne-*N*-hydroxysuccinimide, Figure 5b) are covalently attached to its lysine residues. The DBCO-NHS molecule is commercially available and possesses two key functional groups: a reactive amino-ester group and a strained alkyne triple bond. On the amino-ester portion of the molecule, the condensation reaction with the $-NH_2$ group of a lysine residue side chain of albumin is performed (*Scheme 1*). In such manner albumin-DBCO is formed, the standard platform which is further functionalized by exploiting the reactive, strained alkyne group of DBCO. In this case, the strain-promoted alkyne-azide cycloaddition (SPAAC) was employed, a common click-chemistry reaction in which the azide group rearranges with the alkyne's triple bond to form a triazole ring (*Scheme 2*). Generally, the alkyne-azide cycloaddition requires a metal ion catalyst such as Cu^{2+}; in this case however – due to the strain of the cyclooctyne ring – the click reaction proceeds catalyst-free.

Thus, in our case both the radioprobe and the targeting peptide were functionalized with an azide group for allowing conjugation to the DBCO units. To be noted that the presence of numerous binding sites on albumin allows a large loading of targeting vectors and radioactive payloads, potentially leading to an amplified effect compared the single radioprobe (higher tumor-to-background ratio).

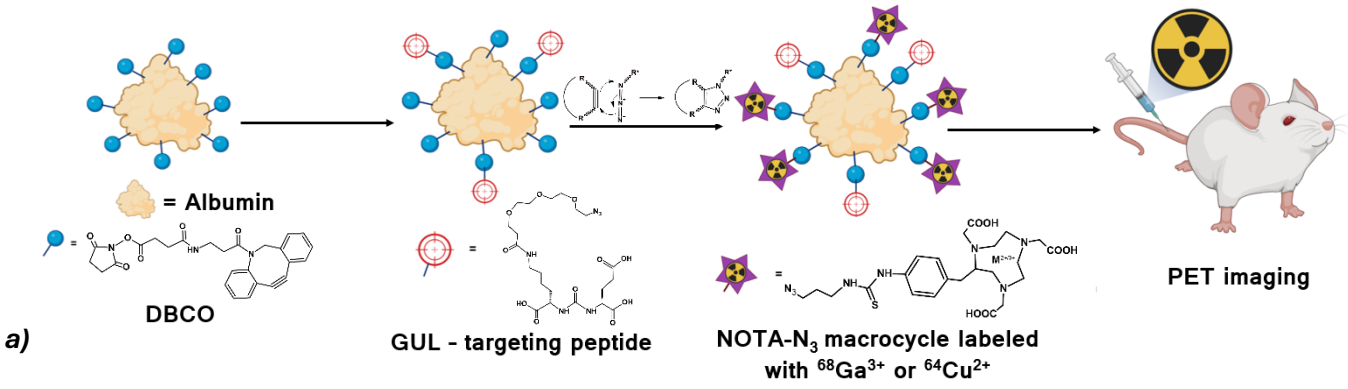

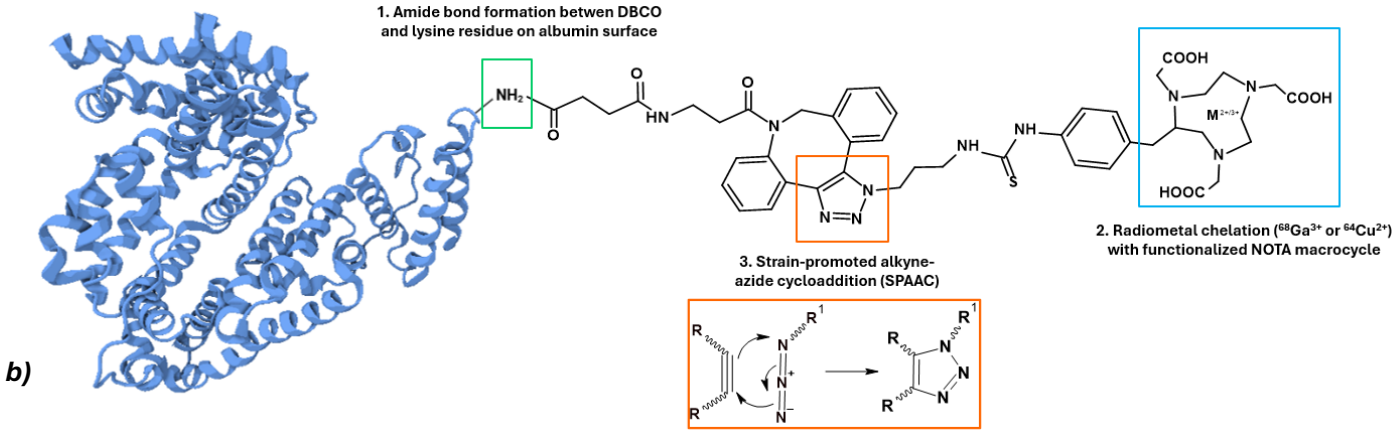

Figure 5. a) Schematic experimental procedure from the functionalization of HSA to PET imaging studies and **b)** HSA functionalized with a Dibenzocyclooctyne-*N*-hydroxysuccinimide (DBCO-NHS) linker molecule which bears a reactive ester group for condensation with lysine aminoacids (green frame), and a strained alkyne for click chemistry with an azide (orange frame).

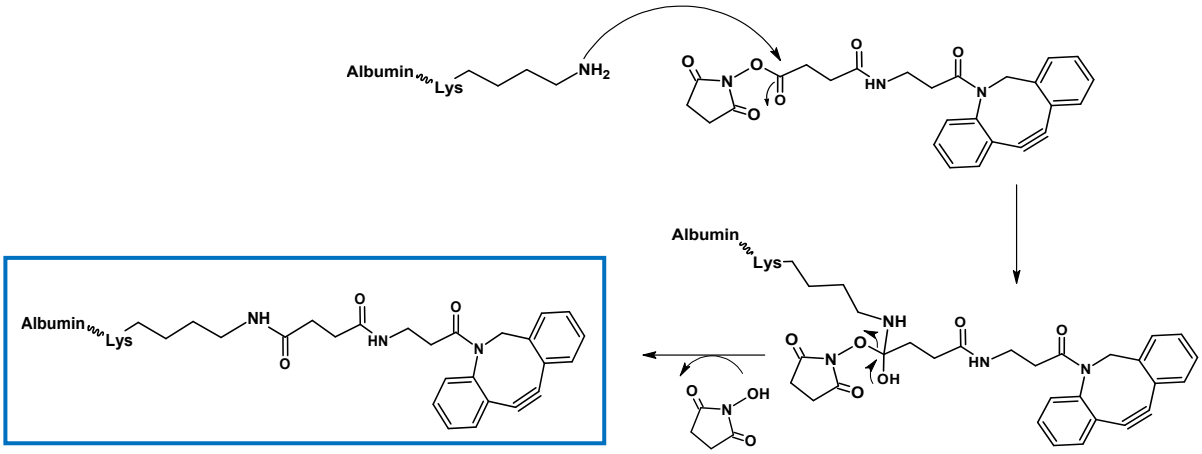

Scheme 1. The functionalization mechanism of albumin with the DBCO linker molecule. It involves the formation of an amide bond with the $-NH_2$ group located on a lysine residue side chain, the most widespread aminoacid on albumin's surface; the species in the blue frame is the end-product of the reaction after elimination of the −NHS leaving group.

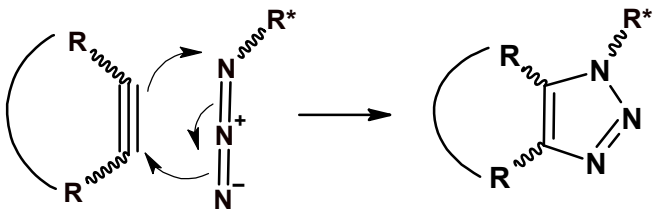

R* = targeting vector and/or radiometal complex

Scheme 2. Simplified reaction scheme of the cycloaddition between the strained alkyne of DBCO and the azide group of R*, which can be either a radioactive moiety (payload) or a targeting peptide.

In the second step, the targeting vector was covalently attached to some of the DBCO residues on the functionalized HSA. In this study, the GUL peptide was the selected targeting vector for prostate cancer receptors as in PSMA-11. However – unlike in PSMA-11 – the chosen linker is a short polyethylene glycol (PEG) moiety functionalized with the aforementioned azide group (*Scheme 3*). While it is obvious that the latter is necessary for the click-chemistry reaction with DBCO on albumin, the PEG fragment was selected due to its biological inertness, *e.g.* resistance to hydrolysis, non-immunogenicity, and well established contribution to increase protein solubility. In previous studies it was found that the optimal length of the PEG fragment corresponds to 2 − 3 units, as using a higher number of PEG units typically causes a decline in cell uptake.[9]

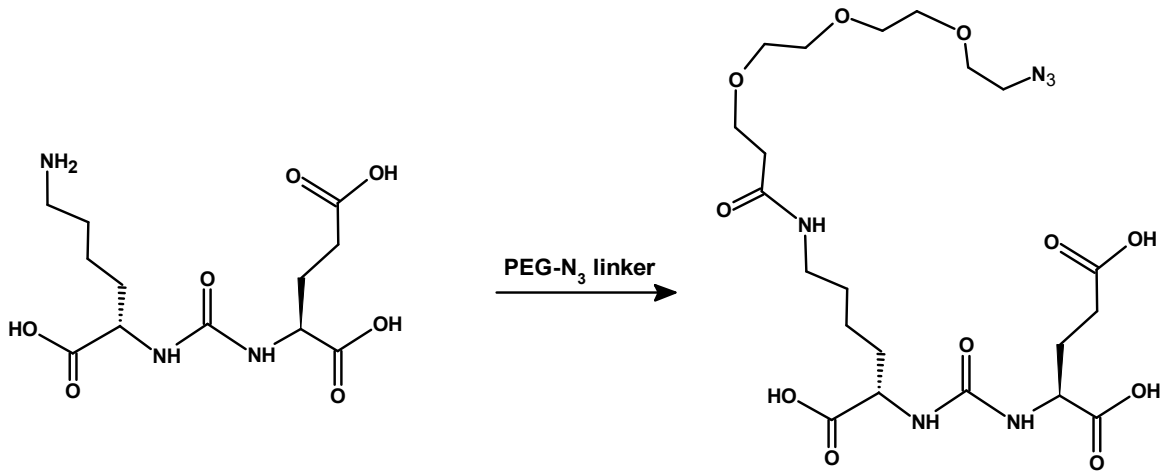

Scheme 3. Glutamate-ureido-lysine (GUL) peptide (left) is connected, through the formation of an amide bond on lysine, with a PEG linker bearing an azide group (right).

In the third and final step the PET radionuclide, the payload, was bound to the remaining DBCO units on the GUL funtionalized HSA. For this purpose, two positron emitter metal ions were selected, namely ^{68}Ga and ^{64}Cu, and both were first inserted into the hexadentate NOTA chelator functionalized with an azide group for DBCO binding (*vide infra*).

The final step was the click chemistry reaction between the formed radiometal-NOTA complex and the DBCO-conjugated albumin, which was conducted at room temperature. In fact, when handling heat-sensitive biomolecules such as proteins, reactions at room temperature are usually preferred, when/if applicable.[10]

Results and discussion

Functionalization of albumin with DBCO and determination of DOF

Considering the abundance of amino groups on the surface of albumin, the first parameter to be taken into account was the optimal number of DBCO moieties to bind to the macromolecule, described by the DOF (degree of functionalization) that gives the average number of DBCO units bound to albumin. An optimal DOF is essential, since it affects both the circulation half-life and biodistribution of the functionalized protein[11] (*vide infra*).

In this study the target DOF was between 8 and 11, as it is considered the optimal number of functionalities for appending molecular probes without changing dramatically endogenous properties of albumin (*vide infra*). In addition, we wanted to improve the conditions, reproducibility, and yield of the reaction as well. Thus, different molar ratios of albumin:DBCO were investigated to achieve a suitable DOF value. The following molar ratios were tested 1:14, 1:15, 1:17, 1:19 and 1:20. Albumin functionalization was performed as detailed in the section „Materials and methods - Albumin conjugation with DBCO-NHS“ (*vide infra*).

UV-Visible spectroscopy and Matrix-Assisted Laser Desorption Ionization Time of Flight (MALDI-TOF MS) spectrometry were employed for determining the number of DBCO units bound to albumin, that provides the degree of functionalization (DOF). Firstly, the UV-Vis spectrum can provide qualitative information owing to the presence of the peak at 312 nm which is specific for the albumin-DBCO conjugate, whereas in the control sample only the characteristic broad peak centered at 280 nm of native albumin is visible (Figure 6). After determining a calibration curve as described in the literature,[12] UV-Vis spectroscopy also enables the determination of DOF by applying the Lambert-Beer law and calculating the ratio between the molar concentrations (*i.e.* ratio of absorbance and molar extinction coefficients) of DBCO-functionalized and native albumin, with the inclusion of an empirically determined correction factor of 0.8658.[12]

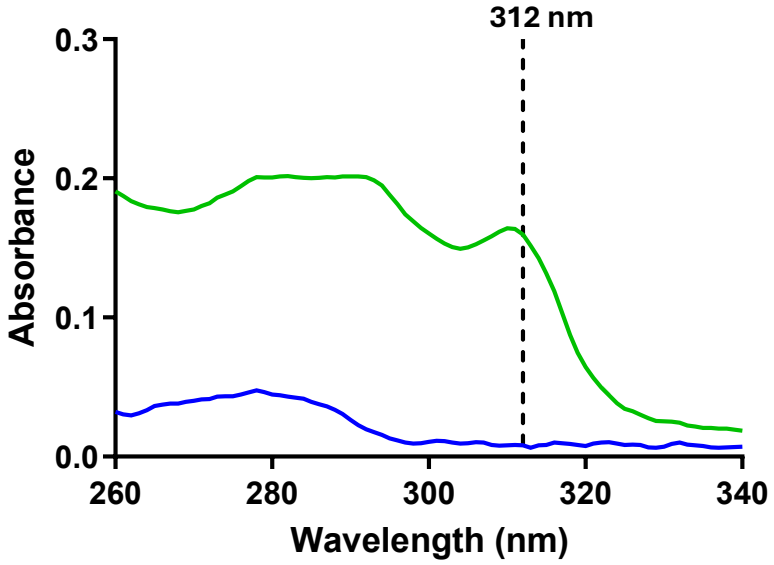

Figure 6. UV-Vis spectrum of native albumin (blue) and albumin functionalized with DBCO (green) with its distinctive peak at 312 nm, absent in the control sample.

On the other hand, MALDI-TOF MS is well-known for its sensitivity and provides a simpler and more accurate way to evaluate quantitatively the degree of functionalization that requires no calibration curve. In fact, determining the DOF is straightforward since, in principle, it consists in calculating the difference between the average mass (*i.e.* the peak centroid) of the functionalized product and that of the initial native albumin, divided by DBCO's molecular weight (Figure 7). Obviously, a prerequisite is to know the chemistry and reaction mechanism that leads to the product of interest. For instance, in the specific case, the functionalization of each lysine of albumin with the DBCO molecule involves the release of an *N*-hydroxysuccinimide (−NHS) group (*vide supra*, *Scheme 1*). Hence, the mass of NHS has to be subtracted from the mass of the DBCO moiety before calculating the DOF (*Eq. 1*).

$$DOF_{(DBCO)} = \frac{MW_{albumin:DBCO} - MW_{albumin}}{MW_{DBCO:NHS} - MW_{NHS}} \qquad Eq.\ 1$$

Given the simple and straightforward MALDI-TOF MS methodology that does not require additional calculations or calibration curves, the latter was chosen as the preferred and standard method.

It was found that the stoichiometry of DBCO should be at least 15 times that of albumin in order to obtain a favourable degree of functionalization (DOF = 8-11). Each experiment/ratio was repeated several times, affording a slight, yet significant, variation in the DOF that might depend on the incomplete dissolution of the reactants, despite the prolonged sonication of albumin in PBS 1x buffer and DBCO in DMSO.

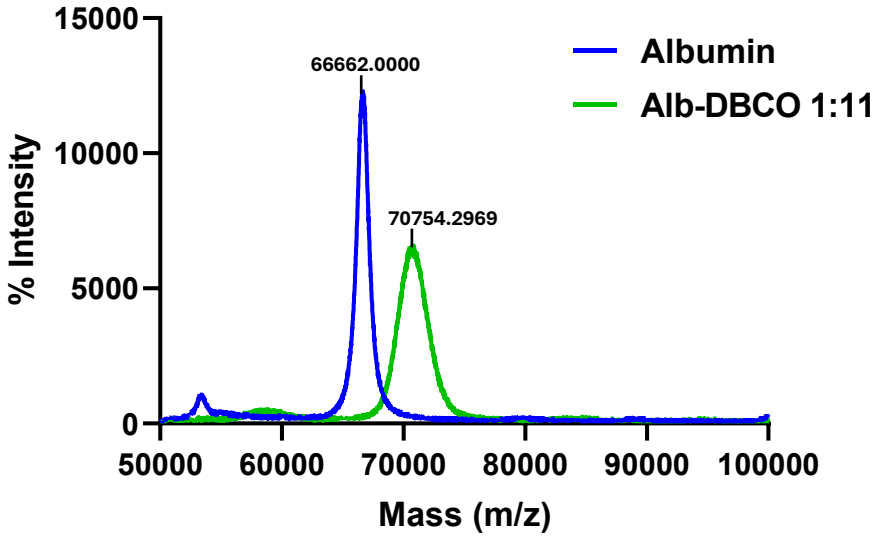

Figure 7. MALDI-TOF spectrum of native albumin (*blue*) and albumin functionalized with DBCO (*green*) to evaluate the average number of bound DBCO units (11 in this case). The number above each peak indicates the respective average (centroid) mass.

Binding of the GUL targeting vector

The binding of the targeting peptide GUL to albumin-DBCO was performed as detailed in „Materials and methods - Albumin conjugation with GUL targeting vector“ (*vide infra*).

The DBCO[11]-GUL conjugation was qualitatively followed through the UV spectra, since the increase of bound GUL units translates into a decrease of the characteristic albumin-DBCO absorbance at 312 nm, due to the fewer available DBCO sites (Figure 8).

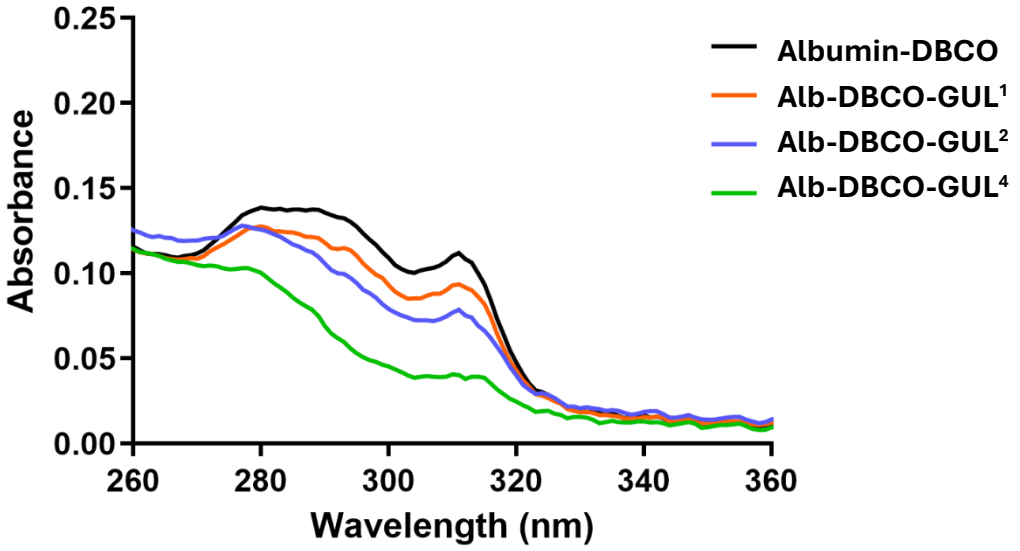

Figure 8. UV-Vis spectra of the pristine albumin-DBCO sample (*black*) and albumin-DBCO functionalized with – on average – one (Alb-DBCO-GUL^1 orange), two (Alb-DBCO-GUL^2 blue), and four units of GUL (Alb-DBCO-GUL^4 green). The distinctive peak at 312 nm decreases as the number of GUL peptides increases and that of free DBCO units correspondingly decreases.

Also in this case a quantitative assessment to determine the average number of GUL units present on the albumin was done through MALDI-TOF MS experiments. A first set of MALDI-TOF MS experiments was performed on each sample of DBCO-functionalized protein to determine the DOF. Then, a subsequent round of measurements was performed after carrying out the functionalization with GUL (Figure 2, Table 1). Each GUL unit leads to an increase of molecular mass of 545.5 Da and the calculation was done similarly as in the case of DBCO, by subtracting the mass of the control sample from the product and dividing the obtained value by the mass of GUL (*Eq. 2*).

$$DOF_{(GUL)} = \frac{MW_{albumin:DBCO:GUL} - MW_{albumin:DBCO}}{MW_{GUL}} \qquad Eq.\ 2$$

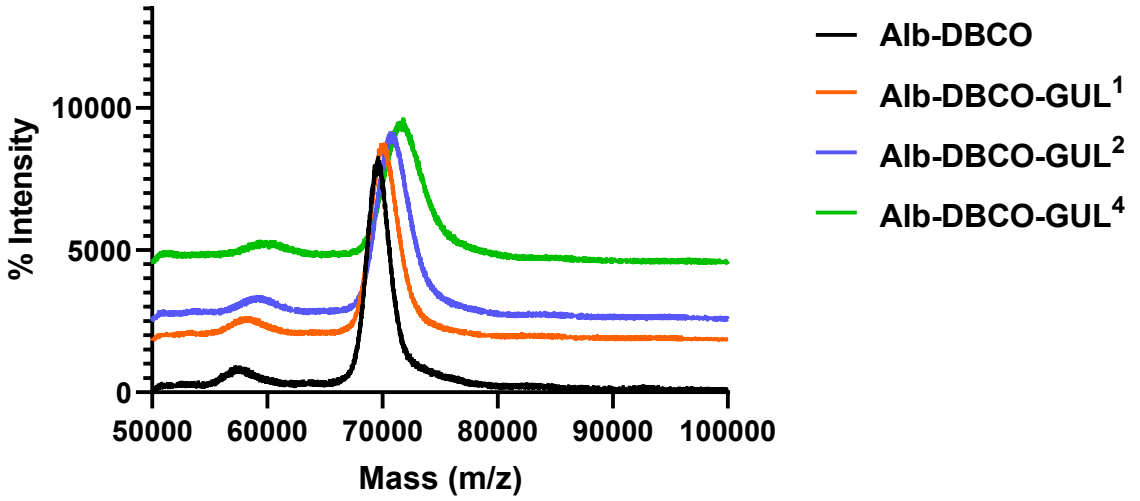

Figure 9. MALDI-TOF spectra of the pristine albumin-DBCO sample (*black*) and albumin-DBCO functionalized with – on average – one (Alb-DBCO-GUL^1 orange), two (Alb-DBCO-GUL^2 blue), and four units of GUL (Alb-DBCO-GUL^4 green).

Table 1. MALDI-TOF determined average mass for pristine albumin-DBCO and Alb-DBCO-GUL$^\times$, where $\times = 1, 2, 4$.

Sample	*Average mass (m/z)*
Albumin-DBCO	69640.9844
Alb-DBCO-GUL^1	70127.4375
Alb-DBCO-GUL^2	70892.5078
Alb-DBCO-GUL^4	71765.1094

The albumin-DBCO-GUL products obtained from the coupling process will be further functionalized with the radioactive NOTA fragment (*vide infra*).

Size, zeta potential and polydispersity index of the functionalized albumin platforms

Albumin is a globular protein with a characteristic size, between 6 and 8 nm of diameter, which may vary slightly in the presence of attached functional groups. Generally, the size of proteins depends on concentration, solvent composition, and temperature. A fine balance between preserving the native protein's characteristics and modifying them according to the desired requirements is needed to engineer an efficient targeted macro-vector for imaging/therapy. If the functionalization of the biomolecule is excessive, it could behave *in-vivo* as a hapten, *i.e.* a large carrier (*e.g.* protein) that upon binding one or more small molecules forms an adduct capable of inducing an immune response in the organism.[13] The severity of immunogenicity

is highly individual and varies widely, from mild allergic reactions to extreme, fatal cases. Conversely, a too mild functionalization might produce an ineffective targeting cargo that will not exert a sufficient therapeutic effect. Moreover, taking into account also the effect of the bound radioactive probe, insufficient targeting properties might lead to accumulation and damage in non-targeted, healthy tissues.

With the purpose of determining the size of the functionalized albumin, Dynamic Light Scattering (DLS) experiments were performed. It was observed that the size of the functionalized protein remained in the standard range below 10 nm, regardless of the functionalization. In fact, when going from native albumin to albumin-DBCO and then increasing the number of GUL units from Alb-DBCO-GUL^{1} to Alb-DBCO-GUL^{5}, no substantial change in dimensions was observed. Upon covalently binding DBCO and GUL an increase in the polydispersity of albumin was measured (Figure 10 and Table 2), which is reasonable considering there is a loss in homogeneity due to the increase of possible combinations of adducts, compared to the native protein. The zeta potential, a parameter describing the surface charge of the protein, was found to be negative, with values decreasing from −12.8 ± 5.93 mV (native albumin) to an average of −18.6 ± 5.56 mV for Alb-DBCO and Alb-DBCO-GUL$^{1\text{-}5}$ (Figure 10 and Table 2). This parameter is crucial for estimating the stability of the particles, especially in terms of tendency to form aggregates. Generally, a standard accepted value associated to stable particles is approximately −30 mV, considering that the higher the charge of the particles the larger is their mutual repulsion. Therefore, values above −30 mV, in the range −11 to −20 mV are still considered acceptable even though closer to the threshold of agglomeration.

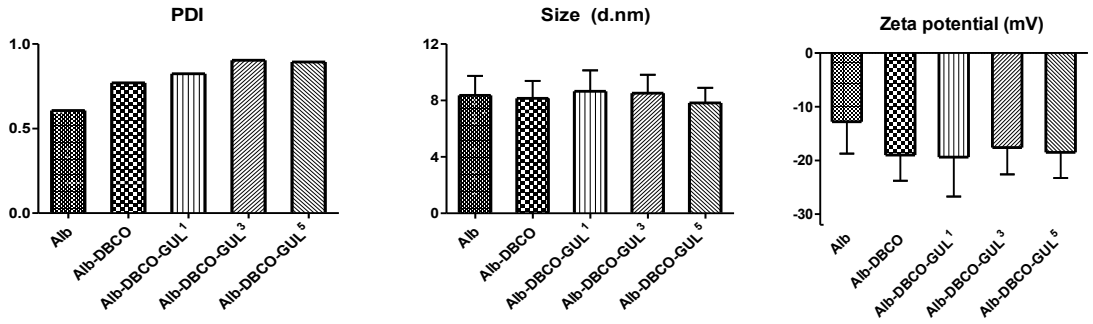

Figure 10. Histograms of the polydispersity index, size and zeta potential of pristine albumin and functionalized albumin derivatives determined through light scattering experiments.

Table 2. Size, zeta potential and polydispersity index (PDI) of pristine albumine and functionalized albumin derivatives determined through light scattering experiments.

Sample	PDI	Size (*d, nm*)	Zeta potential (*mV*)
Albumin	0.607	8.364 ± 1.385	-12.8 ± 5.93
Alb-DBCO	0.770	8.147 ± 1.241	-19.0 ± 4.78
Alb-DBCO-GUL^1	0.824	8.655 ± 1.476	-19.4 ± 7.33
Alb-DBCO-GUL^3	0.904	8.519 ± 1.307	-17.6 ± 5.01
Alb-DBCO-GUL^5	0.894	7.823 ± 1.078	-18.5 ± 4.77

Additional DLS measurements were not performed after click-chemistry with the NOTA-N_3 macrocyle since it is a relatively small fragment compared to the multiple attached DBCO-GUL moieties, hence it was the assumed that its effect on the macro-vector's size is negligible.

The PET probe

As mentioned in the Introduction, the two positron emitter metal ions ^{68}Ga and ^{64}Cu were selected for this study. They significantly differ from each other, both in terms of chemical and radioactive features. In fact, the gallium ion, characterized by a single oxidation state 3+, is a typical hard ion, whereas the copper ion has two accessible oxidation states, 1+ and 2+, which have significantly different properties not only compared to Ga^{3+} (*e.g.* charge, size) but also to one another as well (charge, size, hard-soft features, preferred coordination number and geometry). For example, the ionic radius of Ga^{3+} is 0.62 Å vs 0.73 Å for Cu^{2+}, which in turn is slightly smaller than Cu^{+} (0.77 Å).[14]

In this project, the relatively small hexadentate NOTA macrocycle (Figure 11a) was considered a suitable choice for both metal ions that, from previous studies, were found to form octahedral complexes with it.[15] However, literature data for Cu^{2+} (configuration d^9) suggests that an additional distorted-trigonal-antiprismatic coordination, caused by the Jahn-Teller effect, can be found with NOTA, and was previously characterized.[15] Nonetheless, the NOTA complex with Cu^{2+} has a high thermodynamic stability (log$K$ = 23.3) and kinetic inertness at physiological conditions, undergoing decomplexation only at strongly acidic pH values. Moreover, NOTA and its derivatives became the standard choice when it comes to copper ion complexation also because of their resistance to reduction to Cu^{+} species, which occurs with complexes bearing other types of macrocycles (*e.g.* cyclams).[15] *In-vivo* it is common to have local fluctuations of protons (*e.g.* intra- *vs* extra-cellular environment), with regions of higher and lower concentration, establishing proton gradients. In such cases it is possible that the proton competes for the macrocycle, causing decomplexation and subsequent release of the metal ion. Other scenarios in which a metal complex could be susceptible to decomplexation include trans-metallation reactions with other biologically present metal ions such as Zn^{2+} or Cu^{2+} (*Eq.* 3), or trans-chelation reactions with biologically relevant chelates such as transferrin,

the iron(III)-transport protein which has a high affinity also for Ga^{3+} and other 3+ hard metal ions (*Eq*. 4). Previous studies showed that, surprisingly, the trans-metallation rate for the Cu^{2+}-NOTA complex was extremely slow with Zn^{2+} due to the formation of a stable dinuclear intermediate.[16] As for trans-chelation reaction, Ga^{3+} was found to form with NOTA an even more thermodynamically stable complex than Cu^{2+} (log K = 29.6), which is also several orders of magnitude more stable than the Ga^{3+} complex with transferrin (log K = 20.3).[17] It was shown that this complex dissociates solely in highly acidic conditions, hence showing resistance to trans-chelation as well.[18][19]

$$\mathbf{ML} + \mathbf{*M^{2+}} \rightleftharpoons \mathbf{M^{z+}} + \mathbf{*ML} \quad (\mathbf{*M^{2+}} = \text{endogenous competing metal ion}) \qquad (Eq.\ 3)$$

$$\mathbf{ML} + \mathbf{E} \rightleftharpoons \mathbf{ME} + \mathbf{L} \quad (\mathbf{E} = \text{endogenous competing ligand}) \qquad (Eq.\ 4)$$

Even though the two metal radioisotopes share the same decaying mode, their radiochemical profiles are quite different in terms of half-life, which is quite short for gallium-68 ($t_{1/2}$ = 68 min) and much longer for copper-64 ($t_{1/2}$ = 12.7 h).

In Figure 11b the general structure of the metal complexes with the terminal azide group that undergoes click-chemistry with the DBCO moiety of albumin platforms is shown. The NOTA chelator functionalized with a short benzylthiourea propylazide linker is commercially available and presents optimal properties in terms of solubility and length. Moreover, the linker molecule is bound to a carbon atom and does not affect the binding of the metal ion, considering that all the donor heteroatoms are still available for coordination. The azide-functionalized NOTA chelator is used in excess and undergoes radiolabeling with the mentioned PET metal radiotracers at relatively high temperatures (70 °C) to increase the efficiency of the complexation. In fact, the major setback of macrocycles is the slower complexation kinetics compared to their linear counterparts, thus using a heating source for short time intervals is common practice and often required.

In the final step, the radioactive fragment was bound to the albumin-DBCO-GUL carrier via SPAAC reaction with the DBCO triple bond (Figure 11c). The conjugation was performed for one hour at room temperature using a 20-fold excess concentration of albumin-DBCO with respect to the radiometal complex. The reaction time is a crucial parameter, as the duration of the reaction should be long enough to ensure a good radiolabeling efficiency, but also relatively brief to preserve a substantial radioactivity. This is especially important when operating with gallium-68 given its limited half-life ($t_{1/2}$ = 68 min).

The above-mentioned reactions were monitored through radio-iTLC-SG experiments.

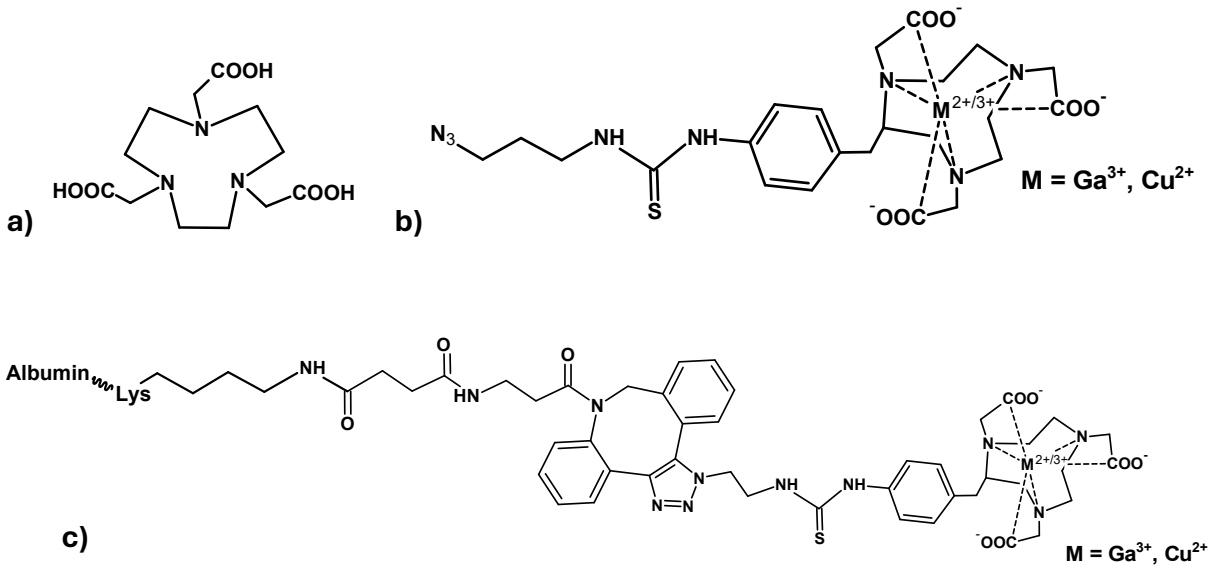

Figure 11. Structure of **a)** NOTA, **b)** functionalized NOTA-N_3 complex with PET imaging radionuclides $^{68}Ga^{3+}$, $^{64}Cu^{2+}$ and **c)** the radio-labeled NOTA complex conjugated to the albumin-DBCO carrier.

Determination of radiochemical purity and efficiency by radio-iTLC-SG

To monitor the formation of the radiometal complexes, radio instant thin-layer chromatography on silica gel (radio-iTLC-SG) experiments were conducted. Radio-iTLC requires a detector capable of identifying radioactive species, which in this case was a proportional counter. This is a type of gaseous ionizing detector which typically uses Ar or a mixture of Ar and CH_4 that once ionized by radiation, produces a detectable current each time an ionizing event occurs. Similarly to standard thin-layer chromatrography, the choice of the mobile phase to elute the radiochemical species on silica gel is fundamental. When working with radioactive species, commonly used eluents are aqueous solutions of inorganic salts or organic acids, such as sodium carbonate or citric acid.[20]

In the first step, the free metal ions were eluted from the generator with 0.1 M HCl, hence the respective chloride salts ($^{68}GaCl_3$ or $^{64}CuCl_2$) were analyzed first. The solutions obtained in such manner typically had a radioactivity in the range of 3 – 6 mCi which corresponds to a concentration of roughly 15 – 30 nmol. Moreover, since the metal ions were initially in acidic conditions, their pH was adjusted by adding sodium acetate buffer to set the pH in the range of 4 − 5 and ensure an efficient complexation with NOTA. After the dilution with the buffer, the radiometal ion solution had a radioactivity in the range of 0.2 – 1 mCi (ca. 1 – 5 nmol).

The radio-iTLC-SG experiments performed on the NOTA radiometal complexes with ^{64}Cu@NOTA and ^{68}Ga@NOTA, as well as on the ^{64}Cu@NOTA-albumin-DBCO, ^{68}Ga@NOTA-albumin-DBCO and ^{68}Ga@NOTA-albumin-DBCO-GUL adducts, enabled us to estimate the efficiency of the radiolabeling process. The albumin-DBCO-GUL adducts were not labelled with $^{64}Cu^{2+}$ due to technical issues with the cyclotron. We found that 0.1 M citric acid was a suitable eluent since it provided a distinct separation between the free radiometal

ions (R_f = 0.55 – 0.70, Figure 12 a, d) and their respective complexes ^{64}Cu@NOTA-N$_3$ (R_f = 0.35 − 0.45, Figure 12b) and ^{68}Ga@NOTA-N$_3$ (R_f = 0.30 – 0.50, Figure 12e).

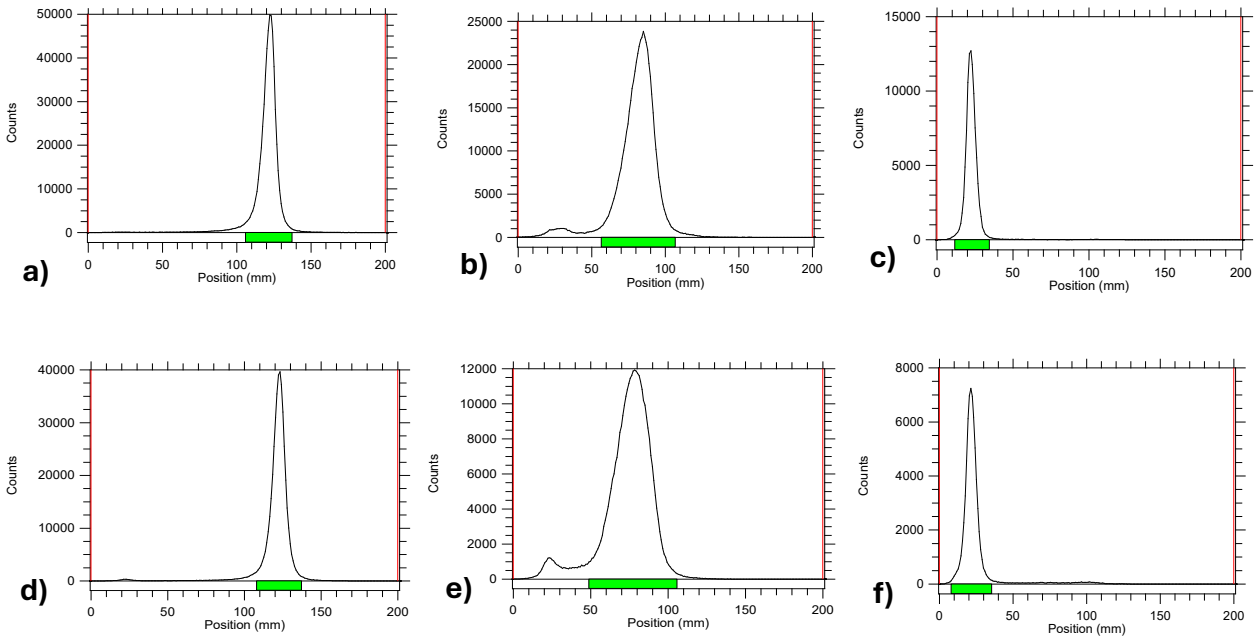

Figure 12. Radio-iTLC-SG of **a)** ^{64}CuCl$_2$ (peak with R_f = 0.55 − 0.70), **b)** ^{64}Cu@NOTA-N$_3$ (peak with R_f = 0.30 – 0.55), **c)** ^{64}Cu@NOTA-Alb-DBCO (peak with R_f = 0.10 − 0.15), **d)** ^{68}GaCl$_3$ (peak with R_f = 0.55 − 0.70), and **e)** ^{68}Ga@NOTA-N$_3$ (peak with R_f = 0.25 − 0.50), and **f)** ^{68}Ga@NOTA-Alb-DBCO (peak with R_f = 0.10 − 0.15).

From the radio-iTLC-SG experiments, it can be observed that both metal ions exhibited similar behaviours during labeling, *i.e.* in the chloride salt form they appear as sharp peaks with higher retention factors, while after the complexation with NOTA they migrate more slowly and appear as broader peaks with lower retention factors. Finally, after labeling albumin-DBCO with either ^{64}Cu@NOTA or ^{68}Ga@NOTA a sharp peak close to the origin was observed (Figure 12c, f), reiterating the analogous behaviour of both radiometal ions in these systems.

The subsequent radio-iTLC-SG experiment consisted in determining the radiolabeling efficiency of the albumin-DBCO-GUL macrovectors. Radiolabeling experiments with ^{68}Ga@NOTA-N$_3$ were performed on albumin-DBCO-GUL^1, albumin-DBCO-GUL^2, and albumin-DBCO-GUL^4. In Figure 13 the comparison between the left (Figure 13a, c, e) and right column (Figure 13b, d, f) shows the effect of the reaction time on the labeling process (30 min *vs* 1 h), whereas each row corresponds to an albumin-DBCO-GUL macrovector with a different DOF for GUL (from 1 to 4), showing how the radiolabeling is affected by the number of GUL moieties present on the albumin macrovector. In fact, as the number of GUL increases, the radiolabeling rate decreases, because fewer triple bonds of DBCO are available to react with the azide group of the ^{68}Ga@NOTA-N$_3$ complex. This was clearly seen especially for ^{68}Ga@NOTA-Alb-DBCO-GUL^4, where only 46% of the albumin was radiolabeled after 30 minutes (Figure 13e). A similar, but less evident behaviour, was observed for ^{68}Ga@NOTA-

Alb-DBCO-GUL[2], where the radiolabelling efficiency was at 83% after 30 min (Figure 13c). Given the slower rate of radiolabeling for multi-GUL platforms, all samples were left to react for additional 30 minutes. After this period, a subsequent radio-iTLC-SG analysis was performed, confirming the progression of the radiolabeling process (Figure 13d, f) with increased efficiencies up to 94-97%. In contrast, the mono-GUL platform labeling efficiency was since the beginning much higher and did not change significantly over time, 96% and 98% after 30 and 60 min, respectively (Figure 13a, b).

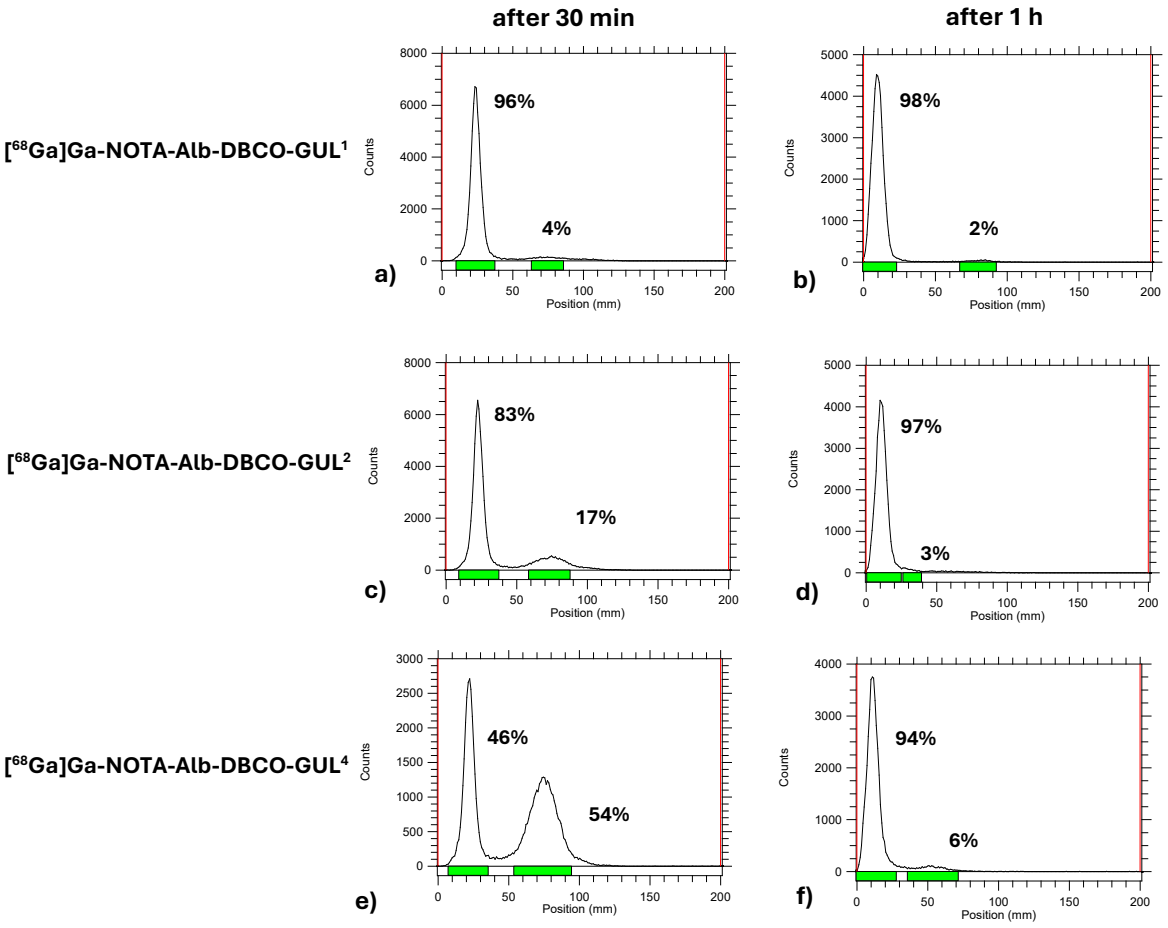

Figure 13. Radiolabeling of functionalized albumin with ^{68}Ga@NOTA (peak with $R_f = 0.10 - 0.15$) after 30 minutes (left column, *a, c, e*) and 1 hour (right column, *b, d, f*). In each figure the peak with $R_f = 0.35 - 0.45$ (that decreases with the reaction time) corresponds to the unbound ^{68}Ga@NOTA-N_3 complex.

After the radiolabeling (1 h), an additional step was performed, which consisted in a rapid one-minute centrifugation on Amicon® ultra filters (30 kDa Molecular Weight Cut-Off) to isolate the functionalized albumin molecules and remove any possible low-molecular weight fragments (Figure 14). As a result, the only functionalized albumin sample displaying a slightly less efficient purification was Alb-DBCO-GUL[4], with some of the remaining NOTA complex still present after centrifugation (Figure 14d).

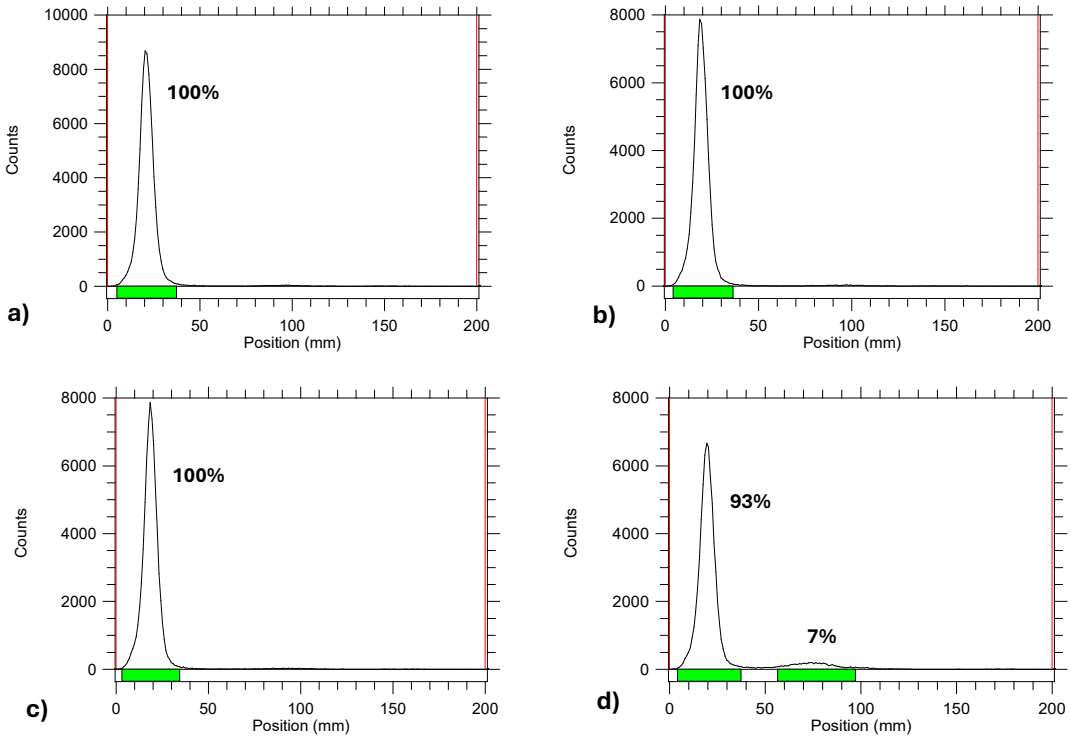

Figure 14. Radio-iTLC-SG after purification of $^{68}Ga^{3+}$-functionalized albumin radioprobes – *a)* ^{68}Ga@NOTA-Alb-DBCO, *b)* ^{68}Ga@NOTA-Alb-DBCO-GUL^{1}, *c)* ^{68}Ga@NOTA-Alb-DBCO-GUL^{2}, *d)* ^{68}Ga@NOTA-Alb-DBCO-GUL^{4}.

In-vivo PET imaging studies of radiolabeled albumin platforms

Furthermore, the synthesized and radiolabeled albumin platforms were tested *in-vivo* by the Seoul National University nuclear medicine team to observe the accumulation and circulation time in normal healthy mice. For the animal imaging studies, it was of interest to determine the biodistribution of the radioprobe in time, hence the PET scans of four time points were collected. The first point was taken right after the intravenous tail injection, followed by imaging after 4, 8 and 24 hours. Given that both radioisotopes ^{68}Ga and ^{64}Cu exhibited the same behaviour during radiolabeling experiments with comparable radiochemical purity, $^{64}Cu^{2+}$ was chosen for the animal experiments mainly for its convenient, longer half-life (12.7 h). From the recorded PET images shown in Figure 15, an initial circulation of the radioprobe in the heart and blood vessels was observed, visible as green and yellow zones in the image. After four hours there was a significant accumulation predominantly in the kidneys and liver, which is expected considering that the liver is the main organ for metabolizing exogenous substances and the kidneys are key components for renal clearance.[21] In the PET scan after eight hours, an overall decrease of the signal intensity due to the decay of the β^{+}-emitter can be observed. It can also be seen that the signal from the GUL-rich platforms is higher compared to the platforms with a single GUL or none. As previous studies suggested, this can be ascribed to the more pronounced alteration of native albumin that can promote the recognition of the labeled macrovectors by the immune system.[12][22] As a consequence, this leads to an accumulation in the liver as opposed to the blood vessels, thus reducing the circulation half-

life. At this time point there is also an increasing accumulation in the bladder, which is a direct consequence of renal clearance that leads to the definite excretion via the urinary tract. Future experiments will involve PET imaging of the albumin radioprobes in patient-derived xenograft mice models and biodistribution studies.

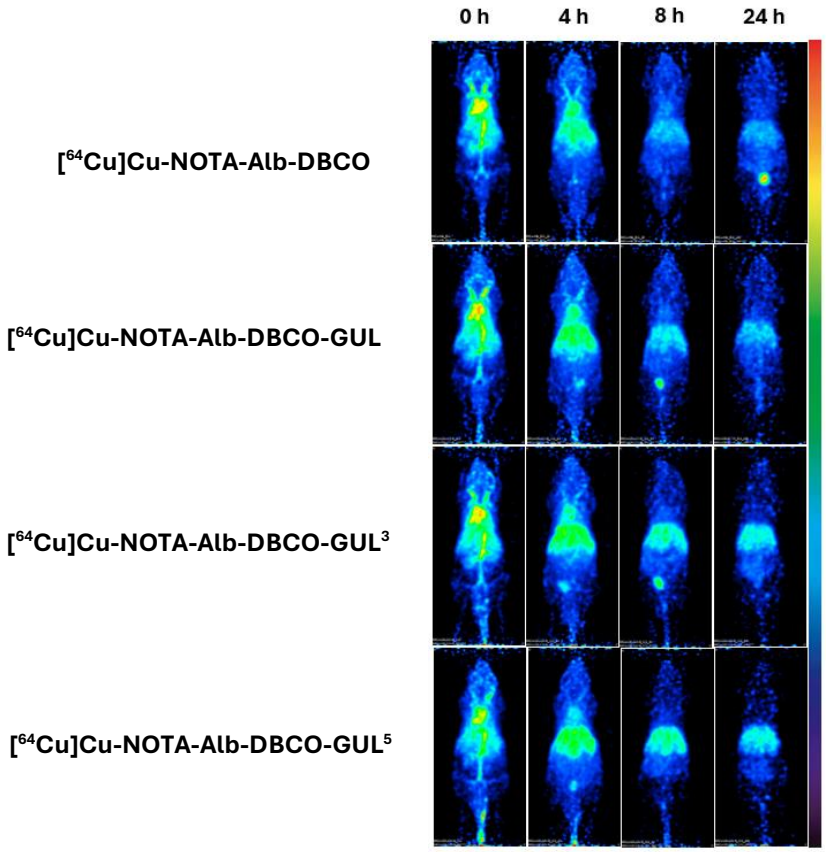

Figure 15. PET scans of ^{64}Cu@NOTA-Alb-DBCO-GUL^{x} (x = 1 – 5) platforms in mice over a 24-hours period.

Conclusions

In this study, albumin–DBCO carriers, capable of binding multiple units of NOTA-based complexes incorporating PET probes ($^{68}Ga^{3+}$ or $^{64}Cu^{2+}$) and the prostate-targeting vector GUL, were synthesized. The carriers were characterized by UV–Vis spectroscopy, which showed the characteristic albumin peak at 280 nm and the albumin–DBCO adduct peak at 312 nm; the latter decreased following GUL conjugation. MALDI-TOF MS was used to precisely determine the ratio between albumin and the conjugated moieties, while DLS provided information on their average size (<10 nm) and on their sufficiently negative zeta potential (−18.6 ± 5.56 mV), which prevents aggregation.

Different albumin:DBCO molar ratios were tested, and ratios in the range of 1:18 – 1:22 were identified as the most suitable for achieving the target DOF of 8 – 11, optimal for conjugating both the azide-functionalized NOTA chelator and the GUL targeting vector. Efficient radiolabeling (≥ 98%) of NOTA with either $^{64}Cu^{2+}$ or $^{68}Ga^{3+}$ was achieved, with both radiometals exhibiting analogous behavior, as confirmed by radio-iTLC-SG.

Additionally, albumin–DBCO:GUL conjugates with variable ratios (1 – 5) were synthesized and radiolabeled with $^{64}Cu^{2+}$ to investigate their biodistribution in mice. PET imaging in healthy mice showed that higher DOFs of GUL led to increased liver accumulation for up to 24 hours. Future work will include PET imaging of these albumin-based radioprobes in patient-derived xenograft mouse models, along with further biodistribution studies.

Experimental Section

Materials and methods

All chemicals were of reagent grade and used without further purification. Reagents azadibenzocyclooctyne NHS ester (DBCO-NHS), 2,2′,2″-(2-(4-(3-(3-azidopropyl)thioureido)benzyl)-1,4,7-triazonane-1,4,7-triyl)triacetic acid (NOTA-N_3), and glutamate-ureido-lysine azide (GUL-N_3) were purchased from FutureChem Co., Ltd (Seoul, Korea). All other reagents and chemicals were provided by Sigma-Aldrich (St. Louis, MO, USA) and used without further purification. Instant thin layer chromatography-silica gel (ITLC-SG) was purchased from Agilent Technologies, Inc. (Santa Clara, CA, USA). All animal PET images were obtained with an eXplore Vista PET/CT scanner (GE Healthcare, Little Chalfont, UK). All animal studies were performed at Seoul National University Hospital (Seoul, Korea) which is fully accredited by AAALAC International (Association for Assessment and Accreditation of Laboratory Animal Care).

Albumin conjugation with DBCO-NHS

The conjugation of DBCO-NHS to albumin occurred via formation of an amide bond between the lysine residues on albumin and the reactive NHS-ester group of DBCO. First, an albumin solution (c = 20 mg/0.5 mL) was prepared and sonicated in phosphate buffered saline (PBS 1x), while preparing a separate solution of DBCO (c = 0.5 mg/µL) in DMSO. Depending on the desired molar ratio (in this work 1:14, 1:15, 1:17, 1:19 and 1:20 were tested) and considering the average volume dilatation of 735 µL upon DMSO addition, a calculated amount of DBCO solution was added. To avoid formation of aggregates, first the albumin solution was placed in a sonicator followed by the slow DBCO addition. The albumin samples with DBCO and the pristine albumin as control sample were then left shaking at room temperature over night. Purification was performed the next day by centrifugating on Amicon® Ultra Centrifugal Filter (30 kDa molecular weight cut-off) at 10,000 rpm for 3 minutes to remove the DBCO in excess. The recovered sample was brought to a final volume of 500 µL with PBS 1x.

Albumin-DBCO conjugation with the GUL targeting vector

In order to conjugate the GUL-azide peptide with a target DOF in the range of 1-5 to albumin-DBCO, four albumin-DBCO solutions in PBS 1x (c = 5 mg/300 µL) were prepared. One of them was used as control sample, whereas the other three were treated with different molar ratios (1:2, 1:6 and 1:12) of a GUL-azide solution (c = 10 nmol/µL) for 6 hours in the dark at room temperature. After the reaction time elapsed, purification on Amicon® Ultra Centrifugal Filter (30 kDa molecular weight cut-off) was performed at 10,000 rpm for 1 minute and the recovered samples brought to a final volume of 500 µL with PBS 1x.

Qualitative UV-Vis and quantitative MALDI-TOF MS analysis

The albumin carriers were analyzed by ultraviolet-visible spectrometry (UV-vis) using NanoDrop® ND-1000 (NanoDrop Technologies, Wilmington, DE, USA). Qualitative UV-Vis spectra were recorded for the albumin-DBCO and albumin-DBCO-GUL samples, by diluting them to a 1 mg/mL concentration in PBS 1x and aliquoting 2 µL of the solution on the measurement pedestal surface. The monitored wavelengths were at 280 nm and 312 nm corresponding to the albumin and albumin-DBCO peak, respectively. All samples were analyzed in triplicate and the average absorbance was considered.

MALDI-TOF MS analysis was performed using the TOF/TOF 5800 system (AB Sciex, Foster City, CA, USA) to determine the DOF of DBCO moieties conjugated to albumin. To prepare the MALDI-TOF sample matrix, an aliquot of albumin solution (10 µL) was mixed with a saturated solution of α-cyano-4-hydroxy-cinnamic acid in a mixture of acetonitrile and water containing 0.1% TFA (1:1 v/v), and each sample (1 µL) was spotted on MALDI plates and allowed to dry at room temperature. Measurements were acquired in linear mode with an accelerating voltage of 25 kV. The analytes were ablated with a 337 nm nitrogen laser. The analysis was performed with 125 scans with 20 laser shots per scan. The molecular weights of

albumin-DBCO and albumin-DBCO-GUL were calculated as the average of the results from 2500 laser shots.

Determination of zeta potential and size of albumin-DBCO-GUL conjugates

The size and zeta potential of the albumin-DBCO-GUL carriers were analyzed using a Dynamic Light Scattering (DLS) Zetasizer Nano ZS90 (Malvern Instruments Ltd, Worcestershire, UK) system. A 10-fold diluted albumin solution (molar range 1 – 10 µM) was prepared for the size measurements using PBS 1x, while the zeta potentials were measured on 100-fold diluted solutions using distilled water (molar range 0.1 – 1 µM) in zeta potential cuvettes.

Production of radioisotopes ^{68}Ga and ^{64}Cu

A total volume of 3 mL of ^{68}Ga radioisotope was eluted with HCl 0.1 M from a ^{68}Ge/^{68}Ga-generator, purchased from Eckert & Ziegler (Eckert & Ziegler EURO-PET Köln/Bonn GmbH, Bonn, Germany). ^{64}Cu was obtained from a cyclotron and received as a $^{64}CuCl_2$ solution, provided by the Korean Institute of Radiological and Medical Sciences (KIRAMS, Seoul, South Korea).

Radiolabeling of NOTA-N_3

The vial containing an HCl solution of ^{64}Cu radioisotope was dried using a stream of nitrogen, while was eluted from a generator as mentioned in *Production of radioisotopes ^{68}Ga and ^{64}Cu* and 900 µL were used for radiolabeling. The pH of the samples were then adjusted to 5 with 100 and 300 µL of sodium acetate buffer for ^{64}Cu and ^{68}Ga, respectively. A solution of NOTA-N_3 (18 nmol/5µL) was added to the radiometal samples and heated at 70 °C for 10 min on a heating block. Radiolabeling efficiency and stability were determined using radio-instant thin layer chromatography-silica gel (radio-iTLC-SG) by spotting the TLC plate with 1 µL of sample and using 0.1 M citric acid as mobile phase. Radioactivity was detected with a proportional counter (DREAM G-10, Shinjin Medics Inc., Korea) using 0.1 M citric acid as mobile phase.

Radiolabeling of albumin-DBCO-GUL with ^{68}Ga-NOTA-N_3

The stock albumin-DBCO-GUL solution was diluted to 1 mg/300 µL with PBS 1x, while the radiometal complex ^{68}Ga-NOTA-N_3 was prepared as mentioned above in *Radiolabeling of NOTA-N_3.* After ensuring successful ^{68}Ga-NOTA-N_3 formation by radio-ITLC-SG monitoring, 0.2 mCi/50 µL of radiometal complex was used to label a 20-fold excess albumin-DBCO-GUL solution (c = 1 mg/300 µL). The radiolabeling efficiency was checked after 30 and 60 minutes again by radio-ITLC-SG, spotting a silica gel TLC plate with 1 µL of sample and using 0.1 M citric acid as mobile phase. Radioactivity was detected with a proportional counter (DREAM

G-10, Shinjin Medics Inc., Korea). Sample purification was performed on Amicon® Ultra Centrifugal Filters (30 kDa molecular weight cut-off) at 10,000 rpm for 3 minutes and volume was adjusted to 200 µL with PBS 1x.

References

(1) Larsen, M. T.; Kuhlmann, M.; Hvam, M. L.; Howard, K. A. Albumin-Based Drug Delivery: Harnessing Nature to Cure Disease. *Molecular and Cellular Therapies* **2016**, *4* (1).

(2) Spada, A.; Emami, J.; Tuszynski, J. A.; Lavasanifar, A. The Uniqueness of Albumin as a Carrier in Nanodrug Delivery. *Molecular Pharmaceutics* **2021**, *18* (5), 1862–1894.

(3) Ji, Q.; Zhu, H.; Qin, Y.; Zhang, R.; Wang, L.; Zhang, E.; Zhou, X.; Meng, R. GP60 and SPARC as Albumin Receptors: Key Targeted Sites for the Delivery of Antitumor Drugs. *Frontiers in Pharmacology* **2024**, *15*.

(4) Zhang, S.; Wang, X.; Gao, X.; Chen, X.; Li, L.; Li, G.; Liu, C.; Miao, Y.; Wang, R.; Hu K. Radiopharmaceuticals and Their Applications in Medicine. *Signal Transduct Target Therapy* **2025**, *10*(1), 1.

(5) Tayyab, S.; Feroz, S. R. Serum Albumin: Clinical Significance of Drug Binding and Development as Drug Delivery Vehicle“ *Advances in Protein Chemistry and Structural Biology* **2021**, 123, 193-218.

(6) Siegel, R. L; Giaquinto, A. N.; Jemal, A. Cancer Statistics. *CA: A Cancer Journal for Clinicians* **2024***, 74*(1), 12-49.

(7) Mehta S., Yang C., Jadvar H., Colletti P. M., Conti P. S., Ma L., Chang E. L., Ye J. C. Advancements and Future Directions in Positron Emission Tomography-Guided Radiotherapy: A Narrative Review“ *Chinese Clinical Oncolology* **2024**, *13*(2):24

(8) Travagin, F.; Lattuada, L.; Giovenzana, G. B. AAZTA: The Rise of Mesocyclic Chelating Agents for Metal Coordination in Medicine. *Coordination Chemistry Reviews* **2021**, *438*, 213908.

(9) Kanellopoulos, P.; Lymperis, E.; Kaloudi, A.; de Jong, M.; Krenning, E. P.; Nock, B. A.; Maina, T. [^{99m}Tc]Tc-DB1 Mimics with Different-Length PEG Spacers: Preclinical Comparison in GRPR-Positive Models. *Molecules* **2020**, *25* (15), 3418.

(10) Mohan, V.; Sengupta, B.; Arusha Acharyya; Yadav, R.; Das, N.; Sen, P. Region-Specific Double Denaturation of Human Serum Albumin: Combined Effects of Temperature and GnHCl on Structural and Dynamical Responses. *ACS Omega* **2018**, *3* (8), 10406–10417.

(11) Chung, H.; Ji Yong Park; Kim, K.; Ran Ji Yoo; Suh, M.; Gyo Jeong Gu; Jin Sil Kim; Tae Hyeon Choi; Jung Woo Byun; Young Wook Ju; Han, W.; Han Suk Ryu; Chung, G.; Do Won

Hwang; Kim, Y.; Kang, H.-R.; Yi Rang Na; Choi, H.; Im, H.-J.; Lee, Y.-S. Circulation Time-Optimized Albumin Nanoplatform for Quantitative Visualization of Lung Metastasis via Targeting of Macrophages. *ACS Nano* **2022**, *16* (8), 12262–12275.

(12) Park, J. Y.; Song, M. G.; Kim, K. W.; Lodhi, N. A.; Choi, J. Y.; Kim, Y. J.; Kim, J. Y.; Chung, H.; Oh, C.; Lee, Y.-S.; Kang, K. W.; Im, H.-J.; Seok, S. H.; Lee, D. S.; Kim, E. E.; Jeong, J. M. Versatile and Finely Tuned Albumin Nanoplatform Based on Click Chemistry. *Theranostics* **2019**, *9* (12), 3398–3409.

(13) Sheedy, C.; MacKenzie, R. C.; Hall, J.C. Isolation and Affinity Maturation of Hapten-Specific Antibodies. *Biotechnology Advances* **2007***, 25*, 333-352.

(14) Tosato, M.; Franchi, S.; Isse, A. A.; Del Vecchio, A.; Zanoni, G.; Alker, A.; Asti, M.; Gyr, T.; Di Marco, V.; Mäcke, H. Is Smaller Better? Cu2+/Cu+ Coordination Chemistry and Copper-64 Radiochemical Investigation of a 1,4,7-Triazacyclononane-Based Sulfur-Rich Chelator. *Inorganic Chemistry* **2023**, *62* (50), 20621–20633.

(15) Kubíček, V.; Böhmová, Z.; Ševčíková, R.; Vaněk, J.; Lubal, P.; Poláková, Z.; Michalicová, R.; Kotek, J.; Hermann, P. NOTA Complexes With Copper(II) and Divalent Metal Ions: Kinetic and Thermodynamic Studies“ *Inorganic Chemistry* **2018**, *57*(6), 3061-3072.

(16) Broan, C. J.; Cox, J. P. L.; Craig, A. S.; Kataky, R.; Parker, D.; Harrison, A.; Randall, A. M.; Ferguson, G. Structure and Solution Stability of Indium and Gallium Complexes of 1,4,7-triazacyclononanetriacetate and of Yttrium Complexes of 1,4,7,10-tetraazacyclo-dodecanetetraacetate and Related Ligands: Kinetically Stable Complexes for Use in Imaging and Radioimmunotherapy. *Journal of the Chemical Society, Perkin Transactions.* **1991***, 2*, 87-99.

(17) Harris, W. R.; Pecoraro, V. L. Thermodynamic Binding Constants for Gallium Transferrin“ *Biochemistry* **1983***, 22*, 292–9.

(18) Seelam, S. R.; Lee, Y. S.; Jeong, J. M. Chelators for 68Ga radiopharmaceuticals“ *Journal of radiopharmaceuticals and molecular probes* **2016**, *2*(1):22-36.

(19) Šimeček, J.; Schulz, M.; Notni, J.; Plutnar, J.; Kubíček, V.; Havlíčková, J.; Hermann, P. Complexation of Metal Ions with TRAP (1,4,7-Triazacyclononane Phosphinic Acid) Ligands and 1,4,7-Triazacyclononane-1,4,7-Triacetic Acid: Phosphinate-Containing Ligands as Unique Chelators for Trivalent Gallium. *Inorganic Chemistry* **2011**, *51* (1), 577–590.

(20) Mutin, J.; Orhon, P.; Choisnard, L.; Lassiaz, M.; Bacot, S.; Ahmadi, M.; De Leiris, N.; Djaileb, L.; Broisat, A.; Ghezzi, C.; Bedouch, P.; Brunet, M.-D.; Leenhardt, J. Validation of HPLC and TLC Analytical Methods to Determine Radiochemical Purity of 99mTc-CAbVCAM1-5, a New Experimental Radiotracer. *Journal of pharmaceutical and biomedical analysis* **2024**, *246*, 116224.

(21) Sarker, A.; Suh, M.; Choi, Y.; Park, J. Y.; Kwon, S.; Kim, H.; Lee, E.; Seo, H.; Lee, Y.-S.; Lee, D. S. [^{64}Cu]Cu-Albumin Clearance Imaging to Evaluate Lymphatic Efflux of Cerebrospinal Space Fluid in Mouse Model. *Nuclear Medicine and Molecular Imaging* **2022**, *56* (3), 137–146.

(22) Gu, G. J.; Chung, H.; Park, J. Y.; Yoo, R.; Im, H.-J.; Choi, H.; Lee, Y.-S.; Seok, S. H. Mannosylated-Serum Albumin Nanoparticle Imaging to Monitor Tumor-Associated Macrophages under Anti-PD1 Treatment. *Journal of Nanobiotechnology* **2023**, *21* (1).

Chapter 4

Synthesis of *macropa*-like macrocycles and their complexes with divalent and trivalent metal ions as models for TAT radiopharmaceuticals

The research described in this Chapter was started during a period of 3 months (at least 6 months abroad are required for PNRR scholarships) in the group of professor Raphaël Tripier at the University of Western Brittany in Brest (France), under the supervision of Dr. Federica Battistin. The remaining work was completed at the University of Trieste, Italy.

Introduction

In the last few years, targeted alpha therapy (TAT) is an emerging therapeutic strategy that combines highly cytotoxic α-emitting radionuclides with selective targeting vectors such as antibodies, peptides, or small molecules.[1,2] Alpha particles release a large amount of energy over only 50 – 100 μm, roughly the size of a few human cells. When this energy is deposited in a tumor cell, it produces severe molecular damage, most notably direct DNA double-strand breaks that cannot be efficiently repaired by the organism.[3] The resulting loss of genomic integrity rapidly compromises the cell viability, leading to apoptosis.[4,5] Because the effectiveness of α-radiation is largely independent of oxygen concentration and proliferation rate, TAT is particularly promising for the treatment of micrometastatic disease and tumors that are resistant to conventional treatments. Aside from the therapeutic radionuclides $^{212}Pb^{2+}/^{212}Bi^{3+}$ discussed in the previous chapter, actinium-225 and radium-223 show great potential for TAT, hence their properties and chelators will be briefly introduced.[6]

Actinium-225

In terms of chemical properties, actinium is generally found in the 3+ oxidation state and is characterized by the largest ionic radius (1.12 Å) among the trivalent *f*-block elements. At pH values slightly above physiological range, it forms hydroxo-species (74% $[Ac(OH)]^{2+}$ and 26% $[Ac(OH)_2]^{+}$, pH = 8).[7][8] Because of the absence of stable actinium isotopes and given the chemical similarities, La^{3+} is often used as a cold analogue of Ac^{3+} to study its properties. Among the various actinium isotopes, ^{225}Ac is considered a promising candidate for radiotherapy due to the stepwise emission of four α particles and two β^- particles throughout its decay, which leads ultimately to the stable isotope ^{209}Bi (Scheme 1). One method for obtaining ^{225}Ac is from a ^{229}Th generator, which in turn is obtained from ^{233}U nuclear fuel.[9] However, to meet the potential future global demand, new methods for ^{225}Ac production are currently being investigated, such as the irradiation of long half-life target radionuclides (^{232}Th

and ^{226}Ra) in accelerators and nuclear reactors.[10] The development of selective chelators for $^{225}Ac^{3+}$ is negatively affected by the decay chain of this nucleide. In fact, during the decay events, two subsequent α emissions generate two nuclei with entirely different chemistry, the short-lived intermediate daughter radionuclides ^{221}Fr ($t_{1/2}$ = 4.9 min, an alkaline metal) and ^{217}At ($t_{1/2}$ = 32 ms, a halogen). Consequently, they are most likely to be released from the ligand designed for the initial parent isotope $^{225}Ac^{3+}$.[11] Furthermore, if the conservation of momentum of the system is considered, the generated recoil energy caused by the alpha emission from ^{225}Ac is several orders of magnitude higher (~100 – 160 keV) than a typical coordination bond (~10 eV), which might cause the release of the recoiling radionuclide and thus undesired radiation in healthy tissues.[12] Nevertheless, its use in TAT is being actively studied and several ^{225}Ac-based radiopharmaceuticals are in clinical trials, namely for neuroendocrine, prostate, breast and blood cancers.[13]

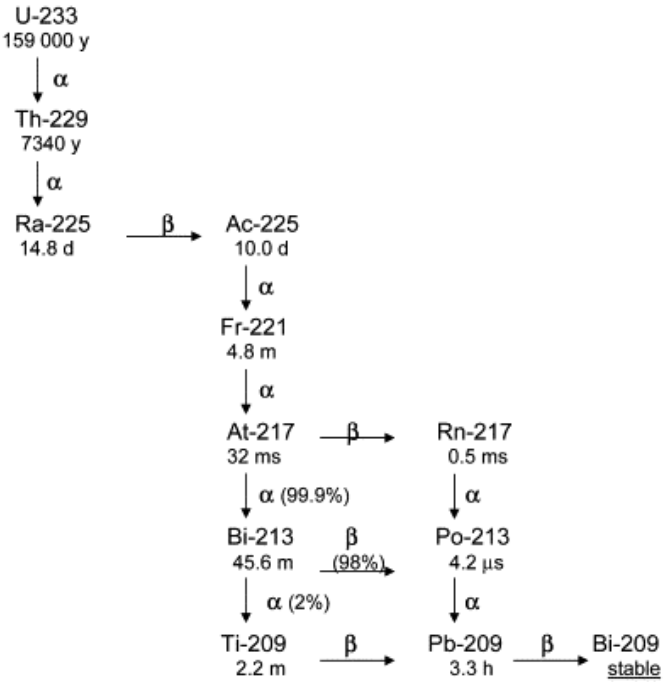

Scheme 1. Decay chain of ^{233}U leading to alpha emitter isotope ^{225}Ac.

Radium-223

Radium is characterized by the largest ionic radius (1.48 Å) among the elements of Group 2, and its predominantly electrostatic coordination behavior makes forming stable complexes particularly challenging. Ra^{2+} exhibits a strong preference for high coordination numbers, typically 8 to 12, and forms predominantly ionic interactions with oxygen-donor ligands. In fact, in terms of ligand affinity, Ra^{2+} shows a marked preference towards hard donor atoms, such as carboxylates, phosphates, and ether oxygens. However, its large size results in low charge density, making its complexes generally more labile and less thermodynamically stable compared to those of smaller alkaline-earth ions such as Sr^{2+} or Ca^{2+}.[14] Moreover, only chelators with very large and flexible cavities that are capable of accommodating its size, can

bind it effectively. This is why Ba^{2+}, the closest non-radioactive analogue in terms of radius and chemical behavior, is often used as a cold surrogate in coordination studies.[15,16] Overall, the combination of large ionic radius, high coordination number, and weak binding strength makes the design of stable Ra^{2+} chelators particularly challenging for radiopharmaceutical applications.

In terms of radiochemical properties, the isotope ^{223}Ra has a relatively long half-life of 11.4 days and undergoes a cascade decay (Scheme 2), emitting four alpha particles and two beta particles, ultimately forming the stable isotope ^{207}Pb. Similar to actinium-225, the fact that ^{223}Ra undergoes four consecutive decays presents a significant challenge in designing chelators capable of forming complexes that retain both the parent isotope, and its radioactive daughter products. Furthermore, during radium-223 decay, radon-219 is formed, and despite its short half-life, a noble gas can easily decoordinate and diffuse throughout the body, potentially increasing the toxicity of radium-based radiopharmaceuticals.

Currently, the only FDA- and EMA-approved radiopharmaceutical based on α-emitting metal ions is the simple radium chloride salt, [^{223}Ra]-$RaCl_2$, used in the treatment of bone metastases.[17,18] Therefore, there is an increasing interest in developing ^{223}Ra-based radiopharmaceuticals for targeted alpha therapy (TAT) to treat other types of cancer. However, this would require not only the identification of suitable targeting vectors, but also the development of chelating ligands capable of complexing Ra^{2+} with sufficient thermodynamic and kinetic stability to minimize its release *in vivo*.[19]

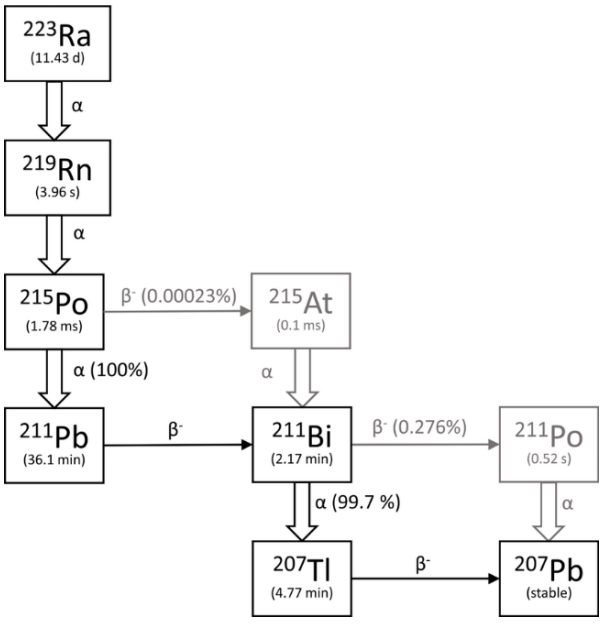

Scheme 2. Decay chain of radium-223.[20]

A series of acyclic and macrocyclic chelators (Figure 1), including DOTA, DTPA, cryptands such as Kryptofix (4,7,13,16,21,24-hexaoxa-1,10-diazabicyclohexacosane), and functionalized calixarenes such as calix[4]arene tetraacetic acid, have been investigated in previous works.[16][20] While DOTA shows a higher affinity for Ra^{2+} (logK = 11.75) than DTPA (logK = 8.78), Kryptofix and calix[4]arene tetraacetic acid form even more thermodynamically stable complexes. However, even these are kinetically labile: for example, 35% of Ra^{2+} is decomplexed from calix[4]arene tetraacetic acid within 10 minutes in water.[21]

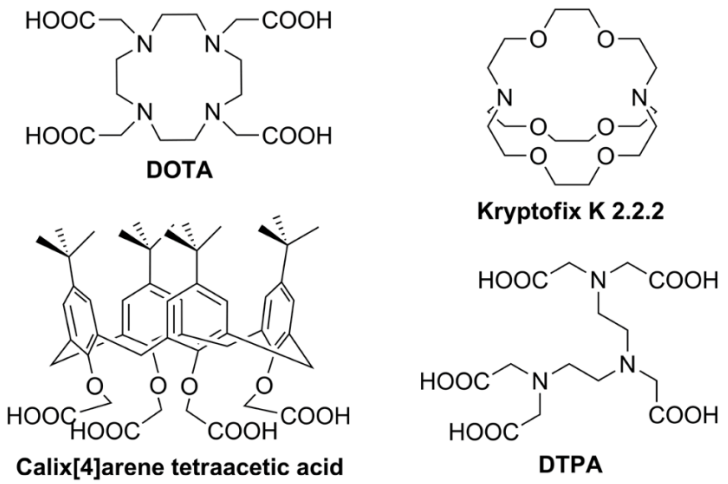

Figure 1. Investigated chelating agents used for ^{223}Ra.[17]

Chelation of large metal ions with *macropa*

A recent breakthrough in the stable chelation of metal ions with large ionic radii involved the development of a decadentate ligand, *macropa*, featuring a functionalized diaza-18-crown-6 core with two picolinate arms.[22] *Macropa* contains four donor atom types − sp^3 amine nitrogens, sp^2 pyridine nitrogens, carboxylate oxygens, and ether oxygens − and coordinates metal ions in its deprotonated dianionic form. It preferentially binds larger ions, such as La^{3+}, Ac^{3+}, and Ba^{2+}, the latter being a cold model for Ra^{2+} due to their similar ionic radii and hard acid characteristics. For example, the [Ba(*macropa*)] complex is characterized by a high formation constant (logK = 10.74, pH = 7.4, I = 0.1 M KCl, 25°C).[23] Moreover, the high affinity of *macropa* for radium was confirmed both by DFT computational studies and experimentally via complexation of $^{223}Ra^{2+}$ at pH = 6, achieving 95% complexation within 5 minutes at room temperature (Figure 2).[23]

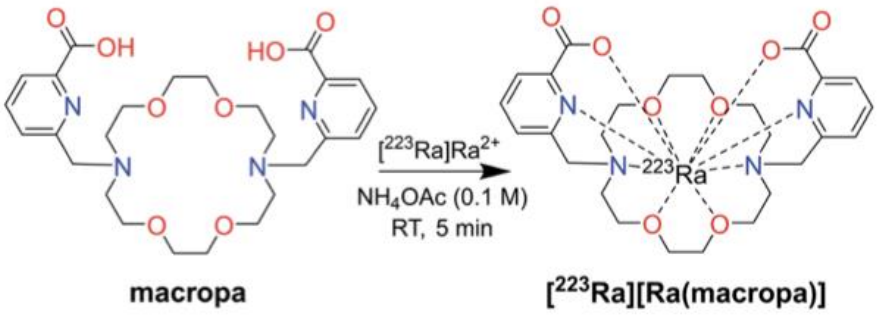

Figure 2. Formation of the [^{223}Ra]-[Ra(*macropa*)] complex.

The [^{223}Ra]-[Ra(*macropa*)] complex exhibits good stability even in biological conditions, with no observed bone uptake, indicating negligible *in vivo* release of Ra^{2+} (Figure 3).[23]

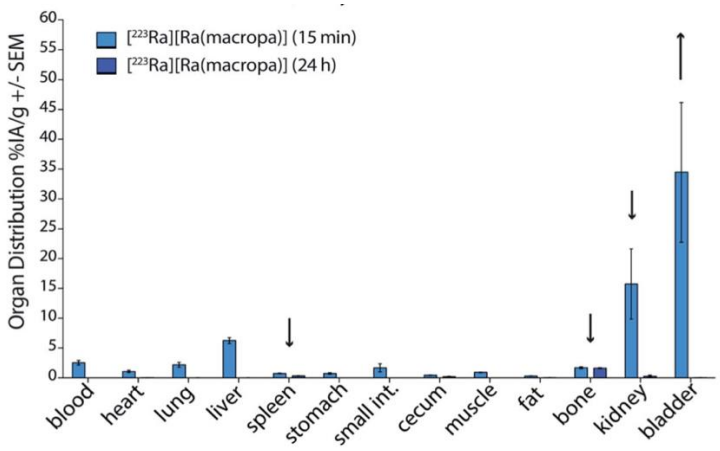

Figure 3. Biodistribution of [^{223}Ra]-[Ra(*macropa*)] after 15 minutes and 1 day.[23]

However, the bioconjugation of *macropa* to a peptide targeting vector through one of its picolinate rings resulted in decreased *in vivo* stability of the radium complex, as indicated by the accumulation of the ion in bone tissue. Specifically, the *macropa* bioconjugate containing the glutamate–urea–glutamate polypeptide (DUPA, Figure 4), which binds efficiently to the prostate-specific membrane antigen (PSMA), produces an *in vivo* Ra^{2+} distribution similar to that observed for $RaCl_2$. This suggests that Ra^{2+} is released, likely due to interactions between the bifunctional chelator and the linker + targeting vector fragment.

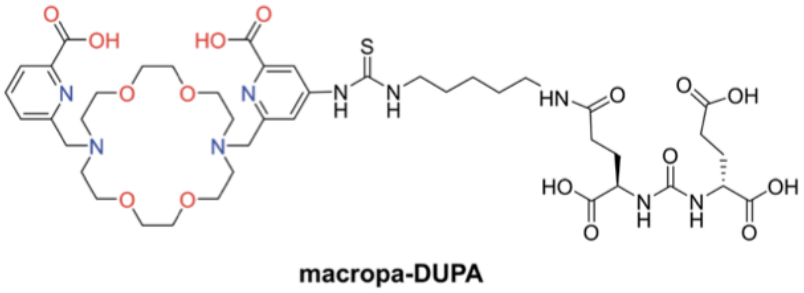

Figure 4. Structure of *macropa*-DUPA.[24]

One possible strategy to improve the chelating properties of *macropa* is to rigidify the macrocycle by introducing aromatic rings, thereby reducing the perturbing effect of the linker + targeting vector on the chelator. This approach was applied to two *macropa* derivatives shown in Figure 5.[24]

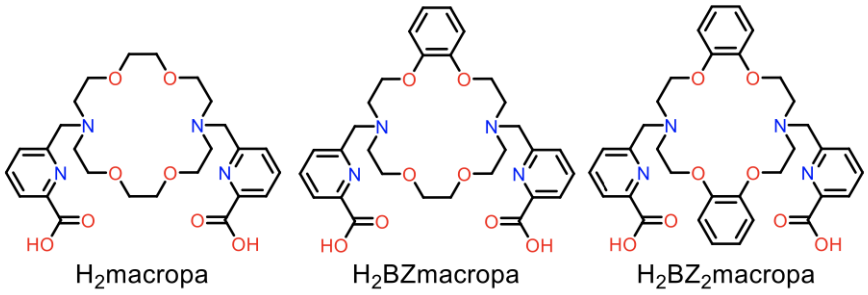

Figure 5. Structure of *macropa*-derived ligands containing one or two benzene rings in the macrocycle.[24]

Surprisingly, the incorporation of benzene rings did not increase formation constants with large metal ions such as La^{3+} ([La(*macropa*)]$^+$ logβ = 14.99; [La(*BZmacropa*)]$^+$ logβ = 13.99; [La(*BZ2macropa*)]$^+$ logβ = 12.04). However, an advantage of bioconjugation via the benzene rings was given by the reduced hydrolysis rates of La^{3+} ($t_{1/2}$ = 56 h in $NaHCO_3$ buffer at pH 9.1, RT) compared to conjugation via the picolinate arm ($t_{1/2}$ = 1.5 h), indicating enhanced kinetic stability upon linker relocation.[24]

The co-supervisor of this work, Dr. Federica Battistin, proposed the synthesis of two new *macropa*-like chelators containing either 2,2′-bipyridine or 1,10-phenanthroline in place of an O–CH_2–CH_2–O fragment of the macrocycle. These derivatives, named *bpycropa* and *phencropa* respectively (Figure 6),[25] were designed with the purpose of increasing the macrocycle rigidity with the bipyridyl/phenanthroline moieties, while the substitution of two ether oxygens with two sp² nitrogen donors renders the donor orbitals more directional, which could reasonably improve metal-complex stability.

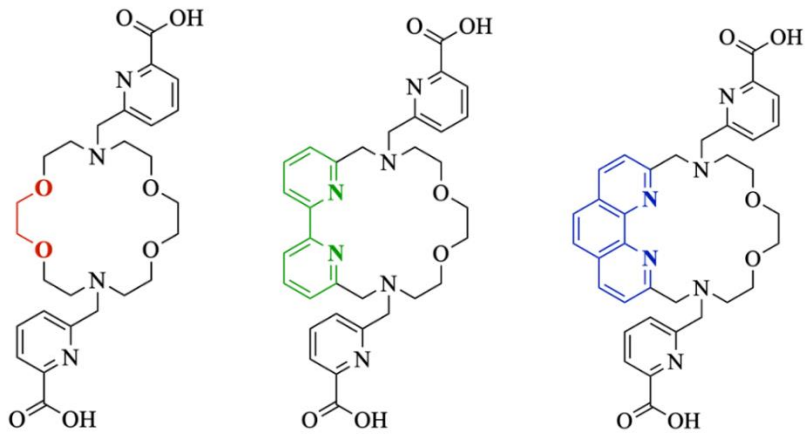

Figure 6. Comparison between the structures of *macropa*, *bpycropa,* and *phencropa*.

Moreover, the presence of bipyridine or phenanthroline allows the linker for bioconjugation, or additional functional groups, to be positioned further removed from the coordination site, reducing deleterious interactions with the metal ion that could cause its decomplexation. In fact, the binding of the linker to the picolinate ring, located close to the coordinated metal, may be responsible for the decomplexation of Ra^{2+} observed in the *macropa* complex. Thus, these newly proposed structures could allow multiple functionalization options (Figure 7), that might better preserve the hopefully high thermodynamic and kinetic stabilities of the complexes.

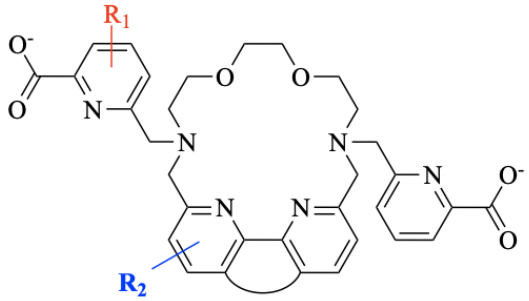

Figure 7. Different positions where *bpycropa/phencropa* can be conjugated to different targeting vectors.

Results and Discussion

Synthesis and characterization of the *bpycropa* ligand (D)

The macrocyclic ligand *bpycropa* was synthesized by following a procedure similar to that found in the literature for cryptates containing bipyridine units.[22,26] The starting material 2,2′-bipyridine-6,6′-dicarbaldehyde (**A)** was condensed with 1,8-diamino-3,6-dioxaoctane to form a cyclic diimine, followed by $NaBH_4$ reduction to afford the corresponding cyclic diamine (*bpycrown* **B**, Scheme 3). The macrocycle **B** was then N-alkylated with 6-(chloromethyl)pyridin-2-carboxylate methyl ester in a microwave reactor to obtain the dimethyl ester intermediate **C**. After chromatographic purification on an alumina column, acidic hydrolysis of the ester groups yielded the final ligand as its hydrochloride salt (**D**).

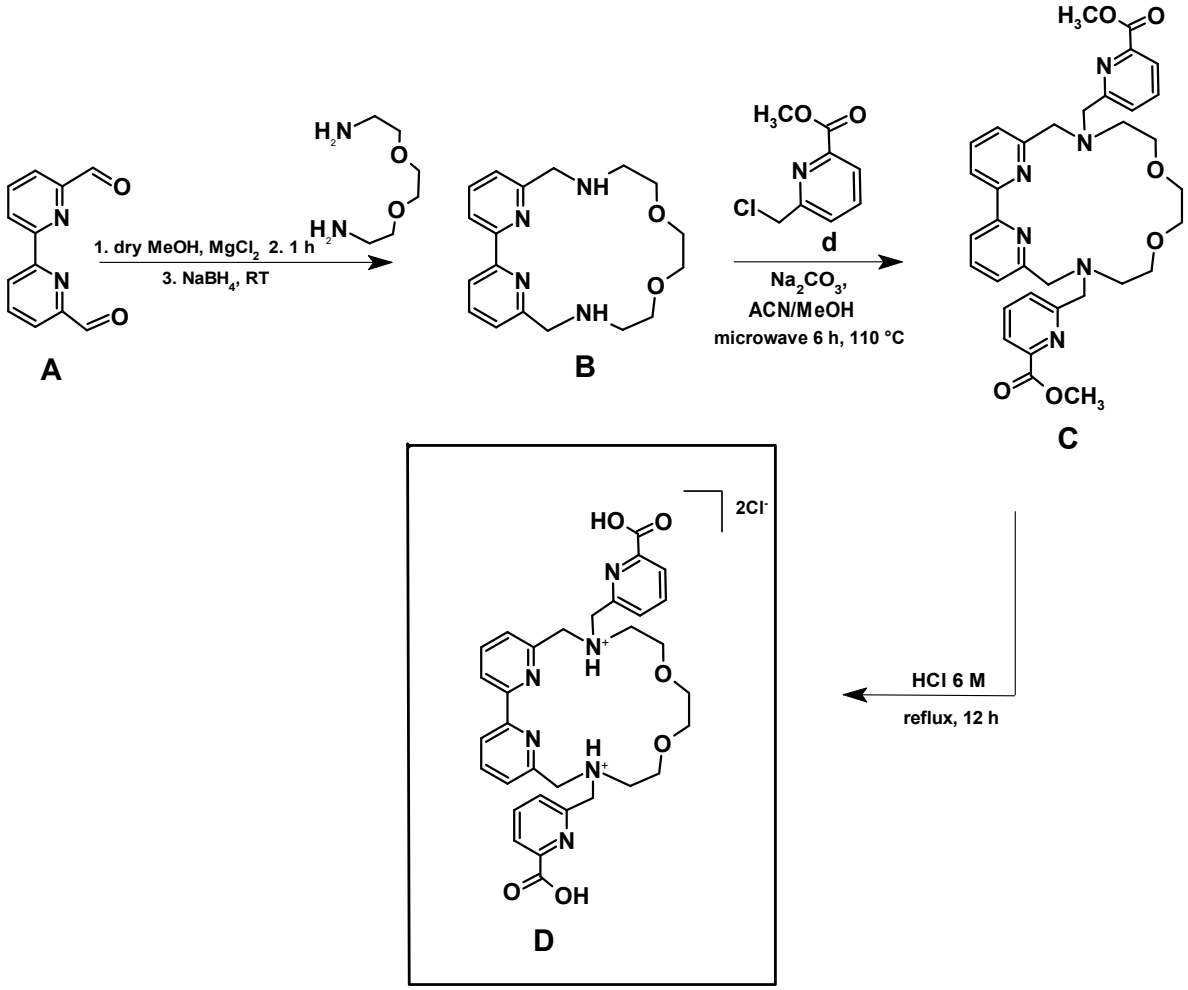

Scheme 3. Synthetic steps for obtaining the *bpycropa* ligand (**D**).

Reaction intermediates and the final compound were characterized by NMR spectroscopy and mass spectrometry. The characterization of the free ligand **D** in CD_3OD is reported below (Figure 8).

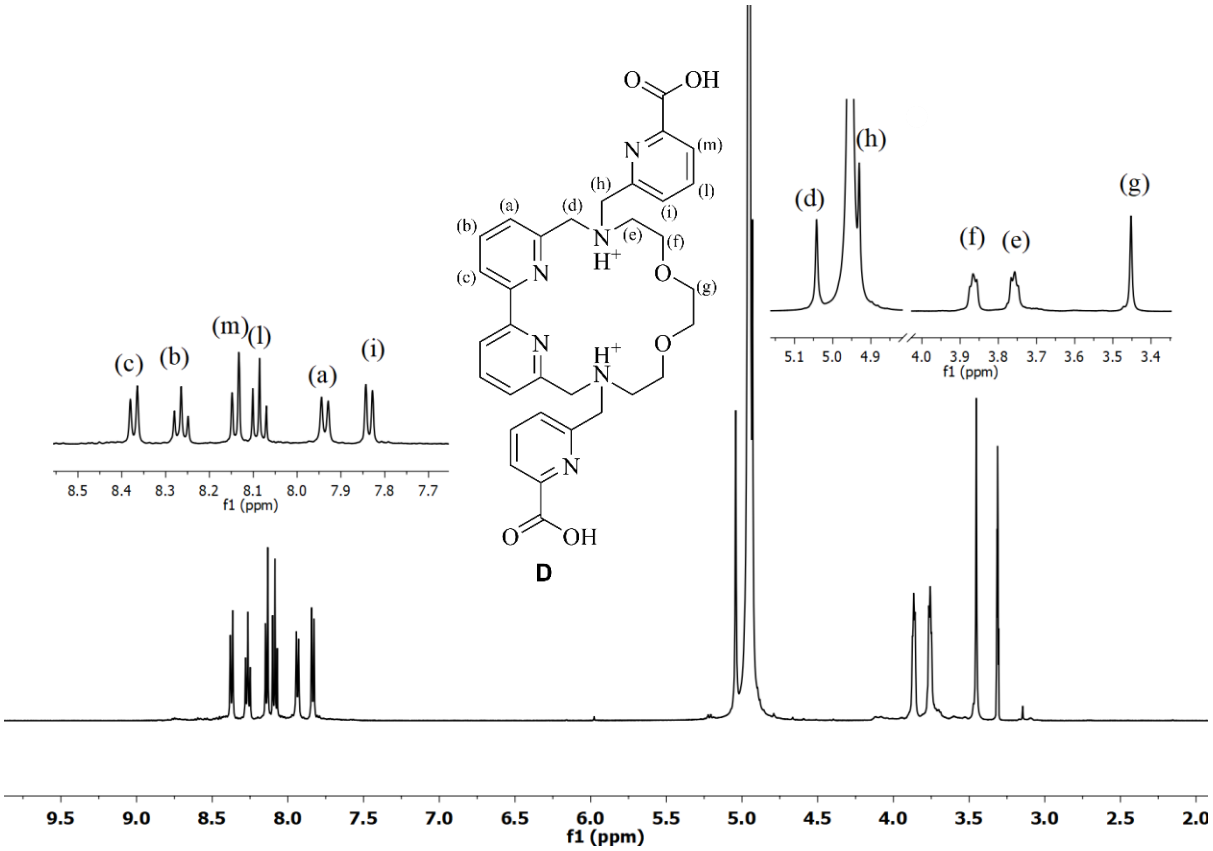

Figure 8. ^1H NMR spectrum (500 MHz) of the *bpycropa* ligand (**D**) in CD_3OD with labeling scheme.

The ^1H NMR spectrum of **D** is consistent with its symmetric structure, showing only half the number of proton resonances expected for the full molecule, *i.e.* chemically equivalent proton pairs are also magnetically equivalent. In the aromatic region, six signals – four doublets and two triplets of equal intensity, each integrating for two protons − are observed. Five additional resonances appear in the aliphatic region, one of which partially overlaps with the solvent peak.

Assignments of the aromatic doublets and triplets were done through a $^1H - ^1H$ COSY spectrum (Figure 9), which also revealed long-range couplings between aromatic and aliphatic protons (Figure 10). The resonances of the picolinate protons (H_m, H_l, H_i) were distinguished from those of the bipyridyl unit (H_a, H_b, H_c) by comparing the ^{13}C NMR spectrum of the ligand with that of its precursor *bpycrown* (**B**) and with the spectra of relevant building-block analogues (6,6′-dimethyl-2,2′-bipyridine and 6-methyl-pyridin-2-carboxylic acid).[27] Further confirmation was provided by the $^1H - ^{13}C$ HSQC and HMBC spectra, which display the C–H connectivities (Figures 11a,b) and the correlations to quaternary carbons, including the picolinate carboxylate carbon and the quaternary carbon of the bipyridyl moiety (Figures 12a,b).

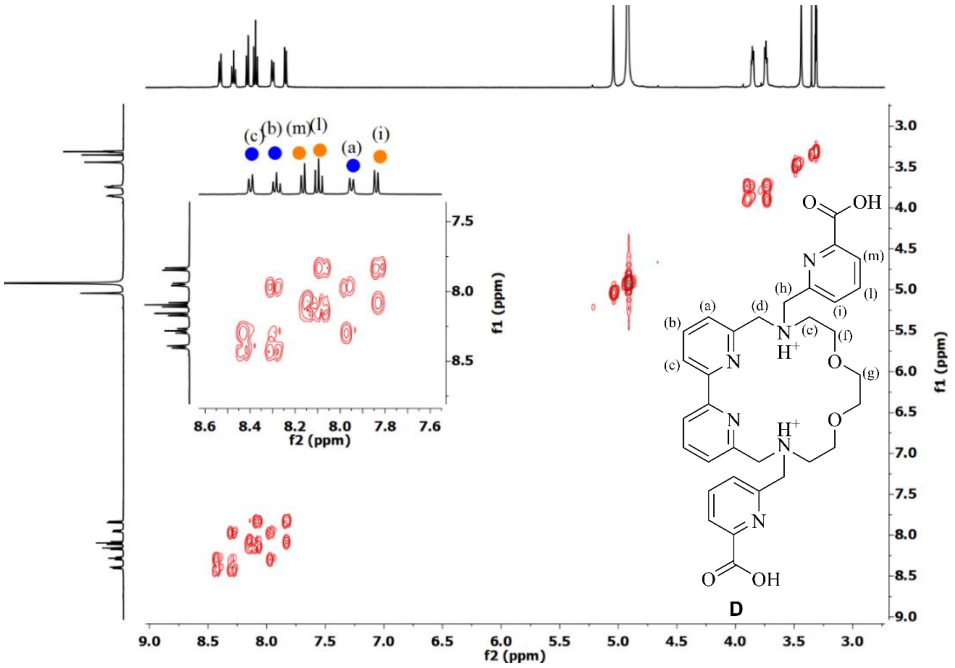

Figure 9. $^{1}H - {}^{1}H$ COSY spectrum (500 MHz) of the *bpycropa* ligand (**D**) in CD_3OD with labeling scheme. In the insert, the enlarged aromatic region. Blue dots = resonances of bpy unit, orange dots = resonances of picolinate unit.

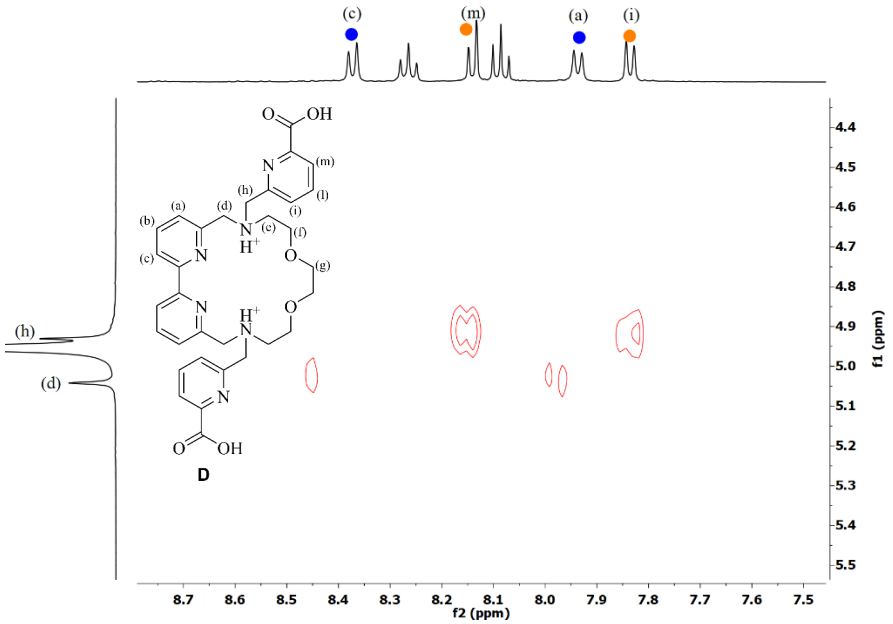

Figure 10. $^{1}H - {}^{1}H$ COSY spectrum (500 MHz) of *bpycropa* (**D**) in CD_3OD highlighting long-range coupling between the resonances of aromatic (H_c, H_m, H_a, H_i) and aliphatic (H_d, H_h) protons. Blue dots = resonances of bpy unit, orange dots = resonances of picolinate unit.

At lower frequencies of the aliphatic proton region, H_g protons resonate as a singlet (3.48 ppm, Figure 11b, green frame), followed by two triplets at higher frequencies corresponding to the methylene groups of the macrocycle, H_f and H_e at 3.83 and 3.74 ppm, respectively. These assignments were done by considering the $^{1}H - {}^{13}C$ HSQC spectrum of the reference *macropa* ligand.[21] Specifically, the carbon resonances adjacent to the nitrogen atoms can be distinguished from those adjacent to oxygens.[22] For instance, the ^{13}C resonance of C14 falls at 54.3 ppm in free *macropa*, and at 55.89 ppm in *bpycropa* (Figure 11b, black frame), while the CH_2–O peaks of C15 and C16 resonate at higher frequencies, from 64.7 to 70.2 ppm in free *macropa*, and at 65.01 and 64.66 ppm in *bpycropa* (Figure 11b, orange and green frames).

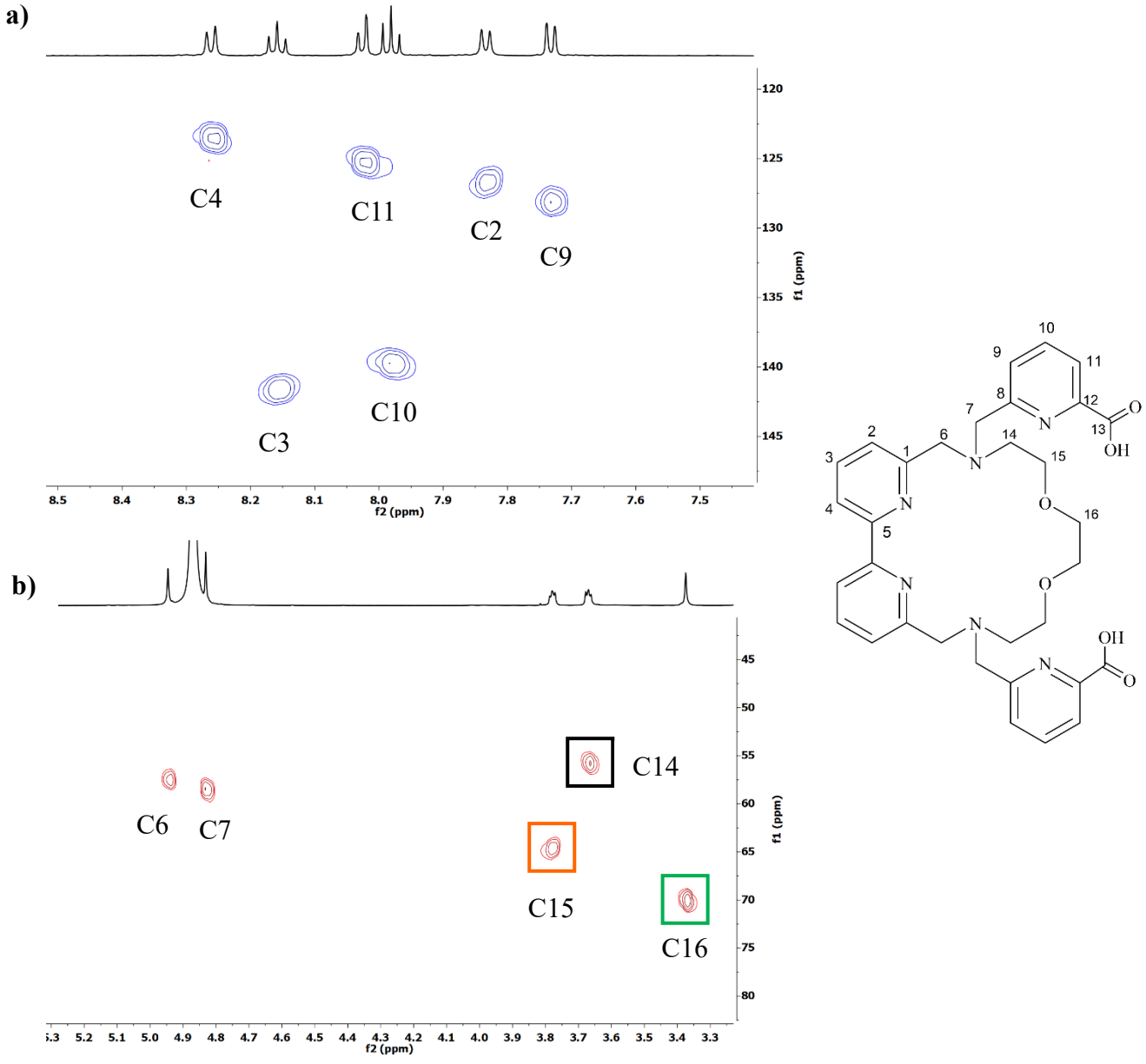

Figure 11. Enlarged view of the aromatic (**a**) and aliphatic (**b**) region of the $^{1}H - {}^{13}C$ HSQC spectrum (500 MHz) of *bpycropa*.

In the deshielded aliphatic region, two singlets are observed at 5.03 ppm (H_d) and 4.73 ppm (H_h) that in the $^1H - ^{13}C$ HSQC spectrum have cross peaks with C6 and C7, respectively (Figure 11b). In addition to the long-range couplings evident in the $^1H - ^1H$ COSY spectrum, the distinction between H_d and H_h was achieved through their correlations in the $^1H - ^{13}C$ HMBC spectrum. The H_h protons correlate with carbons C8 and C9 at 150.11 and 127.52 ppm, respectively − carbons that also show correlations with protons H_i and H_l (Figure 12a, red frames). Conversely, the H_d protons correlate with carbons C1 and C2 at 149.20 and 125.91 ppm, which in turn correlate with the bipyridyl protons H_c and H_b (Figure 12a, blue frames).

This assignment was further supported by cross peaks between the picolinate protons H_l and H_m and the deshielded carboxylate carbon at 164.9 ppm in the $^1H - ^{13}C$ HMBC spectrum (Figure 12b). The chemical shift of this carboxylate carbon matches that observed in the ^{13}C NMR spectrum of the 6-methyl-pyridin-2-carboxylic acid fragment, which served as an additional reference.[27]

a)

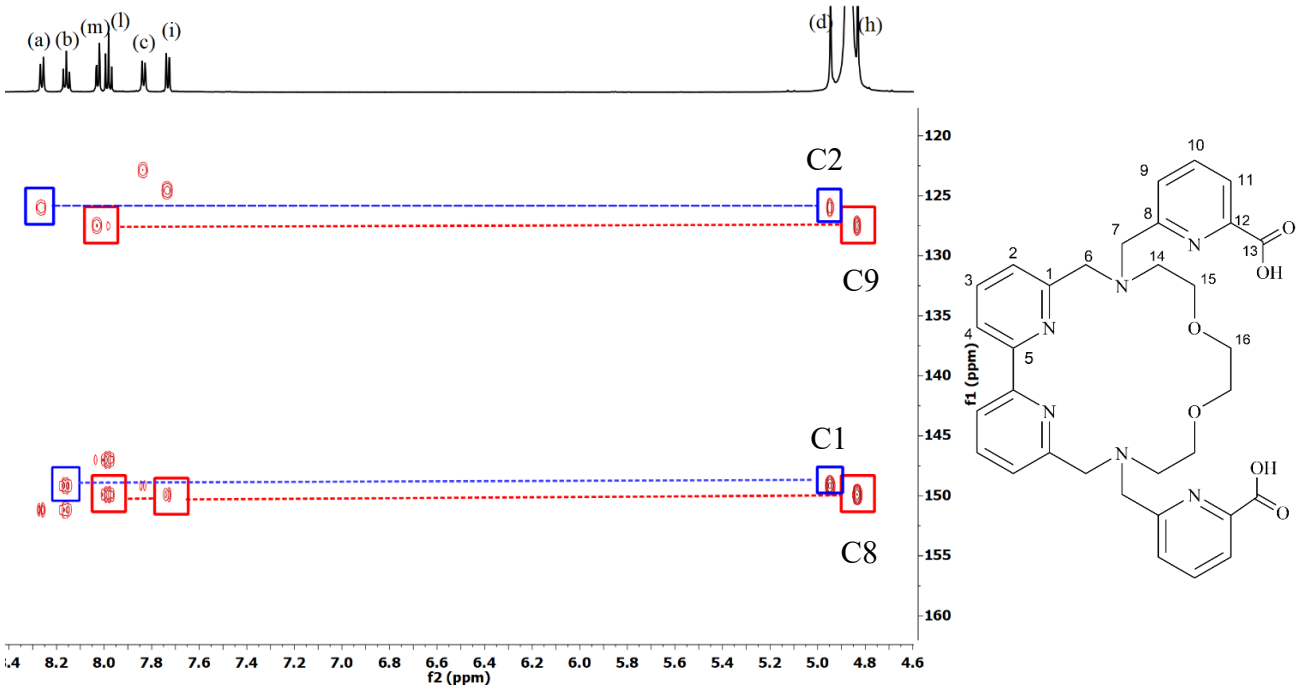

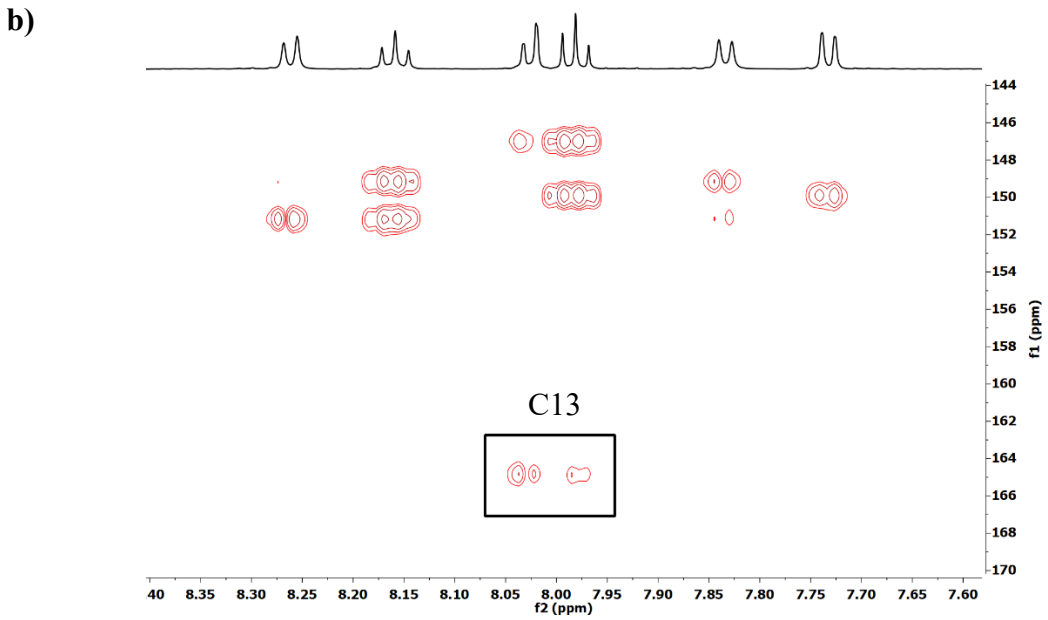

Figure 12. Enlarged sections of the $^{1}H - {}^{13}C$ HMBC spectrum of *bpycropa*. In panel **a**, correlations between aromatic carbons C8, C9 and the protons H_i, H_l and H_h (red frames) are visible, along with correlations between aromatic carbons C1, C2 and H_b, H_c and H_d protons (blue frames). Panel **b** displays the correlations between the aromatic protons H_m, H_l and the carboxylate carbon C13 of the picolinate group.

Finally, the synthesized ligand was confirmed by ESI-MS spectra in both positive and negative modes, where the peaks relative to $[M + H]^+$ and $[M - H]^-$ were observed, respectively (Figure 13 and 14).

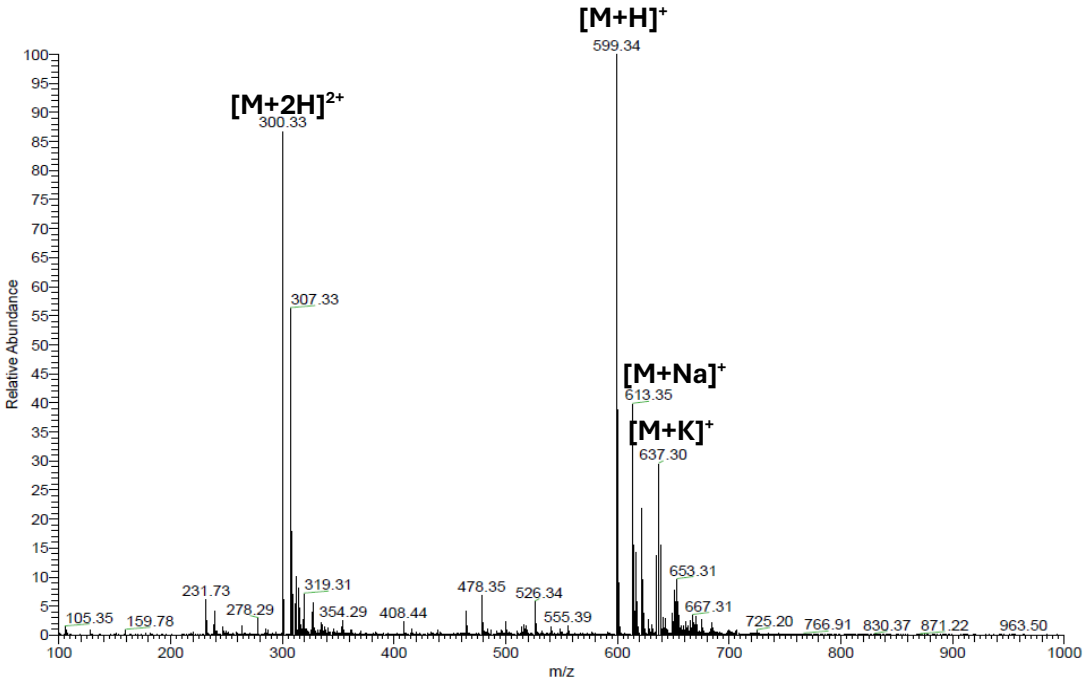

Figure 13. ESI-MS$^{(+)}$ spectrum of *bpycropa* (**D**).

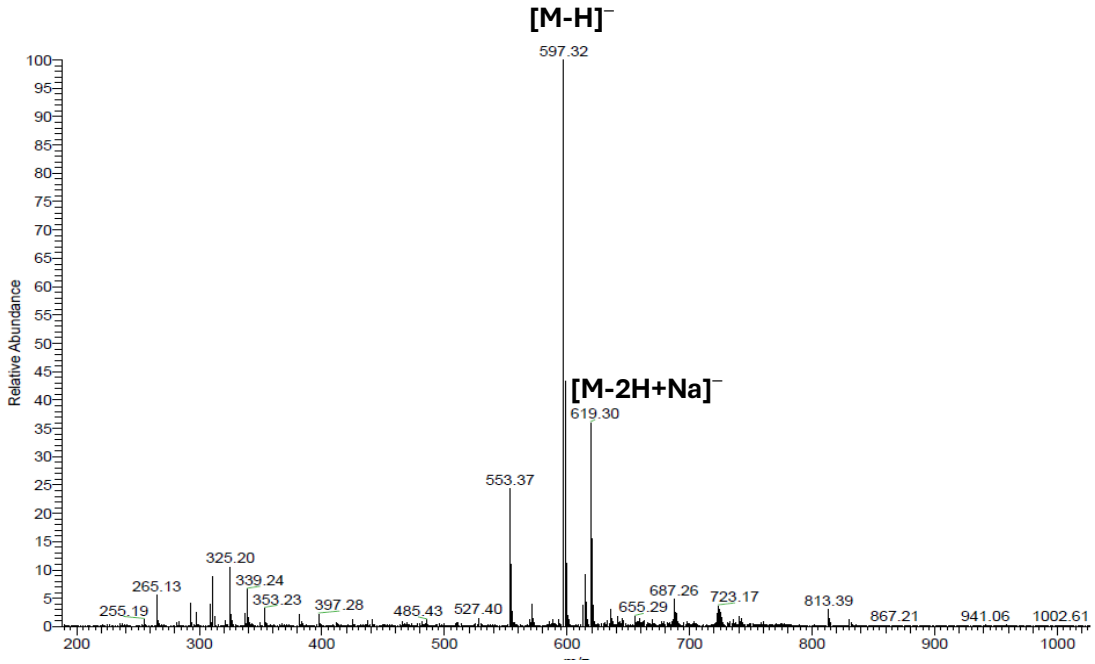

Figure 14. ESI-MS$^{(-)}$ spectrum of *bpycropa* (**D**).

Synthesis and characterization of *bpycropa* complexes with the divalent Ba(II) and Pb(II) cations

[Ba(*bpycropa*)] (1)

The [Ba(*bpycropa*)] complex (**1**) was obtained as a white solid by reacting, at room temperature, a slight excess of $BaCl_2$ (1.1 eq) with a concentrated aqueous solution of *bpycropa*, previously adjusted to pH 7 with a KOH solution (Scheme 4). The complex was characterized by single crystal X-ray diffraction and NMR spectroscopy (*vide infra*).

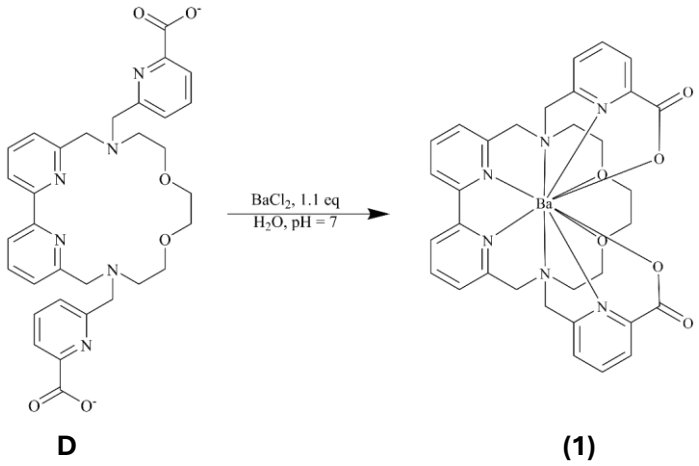

Scheme 4. Synthesis of the [Ba(*bpycropa*)] (**1**) complex.

X-ray crystallographic studies of the [Ba(*bpycropa*)] (1) complex

Single crystal X-ray diffraction studies performed by Prof. Gabriele Balducci (DSCF) on single crystals of [Ba(*bpycropa*)] (**1**) afforded its solid-state structure. The complex is neutral, with no additional counterions, consistent with the deprotonation of both carboxylic groups of the picolinate rings. In the solid state, it adopts an asymmetric geometry in which the Ba^{2+} cation is deca-coordinate, *i.e.* all donor atoms of the ligand are coordinated to barium. The bond lengths of the coordination sphere of the complex are reported in Table 1.

In the complex, the macrocycle exhibits a highly distorted geometry, with the bent ether portion nearly perpendicular to the bipyridyl plane. Within the barium coordination sphere, two approximately perpendicular mean planes can be identified, each defined by six donor atoms. One is defined by the bipyridyl nitrogens N1 and N2, the tertiary amine nitrogens N3 and N5, and N4 and O3 of one picolinate, which is *trans* with respect to the bipyridyl ring. The other plane contains – besides N3 and N5 – O4 and N6 of the second picolinate moiety and the ether oxygens O1 and O2 (Figure 15). The angle between the bipyridine moiety and the average plane containing N1 – N5 and O3 was found to be around ~19°The solid-state geometry of complex **1** is fully consistent with the NMR spectra in solution, which point to the absence of symmetry elements (*vide infra*).

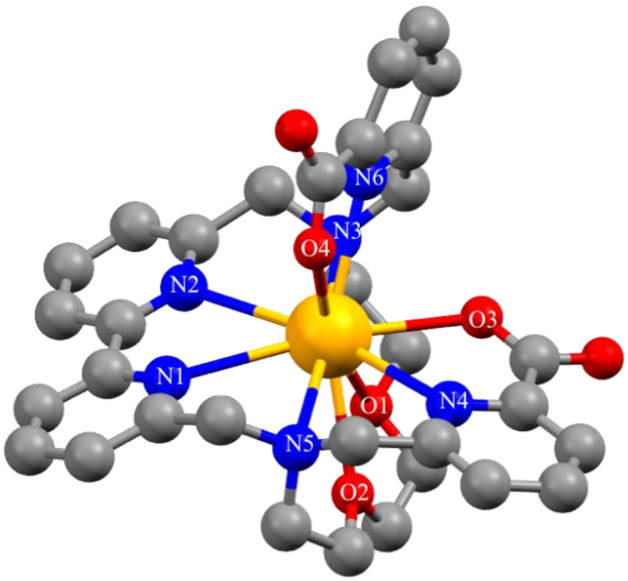

Figure 15. Single crystal X-ray structure of [Ba(*bpycropa*)] (**1**).

Table 1. Coordination bond lengths from the single crystal X-ray structure of complex **1**.

	[Ba(*bpycropa*)]	
	bond	***length (Å)***
N-bpy/phen(1)	Ba–N1	2.964(4)
N-bpy/phen(2)	Ba–N2	3.019(4)
N-amine(1)	Ba–N3	2.967(5)
N-picolinate(1)	Ba–N4	2.943(4)
N-amine(2)	Ba–N5	2.957(4)
N-picolinate(2)	Ba–N6	2.856(5)
O-ether(1)	Ba–O1	2.975(4)
O-ether(2)	Ba–O2	2.864(3)
O-carboxylate(1)	Ba–O3	2.739(4)
O-carboxylate(2)	Ba–O4	2.758(4)

NMR studies of the [Ba(*bpycropa*)] (1) complex

The ^{1}H NMR spectrum of [Ba(*bpycropa*)] (**1**) (Figure 16) immediately reveals a substantial increase in the number of resonances compared to the free ligand **D**. Thirteen well-resolved signals, each integrating for 1H, are observed − five in the aromatic region and eight in the aliphatic region − while the resonances of the remaining 19 protons appear in partially overlapping multiplets. This indicates that all protons become magnetically non-equivalent and resonate at distinct frequencies due to the loss of ligand symmetry upon metal coordination, which is also in an agreement with the X-ray crystal structure of the complex.

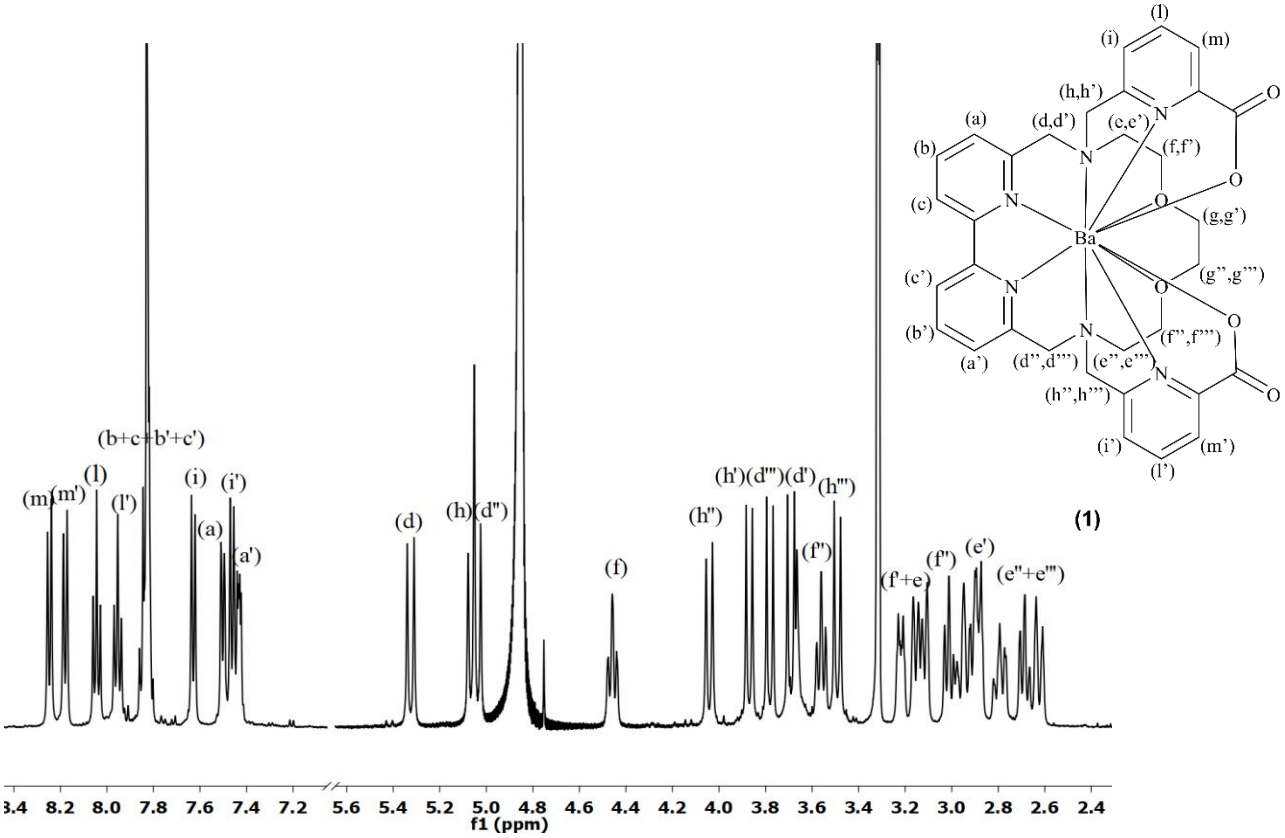

Figure 16. ^{1}H NMR spectrum (500 MHz) of the [Ba(*bpycropa*)] (**1**) complex in CD_3OD with labeling scheme.

In the aromatic region, the two doublets and two triplets at highest frequencies belong to the $H_{m\text{-}m'}$ and $H_{l\text{-}l'}$ picolinate protons, that are more deshielded compared to $H_{i\text{-}i'}$ due to resonance effects. The signals of the remaining picolinate protons ($H_{i\text{-}i'}$) appear as doublets at slightly lower frequencies and were assigned through the ^{1}H – ^{1}H COSY spectrum (Figure 17a). The resonances of the bipyridyl protons $H_{b\text{-}b'}$ and $H_{c\text{-}c'}$ overlap in a multiplet that shows correlation with the doublets of the $H_{a\text{-}a'}$ protons.

In the aliphatic region of the ^{1}H – ^{1}H COSY spectrum (Figure 17b), several cross peaks between doublets, corresponding to diastereotopic CH_2 protons, are observed. The resonances of the

most deshielded protons $H_{d\text{-}d'''}$ and $H_{h\text{-}h'''}$, due to their proximity to the sp^3 N atoms and the aromatic fragments, appear at higher frequencies. Similarly to what was observed in the free ligand, these protons presented long-range couplings with nearby aromatic partners: for example, the resonance of H_d correlates with the H_b/H_c multiplet and the H_a doublet (Figure 17c, coupling highlighted in orange), while the resonance of $H_{h''}$ shows correlations with those of the picolinate protons $H_{m'}$ and $H_{i'}$ (Figure 17c, coupling highlighted in magenta). All resonances relative to the remaining protons ($H_{e\text{-}e'''}$, $H_{f\text{-}f'''}$ and $H_{g\text{-}g'''}$) fall in partially overlapping multiplets at lower frequencies and were further analyzed via $^1H - {}^{13}C$ HSQC and $^1H - {}^{13}C$ HMBC experiments for completeness (See Supplementary Information, Figures S6 and S7).

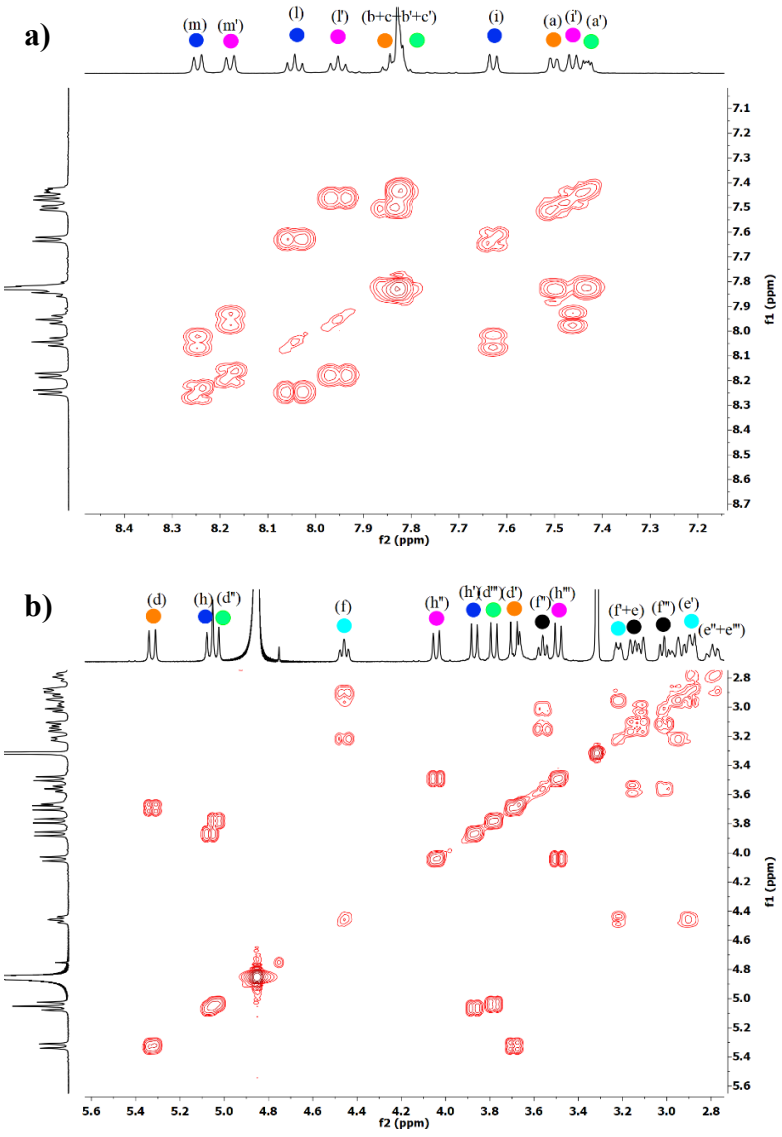

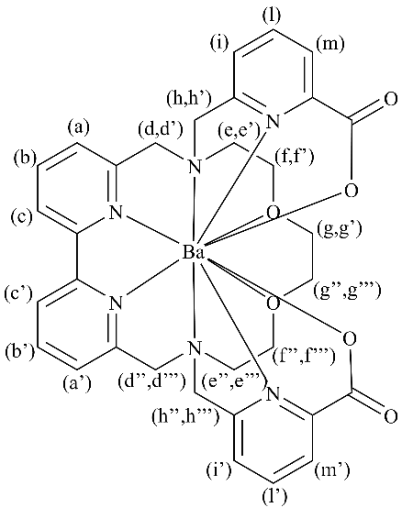

(1)

c)

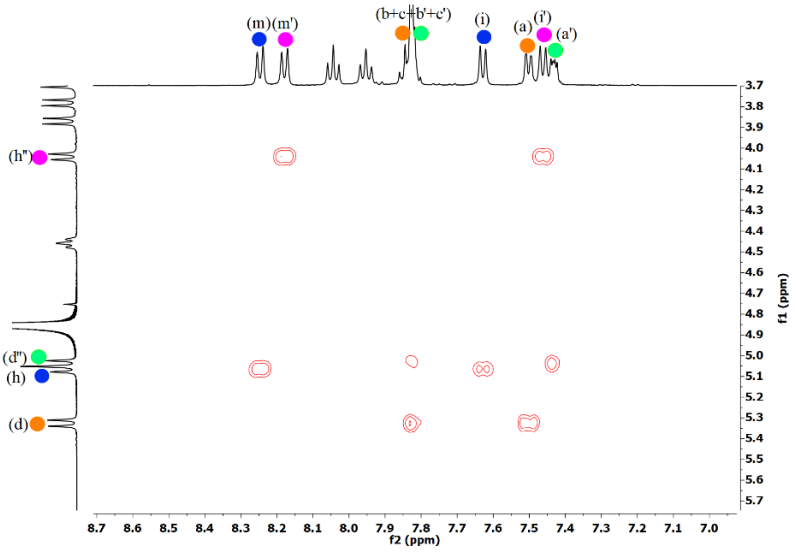

Figure 17. ^{1}H – ^{1}H COSY spectrum (500 MHz) of complex (**1**) highlighting the aromatic (**a**), aliphatic (**b**), and long range aromatic-aliphatic couplings (**c**). Color coding identifies couplings between proton pairs with at least one resolved resonance.

Lastly, an ^{1}H – ^{1}H ROESY experiment showed that the resonances of chemically equivalent protons are pairwise connected by exchange cross peaks, indicating the occurrence of a dynamic process that exchanges them, and is slow on the NMR time scale (Figure 18, orange frames).

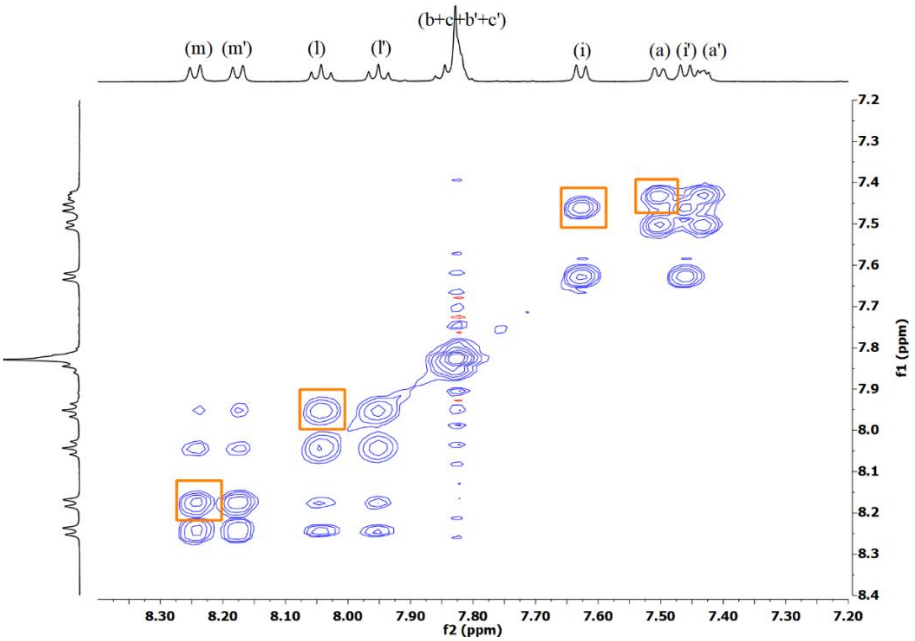

Figure 18. ^{1}H – ^{1}H ROESY spectrum (500 MHz) of the aromatic region of [Ba(*bpycropa*)] (**1**). Mixing time = 300 ms. Exchange cross peaks are evidenced by orange frames.

It was hypothesized that this phenomenon arises from the physical exchange of the coordinative positions of the two picolinate pendant arms, possibly through their dissociation/recomplexation, that leads to an exchange of all pairwise chemically equivalent (but magnetically inequivalent) protons. To further illustrate this process, the two possible conformers were modeled using Blender 4.3 software, as shown in Figure 19. In this scenario, the bipyridyl N atom that lies opposite to the N atom of one picolinate in one conformer becomes positioned opposite to the O atom of the other picolinate in the other conformer (Figure 19, highlighted in yellow). The same positional inversion occurs for the second nitrogen atom of the bipyridyl unit.

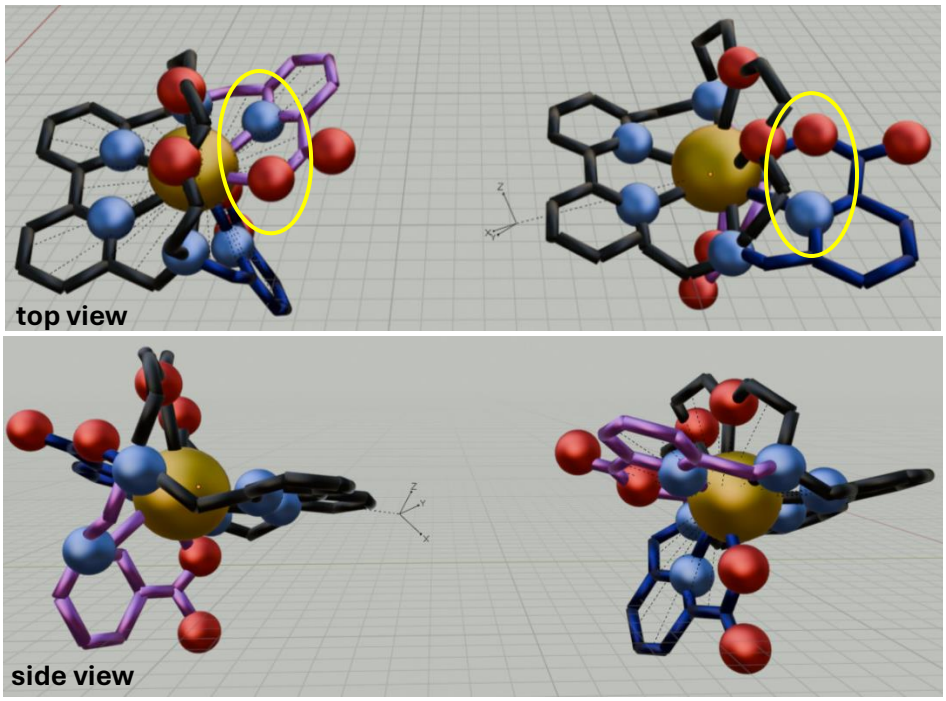

Figure 19. Hypothesized conformational exchange of the picolinate moieties (shown in blue and violet) of the [Ba(*bpycropa*)] (**1**) complex.

[Pb(*bpycropa*)] (2)

The [Pb(*bpycropa*)] complex (**2**) was obtained using the same procedure described for [Ba(*bpycropa*)] (**1**) (Scheme 4), using $Pb(NO_3)_2 \cdot 5H_2O$ as source of Pb(II). The ^1H NMR spectrum of **2** shown in Figure 20 displays a pattern very similar to that observed for the barium complex **1**, though with more pronounced signal overlap. Nonetheless, it was possible to perform the full characterization with $^1H - ^1H$ COSY, $^1H - ^{13}C$ HSQC, $^1H - ^{13}C$ HMBC spectra (See Supplementary Information, Figures S9 – S11). The $^1H - ^1H$ ROESY NMR spectrum evidenced the occurrence of an analogous exchange processes as in complex **1**. It should be noted however that in this case the exchange cross peaks are less intense (same mixing time of 300 ms), suggesting that the exchange process with Pb(II) is slower than with Ba(II).

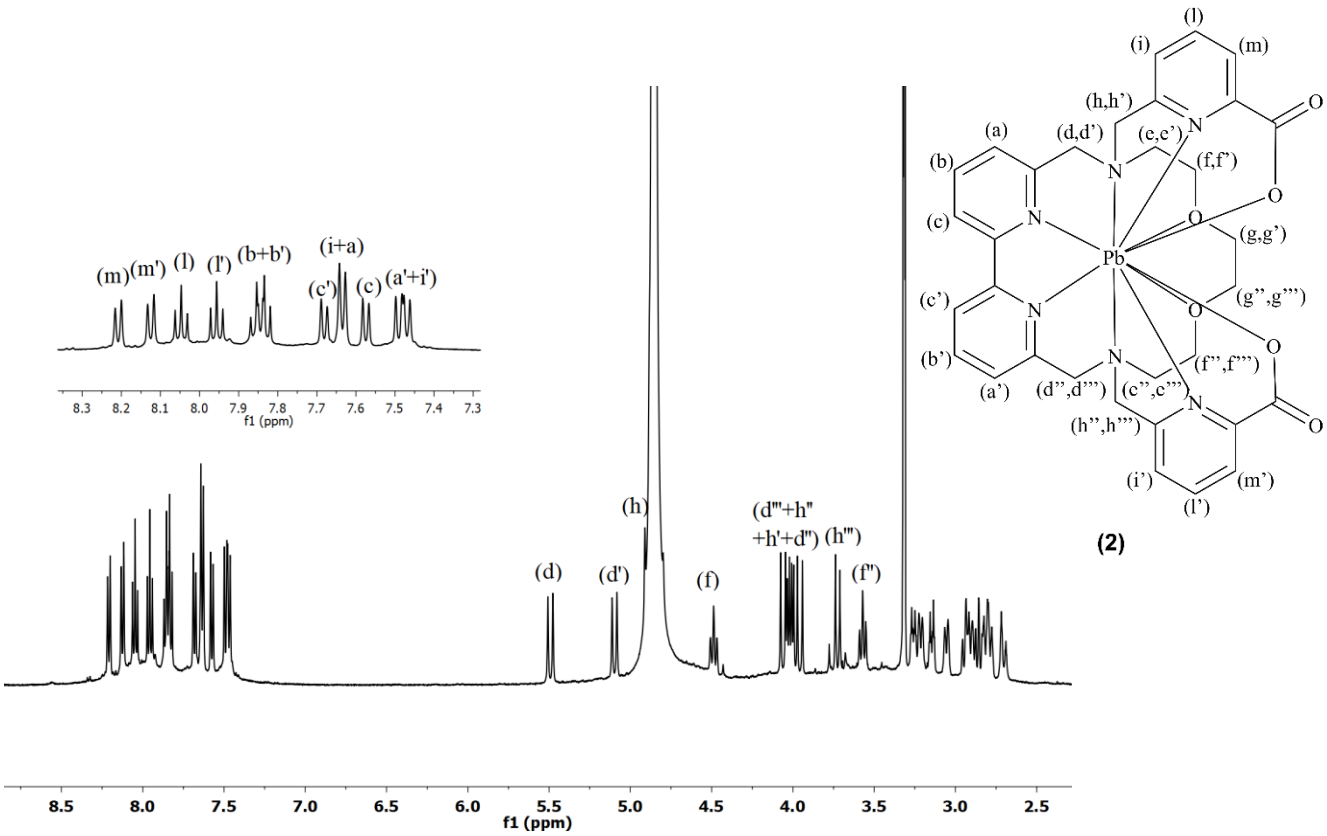

Figure 20. ^{1}H NMR spectrum (500 MHz) of the [Pb(*bpycropa*)] (**2**) complex in CD_3OD with labeling scheme.

Synthesis and characterization of *bpycropa* complexes with the trivalent cations La(III) and Bi(III)

[La(*bpycropa*)][NO_3] (3)

The [La(*bpycropa*)][NO_3] complex (**3**) was obtained at room temperature by adding $La(NO_3)_3 \cdot 5H_2O$ (1.5 eq.) to an aqueous solution of the ligand, previously set to pH = 6.45. The white complex, isolated after 12 h of magnetic stirring at room temperature, displayed high solubility in water and was only slightly soluble in methanol. For this reason, the NMR characterization of **3** was performed in D_2O. In this solvent, the ^{1}H NMR spectrum of **3** (Figure 21) is similar to those of **1** and **2** in CD_3OD, suggesting a similar coordination sphere and geometry. The resonances of the $H_{h-h'''}$, $H_{d-d'''}$ protons significantly overlap with the solvent peak (4.5 – 4.9 ppm range), however based on the typical ^{1}H – ^{1}H COSY couplings seen for the barium and lead complexes, all assignments could be done.

Significantly, for complex **3**, contrary to what found for **1** and **2**, no exchange process was observed in the ^{1}H – ^{1}H ROESY spectrum (Figure 22), even when the mixing time was extended to 400 ms. This finding is consistent with the mechanism proposed for the exchange process in the complexes with the divalent cations: the stronger bonds of the picolinate arms with the trivalent cation hamper their dissociation, and thus the whole exchange process.

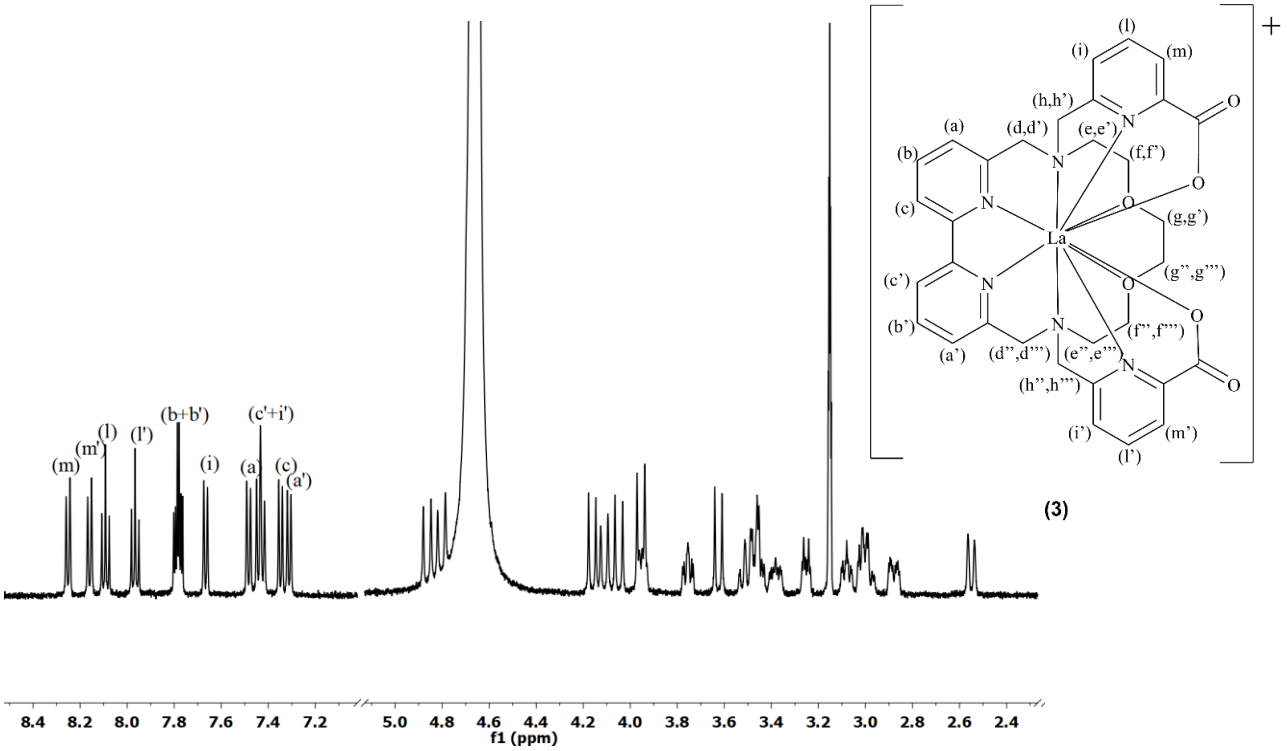

Figure 21. ^{1}H NMR spectrum (500 MHz) of the [La(*bpycropa*)][NO_3] (**3**) complex in D_2O with labeling scheme.

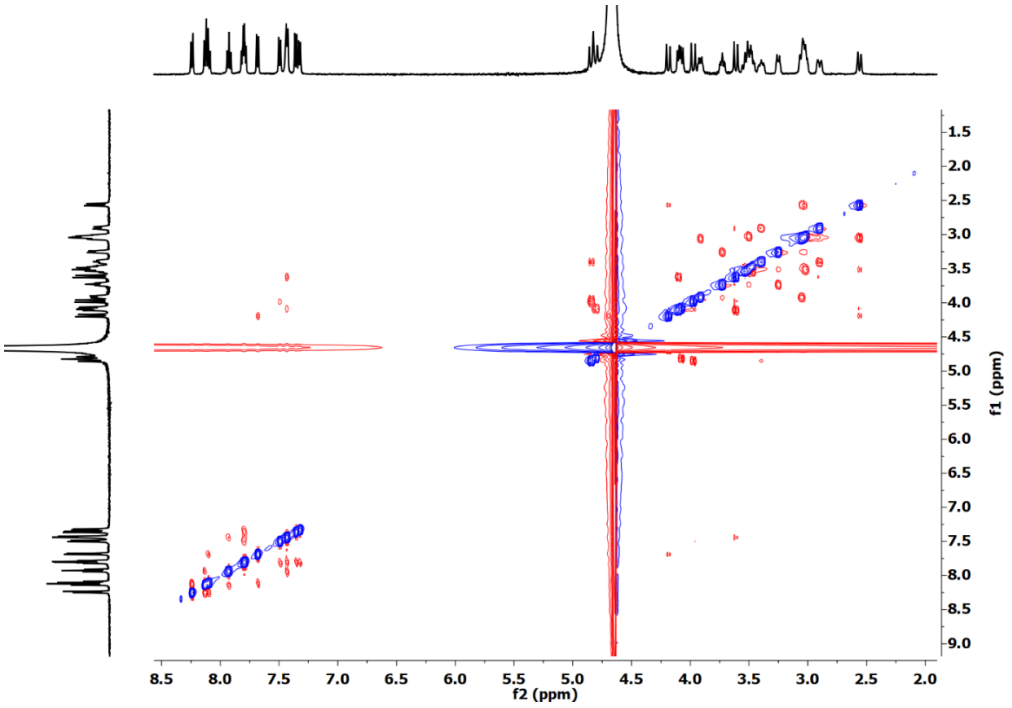

Figure 22. ^{1}H – ^{1}H ROESY spectrum (600 MHz) of the [La(*bpycropa*)][NO_3] (**3**) complex in D_2O. Mixing time = 300 ms. Only NOE cross peaks (in red) are seen.

[Bi(*bpycropa*)][NO_3] (4)

The complex [Bi(*bpycropa*)][NO_3] (**4**) was synthesized by treating the ligand with a slight excess of $Bi(NO_3)_3 \cdot 5H_2O$ in an aqueous solution at acidic pH (3.7) for minimizing the hydrolytic processes of bismuth (see Experimental Section). Figure 23 shows the ^1H NMR spectrum of **4** in CD_3OD, that is similar to those of the analogous complexes **1** – **3**, again suggesting a similar coordination environment The major difference is that the resonance attributed to proton H_l is particularly more deshielded with respect to those of the other picolinic protons ($H_{l'}$, $H_{m/m'}$ and $H_{i/i'}$).

As seen for the La^{3+} complex (**3**), also in this case no exchange cross peaks were observed in the ^1H – ^1H ROESY spectrum.

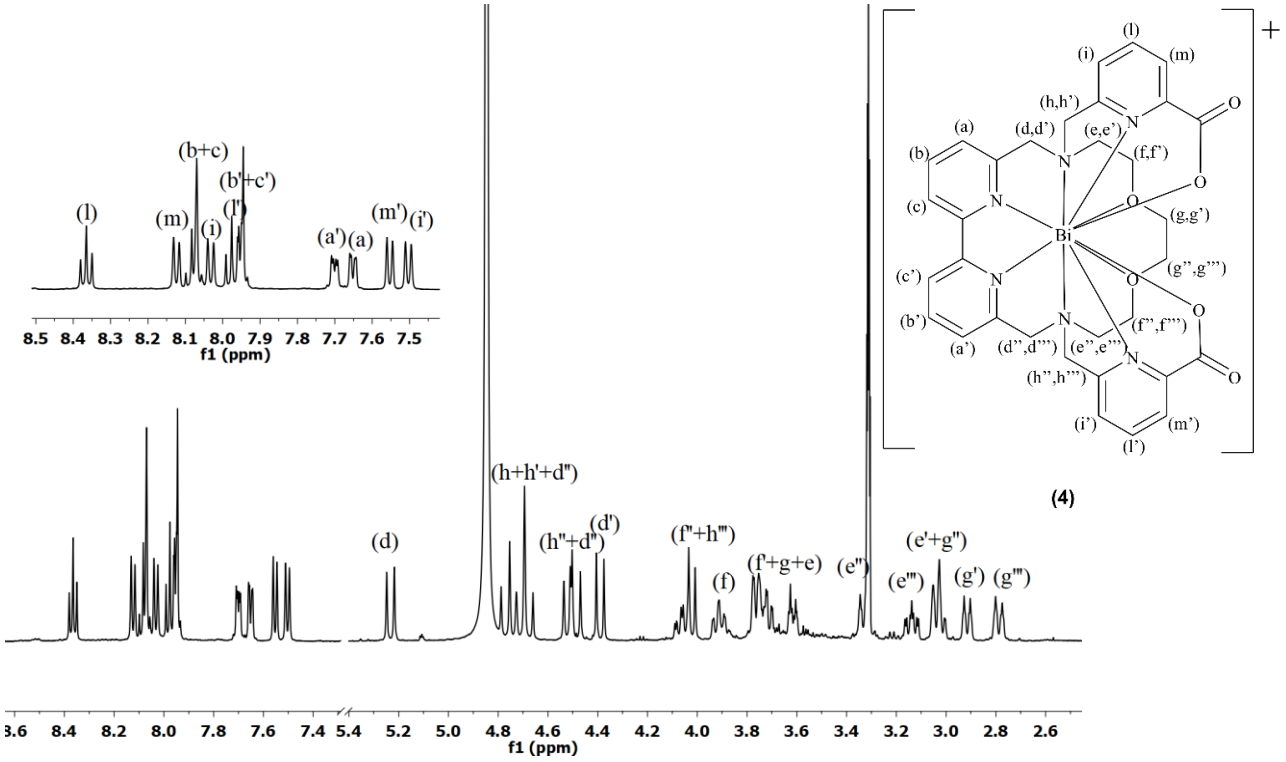

Figure 23. ^1H NMR spectrum (500 MHz) of the [Bi(*bpycropa*)][NO_3] complex (**4**) in CD_3OD with labeling scheme.

Synthesis and characterization of the *phencropa* ligand (D')

The synthetic procedure for the *phencropa* ligand (**D'**) was similar to that for *bpycropa* (Scheme 5,). The major difference concerned the addition of the diamine in the first step. In fact, it was observed that in order to limit the formation of undesired byproducts − such as the *2+2* macrocycle resulting from the condensation of two molecules of 1,10-phenanthroline-2,9-dicarbaldehyde with two molecules of diamine – the amine was best added in small aliquots over the course of 6 hours. The following steps were identical to those of the *bpycropa* synthesis, affording *phencropa* as an orange solid.

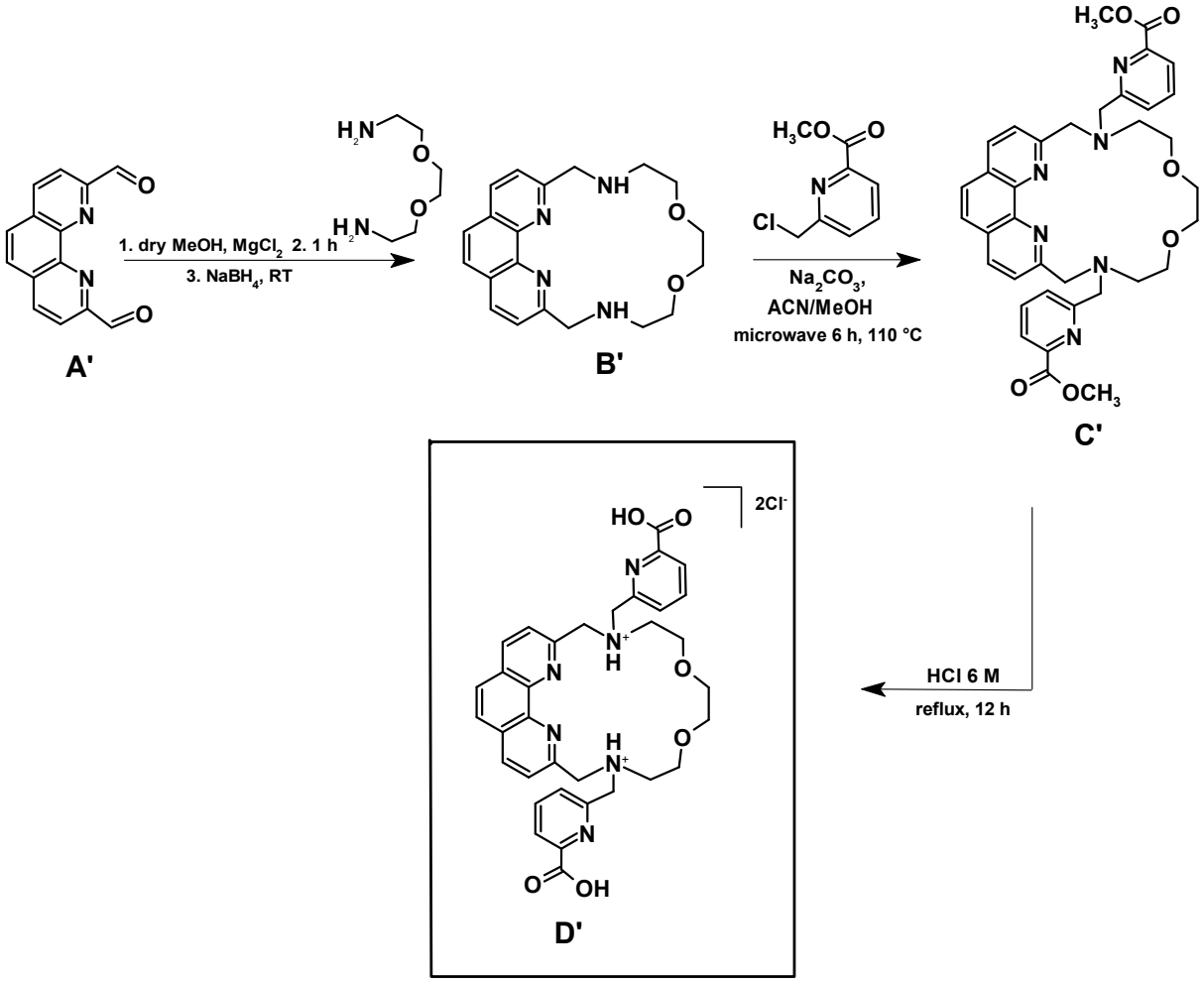

Scheme 5. Synthetic steps to obtain the *phencropa* ligand (**D'**).

The reaction intermediates were characterized by NMR spectroscopy (see Supplementary Information and Experimental Section), whereas the characterization of the free ligand in CD_3OD is reported below (Figure 24).

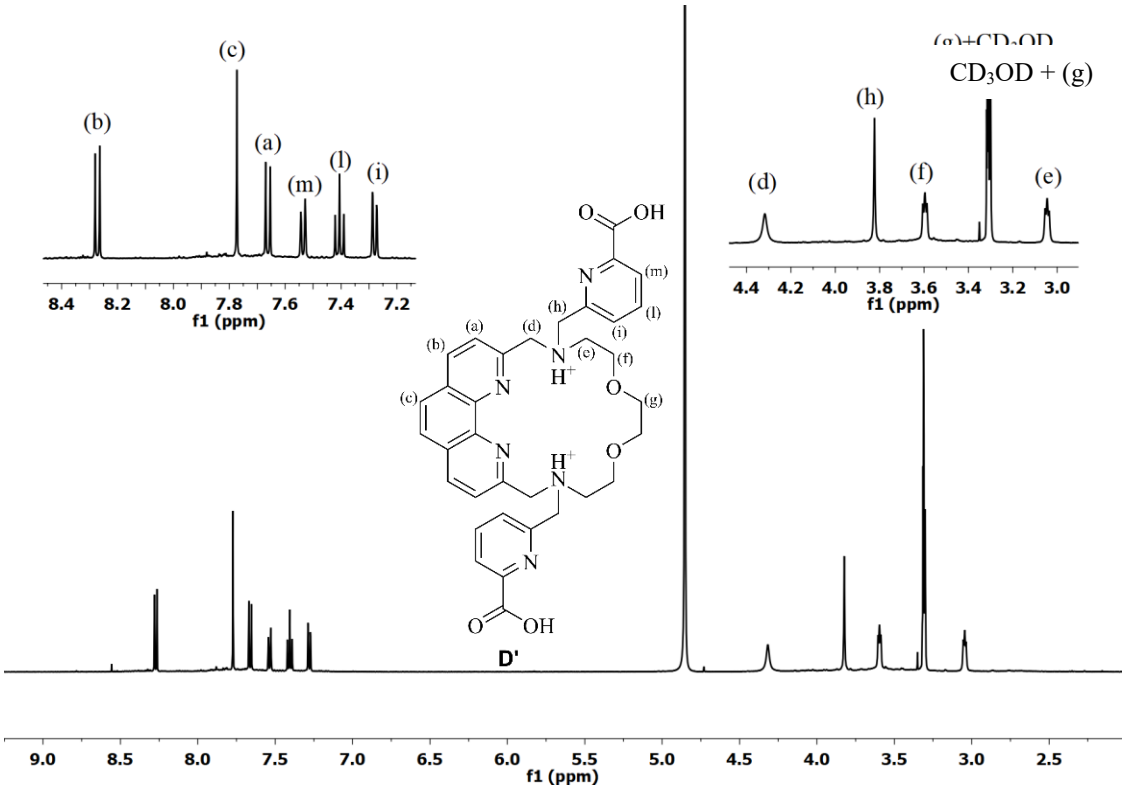

Figure 24. ^{1}H NMR spectrum (500 MHz) of *phencropa* (**D'**) in CD_3OD with labeling scheme.

The spectrum of *phencropa* is similar to that of *bpycropa* (Figure 8): also in this case the number of resonances corresponds to half the total number of protons present in the molecule, in agreement with its symmetry (*i.e.* chemically equivalent protons are also magnetically equivalent). In total six resolved resonances of equal intensity (2H) in the range 7.2 – 8.3 ppm can be observed. The singlet at 7.79 ppm is unequivocally assigned to the H_c protons of the phenanthroline moiety. The remaining multiplets were readily attributed either to phenanthroline − doublets H_b and H_a at 8.29 ppm and 7.69 ppm, respectively − or to the picolinate rings – H_l, H_m and H_i via a ^{1}H – ^{1}H COSY spectrum (Figure 25). The doublet at highest frequency is assigned to the two H_b protons positioned *para* to the nitrogen atom of the phenanthroline ring, which are deshielded due to resonance effects.

In the aliphatic region, four of the five expected resonances (4H each) are observed. The two triplets correspond to the methylene groups of the macrocycle, H_e and H_f. The assignment of these resonances was performed through the ^{1}H – ^{13}C HSQC spectrum (Figures 26 and 27), as for *bpycropa*. In particular, carbons C15 and C16 that resonate at 54.97 and 65.03 ppm, are bound to protons H_e and H_f, respectively (Figure 27). Further confirmation of the H_e and H_f assignments came from the pH dependence of their chemical shifts (*vide infra*, ^{1}H NMR titration studies). In fact, the resonance of H_e, located closer to the tertiary nitrogen, exhibited a larger chemical shift change upon protonation of the amino group compared to H_f.

Lastly, by analyzing the long-range couplings between aliphatic and aromatic protons of the ^{1}H – ^{1}H COSY spectrum (not shown in Figure 25), it was possible to assign the broadened singlet at 4.33 ppm, which displays a cross peak with the resonance of H_a, to the H_d protons, and the slightly broadened singlet at 3.84 ppm to the H_h protons due to long-range coupling with the resonance of H_i. The signal of the four H_g protons overlaps with the quintet of the solvent CD_3OD.

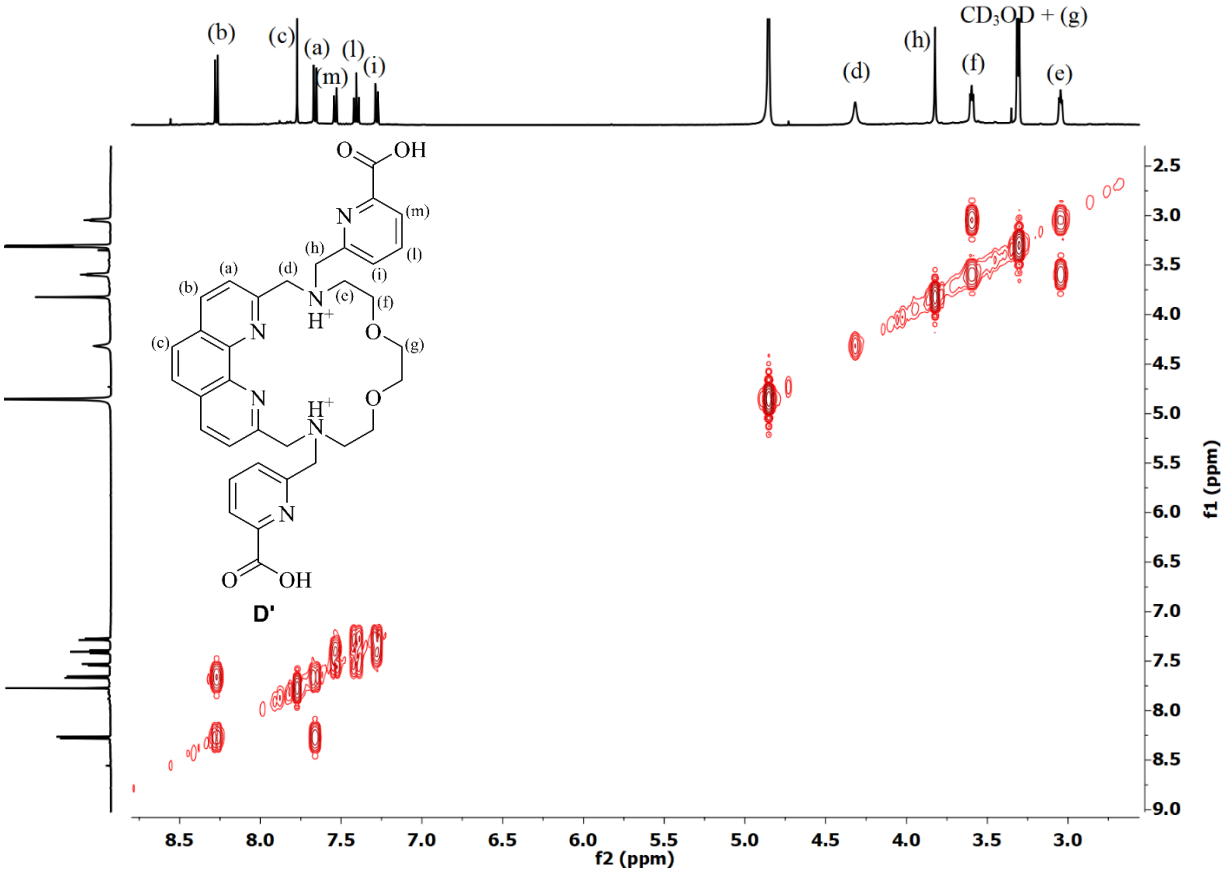

Figure 25. ^{1}H – ^{1}H COSY spectrum (500 MHz) of *phencropa* (**D'**) in CD_3OD.

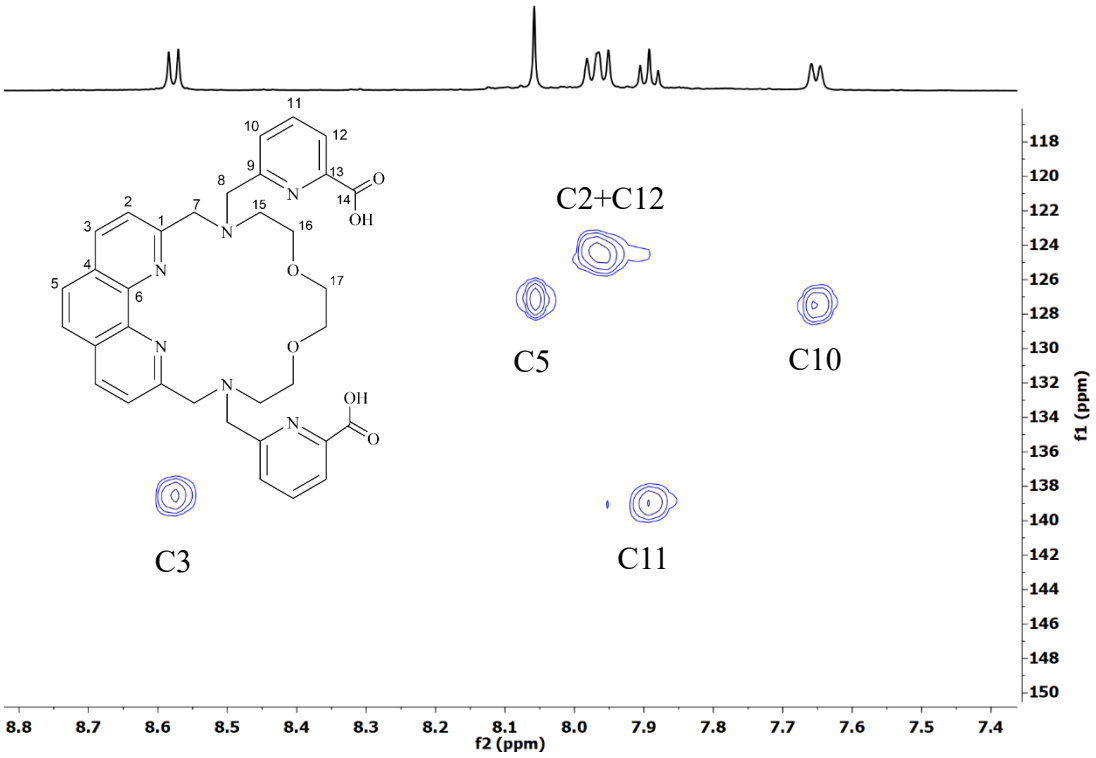

Figure 26. $^{1}H - ^{13}C$ HSQC spectrum (500 MHz) of the aromatic region of *phencropa* (**D'**) in CD_3OD.

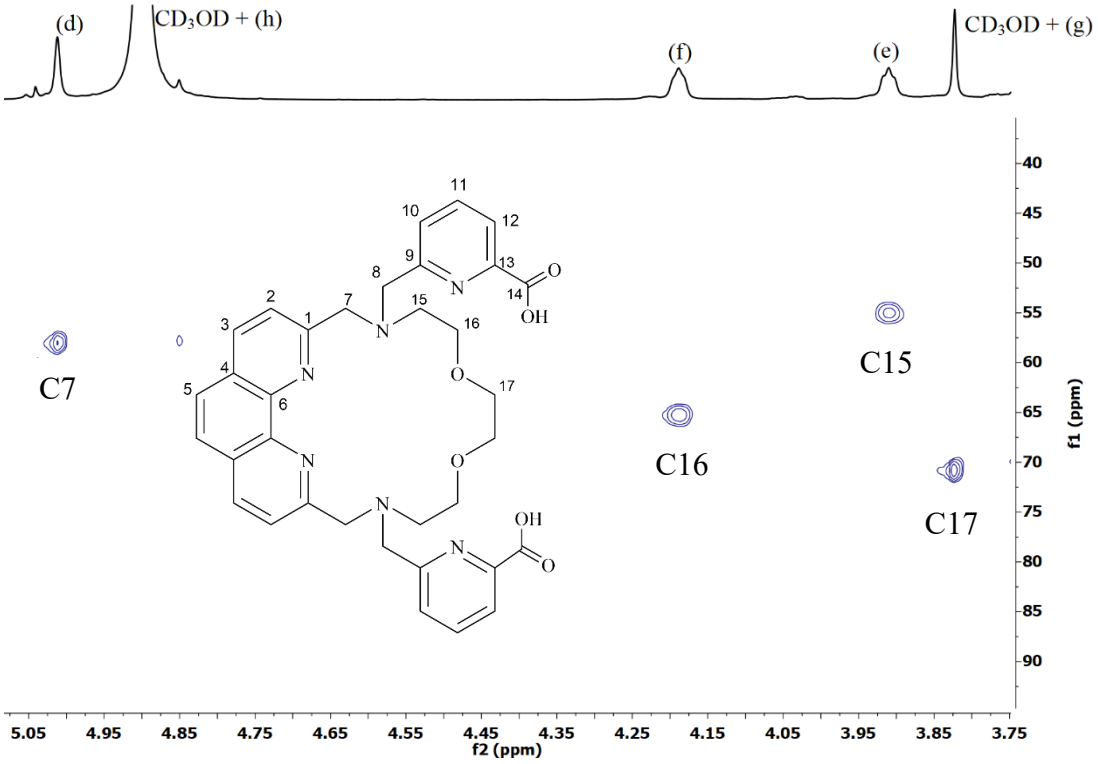

Figure 27. $^{1}H - ^{13}C$ HSQC spectrum (500 MHz) of the aliphatic region of *phencropa* (**D'**) in CD_3OD.

In addition, the ESI-MS spectra, recorded both in positive and in negative mode (Figures 28 and 29), are consistent with the proposed structure of the ligand.

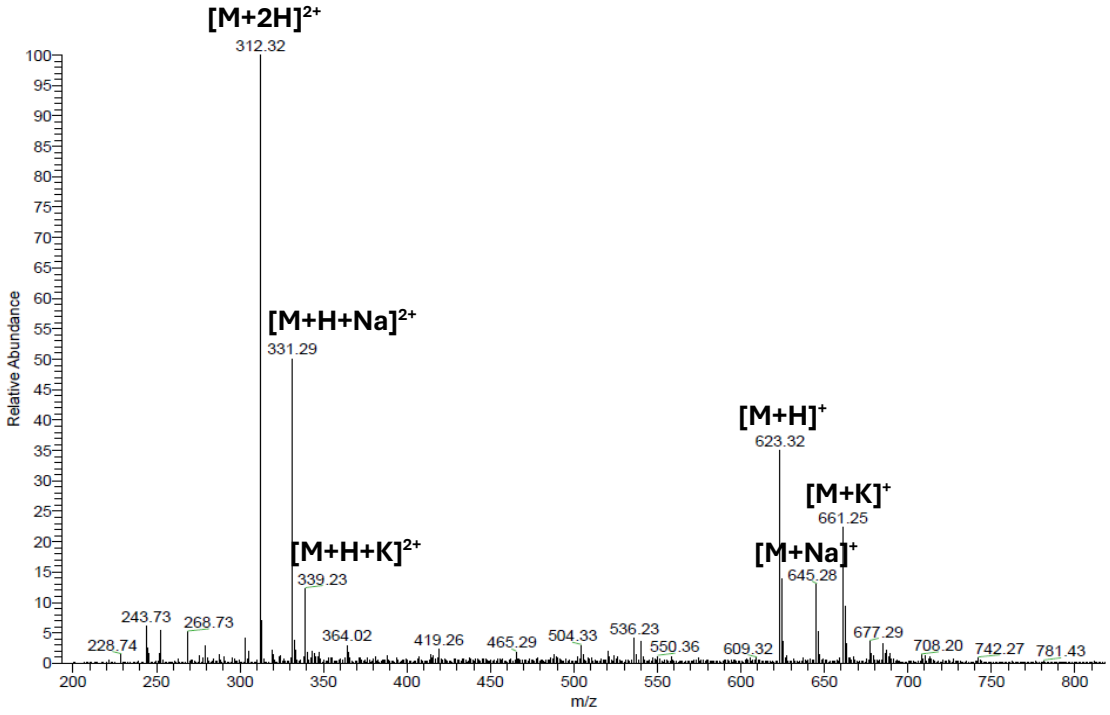

Figure 28. ESI-MS$^{(+)}$ spectrum of *phencropa* (**D'**).

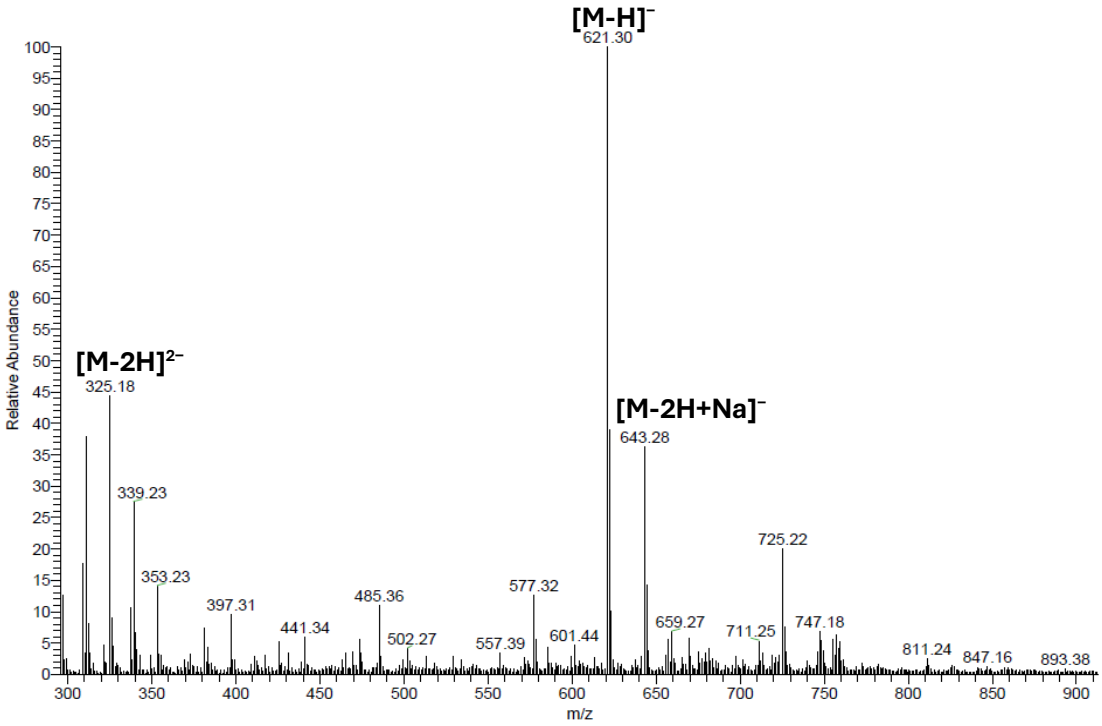

Figure 29. ESI-MS$^{(-)}$ spectrum of *phencropa* (**D'**).

Synthesis and characterization of *phencropa* complexes with the divalent cations Ba(II) and Pb(II)

[Ba(*phencropa*)] (5)

The [Ba(*phencropa*)] complex (**5**) was obtained by reacting, at room temperature, a slight excess of $BaCl_2$ with a concentrated aqueous solution of *phencropa*, previously adjusted to pH 7. The resulting complex precipitated as a beige solid within 5 minutes and was subsequently isolated by centrifugation. As done for complex **1**, characterization was performed by X-ray diffraction and NMR spectroscopy (*vide infra*).

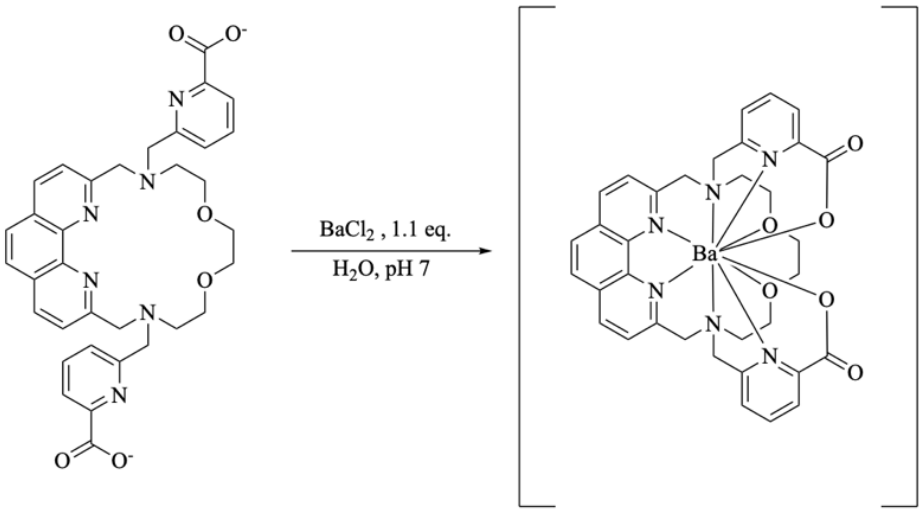

D' **(5)**

Scheme 6. Schematic representation of the synthesis of [Ba(*phencropa*)] (**5**).

X-ray crystallographic studies of the [Ba(*phencropa*)] (5) complex

Single crystal X-ray crystallography showed that [Ba(*phencropa*)] (**5**) has a molecular structure similar to **1**, *i.e.* it is a neutral complex with no additional counterions, adopting an asymmetric geometry in which the Ba^{2+} cation is deca-coordinated (Figure 30). In the case of **5**, two molecules of the complex were detected in the unit cell. However, since their structures are practically identical, the coordination bond distances of only one of them are reported (Table 2). Moreover, in this case angle formed by the phenanthroline fragment with the average plane that contains N1 – N5 and O3 is slightly larger compared to the similar one in [Ba(*bpycropa*)] (**1**) (~30° in **5** vs ~19° in **1**).

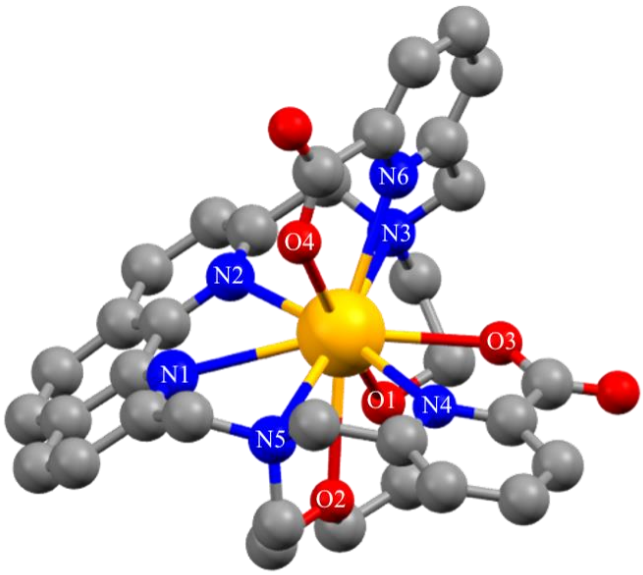

Figure 30. Single crystal X-ray structure of [Ba(*phencropa*)] (**5**).

Table 2. Coordination bond lengths from the single crystal X-ray structure of the [Ba(*phencropa*)] complex (**5**).

	[Ba(*phencropa*)]	
	bond	***length (Å)***
N-bpy/phen(1)	Ba–N1	2.974(4)
N-bpy/phen(2)	Ba–N2	2.934(5)
N-amine(1)	Ba–N3	2.993(4)
N-picolinate(1)	Ba–N4	2.897(4)
N-amine(2)	Ba–N5	3.031(4)
N-picolinate(2)	Ba–N6	2.869(4)
O-ether(1)	Ba–O1	2.895(3)
O-ether(2)	Ba–O2	2.920(3)
O-carboxylate(1)	Ba–O3	2.761(3)
O-carboxylate(2)	Ba–O4	2.736(4)

The coordination distances in the Ba(II) complexes **1** and **5** are rather similar; it is worth noting, however, that in **5** the two opposite bonds Ba–N2 and Ba–N4 are sensibly shorter that in **1** (bond length 2.934(5) and 2.897(4) Å vs 3.019(4) and 2.943(4) Å, respectively), suggesting a tighter coordination in *phencropa*.

On the other hand, the solid state geometries of **1** and **5** differ greatly from that of [Ba(*macropa*)], in which the ligand coordination to the metal center exhibits a higher degree of symmetry. In particular, the crystal structure of the complex [Ba(*Hmacropa*)(DMF)][ClO_4] (Figure 31) has been resolved,[21] showing that one of the two picolinate groups is protonated, and the overall charge is neutralized by a perchlorate anion. In this case, the barium ion displays a coordination number of eleven. The six donor atoms of the macrocyclic framework, *i.e.* the two amine nitrogens (N1 and N2) and the four ether oxygens (O1 – O4), define a mean plane around the cation, while the two picolinate rings chelate the metal from above in an antisymmetric arrangement. The barium coordination sphere is completed by a DMF molecule bound on the face opposite to the picolinate groups. It is worth noting that similar solid state structures were found for the complexes of *macropa* with radium, lanthanum, and lutetium ions, suggesting that this coordination mode is a common feature for this ligand.[21][28][23]

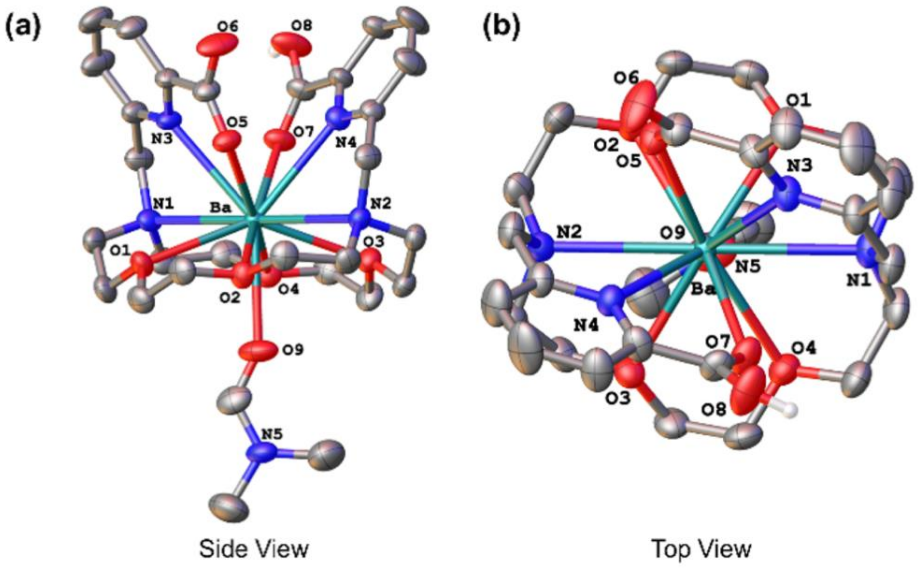

Figure 31. X-ray crystal structure of the [Ba(*Hmacropa*)(DMF)][ClO_4] complex.[21]

The presence of a C_2 symmetry axis in the [Ba(*Hmacropa*)(DMF)]$^+$ complex, clearly visible in the top-down view shown in Figure 31, is consistent with its solution NMR spectrum. Unlike those of the [Ba(*phencropa*)] and [Ba(*bpycropa*)] complexes, this spectrum displays a number of resonances equal to half of the total number of protons in the molecule, reflecting the higher symmetry of the compound.[21] Thus, if in the macropa complexes an exchange process of the two picolinate pendant arms should also occur, it would not be visible in the ^{1}H NMR spectra due to the higher symmetry.

NMR studies of the [Ba(*phencropa*)] (5) complex

The neutral complex **5** is soluble in methanol and poorly soluble in water. The ^{1}H NMR spectrum of **5** in CD_3OD, shown in Figure 32, closely resembles that of the analogous complex [Ba(*bpycropa*)] (**1**) (Figure 16), suggesting that the two have similar coordination environments and geometries in solution (as in the solid state).

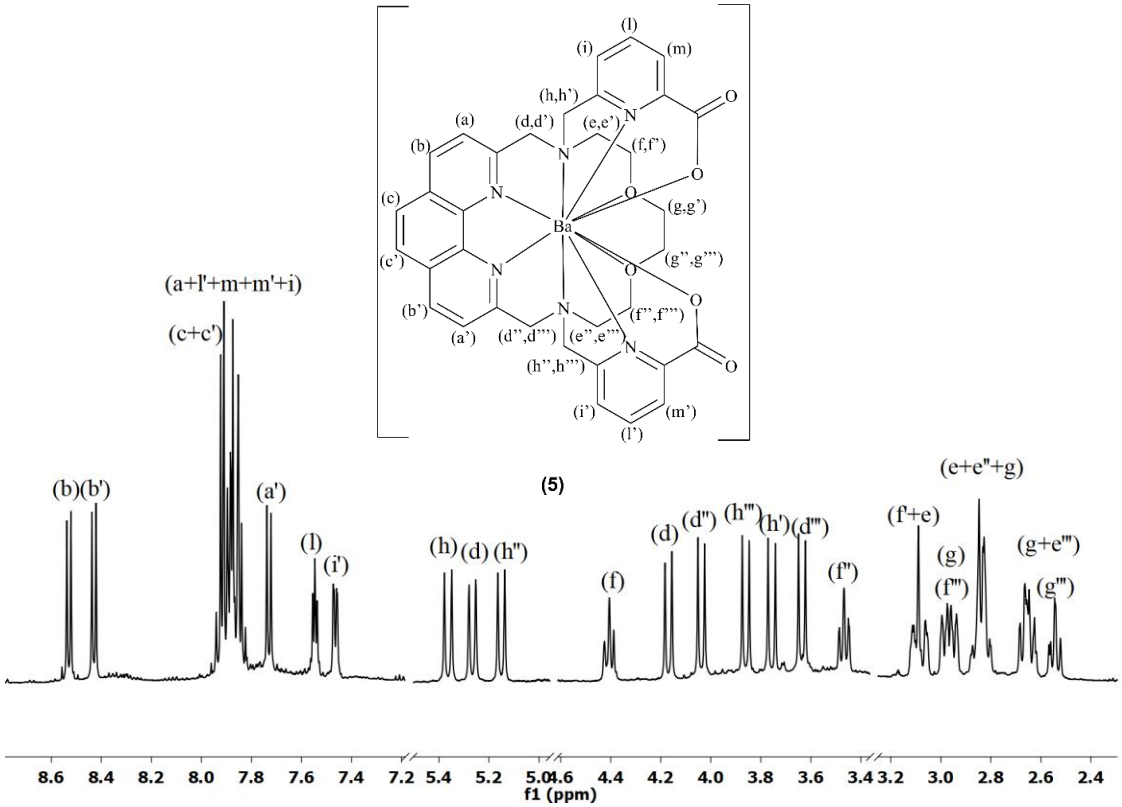

Figure 32. ^{1}H NMR spectrum (500 MHz) of [Ba(*phencropa*)] (**5**) in CD_3OD with labeling scheme.

As for the [Ba(*bpycropa*)] (**1**) complex, the ^{1}H NMR spectrum of [Ba(*phencropa*)] (**5**) also shows a number of resonances significantly larger compared to the free ligand. Sixteen well-resolved resonances are observed (five in the aromatic region and eleven in the aliphatic region, each integrating for 1H). The remaining 16 protons give resonances that partially overlap in four additional multiplets. Thus, in this case as well, all protons are magnetically inequivalent and resonate at different frequencies due to the loss of ligand symmetry upon coordination. All resonances were assigned through a ^{1}H – ^{1}H COSY spectrum (Figures 33a and 33b), followed by analysis of ^{1}H – ^{13}C HSQC and ^{1}H – ^{13}C HMBC spectra (see Supplementary Information, Figures S27 and S28), as done for [Ba(*bpycropa*)] (**1**).

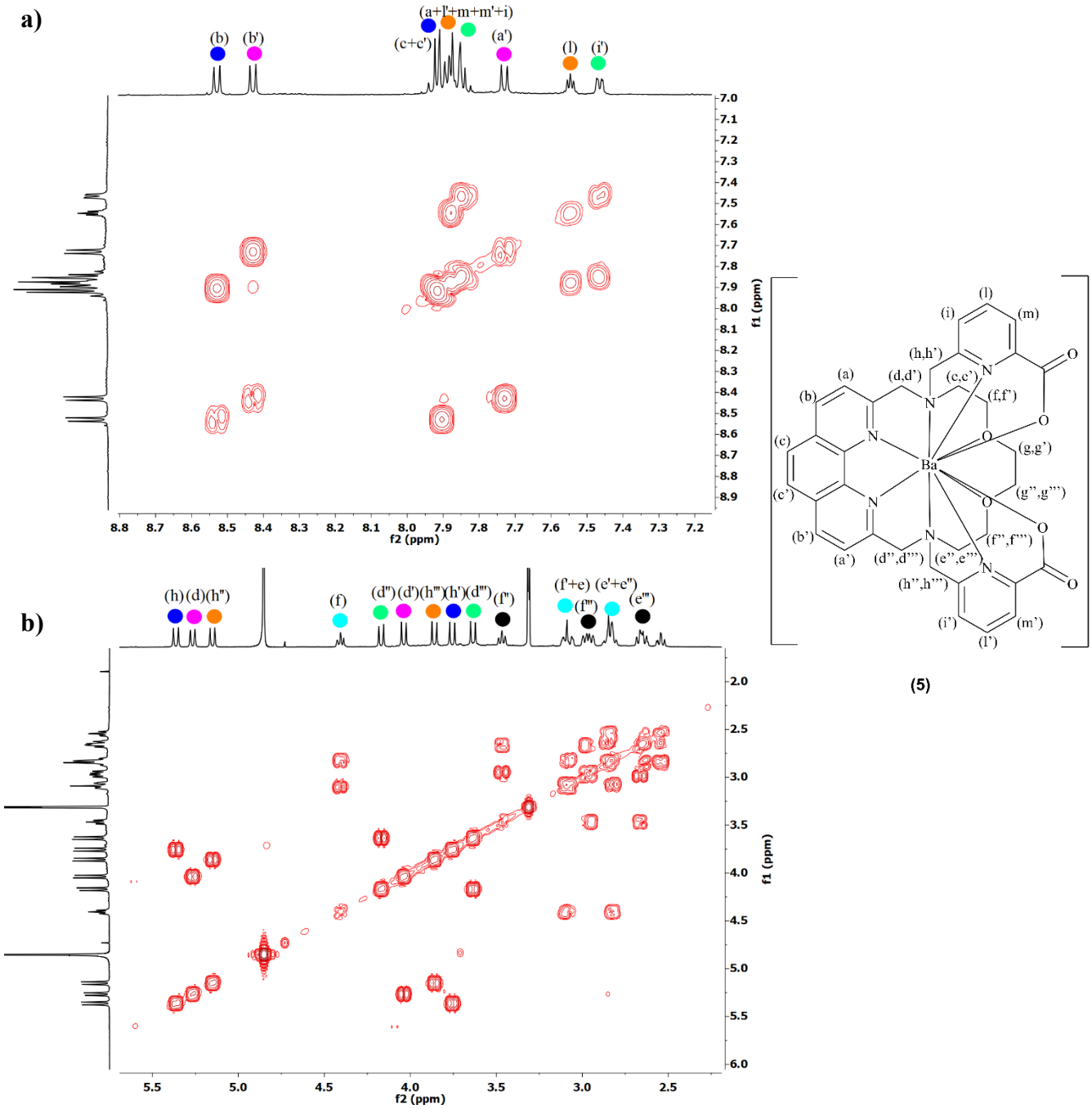

Figure 33. ^{1}H – ^{1}H COSY spectrum (500 MHz) of [Ba(*phencropa*)] (**5**) in CD_3OD with labeling scheme: (**a**) aromatic region, (**b**) aliphatic region. Color coding identifies couplings between proton pairs with at least one resolved resonance.

Furthermore, as for [Ba(*bpycropa*)], the ^{1}H – ^{1}H ROESY spectrum of complex **5** shows exchange cross peaks between the resonances of the chemically equivalent proton pairs, e.g the pairs of phenanthroline protons $H_b/H_{b'}$ and $H_a/H_{a'}$, as well as the pairs of picolinate protons $H_l/H_{l'}$ and $H_i/H_{i'}$ (Figure 34).

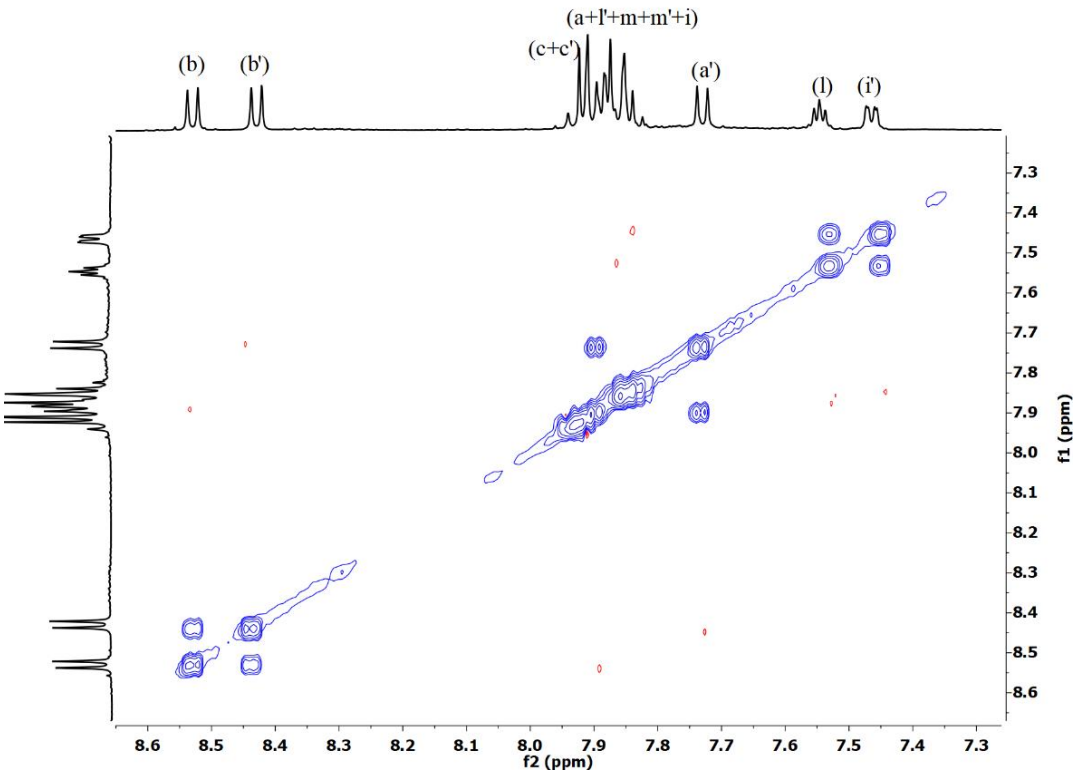

Figure 34. $^{1}H - {}^{1}H$ ROESY spectrum (600 MHz) of the [Ba(*phencropa*)] complex (aromatic region).

[Pb(*phencropa*)] (6)

[Pb(*phencropa*)] (**6**) was obtained using the same procedure described for the *bpycropa* analogous complex **2**. The ^{1}H NMR spectrum of **6** shown in Figure 35 displays a pattern similar to that of the barium complex **5**, with a more pronounced overlapping of signals. However, a major difference resided in the $^{1}H - {}^{1}H$ ROESY spectrum (Figure 36), in which no exchange cross peaks were observed for the same mixing time (300 ms) used for the corresponding complex with *bpycropa* **2**. This finding suggests that the exchange process in the *phencropa* complexes is slower than in those with *bpycropa* and is consistent also with the slower exchange rate found in [Pb(*bpycropa*)] compared to [Ba(*bpycropa*)] (*vide supra*).

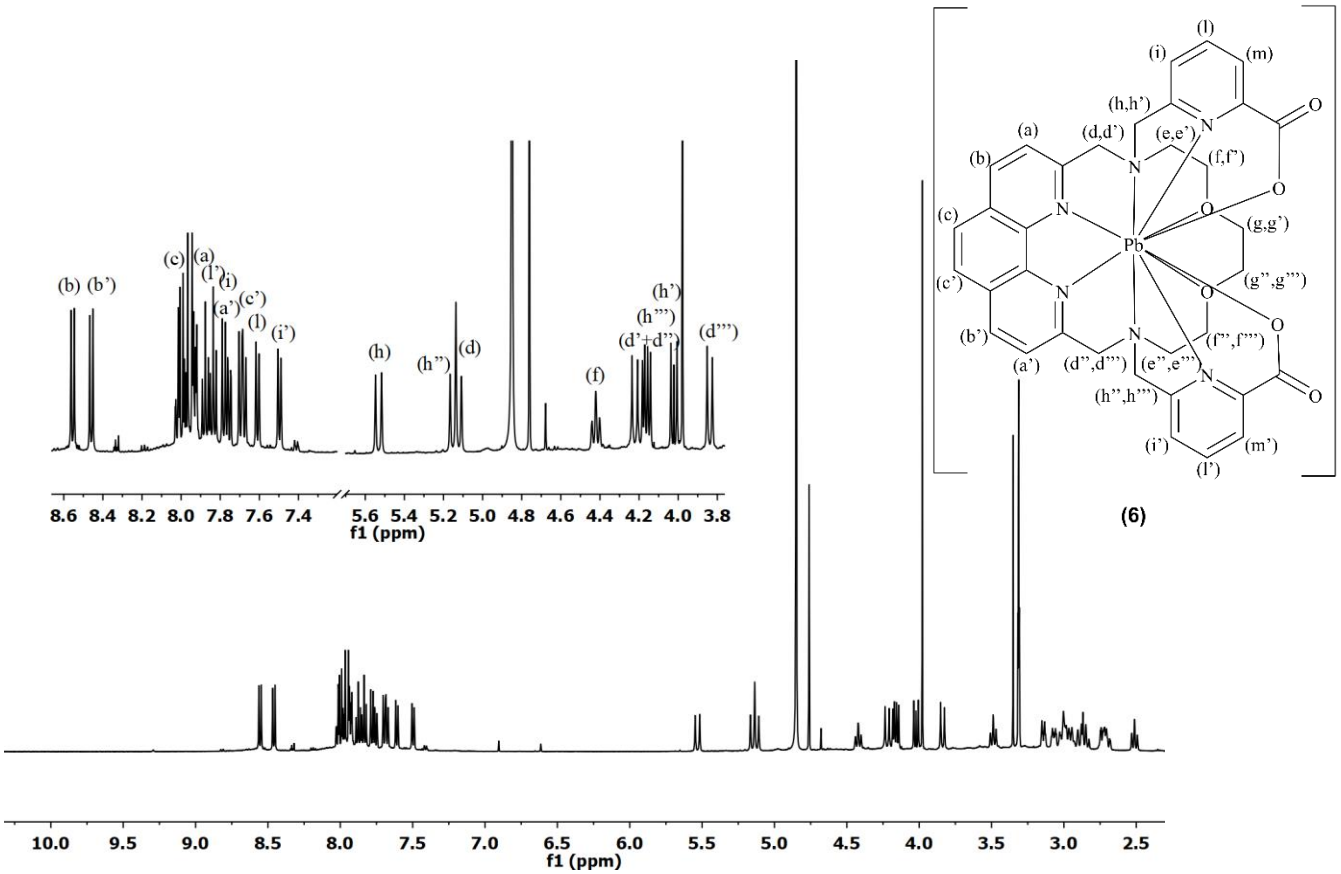

Figure 35. ^{1}H NMR spectrum (500 MHz) of [Pb(*phencropa*)] (**6**) in CD_3OD with labeling scheme.

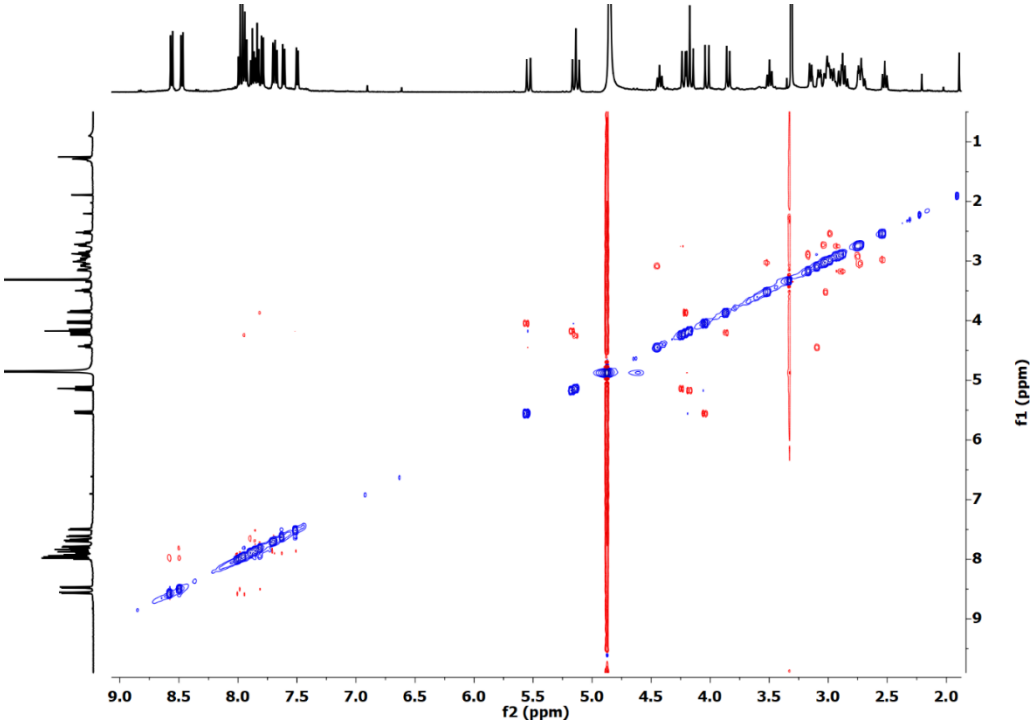

Figure 36. ^{1}H – ^{1}H ROESY spectrum (600 MHz) of [Pb(*phencropa*)] in CD_3OD; only NOE cross peaks (red) are evident.

Synthesis and characterization of *phencropa* complexes with the trivalent cations La(III) and Bi(III)

[La(*phencropa*)][NO_3] (7)

The complex [La(*phencropa*)][NO_3] (**7**) was synthesized with the same procedure used for the analogous *bpycropa* complex **3**.

However, contrary to **3**, complex **7** is soluble in both methanol and water. The ^{1}H NMR spectrum of [La(*phencropa*)][NO_3] in CD_3OD (Figure 37) closely resembles that of [Ba(*phencropa*)] (**5**) described above, as well as that of the analogous [La(*bpycropa*)][NO_3] (**3**) complex, indicating a similar coordination environment and geometry. Ten well-resolved resonances were identified − five in the aromatic region and five in the aliphatic region − each integrating for one proton, in addition to ten multiplets resulting from overlapping signals. Moreover, as seen for complex **3**, the ^{1}H – ^{1}H ROESY spectrum did not exhibit exchange cross peaks.

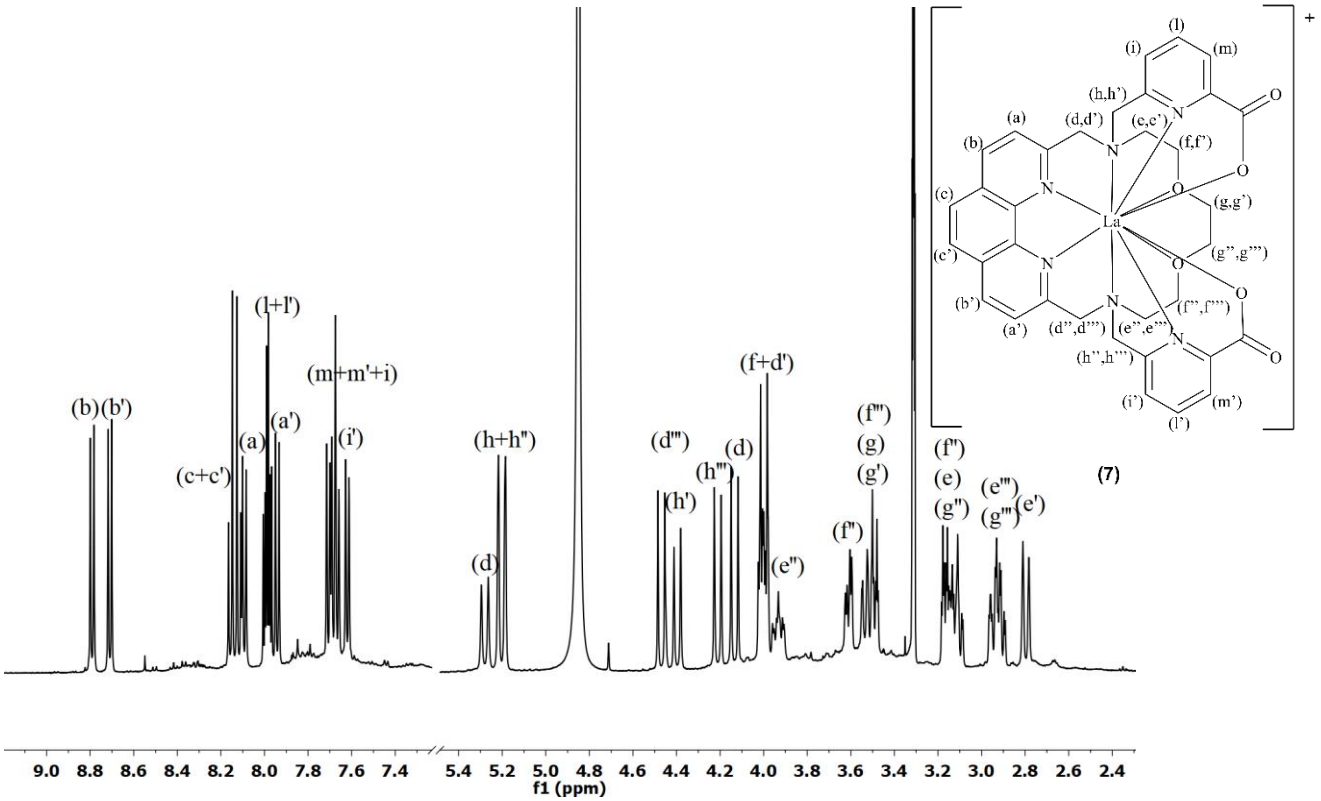

Figure 37. ^{1}H NMR spectrum (500 MHz) of [La(*phencropa*)]$^+$ (**7**) in CD_3OD with labeling scheme.

[Bi(*phencropa*)][NO_3] (8)

The complex [Bi(*phencropa*)][NO_3] (**8**) was synthesized with the same procedure used for [Bi(*bpycropa*)][NO_3] (**4**) (*vide supra*). However, the CD_3OD samples for the NMR characterization were found to become increasingly turbid for the formation of a white precipitate, presumably a bismuth hydroxide due to Bi^{3+} hydrolysis. This finding might be due either to the decomposition of the complex over time or to the presence in the NMR sample of unreacted bismuth salt. Further investigations on this system are needed and at present we cannot favor either hypothesis, even though we notice that the corresponding *bpycropa* complex **4** was stable in methanol solution. In Figure 38 the ^1H NMR spectrum of a diluted sample of the complex in CD_3OD is shown. The aromatic proton region clearly displays the characteristic resonances observed in the previously discussed *phencropa* complexes, corresponding to the phenanthroline ($H_{b/b'}$, $H_{a/a'}$ and $H_{c/c'}$) and picolinate moieties ($H_{l/l'}$, $H_{m/m'}$ and $H_{i/i'}$) suggesting, also in this case, the usual coordination environment and geometry.

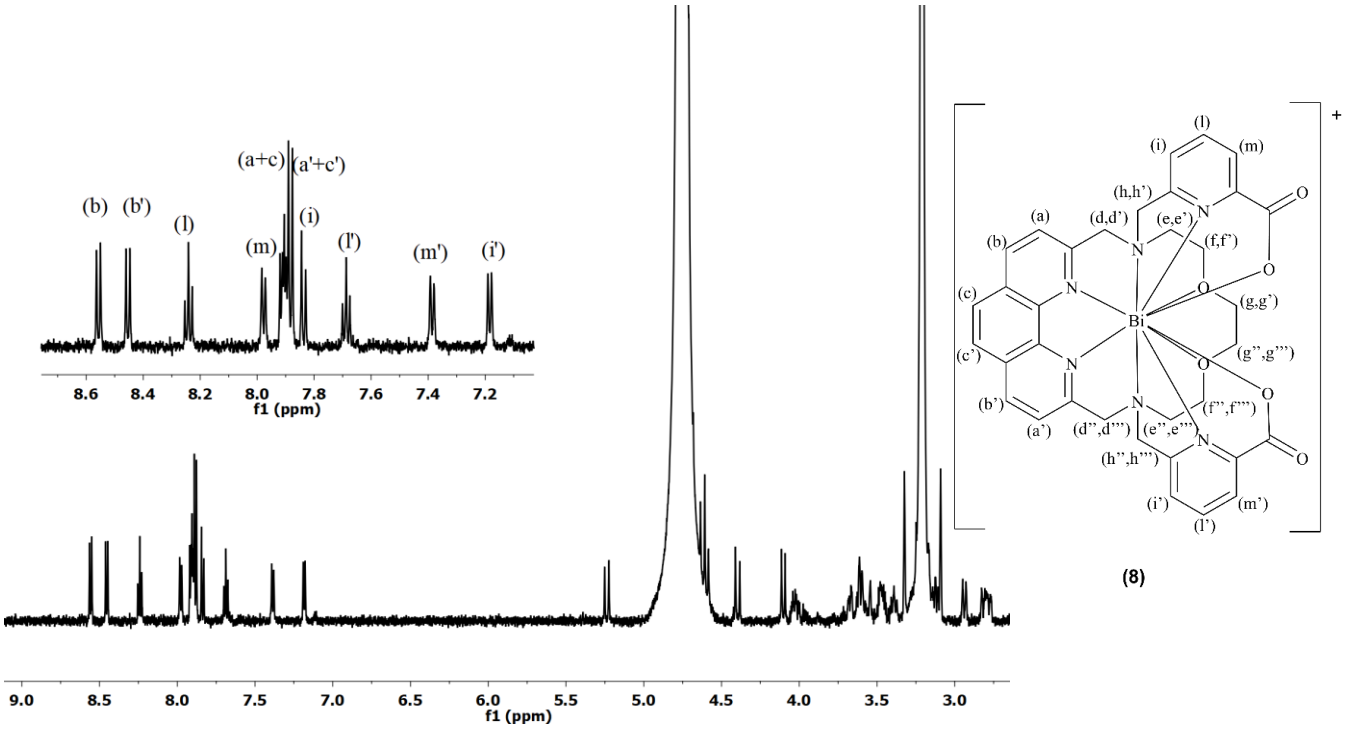

Figure 38. ^1H NMR spectrum (600 MHz) of [Bi(*phencropa*)][NO_3] (**8**) in CD_3OD with labeling scheme.

Thermodynamic studies of *bpycropa* and *phencropa* ligands and complexes

pH-potentiometry

Potentiometric titrations – performed at the University of Western Brittany in Brest (France), – were employed to determine the protonation constants of the ligands and the stability constants of their respective metal complexes under well-defined equilibrium conditions. This technique is known to provide accurate macroscopic protonation equilibrium constants over wide pH ranges and, in this work, served as a reference method for comparison with protonation constants obtained by ^{1}H NMR spectroscopy (*vide infra*).

All measurements were carried out in 0.15 M KNO_3 to maintain constant ionic strength and were performed over the pH range 1.8 – 12.0, enabling characterization of both the protonation equilibria of the free ligands and the formation equilibria of the corresponding metal complexes. A standardized 0.1 M KOH solution was used as the titrant, and the pH was monitored with a calibrated glass electrode connected to an automated titration system.

^{1}H NMR spectroscopy titrations of *bpycropa* and *phencropa* ligands

^{1}H NMR titrations afford the experimental determination of protonation constants (pK_a values) for molecules containing multiple (de)protonable sites by analyzing how the chemical shift of one or more protons changes as a function of pH. Similarly to pH-potentiometry, in NMR titrations it is also necessary to maintain a constant ionic strength by adding a high concentration of a non-interacting salt, both to ensure accurate pH readings and because the ionic strength – that also affects the resonance frequencies of the various spin systems – should not significantly depend on incremental additions of OH^- ions. Moreover, prior to data analysis, the experimentally measured pD values obtained from the pH-meter were corrected for isotopic effects of the D_2O solvent by subtracting a value of 0.4.[29] The pK_a values were then determined by processing the data with softwares that allow different types of curve fitting. This method, in combination with potentiometric titrations, was essential for determining and validating the speciation of the synthesized macrocycles *bpycropa* and *phencropa*. Moreover, the protonation constants determined by ^{1}H NMR spectroscopy were compared to those of the reference chelator *macropa*.

Protonation constants of *macropa*

In principle, *macropa* has six sites that might undergo (de)protonation processes: the two sp^3 N atoms in the macrocycle, plus the two sp^2 N atoms and the two carboxylate groups of the picoline arms.

From the literature,[22][30] ^{1}H NMR and potentiometric titrations of *macropa* identified four distinct protonation constants in the pH range 2 – 8 (Table 3). The two pK_a values of 2.40 and 3.13 were ascribed to the protonation of the carboxylic groups on the two picolinate rings, while the higher pK_a values of 6.80 and 7.73 were assigned to the protonation processes of the

basic tertiary nitrogens of the macrocycle. In another work,[22] an additional protonation process at very acidic pH (pK_a = 1.69) was observed and attributed to the protonation of a picolinate nitrogen atom. This value is considerably lower compared to the corresponding picolinic N-atom as a free ligand, which has a $pK_a \approx 5.3$.[31]

Table 3. Protonation constants of *macropa* from the literature ([*macropa*] = 0.001 M, 25 °C).[22][30]

macropa
1.69(1)[22]
2.40(1)[30]
3.13(1)[30]
6.80(1)[30]
7.73(1)[30]

[2] [KCl] = 0.1 M

[30] [NaCl] = 0.1 M

In our case, the *bpycropa* and *phencropa* ligands have two additional sp^2 N atoms that might undergo protonation processes, with pK_a values of 4.44 and 4.92 for the free 2,2'-bipyridine and 1,10-phenantroline ligands, respectively.[32]

^{1}H NMR titration of the *bpycropa* ligand (D)

The ^{1}H NMR titration of *bpycropa* was performed on a 10 mM sample of the ligand in D_2O, with 0.15 M $NaNO_3$ for constant ionic strength and 2,2-dimethyl-2-silapentane-5-sulfonate sodium salt (DSS), which was used as reference at 0.0 ppm. In Figure 39 the ^{1}H NMR spectrum of the ligand dissolved in D_2O is shown before starting the titration. The low pH value of this sample, 1.38, is due to the fact that the ligand was isolated in the form of hydrochloride salt. The sample was then titrated by adding small amounts of a NaOD solution in D_2O.

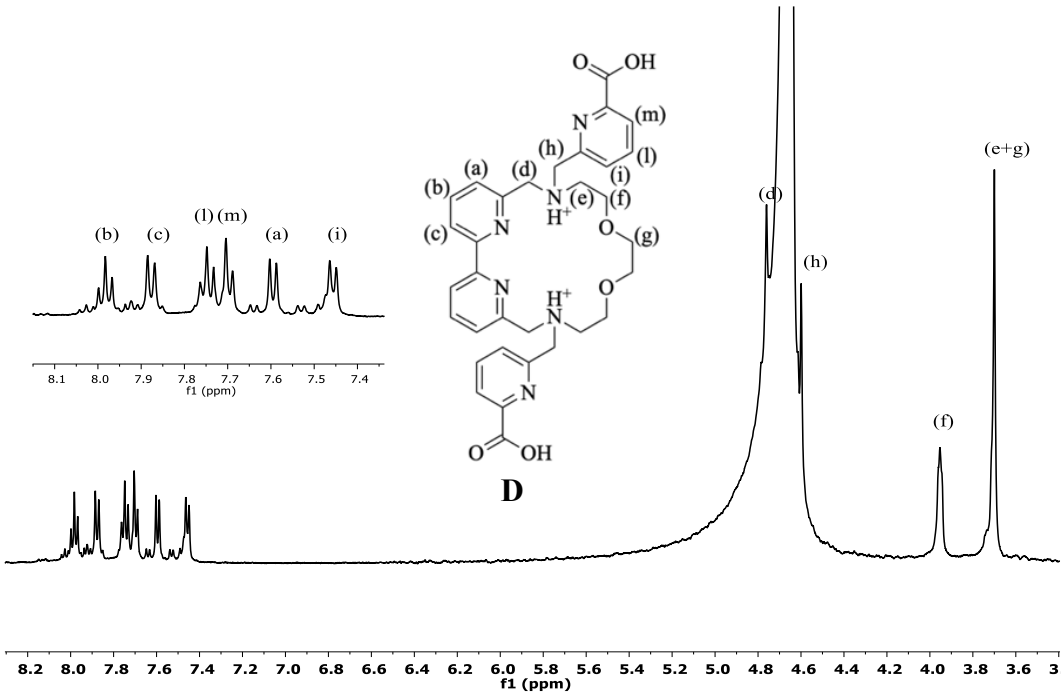

Figure 39. ^{1}H NMR spectrum (500 MHz) of the *bpycropa* ligand (**D**) in D_2O at pH = 1.38 with labeling scheme.

Figures 40 and 41 show the trends observed during the NMR titration in the aromatic and aliphatic regions, respectively. For the determination of the pK_a values, the chemical shifts of well-resolved resonances that significantly vary with pH and remain free from overlap are typically plotted, allowing them to be reliably tracked across the titration.

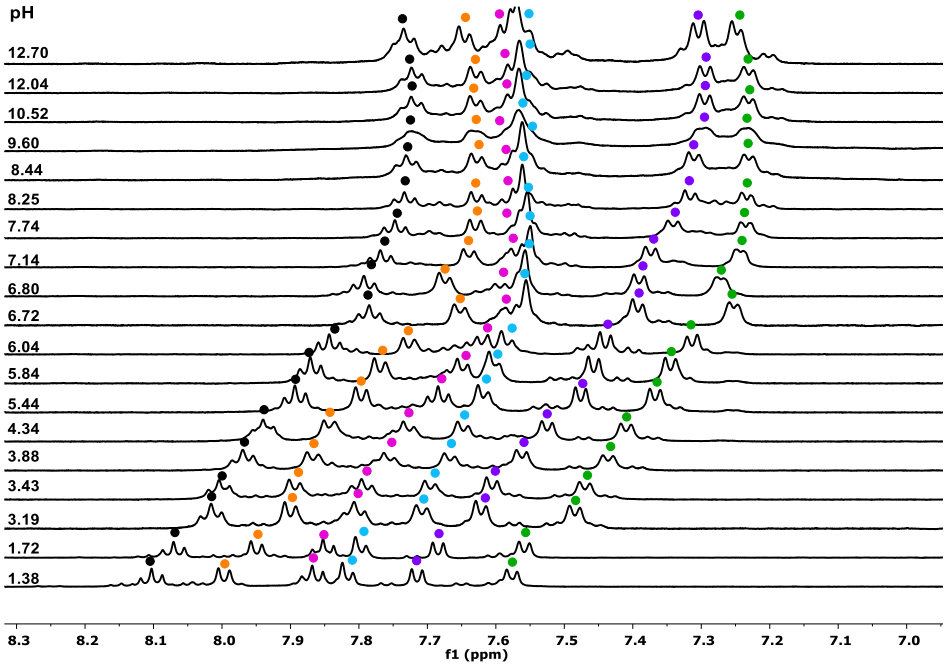

Figure 40. ^{1}H NMR titration of the *bpycropa* ligand (**D**) in D_2O (aromatic region). See Figure 39 for the labeling scheme. Color coding identifies and tracks the protons of the system as a function of pH: H_b (black), H_c (orange), H_l (magenta), H_m (blue), H_a (purple) and H_i (green).

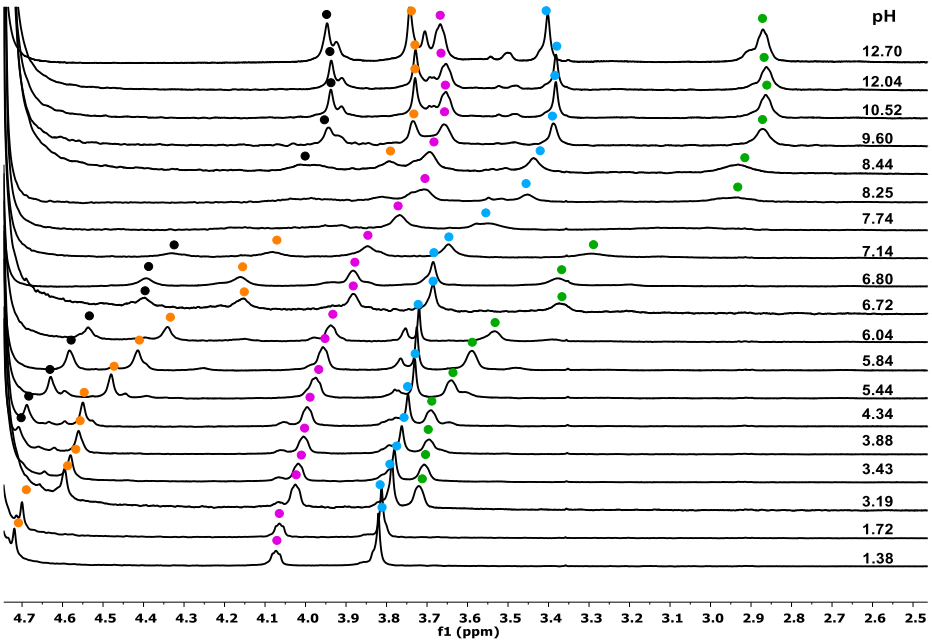

Figure 41. ^{1}H NMR titration of the *bpycropa* ligand (**D**) in D_2O (aliphatic region). See Figure 39 for the labeling scheme. Color coding identifies and tracks the protons of the system as a function of pH: H_d (black), H_h (orange), H_f (magenta), H_g (blue) and H_e (green).

It can be observed that all signals shift to lower frequencies as the pH increases, in agreement with the ligand becoming deprotonated and thus possessing higher electron density. Moreover, in the pH range 6.9 – 8.5, substantial signal broadening occurs in the aliphatic region (Figure 41), likely due to a conformational or protonation/deprotonation equilibrium of intermediate rate that involves mainly the flexible part of the macrocycle.

The chemical shifts δ_i and protonation constants of *bpycropa* were fitted using a population-weighted average over all the protonation states of the ligand, by considering a five pK_a model (*Eq.1,* Figures 42a,b):

$$\delta(pH) = \frac{\sum_{i=0}^{5} \delta_i \beta_i [H]^{5-i}}{\sum_{i=0}^{5} \beta_i [H]^{5-i}} \qquad Eq.1$$

where δ_i is the intrinsic chemical shift of the protonation state „*i*“, [H] = 10^{-pH} and $\beta_i = \prod_{k=1}^{i} K_k$ is the cumulative protonation constant. Furthermore, the protonation constants determined by ^{1}H NMR spectroscopy were compared to those obtained by pH-potentiometry (Table 4).

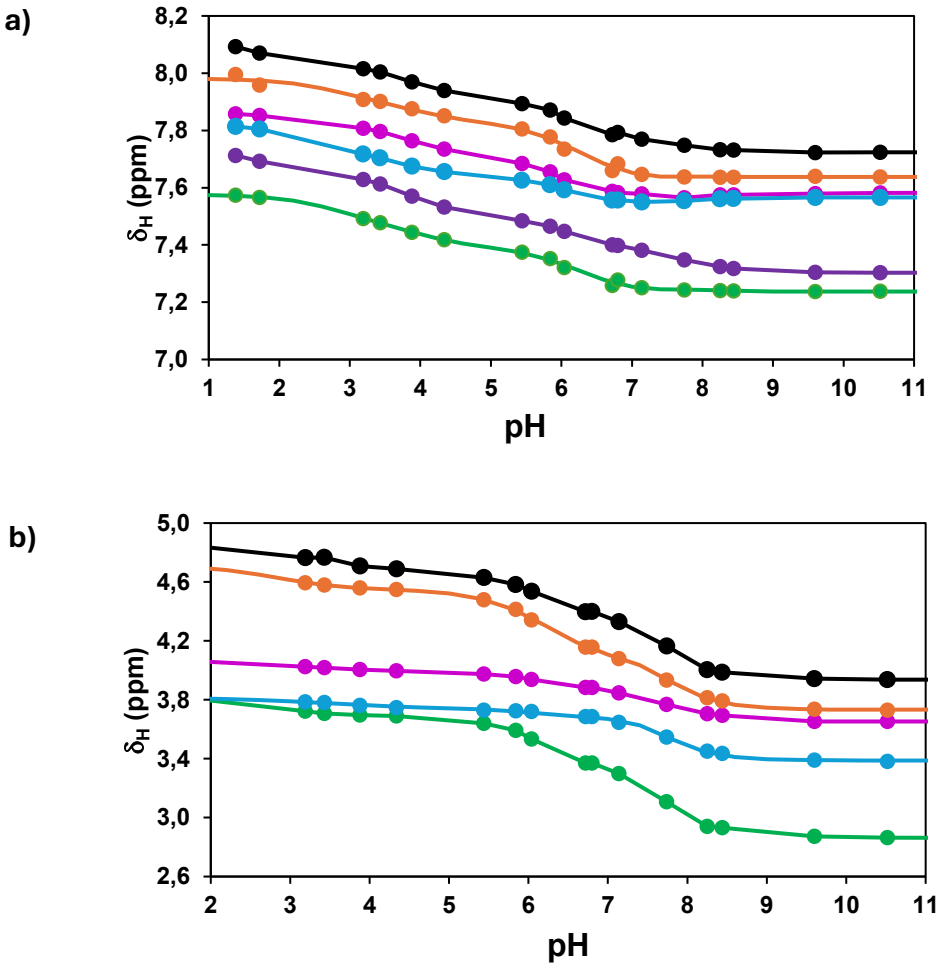

Figure 42. Fitted chemical shifts for the resonances of the aromatic protons (**a**) and aliphatic protons (**b**) *vs* pH.

Table 4. Protonation constants (pK_a values) of *bpycropa* obtained by ^{1}H NMR spectroscopy and pH-potentiometry, respectively.

$pKa_i^{H\ NMR}$	pKa_i^{pot}
I = 0.15 M $NaNO_3$	I = 0.15 M KNO_3
1.80(2)	1.82(2)
2.9(1)	2.90(2)
3.91(1)	3.84(2)
6.09(2)	6.47(1)
7.72(1)	7.74(1)

Analogously to *macropa*, the two larger protonation constants (6.1 − 7.9) are attributed to the sp^3-nitrogens, whereas the third one, in the range 3.84 − 3.91, is attributed to the protonation of the sp^2-nitrogens of the bipyridine unit, which is lower compared to the free bipyridine (pK_a = 4.44). Finally the two lowest protonation constants in the range 1.8 − 2.9 can be attributed to the acidic picolinate pendant arms.

Based on the determined pK_a values, the speciation diagram for *bpycropa* as a function of pH was calculated (Figure 43).

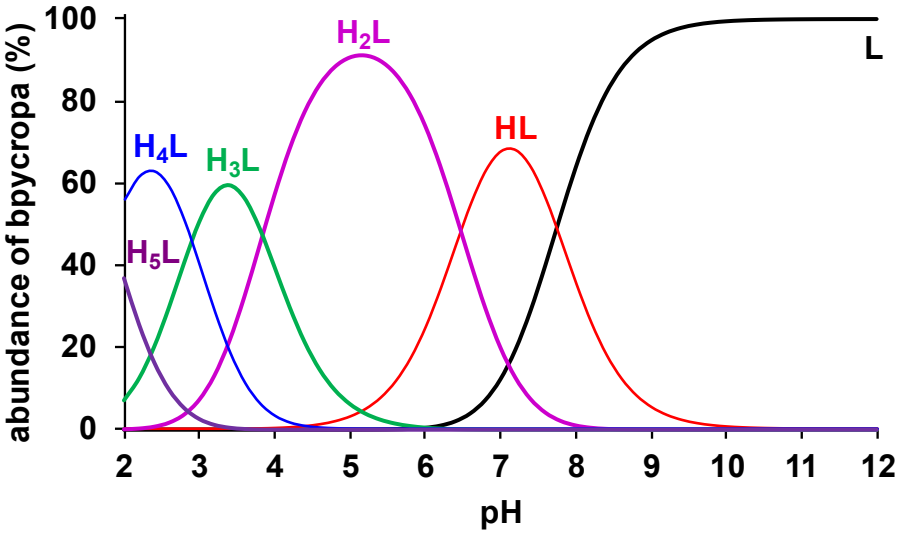

Figure 43. Speciation diagram for the *bpycropa* ligand (here labelled as **H_2L**) as a function of pH. [*bpycropa*] = 0.002 M, [KNO_3] = 0.15 M.

^{1}H NMR titration of the *phencropa* ligand (D')

In Figure 44 the initial ^{1}H NMR spectrum of *phencropa* (**D'**) in D_2O is shown. Also in this case the initial pH value is low (pH = 1.69). The ^{1}H NMR spectrum of the ligand displayed an analogous behaviour to *bpycropa* when titrated (Figures 45 and 46).

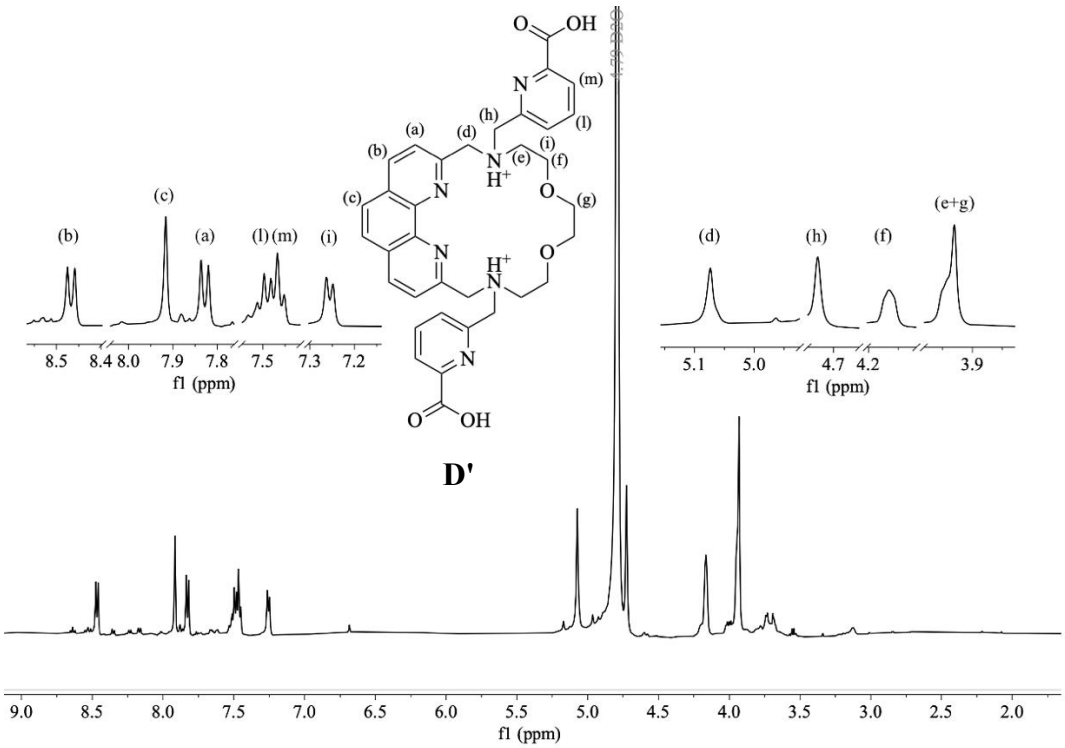

Figure 44. ^{1}H NMR spectrum (500 MHz) of *phencropa* (**D'**) in D_2O at pH = 1.69 with labeling scheme.

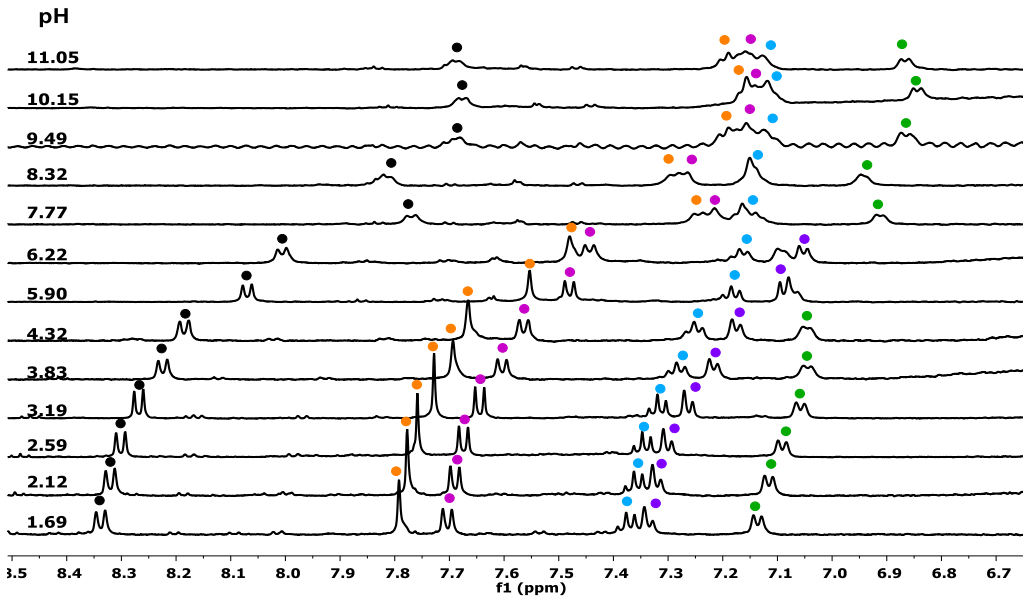

Figure 45. ^{1}H NMR titration of *phencropa* ligand (**D'**) in D_2O (aromatic region). See Figure 44 for the labeling scheme. Color coding identifies and tracks the protons of the system as a function of pH: H_b (black), H_c (orange), H_a (magenta), H_l (blue), H_m (purple) and H_i (green).

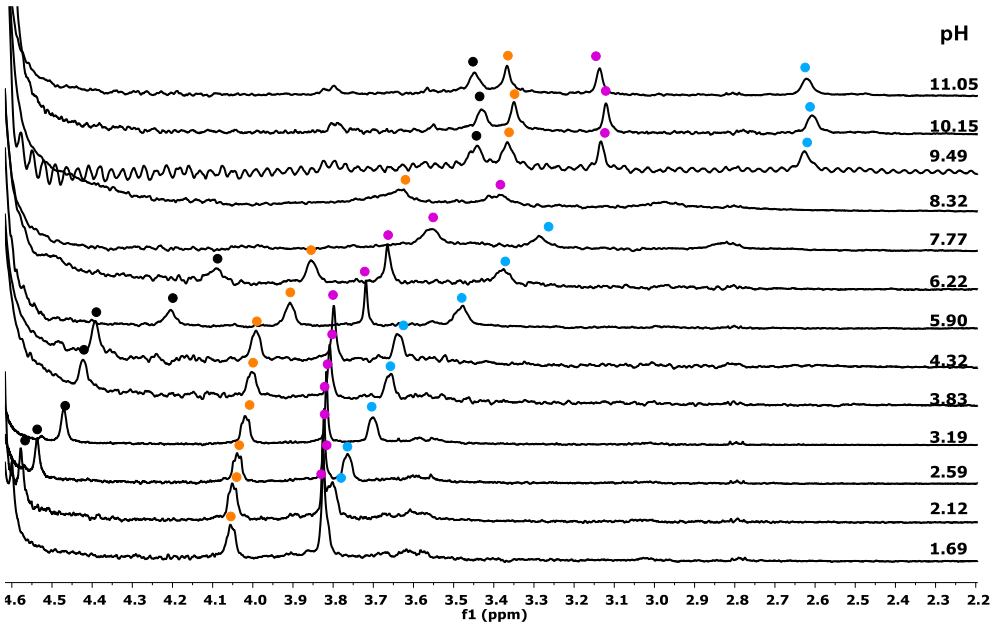

Figure 46. ^{1}H NMR titration of *phencropa* ligand (**D'**) in D_2O (aliphatic region). See Figure 44 for the labeling scheme. Color coding identifies and tracks the protons of the system as a function of pH: H_h (black), H_f (orange), H_g (magenta), and H_e (blue).

Compared to *bpycropa*, the resonances in the aromatic region show a larger overlapping as a function of pH (Figure 47a). Thus, for an accurate determination of the pK_a values, the resonances of the aromatic H_b proton (Figure 47a, black curve) and of four aliphatic protons (Figure 47b) were considered, as they are non-overlapping over the entire pH range and readily distinguishable from other signals. Moreover, the selected resonances exhibited considerable chemical shift variations, thus reflecting their sensitivity to the protonation processes.

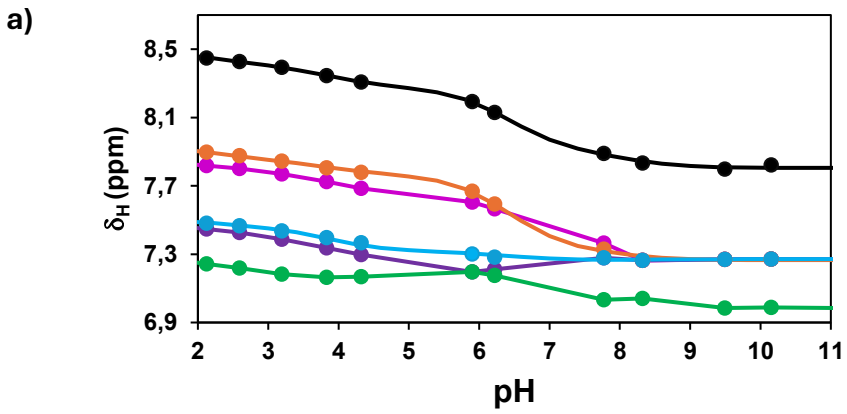

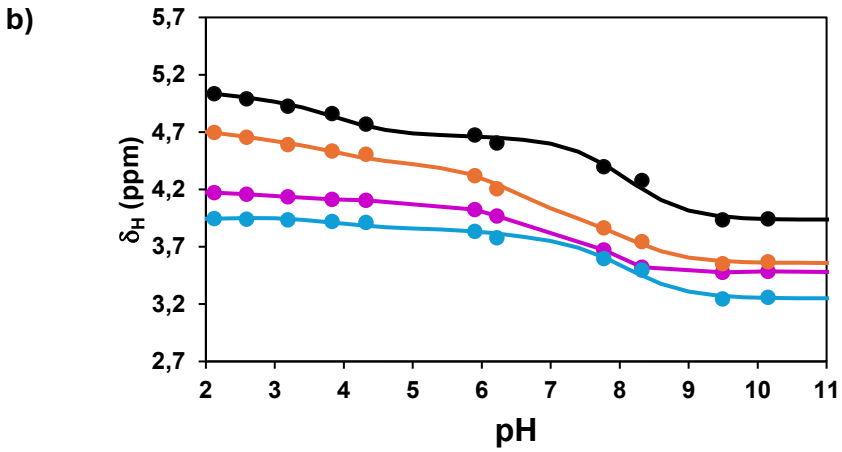

Figure 47. Fitted chemical shifts for the resonances of the aromatic protons (**a**) and aliphatic protons (**b**) *vs* pH.

In this case the best fit process afforded four (rather than five in the case of *bpycropa*) protonation constants. As seen previously for both *macropa* and *bpycropa*, the protonation constant with $pK_a = 2.9$ is assigned to the carboxylic group of the picolinate pendant arm. The remaining acidic protonation occurs at even lower pH and could not be reliably determined by fitting the ^{1}H NMR data. The pK_a value of 3.8 is attributed to protonation of the phenanthroline sp^2 nitrogens, which is shifted to lower values relative to the free ligand ($pK_a = 4.92$). The two higher pK_a values (6.42 and 8.11) are reasonably assigned to the protonation of the tertiary amine groups of the macrocycle.

Table 5 compares the pK_a values obtained for *phencropa* by ^{1}H NMR spectroscopy and pH-potentiometric measurements. The latter method enabled the determination of the lowest protonation constant, obtaining for it a pK_a of 1.31. Furthermore, the highest protonation constant assigned to one of the sp^3-hybridized nitrogen atoms resulted higher when determined by NMR than by potentiometry (8.11 *vs* 7.26). This discrepancy can be attributed to differences in the ionic background of the two experiments: the potentiometric measurements were conducted in 0.15 M KNO_3, whereas the NMR studies employed 0.15 M $NaNO_3$, suggesting an effect related to the different ionic radii of the cations.

Table 5. Protonation constants (pK_a values) of *phencropa* (**D'**) obtained by ^{1}H NMR spectroscopy and potentiometry, respectively.

$pKa_i^{H\ NMR}$	pKa_i^{pot}
I = 0.15 M $NaNO_3$	I = 0.15 M KNO_3
–	1.31(2)
2.9(1)	2.89(1)
3.88(5)	3.82(1)
6.42(1)	6.25(1)
8.11(1)	7.26(1)

Similarly to *bpycropa*, the pH-dependent speciation diagram for *phencropa* was calculated and is shown in Figure 48.

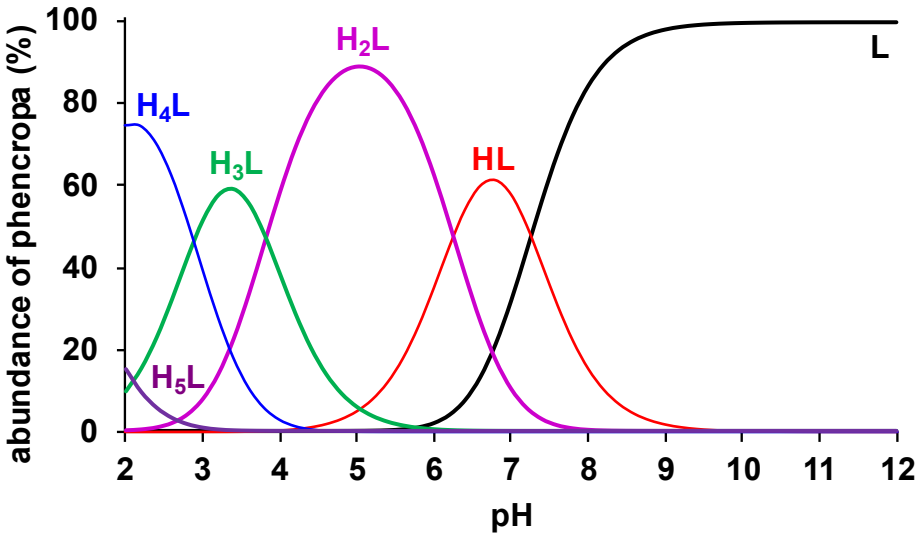

Figure 48. Speciation diagram for the *phencropa* ligand (here labelled as **H_2L**) as a function of pH. [*phencropa*] = 0.002 M, [KNO_3] = 0.15 M.

The NMR-obtained protonation constants for *phencropa* are very similar to those of *macropa*[22][30] and *bpycropa* at the same temperature (Table 6). It should be noted, however, that in the case of *macropa*, the ionic strength used was 0.1 M NaCl, and that the lowest protonation constant was determined in KCl, rather than $NaNO_3$.

Table 6. Comparison of pK_a values for the *phencropa*, *bpycropa* and *macropa* ligands obtained by NMR spectroscopy. [$NaNO_3$] = 0.15 M, 25 °C

	macropa	***bpycropa***	***phencropa***
pKa_1'	1.69(1)[22]	1.80(2)	–
pKa_1	2.40(1)[30]	2.9(1)	2.9(1)
pKa_2	3.13(1)[30]	3.91(1)	3.88(5)
pKa_3	6.80(1)[30]	6.09(2)	6.42(1)
pKa_4	7.73(1)[30]	7.72(1)	8.11(1)

[2][KCl] = 0.1 M, 25°C, [*macropa*] = 0.001 M

[30][NaCl] = 0.1 M, 25°C, [*macropa*] = 0.001 M

Determination of stability constants of *bpycropa* and *phencropa* complexes with Ba^{2+}, Pb^{2+} and La^{3+}

The stability constants of the metal complexes formed by *bpycropa* or *phencropa* with the divalent and trivalent cations Ba^{2+}, Pb^{2+}, and La^{3+} were determined by potentiometric titrations.

The measurements were performed under the same conditions employed for the free ligands, namely in 0.15 M KNO_3 and over the pH range 1.8 – 12.0, using a standardized 0.1 M KOH solution as titrant. The experimental data were fitted by using the protonation constants of the free macrocycles, and including the formation of the species ML, M(HL) and M(H_2L) (metal complex, mono- and diprotonated complexes, respectively) to obtain the overall formation constants (log*K* values) for each metal-ligand system (Table 7). This approach afforded an accurate characterization of the complexes across a wide pH range and provided direct comparison of the relative binding affinities of Ba^{2+}, Pb^{2+}, and La^{3+} under the same conditions. In addition, conditional stability constants (K_{ML}^{cond}) for pH = 7.4 were calculated for each complex using *Eq.2* to provide insight into their behavior under physiological conditions. For the calculation, the portion of the protonated ligand, the protonated metal-complex, and the hydrolysis of the metal ions have been taken into account by the alpha coefficients for the ligand (α_L), the metal complex (α_{ML}), and the metal ion (α_M), respectively.

$$K_{ML}^{cond} = \frac{[ML]_t}{[M]_t[L]_t} = \frac{[ML]}{[M][L]}\frac{\alpha_{ML}}{\alpha_M\alpha_L} = K_{ML}\frac{\alpha_{ML}}{\alpha_M\alpha_L} \qquad Eq.2$$

where $[M]_t = [M] + [M(OH)] + [M(OH)_2]$; $[L]_t = [L] + [HL] + [H_2L] + \ldots + [H_5L]$, $[ML]_t = [ML] + [MHL] + [MH_2L]$; $\alpha_M = 1 + K_{MOH}/[H^+] + K_{MOH}K_{M(OH)2}/[H^+]^2$; $\alpha_L = 1 + K_1[H^+] + K_1K_2[H^+]^2 + \ldots + K_1K_2\ldots K_5[H^+]^5 +$, $\alpha_{ML} = 1 + K_{MHL}[H^+] + K_{MHL}K_{MH2L}[H^+]^2$

Table 7. Comparison of the stability constants of *macropa*, *bpycropa*, *phencropa* complexes with Ba^{2+}, Pb^{2+} and La^{3+} ions, and respective conditional stability constants ($\log K_{ML}^{cond}$) for pH = 7.4. [KNO_3] = 0.15 M, 25 °C.

	macropa	***bpycropa***	***phencropa***
$\log K_{BaL}$	**11.11** ± 0.04[30]	**8.70** ± 0.10	**11.44** ± 0.10
$\log K_{BaHL}$	3.76 ± 0.02[30]	5.63 ± 0.07	4.32 ± 0.04
$\log K_{BaH_2L}$	2.49 ± 0.07[30]	3.16 ± 0.08	2.89 ± 0.07
$\log K_{ML}^{cond}$ (pH = 7.4)	10.58	8.18	11.19
$\log K_{PbL}$	**18.50** ± 0.01[30]	**13.68** ± 0.02	**14.78** ± 0.15
$\log K_{PbHL}$	-	5.21 ± 0.10	3.60 ± 0.07
$\log K_{PbH_2L}$	-	-	-
$\log K_{ML}^{cond}$ (pH = 7.4)	17.57	12.75	13.34
$\log K_{LaL}$	**14.99** ± 0.02[2]	-	**15.25** ± 0.02
$\log K_{LaHL}$	-	-	3.04 ± 0.01
$\log K_{ML}^{cond}$ (pH = 7.4)	14.43		14.97

Based on the potentiometric data reported in Table 7, the barium complexes of *phencropa* and *macropa* display similar stability constants ($\log K$ = 11.44 and 11.11, respectively), whereas the *bpycropa* complex is nearly three orders of magnitude less stable ($\log K$ = 8.70). A similar trend is observed for Pb^{2+}, for which the *bpycropa* complex is approximately one order of magnitude less stable ($\log K$ = 13.68) than the corresponding *phencropa* complex ($\log K$ = 14.78), while *macropa* again provides the highest thermodynamic stability ($\log K$ = 18.50). For the trivalent cation La^{3+}, *phencropa* forms a slightly more stable complex than *macropa* ($\log K$ = 15.25 and 14.99, respectively). The stability constant of [La(*bpycropa*)]$^+$ complex has not yet been determined, but preliminary experiments suggest that its stability will be comparable to those of the *phencropa* and *macropa* complexes. Lastly, the conditional stability constants calculated at physiological pH are lower about 0.25 − 1.4 orders of magnitude depending on the complex,

reflecting the partial protonation of the ligands and hydrolysis of the respective metal ions, thus reducing the effective concentration in solution of the metal complexes.

Kinetic inertness studies monitored by UV spectroscopy

The kinetic inertness of seven complexes, namely the *bpycropa* and *phencropa* complexes of Ba^{2+}, Pb^{2+}, and La^{3+}, as well as [Bi(*bpycropa*)]$^{+}$, was evaluated through transchelation experiments with EDTA. The reactions were monitored by UV spectroscopy over the 200 – 400 nm range for a period of two weeks at 20 °C. In all samples the complex concentration was 0.1 mM, while EDTA was added in 50-fold excess (5 mM) to ensure pseudo-first-order conditions, thus was incorporated in the observed rate constant k_{obs} (*Eq. 3*), from which the respective half-lives were calculated with *Eq.4*. Additionally, the experiments were conducted in aqueous solutions containing 10 mM HEPES buffer to maintain a constant pH of 7.4, and $NaNO_3$ was added to fix constant the ionic strength at I = 0.15 M.

$$-\frac{d[\mathrm{ML}]}{dt} = k_{obs}[\mathrm{ML}], \quad k_{obs} = k[\mathrm{EDTA}] \qquad \textit{Eq. 3}$$

$$t_{1/2} = \frac{ln2}{k_{obs}} \qquad \textit{Eq. 4}$$

For both barium complexes, as well as for [Pb(*phencropa*)] and [La(*phencropa*)]$^{+}$, the progress of transchelation was followed at λ = 275 nm, which corresponds to an increase in absorbance associated with the release of the picolinate moieties from the metal ions (Figures 49a, b, d, f).[33,34] In the case of [Bi(*bpycropa*)]$^{+}$ (Figure 49g), the most pronounced absorbance change occurred at λ = 255 nm, reflecting the formation of the [Bi(EDTA)]$^{-}$ complex, which absorbs in the 240 – 265 nm region.[35,36] For [Pb(*bpycropa*)] and [La(*bpycropa*)]$^{+}$, absorbance changes were monitored at λ = 315 nm, where their decrease in absorbance accompanies the formation of the respective EDTA complexes at the corresponding wavelength (Figure 49c, e). Further studies will be conducted on the [Bi(*phencropa*)]$^{+}$ complex, as it was not included in the kinetic analysis because it could not be tracked consistently over time due to the formation of precipitates (see its NMR characterization).

The observed transchelation rate constants (k_{obs}) for all analyzed complexes are summarized in Table 8, and were obtained by fitting the kinetic data according to *Eq. 5*.

$$A_t = (A_0 - A_e)e^{-k_{obs}t} + A_e \qquad \textit{Eq. 5}$$

in which the parameters A_t, A_0, and A_e are the absorbance values at time t, at the start of the reaction and at equilibrium, respectively.

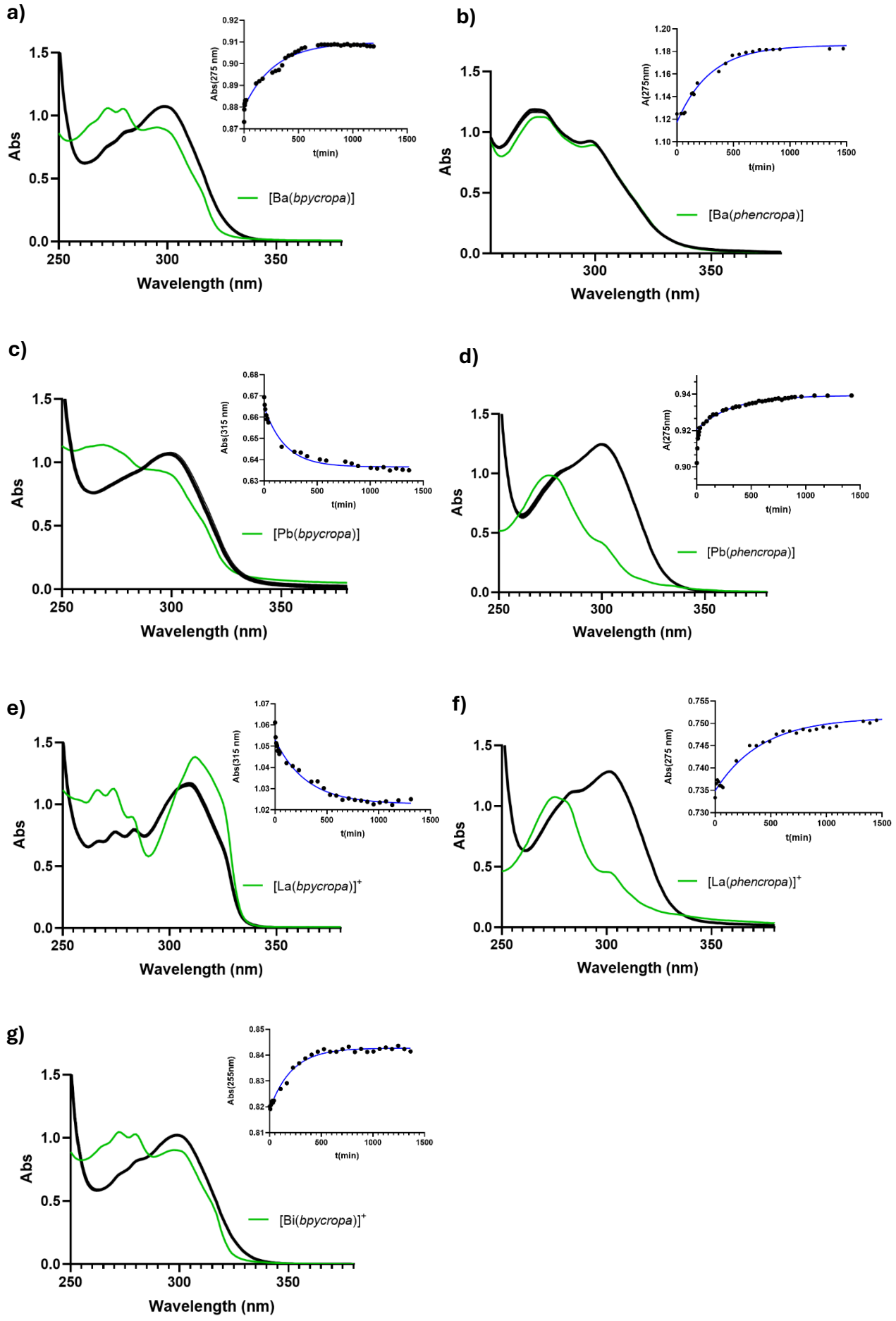
a)
Abs
Wavelength (nm)
Abs(275 nm)
t(min)
[Ba(bpycropa)]
b)
Abs
Wavelength (nm)
A(275nm)
t(min)
[Ba(phencropa)]
c)
Abs
Wavelength (nm)
Abs(315 nm)
t(min)
[Pb(bpycropa)]
d)
Abs
Wavelength (nm)
A(275nm)
t(min)
[Pb(phencropa)]
e)
Abs
Wavelength (nm)
Abs(315 nm)
t(min)
[La(bpycropa)]+
f)
Abs
Wavelength (nm)
Abs(275 nm)
t(min)
[La(phencropa)]+
g)
Abs
Wavelength (nm)
Abs(255nm)
t(min)
[Bi(bpycropa)]+

Figure 49. UV spectra of EDTA-mediated transchelation reactions of [Ba(*bpycropa*)] (**a**), [Ba(*phencropa*)] (**b**), [Pb(*bpycropa*)] (**c**), [Pb(*phencropa*)] (**d**), [La(*bpycropa*)]$^+$ (**e**), [La(*phencropa*)]$^+$ (**f**) and [Bi(*bpycropa*)]$^+$ (**g**) with a 50-fold excess of EDTA at pH = 7.4, T = 20 °C, I = 0.15 M. The green curves represent the spectra of the complexes before the addition of EDTA; the black curves correspond to the spectra after adding EDTA. The curves in blue reported in the inserts were fitted with *Eq.5*, and correspond to the change in absorbance *vs* time monitored at λ = 275 nm for (**a**), (**b**), (**d**), (**f**); at λ = 315 nm for (**c**), (**e**) and at λ = 255 nm for (**g**).

Table 8. Observed dissociation rate constants k_{obs} and half-lives $t_{1/2}$ of the examined complexes determined via EDTA-mediated transchelations at pH = 7.4, 20 °C.

	k_{obs} (s^{-1})	$t_{1/2}$ (h)
[Ba(*bpycropa*)]	5.95×10^{-5}	3.24
[Ba(*phencropa*)]	5.69×10^{-5}	3.39
[Pb(*bpycropa*)]	8.53×10^{-5}	2.26
[Pb(*phencropa*)]	5.18×10^{-5}	3.72
[La(*bpycropa*)]$^+$	5.52×10^{-5}	3.49
[La(*phencropa*)]$^+$	4.05×10^{-5}	4.81
[Bi(*bpycropa*)]$^+$	7.83×10^{-5}	2.46

As summarized in Table 8, all analyzed complexes display comparable observed rate constants (k_{obs}) in the range of 4.1 – 8.5 × 10^{-5} s^{-1}, corresponding to half-lives ($t_{1/2}$) of 2.3 – 5.0 h. Comparison of *bpycropa* and *phencropa* complexes containing the same metal ion reveals that the *phencropa* derivatives are consistently more kinetically inert, which is especially evident for the lead cation (k_{obs} = 5.18 × 10^{-5} *vs* 8.53 × 10^{-5}, Table 8).

Among all systems investigated, [La(*phencropa*)]$^+$ is the most inert complex (k_{obs} = 4.05 × 10^{-5}, Table 8), which may be attributed to the trivalent oxidation state of La^{3+} in combination with the rigid phenanthroline moiety, resulting in stronger metal–ligand interactions compared to those observed for divalent ions, such as Ba^{2+} and Pb^{2+}. Nevertheless, [La(*phencropa*)]$^+$ is considerably more labile than the analogous [La(*macropa*)]$^+$ complex, which was reported to remain intact for 21 days under the same pH conditions when challenged with an excess of

DTPA ligand.[37] For the Pb^{2+} cation, the kinetic inertness of the studied ligands and *macropa* is comparable, as the half-life of [Pb(*macropa*)] was reported to be $t_{1/2} \approx 2$ h at pH = 7.4.[34]

In contrast, compared to [Ba(*macropa*)] which has a notably short half-life of 5.45 minutes,[21] [Ba(*bpycropa*)] and [Ba(*phencropa*)] are considerably more inert exhibiting a half-life $t_{1/2} \approx 3$ h (Table 8), suggesting that the rigid aromatic structures may improve kinetic features of barium complexes.

Conclusions

In this work, the synthesis and full characterization of two new decadentate macrocyclic chelators, *bpycropa* and *phencropa*, is reported. Relative to the parent ligand *macropa*, *bpycropa* and *phencropa* incorporate a 2,2′-bipyridine or a 1,10-phenanthroline unit, respectively, replacing one RO–CH_2CH_2–OR fragment of the macrocyclic backbone. The introduction of these rigid aromatic moieties was intended to increase the structural rigidity of the resulting Ba^{2+}, Pb^{2+}, La^{3+}, and Bi^{3+} complexes, a feature expected to positively influence both thermodynamic stability and kinetic inertness. These metal ions were selected as "cold" analogues of the clinically relevant radiotherapeutic nuclides $^{223}Ra^{2+}$, $^{212}Pb^{2+}$, $^{225}Ac^{2+}$ and ^{212}Bi, owing to their comparable ionic radii and hard-soft properties.

The syntheses of *bpycropa* and *phencropa* were optimized, and both ligands were fully characterized by NMR spectroscopy and mass spectrometry. Their solution speciation was investigated by ^1H NMR and potentiometric titrations, enabling the determination of five protonation constants. The two larger protonation constants (6 − 8) were attributed to the sp^3-nitrogens, whereas the third one, in the range 3.6 − 3.9, is attributed to the protonation of the sp^2-nitrogens of the bipyridine or phenanthroline moiety. Finally, the two lowest protonation constants in the range 1.3 − 2.9 can be attributed to the acidic picolinate pendant arms. Overall, the pK_a values of both ligands are comparable to those previously reported for *macropa* (where the pK_a value at 3.13 was however attributed to the protonation of one carboxylate).[22,30]

All eight metal complexes, Ba^{2+}, Pb^{2+}, La^{3+}, and Bi^{3+} with *bpycropa* and *phencropa*, were characterized by mass spectrometry and ^1H NMR spectroscopy. In each case, the proton NMR spectra display approximately twice the number of resonances observed for the free ligands, indicating that chemically equivalent protons are no longer magnetically equivalent due to reduced symmetry upon metal coordination. The solution NMR spectra are consistent with the asymmetric geometry found in the solid state for [Ba(*bpycropa*)] and [Ba(*phenycropa*)] by single-crystal X-ray diffraction. The strong similarity among the NMR spectra suggests that the remaining complexes adopt similar asymmetric structures in solution. In contrast, *macropa* complexes, such as [Ba(*macropa*)], [Yb(*macropa*)]$^+$, and [Gd(*macropa*)]$^+$, exhibit higher symmetry both in solution and in the solid state, consistent with the presence of a C_2 rotational axis.[21,28,38]

Potentiometric titrations of the metal complexes enabled determination of their overall stability constants. The stability constant of [Ba(*phencropa*)] (log$K$ = 11.44) is comparable to that of [Ba(*macropa*)] (log$K$ = 11.11), whereas [Ba(*bpycropa*)] is significantly less stable (log$K$ =

8.70). Likewise, the lead complexes show lower stability with *bpycropa* (log*K* = 13.68) than with *phencropa* (log*K* = 14.78). In the case of the lanthanum ion, *phencropa* forms a slightly more stable complex (log*K* = 15.25) than *macropa* (log*K* = 14.99).

Finally, kinetic transchelation studies revealed an overall higher inertness for *phencropa* complexes compared to their *bpycropa* counterparts. Among all systems investigated, [La(*phencropa*)]$^{+}$ was identified as the most inert complex at physiological pH (pH = 7.4, k_{obs} = 4.05 × 10^{-5} s^{-1}, $t_{1/2}$ = 4.81 h), likely reflecting the combined effect of the trivalent metal center and the rigid phenanthroline unit. However, it was still significantly more labile than [La(*macropa*)]$^{+}$ ($t_{1/2}$ ≥ 21 d). In contrast, the barium complexes were considerably more inert ($t_{1/2}$ ≈ 3 h) compared to their congener [Ba(*macropa*)] ($t_{1/2}$ = 5.45 min), whereas the lead complexes of all three macrocycles exhibited a similar kinetic stability ($t_{1/2}$ ≈ 2 h). Nevertheless, for *in vivo* and radiopharmaceutical applications, substantially higher kinetic inertness is required, as the half-lives of α-emitting radionuclides such as ^{223}Ra and ^{225}Ac are on the order of days ($t_{1/2}$ = 11.4 d and 9.9 d, respectively).

Experimental Section

Materials and methods

All chemicals were of reagent grade and purchased from Sigma Aldrich, while 2,2'-bipyridine-6,6'-dicarbaldehyde and 1,10-phenanthroline-2,9-dicarbaldehyde were purchased from Fluorochem.

The 1D and 2D NMR spectra were recorded using Varian 500 MHz, Varian 400 MHz, and Bruker 600 MHz NMR spectrometers. The mass spectra were obtained with the LTQ XL – Thermo Fisher mass spectrometer, while the UV-Vis absorption spectra were recorded on an Agilent Cary 60 UV-Vis spectrophotometer. The pH of the analyzed solutions was measured with a sensION+ PH31 (Hach) pH-meter equipped – when necessary – with a Mettler Toledo™ InLab™ NMR glass electrode.

Synthesis[26] **of *bpycrown* (B)**

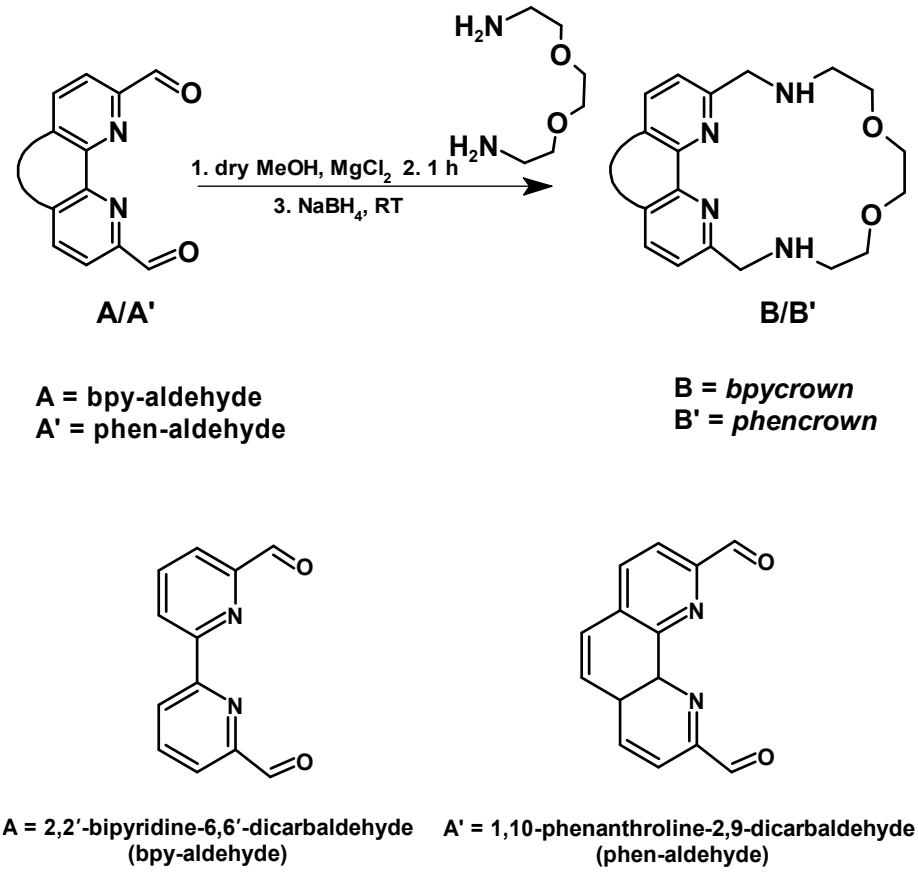

Scheme 1. Synthetic steps to obtain *bpycrown* (**B**) and *phencrown* (**B'**) from the respective aldehydes (**A** and **A'**).

In a system kept under stirring at 40 °C and connected to a continuous argon flow, 500 mg (2.357 mmol, 1 eq.) of 2,2'-bipyridine-6,6'-dicarbaldehyde for *bpycrown* was reacted with 448 mg (4.714 mmol, 2 eq.) of $MgCl_2$ in 75 mL of anhydrous methanol. Once the reagents had completely dissolved, a mixture consisting of 346 µL (1 eq.) of 1,8-diamino-3,6-dioxaoctane (d = 1.01 g/mL) in 9 mL of anhydrous methanol was added to the yellowish solution.

After the addition was completed, the mixture was stirred for an additional hour to ensure full reaction of the amine. During this stage, a white-grey precipitate formed, which was removed by filtration. The orange solution containing the macrocycle with two imine groups was then reduced carefully with an excess of $NaBH_4$ (446 mg, 5.0 eq.), causing effervescence due to the release of hydrogen gas, H_2(g).

The mixture was stirred for 12 hours. The yellowish solution containing the reduced macrocycle was diluted with 60 mL of distilled water and the methanol was subsequently removed by rotary evaporation. The product was extracted from the aqueous solution with three 10 mL portions of dichloromethane, and the organic phase was dried over Na_2SO_4 evaporated,

yielding a yellow oil (62%) which was used for the next synthetic steps without further purification.

^{1}H NMR (500 MHz, $CDCl_3$, 298 K): δ_H 7.71 (t, J = 7.7, 2H), 7.62 (d, J = 7.7, 2H), 7.22 (d, J = 7.7, 2H), 3.99 (s, 4H), 3.67 (t, J = 4.6 Hz, 4H) 3.57 (s, 4H), 2.92 (t, J = 4.6 Hz, 4H).

^{13}C NMR (126 MHz, $CDCl_3$, 298 K): δ_C 155.71, 148.87, 148.85, 137.28, 123.89, 123.87, 121.21, 70.31, 70.06, 53.91, 48.12.

Synthesis[26] of *phencrown* (B')

The synthesis of *phencrown* (**B'**) was conducted analogously to that of **B**. In this case the starting material aldehyde was 1,10-phenanthroline-2,9-dicarbaldehyde (500 mg, 2.117 mmol), which was reacted with $MgCl_2$ (424 mg, 2 eq.) and 1,8-diamino-3,6-dioxaoctane (310 µL, 1 eq., d = 1.01 g/mL). The addition of the amine was carried out gradually and uniformly in small aliquots over the course of 6 hours, to limit the formation of undesired byproducts (*e.g.* the *2+2* macrocycle resulting from the condensation of two molecules of 1,10-phenanthroline-2,9-dicarbaldehyde with two molecules of diamine). The obtained macrocycle appears as an orange solid (yield 88%) and was used for the next synthetic step without further purification.

^{1}H NMR (500 MHz, $CDCl_3$, 298 K): δ_H 8.13 (d, J = 8.2 Hz, 2H); 7.70 (s, 2H); 7.48 (d, J = 8.1 Hz, 2H), 4.22 (s, 4H); 3.75 (t, J = 4.7 Hz, 4H); 3.69 (s, 4H); 2.98 (t, J = 4.9 Hz, 4H) ppm.

^{13}C NMR (126 MHz, $CDCl_3$, 298 K): δ_C 159.05, 145.66, 136.60, 127.86, 126.01, 122.60, 70.67, 70.51, 55.48, 49.46 ppm.

Synthesis of dimethyl pyridine-2,6-dicarboxylate (b)

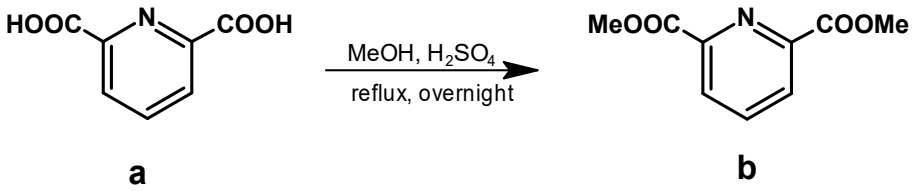

Scheme 2. Esterification of 2,6-pyridinedicarboxylic acid (**a**).

The synthesis to obtain **b** consisted in the esterification of 2,6-pyridinedicarboxylic acid (5.10 g, 30.52 mmol) in the presence of 50 mL of methanol and 12 mL of concentrated sulfuric acid to activate the carboxylates and favor dehydration. The reaction mixture was left overnight at reflux (70°C). The following day the work-up consisted in adding 75 mL of distilled water and neutralizing the acid with a saturated solution of $NaHCO_3$ to pH = 7. Since the addition of sodium bicarbonate caused CO_2 formation, precautions were taken by neutralizing the acid gradually and by selecting a suitable round-bottom flask to ensure a larger volume to limit the

developed effervescence. Following that, the aqueous phase was extracted three times with 20 mL of dichloromethane, the organic phases were united, dried over Na_2SO_4 and filtrated. After rotary evaporation, a white solid was obtained (4.68 g, 79%). The resulting product was solubilized in $CDCl_3$ and characterized by ^1H NMR spectroscopy. In the ^1H NMR spectrum all observed resonances could be assigned to desired product and no observed signals of the starting material were present.

^1H NMR (500 MHz, $CDCl_3$, 298 K): δ_H 8.30 (d, J = 7.8 Hz, 2H), 8.02 (t, J = 7.8 Hz, 1H), 4.01 (s, 6H).

Synthesis[39] of 6-hydroxymethylpyridine-2-carboxylic acid methyl ester (c)

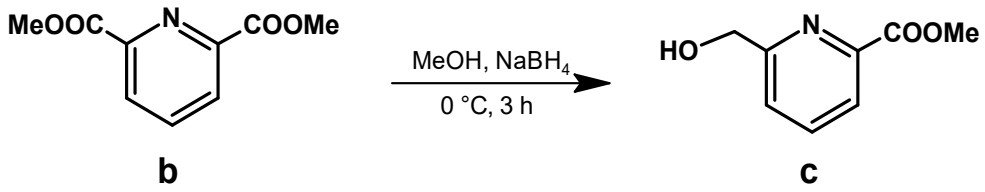

Scheme 3. Asymmetric reduction of the dimethyl ester (**b**) to primary alcohol 6-hydroxymethylpyridine-2-carboxylic acid methyl ester (**c**).

Dimethyl pyridine-2,6-dicarboxylate (4.68 g, 23.98 mmol) was dissolved in MeOH and 2.72 g (71.94 mmol, 3 eq.) of $NaBH_4$ were added in small portions (0.5 eq. each) every 30 min. The resulting reaction mixture was stirred at 0 °C for 3 hours. After this period, the work-up consisted in the addition of a saturated solution of $NaHCO_3$. Methanol was removed via rotary evaporation, and the resulting aqueous solution was extracted with $CHCl_3$ (3 × 50 mL). The combined organic extracts were dried over Na_2SO_4 and evaporated to give the crude product as a white solid (4.23 g). The ^1H NMR spectrum in $CDCl_3$ of the solid presented additionally the symmetric diol product, hence purification by column chromatography on alumina with a DCM/MeOH gradient was performed, yielding the purified product (2.13 g, 53%).

^1H NMR (500 MHz, $CDCl_3$, 298 K): δ_H 8.04 (d, J = 7.7 Hz, 1H), 7.86 (t, J = 7.8 Hz, 1H), 7.54 (d, J = 7.8 Hz, 1H), 4.87 (d, J = 5.4 Hz, 2H), 4.00 (s, 3H).

Synthesis[39] of 6-chloromethylpyridine-2-carboxylic acid methyl ester (d)

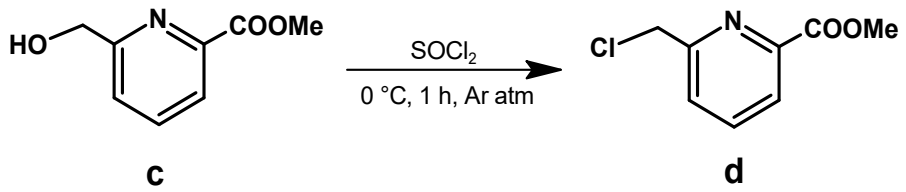

Scheme 4. Chlorination of the hydroxyl group of (**c**) with thionyl chloride to obtain 6-chloromethylpyridine-2-carboxylic acid methyl ester (**d**).

An excess of thionyl chloride (9 mL, 10 eq.) was added in excess over 6-hydroxymethylpyridine-2-carboxylic acid methyl ester (2.13 g, 12.72 mmol) at 0 °C under inert atmosphere (Ar). The reaction mixture was stirred at 0 °C for 1 h, and the excess of $SOCl_2$ was removed under reduced pressure. The obtained residue was dissolved in toluene (100 mL), and the organic solution, washed 3 times with a 1 M $NaHCO_3$ aqueous solution to neutralize the remaining acid. The organic extract was dried over Na_2SO_4 before evaporating it, and the resulting oil was dried under vacuum until a yellow pale solid was obtained (1.51 g, 64%).

^{1}H NMR (500 MHz, $CDCl_3$, 298 K): δ_H 8.05 (d, J = 7.8 Hz, 1H), 7.87 (t, J = 7.8 Hz, 1H), 7.70 (d, J = 7.8 Hz, 1H), 4.75 (d, 2H), 3.98 (s, 3H).

Synthesis of bpycrown-N,N′-dipicolinate methyl ester (C)

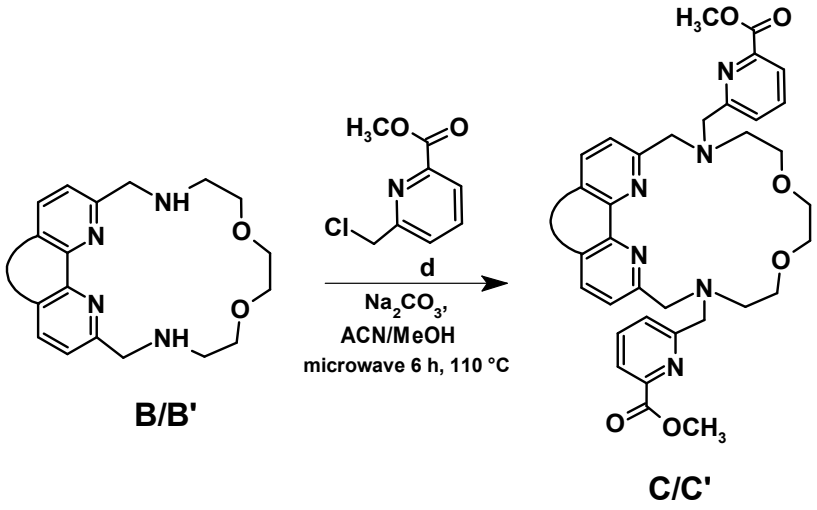

Scheme 5. Alkylation reaction of *bpycrown/phencrown* (**B**/**B'**) with 6-chloromethylpyridine-2-carboxylic acid methyl ester (**d**).

A total of 200 mg (0.6090 mmol, 1 eq.) of *bpycrown* (**B**) was weighed and introduced in a 10 mL microwave vessel with 4 mL of acetonitrile, 0.3 mL of methanol, and 10 eq. of Na_2CO_3. Subsequently, 226 mg (1.218 mmol, 2 eq.) of 6-chloromethylpyridin-2-carboxylate methyl ester were added to the vessel. The reaction mixture was heated in a microwave reactor for 6 hours at 110 °C.

The solvent was removed using a rotary evaporator, and the resulting product was completely redissolved in 10 mL of dichloromethane and washed three times with distilled water. The organic phase was again evaporated to dryness and further dried under vacuum. A TLC plate of the crude product on alumina using a DCM/MeOH 95:5 eluent displayed two spots (R_{f1} = 0.58 and R_{f2} = 0.41). Therefore, purification by alumina column chromatography was conducted using a DCM/MeOH gradient. The second spot (R_{f2} = 0.41) was successfully isolated and identified as the desired product (yield 45%).

^{1}H NMR (500 MHz, $CDCl_3$, 298 K): δ_H 7.87 (d, J = 7.7 Hz, 2H), 7.84 – 7.73 (m, 6H), 7.56 (d, J = 7.7 Hz, 2H), 7.41 (d, J = 7.3 Hz, 2H), 4.07 (s, 4H), 3.88 (s, 6H), 3.70 (t, J = 5.0 Hz, 4H), 3.48 (s, 4H), 2.85 (t, J = 5.0 Hz, 4H), 2.67 – 2.57 (m, 4H).

MS (ESI$^+$, CH_3OH): *m/z (%)* = 627.40 (100, $[M+H]^+$); 314.34 (96, $[M+2H]^{2+}$), 665.35 (40, $[M+K]^+$), 673.36 (30, $[M+Na]^+$).

Synthesis of *bpycropa* (D)

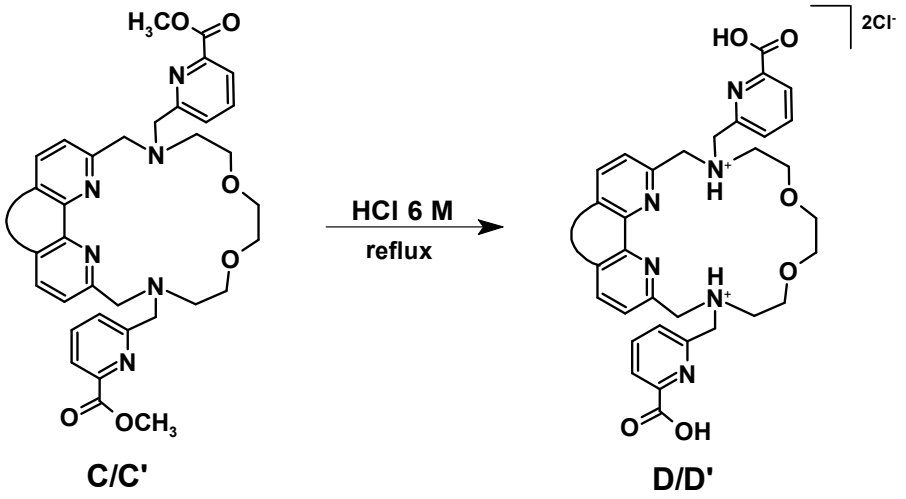

C/C' D/D'

Scheme 6. Deprotection reaction of *bpycrown/phencrown-N,N´-dipicolinate-methyl-ester* (**C** and **C'**) in acidic conditions (HCl 6 M).

The deprotection reactions of *bpycrown*-N,N′-dipicolinate methyl ester was carried out by adding 200 mg of the ester in 10 mL of 6 M aqueous HCl. The yellow solution was left under magnetic stirring and reflux at 100 °C for a total of 12 hours. Subsequently, the acid aqueous solution product was concentrated to dryness using a rotary evaporator. The macrocycle was obtained as a yellowish oil and was further purified by precipitation. Specifically, it was redissolved in a minimal amount of water and precipitated by slowly adding acetone. The isolated macrocycle was obtained as a white-yellowish solid (yield 71%).

The characterization of the compound was carried out by mass spectrometry in methanol and NMR spectroscopy (CD_3OD and D_2O for the NMR titrations, *vide infra*). The spectra with the detailed assignments are reported in the Results and Discussion section.

^{1}H NMR (500 MHz, CD_3OD, 298 K): δ_H 8.40 (d, J = 7.9 Hz, 2H), 8.28 (t, J = 7.8 Hz, 2H), 8.17 (d, J = 7.7 Hz, 2H), 8.10 (t, J = 7.8 Hz, 2H), 7.95 (d, J = 7.7 Hz, 2H), 7.84 (d, J = 7.7 Hz, 1H), 5.04 (s, 4H), 4.93 (s, 4H), 3.85 (t, J = 4.7 Hz, 4H), 3.74 (t, J = 4.7 Hz, 4H), 3.44 (s, 4H).

^{1}H NMR (500 MHz, D_2O, 298 K): δ_H 7.98 (t, J = 7.8 Hz, 2H), 7.88 (d, J = 8.2 Hz, 2H), 7.75 (t, J = 7.7 Hz, 2H), 7.70 (d, J = 7.7 Hz, 2H), 7.60 (d, J = 7.7 Hz, 2H), 7.46 (d, J = 7.6 Hz, 3H), 3.95 (m, 6H), 3.71 (m, 11H).

MS (ESI$^+$, CH_3OH): *m/z* (%) = 599.34 (100, $[M+H]^+$), 300.33 (85, $[M+2H]^{2+}$), 637.30 (30, $[M+K]^+$), 621.32 (25, $[M+Na]^+$).

MS (ESI$^-$, CH_3OH): *m/z* (%) = 597.32 (100, $[M-H]^-$), 619.37 (40, $[M-2H+Na]^-$).

Synthesis of phencrown-N,N′-dipicolinate methyl ester (C')

The synthesis was performed similarly as for **C**. A total of 198 mg (0.5622 mmol, 1 eq.) of *phencrown* (**B'**) was weighed and introduced in a 10 mL microwave vessel with 4 mL of acetonitrile, 0.3 mL of methanol, and 10 eq. of Na_2CO_3. Subsequently, 209 mg (1.124 mmol, 2 eq.) of 6-chloromethylpyridin-2-carboxylate methyl ester were added to the vessel. The reaction mixture was heated in a microwave reactor for 6 hours at 110 °C. The work-up was performed as for **C**. After evaporation and drying under vacuum, *phencrown*-N,N′-dipicolinate methyl ester (**C'**) was obtained (yield 51%). A TLC plate on alumina using a DCM/MeOH 95:5 eluent displayed a single spot with an R_f = 0.47, corresponding to the alkylated product as confirmed by ^{1}H NMR spectroscopy, hence no further purification was required.

^{1}H NMR (500 MHz, $CDCl_3$, 298 K): δ_H 8.20 (d, J = 8.2 Hz, 2H), 8.01 (d, J = 7.7 Hz, 2H), 7.99 (d, J = 7.7 Hz, 2H), 7.84 (t, J = 7.7 Hz, 2H), 7.77 (s, 2H); 7.72 (d, J = 8.2 Hz, 2H), 4.31 (s, 3H), 4.19 (s, 3H), 4.01 (m, 8H), 3.89 (t, J = 6.5 Hz, 4H), 3.66 (s, 4H), 2.86 (t, J = 6.5 Hz, 4H) ppm.

MS (ESI$^+$, CH_3OH): *m/z (%)* = 651.37 (100, $[M+H]^+$); 326.36 (60, $[M+2H]^{2+}$), 689.30 (37, $[M+K]^+$), 373.40 (30, $[M+H+K]^{2+}$), 673.36 (28, $[M+Na]^+$).

Synthesis of *phencropa* (D')

The synthesis of *phencropa* (**D'**) was conducted in an analogous way to **D**. Moreover, after the 12 hours of stirring under reflux in HCl 6 M, a color change was observed, *i.e.* the solution shifted from orange to brown. The macrocycle **D'** was precipitated by adding diethyl ether dropwise to its concentrated methanol solution. The isolated product was obtained as a brown solid (yield 82%) and characterized by ^{1}H NMR spectroscopy (in CD_3OD and D_2O for the NMR titrations, *vide infra*), and mass spectrometry (see Results and Discussion section).

^{1}H NMR (500 MHz, CD_3OD, 298 K): δ_H 8.29 (d, J = 8.2 Hz, 2H), 7.79 (s, 2H), 7.68 (d, J = 8.2 Hz, 2H), 7.55 (d, J = 7.6 Hz, 2H), 7.42 (t, J = 7.6 Hz, 2H), 7.30 (d, J = 7.6 Hz, 2H), 4.33 (s, 4H), 3.84 (s, 4H), 3.61 (t, J = 4.7 Hz, 4H), 3.32 (s, 4H), 3.06 (t, J = 4.7 Hz, 4H) ppm.

^{1}H NMR (500 MHz, D_2O, 298 K): δ_H 8.47 (d, J = 8.2 Hz, 2H), 7.92 (s, 2H), 7.83 (d, J = 8.2 Hz, 2H), 7.50 (t, J = 7.7 Hz, 2H), 7.46 (d, *J = 7.6 Hz*, 2H), 7.26 (d, J = 7.5 Hz, 2H), 5.07 (s, 4H), 4.73 (s, 4H), 4.17 (t, J = 4.6 Hz, 4H), 3.94 (m, 8H), 3.66 (s, 4H) ppm.

MS (ESI$^+$, CH_3OH): *m/z* (%) = 312.32 (100, $[M+2H]^{2+}$), 331.29 (51, $[M+H+Na]^{2+}$), 623.32 (35, $[M+H]^+$), 661.25 (24, $[M+K]^+$), 645.28 (13, $[M+Na]^+$), 339.23 (13, $[M+H+K]^{2+}$).

MS (ESI$^-$, CH_3OH): *m/z* (%) = 621.30 (100, $[M-H]^-$), 325.18 (45, $[M-2H]^{2-}$), 643.28 (37, $[M-2H+Na]^-$).

^{1}H NMR titration of *bpycropa* (D) and *phencropa* (D')

For the ^{1}H NMR titration of the *bpycropa* and *phencropa*, a vial containing respectively 1 mL of a 0.01 M solution of the ligand, 0.15 M $NaNO_3$ and 0.001 M of 2,2-dimethyl-2-silapentane-5-sulfonate sodium salt (DSS), which was used as reference at 0.0 ppm in D_2O, was prepared. The ^{1}H NMR spectra (500 MHz) were recorded at 298 K, with each spectrum acquired at approximately 0.5-pH-unit intervals over a range between pH 1.3 and 12.1. The pH of the solutions was adjusted through small additions of diluted D_2SO_4 and NaOD solutions in D_2O.

Synthesis of [Ba(*bpycropa*)] (1)

The synthesis of the complex was carried out by dissolving in a vial 17.1 mg (0.0253 mmol, 1 eq.) of the **D** in 2 mL of water. The aqueous ligand solution was set to pH 7 via additions of a KOH solution and monitored with a pH-meter. Subsequently, 304 μL (0.0304 mmol, 1.2 eq.) of a 0.1 M $BaCl_2$ solution were added. Shortly after adding the barium salt, a beige solid precipitated and was isolated by centrifugation. The solid is soluble in methanol and, depending on the pH, soluble in water as well.

NMR spectra were recorded in CD_3OD, and the solution for mass spectrometry in methanol. The detailed characterization and assignments of complex **1** is reported in the Results and Discussion section and Supplementary Information.

^{1}H NMR (500 MHz, CD_3OD, 298 K): δ_H 8.25 (d, J = 8.0 Hz, 1H), 8.18 (d, J = 8.0 Hz, 1H), 8.04 (t, J = 7.8 Hz, 1H), 7.95 (t, J = 7.8 Hz, 1H), 7.87 – 7.79 (m, 4H), 7.63 (d, J = 7.6 Hz, 1H), 7.50 (d, J = 7.3 Hz, 1H), 7.46 (d, J = 7.7 Hz, 1H), 7.43 (dd, J = 5.7, 3.0 Hz, 1H), 5.33 (d, J = 14.7 Hz, 1H), 5.05 (m, J = 13.5 Hz, 2H), 4.46 (t, J = 10 Hz, 1H), 4.04 (d, J = 13.5 Hz, 1H), 3.87 (d, J = 13.2 Hz, 1H), 3.78 (d, J = 13.9 Hz, 1H), 3.73 – 3.64 (m, 2H), 3.56 (t, J = 9.4 Hz, 1H), 3.49 (d, J = 13.6 Hz, 1H), 3.22 (dd, J = 10.1, 3.7 Hz, 1H), 3.18 – 3.08 (m, 2H), 3.04 – 2.85 (m, 3H), 2.83 – 2.75 (m, 1H), 2.72 – 2.59 (m, 2H).

MS (ESI$^+$, CH_3OH): *m/z* (%) = 735.24 (100, $[M+H]^+$), 367.99 (30, $[M+2H]^{2+}$).

Synthesis of [Pb(*bpycropa*)] (2)

The synthesis of the complex was carried out by dissolving in a vial 14.6 mg (0.0217 mg, 1 eq.) of **D** in 2 mL of water. The aqueous ligand's solution was set to pH 7 via additions of a KOH solution and monitored with a pH-meter. Subsequently, 11 mg (0.0261 mmol, 1.2 eq.) of $Pb(NO_3)_2 \cdot 5H_2O$ were added, respectively. After the addition of the lead salt, no observable precipitate was found. The excess salt was removed by evaporating the complex to dryness and redissolving it in methanol, followed by filtration on a 0.20 µm nylon membrane. After drying under vacuum, a white solid was obtained, soluble in methanol and water. NMR spectra were recorded in CD_3OD, and the solution for mass spectrometry in methanol. The detailed characterization and assignments of complex **2** is reported in the Results and Discussion section and Supplementary Information.

^{1}H NMR (500 MHz, CD_3OD, 298 K): δ_H 8.20 (d, J = 7.9 Hz, 1H), 8.11 (d, J = 8.0 Hz, 1H), 8.03 (t, J = 7.8 Hz, 1H), 7.94 (t, J = 7.8 Hz, 1H), 7.83 (dt, J = 9.7, 7.6 Hz, 2H), 7.67 (d, J = 7.6 Hz, 1H), 7.62 (d, J = 7.6 Hz, 2H), 7.56 (d, J = 7.7 Hz, 1H), 7.47 (dd, J = 10.5, 7.6 Hz, 2H), 5.48 (d, J = 15.4 Hz, 1H), 5.09 (d, J = 14.7 Hz, 1H), 4.50 – 4.45 (m, 2H), 4.07 – 3.92 (m, 4H), 3.74 – 3.69 (m, 1H), 3.56 (td, J = 9.9, 1.8 Hz, 1H), 3.25 (dt, J = 10.0, 3.4 Hz, 1H), 3.20 (dt, J = 10.5, 2.1 Hz, 1H), 3.13 (dt, J = 10.2, 3.2 Hz, 1H), 3.04 (dt, J = 10.4, 2.1 Hz, 1H), 2.96 – 2.75 (m, 5H), 2.69 (dt, J = 13.7, 2.5 Hz, 1H).

MS (ESI$^+$, CH_3OH): *m/z* (%) = 805.30 (100, $[M+H]^+$).

Synthesis of [La(*bpycropa*)][NO_3] (3)

In a vial, 8.2 mg (0.0122 mmol, 1 eq.) of *bpycropa* were dissolved in 2 mL of distilled water. The aqueous ligand solution was adjusted to pH = 6.45 by adding aliquots of a KOH solution, using a pH-meter for monitoring. Subsequently, 134 µL (0.0134 mmol, 1.1 eq.) of a 0.1 M $La(NO_3)_3$ solution were added. The reaction mixture was stirred at room temperature for 24 hours. Afterward, the solution was evaporated to dryness using a rotary evaporator and dried under vacuum. The complex appeared as a white-beige solid, soluble in water and slightly in methanol, hence the NMR characterization was performed in D_2O.

^{1}H NMR (600 MHz, D_2O, 298 K): δ_H 8.25 (d, J = 8.0 Hz, 1H), 8.16 (d, J = 8.0 Hz, 1H), 8.09 (t, J = 8.0 Hz, 1H), 7.97 (t, J = 8.0 Hz, 1H), 7.78 (td, J = 7.8, 3.7 Hz, 2H), 7.67 (d, J = 7.8 Hz,

1H), 7.48 (d, J = 7.8 Hz, 1H), 7.45 – 7.41 (m, 2H), 7.35 (d, J = 7.6 Hz, 1H), 7.31 (d, J = 7.8 Hz, 1H), 4.83 (dd, *J* = 30.4, 16.3 Hz, 4H), 4.19 – 4.01 (m, 4H), 3.96 (d, *J* = 16.3 Hz, 2H), 3.80 – 3.69 (m, 1H), 3.63 (d, *J* = 15.3 Hz, 1H), 3.56 – 3.42 (m, 1H), 3.41 – 3.34 (m, 1H), 3.25 (dt, J = 11.7, 3.7 Hz, 1H), 3.11 – 3.05 (m, 2H), 3.04 – 2.94 (m, 1H), 2.92 – 2.84 (m, 1H), 2.55 (d, J = 13.9 Hz, 1H).

MS (ESI$^+$, CH_3OH): *m/z* (%) = 735.25 (100, $[M]^+$), 368.17 (30, $[M+H]^{2+}$).

Synthesis of [Bi(*bpycropa*)][NO_3] (4)

For the synthesis of the bismuth complex, 7.5 mg (0.0111 mmol, 1 eq.) of *bpycropa* were dissolved in 2 mL of distilled water and set to pH = 3.7 to limit Bi^{3+} hydrolysis, followed by the addition of 5.9 mg (0.0123 mmol, 1.1 eq) of $Bi(NO_3)_3 \cdot 5H_2O$. The mixture was stirred for 24 h and then 2 mL of methanol were added to precipitate the bismuth hydroxo species. The white suspension was then filtered through a 0.20 µm nylon membrane, and the clear filtrate was concentrated under vacuum, yielding a white-beige solid. The complex was characterized by NMR spectroscopy in CD_3OD.

^{1}H NMR (600 MHz, CD_3OD, 298 K): δ_H 8.37 (t, *J* = 7.7 Hz, 1H), 8.12 (d, *J* = 7.6 Hz, 1H), 8.10 – 8.05 (m, 2H), 8.03 (d, *J* = 7.7 Hz, 1H), 8.00 – 7.93 (m, 3H), 7.70 (dd, *J* = 5.9, 2.6 Hz, 1H), 7.65 (dd, *J* = 6.3, 2.1 Hz, 1H), 7.55 (d, *J* = 7.5 Hz, 1H), 7.50 (d, *J* = 7.7 Hz, 1H), 5.23 (d, *J* = 15.2 Hz, 1H), 4.80 – 4.65 (m, 4H), 4.56 – 4.46 (m, 2H), 4.39 (d, *J* = 15.2 Hz, 1H), 4.10 – 3.99 (m, 2H), 3.91 (td, *J* = 11.5, 2.7 Hz, 1H), 3.80 – 3.68 (m, 3H), 3.61 (dt, *J* = 10.9, 3.6 Hz, 1H), 3.14 (ddd, *J* = 13.6, 10.2, 3.6 Hz, 1H), 3.03 (ddt, *J* = 15.0, 11.9, 2.4 Hz, 2H), 2.91 (dt, *J* = 12.4, 2.8 Hz, 1H), 2.79 (dt, *J* = 13.4, 3.0 Hz, 1H).

MS (ESI$^+$, CH_3OH): *m/z* (%) = 805.36 (100, $[M]^+$).

Synthesis of [Ba(*phencropa*)] (5)

The synthesis was performed analogously to complex **1**, by dissolving 13.8 mg (0.0198 mmol, 1 eq.) of *phencropa* (**D'**), setting the pH with KOH at 7 and mixing with 238 µL (0.0237 mmol 1.2 eq.) of a 0.1 M $BaCl_2$ solution. As seen for complex **1**, after mixing the two solutions, a yellow solid formed and was isolated by centrifugation. The solid is soluble in methanol and, depending on the pH, soluble in water as well.

^{1}H NMR (500 MHz, CD_3OD, 298 K): δ_H 8.55 (d, *J = 8.2 Hz*, 1H), 8.45 (d, *J = 8.2 Hz*, 1H), 8.00 – 7.80 (m, 7H), 7.75 (d, *J = 8.2 Hz*, 1H), 7.56 (t, *J = 4.7 Hz*, 1H), 7.48 (dd, *J = 6.7 Hz, J' = 2.0 Hz*, 1H), 5.38 (d, *J = 14.6 Hz*, 1H), 5.28 (d, *J = 13.4 Hz*, 1H), 5.17 (d, *J = 13.8 Hz*, 1H), 4.42 (t, *J = 9.3 Hz*, 1H), 4.19 (d, *J = 13.6 Hz*, 1H), 4.05 (d, *J = 13.5 Hz*, 1H), 3.88 (d, *J = 13.8 Hz*, 1H), 3.77 (d, *J = 14.6 Hz*, 1H), 3.65 (d, *J = 13.7 Hz*, 1H), 3.49 (t, *J = 9.2 Hz*, 1H), 3.15 – 3.05 (m, 2H), 2.98 (m, 2H), 2.84 (m, 3H), 2.72 – 2.62 (m, 2H), 2.60 – 2.52 (m, 1H) ppm.

MS (ESI$^+$, CH_3OH): *m/z* (%) = 759.34 (100, $[M+H]^+$), 380.02 (42, $[M+2H]^{2+}$).

Synthesis of [Pb(*phencropa*)] (6)

The synthesis of the complex was carried out as for its analog, complex **2**. A quantity of 10.3 mg (0.0148 mmol, 1 eq.) of ligand **D'** was weighed and dissolved in 2 mL of distilled water, set to pH 7 via additions of a KOH solution and, subsequently, 7.5 mg (0.0178 mmol, 1.2 eq.) of $Pb(NO_3)_2 \cdot 5H_2O$ were added. No observable precipitate was present after mixing. The excess salt was removed by evaporating the complex to dryness and redissolving it in methanol, followed by filtration on a 0.20 µm nylon membrane. After drying under vacuum, a yellow solid was obtained, soluble in methanol and water.

^{1}H NMR (500 MHz, CD_3OD, 298 K): δ_H 8.55 (d, J = 8.2 Hz, 1H), 8.46 (d, J = 8.1 Hz, 1H), 8.04 – 7.95 (m, 3H), 7.95 – 7.92 (m, 2H), 7.86 (dt, J = 20.1, 7.7 Hz, 2H), 7.80 – 7.74 (m, 2H), 7.71 – 7.66 (m, 2H), 7.61 (d, J = 7.8 Hz, 1H), 7.50 (d, J = 7.6 Hz, 1H), 5.53 (d, J = 15.4 Hz, 1H), 5.14 (t, J = 14.3 Hz, 2H), 4.76 (s, 2H), 4.46 – 4.39 (m, 1H), 4.25 – 4.20 (m, 1H), 4.16 (dd, J = 14.0, 6.6 Hz, 2H), 4.05 – 3.99 (m, 1H), 3.84 (d, J = 13.2 Hz, 1H), 3.49 (td, J = 9.9, 1.6 Hz, 1H), 3.14 (dt, J = 9.9, 2.6 Hz, 1H), 3.10 – 2.81 (m, 6H), 2.78 – 2.67 (m, 2H), 2.51 (td, J = 9.8, 1.6 Hz, 1H).

MS (ESI$^+$, CH_3OH): *m/z* (%) = 829.29 (100, $[M+H]^+$).

Synthesis of [La(*phencropa*)][NO_3] (7)

The synthesis was performed as for lanthanum complex **3**. In a vial, 11.4 mg (0.0164 mmol, 1 eq.) of ligand **D'** were dissolved in 2 mL of distilled water. After setting the ligand solution to pH 6.45 by adding aliquots of a KOH solution, 180 µL (0.0180 mmol, 1.1 eq.) of a 0.1 M $La(NO_3)_3$ solution were added. The reaction mixture was stirred at room temperature for 24 hours. Afterward, the solution was evaporated to dryness, redissolved in methanol and filtered through a 0.20 µm nylon membrane to remove the excess lanthanum salt. After drying under vacuum, the complex was obtained as a yellow-orange solid, soluble in methanol and water.

^{1}H NMR (500 MHz, CD_3OD, 298 K): δ_H 8.84 (d, *J = 8.3 Hz*, 1H), 8.76 (d, *J = 8.2 Hz*, 1H), 8.22 (d, *J = 8.8 Hz*, 1H), 8.18 (d, *J = 8.8 Hz*, 1H), 8.13 (d, *J = 8.4 Hz*, 1H), 8.04 – 7.96 (m, 3H), 7.74 (d, *J = 7.5 Hz*, 1H), 7.71 (d, *J = 7.9 Hz*, 1H), 7.69 (d, *J = 7.6 Hz*, 1H), 7.65 (d, *J = 7.9 Hz*, 1H), 5.32 (d, *J = 15.7 Hz*, 1H), 5.22 (d, *J = 15.7 Hz*, 2H), 4.50 (d, *J = 15.8 Hz*, 1H), 4.43 (d, *J = 15.1 Hz*, 1H), 4.24 (d, *J = 15.7 Hz*, 1H), 4.16 (d, *J = 15.9 Hz*, 1H), 4.03 (d, *J = 14.8 Hz*, 2H), 3.75 (d, *J = 11.2 Hz*, 1H), 3.68 – 3.61 (m, 1H), 3.55 (m, 2H), 3.17 (m, 3H), 3.01 – 2.92 (m, 3H), 2.83 (m, 2H) ppm.

MS (ESI$^+$, CH_3OH, +): *m/z* (%) = 759.29 (100, $[M]^+$).

Synthesis of [Bi(*phencropa*)][NO_3] (8)

In this case, the same synthesis was applied as for complex **4**, *i.e.* 9.2 mg (0.0132 mmol, 1 eq.) of ligand **D'** were dissolved in 2 mL of distilled water and set to pH = 3.7 to limit Bi^{3+} hydrolysis, followed by the addition of 7.1 mg (0.0145 mmol, 1.1 eq) of $Bi(NO_3)_3 \cdot 5H_2O$. After stirring the mixture for 24 h, 2 mL of methanol were added to precipitate the bismuth hydroxo species.

Subsequently, the white suspension was filtered through a 0.20 μm nylon membrane, and the colorless filtrate was dried under vacuum, yielding a yellowish solid. The complex was characterized by NMR spectroscopy in CD_3OD, however, it was observed that the NMR sample became incresingly turbid over time due to the formation of a white precipitate, possibly a bismuth hydroxide deriving from Bi^{3+} hydrolysis.

^{1}H NMR (600 MHz, CD_3OD, 298 K): δ_H 8.56 (d, J = 8.2 Hz, 1H), 8.45 (d, J = 8.2 Hz, 1H), 8.24 (t, J = 7.7 Hz, 1H), 7.98 (d, J = 7.4 Hz, 1H), 7.93 – 7.86 (m, 4H), 7.84 (d, J = 8.8 Hz, 1H), 7.69 (t, J = 7.6 Hz, 1H), 7.39 (d, J = 7.7 Hz, 1H), 7.18 (d, J = 7.7 Hz, 1H), 5.24 (d, J = 16.2 Hz, 1H), 4.40 (d, J = 16.5 Hz, 1H), 4.10 (d, J = 13.7 Hz, 1H), 3.72 – 3.37 (m, 5H), 3.32 (m, 2H), 3.09 (m, 2H), 2.94 (d, J = 13.2 Hz, 1H), 2.86 – 2.75 (m, 2H).

MS (ESI$^+$, CH_3OH, +): *m/z* (%) = 829.36 (100, $[M]^+$).

Potentiometric titrations

The stability and protonation constants of the macrocycles and complexes were determined by Dr. Federica Battistin at the University of Western Brittany in Brest, France. The pH-potentiometric titrations of the solutions contained metal and ligand in a 1:1 molar ratio (ligand concentration typically 2 mM) and were carried out with a Metrohm 888 Titrando automatic titration workstation equipped with a Metrohm 6.0234.110 combined glass electrode. Measurements were carried out at 298 K in 6 mL samples with continuous magnetic stirring, maintaining a constant ionic strength of 0.15 M KNO_3. The pH range investigated was 1.7 – 12.0. A waiting time of 60 s between consecutive measurements was used for the ligands, while a longer interval of 180 s was applied for the complexes to ensure that equilibrium was reached. In the equilibrium calculations, the stoichiometric ionic product of water (pK_w) was also taken into account for the determination of $[OH^-]$ under basic conditions. The protonation and stability constants were fitted using Hyperquad2008 software.

Kinetic inertness studies monitored by UV spectroscopy

The kinetic inertness of a total of seven complexes (*bpycropa* and *phencropa* complexes with Ba^{2+}, Pb^{2+}, La^{3+} and [Bi(*bpycropa*)]$^+$) was studied by performing transchelation reactions with the EDTA ligand and monitoring them by UV spectroscopy in the range 200 – 400 nm for a period of two weeks at 20 °C. The concentration of the complexes in the reaction quartz cuvette was 0.1 mM, while the competing ligand, EDTA, was in a 50-fold excess (5 mM). Additionally, the assays were performed in aqueous solutions containing 10 mM HEPES buffer to maintain a constant pH of 7.4 and constant ionic strength I = 0.15 M with $NaNO_3$.

References

(1) Grieve, M. L.; Paterson, B. M. The Evolving Coordination Chemistry of Radiometals for Targeted Alpha Therapy. *Aust. J. Chem.* **2021**, *75(2)*, 65-88.

(2) Hatcher-Lamarre, J. L.; Sanders, V. A.; Rahman, M.; Cutler, C. S.; Francesconi, L. C. Alpha Emitting Nuclides for Targeted Therapy. *Nucl. Med. Biol.* **2021**, *92*, 228–240..

(3) Pouget, J.-P.; Constanzo, J. Revisiting the Radiobiology of Targeted Alpha Therapy. *Front. Med.* **2021**, *8*, 692436.

(4) Carter, R. J.; Nickson, C. M.; Thompson, J. M.; Kacperek, A.; Hill, M. A.; Parsons, J. L. Complex DNA Damage Induced by High Linear Energy Transfer Alpha-Particles and Protons Triggers a Specific Cellular DNA Damage Response. *Int. J. Radiat. Oncol.* **2018**, *100* (3), 776–784.

(5) Bannik, K.; Madas, B.; Jarzombek, M.; Sutter, A.; Siemeister, G.; Mumberg, D.; Zitzmann-Kolbe, S. Radiobiological Effects of the Alpha Emitter Ra-223 on Tumor Cells. *Sci. Rep.* **2019**, *9* (1), 18489.

(6) Eychenne, R.; Chérel, M.; Haddad, F.; Guérard, F.; Gestin, J. F. Overview of the Most Promising Radionuclides for Targeted Alpha Therapy: The "Hopeful Eight". *Pharmaceutics.* **2021**, *13(6):906.*

(7) Kirby, H. W.; Morss, L. R. Actinium. In *The Chemistry of the Actinide and Transactinide Elements*; Morss, L. R., Edelstein, N. M., Fuger, J., Eds.; Springer Netherlands: Dordrecht, **2006**; pp 18–51.

(8) Deblonde, G. J.-P.; Zavarin, M.; Kersting, A. B. The Coordination Properties and Ionic Radius of Actinium: A 120-Year-Old Enigma. *Coord. Chem. Rev.* **2021**, *446*, 214130.

(9) Perron, R.; Gendron, D.; Causey, P. W. Construction of a Thorium/Actinium Generator at the Canadian Nuclear Laboratories. *Appl. Radiat. Isot.* **2020**, *164*, 109262.

(10) Robertson, A. K. H.; Ramogida, C. F.; Schaffer, P.; Radchenko, V. Development of ^{225}Ac Radiopharmaceuticals: TRIUMF Perspectives and Experiences. *Curr. Radiopharm.* **2018**, *11* (3), 156–172.

(11) Kim, Y. S.; Brechbiel, M. W. An Overview of Targeted Alpha Therapy. *Tumor Biol.* **2012**, *33* (3), 573–590.

(12) Kozempel, J.; Mokhodoeva, O.; Vlk, M. Progress in Targeted Alpha-Particle Therapy. What We Learned about Recoils Release from *In Vivo* Generators. *Molecules* **2018**, *23* (3), 581.

(13) Kleynhans, J.; Ebenhan, T.; Cleeren, F.; Sathekge, M. M. Can Current Preclinical Strategies for Radiopharmaceutical Development Meet the Needs of Targeted Alpha Therapy? *Eur. J. Nucl. Med. Mol. Imaging* **2024**, *51* (7), 1965–1980.

(14) Ivanov, A. S.; Simms, M. E.; Bryantsev, V. S.; Benny, P. D.; Griswold, J. R.; Delmau, L. H.; Thiele, N. A. Elucidating the Coordination Chemistry of the Radium Ion for Targeted Alpha Therapy. *Chem. Commun.* **2022**, *58* (71), 9938–9941.

(15) Yokoo, H.; Oki, T.; Uehara, M.; Dwi Winarni, I.; Yamaji, K.; Fukuyama, K.; Ohara, Y.; Ohnuki, T.; Hochella, M. F.; Utsunomiya, S. Geochemistry of Barium Ions Associated with Biogenic Manganese Oxide Nanoparticles Generated by a Fungus Strain: Implications for Radium Sequestration in Uranium Mill Tailings. *Gondwana Res.* **2022**, *110*, 270–282.

(16) Franchi, S.; Asti, M.; Blei, M. K.; Pozzo, S.; Madabeni, A.; Graiff, C.; Menegazzo, I.; Volpato, F.; Gentile, S.; Orian, L.; Mancin, F.; Stadlbauer, S.; Kopka, K.; Mamat, C.; Di Marco, V.; Tosato, M. Heavy Alkaline Earth Radiometals for Cancer Theranostics: Coordination and Radiochemistry of Radium-223 and Barium-131 with Kryptofix 22-Based Chelators. *Inorg. Chem.* **2025**, *64* (45), 22422–22440.

(17) Gott, M.; Steinbach, J.; Mamat, C. The Radiochemical and Radiopharmaceutical Applications of Radium. *Open Chem.* **2016**, *14* (1), 118–129.

(18) Vermeulen, K.; Vandamme, M.; Bormans, G.; Cleeren, F. Design and Challenges of Radiopharmaceuticals. *Semin. Nucl. Med.* **2019**, *49* (5), 339–356.

(19) Franchi, S.; Madabeni, A.; Tosato, M.; Gentile, S.; Asti, M.; Orian, L.; Di Marco, V. Navigating through the Coordination Preferences of Heavy Alkaline Earth Metals: Laying the Foundations for ^{223}Ra- and $^{131/135m}$Ba-Based Targeted Alpha Therapy and Theranostics of Cancer. *J. Inorg. Biochem.* **2024**, *256*, 112569.

(20) Abou, D. S.; Ulmert, D.; Doucet, M.; Hobbs, R. F.; Riddle, R. C.; Thorek, D. L. J. Whole-Body and Microenvironmental Localization of Radium-223 in Naïve and Mouse Models of Prostate Cancer Metastasis. *J. Natl. Cancer Inst.* **2016**, *108* (5), djv380.

(21) Thiele, N. A.; MacMillan, S. N.; Wilson, J. J. Rapid Dissolution of $BaSO_4$ by Macropa, an 18-Membered Macrocycle with High Affinity for Ba^{2+}. *J. Am. Chem. Soc.* **2018**, *140* (49), 17071–17078.

(22) Roca-Sabio, A.; Mato-Iglesias, M.; Esteban-Gómez, D.; Tóth, É.; Blas, A. D.; Platas-Iglesias, C.; Rodríguez-Blas, T. Macrocyclic Receptor Exhibiting Unprecedented Selectivity for Light Lanthanides. *J. Am. Chem. Soc.* **2009**, *131* (9), 3331–3341.

(23) Abou, D. S.; Thiele, N. A.; Gutsche, N. T.; Villmer, A.; Zhang, H.; Woods, J. J.; Baidoo, K. E.; Escorcia, F. E.; Wilson, J. J.; Thorek, D. L. J. Towards the Stable Chelation of Radium for Biomedical Applications with an 18-Membered Macrocyclic Ligand. *Chem. Sci.* **2021**, *12* (10), 3733–3742.

(24) Kadassery, K. J.; King, A. P.; Fayn, S.; Baidoo, K. E.; MacMillan, S. N.; Escorcia, F. E.; Wilson, J. J. H_2 BZmacropa-NCS: A Bifunctional Chelator for Actinium-225 Targeted Alpha Therapy. *Bioconjug. Chem.* **2022**, *33* (6), 1222–1231.

(25) Battistin, F.; Merdžo, I.; Alessio, E.; Balducci, G.; Tripier, R. Unpublished Results.

(26) Alzakhem, N.; Bischof, C.; Seitz, M. Dependence of the Photophysical Properties on the Number of 2,2′-Bipyridine Units in a Series of Luminescent Europium and Terbium Cryptates. *Inorg. Chem.* **2012**, *51* (17), 9343–9349.

(27) *SDBS, Spectral Database for Organic Compounds, AIST. Sdbs.Db.Aist.Go.Jp. Https://Sdbs.Db.Aist.Go.Jp.*

(28) Kovács, A.; Varga, Z. H_2O Coordination in Macropa Complexes of f Elements (Ac, La, Lu): Feasibility of the 11th Coordination Site. *Struct. Chem.* **2021**, *32* (2), 643–653.

(29) Glasoe, P. K.; Long, F. A. Use of glass electrodes to measure acidities in deuterium oxide. *J. Phys. Chem.* **1960**, *64* (1), 188–190.

(30) Blei, M. K.; Waurick, L.; Reissig, F.; Kopka, K.; Stumpf, T.; Drobot, B.; Kretzschmar, J.; Mamat, C. Equilibrium Thermodynamics of Macropa Complexes with Selected Metal Isotopes of Radiopharmaceutical Interest. *Inorg. Chem.* **2023**, *62* (50), 20699–20709.

(31) Smith, R.M., Martell, A.E. Pyridinecarboxylic Acids. In *Critical Stability Constants*; Springer: Boston, MA; **2007**, Vol. 6.

(32) Yasuda, M.; Sone, K.; Yamasaki, K. Stability of Zinc and Cadmium Complexes with Some Methyl Derivatives of 1,10-Phenanthroline and 2,2′-Bipyridine. *J. Phys. Chem.* **1956**, *60* (12), 1667–1668.

(33) Faltejsek, J.; Urbanovský, P.; Kubíček, V.; Havlíčková, J.; Císařová, I.; Kotek, J.; Hermann, P. Extraordinary Kinetic Inertness of Lanthanide(III) Complexes of Pyridine-Rigidified 18-Membered Hexaazamacrocycles with Four Acetate Pendant Arms. *Chem. Sci.* **2025**, *16* (27), 12558–12567.

(34) Randhawa, P.; Kadassery, K. J.; McNeil, B. L.; MacMillan, S. N.; Wharton, L.; Yang, H.; Wilson, J. J.; Ramogida, C. F. The H_2 S $_x$ Macropa Series: Increasing the Chemical Softness of H_2 Macropa with Sulfur Atoms to Chelate Radiometals $[^{213}Bi]Bi^{3+}$ and $[^{203}Pb]Pb^{2+}$ for Radiopharmaceutical Applications. *Inorg. Chem.* **2024**, *63* (44), 21177–21193.

(35) Den Boef, G.; Van Der Linden, W. E.; Beyer, S. Photometric Titrations of Metal Ions Based on UV Absorption of Bi(III)-EDTA. *Microchim. Acta* **1971**, *59* (5), 761–766.

(36) Beltran-Torres, M.; Sugich-Miranda, R.; Santacruz-Ortega, H.; Lopez-Gastelum, K. A.; Ayala-Zavala, J. F.; Rocha-Alonzo, F.; Velazquez-Contreras, E. F.; Vazquez-Armenta, F. J. Synthesis and Characterization of Bismuth(III) Complex with an EDTA-Based Phenylene Ligand and Its Potential as Anti-Virulence Agent. *PeerJ Inorg. Chem.* **2022**, *4*, e4.

(37) Aluicio-Sarduy, E.; Thiele, N. A.; Martin, K. E.; Vaughn, B. A.; Devaraj, J.; Olson, A. P.; Barnhart, T. E.; Wilson, J. J.; Boros, E.; Engle, J. W. Establishing Radiolanthanum Chemistry for Targeted Nuclear Medicine Applications. *Chem. – Eur. J.* **2020**, *26* (6), 1238–1242.

(38) Kovács, A. Theoretical Study of Actinide Complexes with Macropa. *ACS Omega* **2020**, *5* (41), 26431–26440.

(39) Mato-Iglesias, M.; Roca-Sabio, A.; Pálinkás, Z.; Esteban-Gómez, D.; Platas-Iglesias, C.; Tóth, É.; De Blas, A.; Rodríguez-Blas, T. Lanthanide Complexes Based on a 1,7-Diaza-12-Crown-4 Platform Containing Picolinate Pendants: A New Structural Entry for the Design of Magnetic Resonance Imaging Contrast Agents. *Inorg. Chem.* **2008**, *47* (17), 7840–7851.

Supplementary Information

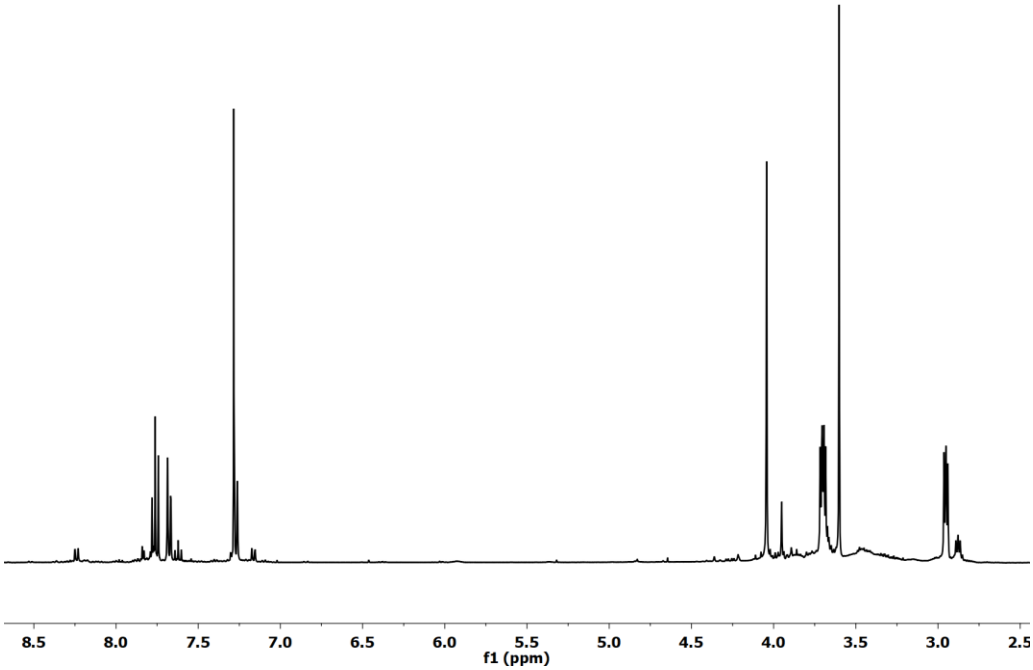

Figure S1. ^{1}H NMR spectrum (400 MHz) of *bpycrown* (**B**) in $CDCl_3$.

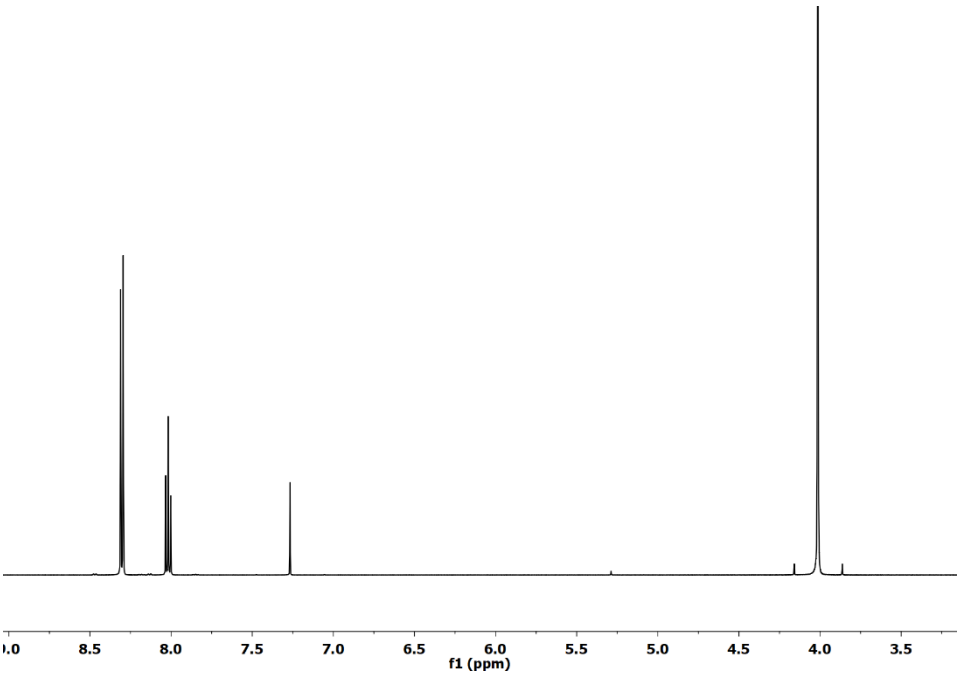

Figure S2. ^{1}H NMR spectrum (500 MHz) of dimethyl pyridine-2,6-dicarboxylate (**b**) in $CDCl_3$.

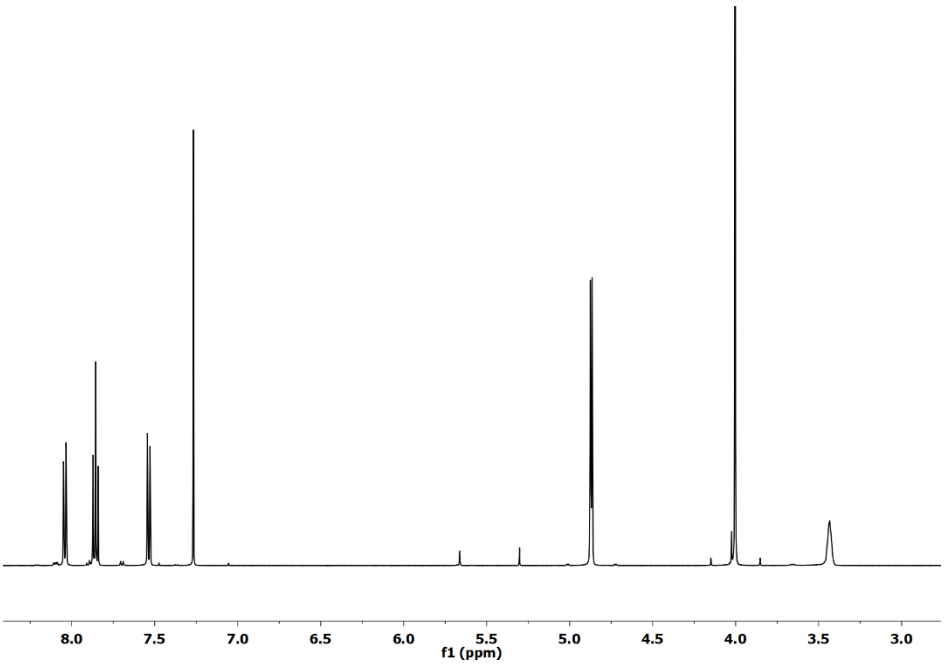

Figure S3. ^{1}H NMR spectrum (500 MHz) of 6-hydroxymethylpyridine-2-carboxylic acid methyl ester (**c**) in $CDCl_3$.

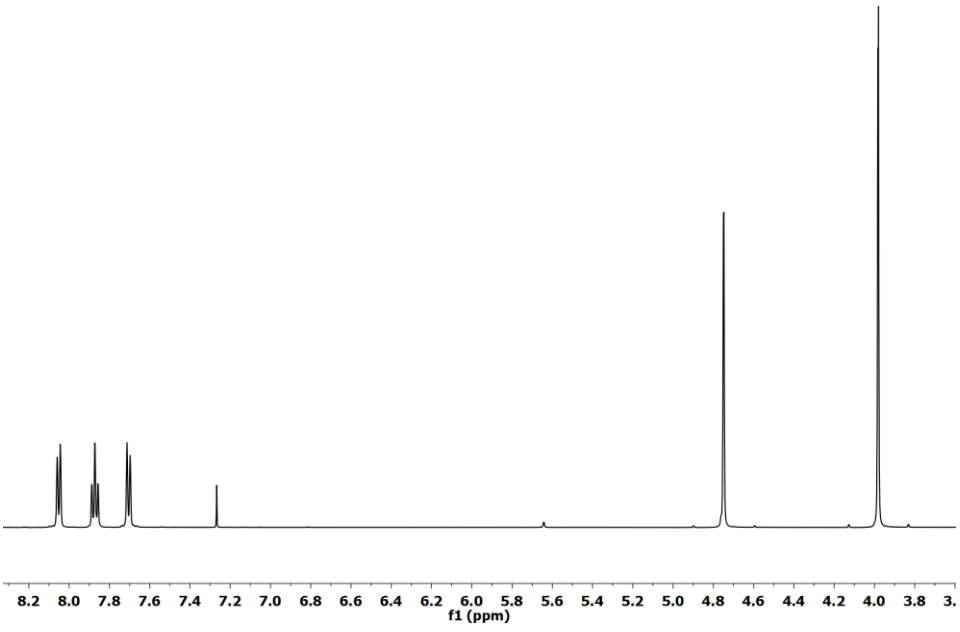

Figure S4. ^{1}H NMR spectrum (500 MHz) of 6-chloromethylpyridine-2-carboxylic acid methyl ester (**d**) in $CDCl_3$.

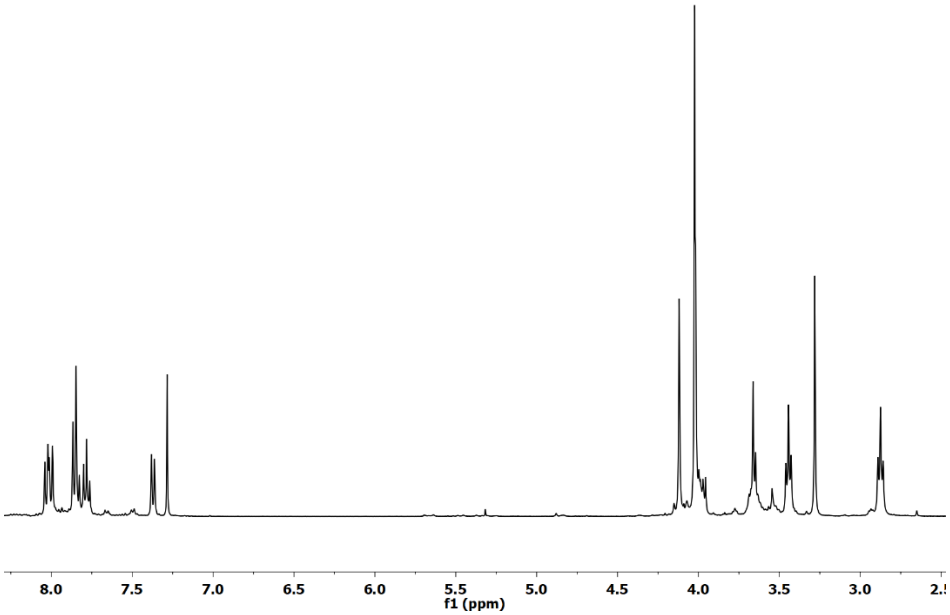

Figure S5. ^{1}H NMR spectrum (500 MHz) of *bpycrown-N,N'*-dipicolinate methyl ester (**C**) in $CDCl_3$.

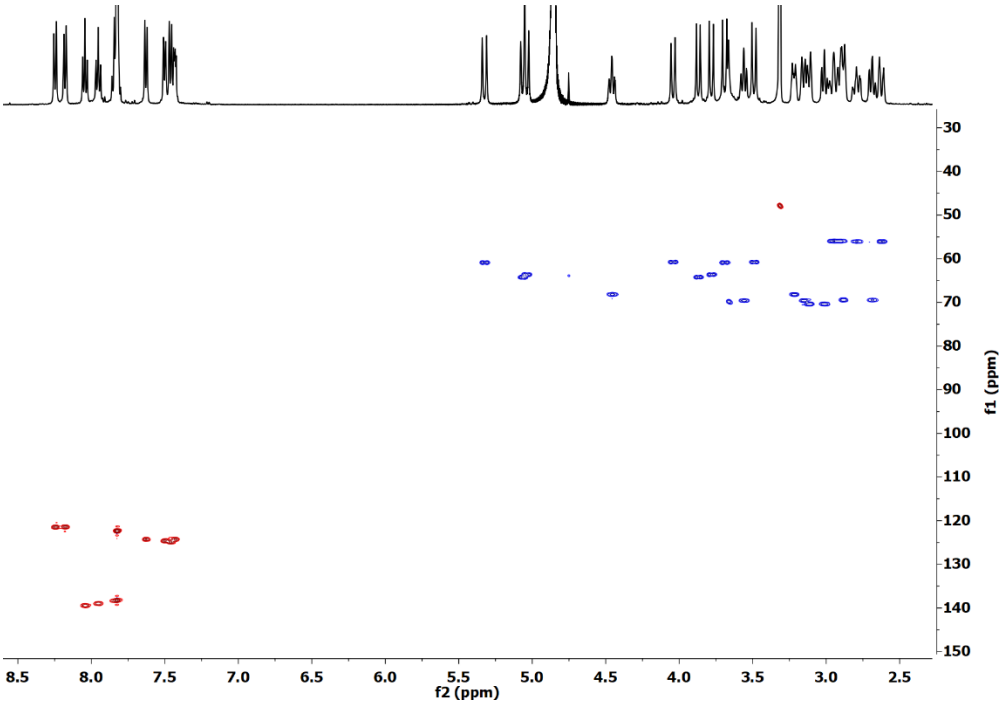

Figure S6. ^{1}H – ^{13}C HSQC spectrum (500 MHz) of [Ba(*bpycropa*)] (**1**).

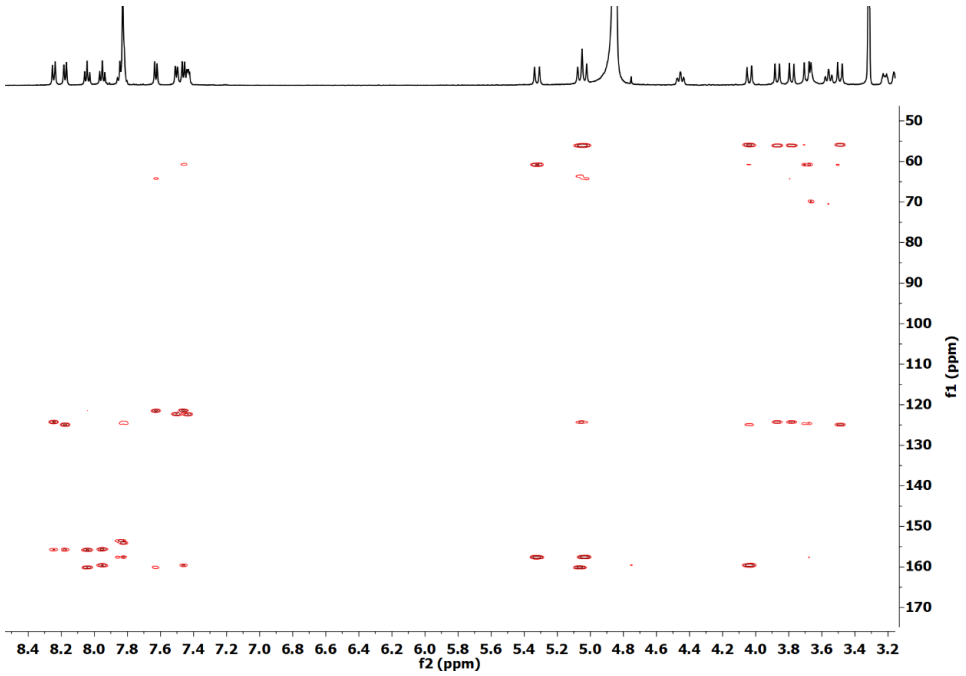

Figure S7. ^{1}H – ^{13}C HMBC spectrum (500 MHz) of [Ba(*bpycropa*)] (**1**).

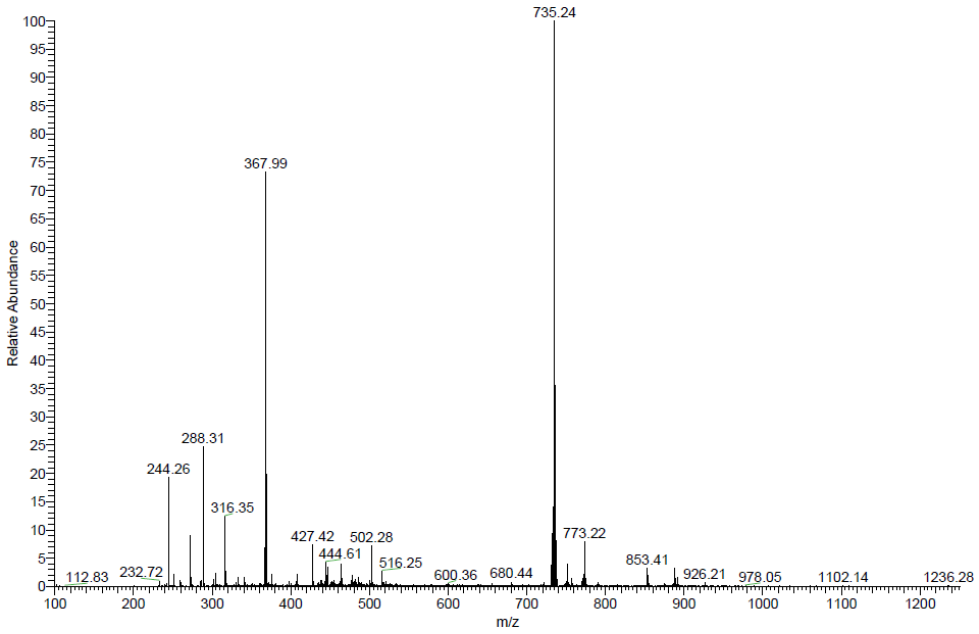

Figure S8. ESI-MS^{+} spectrum of [Ba(*bpycropa*)] (**1**).

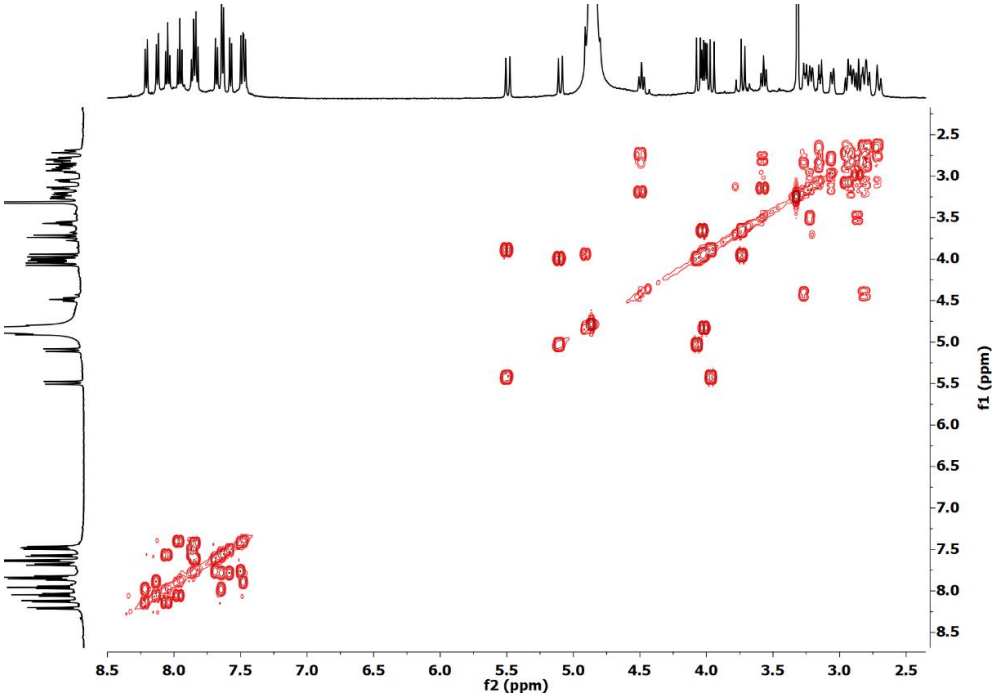

Figure S9. ^{1}H – ^{1}H COSY spectrum (500 MHz) of [Pb(*bpycropa*)] (**2**).

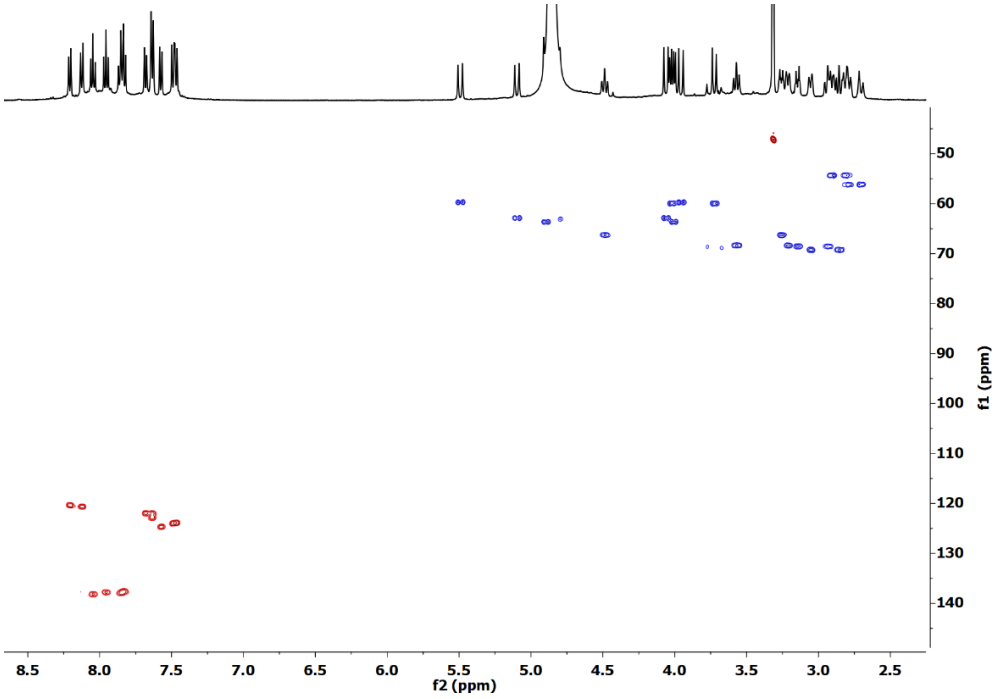

Figure S10. ^{1}H – ^{13}C HSQC spectrum (500 MHz) of [Pb(*bpycropa*)] (**2**).

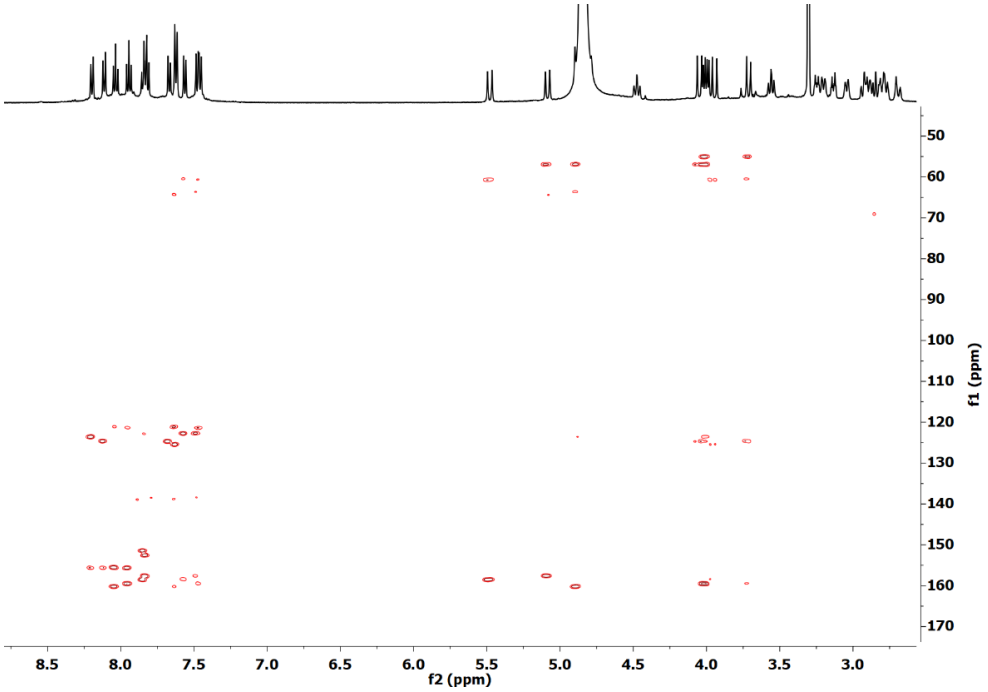

Figure S11. ^{1}H – ^{13}C HMBC spectrum (500 MHz) of [Pb(*bpycropa*)] (**2**).

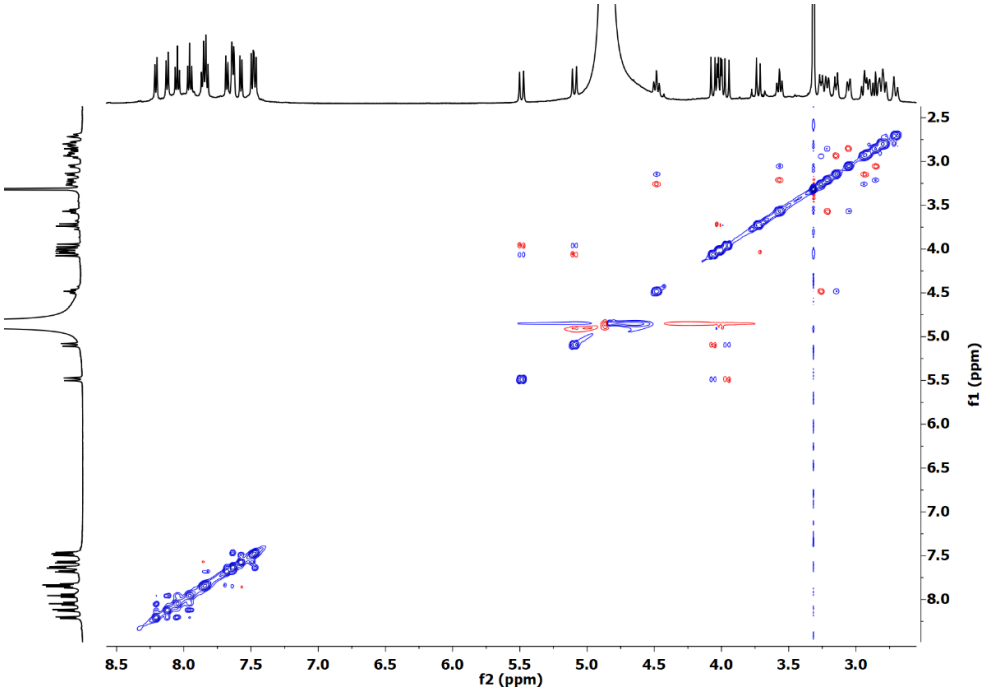

Figure S12. ^{1}H – ^{1}H ROESY spectrum (500 MHz) of [Pb(*bpycropa*)] (**2**).

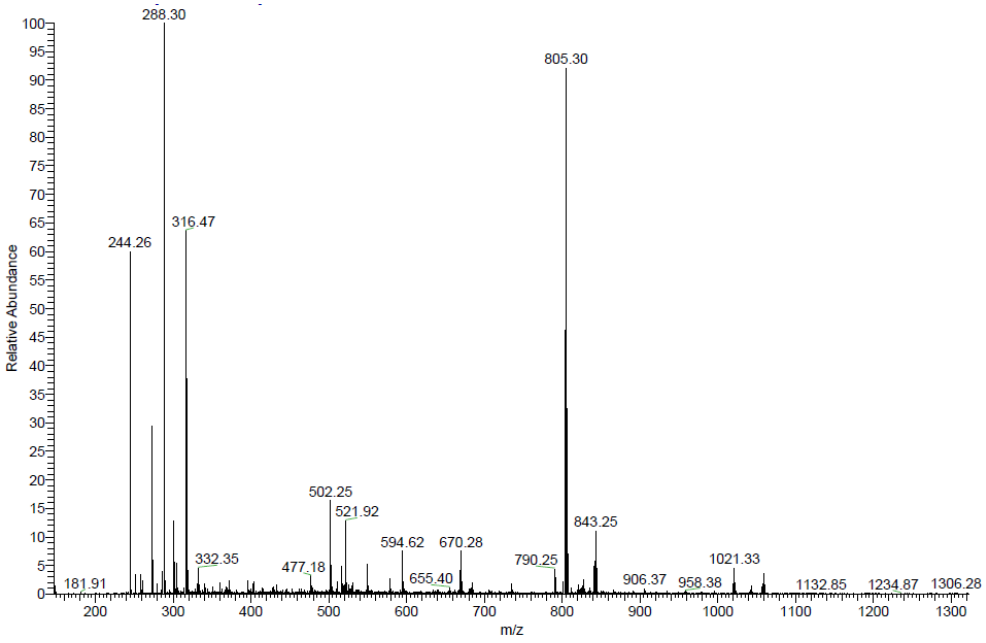

Figure S13. ESI-MS^{+} spectrum of [Pb(*bpycropa*)] (**2**).

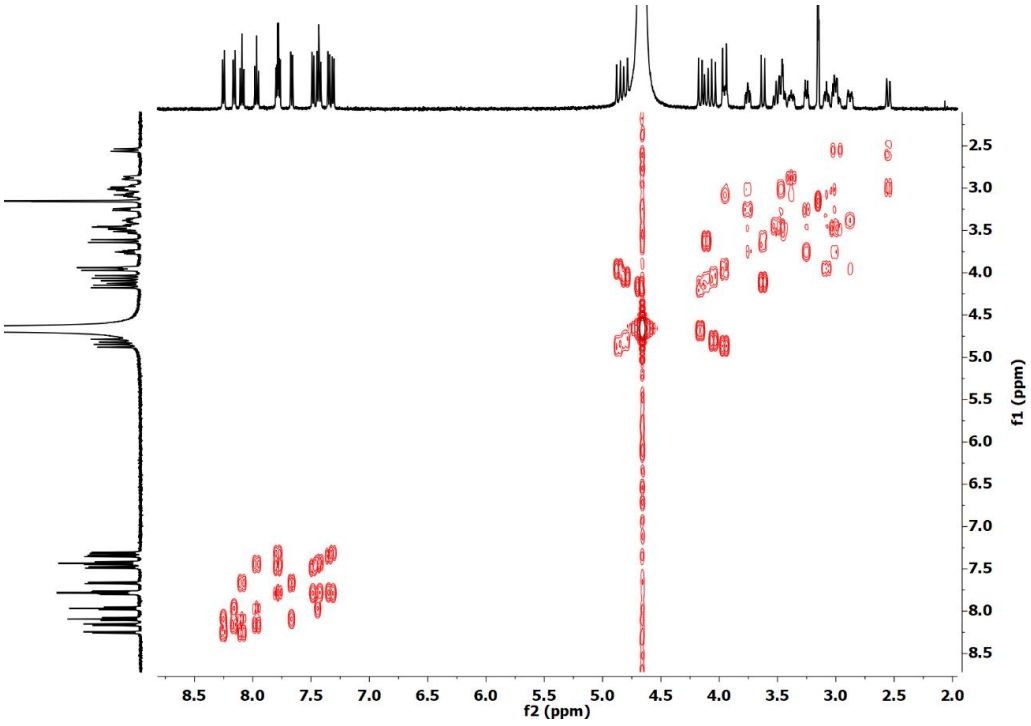

Figure S14. ^{1}H – ^{1}H COSY spectrum (500 MHz) of [La(*bpycropa*)]$^{+}$ (**3**).

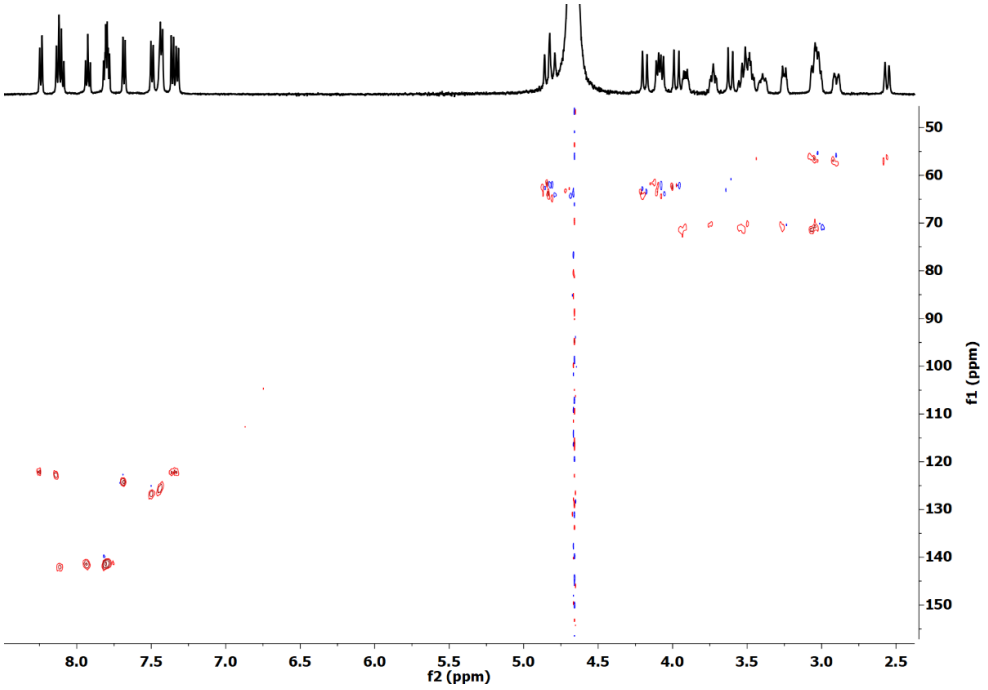

Figure S15. ^{1}H – ^{13}C HSQC spectrum (500 MHz) of [La(*bpycropa*)]$^{+}$ (**3**).

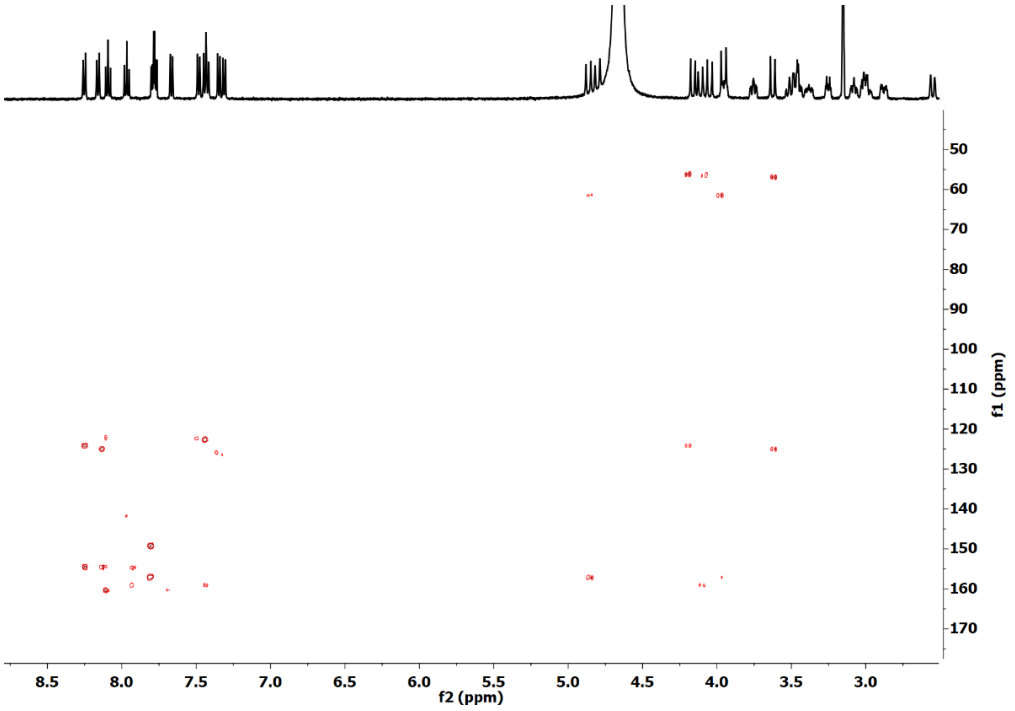

Figure S16. ^{1}H – ^{13}C HMBC spectrum (500 MHz) of [La(*bpycropa*)]$^{+}$ (**3**).

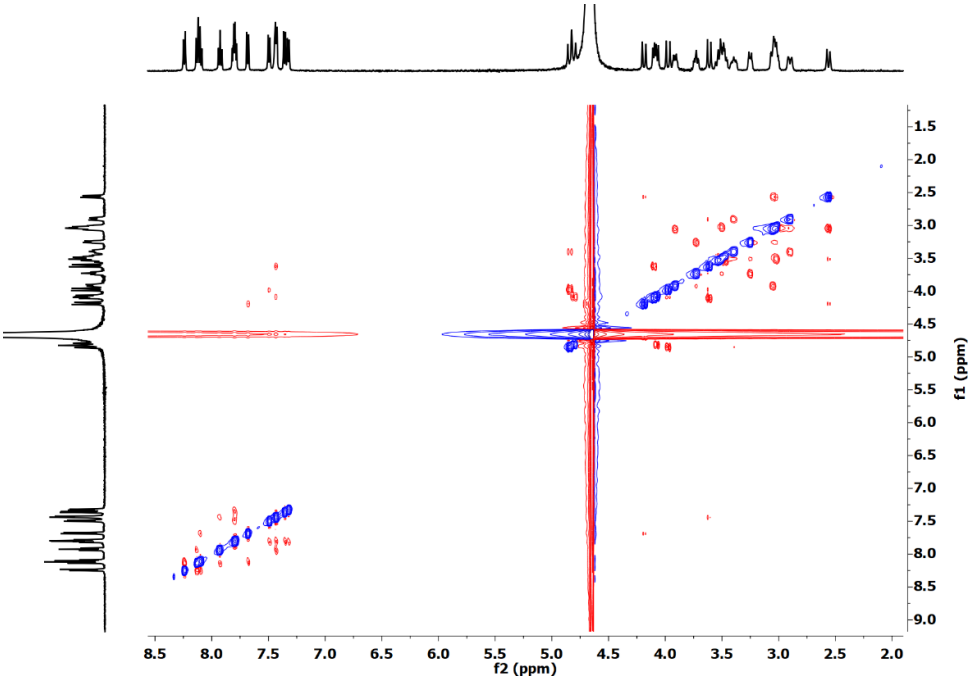

Figure S17. $^{1}H - {}^{1}H$ ROESY spectrum (500 MHz) of [La(*bpycropa*)]$^{+}$ (**3**).

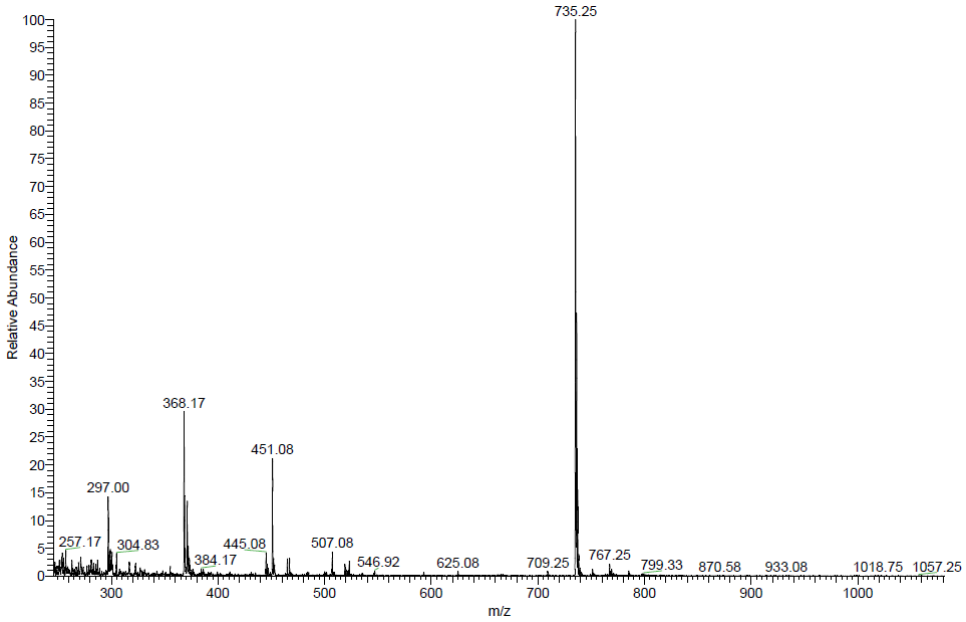

Figure S18. ESI-MS^{+} spectrum of [La(*bpycropa*)]$^{+}$ (**3**).

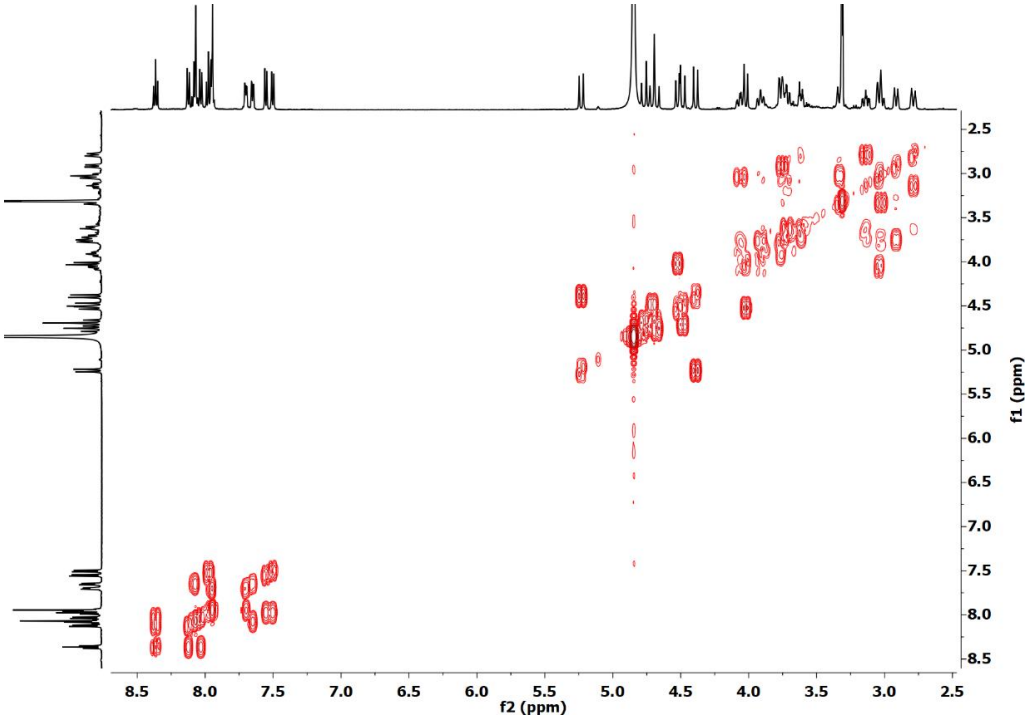

Figure S19. ^{1}H – ^{1}H COSY spectrum (500 MHz) of [Bi(*bpycropa*)]$^{+}$ (**4**).

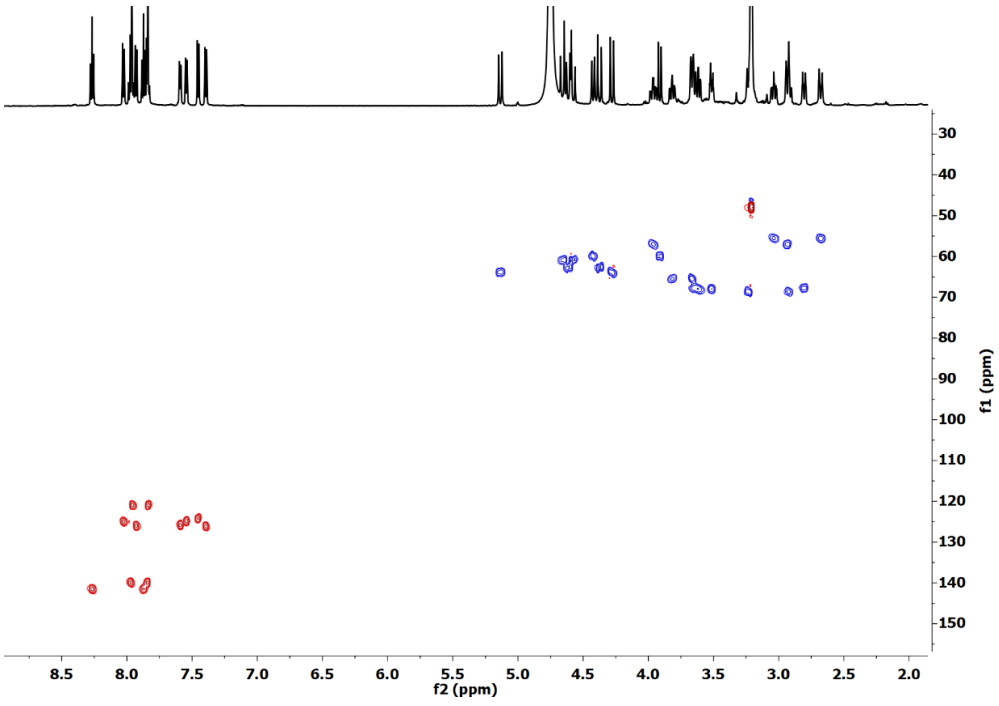

Figure S20. ^{1}H – ^{13}C HSQC spectrum (600 MHz) of [Bi(*bpycropa*)]$^{+}$ (**4**).

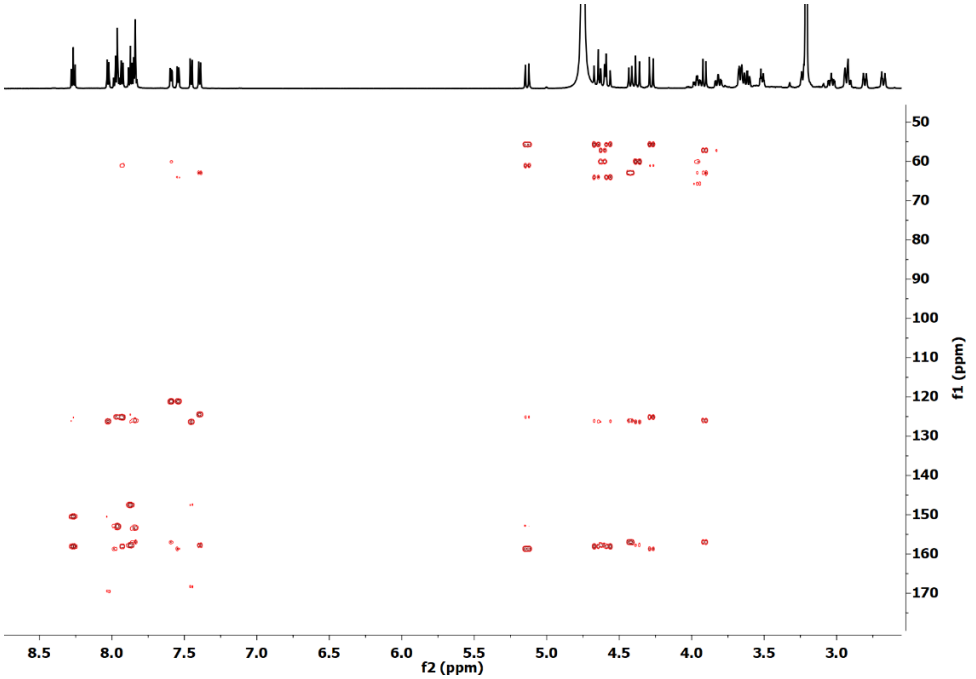

Figure S21. ^{1}H – ^{13}C HMBC spectrum (600 MHz) of [Bi(*bpycropa*)]$^{+}$ (**4**).

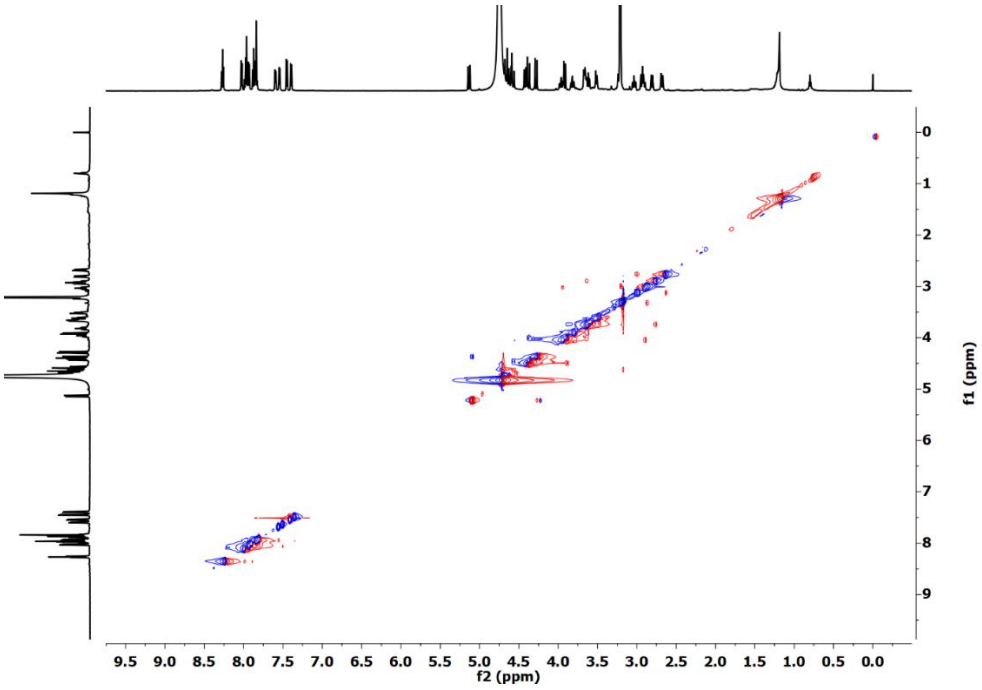

Figure S22. ^{1}H – ^{1}H ROESY spectrum (600 MHz) of [Bi(*bpycropa*)]$^{+}$ (**4**).

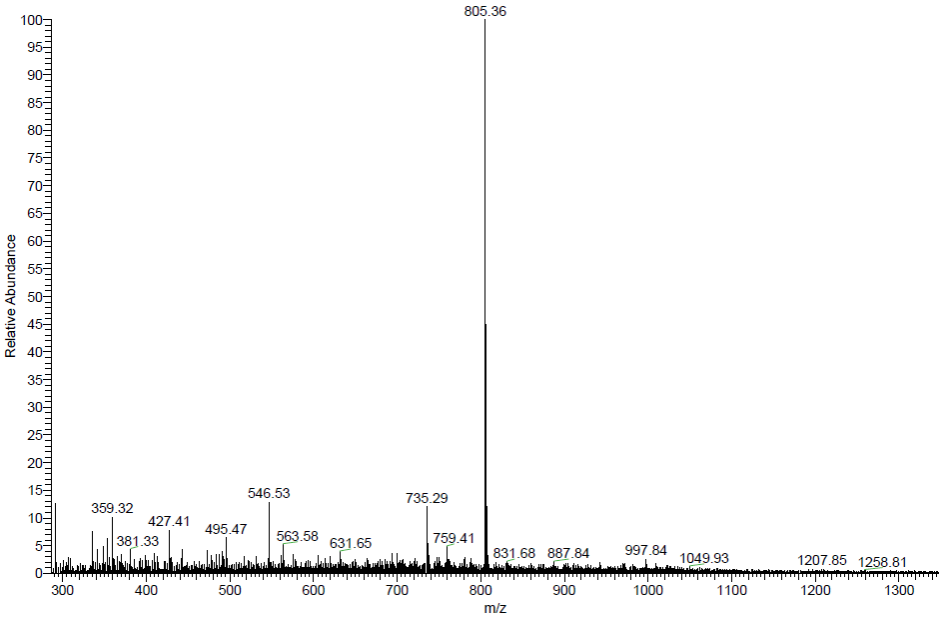

Figure S23. ESI-MS^{+} spectrum of [Bi(*bpycropa*)]$^{+}$.

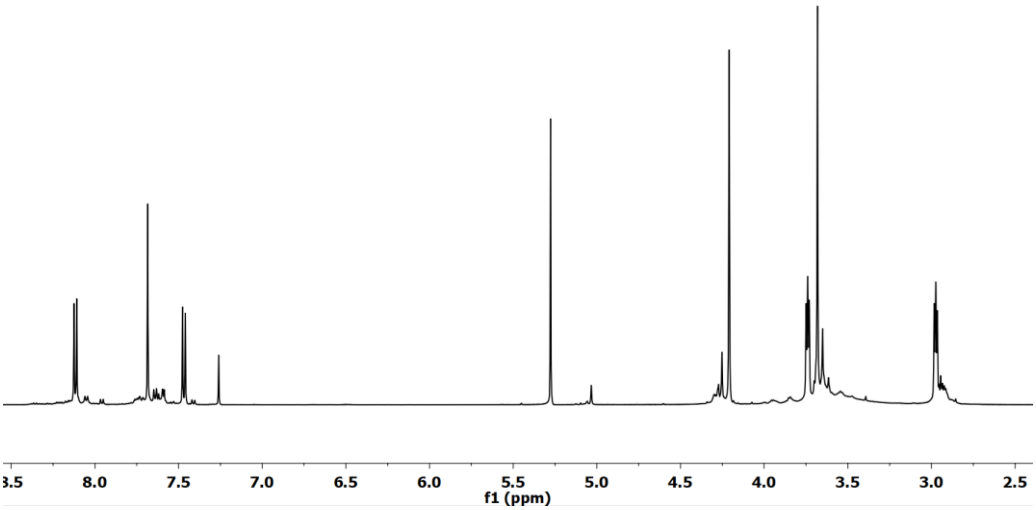

Figure S24. ^{1}H NMR spectrum (500 MHz) of *phencrown* (**B'**).

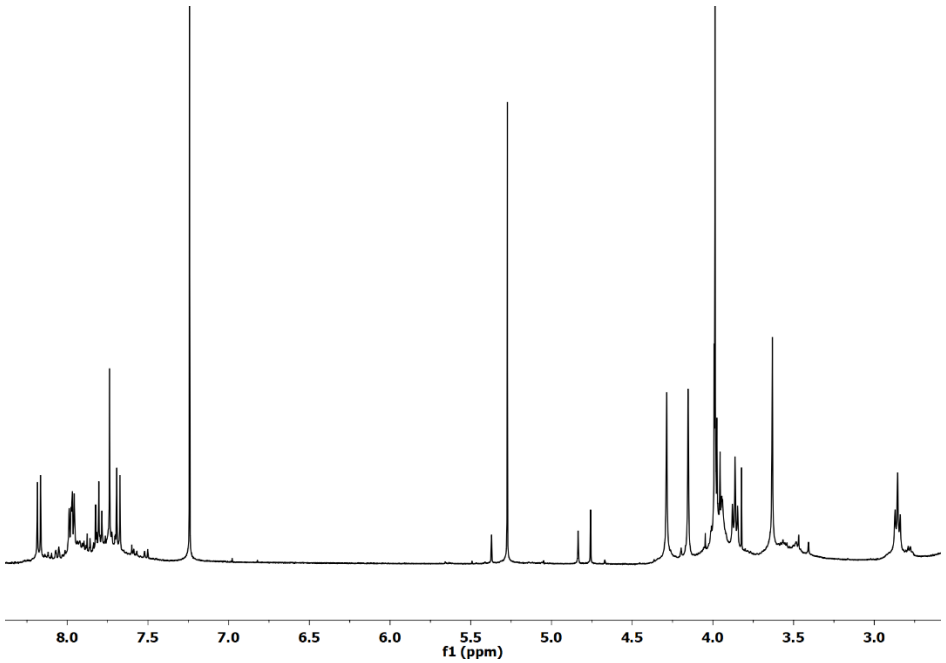

Figure S25. ^{1}H NMR spectrum (500 MHz) of *phencrown-N,N'-dipicolinate methyl ester* (**B'**).

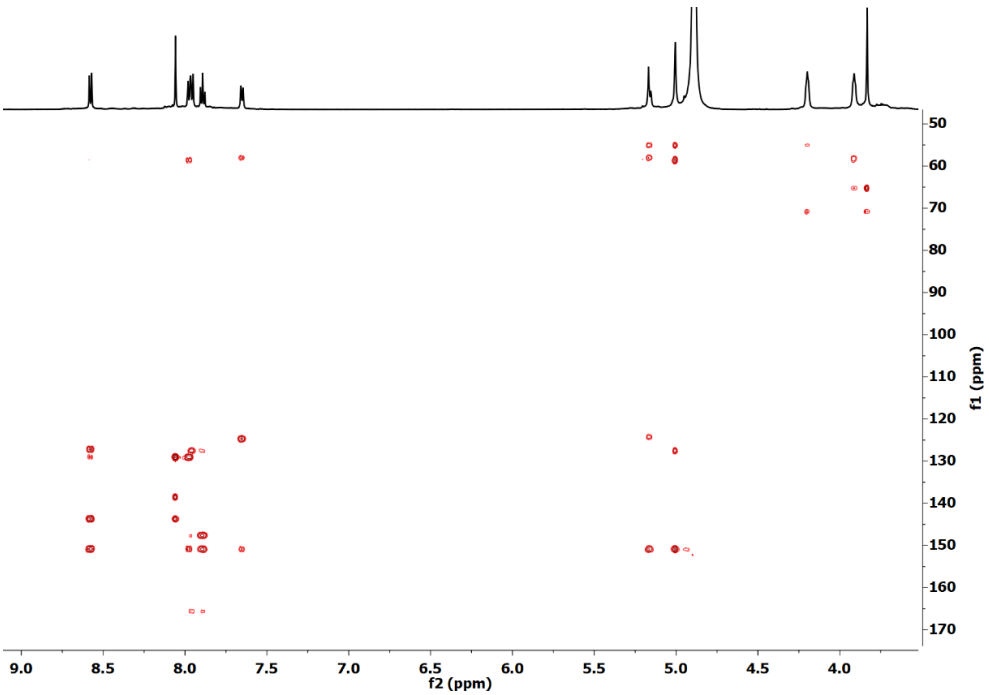

Figure S26. ^{1}H – ^{13}C HMBC spectrum (600 MHz) of *phencropa* (**D'**).

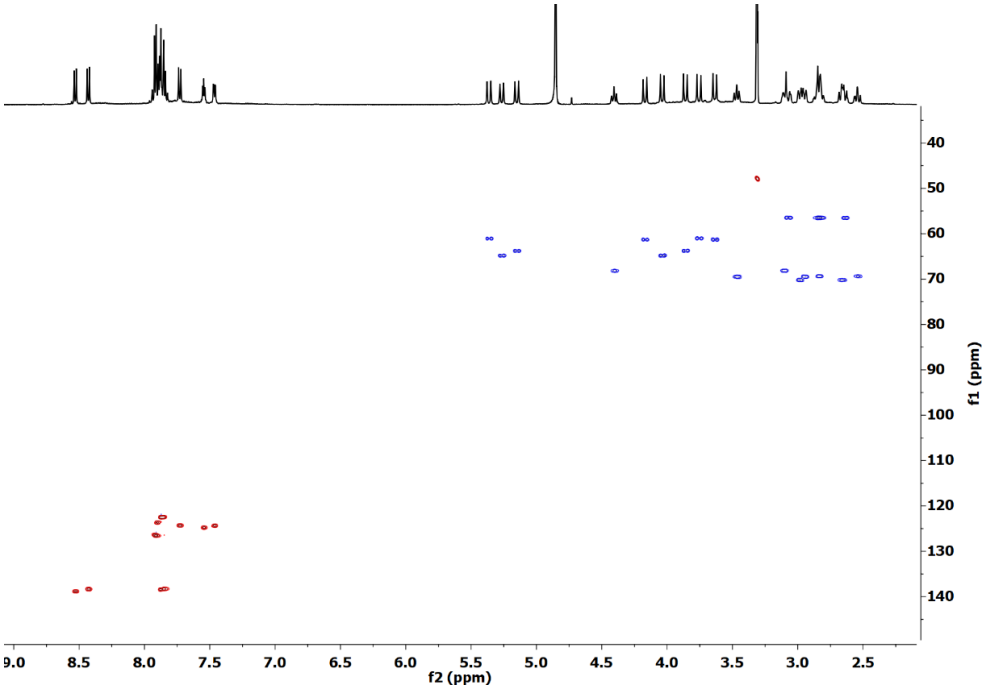

Figure S27. ^{1}H – ^{13}C HSQC spectrum (600 MHz) of [Ba(*phencropa*)] (**5**).

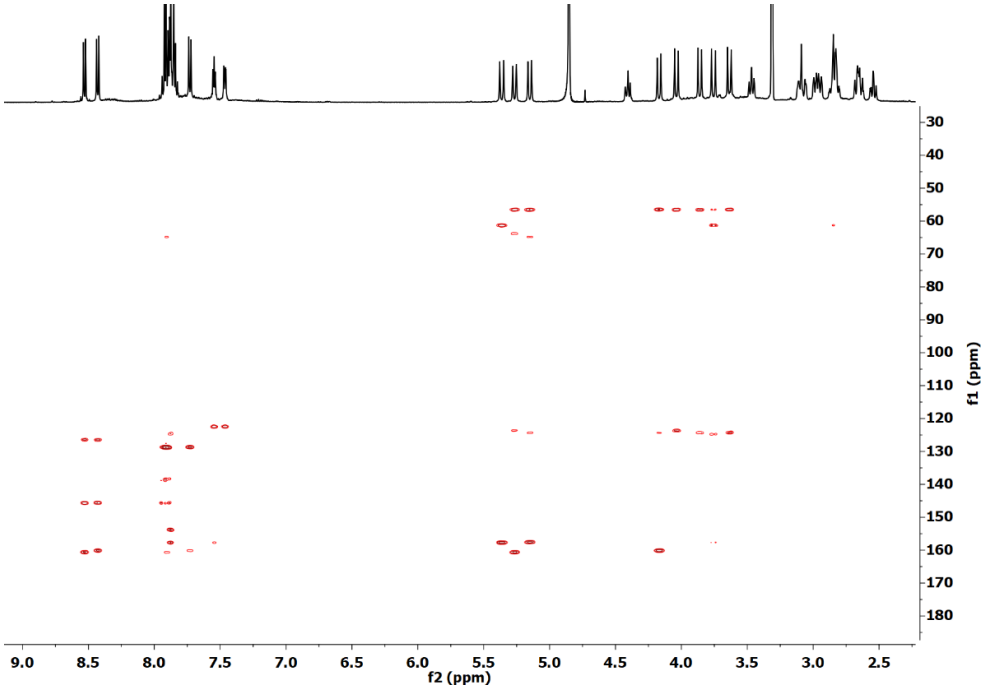

Figure S28. ^{1}H – ^{13}C HMBC spectrum (600 MHz) of [Ba(*phencropa*)] (**5**).

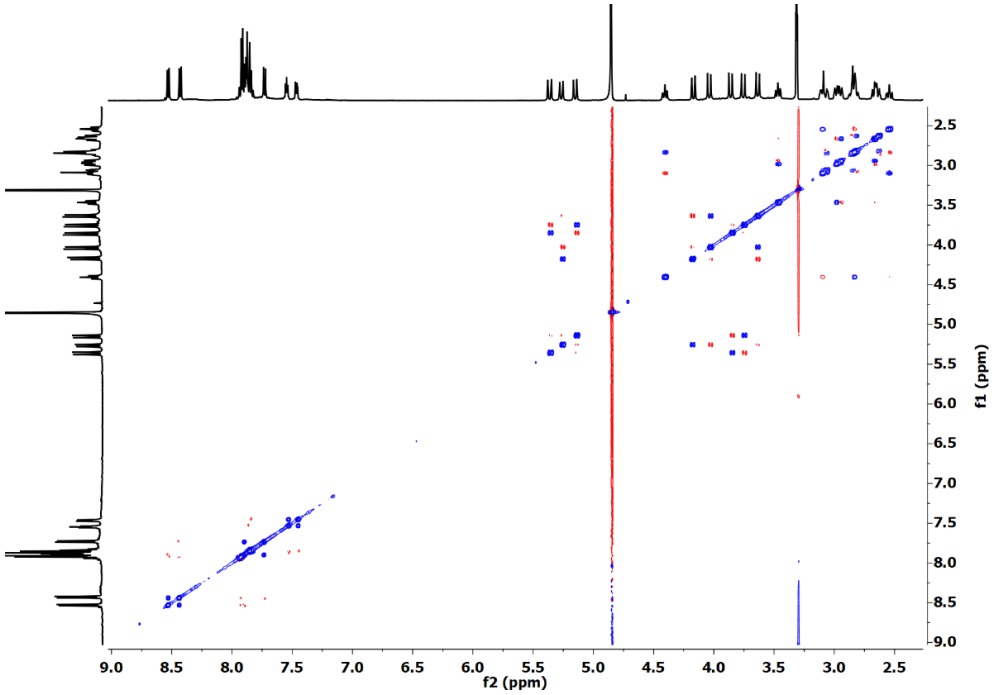

Figure S29. ^{1}H – ^{1}H ROESY spectrum (600 MHz) of [Ba(*phencropa*)] (**5**).

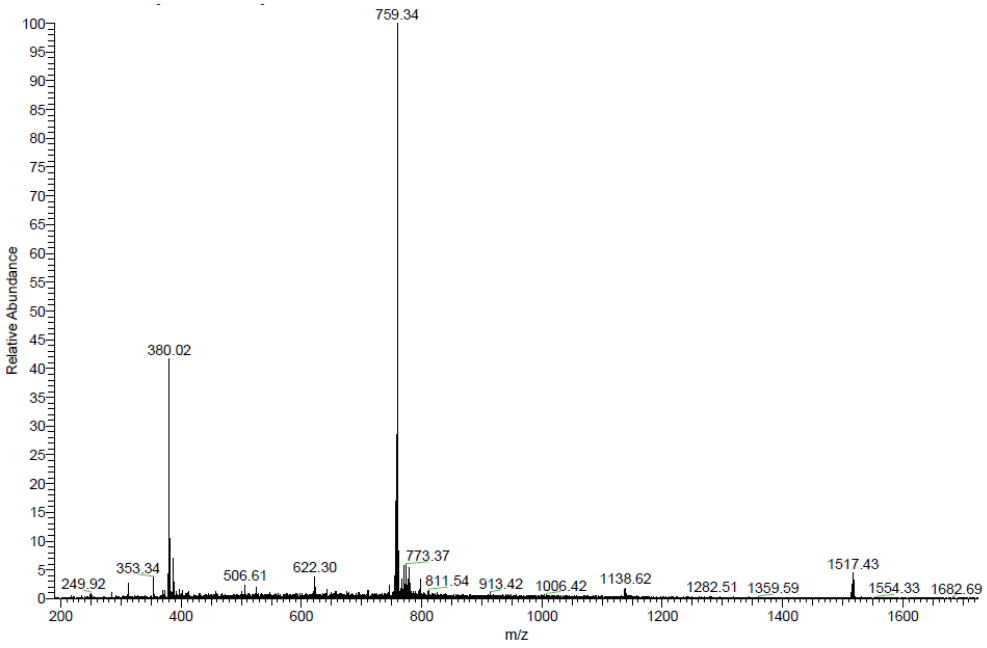

Figure S30. ESI-MS^{+} spectrum of [Ba(*phencropa*)] (**5**).

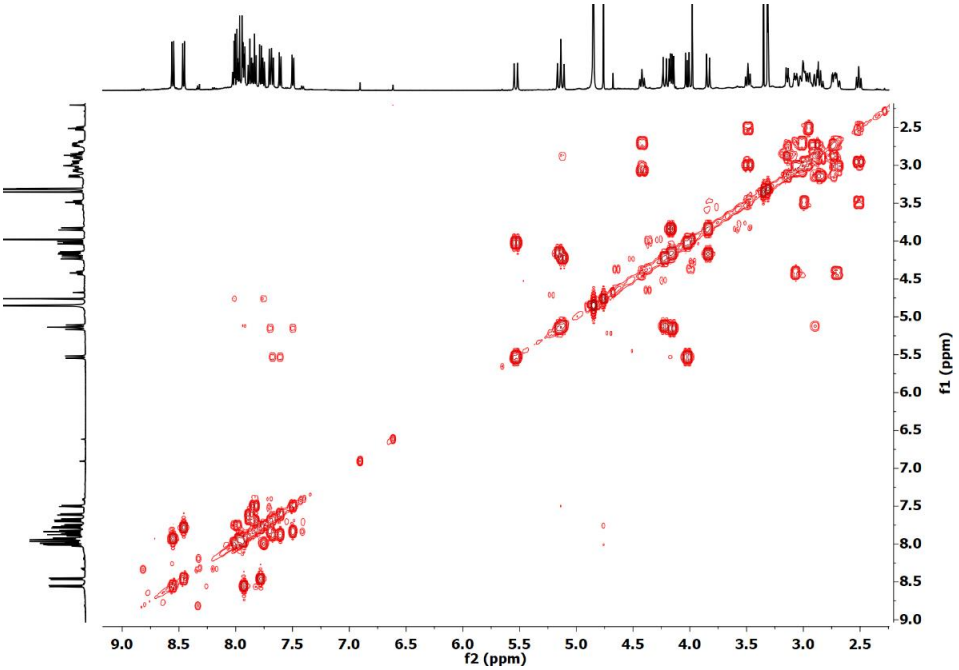

Figure S31. ^{1}H – ^{1}H COSY spectrum (500 MHz) of [Pb(*phencropa*)] (**6**).

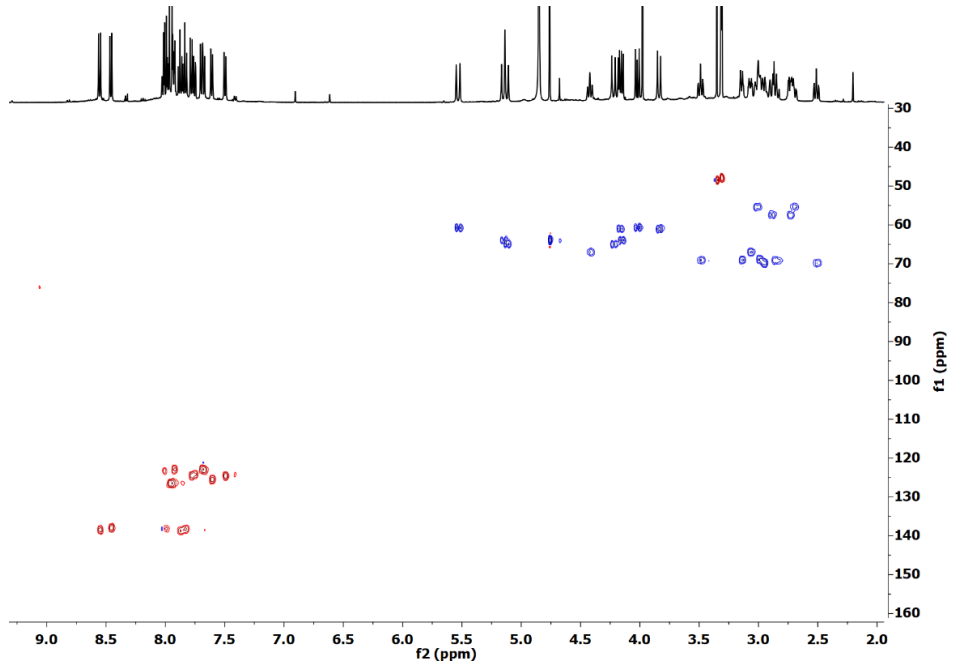

Figure S32. ^{1}H – ^{13}C HSQC spectrum (500 MHz) of [Pb(*phencropa*)] (**6**).

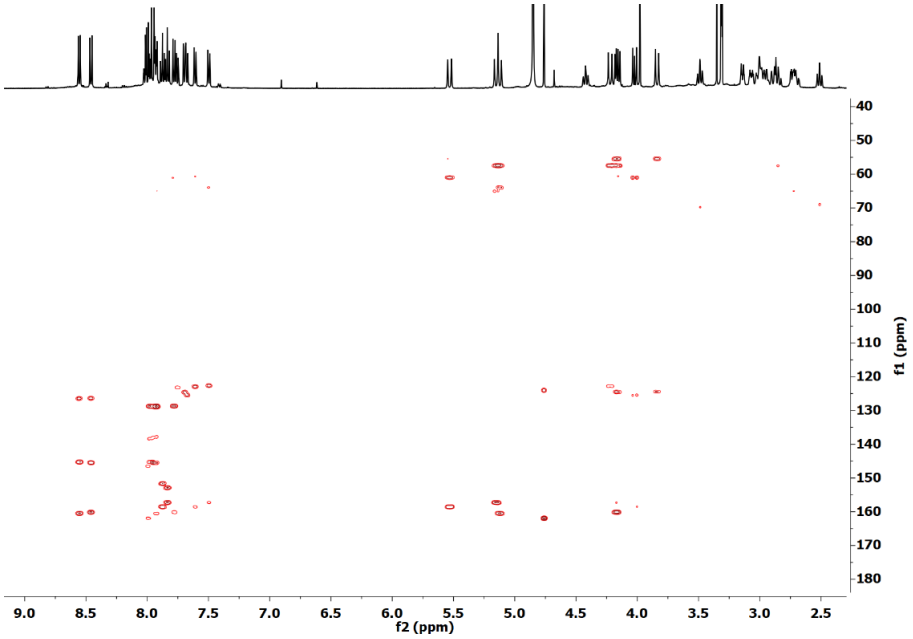

Figure S33. ^{1}H – ^{13}C HMBC spectrum (500 MHz) of [Pb(*phencropa*)] (**6**).

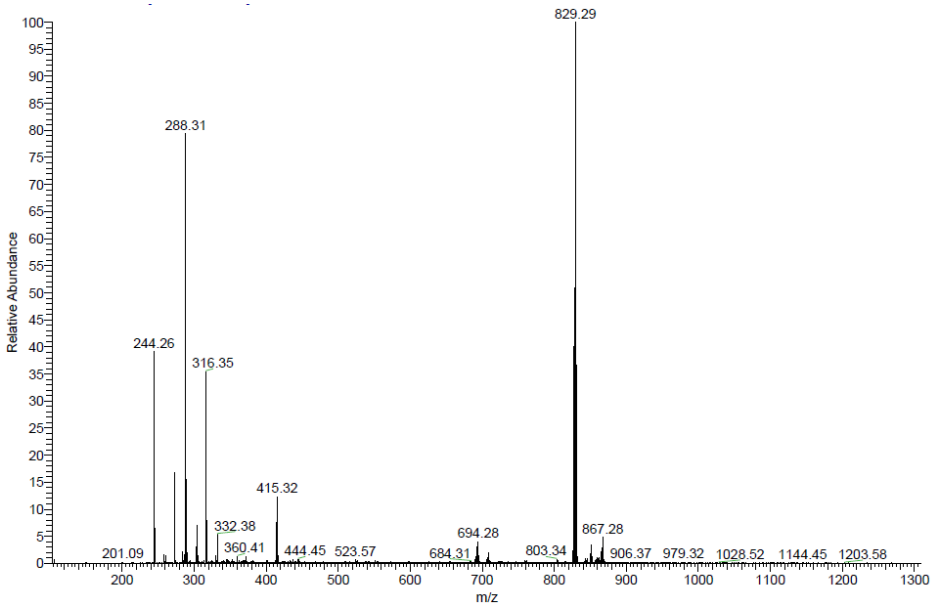

Figure S34. ESI-MS^{+} spectrum of [Pb(*phencropa*)] (**6**).

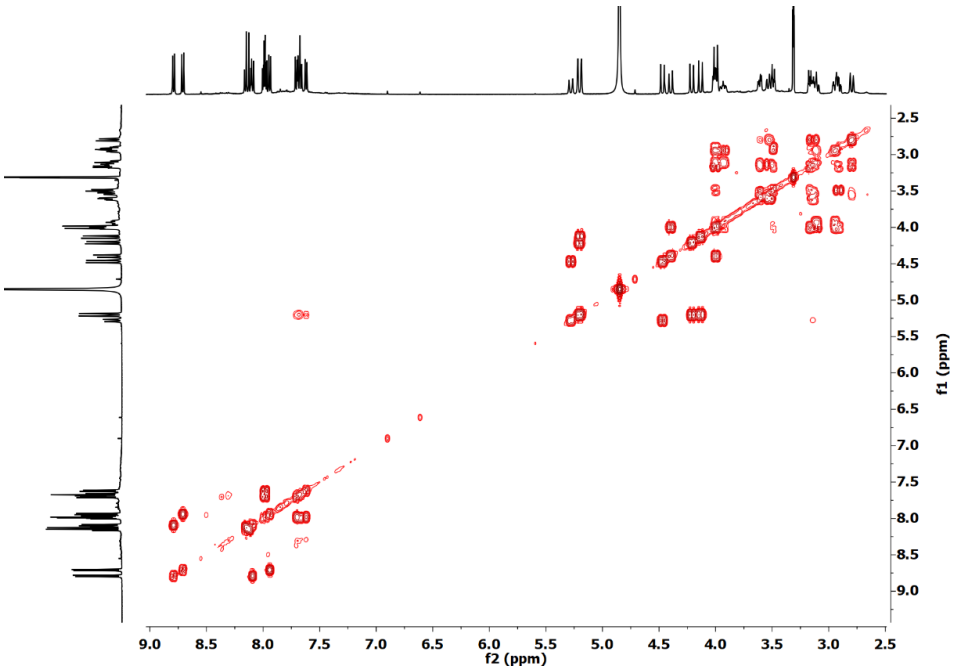

Figure S35. ^{1}H – ^{1}H COSY spectrum (500 MHz) of [La(*phencropa*)]$^{+}$ (**7**).

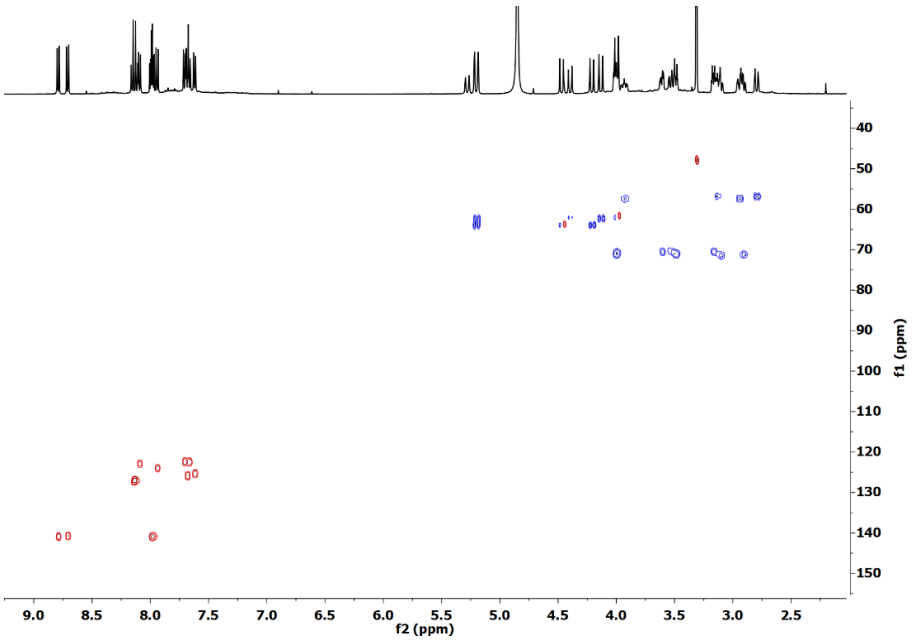

Figure S36. ^{1}H – ^{13}C HSQC spectrum (500 MHz) of [La(*phencropa*)]$^{+}$ (**7**).

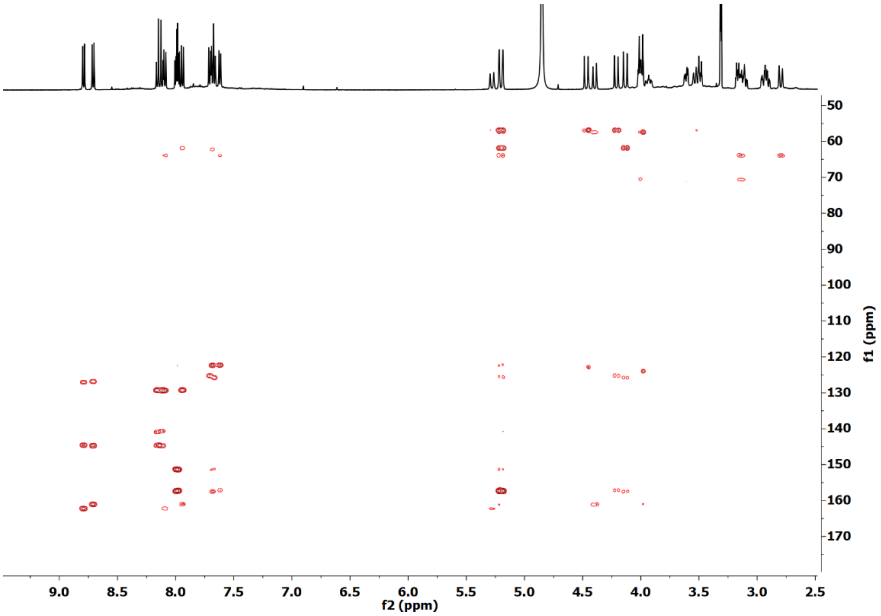

Figure S37. ^{1}H – ^{13}C HMBC spectrum (500 MHz) of [La(*phencropa*)]$^{+}$ (**7**).

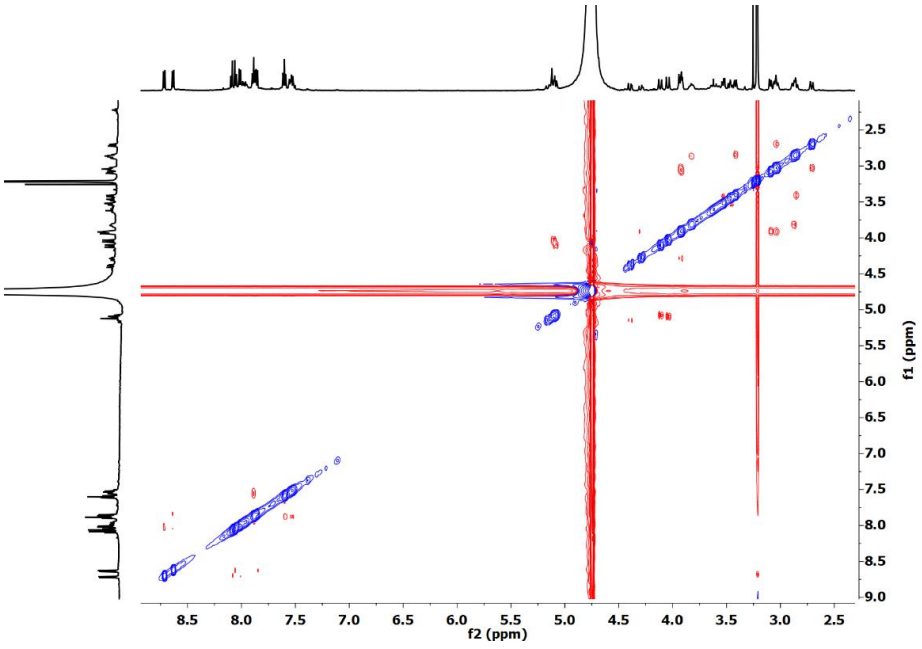

Figure S38. ^{1}H – ^{1}H ROESY spectrum (600 MHz) of [La(*phencropa*)]$^{+}$ (**7**).

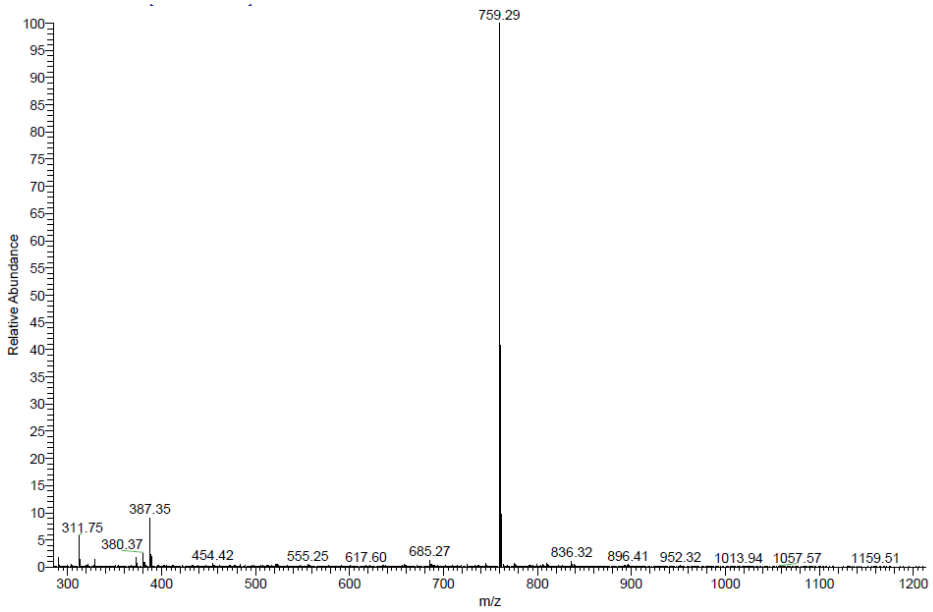

Figure S39. ESI-MS$^+$ spectrum of [La(*phencropa*)]$^+$ (**7**).

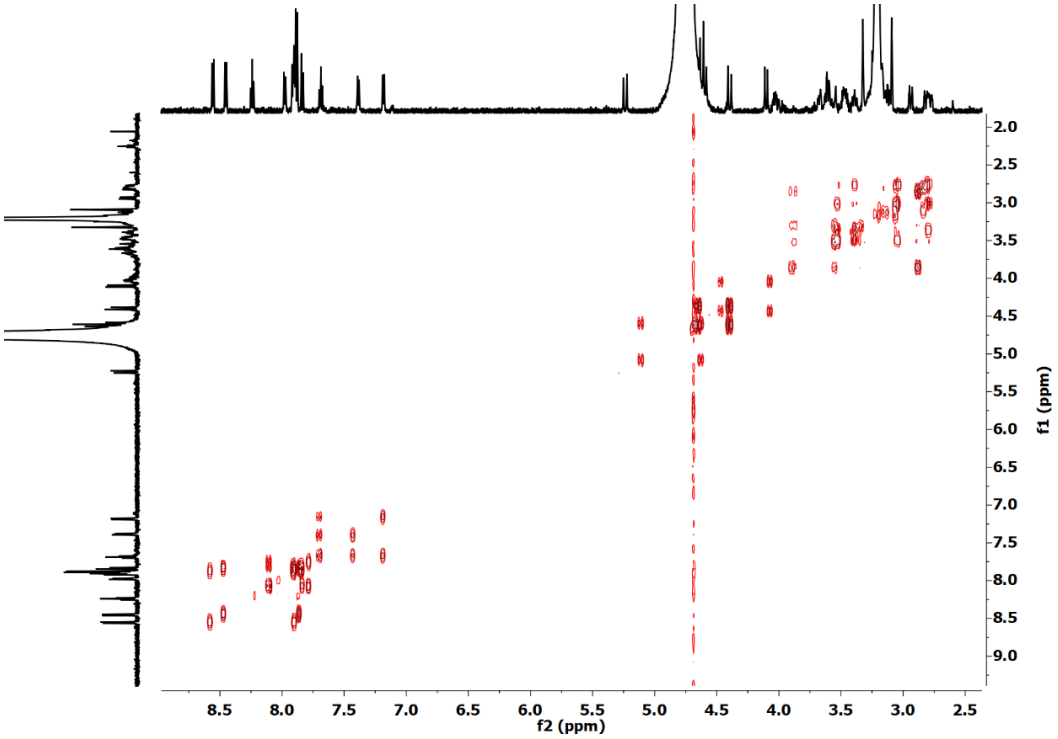

Figure S40. ^{1}H – ^{1}H COSY spectrum (600 MHz) of [Bi(*phencropa*)]$^+$ (**8**).

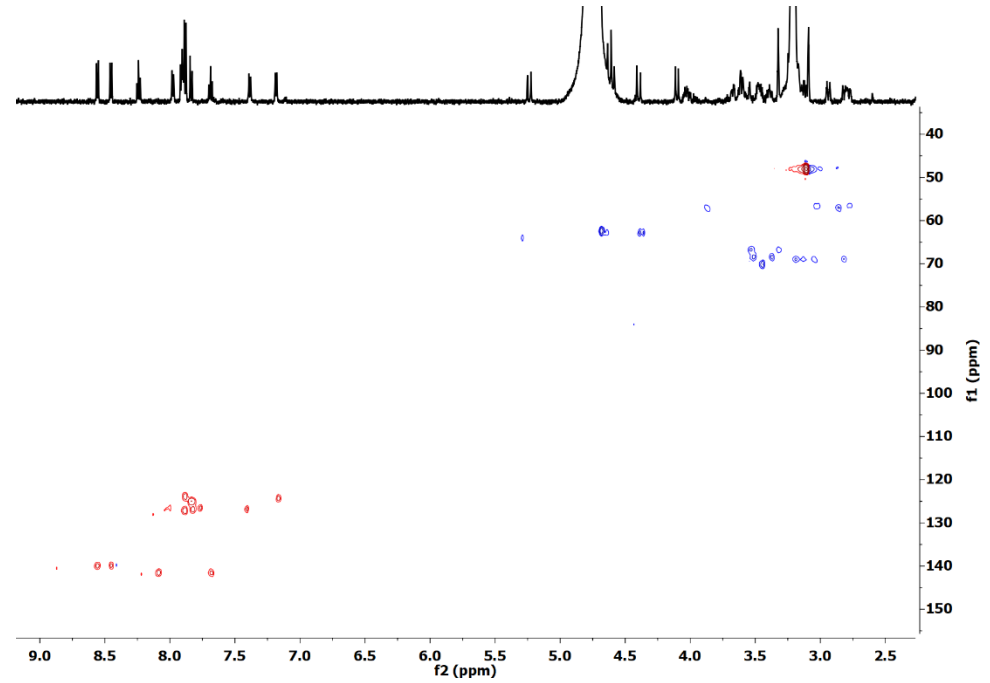

Figure S41. ^{1}H – ^{13}C HSQC spectrum (600 MHz) of [Bi(*phencropa*)]$^{+}$ (**8**).

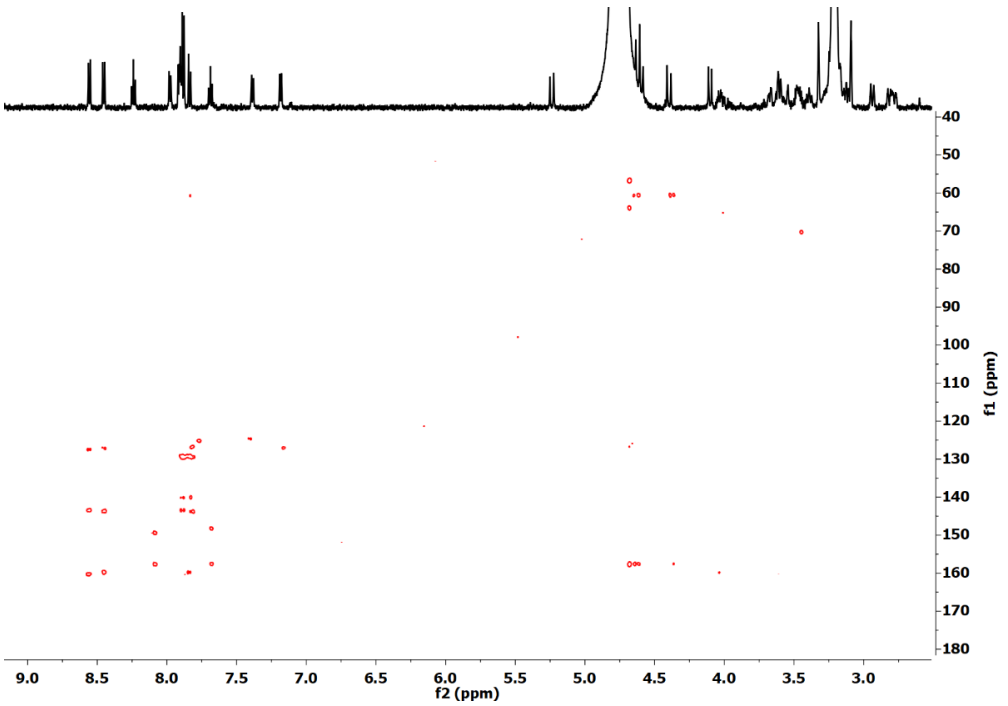

Figure S42. ^{1}H – ^{13}C HMBC spectrum (600 MHz) of [Bi(*phencropa*)]$^{+}$ (**8**).

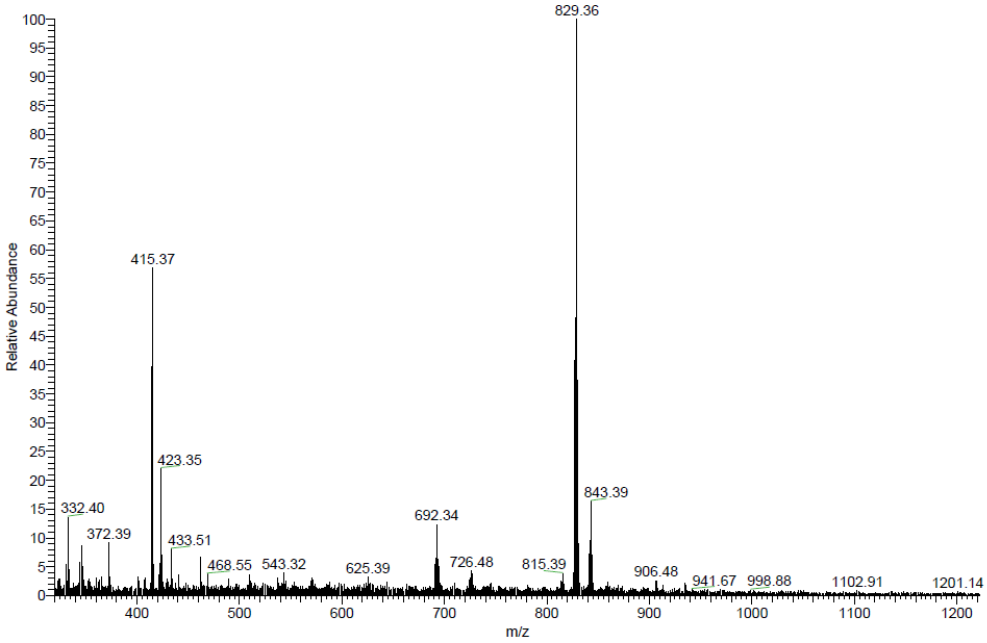

Figure S43. ESI-MS$^+$ spectrum of [Bi(*phencropa*)]$^+$ (**8**).

Acknowledgements

First of all, I would like to thank my supervisor, Prof. Enzo Alessio, for his patience, invaluable advice, and for instilling in me a sense of critical thinking that is essential, yet too often taken for granted, in our field.

I am grateful to Bracco Imaging SpA for the opportunity to work with them, an experience that allowed me to expand my scientific knowledge, skills, and productivity. In particular, I would like to express my sincere thanks to Dr. Mariangela Boccalon and Dr. Nicol Guidolin, exceptional colleagues who consistently supported me and always had my back.

A special thank you goes to Dr. Federica Battistin, who embodies pure logic while remaining deeply empathetic. Her guidance helped me overcome many challenges and grow both scientifically and personally.

My heartfelt gratitude goes to my family, friends and to my boyfriend David, who always supported and trusted me unconditionally, even when they did not fully understand the scientific concepts or the details of my project (and, truthfully, there were moments when I did not either).

I am also deeply thankful to my colleagues, who were a fundamental presence throughout these years. You helped me when I first arrived in the laboratory, and together we shared many meaningful and memorable moments.

Last but not least, I wish to pay a heartfelt tribute to my colleague Marta. Although you have not been here for some time, remembering your passion for science and your out-of-the-box approach gave me strength during moments when I felt I could not continue this project. This work is also for you.

La borsa di dottorato è cofinanziata con risorse dell'Unione europea, NextGeneration EU - Piano Nazionale di Ripresa e Resilienza, Missione 4 – Componente 2 – Investimento 3.3 CUP J92B22001010007.